Lecture Notes in Mechanical Engineering

Holm Altenbach · Xiao-Wei Gao · Stavros Syngellakis · Alexander H.-D. Cheng · Piotr Lampart · Anton Tkachuk *Editors*

Advances in Mechanical and Power Engineering III

Selected Papers from The International Conference on Advanced Mechanical and Power Engineering (CAMPE 2025), October 20–21, 2025, Kharkiv, Ukraine

Springer

Lecture Notes in Mechanical Engineering

Lecture Notes in Mechanical Engineering (LNME) publishes the latest developments in Mechanical Engineering—quickly, informally and with high quality. Original research or contributions reported in proceedings and post-proceedings represents the core of LNME. Volumes published in LNME embrace all aspects, subfields and new challenges of mechanical engineering.

To submit a proposal or request further information, please contact the Springer Editor of your location:

Europe, USA, Africa: Leontina Di Cecco at Leontina.dicecco@springer.com

China: Ella Zhang at ella.zhang@cn.springernature.com

India, Rest of Asia, Australia, New Zealand: Swati Meherishi at swati.meherishi@springer.com

Topics in the series include:

- Engineering Design
- Machinery and Machine Elements
- Mechanical Structures and Stress Analysis
- Automotive Engineering
- Engine Technology
- Aerospace Technology and Astronautics
- Nanotechnology and Microengineering
- Control, Robotics, Mechatronics
- MEMS
- Theoretical and Applied Mechanics
- Dynamical Systems, Control
- Fluid Mechanics
- Engineering Thermodynamics, Heat and Mass Transfer
- Manufacturing Engineering and Smart Manufacturing
- Precision Engineering, Instrumentation, Measurement
- Materials Engineering
- Tribology and Surface Technology

Indexed by SCOPUS, EI Compendex, and INSPEC.

All books published in the series are evaluated by Web of Science for the Conference Proceedings Citation Index (CPCI).

To submit a proposal for a monograph, please check our Springer Tracts in Mechanical Engineering at https://link.springer.com/bookseries/11693.

Holm Altenbach · Xiao-Wei Gao ·
Stavros Syngellakis · Alexander H.-D. Cheng ·
Piotr Lampart · Anton Tkachuk
Editors

Advances in Mechanical and Power Engineering III

Selected Papers from The International Conference on Advanced Mechanical and Power Engineering (CAMPE 2025), October 20–21, 2025, Kharkiv, Ukraine

Springer

Editors
Holm Altenbach
Fakultät für Maschinenbau
Otto-von-Guericke-Universität
Magdeburg, Germany

Xiao-Wei Gao
School of Aeronautics and Astronautics
Dalian University of Technology
Dalian, China

Stavros Syngellakis
School of Engineering
Wessex Institute of Technology
Southampton, UK

Alexander H.-D. Cheng
School of Engineering
University of Mississippi
Oxford, MS, USA

Piotr Lampart
The Szewalski Institute of Fluid-Flow
Machinery, Polish Academy of Science
Gdańsk, Poland

Anton Tkachuk
Department of Engineering and Physics
Karlstad University
Karlstad, Sweden

ISSN 2195-4356 ISSN 2195-4364 (electronic)
Lecture Notes in Mechanical Engineering
ISBN 978-3-032-16380-6 ISBN 978-3-032-16381-3 (eBook)
https://doi.org/10.1007/978-3-032-16381-3

This Springer imprint is published by the registered company Springer Nature Switzerland AG
The registered company address is: Gewerbestrasse 11, 6330 Cham, Switzerland

Preface

This volume of Lecture Notes in Mechanical Engineering gathers selected papers presented at the 16th International Conference on Advanced Mechanical and Power Engineering (CAMPE-2025), held online from Kharkiv, Ukraine, on October 20–21, 2025. Between 1972 and 2025, XXIII CAMPE Editions were carried out. The first 7 conferences did not include international authors (1972–1993), and the other 16 conferences held in 1994–2025 were international events. CAMPE-2025 was organized by the National Academy of Sciences of Ukraine, the Anatolii Pidhornyi Institute of Power Machines and Systems of the National Academy of Sciences of Ukraine, and the Engineering Academy of Ukraine.

The aim of the conference was to present the latest achievements in mechanical and power engineering and to provide an opportunity for discussion and exchange of views and opinions. The conference covered the following topics:

Development and Improvement of Numerical Methods of Calculation of Fluid Flow and/or Heat Transfer.
Numerical Analysis of Fluid Flow and/or Heat Transfer in Power Equipment.
Identification and Optimization of Fluid Flow and/or Heat Transfer in Power Equipment
Profiling of Flow Parts of Turbomachines.
Development of Thermal Circuits and Improvement of Thermodynamic Characteristics of Power Equipment.
Efficient Fuel Combustion.
Renewable Energy Sources.
Resource-Saving and Energy Efficient Technologies.
Energy Storage.
Environmental Safety Issues of Power Engineering.
Hydrogen Technologies.
Theoretical and Applied Mechanics.
Mechanical Structures and Stress Analysis.
Engineering Design.
Materials Engineering.
Nanotechnology and Microengineering.
Methods and Technologies for Additive Manufacturing.
Engine Technology.
Aerospace Technology and Astronautics.

The book “Advances in Mechanical and Power Engineering” has been organized in three parts, according to the main topic covered by the respective contributions:

1. Fluid Mechanics and Heat Transfer in Power Engineering.
2. Energy Saving Technologies and Environmental Safety.
3. Dynamics and Strength of Power Equipment.

The first part "Fluid Mechanics and Heat Transfer in Power Engineering" covers recent developments of advanced computational and analytical methods for applications in mechanical engineering, turbomachinery, heat and power engineering. It reports on both theoretical and experimental research, and the use of modern computer technology and effective mathematical methods for the analysis of fluid mechanics and heat transfer problems, as well as for the identification and optimization of fluid flow. It highlights new strategies for implementing intelligent solutions for the purpose of improving compressor and turbine stages and effective methods for profiling flow parts of turbomachines.

The second part "Energy Saving Technologies and Environmental Safety" presents some comparative analysis of computational methods adopted for renovation projects in mechanical engineering, such as those relating to the development of thermal circuits, and the improvement of thermodynamic characteristics of power equipment. The works belonging to this part are also devoted to methods for ensuring ecological and human safety and for reducing material costs and environmental pollution. New advancements in energy saving technologies, renewable energy sources, topical issues in environmental safety, resource-saving, and hydrogen technologies are presented.

The third part "Dynamics and Strength of Power Equipment" reports on recent developments in mathematical models and methods to simulating the dynamics characteristics and durability of machines, and engineering designs applications. It describes advanced mathematical models for simulating the behavior of power equipment under static and dynamic loads and for making qualitative predictions on reliability and durability. It also covers topics related to stress-strain state, stability, structure optimization, and dynamic processes of mechanical systems and objects. It shows applications in nanotechnology, microengineering, engine and aerospace technologies, astronautics, materials engineering, and additive manufacturing.

CAMPE-2025 program comprises an impressive range of topics addressing important issues relating to energy production and its effects on the environment. Solutions that are proposed would enhance the performance of power engineering systems for the benefit of society. There are high-quality and innovative contributions on modelling and experimentation in material science, structural engineering as well as heat and mass transfer.

The Program Committee and the Organizing Committee of the conference express their sincere gratitude to all our international partners, friends and colleagues who stand with Ukraine in these difficult times. Your support—humanitarian, institutional, scientific—is invaluable.

This year we had a record number of participants. CAMPE-2025 received 44 contributions. After a two-stage single-blind review, the Program Committee accepted 35 papers written by 114 authors from 16 countries around the world (Austria, Algeria, Bulgaria, Brazil, Great Britain, India, China, Lithuania, Mexico, Moldova, Netherlands, Germany, New Zealand, Poland, Ukraine, Sweden). Each paper was peer-reviewed by at least three members of the Program Committee, along with invited external reviewers.

Each submission was evaluated for originality, scientific significance, research methodology, accuracy of the research content, discussion of the obtained results, validity of the conclusions, completeness, clarity of presentation, and overall readability. The originality of the submissions was checked by Ithenticate plagiarism software.

We appreciate the partnership with Springer Nature, Ithenticate, and Meteor Team for their essential support during the preparation of CAMPE-2025. We would like to thank the members of the International Program Committee for their hard work during the review process. Their involvement and commitment were crucial for both the success of CAMPE-2025 and for the realization of this book.

Our special thanks to Prof. Svitlana Alyokhina (Fachhochschule Technikum Wien Vienna, Austria), Prof. Alexander Steinwolf, (AST Consulting Ltd., Auckland, New Zealand), Prof. Carlos Gustavo Martínez Gomez (Faculty of Mechanical and Electrical Engineering, Autonomous University of Nuevo Leon, Monterrey 66455, Mexico).

We sincerely appreciate the youngest reviewer and editor: Dr.-Ing., habil. Anton Tkachuk (Department of Engineering and Physics Karlstad University Karlstad, Sweden).

Thank you very much to the CAMPE Team. Their outstanding involvement and hard work were crucial to the success of the conference.

October 2025

Holm Altenbach
Alexander H.-D. Cheng
Xiao-Wei Gao
Piotr Lampart
Stavros Syngellakis
Anton Tkachuk

Organization

Honorary Chairs

Olexandr Kyrylenko	National Academy of Sciences of Ukraine, Kyiv, Ukraine
Victor Subotin	Joint Stock Company «Ukrainian Energy Machines», Kharkiv, Ukraine
Igor Kravchenko	SE Ivchenko-Progress, Zaporizhzhia, Ukraine
Anatolii Boiko	National Technical University «Kharkiv Polytechnic Institute», Kharkiv, Ukraine
Oleksandr Shubenko	Anatolii Pidhornyi Institute of Power Machines and Systems of the National Academy of Sciences of Ukraine, Kharkiv, Ukraine
Anatolii Tarelin	Anatolii Pidhornyi Institute of Power Machines and Systems of the National Academy of Sciences of Ukraine, Kharkiv, Ukraine

General Chair

Andrii Rusanov	Anatolii Pidhornyi Institute of Power Machines and Systems of the National Academy of Sciences of Ukraine, Kharkiv, Ukraine

Co-chair

Andrii Kostikov	Anatolii Pidhornyi Institute of Power Machines and Systems of the National Academy of Sciences of Ukraine, Kharkiv, Ukraine

Steering Committee

Svitlana Alyokhina	Fachhochschule Technikum Wien Vienna, Austria
Vitaliy Homan	Anatolii Pidhornyi Institute of Power Machines and Systems of the National Academy of Sciences of Ukraine, Kharkiv, Ukraine

Denis Kriutchenko	Anatolii Pidhornyi Institute of Power Machines and Systems of the National Academy of Sciences of Ukraine, Kharkiv, Ukraine
Sergii Misiura	Anatolii Pidhornyi Institute of Power Machines and Systems of the National Academy of Sciences of Ukraine, Kharkiv, Ukraine
Tetiana Protasova	Anatolii Pidhornyi Institute of Power Machines and Systems of the National Academy of Sciences of Ukraine, Kharkiv, Ukraine
Andrii Shpak	Anatolii Pidhornyi Institute of Power Machines and Systems of the National Academy of Sciences of Ukraine, Kharkiv, Ukraine
Natalia Smetankina	Anatolii Pidhornyi Institute of Power Machines and Systems of the National Academy of Sciences of Ukraine, Kharkiv, Ukraine
Anna Vorontsova	Anatolii Pidhornyi Institute of Power Machines and Systems of the National Academy of Sciences of Ukraine, Kharkiv, Ukraine
Mykola Zipunnikov	Anatolii Pidhornyi Institute of Power Machines and Systems of the National Academy of Sciences of Ukraine, Kharkiv, Ukraine

Program Committee

Imran Ali	Jamia Millia Islamia, New Delhi, India
M. H. Ferri Aliabadi	Imperial College London, London, UK
Almeida Júnior	José Humberto Santos Queen's University Belfast UK
Holm Altenbach	Otto-von-Guericke Magdeburg University, Magdeburg, Germany
Svitlana Alyokhina	Fachhochschule Technikum Wien Vienna, Austria
Ali Abdulateef Kareem Alzubadi	Physics department, College of Science, Baghdad University, Iraq
Marco Amabili	McGill University, Montreal, QC, Canada
Igor Andrianov	Rheinisch-Westfälische Technische Hochschule Aachen, Aachen, Germany
Andrii Avramenko	Anatolii Pidhornyi Institute of Power Machines and Systems of the National Academy of Sciences of Ukraine, Kharkiv, Ukraine
Kostiantyn Avramov	Anatolii Pidhornyi Institute of Power Machines and Systems of the National Academy of Sciences of Ukraine, Kharkiv, Ukraine
Jan Awrejcewicz	Lodz University of Technology, Lodz, Poland

Jean-Michel Bergheau	École Centrale de Lyon, Ecully, France
Omar El Bounagui	Université Mohammed V de Rabat Faculté des Sciences in Rabat, Morocco
Ivan Breslavsky	McGill University, Montreal, Quebec, Canada
Weiqiu Chen	State Key Lab of CAD&CG, Zhejiang University, Hangzhou, China
Alexander Cheng	School of Engineering, University of Mississippi, Oxford, USA
Giuseppe Ciaburro	Università degli Studi della Campania Luigi Vanvitelli, Naples, Italy
Olga Chernousenko	National Technical University of Ukraine «Igor Sikorsky Kyiv Polytechnic Institute»
Neelam Choudhary	Bennett University, Greater Noida, India
Dmitriy Dikin	Temple University, Philadelphia, USA
Ney Augusto Dumont	Pontifical Catholic University of Rio de Janeiro, Brazil
Alaa Abd El-Bary	Arab Academy for Science, Technology and Maritime Transport, Alexandria, Egypt
Igor Emri	Faculty of Mechanical Engineering, University of Ljubljana, Slovenia
Hamid Ez-Zahraouy	Université Mohammed V de Rabat Faculté des Sciences in Rabat, Morocco
Chia-Ming Fan	National Taiwan Ocean University, Keelung, Taiwan
Alexander Fidlin	Karlsruhe Institute of Technology, Germany
Andreas Fischer	Technische Universität Dresden, Dresden, Germany
Xiao-Wei Gao	School of Aeronautics and Astronautics, Dalian University of Technology, Dalian, China
Oleg Gendelman	Israel Institute of Technology, Haifa, Israel
Gillich Gilbert-Rainer	Babeş-Bolyai University, Cluj-Napoca, Romania
Luís Godinho	University of Coimbra, Portugal
Oleksandr Grygorenko	Taras Shevchenko National University of Kyiv, Ukraine
Wei Han	International Center of Future Science, Jilin University, Changchun, China
Shoukry Hassan	University of Bahrain, Sakhir, Bahrain
Xingxing Huang	S.C.I. Energy, Zurich, Switzerland
Ahmed Kadhim Hussein	University of Babylon, Babylon, Iraq
Vitalii Ivanov	Sumy State University, Sumy, Ukraine
Mohammed Kaabar	Washington State University, Pullman, WA, USA
Kirill Kabalyk	Lodz University of Technology, Lodz, Poland
Andreas Karageorghis	University of Cyprus, Cyprus

Dariusz Kardaś	Institute of Fluid-Flow Machinery Polish Academy of Sciences, Gdansk, Poland
John Katsikadelis	National Technical University of Athens, Greece
Piotr Klonowicz	Robert Szewalski Institute of Fluid-Flow Machinery of the Polish Academy of Sciences, Gdansk, Poland
Andrii Kondratiev	O.M. Beketov National University of Urban Economy, Kharkiv, Ukraine
Endre Kovács	University of Miskolc, Department of Physics and Electrical Engineering, Miskolc, Hungary
Oleg Kravchenko	Anatolii Pidhornyi Institute of Power Machines and Systems of the National Academy of Sciences of Ukraine, Kharkiv, Ukraine
Leopold Kruszka	Wojskowa Akademia Techniczna, Warsaw, Poland
Volodymyr Kvasnikov	National Aviation University, Kyiv, Ukraine
Alaaeddine Lahbas	Université Mohammed V de Rabat Faculté des Sciences in Rabat, Morocco
Piotr Lampart	Robert Szewalski Institute of fluid-flow machinery of Polish Academy of Sciences, Gdańsk, Poland
Oleksiy Larin	National Technical University «Kharkiv Polytechnic Institute», Kharkiv, Ukraine
Mathias Legrand	McGill University, Montreal, Quebec, Canada
Vitor Leitao	Instituto Superior Técnico, Lisbon, Portugal
Edson Denner Leonel, University of São Paulo, Brazil	Edson Denner Leonel, University of São Paulo, Brazil
Yevgen Levchenko	Joint Stock Company «Ukrainian Energy Machines», Kharkiv, Ukraine
Mykhaylo Lototskyy	University of the Western Cape, Bellville, South Africa
Martin Luxa	Institute of Thermomechanics Academy of Sciences of the Czech Republic, Praha, Czech Republic
Gennadiy Lvov	National Technical University «Kharkiv Polytechnic Institute», Kharkiv, Ukraine
Kyrylo Maksymenko-Sheiko	Anatolii Pidhornyi Institute of Power Machines and Systems of the National Academy of Sciences of Ukraine, Kharkiv, Ukraine
José-Antonio Marmolejo-Saucedo	Universidad Panamericana, Ciudad de Mexico, Mexico
Gennadii Martynenko	National Technical University «Kharkiv Polytechnic Institute», Kharkiv, Ukraine
Oleksandr Menshykov	University of Aberdeen, Aberdeen, UK

Minavar Mir-Salim-Zada	Institute of Mathematics and Mechanics Azerbaijan National Academy of Sciences, Baku, Azerbaijan
Francisco Monticeli	Department of Aeronautical Engineering, Technological Institute of Aeronautics (ITA), São José dos Campos, Brazil
Darkhan Myrzaliyev	M. Auezov South Kazakhstan University, Shymkent, Kazakhstan
Jose Fernando da Costa Oliveira	University of Porto, Porto, Portugal
Ernian Pan	National Yang Ming Chiao Tung University, Hsinchu, Taiwan
Chitaranjan Pany	Vikram Sarabhai Space Centre, Trivandrum, India
Anatoliy Pavlenko	Kielce University of Technology, Kielce, Poland
Dimitrios Pavlou	University of Stavanger, Norway
Francesco Pellicano	University of Modena and Reggio Emilia, Modena, Italy
Evgeny Petrov	University of Sussex, Brighton, UK
Valery Pilipchuk	Wayne State University, Detroit, USA
Christophe Pierre	Stevens Institute of Technology, Hoboken, USA
Ján Piteľ	Technical University of Kosice, Slovakia
Sergiy Plankovskyy	O.M. Beketov National University of Urban Economy, Kharkiv, Ukraine
Viktor Popov	Ascend Technologies Limited, Eastleigh, UK
Robertas Poškas	Lithuanian Energy Institute, Kaunas, Lithuania
Jure Ravnik	University of Maribor, Slovenia
Tetiana Romanova	University of Leeds, Maurice Keyworth Building, Leeds, LS2 9JT, UK
Božidar Šarler	Institute of Metals and Technology Ljubljana, Ljubljana, Slovenia
David Šimurda	Institute of Thermomechanics of the Academy of Sciences of the Czech Republic, Prague, Czech Republic
Vladimir Sladek	Institute of Construction and Architecture, Slovak Academy of Sciences, Bratislava, Slovak Republic
Stavros Syngellakis	Wessex Institute of Technology, Southampton, UK
Natalia Smetankina	Anatolii Pidhornyi Institute of Power Machines and Systems of the National Academy of Sciences of Ukraine, Kharkiv, Ukraine
Victor Solovey	Anatolii Pidhornyi Institute of Power Machines and Systems of the National Academy of Sciences of Ukraine, Kharkiv, Ukraine

Yurii Stoyan	Anatolii Pidhornyi Institute of Power Machines and Systems of the National Academy of Sciences of Ukraine, Kharkiv, Ukraine
Elena Strelnikova	Anatolii Pidhornyi Institute of Power Machines and Systems of the National Academy of Sciences of Ukraine, Kharkiv, Ukraine
Matteo Strozzi	Department of Sciences and Methods for Engineering, University of Modena and Reggio Emilia, Italy
Ulanbator Suleimenov	M. Auezov South Kazakhstan University, Shymkent, Kazakhstan
Antonio Tadeu	University of Coimbra, Portugal
Najim Tahiri	Université Mohammed V de Rabat Faculté des Sciences in Rabat, Morocco
Anton Tkachuk	Department of Engineering and Physics, Karlstad University, 658 88, Karlstad, Sweden
Amit Kumar Verma	Indian Institute of Technology Patna, Patna, India
Jerzy Warminski	Lublin University of Technology, Lublin, Poland
Alexandre Wahrhaftig	Universidade Federal da Bahia, Salvador, Brazil
Łukasz Witanowski	Robert Szewalski Institute of Fluid-Flow Machinery of the Polish Academy of Sciences, Gdansk, Poland
Luiz Wrobel	Brunel University London, Uxbridge, UK
Ihor Yanchevskii	National Technical University of Ukraine «Igor Sikorsky Kyiv Polytechnic Institute»
Chuanzeng Zhang	Universität Siegen, Siegen, Germany
Krzysztof Kamil Zur	Bialystok University of Technology, Bialystok, Poland

Contents

Fluid Mechanics and Heat Transfer in Power Engineering

In-Phase Self-Excited Vibrations of Fan Blades

Yuriy Bykov[1](✉), Lyubov Kolodyazhna[1], Mykola Kostin[2], Oleksii Petrov[2], and Romuald Rządkowski[3]

[1] Anatolii Pidhornyi Institute of Power Machines and Systems of the National Academy of Sciences of Ukraine, 2/10 Komunalnykiv Street, Kharkiv 61046, Ukraine
yubykoff@gmail.com
[2] SE Ivchenko-Progress, 2 Ivanova Street, Zaporizhzhia 69068, Ukraine
[3] Robert Szewalski Institute of Fluid-Flow Machinery of the Polish Academy of Sciences, 14 Fiszera Steet, Gdansk, Poland

Abstract. In modern aviation, gas turbine engines are the main energy source, and their gas-dynamic stability is one of the prerequisites for the robustness, operational lifetime and safety of the aircraft as a whole. Gas turbine engine fans, due to the absence of a bandage, long blades, and wide chord width, are most susceptible to vibrations caused by interaction with the air flow. This paper presents the results of numerical simulation of blade aeroelasticity of aircraft engine fan in off-design mode. The equations of motion of unsteady fluid flow were integrated using the ANSYS Fluent software package, simulation of motion of the blades, as well as two-way coupling between the equations, was implemented in additional software to speed up the simulation process. The blade motion was simulated using the natural mode decomposition method for the first five natural modes of vibration. The aerodynamic damping values were obtained for five modes and four interblade angles, as well as the distribution of damping along the blade length. As a result, negative damping of vibrations was revealed in the first natural mode and synchronous vibrations of the blades. Subsequent modeling of coupled blade vibrations revealed self-excitation of blade vibrations in zero phase shift mode and damping for other vibration modes.

Keywords: Aeroelasticity · Flutter · Fan · Aircraft Engine · Blade Vibrations

1 Introduction

In modern aviation, gas turbine engines are the most common, and their gas-dynamic stability is one of the essential conditions for the robustness, safety, and operational lifetime of the aircraft as a whole. The technical characteristics of aircraft, maximum altitude and flight speed, and maneuverability of aircraft largely depend on the perfection of aviation gas turbine engines (GTE) [1]. Therefore, finding ways to increase the stability reserves of GTE and eliminating modes of instability, as in the case of self-excited vibrations associated with energy exchange between the vibrating structure and the main flow (flutter), is an important and relevant task [2].

H. Altenbach et al. (Eds.): CAMPE 2025, LNME, pp. 3–12, 2026.
https://doi.org/10.1007/978-3-032-16381-3_1

The instability mode of blade vibrations, known as flutter, causes an intense increase in the amplitude of vibrations of the rotor blades and can lead to blade failure and even an accident in a very short time [3]. Therefore, the study of flutter, the causes of aeroelastic instability of vibrating blades in a gas flow, is of considerable theoretical and practical interest. GTE fan, subjected to blade flutter, is one of the most serious difficulties in gas turbine engine design, as it limits the range of safe operating modes and engine performance [4].

Blade flutter also occurs in steam turbines and can occur during transient and off-design operating modes [5], with the aeroelastic characteristics being influenced by the structural design of the blade attachment [6], friction damping and mistuning of the blades is also important [7]. It has also been found strong dependency of turbine stage Mach number and the vibration amplitude of blades [8]. Predicting flutter is also a key task for industrial gas turbines with multistage compressors [9].

The reflection of acoustic waves in the air intake plays a significant role in the excitation of fan blade vibrations, which can either increase or decrease the stability of blade vibrations [10]. This factor is considered key in the analysis of a physical event known as flutter-bite [11].

Currently, there are many methods for assessing the probability of flutter, including a combination of machine learning methods with reduced-order models [12]. In general, classical modeling methods require significant time and computational resources [13]. The search continues for more efficient methods, such as methods based on graph convolutional neural networks [14], using simplified numerical models [16], as well as using the Fourier decomposition to solve the problem in terms of frequency [15].

Correctly capturing the energy transfer between flow and structure demands a coupled solution of fluid dynamics and structural dynamics [16]. The results of such methods show good agreement with experimental data [17, 18]. At the same time, it is necessary to verify the methods using new experimental data [19, 20].

In this study, based on the aerodynamic model described in the article [21] and the modal approach to solving the blade dynamics problem, a numerical analysis of the blade aeroelasticity of an aircraft engine fan is presented.

2 Object and Methodology of Research

Under investigation is a 24-blade wide-chord fan, which is the first rotor of an aircraft engine compressor. The visual appearance of the fan is shown in Fig. 1. The fan operates at medium speed under the following boundary conditions:

- inlet total pressure: 100240 ÷ 101230 Pa;
- inlet total temperature: 282 K;
- axial flow direction at the inlet;
- static pressure at the outlet in range 99200 ÷ 112600 Pa;
- rotational speed of the fan: 4123 rpm.

To obtain the aeroelastic characteristics of the fan blade cascade, the problem of coupled fluid flow and elastic blade vibration simulation was solved. The fluid flow is simulated by RANS pressure-based solver, with SST Menter turbulence model [22]. The

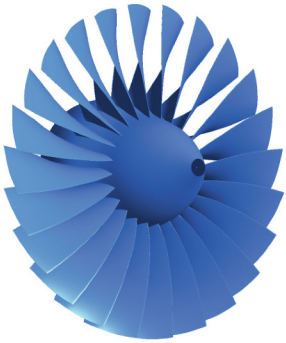

Fig. 1. Appearance of the fan.

elastic vibrations of the blades are assumed to be small, so the natural form decomposition method is used, with the first five forms being used in this case [21]. The flow equations are solved using the ANSYS Fluent software package [23]. The vibrations of the blades are simulated with second-order scheme and implemented in additional software, where two-way coupling is also performed. The state of the air is modeled by the equations of state of an ideal gas [24]. This approach to obtaining aeroelastic characteristics has been verified and used in different cases [25], as well as in problems of fluid-structure interaction [26].

The primary aeroelastic characteristics are determined using the energy method, with blade vibrations set according to a harmonic law, initial amplitude of vibrations was 0.5 mm. Initial inter-blade phase angles (IBPA) has four values differing by 90 degrees. Table 1 shows the values of blade natural frequencies for the corresponding natural forms in the modeling of vibrations.

Table 1. Natural frequencies of blade vibrations.

Natural form	1	2	3	4	5
Natural frequency, Hz	98	217	410	478	632

3 Results and Discussion

The fan's operating mode is characterized by transonic flow, with a shock wave on the suction side and a small separation zone on the suction side, most developed in the middle section. The isolines of the relative Mach number in the middle section are shown in Fig. 2.

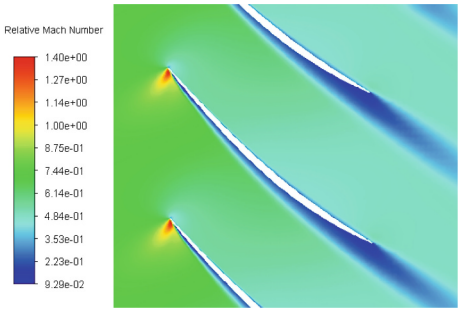

Fig. 2. Relative Mach number isolines in the middle section.

The resistance of blades to self-excited vibrations is determined by the aerodamping coefficient, which is the opposite to the dimensionless aerodynamic work on excitation of vibrations. The sign of the aerodamping coefficient determines the possibility of self-excited vibrations.

For the five natural forms in Fig. 3, the aerodamping coefficient D is shown as a function of IBPA.

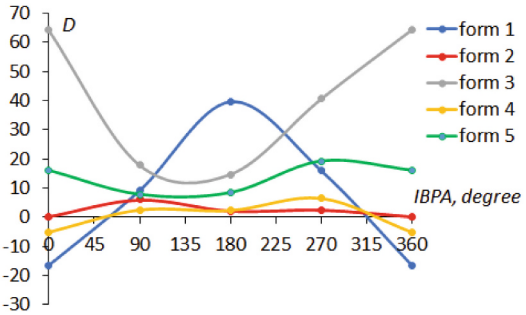

Fig. 3. Dependency of aerodamping coefficient on IBPA for five natural forms of blade vibration.

In Fig. 3, almost all modes have positive damping, except for the first and fourth modes for IBPA close to 0°, with the value for the first mode being significantly lower than zero compared to the values for other modes.

Figure 4 shows the change along the blade of the aerodamping coefficient D for same natural forms and IBPA.

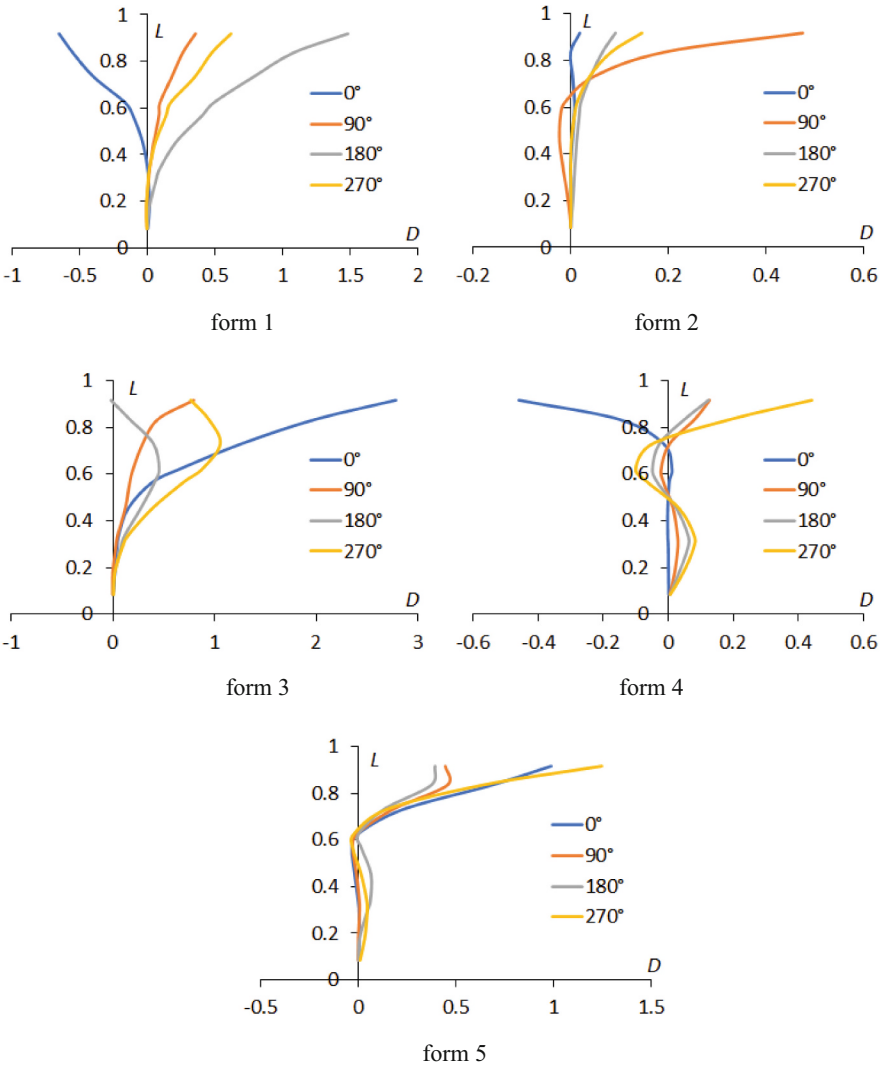

Fig. 4. Change by blade length of aerodamping coefficient for five natural forms and four IBPA.

According to Fig. 4, for the third and fifth natural forms, damping is positive, so there is no danger of self-excitation for these forms. For the second form and an angle of 90° in the middle section, there is energy feed, but it is compensated by the work in the peripheral part of the blade. As for the first and fourth modes, for IBPA = 0°, energy feed is present for whole blade, thereby indicating the possibility of uncontrolled self-excitation of vibrations.

The results of coupled simulation of blade vibrations and flow, with mutual energy exchange, are closest to reality. The initial conditions for coupled vibrations were set as harmonic blade vibrations with the same amplitude for all natural modes and four

values of IBPA. The simulation was performed over a period of 10 rotor revolutions. Figure 5 shows the simulation result for IBPA = 0° in the form of circumferential force and displacement for the blade tip region, as well as their spectrum.

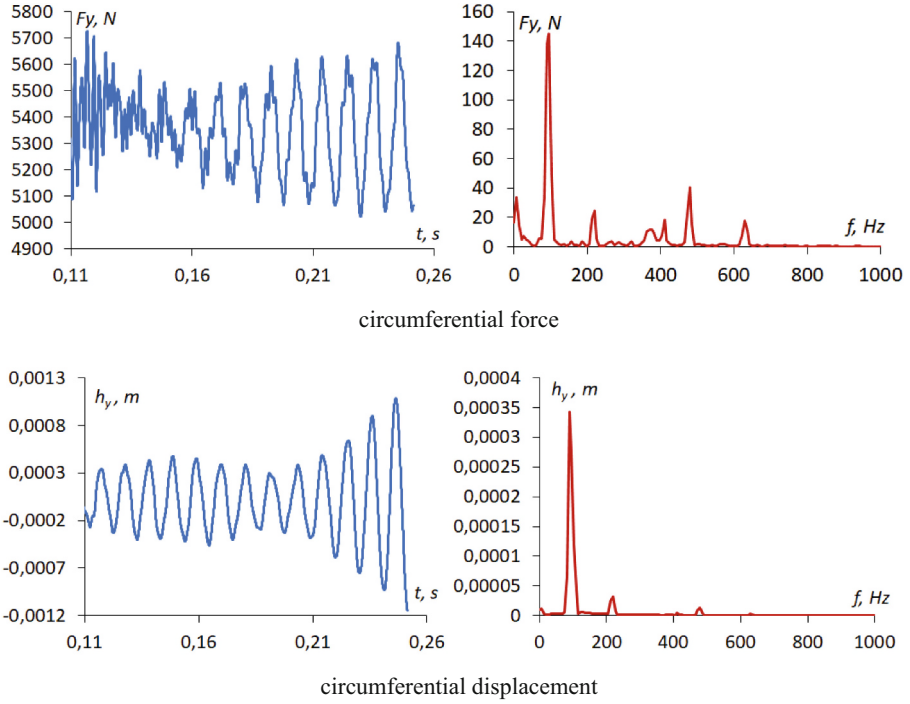

Fig. 5. Force and displacement of the blade tip region for IBPA = 0°, and their spectrum.

Figure 5 clearly shows that from chaotic vibrations, which are the sum of five natural forms, only vibrations with the frequency of the first natural form remain, while the amplitude of the vibrations increases. The force and displacement spectra show the dominance of the first natural frequency with a negligible amplitude of the exciting forces of other frequencies.

The situation for IBPA = 90°, 180°, and 270° is approximately the same and develops according to the following scenario: attenuation of vibrations in all modes except the first, for which an initial decrease in amplitude is observed, followed by an increase. For example, Fig. 6 shows the result of modeling coupled vibrations for IBPA = 180°.

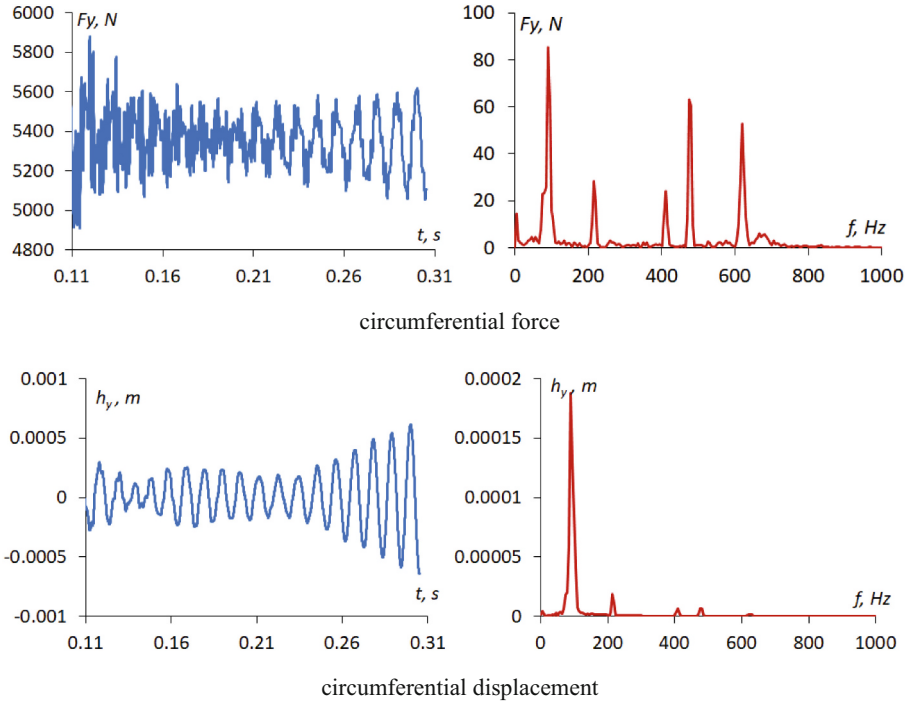

Fig. 6. Force and displacement of the blade tip region for IBPA = 180°, and their spectrum.

Here, despite the presence of exciting forces with the fourth and fifth natural frequencies, the first natural frequency also dominates. The graph from the displacement spectrum shows that vibrations in forms other than the first quickly decay, while those in the first form begin to increase. In this process, there is an effect of changing the phase of vibrations – from values different from 0° to IBPA = 0°, at which the minimum damping is revealed for the first form. This is clearly visible in Fig. 7, which shows the displacement of the peripheral section of two adjacent blades.

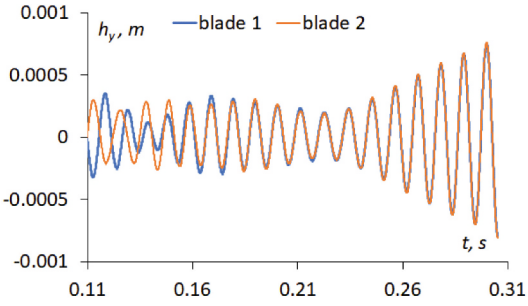

Fig. 7. Displacement of adjacent blades for initial IBPA = 180°.

Figure 7 shows that the initial phase shift of 180 degrees changes to 0 over four vibrations, while the decrease in vibration amplitude changes to a noticeable increase. This shows how quickly the conditions for damping vibrations can change to favorable conditions for self-excitation of vibrations.

Previously, using another method of flow modeling with a simpler turbulence model by Baldwin and Lomax, a numerical investigation of the aeroelasticity of the blades of the same aircraft engine fan in close mode was conducted [27]. The aerodynamic damping coefficient dependence on interblade phase angle was also calculated using the energy method. Subsequent analysis of coupled vibrations showed the presence of self-oscillations with a small amplitude. A comparison of the research results showed a similarity in the dependence of the aerodynamic damping coefficient on interblade phase angle, but the absence of negative values for IBPA $= 0°$. Thus, the application of a more advanced turbulence model and modern methodology can produce quantitatively different outcomes, yet retain strong qualitative consistency with results from other approach.

4 Conclusion

The blade aeroelasticity of an aircraft engine fan for an off-design operating mode was numerically analyzed, including the energy method analysis for the five natural forms and four values of the interblade phase angle, and solutions to the coupled problem of fluid flow and blade dynamics for the same modes and angles. Fluid motion simulation was performed in the ANSYS Fluent software package, with solution of the differential equations of blade dynamics and two-way fluid-structure coupling supplied by custom software developed for this purpose.

At the first step, the aerodynamic damping coefficient dependency on the interblade phase angles were obtained for the five natural vibration modes of the blades. At the second step of the study, the coupled vibrations were simulated for the same five natural modes and four values of angles.

It was found that for the first and fourth modes and interblade phase angles close to zero, the aerodynamic damping becomes negative, and this is a factor determining the possibility of flutter.

Subsequent modeling of coupled vibrations showed that for IBPA $= 0°$, self-excited vibrations are observed, which have the frequency of the first blade vibration natural mode. At other values of IBPA, damping of vibrations is observed for all natural modes, which at some point in time change the inter-blade phase angle to $0°$, leading to subsequent self-excited blade vibrations of the first natural mode. Such aeroelastic performance of the fan blade cascade is caused by the compressor operating in off-design mode.

References

1. Kulkarni, D.Y., Lad, B., di Mare, L.: Multi-aeroelastic phenomena modelling Part I: the development of whole LPC model for civil turbofan engine. Proceedings of the ASME Turbo Expo **12C**, V12CT32A041 (2024). https://doi.org/10.1115/GT2024-128191

2. Šnábl, P., Prasad, C.S., Procházka, P., Pešek, L., Uruba, V., Skála, V.: Innovative design of experimental blade cascade model for in-depth analysis of stall flutter. Bulletin of the Polish Academy of Sciences: Technical Sciences **72**(5), e150806 (2024). https://doi.org/10.24425/bpasts.2024.150806
3. Procházka, P., Šnábl, P., Chindada, S., Prasad, C.S., Uruba, V., Pešek, L.: The broad study of blade cascade under controlled torsional flutter: dynamics of the flow and stability analysis. European Journal of Mechanics, B/Fluids **109**, 66–79 (2025). https://doi.org/10.1016/j.euromechflu.2024.08.006
4. Tharreau, P., Hardy-Falch, M., Stapelfeldt, S., Brandstetter, C.: Non-synchronous vibration: characterisation of the aerodynamic disturbance and its dependency on local tip clearance. Proceedings of the ASME Turbo Expo **10A**, V10AT21A021 (2024). https://doi.org/10.1115/GT2024-129186
5. Pinelli, L., et al.: The role of operating conditions on flutter instability of a low-pressure turbine rotor. Proceedings of the ASME Turbo Expo **10A**, V10AT21A014 (2024). https://doi.org/10.1115/GT2024-127528
6. Gallardo, J.M., Pérez Escobar, Ó.: A conceptual model for the flutter mechanism in interlocked turbine blades. J. Eng. Gas Turbines Power **145**(11), 111015 (2023). https://doi.org/10.1115/1.4063313
7. Rodríguez-Blanco, S., González-Monge, J., Martel, C.: Interaction of flutter and forced response in a low pressure turbine rotor with friction damping and mistuning effects. J. Sound Vib. **572**, 118181 (2024). https://doi.org/10.1016/j.jsv.2023.118181
8. Escudero, A., Corral, R., Blando, Y.: Mach number influence on low-pressure turbine flutter Journal of the Global Power and Propulsion Society **8**, 62–72 (2024). https://doi.org/10.33737/jgpps/182890
9. Kang, H.-S., Kim, Y.-J.: Aeroelasticity design and evaluation methodologies for gas turbine axial compressor: focus on fluttering phenomena. J. Mech. Sci. Technol. **38**, 3953–3962 (2024). https://doi.org/10.1007/s12206-024-2108-3
10. Yang, H., Liang, H., Zheng, Y.: Effect of intake acoustic reflection on blade vibration characteristics. Aerospace **11**(5), 358 (2024). https://doi.org/10.3390/aerospace11050358
11. Perez, J.M., Corral, R.: Parametric study on the duct intake reflection coefficients for fan flutter analyses. Proceedings of the ASME Turbo Expo **10A**, V10AT21A019 (2024). https://doi.org/10.1115/GT2024-129159
12. Rauseo, M., Zhao, F., Vahdati, M.: Physics guided machine learning modelling of compressor stall flutter. Journal of the Global Power and Propulsion Society **8**, 295–309 (2024). https://doi.org/10.33737/jgpps/187996
13. Rusanov, R., et al.: Application of innovative solutions to improve the efficiency of the low-pressure cylinder flow part of a 1000 MW steam turbine for nuclear power plant. Archives of Thermodynamics **45**(4), 141–152. https://doi.org/10.24425/ather.2024.152003 (2024)
14. Liu, Y., Li, Y., Li, L., Xie, Y., Zhang, D.: A fast prediction model of blade flutter in turbomachinery based on graph convolutional neural network. Aerosp. Sci. Technol. **148**, 109119 (2024). https://doi.org/10.1016/j.ast.2024.109119
15. Berthold, C., Gross, J., Frey, C., Krack, M.: Fully coupled analysis of flutter induced limit cycles: frequency versus time domain methods. J. Eng. Gas Turbines Power **145**(7), 071009 (2023). https://doi.org/10.1115/1.4062408
16. Ombret, N., Daon, R., Dugeai, A., Thouverez, F., Blanc, L.: A frequency-time partitioned approach for computing fan blade flutter induced limit cycle oscillations with nonlinear friction on contact interfaces. Proceedings of the ASME Turbo Expo **11A**, v11at21a010 (2023). https://doi.org/10.1115/GT2023-102568

17. Bublík, O., Pecka, A., Vimmr, J., Šnábl, P., Pešek, L.: Investigation of blade cascade torsional flutter using the discontinuous galerkin approach in correlation with experimental measurements. International Journal of Computational Fluid Dynamics **38**(1), 45–60 (2024). https://doi.org/10.1080/10618562.2024.2395568
18. Zoepke-Sonntag, R., Hill, G., Stapelfeldt, S.: Analysis of flutter mechanisms and unsteady aerodynamics of a transonic fan blade near stall. Proceedings of the ASME Turbo Expo **13D**, v13dt36a012 (2023). https://doi.org/10.1115/GT2023-102237
19. Gallardo, J.M., et al.: Experimental research into aeroelastic phenomena in turbine rotor blades inside ARIAS EU project. J. Turbomach. **146**(7), 071009 (2024). https://doi.org/10.1115/1.4065621
20. Eggers, T., et al.: Effect of 3D blade design on the aerodynamic, aeroelastic and structural behavior of a scaled UHBR fan. Journal of Physics: Conference Series **2526**(1), 012032 (2023). https://doi.org/10.1088/1742-6596/2526/1/012032
21. Kolodyazhna, L., Bykov, Y., Rządkowski, R., Panamariova, O.: Simulation of fluid-structure interaction in last stage of steam turbine. Lecture Notes in Networks and Systems 1091 LNNS, 56–69 (2024). https://doi.org/10.1007/978-3-031-67348-1_5
22. Rusanov, R.A., Rusanov, A.V., Chugay, M.O.: Analysis of the influence of operational and geometrical characteristics on the efficiency of axial turbine stage profile cascades. Science and Innovation **21**(2), 73–87 (2025). https://doi.org/10.15407/scine21.02.073
23. ANSYS Fluent Theory Guide. ANSYS, Inc., Canonsburg, PA (2019)
24. Rusanov, A., Rusanov, R., Klonowicz, P., Lampart, P., Żywica, G., Borsukiewicz, A.: Development and experimental validation of real fluid models for CFD calculation of ORC and steam turbine flows. Materials **14**(22), 6879 (2021). https://doi.org/10.3390/ma14226879
25. Strelnikova, E., Choudhary, N., Degtyariov, K., Kriutchenko, D., Vierushkin, I.: Boundary element method for hypersingular integral equations: Implementation and applications in potential theory. Eng. Anal. Boundary Elem. **169**, 105999 (2024). https://doi.org/10.1016/j.enganabound.2024.105999
26. Degtyariov, K., Gnitko, V., Kononenko, Y., Kriutchenko, D., Sierikova, O., Strelnikova, E.: Fuzzy methods for modelling earthquake induced sloshing in rigid reservoirs. 2022 IEEE 3rd KhPI Week on Advanced Technology, KhPI Week 2022 - Conference Proceedings, pp. 1–6 (2022). IEEE. https://doi.org/10.1109/KhPIWeek57572.2022.9916466
27. Gnesin, V., Bykov, Y., Kolodyazhnaya, L., Donchenko, V., Petrov, O.: Modeling of aeroelastic instability of fan blades. In: Advances in Mechanical and Power Engineering, CAMPE 2021, LNME, pp. 14–23 (2023). Springer, Cham. https://doi.org/10.1007/978-3-031-18487-1_2

Impact of Stay Vane Number on Pump-Turbine Characteristics

Oleg Khoryev, Yuriy Bykov(✉), Pavlo Korotaiev, Sergii Agibalov, and Anton Panov

Anatolii Pidhornyi Institute of Power Machines and Systems of the National Academy of Sciences of Ukraine, 2/10 Komunalnykiv Street, Kharkiv 61046, Ukraine
yubykoff@gmail.com

Abstract. The numerical and experimental investigation of impact of stay vane number on the flow patterns and efficiency of a pump-turbine model at heads up to 200 m in turbine and pump modes are presented. The study was conducted for two variants of flow parts, which consisted of spiral casing with stay vanes, guide vanes, runner, and draft tube, and differed in the number of stay vanes: 20 in the original variant and two times less in the modernized one. Numerical studies of incompressible viscous flow were carried out using the Ansys CFX software. The flow structure was presented and analyzed, the distribution of radial and circumferential velocity components was compared, as well as the flow angle in the gap between the stay vanes and the guide vanes blades. Experimental tests were performed on the hydrodynamic test stand of the IEMS hydraulic machinery laboratory. The blades and rim of the runner were manufactured using 3D printing technology. The efficiency hill chart in turbine mode at the given speeds, which correspond to the best efficiency mode and the minimum, nominal, and maximum heads at the Dniester PSP are shown. In pumping mode, a comparison of efficiency and head at the optimal opening of the guide vanes is given. It is concluded that the double reduction of the stay vanes worsens the energy characteristics in turbine mode, but improves them in pump mode.

Keywords: Pump-Turbine · Flow Part · Spiral Casing · Stay Vanes · Guide Vanes · Numerical Studies · Experimental Studies · Hydrodynamic Test Stand

1 Introduction

Reaching the target of the Paris Climate Agreement by 2050 will require more than doubling hydropower capacity, including the capacity of pumped storage plants. This requires investing approximately $85 billion in conventional hydropower and $8.8 billion in plants with pumped storage (PSP) every year. With the rapid development of solar and wind power generation, the role of hydroelectric units, which flexibly balance the peak part of the overall load schedule and serve as an emergency and frequency reserve for power systems, is growing significantly [1].

The hydroelectric power market has been growing steadily over the past few years and, according to experts, reached $246.51 billion in 2024. The hydroelectric power

H. Altenbach et al. (Eds.): CAMPE 2025, LNME, pp. 13–22, 2026.
https://doi.org/10.1007/978-3-032-16381-3_2

market is expected to continue growing in the near future. According to experts, by 2028, it will amount to $286.40 billion with an average annual growth rate of 3.8%. Among the prerequisites for growth are increased demand for renewable energy sources, increased government support for hydropower projects, rapid urbanization, and industrialization.

Hydropower not only generates electricity but also plays a key role in energy storage. Modern pumped storage power plants act as natural "batteries," storing excess electricity during periods of low demand and releasing it during peak loads. This ensures the stability of the power system, reduces the load on the grid, and promotes the effective integration of solar and wind energy by balancing their variable generation [2]. In 2025, hydropower will strengthen its position as one of the main tools of the global energy transition, contributing to the reduction of carbon emissions and ensuring a stable, reliable energy supply for future generations [3]. Improving the energy performance of turbines is a priority for researchers.

One of the main trends is to establish dependencies between efficiency and the geometric parameters of flow parts, based on which their characteristics can be improved [4]. When operating as part of a PSP, pump-turbines are subject to special requirements, including stable operation in partial and transient modes. To this purpose, the entire flow section, in particular the blades of the runner, is optimized [5].

Optimizing the runner of a pump-turbine is the most demanding process, but it often gets the objective achieved [6]. To this aim, comprehensive methods are being developed that utilize the greatest number of parameters [7]. The flow part can also be optimized by installing new elements in the runner, in particular, splitter blades [8]. The number of parameters used to describe the geometric characteristics of the flow -part is of great importance for the convenience of design and speed of optimization [9], and a successful description method can also be applied to other types of hydraulic [10] and steam [11] turbines. Improvements can also be made to other components of the turbine unit, including the draft tube [12]. When optimizing the flow part, it is also necessary to take into account the parameters of erosion wear [13].

Special attention is now being paid to the guide vanes and stay vanes, as these elements ensure optimal flow characteristics at the runner inlet in turbine mode and reduce losses in pump mode. This area also experiences significant unsteady loads associated with the interaction between the runner and the stationary blades [14]. The number of stay vanes, their characteristics, and their interaction with the flow from the spiral case and the guide vanes blades also influence unsteady phenomena, both during the start-up process [15] and under constant load [16].

An important and necessary part of the method of developing and improving the flow parts of hydraulic turbines is conducting experimental research to confirm theoretical developments or numerical studies [17]. Some cavitation characteristics of pump-turbines can only be reliably obtained experimentally [18].

The proposed article considers comprehensive studies – numerical and experimental – of the impact of the number of stay vanes on the flow patterns and efficiency of a pump-turbine at heads up to 200 m in turbine and pump modes.

2 Object and Method of Study

The ORO170/5252M7 pump-turbine model, developed at IEMS and transferred to JSC "Ukrainian Energy Machines" for implementation in the project of 5–7 hydroelectric units of the Dniester pumped storage power plant, was selected as the study object. The main features of the object are as follows:

- spiral casing with a coverage angle of $\varphi = 360°$, having round cross-sections designed according to the assumption of constant circular velocity $V_u = const$;
- a stator with flat rings, having 20 (in the original version) or 10 (in the modernized version) profiled stay vanes, including a spiral case tongue. It is possible to install a ring valve;
- the guide vanes of 20 blades, height $b_0 = 0.14D_1$, rotation axis at diameter of $D_0 = 1.2D_1$;
- runner with 7 blades and diameter of $D_1 = 350$ mm.
- draft tube with vertical 5° taper diffuser, an elbow of KU-3RO type, discharge pipe of constant diameter. The overall height of the draft tube is $h = 3.19D_1$, and the length is $L = 4.5D_1$.

To reduce the production cost of the model unit and shorten the testing time, the runner blades and shroud were printed on a PLA plastic printer (Fig. 1).

Fig. 1. Model of the R5252M7 runner (after testing on a hydrodynamic test stand).

The hub is made of stainless steel. Calculations of the strength of the blades and the structure as a whole have shown that such a model can be tested on a hydrodynamic test stand in turbine mode at heads up to 15 m, which allows reliable results to be obtained.

3 Results of Numerical Study

Using the ANSYS software, for which IEMS has an academic license, a numerical study of the flow of viscous incompressible fluid was conducted in models containing all elements of the flow section, in turbine and pump modes. A tetrahedral mesh with wall refinement was selected [19]. The total number of cells was approximately 7.1

million. The parameter $y+$ was controlled and did not exceed 10 [20]. Water motion was simulated using the ANSYS CFX RANS solver, supplemented by the k-ε turbulence model [19]. For the turbine mode, the mass flow at the inlet of the spiral case and the static pressure at the outlet of the draft tube were set. For the pumping mode, the mass flow at the inlet of the draft tube and the static pressure at the outlet of the spiral case were set.

Numerical studies have shown that the flow structure in the turbine mode is practically independent of the flow rate; only the values of the absolute velocity components change, proportionally to the flow rate.

Figure 2 shows the distribution of streamlines for two variants of spiral casings (the original one with 20 stay vanes and the modernized one with 10) in turbine mode, close to best efficiency when the opening of the guide vanes is $a_0 = 20$ mm, the unit rotation frequency is 91 min^{-1}, and the unit flow rate is 0.303 m^3/s. The results show that the distribution of streamlines in the stator column area is quite smooth in both model variants.

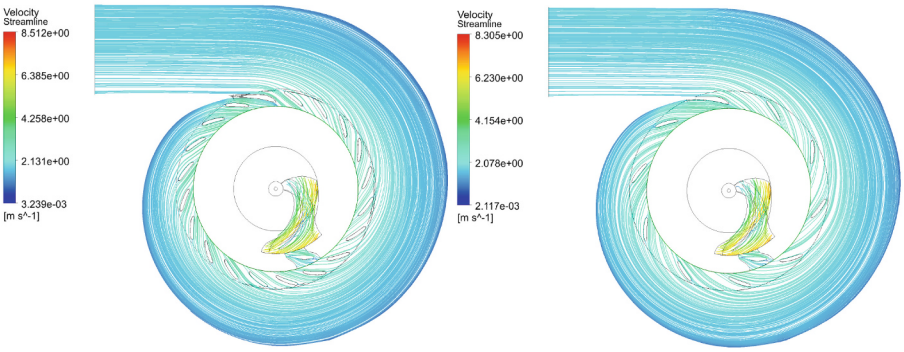

Fig. 2. Distribution of streamlines in spiral casings of pump-turbine models with different numbers of stay vanes in turbine mode: a – 20 stay vanes; b – 10 stay vanes.

Figure 3 shows the distribution by the angle of coverage from 0 to 360° in the middle horizontal cross-section of the spiral of the radial V_r and circumferential V_u components of the velocity and flow angle α, which forms the inflow, behind the stay vanes for two model variants at the above-mentioned turbine mode. It can be seen that the distribution of the flow velocity in both variants of the flow parts up to the angle of coverage $\varphi < 270°$ is uniform, while at $\varphi > 270°$ the unevenness of the distribution increases in the variant with 10 stay vanes. The same pattern is observed in the distribution of the circular velocity. Accordingly, in the model with 10 stay vanes, a greater difference in the values of the angle α over the spiral wrap φ is obtained. Thus, at spiral coverage angles from 15 to 345°, the flow angle behind the stator in the R5252M7 model varies in the range of 25.6–28.5°, and in the R5252M7–10 model from 23.1 to 30°. This leads to an increase in the circumferential uniformity of the flow onto the guide vane blades and may lead to an increase in hydraulic losses.

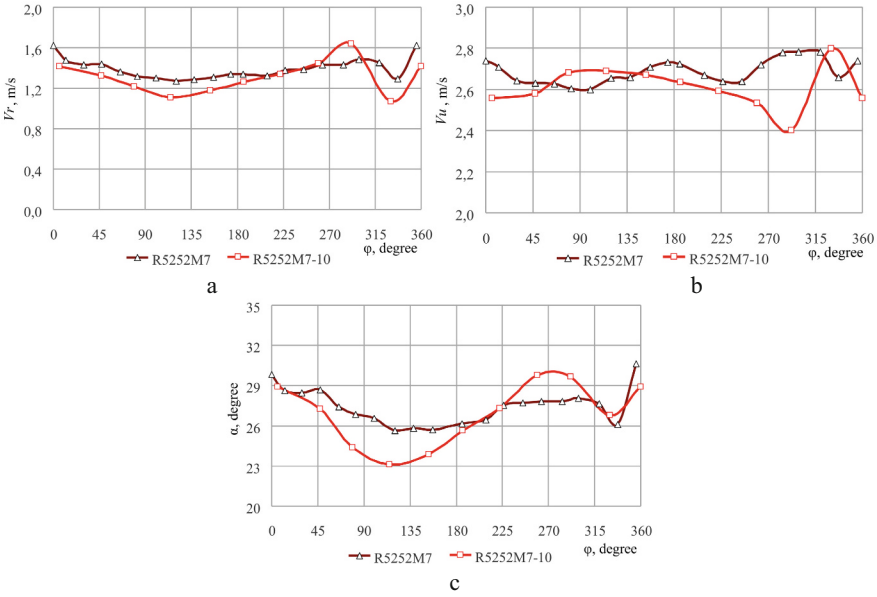

Fig. 3. Distribution by angle of coverage in the middle horizontal section of the spiral case of kinematic characteristics in turbine mode: a – radial velocity V_r; b – circumferential velocity component V_u, c – flow angle α.

In pump mode, numerous studies were conducted with the opening of the guide vanes at 26 mm, close to the best efficiency at a rotor speed of 700 rpm, at different flow rates. Figure 4 shows the distribution of streamlines at flow rates corresponding to the maximum efficiency. Both models have a fairly uniform distribution of streamlines. At the same time, the variant with 10 stay vanes demonstrates better flow around the tongue. This, taking into account the decrease in profile losses due to the reduction in the number of stay vanes, should lead to an increase in the efficiency of the flow part of the model in pump mode.

Figure 5 shows the distribution by angle of coverage from 0 to 360º in the middle horizontal section of the spiral case of the radial V_r and circumferential V_u components of velocity and flow angle α behind the guide vanes in front of the stay vanes for two model variants at the best efficiency pumping mode when the opening of the guide vanes is $a_0 = 26$ mm.

As can be seen from the Fig. 5, the impact of the number of stay vanes on the kinematic characteristics of the flow between the guide vanes and the stay vanes is less than in the turbine. This is explained by the fact that the flow structure in the pump mode in front of the stator is mainly determined by the guide vanes and, to some extent, by the runner, which is identical in the two models under consideration. The reverse effect of the stay vanes also occurs, which is especially evident in the cross-sections corresponding to the spiral case coverage angles from 270 to 360º. At coverage angles from 0 to 270º, the distribution of both the flow rate and the flow angle is more uniform

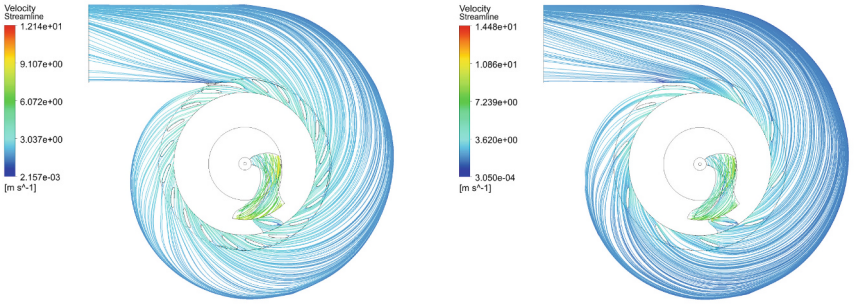

Fig. 4. Distribution of streamlines in spiral casing of pump-turbine models with different numbers of stay vanes in pump mode: a – R5252M7, 20 stay vanes; b – R5252M7–10, 10 stay vanes.

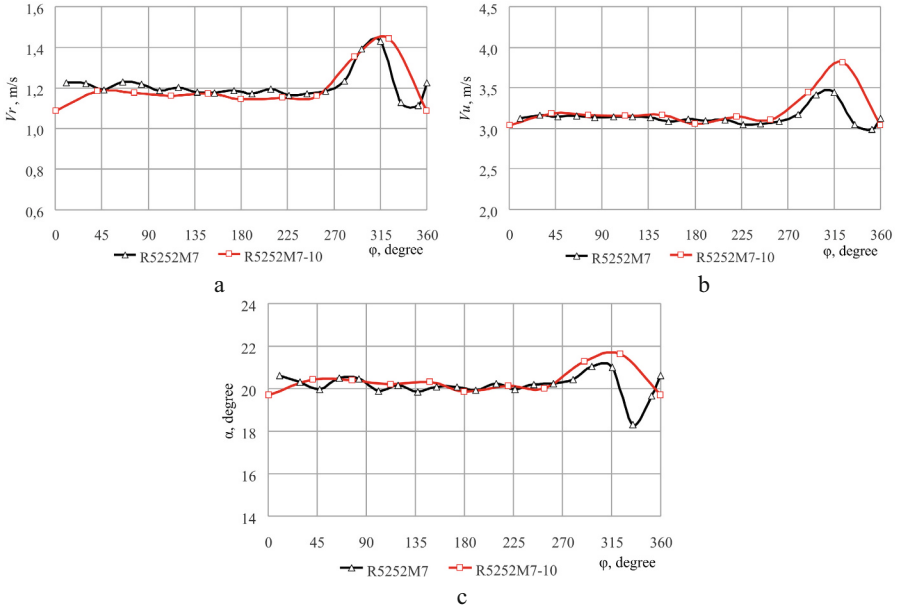

Fig. 5. Distribution by angle of coverage in the middle horizontal section of the spiral case of kinematic characteristics in pump mode: a – radial velocity V_r; b – circumferential velocity component V_u, c – flow angle α.

in the R5252M7–10 model with 10 stay vanes. This should lead to an improvement in the energy characteristics of this flow part.

4 Results of Experimental Study

The pump-turbine models were studies on the hydrodynamic test stand of the IEMS hydromachinery laboratory. The test stand is equipped with set of modern measuring instruments and has undergone metrological certification. All technical indicators of the test stand correspond to the IEC 60193 standard for model testing, primarily in terms of efficiency measurement error ± 0.25%. The main parameters of the equipment are: diameter of runner models up to 500 mm; flow rate up to 0.500 m^3/s; test heads up to 30 m; motor-generator power 200 kW. The Reynolds number in the studies were in the range $Re = 2.5 \cdot 10^6 \ldots 3.0 \cdot 10^6$ and were recorded in the protocols for each operating point. For a more detailed description of the stand, please refer to [21, 22].

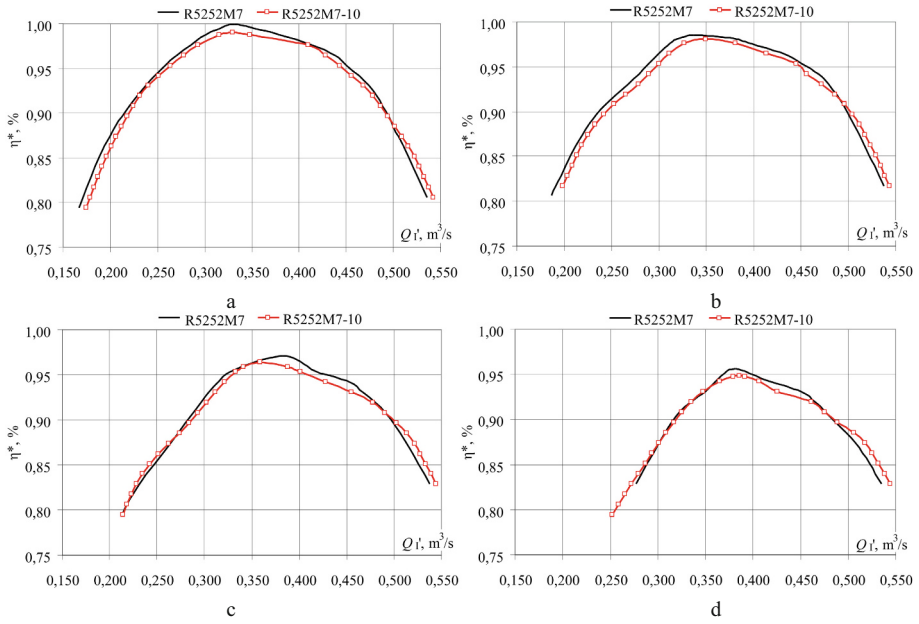

Fig. 6. Dependency of η* on unit flow rate for models R5252M7 (with 20 stay vanes) and R5252M7–10 (10 stay vanes): a – $n_I' = 80\ min^{-1}$; b – $n_I' = 85\ min^{-1}$; c – $n_I' = 91\ min^{-1}$; d – $n_I' = 95\ min^{-1}$.

Experimental studies of models were conducted at a head of 6 m in turbine mode, and rotor speed was set to 700 min^{-1} in pump mode. The opening of guide vanes varied from 12 to 34 mm in the range of unit flow rate Q_I' from 0.100 to 0.600 m^3/s. Operating characteristics were obtained and used to construct efficiency hill chart.

In turbine mode, the use of a stator with 10 stay vanes led to a decrease in the maximum efficiency relative to the initial variant by 0.72% with a decrease in the optimal unit flow rate by 0.008 m^3/s, while the best efficiency unit rotation speed remained unchanged.

Figure 6 shows a comparison of the distribution of the relative efficiency (η*) of two variants of pump-turbine models in the form of sections of hill chart at unit rotation speeds

n_{1}' of 80, 85, 91, and 95 min^{-1} ($n_{1}' = nD_1/\sqrt{H}$, here n is rotation speed, D_1 – runner diameter, H – head). The values of 85, 91, and 95 correspond to the highest, nominal, and lowest heads at the Dniester PSP, respectively. Hereinafter, relative efficiency η* is defined as the ratio to the maximum efficiency of the model with 20 stay vanes.

As can be seen from the data presented, at almost all heads at the station and across the entire range of flow rate, the efficiency of the initial version is higher than that of the model with a reduced number of stay vanes. The exception is flow rates greater than 0.500 m^3/s, but these values are beyond the power limitation lines, and hydraulic units are not operated at such modes.

Figure 7 shows a comparison of the relative efficiency and heads in pump mode when the guide vanes opening is $a_0 = 26$ mm, which is practically optimal for both models.

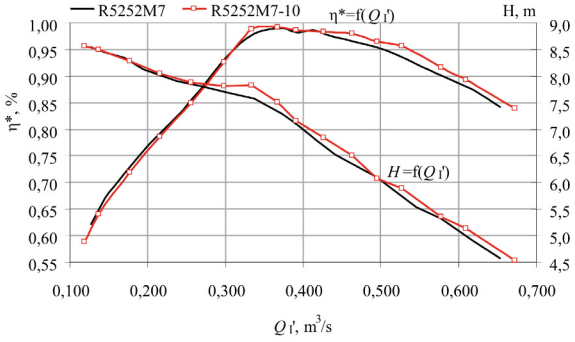

Fig. 7. Dependency of η* and head on unit flow rate for models R5252M7 (with 20 stay vanes) and RK5252M7–10 (10 stay vanes) when the opening of the guide vanes is $a_0 = 26$ mm.

The figure shows that in the flow rate range from 0.300 m^3/s to 0.500 m^3/s, i.e. almost throughout the entire operating range, the R5252M7–10 model with a reduced number of stay vanes has better characteristics of efficiency and head (to an even greater extent). A similar picture can be observed at other values of openings of the guide vanes. The maximum efficiency of this model exceeds that of the original version by almost 0.60% with a 3% increase in head.

5 Conclusion

The results obtained allow us to draw the following conclusions:

1. As a result of experimental and numerical investigations, the impact of the number of stay vanes on the flow patterns in the pump-turbine inlet on the parameters of the Dniester PSP and on the energy characteristics of the flow part model was determined.
2. The use of 10 stay vanes instead of 20 in the turbine mode increases the circumferential irregularity of the distribution of the flow and circumferential velocity components, as well as the flow angle in front of the guide vanes. This resulted in a 0.72% decrease in maximum efficiency and worsened its level over almost the entire operating range.

3. In the pump mode, a double reduction in the number of stay vanes led to better flow pattern in the stay vane-guide vane region, but the effect is less than in the turbine mode. Experimental studies have confirmed the improvement of energy and pressure characteristics. The maximum efficiency in this model increased by 0.60% with a simultaneous increase in head by 3%.

References

1. Hydropower capacity should more than double by 2050 to meet climate goals, Irena says. The National News. https://www.thenationalnews.com/business/energy/2023/02/14/hydropower-capacity-should-more-than-double-by-2050-to-meet-climate-goals-irena-says/. Accessed 15 Aug 2025
2. Hunt, J.D., Zakeri, B., Nascimento, A., Brandão, R.: Pumped hydro storage (PHS). In: Storing Energy, 2nd edn. Elsevier (2022). https://doi.org/10.1016/B978-0-12-824510-1.00008-8
3. Hydropower in 2025: what to expect for the industry?. https://uhe.gov.ua/media_tsentr/novyny/hidroenerhetyka-u-2025-rotsi-shcho-chekaye-na-haluz. Accessed 15 Aug 2025
4. Du, J., et al.: Study on the effects of runner geometric parameters on the performance of micro Francis turbines used in water supply system of high-rise buildings. Energy **256**, 124616 (2022). https://doi.org/10.1016/j.energy.2022.124616
5. Sun, L., Li, Y., Zhang, Q., Wang, Z., Guo, P.: Beyond the S-region instability: a 3D blade reshaping strategy to unlock stable pump-turbine operation for enhanced grid flexibility. Energy **332**, 137244 (2025). https://doi.org/10.1016/j.energy.2025.137244
6. Tengs, E., Charrassier, F., Jordal, M.R., Iliev, I.: Fully automated multidisciplinary design optimization of a variable speed turbine. IOP Conference Series: Earth and Environmental Science **774**, 012031 (2021). https://doi.org/10.1088/1755-1315/774/1/012031
7. Lestriez, R., Calvo, D., Mendicino, D.: Advanced optimization tools for hydro turbine runner design. IOP Conference Series: Earth and Environmental Science **774**, 012001 (2021). https://doi.org/10.1088/1755-1315/774/1/012001
8. Wang, H., Liu, X., Jiang, Q., Hua, H., Ou, S.: Numerical simulation of cavitation turbulence in Francis turbine runner with splitter blades. Journal of Drainage and Irrigation Machinery Engineering **38**(1), 45–51 (2020). https://doi.org/10.3969/j.issn.1674-8530.18.1275
9. Cerriteño, A., Delgado, G., Galván, S., Dominguez, F., Ramírez, R.: Reconstruction of the Francis 99 main runner blade using a hybrid parametric approach. IOP Conference Series: Earth and Environmental Science **774**, 012074 (2021). https://doi.org/10.1088/1755-1315/774/1/012074
10. Abeykoon, C.: Modelling and optimisation of a kaplan turbine - a comprehensive theoretical and CFD study. Cleaner Energy Systems **3**, 100017 (2022). https://doi.org/10.1016/j.cles.2022.100017
11. Rusanov, A., et al.: Application of innovative solutions to improve the efficiency of the LPC flow part of the 220 MW NPP steam turbine. Archives of Thermodynamics **43**(1), 63–87 (2022). https://doi.org/10.24425/ather.2022.140925
12. Zhou, X., Wu, H., Cheng, L., Huang, Q., Shi, C.: A new draft tube shape optimisation methodology of introducing inclined conical diffuser in hydraulic turbine. Energy **265**, 126374 (2023). https://doi.org/10.1016/j.energy.2022.126374
13. Aponte, R.D., et al.: Minimizing erosive wear through a CFD multi-objective optimization methodology for different operating points of a Francis turbine. Renewable Energy **145**, 2217–2232 (2020). https://doi.org/10.1016/j.renene.2019.07.116

14. Ye, W., Geng, C., Luo, X.: Unstable flow characteristics in vaneless region with emphasis on the rotor-stator interaction for a pump turbine at pump mode using large runner blade lean. Renewable Energy **185**, 1343–1361 (2022). https://doi.org/10.1016/j.renene.2021.12.129
15. Xia, M., Wang, Z., Wang, W., Yang, J., Zhao, W., Qiao, M.: Hidden hydraulic instability: clearance flow dynamics during pump-turbine pump mode startup. Renewable Energy **252**, 123312 (2025). https://doi.org/10.1016/j.renene.2025.123312
16. Rode, B.R., Kumar, A.: Rotor-stator interaction investigations in variable speed reversible pump-turbine at higher head. Phys. Fluids **36**(3), 035122 (2024). https://doi.org/10.1063/5.0191202
17. Joy, J., Raisee, M., Cervantes, M.J.: Experimental investigation of an adjustable guide vane system in a Francis turbine draft tube at part load operation. Renewable Energy **210**, 737–750 (2023). https://doi.org/10.1016/j.renene.2023.04.096
18. Krzemianowski, Z., Steller, J.: High specific speed Francis turbine for small hydro purposes - Design methodology based on solving the inverse problem in fluid mechanics and the cavitation test experience. Renewable Energy **169**, 1210–1228 (2021). https://doi.org/10.1016/j.renene.2021.01.095
19. Rusanov, A., Rusanov, R.: The influence of stator-rotor interspace overlap of meridional contours on the efficiency of high-pressure steam turbine stages. Archives of Thermodynamics **42**(1), 97–114 (2021). https://doi.org/10.24425/ather.2021.136949
20. Rusanov, R., et al.: Development of the turbocompressor unit flow part for a biofuel power generation plant. Vidnovluvana Energetika **1**(80), 124–132 (2025). https://doi.org/10.36296/1819-8058.2025.1(80)124-132
21. Khoryev, O., Lynnyk, O., Korotaiev, P., Bykov, Yu., Ahibalov, Y.: Effect of circumferential lean of pump-turbine runner blades on energy characteristics. Naukovyi Visnyk Natsionalnoho Hirnychoho Universytetu **3**, 56–62 (2024). https://doi.org/10.33271/nvngu/2024-3/056
22. Khoryev, O., Korotaiev, P., Agibalov, Y., Bykov, Y., Maksymenko-Sheiko, K.: Experimental studies of pump-turbine flow part models at heads of 80–120 m. In: Altenbach, H., et al. Advances in Mechanical and Power Engineering. CAMPE 2021, LNME, pp. 24–33. Springer, Cham (2023). https://doi.org/10.1007/978-3-031-18487-1_3

Analysis of Boundary Layer Hydrodynamic Parameters on Flat Building Surfaces Under Air Leakage

Natalya Orlova[1(✉)] and Svitlana Alyokhina[2]

[1] Anatolii Pidhornyi Institute of Power Machines and Systems of the National Academy of Sciences, Vul. Komunalnykiv 2/10, Kharkiv 61046, Ukraine
naorl@ukr.net

[2] University of Applied Sciences Technikum Wien, Höchstädtplatz 6, 1200 Vienna, Austria

Abstract. This study proposes an integrated methodology for evaluating the boundary layer thickness on building façades under airflow impingement. The objective is to find spatial characteristics of boundary layer formation on building surfaces for different types of urban development, considering microclimatic parameters. The scientific novelty lies in the development methodology, which combines theoretical analysis, experimental measurements, and CFD simulations, ensuring higher accuracy in predicting building thermal performance and improving energy-efficient heating strategies. For the first time, it is shown that the coordinate, where the transition from gradient to non-gradient flow regimes happened, depends on both airflow velocity and temperature, allowing precise prediction of this critical phenomenon. Furthermore, unlike existing models, the proposed approach considers wind flow angle and velocity, which significantly impact local boundary layer characteristics and heat loss distribution. The practical significance of the study is the ability to accurately forecast façade heat losses, assess wind loads, and optimize energy efficiency. The obtained analytical dependencies and approximation functions for boundary layer thickness distribution can be applied in urban planning and architectural design to ensure microclimatic comfort and durability of building envelopes.

Keywords: Boundary Layer Thickness · Airflow · Building Surface

1 Introduction

Increasing demands for building energy efficiency and urban microclimate optimization require a detailed analysis of heat transfer through building envelopes. Heat losses depend strongly on boundary layer structure, shaped by airflow, solar radiation, thermal gradients, and façade geometry. The spatiotemporal variability of flow around buildings limits the accuracy of standard stationary models, highlighting the need to consider boundary layer thickness. Combining experimental measurements with CFD simulations is therefore essential for predicting heat losses, optimizing heating systems, and maintaining comfortable indoor microclimates across diverse urban environments.

H. Altenbach et al. (Eds.): CAMPE 2025, LNME, pp. 23–32, 2026.
https://doi.org/10.1007/978-3-032-16381-3_3

2 Literature Review

The study of airflow impingement on building envelopes combines experiments and numerical simulations to clarify boundary layer formation, separation, and vortex dynamics. Prior works [1–3] showed that corners, projections, and balconies create accelerated flows and low-pressure zones, strongly affecting boundary layer thickness and structure. These localized effects alter near-wall velocity distributions and generate secondary vortices.

Comparisons of simulations and field data [4–6] reveal that classical laminar and turbulent flat-plate models fail near complex façades, especially in corner regions with recirculation. Even high-resolution CFD requires experimental validation, particularly for façades with pronounced projections [5, 6]. Studies on transition location x_* [7–9] demonstrated dependence on free-stream velocity and temperature, governed by flow acceleration and stabilization of velocity profiles. Atmospheric parameters, including temperature and pressure, also critically influence separation zones and velocity evolution [10–12].

Urban microclimatic effects on buildings of different heights [13–15] show that interactions between high- and low-rise structures create complex circulation patterns, but dynamic variations (wind, temperature gradients, humidity) remain insufficiently studied. Experiments in upper façade regions [16, 17] confirmed increased local velocities, while numerical models often mispredict due to geometric simplifications and inadequate vortex representation. Minor architectural elements (balconies, cornices, canopies) also lack systematic analysis.

Correlation-based flat-surface models [18–20] lose accuracy for façades with discontinuities. Study [20] highlights the need to combine CFD with detailed experiments, particularly in heterogeneous urban environments.

In summary, current research outlines boundary layer behavior over façades, but a generalized model accounting for geometry, architectural details, urban microclimates, and unsteady atmospheric effects is lacking. Future work should refine transition criteria, separation and vortex modeling, include dynamic meteorological effects, and validate CFD models with comprehensive experiments.

The aim of this study is to develop a comprehensive methodology for determining the spatial characteristics of boundary layer thickness under airflow impingement on façades of different urban building types, taking into account microclimatic parameters. The methodology integrates theoretical calculations, experimental measurements, and numerical modeling to enhance the accuracy of predicting building thermal performance and optimizing energy-efficient heating strategies.

3 Research Methodology

The determination of boundary layer thickness under airflow impingement on building façades is based on a multi-stage approach. At the first stage, theoretical calculations of boundary layer thickness and the transition coordinate from gradient to non-gradient flow regimes are carried out. The theoretical study is refined by experimental velocity field measurements, which allow localization of the boundary layer edge and confirmation of the transition point.

At the third stage, numerical modeling is conducted using CFD, incorporating theoretical and experimental results. Appropriate turbulence models are selected to account for the specifics of urban development, façade geometry, and meteorological variability. The numerical model is calibrated using experimental data to improve predictive accuracy.

This stepwise approach ensures a comprehensive analysis of boundary layer structure, which serves as a foundation for developing effective measures to enhance building energy efficiency and optimize thermal regimes in residential areas.

3.1 Theoretical Background

The formation of the boundary layer during airflow over solid surfaces is described by the Reynolds-averaged Navier–Stokes equations, consisting of continuity, momentum, energy, and state equations. For building-scale flow, a turbulent boundary layer is formed with Reynolds numbers $\mathrm{Re} > > 1{\cdot}10^6$; thus, the flow can be considered self-similar. The laminar and transitional sublayers are neglected due to the high roughness of external walls, which promotes turbulence.

Here is considered the boundary layer developing in a region of increased pressure, where the airflow originates from the stagnation. The characteristic parameter of interest is the momentum thickness of the boundary layer, which represents the integral measure of momentum loss relative to the inviscid flow.

$$\delta_2 = \int_0^{\delta} \frac{u}{U_0} \cdot \left(1 - \frac{u}{U_0}\right) dy \tag{1}$$

The displacement thickness δ_1 is defined as:

$$\delta_1 = \int_0^{\delta} \left(1 - \frac{u}{U_0}\right) dy, \tag{2}$$

where U_0 is the free-stream velocity at the boundary layer edge in the region of non-gradient flow, and δ is the boundary layer thickness.

To characterize the velocity profile under conditions influenced by the pressure gradient, a shape factor is introduced [21]:

$$H_{12} = \frac{\delta_1}{\delta_2} \tag{3}$$

Experimental studies of turbulent boundary layers demonstrate that velocity profiles can be approximated by a one-parameter family of curves, described by a power-law distribution of the form.

The velocity of the approaching air flow under potential flow conditions can be represented as

$$\int_0^{x_*} U^{3.8} dx = A \cdot U_0^{3.8} \tag{4}$$

The variation of the shape factor H_{12} over the entire range of the flow $\frac{dP}{dx} \leq 0$ does not exceed ± 2.3%, i.e., for determining $\delta_2(x_*)$ the mean value A = 0.489 can be adopted. In this case, at an air temperature of t = 0 °C, P = 0.098 MPa, wind speed $U_0 = 5$ m/s, and $\nu = 13.75 \cdot 10^{-6}$ m^2/s takes the form

$$\delta_2(x_*) = 0.08276 \cdot \left(\frac{\nu}{U_0}\right)^{0.143} \tag{5}$$

From relation (6), for n = 6, the boundary layer thickness δ

$$\delta = \delta_2 \cdot \frac{(1+n) \cdot (2+n)}{n} = 9.33 \cdot \delta_2 \tag{6}$$

or, for the considered example, δ = 12.4 mm.

Having determined the momentum thickness δ_2, it is possible to calculate the coordinate x_* of the transition point from pressure-gradient flow along the surface to zero-pressure-gradient flow.

3.2 Experimental Study

The experimentally determined values of wall shear stress under pressure-gradient flow, taking into account $H_{12} = 1.3$, are well approximated by the formula

$$\frac{\tau_0}{\rho \cdot U^2} = 0.01383 \cdot \left(\frac{U_0 \cdot \delta_2}{\nu}\right)^{-0.268} \tag{7}$$

The exact solution of the momentum equation for a plate over the length from 0 to x is given by [21]

$$\delta_2(x) = 2 \cdot \frac{\tau_0}{\rho U_0^2} \cdot x \tag{8}$$

By substituting (8) into (9), we obtain

$$x = 36.153 \cdot \left(\frac{U_0}{\nu}\right)^{0.268} \cdot \delta_2(x)^{1.268} \tag{9}$$

Using the value of $\delta_2(x_*)$ with account of (9) for the section $x = x_*$, and performing the transformations, we obtain (taking into account that at $x = x_*$ $U = U_0$)

$$x_* = 1.79 \cdot \left(\frac{U_0}{\nu}\right)^{\frac{1}{8}} \tag{10}$$

Formula (4) shows that the position of the section at which the transition from pressure-gradient to zero-pressure-gradient flow occurs is influenced only by the velocity of the approaching airflow and the air temperature. At a velocity of $U_0 = 5$ m/s, t = 0 °C, and a barometric pressure of P = 0.0981 MPa, $x_* = 7.6$. The values of $\delta_2(x)$, $\delta_1(x_*)$, and x_* are determined under a number of assumptions, including the use of a model for evaluating

τ_0 during pressure-gradient flow as in zero-pressure-gradient flow along a flat plate with a constant potential flow velocity U∞ along the boundary layer edge.

As a result of measuring pressure variations along the boundary layer height, velocity profiles were obtained in different flow sections. The analysis of boundary layer formation conditions on the flat surfaces of building elements requires experimental investigation and generalization in the form of correlation relationships. For this purpose, the test stand shown in Fig. 1 was used.

During the experiment, the main characteristic for comparison was the position of the section x ∗ corresponding to the transition of the flow from pressure-gradient to zero-pressure-gradient conditions.

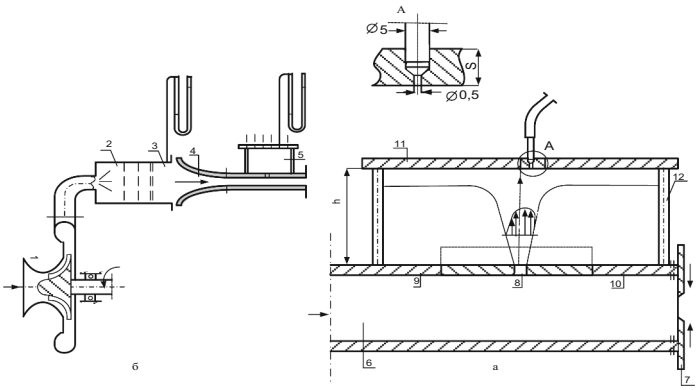

Fig. 1. Schematic diagram of the test rig (a) and working channel (b); 1 – centrifugal blower; 2 – receiver; 3 – flow straightening grids; 4 – nozzle; 5 – experimental setup; 6 – flat channel; 7 – shutters; 8 – flat slit; 9 – side wall; 10 – lateral inserts; 11 – measuring plate.

The measurement results are shown in Fig. 2a, b. The experiment revealed three distinct regions of variation $\overline{\delta}_2(\overline{x})$:

- at $0 \leq \overline{x} \leq 4.1$ - region I, characterized by a high gradient of the decrease in P^*;
- at $4.1 < \overline{x} \leq 10.4$ - region II, corresponding to the reduction of PPP to atmospheric pressure;
- at $\overline{x} > 10.4$ - region III, where a gradient-free flow along the plate is established.

If the value of $\overline{x}$ at the transition from region II to the gradient-free flow region is taken as $\overline{x}_* = 10.4$, and a comparison is made between the calculated value of $\overline{x}_*$, determined using Eq. (11), and the experimental result, we obtain

$$\overline{x}_* = 1.806 \cdot \left(\frac{U_0}{\nu}\right)^{\frac{1}{8}} \tag{11}$$

Experimental results indicate that the deviation associated with Eq. (12) remains within the acceptable error limits. The conducted study on the characteristics of the gradient flow region indicates that its extent depends on the velocity of the incoming flow and the air temperature (through the kinematic viscosity) and is limited in magnitude.

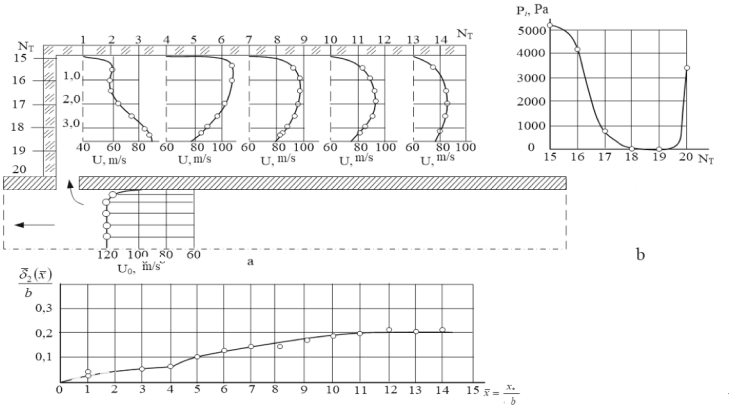

Fig. 2. Variation of the boundary layer thickness during the impingement of a semi-confined jet on a flat surface

The transition coordinate from the gradient to the gradient-free regime defines the spatial boundary beyond which the velocity and temperature gradients in the direction toward the surface diminish, and the flow structure becomes more homogeneous. Since intense heat transfer occurs in the high-gradient region, this results in significant thermal losses and affects the local dynamic loads on the façade.

3.3 CFD Modeling

The numerical experiment was conducted on a personal computer, with the flow around the building modeled in OpenFoam using the equations in steady-state formulation according to [23]. A symmetry condition was applied to the computational model, which reduced the required computational resources by a factor of two and allowed the creation of a finer computational mesh. An adaptive mesh was employed, meaning the grid was automatically refined in regions with rapid parameter changes and near the building.

As a result of the simulation of the air boundary layer thickness distribution on the building's exterior walls under variable flow conditions – depending on height, flow incidence angle (0°, 45°, 90°), and wind speed (2 m/s and 5 m/s) – approximation functions were obtained for each of the 36 building façades, along with the model coefficients A and B, the maximum deviation δ_{max}, and the root-mean-square deviation δ^2.

4 Results and Discussion

A general analysis of the results for airflow angles of 0°, 45°, and 90° at wind speeds of 2 m/s and 5 m/s showed that increasing wind velocity leads to a reduction in the average boundary layer thickness on the building's frontal and side façades due to the enhanced dynamic pressure component of the flow. At the same time, for the leeward façades, the variability of boundary layer thickness increases, along with a higher likelihood of local recirculation zones and flow separation, as indicated by larger spreads in maximum

deviations and the appearance of negative thickness values. At angles of 45° and 90°, boundary layer development becomes more unstable compared to 0°, reflecting increased complexity in the aerodynamic interaction between the flow and the building façades under varying wind directions.

The highest variability was observed for coefficient A, particularly at a 45° incidence angle, where its coefficient of variation reached 471% at 5 m/s. This indicates a high instability in the distribution of parameter A and a potential dependence on the complex turbulent flow structure in this direction. In contrast, at a 90° incidence angle, A showed the lowest variability (<110%) for both speeds, indicating greater stability under normal airflow conditions. Coefficient B generally exhibited lower variability, with coefficients of variation ranging from 77% to 122%. Especially stable B values were observed at 90° (for 2 and 5 m/s), where the spread did not exceed 78% and was accompanied by low dispersion and nearly symmetric distribution (skewness close to zero). To account for the specifics of airflow around the building surfaces, a regression analysis was performed separately for each group of conditions, which significantly reduced residual dispersion and improved the reliability of the estimated regression coefficients. This, in turn, provided higher explanatory power for the model and allowed an accurate description of the influence of wind speed and geometric parameters on boundary layer thickness formation.

Numerical modeling of the boundary layer thickness distribution on the building façades is performed considering height, airflow attack angle (0°, 45°, 90°), and wind speed (2 m/s and 5 m/s). Based on the results, the relationships $\delta = f(A,B,H,\varphi)$ are constructed for 36 building sides, and the model coefficients A and B, as well as the maximum ($\delta_{\delta max}$) and root-mean-square deviations ($\delta_{\delta}{}^2$), are determined to assess accuracy. Comparison of the coefficients makes it possible to evaluate the influence of flow velocity and direction on the boundary layer profile and to predict its distribution without repeated full-scale modeling, while the deviations characterize the acceptable error range. At a wind speed of 2 m/s and an incidence angle of 0°, with $R2 \approx 0.76$, the coefficients were calculated according to the following relationship:

$$A = 114.7C_p^{(-2)} - 114.03 \cdot C_p^{(-2)}.\exp A_p,\ B = -0.2866 \cdot A_p$$

where C_p, A_p – polynomial coefficients for determining static pressure, H -

The analysis of boundary layer thickness modeling results for airflow incidence angles of 0°, 45°, and 90° showed that constructing unified regression relationships for coefficients A and B was statistically unreliable. Specifically, at 0° and a wind speed of 5 m/s, as well as at 45° and 90° across speeds from 2 to 5 m/s, the following were observed: significant discrepancies between mean and maximum boundary layer thickness values, with deviations up to 0.3 m; presence of negative boundary layer thickness values, indicating flow instability, separation, or recirculation zones (especially at 5 m/s); lack of a stable functional relationship between height and layer thickness across different building façades (in some cases increasing, in others decreasing or fluctuating). As a result, regression models built for coefficients A and B under these conditions showed low convergence ($R2 < 0.5$) and, in some cases, could not be approximated due to excessive data variability. Nevertheless, even in the absence of a clear mathematical model, a pattern in boundary layer thickness variation is evident: it clearly depends

on the incidence angle and flow velocity. As the flow velocity increases, the overall boundary layer thickness decreases, but its fluctuations grow, particularly in leeward and side zones.

For a wind speed of 5 m/s and an incidence angle of 90°, with R2 ≈ 0.76, the coefficients are calculated according to the following relationship

$$\begin{aligned} \mathrm{B} &= 5525.29 - 309.28 \cdot \exp\delta \mathrm{P}_{\max} + 735.2 \exp\delta \\ &\mathrm{P}_{\max} \cdot \mathrm{A}_{\mathrm{p}} \cdot \mathrm{C}_{\mathrm{p}} \cos\theta - 108.4 \cdot \delta P_{\max} + 57.47 \exp\delta_{\max} \end{aligned}$$

In this case, the values of the incidence angle in degrees (0°, 45°, 90°) are used without conversion into radians; that is, they are treated as numerical parameters representing the angular configuration of the flow

$$\delta_{\delta max} = -0.00873 \cdot \theta + 0.0641,\ \delta_{\delta}^{2} = -0.004875 \cdot exp\delta_{\delta_{max}} + 0.27795 \cdot \delta_{\delta max}$$

5 Conclusions

As a result, the spatial variability of airflow impingement conditions was revealed, and statistical models were developed to describe the variation of boundary layer thickness as a function of height, wind speed, angle of attack, and hydrodynamic characteristics of the flow. The obtained dependencies have practical significance for assessing convective heat transfer on the external surfaces of building envelope structures.

The boundary layer thickness determines the intensity of heat exchange: in regions with a thin layer (typically frontal surfaces under direct impingement), increased thermal interaction with the surrounding environment is observed, whereas in rear and lateral zones, where the layer is significantly thicker, heat transfer decreases. This allows the implementation of a zonal approach for evaluating facade thermal regimes. In particular, dividing external surfaces into zones with different boundary layer thickness enables:

- assessing the non-uniformity of heat losses;
- refining heat transfer coefficients;
- rationally varying the thermal insulation properties of materials according to the intensity of heat exchange.

The simulation results, complemented by experimental measurements, allowed the derivation of analytical dependencies for determining the boundary layer thickness and the transition location, taking into account variations in the flow incidence angle and the approaching flow velocity. The proposed formulas are adaptive and can be applied to various types of urban buildings and microclimatic conditions, providing more accurate predictions of building thermal regimes.

The studies [24, 25] allow refinement of heat transfer parameters in different zones, considering the microclimatic characteristics of the approaching flow. This approach ensures a more precise analysis of local temperature regimes arising from the complex interaction between the flow and the surface. The integrated application of the derived analytical dependencies and results from other studies enhances the accuracy of predicting thermal regimes in conditions of variable aerodynamic environments.

The practical significance lies in the possibility of using the obtained dependencies to optimize energy-efficient solutions in heating systems, reduce energy consumption, and improve the thermal protection of envelope structures. Moreover, the integration of analytical calculations, experimental validation, and CFD modeling has formed a comprehensive methodology for assessing the spatial characteristics of the boundary layer, which can be effectively applied in the design, reconstruction, and modernization of building facilities in urbanized environments.

References

1. Zhang, Y., Liu, H., Kang, S.-C., Al-Hussein, M.: Virtual reality applications for the built environment. Automation in Construction **118**, Article 103311 (2020). https://doi.org/10.1016/j.autcon.2020.103311
2. Marmar, A., Zouia, S., Ismail, S., Hallik, A.: Twisted buildings: concepts and approaches. Architecture and Planning Journal **27**(2), Article 9 (2021). https://doi.org/10.54729/2789-8547.1152
3. Cheng, X., Huang, G., Yang, Q.S., Zhou, X.: Influence of architectural facades on wind pressures and aerodynamic forces of tall buildings. Journal of Structural Engineering **147**(1), Article 04020303 (2021). https://doi.org/10.1061/(ASCE)ST.1943-541X.0002867
4. Wang, Q., Guo, J., Rongrong: better renewable energy with economic growth without carbon growth: a comparative study of turbine, photovoltaics, and hydropower. Journal of Cleaner Production **426**, Article 139046 (2023). https://doi.org/10.1016/j.jclepro.2023.139046
5. Liu, W., Mattsson, M., Widström, T., Claesson, L.: Wind tunnel and numerical study of wind pressure coefficients on a medieval swedish church. Building and Environment **264**, Article 111905 (2024). https://doi.org/10.1016/j.buildenv.2024.111905
6. Hu, N., Zhu, Y., Lee, C., Smith, C.R.: Experimental and numerical investigation of turbulent spots in a flat plate boundary layer. Journal of Fluid Mechanics **1008**, Article 202 (2025). https://doi.org/10.1017/jfm.2025.202
7. McGuill, C., Keenahan, J.: A parametric study of wind pressure distribution on façades using computational fluid dynamics. Applied Sciences **10**(23), Article 8627 (2020). https://doi.org/10.3390/app10238627
8. Ramezani, R., Vazirizadeh, S.: Investigating the effect of building geometry on outdoor wind flow performance in residential complexes. Journal of Renewable Energy and Environment **9**(2), 20–22 (2022). https://doi.org/20.1001.1.24234931.1401.9.2.8.1
9. Sakiyama, N.R.M., Carlo, J.C., Sakiyama, F.I.H., Abdessemed, N., Frick, J., Garrecht, H.: Impact of wind pressure coefficients on the natural ventilation effectiveness of buildings through simulations. Buildings **14**(9), Article 2803 (2024). https://doi.org/10.3390/buildings14092803
10. Cheng, Y., Yang, M., Xie, S., Liu, J., Zheng, S.: Research on the impact of air temperature and wind speed on ventilation in university dormitories under different wind directions (Northeast China). Buildings **14**(2), Article 361 (2024). https://doi.org/10.3390/buildings14020361
11. Yasa, E., Özdemir, K.: The impacts of air pressure differences on microclimatic wind comfort among low-rise buildings in the historical urban landscape of the bay of Kotor Region, Montenegro (2022). https://doi.org/10.5772/intechopen.101743
12. Kim, G., Lee, G.: Validation of CFD models of urban microclimates under high temperature and humidity conditions during daytime heatwaves in dense low-rise areas. Building and Environment **266**, Article 112087 (2024). https://doi.org/10.1016/j.buildenv.2024.112087

13. Ishida, Y., Yoshida, A., Kamata, S., Yamane, Y., Mochida, A.: Wind tunnel experiments on interference effects of a high-rise building on the surrounding low-rise buildings in an urban block. Wind **3**(1), 97–114 (2023). https://doi.org/10.3390/wind3010007
14. Brozovsky, J., Mandjoupa, L.K., Behera, P., Roman, K.K., Azam, H., Denis, M.: Street-level sensing for assessing urban microclimate (UMC) and Urban Heat Island (UHI) Effects on Air Quality. Environments **12**(6), Article 184 (2025). https://doi.org/10.3390/environments12060184
15. Antoniou, N., Montazeri, H., Neophytou, M., Blocken, B.: CFD simulation of urban microclimate: validation using high-resolution field measurements. Science of The Total Environment **695**, Article 133743 (2019). https://doi.org/10.1016/j.scitotenv.2019.133743
16. Hu, D., Zhang, T., Jin, Q.: Investigation of wind pressure dynamics on low-rise buildings in sand-laden wind environments. Buildings **15**(15), Article 2779 (2025). https://doi.org/10.3390/buildings15152779
17. Wang, Q., Zhang, B.: Wind-induced responses and wind loads on a super high-rise building with various cross-sections and high side ratio—a case study. Buildings **13**(2), Article 485 (2023). https://doi.org/10.3390/buildings13020485
18. Silva, P.U., Bono, G., Greco, M.: Assessing pedestrian comfort in dense urban areas using CFD simulations: A Study on Wind Angle and Building Height Variations (2025). https://doi.org/10.20944/preprints202507.0711.v1
19. Mohajeri Nav, F., Mirfakhar, S.F., Snaiki, R.: A hybrid machine learning framework for wind pressure prediction on buildings with constrained sensor networks. Computer-Aided Civil and Infrastructure Engineering **40**(19), 2816–2832 (2025). https://doi.org/10.1111/mice.13488
20. Sari, D.P., Cho, K.-P.: Performance comparison of different building shapes using a wind tunnel and a computational model. Buildings **12**(2), Article 144 (2022). https://doi.org/10.3390/buildings12020144
21. Prasad, V.R., Silva, V., Cardoso, J.S.: Boundary layer flows: modelling, computation, and applications of laminar, turbulent incompressible and compressible flows. IntechOpen, p. 262 (2023). https://doi.org/10.5772/intechopen.100716. ISBN: 978–1–80356–219–3
22. Wen, X., Wang, L.-P., Guo, Z., Zhakebayev, D.B.: Laminar to turbulent flow transition inside the boundary layer adjacent to isothermal wall of natural convection flow in a cubical cavity. International Journal of Heat and Mass Transfer **167**, Article 120822 (2021). https://doi.org/10.1016/j.ijheatmasstransfer.2020.120822
23. Zhai, Z. (John): Computational Fluid Dynamics for Built and Natural Environments. Springer, p. 263 (2020)
24. Orlova, N., Alyokhina, S.: Identification of the flow parameters of separation area near the building corner. International Journal of Fluid Mechanics Research **48**(2), 47–54 (2021). interjfluidmechres.2021038345
25. Alyokhina, S., Orlova, N.: Framework for dataset development in building energy balance simulations. In: Modeling, Control and Information Technologies: Proceedings of VII International Scientific and Practical Conference, №7 (2024). https://doi.org/10.31713/MCIT.2024.065

Spatial–Angular Distribution of Aerodynamic Coefficients and Static Pressure on Residential Building Facades Under Wind Flow

Andrii Kostikov[1], Natalya Orlova[1(✉)], and Svitlana Alyokhina[2]

[1] Anatolii Pidhornyi Institute of Power Machines and Systems of the National Academy of Sciences, Vul. Komunalnykiv 2/10, Kharkiv 61046, Ukraine
naorl@ukr.net

[2] University of Applied Sciences Technikum Wien, Höchstädtplatz 6, 1200 Vienna, Austria

Abstract. The problem of energy-efficient reconstruction of the housing stock is particularly relevant in the context of damaged urban infrastructure. This study aims to establish a quantitative relationship between experimentally measured aerodynamic pressure coefficients and numerically simulated static pressure on façades of residential buildings with different orientations to the airflow. This provides a basis for constructing spatial–angular wind load maps, which are necessary for predicting heat losses and implementing adaptive façade heating. The novelty of the research lies in the integrated methodology that combines field experiments with numerical simulations to analyze the relationship between aerodynamic coefficients and static pressure. Verification of the CFD model against experimental data significantly improved its reliability and allowed the transition from conventional averaged normative values to detailed façade-specific wind load mapping. The practical significance of the work consists in the development of a methodology for generating spatial–angular wind load maps, enabling precise identification of infiltration heat-loss zones and determination of the most vulnerable façade areas. This creates a foundation for targeted modernization and the design of adaptive heating systems, ultimately increasing the energy efficiency of residential buildings.

Keywords: Airflow · Static Pressure · Aerodynamic Coefficient · Building Facade

1 Introduction

In the modern conditions of urban infrastructure damage resulting from military conflict, the energy-efficient reconstruction of the affected residential buildings has become a critical priority. A significant contributor to thermal losses in buildings is air infiltration through the building envelope, which is strongly influenced by the spatial and angular distribution of wind loads. Accurate quantitative assessment of these effects necessitates consideration of the aerodynamic pressure coefficient ($\overline{P}$) and the static pressure (P_{stat}), as these parameters directly govern the interaction between wind and building facades.

H. Altenbach et al. (Eds.): CAMPE 2025, LNME, pp. 33–42, 2026.
https://doi.org/10.1007/978-3-032-16381-3_4

2 Literature Review

The analysis demonstrates the relevance of applying combined experimental and numerical methods for simulating airflow around buildings. In [1, 2], CFD simulations of airflow over high-rise residential buildings at heights ranging from 0.9 m to 2.2 m were conducted to characterize turbulent flow. However, these studies do not specify the dependence of the aerodynamic pressure coefficient and static pressure on the angle of attack, flow velocity, and facade orientation, which limits the applicability of the results for adaptive design. In [3, 4], wind loads on buildings with various geometries, including skyscrapers and complex-shaped structures, were analyzed, and the wind energy potential in dense urban areas was assessed. Nevertheless, there is no comparison of the obtained coefficients with full-scale measurements, and the effects of extreme wind loads and changes in flow direction are only partially investigated. Works [5, 6] include experimental and numerical results for high-rise buildings, examining mean pressure values, natural ventilation mechanisms, and internal airflow. However, the integration of aerodynamic coefficients with facade thermal losses and infiltration remains insufficient. In [7, 8], data on pressure distribution over historical and high-rise structures are presented, including an analysis of aerodynamic effects on local facade elements. Yet, transitional regimes during wind direction changes are only limitedly studied. In [9, 10], CFD models of complex terrain and urban layouts were developed, considering the influence of building density on aerodynamics. Spatial pressure gradients relative to facade surfaces remain underexplored. Studies [11, 12] investigate the impact of balcony and facade geometry on natural ventilation and thermal comfort, but a direct integration with the assessment of whole-building thermal losses is lacking. In [13, 14], comparisons between aerodynamic experiments and CFD simulations were conducted; however, extreme wind loads and their influence on internal airflow are not addressed. Works [15, 16] utilize cloud-based platforms and large-scale LES simulations to evaluate aerodynamic coefficients and internal airflow. The limitation of these studies is the insufficient assessment of changes in aerodynamic coefficients under angled building configurations and real urban conditions. Studies [16–19] analyze pressure distribution and wind speed variation in urban environments. Nevertheless, the comparison of CFD models with actual measurements is limited, and the effects of microclimatic conditions and air humidity on facade thermal losses are almost entirely neglected.

Thus, the reviewed research demonstrates significant progress in modeling wind effects, pressure characteristics, and internal airflow. At the same time, there remains a critical need for a comprehensive study of the interrelationship between aerodynamic coefficients and static pressure as functions of flow velocity and wind incidence angle, to enable adaptive regulation of heating systems, particularly for residential buildings with variable facade orientations and complex geometries.

The aim of this study is to quantitatively determine the relationship between experimentally obtained aerodynamic pressure coefficients and numerically simulated static pressure on the facades of residential buildings with different orientations relative to the airflow. This analysis is essential for generating spatial-angular maps of wind loading, which are applied in the prediction of thermal losses and adaptive facade heating.

3 Research Methodology

The study is based on two interrelated stages:

experimental determination: data obtained in [20] using a wind tunnel test of a dense urban model were used to generate spatial fields of airflow velocity in the interbuilding environment. Within the present study, these data were systematically processed and grouped according to building height levels and geometric positioning. This approach allowed the formation of generalized relationships for evaluating the local distribution of the aerodynamic pressure coefficient near facades, which serves as a basis for subsequent CFD calculations;
numerical simulation of P_{stat}: a CFD model was used to simulate airflow around the same buildings. The model was chosen based on [21] and near the corners was used methodology described in [22]. The spatial distribution of static pressure on the building envelope was calculated under equivalent velocity and flow incidence conditions.

The results of the P_{stat} analysis are applied to construct pressure distribution maps, which can serve as a basis for assessing infiltration loss zones and managing facade-based heating. The aerodynamic pressure coefficient, in turn, is used to identify aerodynamically active areas of the facade that are subject to maximum local flow impact and may require additional protection or adaptation of building envelope elements.

3.1 Experimental Study

The value adopted as the aerodynamic pressure coefficient is

$$\overline{P} = 2 \cdot P_{exp}/\rho \cdot U_0^2$$

where P is the local value of absolute pressure on the envelope surface, Pa; P_{exp} is the excess pressure, Pa; ρ is the air density at the considered pressure and temperature, kg/m3; U_0 is the wind flow velocity, m/s. Figure 1 presents the variation of the aerodynamic coefficient in five planar sections located at the height of: 0; 0.286; 0.571; 0.857; and 1.0. The main characteristics of the airflow impinging on a flat surface were determined under conditions of a jet flow emerging from a nozzle $\overline{h} = h_{fl}/2 \cdot b$, $\overline{x} = x_i/2 \cdot b_0$, where $2b_0$ is the jet width, x_i is the cross-section position, and h_{fl} is the measured distance (m), h_{fl} - the axial distance from the nozzle exit, m. The value $\overline{P}$ was obtained by dividing the pressure measured at the i-th point by the total pressure of the decelerated flow at U = 21.2, m/s. The cross-section at $\overline{h} = 0{,}286$ passes through the point of complete flow stagnation $\overline{P} = 1{,}0$. As shown in Fig. 1, the character of the pressure variation $\overline{P}$ differs somewhat from that observed for an impinging jet on a flat plate. In the vicinity of point "0", the variation $\overline{P}$ is similar to that of the jet impingement case; however, after reaching $\overline{P} = 0.9$, most cross-sections exhibit a region with an almost constant value of $\overline{P}$. In this case, the distribution for different sections $\bar{x} \approx 0.35$ ($\overline{h} = 0$; ; 0.38; 0.286; 0.571; 1.0).

When $\bar{x} > 0.35$ a reduction is observed across all sections, caused by the end of the wall and, consequently, by the change in the direction of the airflow. In this case, there exists an air stream generated by wind load along the wall surface (an accelerating flow with a negative pressure gradient near the wall) and its deflected motion of the airflow beyond the building boundary.

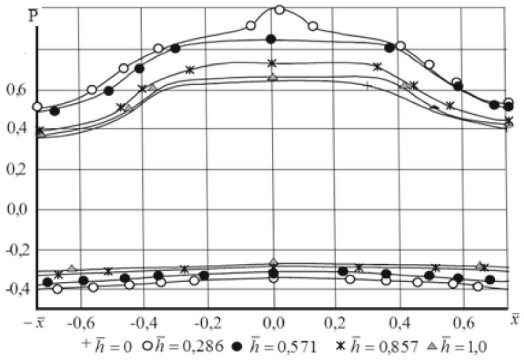

Fig. 1. Variation of relative pressure on the windward and leeward surfaces of the building under impinging airflow conditions.

Considering the high level of $\overline{P}(\overline{x})$ under constant barometric pressure of the surrounding environment, it can be interpreted at each local point as stagnation pressure in the normal component of the velocity vector U at the section $\overline{x}$.

A generalization of experimental wind-tunnel data on a dense urban block model (according to [20]) made it possible to identify patterns of aerodynamic coefficient variation on building surfaces depending on facade height and orientation. The highest coefficient values, up to 1.0, are recorded at stagnation points on the windward side under perpendicular impingement ($\varphi = 90°$), corresponding to the local transformation of dynamic pressure into static pressure under normal airflow impact. With increasing distance from the center of impingement, $\overline{P}(\overline{x})$ decrease to 0.5 and lower due to flow diversion and deflection toward the roof. On lateral and leeward surfaces, stable negative values of $\overline{P}(\overline{x})$ down to –0.6 are recorded, which corresponds to separated flow regions with the formation of low-pressure zones. Such pressure reduction indicates the dominance of reverse flows and local turbulent structures, which can be used for predicting zones of infiltration heat losses.

Thus, the revealed pattern of spatial distribution of $\overline{P}(\overline{x})$ confirms that at points of local maximum pressure, the dynamic pressure is fully transformed into static pressure, and these zones can be identified as key for assessing wind influence on infiltration heat losses. Analysis of $\overline{P}(\overline{x})$ as a function of attack angle and wall height provides a substantiated basis for further calculation of static pressure and its inclusion in models of facade-based heat supply regulation.

3.2 CFD Modeling

Numerical modeling of P_{stat} is performed to transition from a local assessment of peak loads $\overline{P}(\overline{x})$, obtained experimentally, to a comprehensive spatial characterization of pressure, relevant for the analysis of infiltration heat losses and the control of facade-based heating systems. When the airflow impinges on the building surface, flow deceleration occurs; in this case, the velocity of the main stream at the wall is reduced to zero, and, as a consequence, the dynamic pressure is transformed into static pressure. A relationship

is thus established between the static pressure and the parameters of the external air.

$$P^{N}_{stat} = f(U^{N}, \varphi^{N}, H) \text{ at } U = f(t)$$

where P^N – static pressure at point N; U^N – velocity of the incoming airflow at point N; φ^N – angle of incidence of the airflow at point N; H – height at which point N is located.

In this study, numerical simulations were carried out to evaluate the distribution of static pressure along the building height for 37 individual façade surfaces. The simulations were performed for wind velocities of 2 m/s and 5 m/s, and for three representative inflow directions (0°, 45°, and 90°), thereby encompassing a broad range of boundary conditions relevant to real operating environments of buildings. For each façade surface, the pressure–height dependence was approximated using a quadratic regression fit of the form:

$$P_{stat} = C + B \cdot H + A \cdot H^2$$

where A, B, C– polynomial regression coefficients obtained from multifactor analysis. Figures 2–4 present the results of airflow simulations around the building at incident angles of 0°, 45°, and 90° for wind speeds of 2 m/s and 5 m/s.

Changing the airflow direction to 45° leads to a redistribution of pressures between two adjacent façades. Zones of elevated static pressure emerge near the building corner (sides 1 and 2). This flow direction results in an asymmetric distribution of aerodynamic loading and a more complex turbulent wake behind the building. At an incident airflow angle of 0°, a zone of maximum positive static pressure forms on the windward façade (side 1), reaching critical values as the wind speed increases to 5 m/s. On the leeward side of the building, a low-pressure area develops, with pronounced gradients between the windward and leeward façades. This indicates a clearly symmetric flow pattern dominated by frontal pressure forces. The maximum concentration of static pressure occurs on the side facing the airflow, which may cause intensified infiltration (wall 1) and potential air leakage on wall 19, located within the suction zone. Such a distribution generates a vectorized flow through the building, significantly affecting internal thermal dynamics.

At an incident angle of 90°, the airflow bypasses the building's end faces (sides 1 and 19). At 2 m/s, the highest loading occurs on sides 2, 4, and 6–18 (see Fig. 3).

Pressure is distributed relatively evenly along the façade, but a noticeable turbulent low-pressure zone appears on the opposite side. In the case shown in Fig. 4c and 4d, at 5 m/s, pressures increase significantly, consistent with the quadratic dependence of pressure on height. The suction on the leeward side becomes deeper and more widespread. The lateral façades remain in an aerodynamically neutral zone, which reduces the risk of localized infiltration but may create an internal pressure differential between the ends, potentially inducing drafts along the building's axis.

As shown in Figs. 2–4, at a wind speed of 2 m/s, the static pressure distribution on building surfaces is complex and non-uniform. Increasing the wind speed proportionally raises both positive and negative pressures. The results emphasize the importance of considering the wind incidence angle for ensuring energy efficiency and resilience to wind loads.

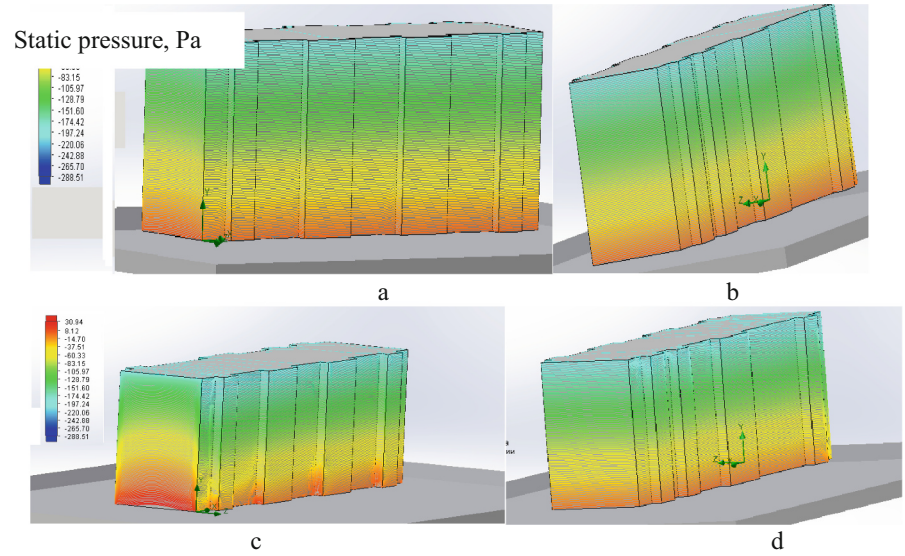

Fig. 2. Results of airflow simulation around the building at an incident angle of 0° for wind speeds of 2 m/s (a, b) and 5 m/s (c, d).

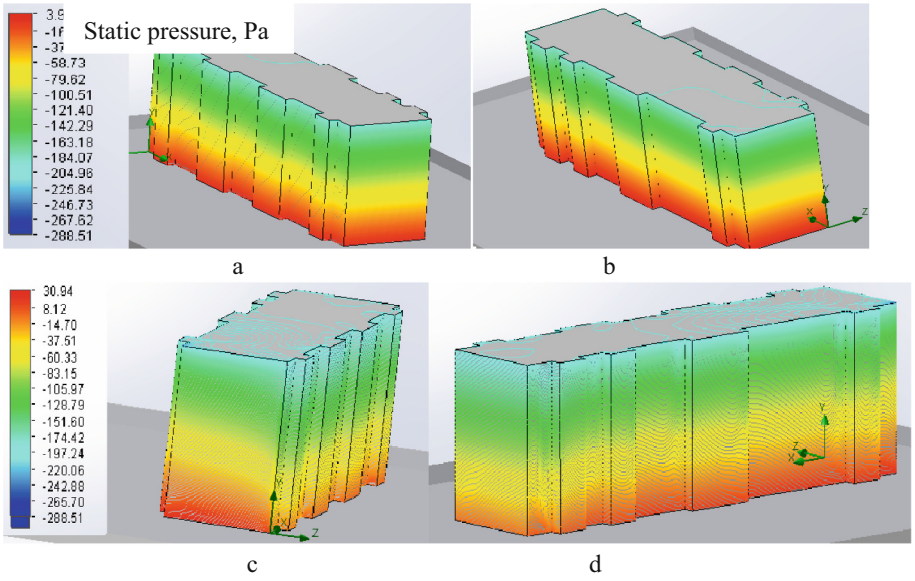

Fig. 3. Results of airflow simulation around the building at an incident angle of 45° for wind speeds of 2 m/s (a, b) and 5 m/s (c, d).

As a result of the simulation of the air boundary layer thickness distribution on the building's exterior walls under variable flow conditions – depending on height, flow

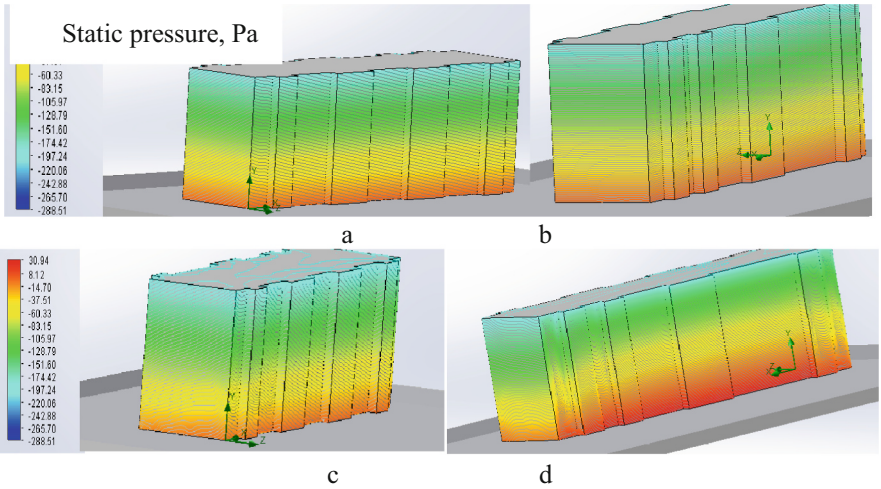

Fig. 4. Results of airflow simulation around the building at an incident angle of 90° for wind speeds of 2 m/s (a, b) and 5 m/s (c, d).

incidence angle (0°, 45°, 90°), and wind speed (2 m/s and 5 m/s) − approximation functions were obtained for each of the 36 building façades, along with the model coefficients A and B, the maximum deviation $ä_{max}$, and the root-mean-square deviation δ^2.

4 Results and Discussion

Based on the obtained results, an analysis of the influence of wind speed and incidence angle on the coefficient C of the polynomial model, as a function of wind speed V and angle φ, , was performed. A two-factor analysis of variance with repetitions was applied to 216 experimental points. The analysis revealed that both wind speed and incidence angle have a statistically significant effect on the coefficient C. Moreover, the interaction between these factors also exerts a significant influence. The coefficient C of the static pressure model exhibits a nonlinear variation as a function of wind speed (U) and angle (φ).

$$P_{stat} = Cf\,(U, \varphi^\circ) + B \cdot H + A \cdot H^2$$

After performing a multifactor regression analysis to model the coefficient C, the obtained coefficient of determination was $R^2 = 0.60$, indicating that the model explains approximately 60% of the variance. This represents an acceptable level of accuracy for tasks related to the wind flow around buildings. Simultaneously, the discrepancies between the observed and predicted values were evaluated.

The initial model was constructed for the normalized value Z_C according to the mean statistical value of the sample $\overline{C} = 1.74$, with a standard deviation $\delta\,C = 8.497$. Reverse normalization was then performed, resulting in an analytical expression for

C: $Z_C = (C_i - \overline{C})/\sigma C$ or $C_i = Z_C \cdot \sigma C + \overline{C}$. The distribution of the normalized Z_C coefficient is characterized by a monotonic increase and symmetry near the mean values, with a moderate left-sided asymmetry. Within 90% of the population, the Z_C value is in the interval [−2.5; 1.5], which indicates the stability of the main part of the data, with the presence of individual extreme values. A significant portion of the data lies in the interval [−0.5; 0.5], but the presence of observations with $Z_C > 2$ indicates the influence of local flow areas (corner regions) that are difficult to account for in a linear model. This explains the moderate accuracy of the constructed model, where $R2 \approx 0.6$. Based on the statistical analysis to determine the nature of the variation and to generalize the value of the coefficient B, the following results were obtained: $\overline{B} = -12.4325$, $\delta B^2 = 0.888$, minimum value $B = -16.9065$, maximum value -9.7801. To determine the value of coefficient A, a multi-parameter regression analysis was performed based on 216 experimental observations. The regression results demonstrated a high level of agreement between the model and the empirical data: the coefficient of determination is $R2 = 0.715$. The value of the Fisher criterion is $F = 57.35$, which indicates that the variation explained by the regression model significantly exceeds the unexplained variance. The low value of the probability of a type I error, $p = 2.54 \times 10^{-5}6$, means that the probability of obtaining such an F-criterion value by chance is practically zero. Thus, the model is valid for practical application in predicting the value of coefficient A.

$$A = -0.0009455 - 0.0002098 \cdot U \cdot \phi + 3.18588 \cdot 10^{-6} \cdot \phi^2 + 0.00001506 \cdot U^2 +$$
$$0.23461 \cdot (\ln U \cdot Zn) + 0.000104476 \cdot (\phi \cdot Zn) + 5.39449 \cdot 10^{-6} \cdot Zn + 0.0022 \cdot Bh + 0.01232Fb$$

As part of the study on the influence of building geometric parameters on coefficient A, a classification system for façade zones was implemented. Each type of zone was assigned a numerical code: lateral zone Bh – 1; rear zone (; frontal balcony Fb – 3. It was found that the most reliable models (with $R^2 > 0.6$) were obtained for angles of 0° and 90°, where the airflow around the building is either symmetrical or uniformly distributed. However, at 45°, a special methodology is needed to account for the complex geometry and increased pressure gradients.

Therefore, the models and statistical characteristics obtained provide the basis for building an integrated predictive system to calculate static pressure, taking into account key meteorological and geometric parameters.

5 Conclusions

The comparison of numerical modeling data and experimental measurements confirms the qualitative agreement of the spatial pressure distribution on building facades under different angles of airflow incidence. Experimental values of the aerodynamic pressure coefficient, obtained in the study conducted in [20] using a wind tunnel model of the building layout, were used for comparison and accuracy assessment of the numerical results. The aerodynamic coefficient at frontal incidence ($\varphi = 90°$) indicates a maximum value in the stagnation zone, extending at a height of $z/H = 0.286$. On the lateral walls, the coefficient decreases to –0.7, and on the leeward side to –0.4. Numerical modeling results

of the static pressure (P_{stat}) under similar conditions exhibit a corresponding distribution: P_{stat} reaches + 32.4 Pa at the stagnation points and –26.7 Pa in the suction zones. In contrast, P_{stat} operates in absolute pressure units, allowing for direct identification of critical infiltration zones and estimation of potential thermal losses with high spatial accuracy. Thus, for further analysis of building heat consumption and heating regulation, it is more appropriate to use P_{stat}, as this parameter: has a clearly defined physical interpretation as the normal component of the total pressure; can be directly associated with the magnitude of air exchange through gaps; allows the construction of infiltration maps for each facade plane without normalization.

In subsequent studies, it is advisable to use P_{stat} as the primary parameter for developing models of thermal losses, adaptive zonal heating, and evaluating the effectiveness of design solutions in damaged urban areas.

References

1. Hubová, O., Macák, M., Franek, M., Lobotka, P., Bujdáková Konečná, L., Ivánková, O.: Numerical analysis of wind effects on a residential building with a focus on the linings, window sills, and lintel. Buildings **13**(1), 183 (2023). https://doi.org/10.3390/buildings13010183
2. Shirzadi, M., Tominaga, Y.: CFD evaluation of mean and turbulent wind characteristics around a high-rise building affected by its surroundings. Build. Environ. **225**, 109637 (2022). https://doi.org/10.1016/j.buildenv.2022.109637
3. Wen, J., Fan, Z., Liu, J.: Effects of complex skyscraper geometries on wind energy potentials of high-density urban central business district: a case study of the Lujiazui blocks. Sustain. Cities Soc. **124**, 106287 (2025). https://doi.org/10.1016/j.scs.2025.106287
4. Alsailani, M., Montazeri, H., Rezaeiha, A.: Towards optimal aerodynamic design of wind catchers: impact of geometrical characteristics. Renewable Energy **168**, 1344–1363 (2021). https://doi.org/10.1016/j.renene.2020.12.053
5. Yang, B., Zhu, H., Zhang, Q., Wüchner, R., Sun, S., Qiu, J.: Identification of wind loads on a 600 m high skyscraper by Kalman filter. Journal of Building Engineering **63**(A), 105440 (2023). https://doi.org/10.1016/j.jobe.2022.105440
6. Zhang, X., Weerasuriya, A.U., Tse, K.T.: CFD simulation of natural ventilation of a generic building in various incident wind directions: comparison of turbulence modelling, evaluation methods, and ventilation mechanisms. Energy and Buildings **229**, 110516 (2020). https://doi.org/10.1016/j.enbuild.2020.110516
7. Wehrle, J., Jung, C., Giometto, M., Christen, A., Schindler, D.: Introducing new morphometric parameters to improve urban canopy air flow modeling: a CFD to machine-learning study in real urban environments. Urban Climate **58**, 102173 (2024)
8. Liu, W., Mattsson, M., Widström, T., Claesson, L.: Wind tunnel and numerical study of wind pressure coefficients on a medieval Swedish church. Build. Environ. **264**, 111905 (2024). https://doi.org/10.1016/j.buildenv.2024.111905
9. Kikuchi, T., et al.: Comparison of wind pressure coefficients between wind tunnel experiments and full-scale measurements using operational data from an urban high-rise building. Build. Environ. **252**, 111244 (2024). https://doi.org/10.1016/j.buildenv.2024.111244
10. Zheng, X., Montazeri, H., Blocken, B.: Large-eddy simulation of pollutant dispersion in generic urban street canyons: guidelines for domain size. J. Wind Eng. Ind. Aerodyn. **211**, 104527 (2021). https://doi.org/10.1016/j.jweia.2021.104527

11. Izadyar, N., Miller, W., Rismanchi, B., Garcia-Hansen, V.: A numerical investigation of balcony geometry impact on single-sided natural ventilation and thermal comfort. Build. Environ. **177**, 106847 (2020). https://doi.org/10.1016/j.buildenv.2020.106847
12. Du, Y., Blocken, B., Abbasi, S., Pirker, S.: Efficient and high-resolution simulation of pollutant dispersion in complex urban environments by island-based recurrence CFD. Environ Model Softw. **145**, 105172 (2021)
13. Karrar, W., Aliewi, J.M., Al Hashimi, S.: Comparison of pressure results between wind tunnel and CFD simulation for university baghdad tower building. International Journal of Modern Research in Engineering and Technology **5**(2), (2020). https://www.ijmret.org/paper/V5I2/05021130.pdf
14. Abdellatif, H.R., El-Shorbagy, E.B.S.: CFD-Based evaluation of elevated coastal residential buildings under hurricane wind loads. Journal of Architectural Engineering **27**(3) (2022). https://doi.org/10.1061/(ASCE)AE.1943-5568.0000472
15. Sakiyama, N.R.M., de Matos, A.M.H., de Souza, F.C.F.F.G.M., Gomes, C.M.A.F.: A cloud-based platform to predict wind pressure coefficients on buildings. Buildings **12**(2), 132 (2022). https://doi.org/10.3390/buildings12020132
16. Hirose, C., Ikegaya, N., Hagishima, A., Tanimoto, J.: Indoor airflow and thermal comfort in a cross-ventilated building within an urban-like block array using large-eddy simulations. Build. Environ. **196**, 107811 (2021)
17. Guo, Q., Meng, X., Li, Y., Lv, X., Liu, C.: A prediction model for the surface residual subsidence in an abandoned goaf for sustainable development of resource-exhausted cities. J. Clean. Prod. **279**, 123803 (2021). https://doi.org/10.1016/j.jclepro.2020.123803
18. Amini, M., Memari, A.M.: CFD-based evaluation of elevated coastal residential buildings under hurricane wind loads. Journal of Architectural Engineering **27**(3) (2021)
19. Bre, F., Gimenez, J.M.: A cloud-based platform to predict wind pressure coefficients on buildings. Build. Simul. **15**, 1507–1525 (2022). https://doi.org/10.1007/s12273-021-0881-9
20. Ivankova, O., Hubová, O., Macák, M., Vojtekova, E.: Wind pressure distribution on the façade of stand-alone atypically shaped high-rise building determined by CFD simulation and wind tunnel tests. Designs **6**(5), 77 (2022). https://doi.org/10.3390/designs6050077
21. Zhai, Z.: Computational Fluid Dynamics for Built and Natural Environments. Springer, p. 263 (2020)
22. Orlova, N., Alyokhina, S.: Identification of the flow parameters of separation area near the building corner. International Journal of Fluid Mechanics Research **48**(2), 47–54 (2021). interjfluidmechres.2021038345.

Energy Saving Technologies and Environmental Safety

Magnetic Silence of an Uncertain Technical Object as a Geometric Inverse Problem of Magnetic Static's

Borys Kuznetsov[1](✉), Ihor Bovdui[1], Konstantin Chunikhin[1], Olena Voloshko[1], and Tetiana Nikitina[2]

[1] Anatolii Pidhornyi Institute of Power Machines and Systems of the National Academy of Sciences of Ukraine, Komunalnykiv Street 2/10, Kharkiv 61046, Ukraine
kuznetsov.boris.i@gmail.com

[2] Bakhmut Education Research and Professional Pedagogical Institute V.N. Karazin, Kharkiv National University, 9a, Nosakov Street, Bakhmut 84511, Ukraine

Abstract. Ensuring technical objects magnetic silence (TOMS) is an important practical problem when designing new types of equipment and technologies, the requirements for electromagnetic compatibility of technical means, as well as issues of magnetic ecology. The study proposes robust prediction and control TOMS method based on geometric inverse magnetostatics problems solution (GIMSPS) using initial magnetic field (MF) compensation with magnetic characteristics uncertainty (MCU). Geometric forward magnetostatics problems solution (GFMSPS) to calculate TOMS with initial magnetic field sources (IMFS) or compensating units known coordinates and these IMFS or compensating units MF multipole coefficients values. Mathematical model (MM) of TOMS for GFMSPS calculated based on Laplace equation solutions (LES) in spherical coordinate system (SCS), prolate spheroidal coordinate systems (PSCS) and Cartesian coordinate systems (CCS). Both prediction and control GIMSPS are reduced to multi-objective nonlinear minimax optimization problems solutions (MONMMOPS). Both vector nonlinear objective function (VNOF) of MONMMOPS calculated based on LES for scalar potential (SP) of MF of TOMS with MCU using COMSOL Multiphysics software. Both MONMMOPS calculated from Pareto optimal solutions (POS) with binary preference relations (BPR) by hybrid heuristic multi-swarm optimization algorithm (HHMSOA). Results of prediction TOMS far MF based on near MF measurements and compensation of initial MF with MCU for ensuring TOMS given to demonstrate the performance of the proposed methodology.

Keywords: Technical Objects · Magnetic Silence · Prediction · Control · Geometric Inverse Magnetostatics Problem · Uncertainty

1 Introduction

When design new types of equipment and technologies, the requirements for electromagnetic compatibility of technical means as well as issues of magnetic ecology occupy a central place in the study and development of methods for purposefully changing the

H. Altenbach et al. (Eds.): CAMPE 2025, LNME, pp. 45–54, 2026.
https://doi.org/10.1007/978-3-032-16381-3_5

external quasi-stationary MF of complex technical objects (TO) outside their shell [1–3]. To ensure the specified accuracy of orientation and control of spacecraft in orbit, an urgent task is to reduce external MF [4, 5]. External MF level also strictly regulated and naval vessel and submarines is main operational characteristics [6].

2 Literature Review

The design of TO with a normalized level of external MF based on three-dimensional quasi-stationary external MF MM created TO outside its shell [7–9]. Currently, when describing the external MF of technical objects, multipole models are mainly used [5].

To ensure a given TOMS, two interrelated GIMSPS solved – prediction and control of TOMS [6]. These both GIMSPS based on GFMSPS – TOMS MF MM calculation generated by its IMFS with known spatial location coordinates and known magnetic characteristics.

TOMS predicting problem is GIMSPS as result of which TOMS MF MM designed based on real TOMS measurements results. IMFS spatial location coordinates and magnetic characteristics calculated. TO resulting MF coincides with actually measured MF.

TOMS control problem is also GIMSPS which result is compensating IMFS spatial location coordinates and magnetic characteristics calculated to ensure TOMS specified requirements.

Naturally, in the course of these both GIMSPS, it is necessary to solve the corresponding GFMSPS many times.

In [4–9] work, TO magnetic characteristics are considered to be precisely known and do not change during the work process. In reality, TO magnetic characteristics depend on their operation modes and change significantly during operation and are MCU [10–14].

The goal of the work is to develop a method for controlling TOMS improving by solving GIMSPS, taking into account TOMS MCU.

3 Research Methodology

TO is a complex electromagnetic system. TO three-dimensional quasi-stationary (TDGS) external MF MM it is advisable spatial harmonic analysis methods (SHAM) used [15–17]. SHAM used to external TO MF control allows to simplify TO MF MM based on harmonic approximation used in multipole coefficients set form [5].

Such mathematical modeling of the MF of a TO allows not only to simplify the calculation of the MF, but also to simplify experimental measurements of parameters of the model of the MF of a TO. In particular, it is possible to directly experimentally measure the spatial harmonics of the external MF of TO based on measuring the MF strength of TO and calculating the multipole coefficients of their spatial harmonics.

The most widespread practical application has found the use of spherical basis solutions of LES, the history of which comes from Gauss representation of the geomagnetic field. The MF strength of a technical object is calculated as the sum of the strengths from

spherical spatial harmonics (SSH) in spherical coordinate system (SCS), taken with the corresponding multipole coefficients:

$$H_r = \sum_{n=1}^{\infty} \sum_{m=0}^{n} \frac{n+1}{r^{n+2}} \left\{ g_n^m \cos m\phi + h_n^m \sin m\phi \right\} \cdot P_n^m(\cos\theta) \tag{1}$$

$$H_\theta = -\sum_{n=1}^{\infty} \sum_{m=0}^{n} \frac{1}{r^{n+2}} \left\{ g_n^m \cos m\phi + h_n^m \sin m\phi \right\} \frac{dP_n^m(\cos\theta)}{d\theta} \tag{2}$$

$$H_\phi = \sum_{n=1}^{\infty} \sum_{m=0}^{n} \frac{m}{r^{n+2}} \left\{ g_n^m \sin m\phi - h_n^m \cos m\phi \right\} \frac{P_n^m(\cos\theta)}{\sin\theta} \tag{3}$$

where $P_n^m(\cos\ \theta)$ – degree n first kind and order m Legendre polynomials;

r, θ, φ – spherical coordinates of the observation point; g_n^m and h_n^m – values of multipole harmonic coefficients.

SHAM application based on MF harmonic composition study. This application result is transition from MF vector measured values to MF harmonics integral characteristics – multipole coefficients. Then MF described based on multipole coefficients values obtained. MF description accuracy depends both on multipole coefficients determining accuracy themselves and spatial harmonics number used of MF source function expansion. For specific problem conclusion made about spatial harmonics qualitative and quantitative composition, which multipole coefficients would provide solution required accuracy.

Thus, SHAM is universal tool for quasi-stationary describing MF regardless of source nature. From the main provisions of such SHAM it follows that choice of both type of basic solutions and coordinate system depends on specific conditions of problem being solved. This makes it possible MF analytically describe for TO wide class and TO measuring apparatus for selected basic solutions practical used.

MF source simplest model is dipole with initial magnetic moment (IMM) components M_{nx}, M_{ny}, M_{nz} in CCS with coordinates (x_n, y_n, z_n), In this case, series (1)–(3) take into account first-order harmonics. Let us imagine TO MF MM in N dipoles form with IMM M_{nx}, M_{ny}, M_{nz} located at points with coordinates (x_n, y_n, z_n). All TO elements undergo strict control for TOMS. All TO elements IMM M_{nx}, M_{ny}, M_{nz} measured before installation and TOMS stringent requirements satisfy.

TO MF components B_{KX}, B_{KY}, B_{KZ} at space any point P_k with coordinates x_k, y_k, z_k in multiple magnetic dipole models (MMDM) form with IMM M_{nx}, M_{ny}, M_{nz} of N dipole located at TO space points with coordinates (x_n, y_n, z_n), calculated [17]

$$\begin{bmatrix} B_{KX} \\ B_{KY} \\ B_{KZ} \end{bmatrix} = \mu_0 \sum_{n=1}^{N} \frac{1}{4\pi r'^5} \begin{bmatrix} 2x'^2 - y'^2 - z'^2 & 3x'y' & 3x'z' \\ 3x'y' & \cdots & 3y'z' \\ 3x'z' & 3y'z' & 2z'^2 - y'^2 - x'^2 \end{bmatrix} \cdot \begin{bmatrix} M_{nx} \\ M_{ny} \\ M_{nz} \end{bmatrix}. \tag{4}$$

TOMS strict requirements imposed MF description accuracy near TO, when TOMS problems solving for magnetic orientation and TOMS ensuring spacecraft magnetic silence means developing. SP spherical expansion for MF TO with predominant overall size does not enable TOMS MF description near their surface. Extended shape TO MF most advisable SHAM in PSCS used, where coordinate surfaces shape makes it possible to bring description region of MF closer TO itself surface.

PSCS feature is parameter c used, which linear scale determines for all three coordinates ξ, η, φ unit vectors

$$\begin{aligned} x &= c \cdot \sqrt{\xi^2 - 1} \cdot \sqrt{1 - \eta^2} \cdot \boldsymbol{cos}(\phi); \\ y &= c \cdot \sqrt{\xi^2 - 1} \cdot \sqrt{1 - \eta^2} \cdot \boldsymbol{sin}(\phi); \Rightarrow \begin{array}{l} \xi \in [1,\ \infty]; \\ \eta \in [0,\ 1]; \\ \phi \in [0,\ 2\pi]; \end{array} \\ z &= c \cdot \xi \cdot \eta; \end{aligned} \tag{5}$$

where coordinates *x, y, z* in CCS, *c* – spheroid interfocal distance half.

Similar SSH MF determined as MF strength projections sum of prolate spheroidal spatial harmonics (PSSH)

$$H_\xi = -\frac{\sqrt{\xi^2 - 1}}{c\sqrt{\xi^2 - \eta^2}} \sum_{n=1}^{\infty} \sum_{m=0}^{n} \frac{dQ_n^m(\xi)}{d\xi} \left\{ c_n^m \cos m\phi + s_n^m \sin m\phi \right\} P_n^m(\cos\eta) \tag{6}$$

$$H_\eta = -\frac{\sqrt{1 - \eta^2}}{c\sqrt{\xi^2 - \eta^2}} \sum_{n=1}^{\infty} \sum_{m=0}^{n} Q_n^m(\xi) \frac{dP_n^m(\cos\eta)}{d\eta} \left\{ c_n^m \cos m\phi + s_n^m \sin m\phi \right\} \tag{7}$$

$$H_\phi = \frac{m}{c\sqrt{(\xi^2 - 1)(1 - \eta^2)}} \sum_{n=1}^{\infty} \sum_{m=0}^{n} Q_n^m(\xi) P_n^m(\cos\eta) \left\{ c_n^m \sin m\phi - s_n^m \cos m\phi \right\} \tag{8}$$

Consider TOMS prediction and control problems by GIMSPS. To solve GIMSPS, it is necessary to solve GFMSPS many times. GFMSPS is TO MF calculated based on IMFS or compensating units known coordinates and these IMFS or compensating units MF multipole coefficients values. GFMSPS accuracy depends both of multipole coefficients calculation accuracy and expansion used for spatial harmonics number original function. GIMSPS result is IMFS or compensating units coordinates and these IMFS or compensating units MF multipole coefficients values. GIMSPS results depend of GFMSPS MF MM choice. When MF MM in SCS using, spherical coordinates *r*, θ, φ – and spatial spherical harmonics g_n^m and h_n^m are sought parameters. When MF MM in dipoles set – MMDM in CCS form used, orthogonal coordinates (x_n, y_n, z_n) and dipoles IMM M_{nx}, M_{ny}, M_{nz} are required parameters. When MF MM in PSCS used spheroidal coordinates *r*, θ, φ – and spatial spheroidal harmonics g_n^m and h_n^m are required parameters.

Let us now consider prediction problem when TO MF MM design based on MF measurements in near zone for MF calculating in far zone. Such prediction MF MM is GIMSPS and called prediction TOMS.

Unlike works [4–9], we introduced TO units MCU vector **δ** in operation various modes [18–21]. Unlike works [1, 2], we consider TO MF MM, created not only by TO blocks dipoles, but also by quadrupoles and octupoles as TO spheroidal units [5].

Introduce this GIMSPS required parameters vector $\boldsymbol{X}_p$ with TO space blocks spatial arrangement coordinates and dipoles, quadrupoles and octupoles multipole harmonic coefficients values and these units spheroidal harmonics. Then, based on accepted TO MF MM it is possible vector $\boldsymbol{H}_c(\boldsymbol{X}_p,\boldsymbol{\delta})$ with predicted MF values at near MF given points calculated. Let's form a vector $\boldsymbol{H}_d(\boldsymbol{X}_p,\boldsymbol{\delta})$ with the squared difference between the vector $\boldsymbol{H}_C(\boldsymbol{X}_p,\boldsymbol{\delta})$ of the calculated MF and the vector $\boldsymbol{H}_C(\boldsymbol{X}_p,\boldsymbol{\delta})$ of actually measured values of MF of TO at given points of the near field

$$\boldsymbol{H}_d(\boldsymbol{X}_p,\boldsymbol{\delta}) = \boldsymbol{H}_m(\boldsymbol{\delta}) - \boldsymbol{H}_c(\boldsymbol{X}_p,\boldsymbol{\delta}) \tag{9}$$

Then, GIMSPS reduced to MONMMOPS by minimizing VNOF (9) with respect to required parameters vector $\boldsymbol{X}_p$, but by maximizing the same VNOF (9) with respect to vector $\boldsymbol{\delta}$ of MCU [22].

Consider TOMS control problem based on introduction of compensating units into TO space for original MF compensated. TO initial MF calculated based on a prediction MM by TOMS GIMSPS. Introduce required parameters vector $\boldsymbol{X}_s$ of this GIMSPS of TOMS with compensating units spatial location coordinates in TO space and spatial harmonic coefficients values these compensating units. Then, based on the designed prediction MF MM of TO, it is possible vector with compensating units values calculated. Let's form vector $\boldsymbol{H}_r(\boldsymbol{X}_s,\boldsymbol{\delta})$ with squares of sum of compensating MF vector $\boldsymbol{H}_s(\boldsymbol{X}_s,\boldsymbol{\delta})$ and TO initial MF vector $\boldsymbol{H}_C(\boldsymbol{X}_p,\boldsymbol{\delta})$, calculated from predicted MF values

$$\boldsymbol{H}_r(\boldsymbol{X}_s,\boldsymbol{\delta}) = \boldsymbol{H}_s(\boldsymbol{X}_s,\boldsymbol{\delta}) + \boldsymbol{H}_C(\boldsymbol{X}_p,\boldsymbol{\delta}) \tag{10}$$

GIMSPS for control TOMS of TO with MCU reduced to MONMMOPS calculated by minimizing VNOF (10) according to required parameters vector $\boldsymbol{X}_s$ of compensating units, but maximizing the same VNOF (10) according to vector $\boldsymbol{\delta}$ of MCU.

of TO [22].

These both prediction and control problems of TOMS of TO with MCU based on both GIMSPS reduced to both MONMMOPS with VNOF (9) and VNOF (10) by minimizing required parameters vector $\boldsymbol{X}_p$ of VNOF (9) or required parameters vector $\boldsymbol{X}_s$ of VNOF (10) of compensating units, including spatial coordinates and spatial harmonics of IMS or compensating units, but maximizing the same VNOF (9) and VNOF (10) according to vector $\boldsymbol{\delta}$ of MCU of TO. Both VNOF (9) and VNOF (10) calculated based on LES for SP of MF for TO with MCU using COMSOL Multiphysics software.

Thus, both GIMSPS solution taking into account MCU of TO reduced to both MONMMOPS with VNOF (9) and VNOF (10). This standard approach for robust systems design for worst case. Both MONMMOPS with VNOF (9) and VNOF (10) associated with both game in which both game payoff are VNOF (9) and VNOF (10). Desired parameters vector $\boldsymbol{X}_p$ or $\boldsymbol{X}_s$ is first player and its strategy is game payoff minimize. Vector $\boldsymbol{\delta}$ of MCU of TO is second player and its strategy is the same game payoff maximize. Moreover, since the game payoff are vectors, such games called multi-objective games with vector payoff or vector games by analogy with multi-objective optimization or vector optimization.

Both MONMMOPS with VNOF (9) and VNOF (10) calculated based on HHMSOA from POS with BPR [23].

When VNOF (9) and VNOF (10) calculated it is necessary for PP GIMSP desired parameters vector $\boldsymbol{X}_p$ and SP GIMSP desired parameters vector $\boldsymbol{X}_s$ minimum calculated. For this purpose VNOF (9) and VNOF (10) minimum calculated by PSO in following procedure. Particle i swarm j movement described by

$$x_{ij}(t+1) = x_{ij}(t) + v_{ij}(t+1) \tag{11}$$

where

$$\begin{aligned} v_{ij}(t+1) &= w_j v_{ij}(t) + c_{1j} r_{1j}(t) H\left(p_{1j} - \varepsilon_{1j}(t)\right) * \ldots \\ &\ldots * \left[y_{ij}(t) - x_{ij}(t)\right] + c_{2j} r_{2j}(t) H\left(p_{2j} - \varepsilon_{2j}(t)\right) * \ldots \\ &\ldots * \left[y_j^*(t) - x_{ij}(t)\right] \end{aligned} \tag{12}$$

Position $x_{ij}(t)$ and velocity $v_{ij}(t)$ vectors components of swarm j particle i for VNOF (9) and VNOF (10) minimum for PP GIMSP desired parameters vector $\boldsymbol{X}_p$, and SP GIMSP desired parameters vector $\boldsymbol{X}_s$ calculated.

To improve convergence in nearly stationary region, second-order methods (SOM) used, which the of objective function second derivatives matrix Hessian matrix used. SOM compared with first-order methods, allow for effective solution in a region close to optimal point, when gradient vector components have sufficiently small values. Recently Levenberg-Marquardt algorithms have become widespread in quasi-Newton methods. Hessian matrix replaced with positive coefficient matrix. Then linear equations system used

$$\boldsymbol{J}(\boldsymbol{F}(\boldsymbol{x}_k))\boldsymbol{J}(\boldsymbol{F}(\boldsymbol{x}_k))^T \boldsymbol{d}_k + \lambda_k \boldsymbol{d}_k + \boldsymbol{J}(\boldsymbol{F}(\boldsymbol{x}_k))\boldsymbol{F}(\boldsymbol{x}_k) = 0 \tag{13}$$

Jacobian matrices $\boldsymbol{J(F(x}_k\boldsymbol{))}$ components along vectors $\boldsymbol{X}_p$ for VNOF (9) or along vectors $\boldsymbol{X}_c$ for VNOF (10) calculated from particle i of swarm j movement velocities $v_{ij}(t)$.

From which recurrent Eq. (9) obtained for desired parameters vector iteratively finding

$$\boldsymbol{x}_{k+1} = \boldsymbol{x}_k + \alpha_k \boldsymbol{d}_k \tag{14}$$

Maximizing VNOF (9) and VNOF (10) according to vector $\boldsymbol{\delta}$ of MCU of TO are calculated similarly (11)–(14).

In conclusion, we note that GIMSPS (9) and (10) are often solved using least squares method (LSM) and without MCU. For prediction GFNSP prediction MF vector $\boldsymbol{H}_c$ calculated in linear dependence form

$$\boldsymbol{H}_c = \boldsymbol{A}\boldsymbol{X}_p \tag{15}$$

Matrix $\boldsymbol{A}$ all elements calculated by GFMSPS process based on (1)–(8).

Equations (15) number usually exceeds unknowns elements vectors $\boldsymbol{X}_p$ number and this linear equations over determined system calculated by generalized LSM. Introduce discrepancy vector $\boldsymbol{H}_d(\boldsymbol{X}_p)$ between measured MF vector $\boldsymbol{H}_m$ and predicted by model (15) MF vector $\boldsymbol{H}_c(\boldsymbol{X}_p)$

$$\boldsymbol{H}_d(\boldsymbol{X}_p) = \boldsymbol{H}_m - \boldsymbol{H}_c(\boldsymbol{X}_p) = \boldsymbol{H}_m - \boldsymbol{A}\boldsymbol{X}_p \tag{16}$$

LSM objective function wrote as squared discrepancy vector $\boldsymbol{H}_d(\boldsymbol{X}_p)$ weighted sum

$$f(\boldsymbol{X}_p) = \boldsymbol{H}_d(\boldsymbol{X}_p)^T \boldsymbol{W}\boldsymbol{H}_d(\boldsymbol{X}_p) = (\boldsymbol{H}_m - \boldsymbol{A}\boldsymbol{X}_p)^T \times \ldots \\ \ldots \times \boldsymbol{W}(\boldsymbol{H}_m - \boldsymbol{A}\boldsymbol{X}_p). \tag{17}$$

This quadratic objective function (17) minimum based on necessary minimum condition LSM calculated

$$\boldsymbol{X}_p = (\boldsymbol{A}^T \boldsymbol{W}\boldsymbol{A})^{-1}\boldsymbol{A}^T \boldsymbol{W}\boldsymbol{H}_d \tag{18}$$

Weight matrix $\boldsymbol{W}$ takes into account different importance of vector $\boldsymbol{H}_d$ error components between measured MF $\boldsymbol{H}_m$ and predicted by model (15) MF $\boldsymbol{H}_c$ values. If weight matrix $\boldsymbol{W}$ used as inverse covariance matrix $\boldsymbol{V}$ of random errors vector $\boldsymbol{H}_d$, than generalized LSM in linear unbiased estimates class is most effective. If measurement MF vector $\boldsymbol{H}_m$ components not correlated with each other, then weight matrix $\boldsymbol{W}$ is diagonal. Then generalized LSM becomes weighted LSM. However, with this approach it is necessary inverse matrix in (18) calculated, which in some cases requires special regularization algorithms used.

Note that when forming nonlinear MONMMOPS for GIMSPS weight matrices $\boldsymbol{W}$ in form (17) also used for VNOF (9)–(10) calculated. Therefore, when GIMSPS used weight matrices $\boldsymbol{W}$ in form of inverse covariance matrix $\boldsymbol{V}$ of random errors vector $\boldsymbol{H}_d$ this GIMSPS in linear unbiased estimates class is also most effective. In addition, GIMSPS (9)–(10) with MCU resulting solution sensitivity significantly reduced with respect to MCU vector $\boldsymbol{\delta}$, since it GIMSPS (9)–(10) calculated for MCU worst case.

4 Results

Let us give an example of TOMS controlling of the «Sich-2» microsatellite family shown in Fig. 1. MF main part at onboard magnetometer LEMI-016 installation point generated by plasma sensor KPNCP [5]. Microsatellite MF MM adopted in dipoles, quadrupoles, and octupoles form. Microsatellite control TOMS it is necessary compensating dipoles, quadropoles and octopoles installed.

Let us give an example of elongated TO TOMS controlled [6]. Elongated TO MF MM described in PSCS. Figure 2 shown MF components dependences of this elongated TO. To TOMS control by such elongated TO, it is necessary 16 compensating dipoles installed in TO space.

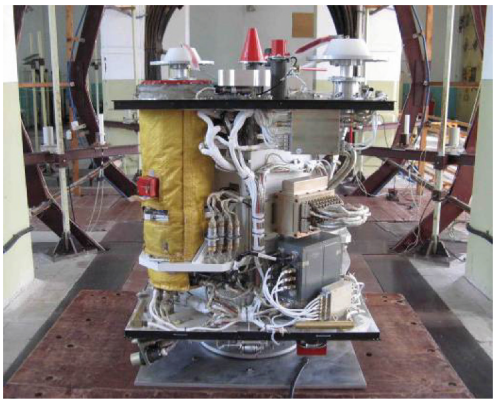

Fig.1. «Sich-2» microsatellite on measuring stand.

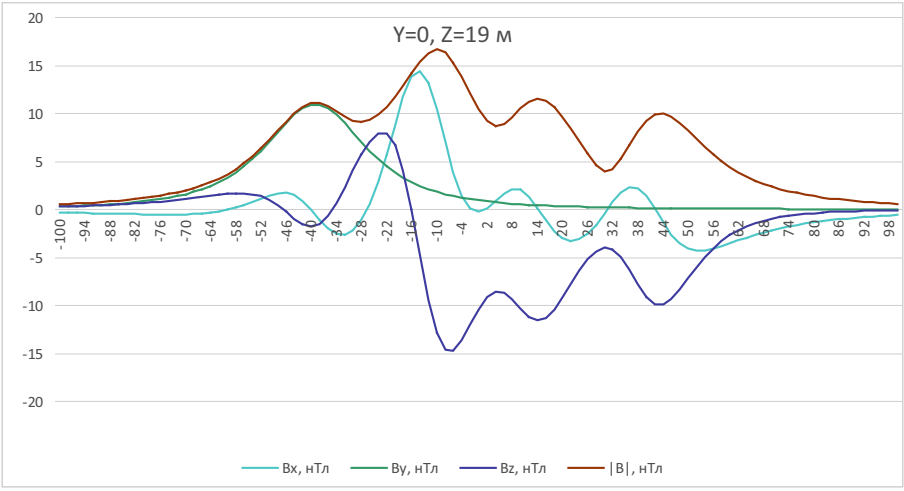

Fig.2. Elongated TO MF components dependencies.

5 Conclusions

Prediction and control by TOMS with MCU method based on SHAM developed. Prediction and control by TO with MCU are GIMSPS. TO TDGS MF MM SSH in SCS and PSSH in PSCS calculated based on LES using the COMSOL Multiphysics software. Both GIMSPS reduced to MONMMOPS calculated based on HHMSOA from POS with BPR.

When TOMS by TO with MCU prediction and control, model and compensating IMFS location coordinates in TO space and MMDM calculated.

TOMS prediction and control by «Sich-2» microsatellite and by elongated TO are given.

References

1. Droughts, S.A., Fedorov, O.P.: Space project Ionosat-Micro. Monograph. Akademperiodika Publ., Kyiv (2013) (Rus)
2. Rozov, V.Y., Getman, A.V., Petrov, S.V.: Spacecraft magnetism. Technical Electrodynamics. Thematic issue «Problems of modern electrical engineering», part 2, pp. 144–147 (2010) (Rus)
3. ECSS-E-HB-20–07A. Space engineering: Electromagnetic compatibility hand-book. ESA-ESTEC. Requirements & Standards Division. Noordwijk, Netherlands, p. 228 (2012)
4. Weikert, S., Mehlem, K., Wiegand, A.: Spacecraft magnetic cleanliness prediction and control. ESA Workshop on Aerospace EMC, Italy, ESA SP-702. http://articles.adsabs.harvard.edu/pdf/2012ESASP.702E..44W. Accessed 15 July 2025
5. Getman, A.V.: Spatial harmonic analysis of the magnetic field of the sensor of the neutral plasma component. Eastern European Journal of Advanced Technologies **6**(5), 35–38 (2010). https://doi.org/10.15587/1729-4061.2010.3326
6. Birsan, M., Holtham, P., Carmen.: Using global optimisation techniques to solve the inverse problem for the computation of the static magnetic signature of ships. Defense Research Establishment Atlantic, 9 Grove St., PO Box 1012, Dartmouth, Nova Scotia, B2Y 3Z7, Canada
7. Acuña, M.H.: The design, construction and test of magnetically clean spacecraft – a practical guide. NASA/GSFC internal report (2004)
8. Mehlem, K., Wiegand, A.: Magnetostatic cleanliness of spacecraft. 2010 Asia-Pacific International Symposium on Electromagnetic Compatibility, pp. 936–944 (2010). https://doi.org/10.1109/APEMC.2010.5475692
9. Boghosian, M., Narvaez, P., Herman, R.: Magnetic testing, and modeling, simulation and analysis for space applications. 2013 IEEE International Symposium on Electromagnetic Compatibility, pp. 265–270 (2013). https://doi.org/10.1109/ISEMC.2013.6670421
10. Shmatko, O., et al.: Synthesis of the optimal algorithm and structure of contactless optical device for estimating the parameters of statistically uneven surfaces. In Radioelectronic and computer systems, issue. 4, pp. 199–213 (2021). https://doi.org/10.32620/reks.2021.4.16
11. Volosyuk, V., et al.: Optimal method for polarization selection of stationary objects against the background of the earth's surface. In International Journal of Electronics and Telecommunications **68**(1), 83–89 (2022). https://doi.org/10.24425/ijet.2022.139852
12. Zhyla, S., et al.: Statistical synthesis of aerospace radars structure with optimal spatio-temporal signal processing, extended observation area and high spatial resolution. In Radioelectronic and Computer Systems **101**(1), 178–194 (2022). https://doi.org/10.32620/reks.2022.1.14
13. Solomentsev, O., et al.: Method of optimal threshold calculation in case of radio equipment maintenance. In Data Science and Security. Lecture Notes in Networks and Systems, vol. **462**, Springer, Singapore, pp. 69–79 (2022). https://doi.org/10.1007/978-981-19-2211-4_6
14. Sushchenko, O., et al.: Algorithms for design of robust stabilization systems. In. Computational Science and Its Applications – ICCSA 2022. Lecture Notes in Computer Science, vol. **13375**, Springer, Cham, pp. 198–213 (2022). https://doi.org/10.1007/978-3-031-10522-7_15
15. Dergachov, K., et al.: GPS usage analysis for angular orientation practical tasks solving. 2022 IEEE International Conference on Problems of Infocommunications. Science and Technology, Kyiv, Ukraine, pp. 1–6 (2022)
16. Popov, A., Tserne, E., Zhyla, S., Volosyuk, V., Pavlikov, V., Ruzhentsev, N.: Invariant polarization signatures for recognition of hydrometeors by airborne weather radars. In. Computational Science and Its Applications – ICCSA 2023. Lecture Notes in Computer Science, vol. 13956, Springer, Cham, pp. 1–14 (2023)

17. Zhyla, S., et al.: Practical imaging algorithms in ultra-wideband radar systems using active aperture synthesis and stochastic probing signals. In Radioelectronic and computer systems, **105**(1), 55–73 (2023). https://doi.org/10.32620/reks.2023.1.05
18. Rusanov, A., Chugay, M., Rusanov, R.: Advanced computer technologies in the new flow part development for reactive type HPC steam turbine of T-100 Series. Advances in Mechanical and Power Engineering. Selected Papers from The International Conference on Advanced Mechanical and Power Engineering (CAMPE 2021), October 18–21, 2021, pp. 55–63 (2021)
19. Tarasova, V., Kostikov, A., Kuznetsov, M.: Thermodynamic analysis and optimization of the cycle of a CHP plant power unit operating with ultra-supercritical steam parameters. Advances in Mechanical and Power Engineering. Selected Papers from The International Conference on Advanced Mechanical and Power Engineering (CAMPE 2021), October 18–21, 2021, pp. 44–54 (2021)
20. Ugrimov, S., Smetankina, N., Kravchenko, O.: A study of the dynamic response of materials and multilayer structures to shock loads. advances in mechanical and power engineering. Selected Papers from The International Conference on Advanced Mechanical and Power Engineering (CAMPE 2021), October 18–21, 2021, pp. 304–313 (2021)
21. Solovey, V., Rusanov, A.: Integrated energy technologies when using natural gas in utility heat power engineering. advances in mechanical and power engineering. Selected Papers from The International Conference on Advanced Mechanical and Power Engineering (CAMPE 2021), October 18–21, 2021, pp. 78–87 (2021)
22. Sushchenko, O., et al.: Algorithms for design of robust stabilization systems. In. Computational Science and Its Applications – ICCSA 2022. Lecture Notes in Computer Science, vol. 13375, Springer, Cham, pp. 198–213 (2022). https://doi.org/10.1007/978-3-031-10522-7_15
23. Hashim, F.A., Hussain, K., Houssein, E.H., Mabrouk, M.S., Al-Atabany, W.: Archimedes optimization algorithm: a new metaheuristic algorithm for solving optimization problems. Applied Intelligence **51**, 1531–1551 (2021). https://doi.org/10.1007/s10489-020-01893-z

Combined Active and Electromagnetic Passive Silencing of Power Lines Magnetic Field Based on Geometric Inverse Magneto Quasi Static's Problem

Ihor Bovdui[1](✉), Borys Kuznetsov[1], Konstantin Chunikhin[1], Olena Voloshko[1], and Tetiana Nikitina[2]

[1] Anatolii Pidhornyi Institute of Power Machines and Systems of the National Academy of Sciences of Ukraine, Komunalnykiv Street 2/10, Kharkiv 61046, Ukraine
ibovduj@gmail.com

[2] Bakhmut Education Research and Professional Pedagogical Institute V.N. Karazin Kharkiv National University, 9a, Nosakov Street, Bakhmut 84511, Ukraine

Abstract. Combined electromagnetic active and passive silencing (CEAPS) design method of overhead power lines (OPL) magnetic field (MF) based on geometric inverse magneto-quasi-static problem solution (GIMSPS), taking into account the uncertainties of the geometric forward magneto-quasi-static problem solution (GFMSPS) developed. In course of CEAPS designing passive electromagnetic silencing (PES) and active electromagnetic silencing (AES) spatial location geometric coordinates, and AES silencing windings (SW) currents and phases calculated. GIMSPS for CEAPS designing to compensate initial MF reduced to multi-objective nonlinear minimax optimization problems solutions (MONMMOPS). Vector nonlinear objective function (VNOF) calculated based on Maxwell equations solutions (MES) using COMSOL Multiphysics software. MONMMOPS calculated based on Pareto optimal solutions (POS) and binary preference relations (BPR) based on hybrid heuristic multi-swarm optimization algorithm (HHMSOA). Designed CEAPS computer modeling and experimental studies results to reduce OPL MF level are given.

Keywords: Magnetic Silence · Geometric Inverse Problem · Uncertainty · Computer Modeling · Field Experimental Study

1 Introduction

Recently in world developed countries more and more attention being electromagnetic pollution population protecting problem which intensity increasing from year to year. Power frequency (PF) MF main source are OPL. PF MF leads to changes in the hematological parameters of the blood and the immune status of a person, affects the reproductive, central and neurovascular systems, affects the bioelectrical activity of the brain, causes genetic mutations in the human body and has carcinogenic properties [1]. In

H. Altenbach et al. (Eds.): CAMPE 2025, LNME, pp. 55–64, 2026.
https://doi.org/10.1007/978-3-032-16381-3_6

world developed countries strict state sanitary regulations on the permissible PF MF levels in the environment of long-term stay of people. The social significance of the work consists in ensuring the protection of the health of the population living near OPL from the negative impact of a long-lasting PF MF. Work economic significance consists in MF reducing methods and means development to a sanitary-reasonable level in residential and public areas of people long-term stay without OPL route changing or resettling people [2, 3].

2 Literature Review

The most common reducing MF level method is PES [4–6]. The operating principle of PES is: primary MF action conduction currents induced in silence; secondary MF create these current; resulting MF formed by primary MF with secondary MF, which is weaker as primary MF in silencing area [7]. Consequently, for PES materials manufacture high electrical conductivity used. PES made of aluminum most widely used, which is relatively low cost. Silence increases by PES thickness. Silencing efficiency increases linear dependence in certain. With a further increase in thickness, the silencing efficiency reaches saturation and behaves asymptotically. Required shielding efficiency ensuring by silence thickness increasing leads to required metal volume increase for its manufacture.

MF silencing efficiency increase without silence volume increasing CEAPS consisting of PES and AES used [8]. Designing such CEAPS is a GIMSPS. Initial MF generated by OPL calculated based on GFMSPS. In the course of CEAPS designing it is necessary to solve GIMSPS – to calculate AES and PES spatial location geometric coordinates and AES SW currents and phases in such a way that CEAPS using generated compensating MF directed opposite to original MF [9, 10].

GFMSPS uncertainties caused by GFMSPS parameters inaccurate knowledge and their changes during operation it is necessary to take into account [11–13].

The goal of the work is CEAPS design method developed of OPL MF based on GIMSPS taking into account GFMSPS uncertainties.

3 Research Methodology

Initial MF generated by OPL. Let us consider GFMSPS – calculating MF at points in the silencing space (SS) for OPL wires spatial location given coordinates and OPL wires currents given values. Analysis and MF MM reduced to MES, which MF describe in media with characteristics that vary continuously or piecewise continuously and are the basis for analytical and numerical modeling of any electromagnetic processes, both in vacuum and in material media. MES are systems of partial differential equations that are subject to mathematical study and numerical solution [14–16].

When calculating MF of OPL significant simplifications made to MES [17–19]. In this approximation, displacement currents neglected compared to conduction currents [20–22]. From these MES it follows that determined by electric currents distribution. MF calculated by integration over distributed sources. When modeling three-phase OPL MF following assumptions often made: wires have the form of endless linear conductors

with a uniformly distributed current, processes of current redistribution within the cross-section of wires are not considered, currents in the wires are strictly harmonious, equal in amplitude and in different phases shifted by 120 degrees.

In this case, the Biot-Savart's laws has the form

$$\boldsymbol{H}(P,t) = \frac{i(t)}{4\pi}\int\limits_{L}\frac{(d\boldsymbol{l}\times\boldsymbol{R})}{R^3} \tag{1}$$

Thus, to solve GFMSPS – calculating MF generated by OPL wires, this formula is widely used instead of MES.

This formula is also widely used to solve the second GFMSPS – calculating the compensation MF, generated by SW of AES of CEAPS at SS points for SW spatial location coordinates and SW currents and phases of AES of CEAPS.

Let us now consider third GFMSPS – calculating the compensating MF generated by PES part of CEAPS – a solid PES at SS points for solid PES spatial location coordinates of the and thickness, material and etc. When considering PF MF PES problems can assume that MF wavelength is significantly larger than PES main dimensions. This circumstance makes it possible to solve MES in a quasi-stationary approximation:

$$\begin{cases} rot\,\boldsymbol{H} = \sigma\,\boldsymbol{E} + \boldsymbol{J}\,, \\ rot\,\boldsymbol{E} = -j\,\omega\,\mu_0\,\mu\,\boldsymbol{H}\,, \end{cases} \tag{2}$$

where $\boldsymbol{H}$, $\boldsymbol{E}$ are magnetic and electric fields strengths; $\boldsymbol{J}$ – external currents density;

σ – specific conductivity; μ – relative magnetic permeability; μ_0 – magnetic constant; ω – field circular frequency; j is a complex unit.

The distribution of OPL MF silencing by CEAPS, consisting of active contour and electromagnetic components, can be found from Ampere law, written in differential form with respect to vector potential of the electromagnetic field:

$$\frac{1}{\mu_0\mu}rot(rot\boldsymbol{A}) + \sigma\frac{\partial\boldsymbol{A}}{\partial t} + \varepsilon_0\varepsilon\frac{\partial^2\boldsymbol{A}}{\partial t^2} = \boldsymbol{J} \tag{3}$$

where $\boldsymbol{A}$ – electromagnetic field vector potential, σ – electrical conductivity,

$\boldsymbol{J}_{\mathrm{CT}}$ – extraneous current density.

Finite element method application is conducting numerical experiments effective ways [16–18]. This method is the basis of most modern software environments COMSOL Multiphysics. If we assume that OPL wires parallel to each other and silencing length is much greater than its width, then the resulting silencing MF will be plane-parallel. In this case, the problem considered in a two-dimensional formulation. However, for silencing residential buildings, combined AES and PES of finite length, comparable to the length of the house used. Therefore, to calculate the effectiveness of silencing along the edges of a house, it is necessary to use a three-dimensional formulation of the problem of MF calculating.

Let us now consider the CAMPECS designing problem to compensate for the initial MF. Let us introduce this GIMSPS desired parameters vector $\boldsymbol{X}$ with AES and PES spatial location geometric coordinates and SW AES currents and phases that compensating MF CAMPECS generated directed opposite to original MF.

In works [6–8] contrast initial MF MM uncertainties vector $\boldsymbol{\delta}$ introduced with original MF parameters inaccuracy and their changes during operation [20]. Let's form a squares of sum $\boldsymbol{B}_R(\boldsymbol{X},\boldsymbol{\delta},P_i)$ compensating MF vector and original MF vector in silencing space (SS) points P_i. Let's form a vector

$$\boldsymbol{B}_R(\boldsymbol{X},\boldsymbol{\delta}) = \langle \{\boldsymbol{B}_R(\boldsymbol{X},\boldsymbol{\delta},P_1), \boldsymbol{B}_R(\boldsymbol{X},\boldsymbol{\delta},P_2)...\boldsymbol{B}_R(\boldsymbol{X},\boldsymbol{\delta},P_{\mathrm{n}})\}\rangle \tag{4}$$

With resulting MF $\boldsymbol{B}_R(\boldsymbol{X},\boldsymbol{\delta},P_i)$ in SS points P_i. Then GIMSPS for multi objective CEAPS designing for initial MF compensated taking into account uncertainties vector $\boldsymbol{\delta}$ reduced to MONMMOPS [22–24]

$$\min_{X}\max_{\delta}\boldsymbol{B}_R(\boldsymbol{X},\boldsymbol{\delta}) = \langle \boldsymbol{B}_R(\boldsymbol{X},\boldsymbol{\delta},P_{\mathrm{i}})\rangle \tag{5}$$

In this MONMMOPS (5) it's necessary minimizing VNOF $\boldsymbol{B}_R(\boldsymbol{X},\boldsymbol{\delta})$ (4) according to designed CEAPS desired parameters vector $\boldsymbol{X}$, but maximizing the same VNOF $\boldsymbol{B}_R(\boldsymbol{X},\boldsymbol{\delta})$ according to uncertainties parameters vector $\boldsymbol{\delta}$ of original MF.

MONMMOPS (5) associated with game solving [25]. Desired parameters vector $\boldsymbol{X}$ is first player. Its strategy is to minimize vector payoff $\boldsymbol{B}_R(\boldsymbol{X},\boldsymbol{\delta})$. Parameters uncertainties vector $\boldsymbol{\delta}$ is second player. Its strategy is to maximize same vector payoff $\boldsymbol{B}_R(\boldsymbol{X},\boldsymbol{\delta})$. Moreover, since game payoff (4) is vector, such game is called multi objective or vector game by analogy with multi objective or vector optimization.

VNOF $\boldsymbol{B}_R(\boldsymbol{X},\boldsymbol{\delta})$ (4) is calculated using COMSOL Multiphysics software. A feature of finite-difference methods is that the spatial grid is applied to the entire computational domain [14–16]. In the problem under consideration, the area of study of the MF distribution contains OPL conductors, AES SW conductors, PES and the SS. Since the diameter of OPL and SW conductors are much smaller than the distance between them, they are considered as current threads and the distribution of the current density that flows through them is represented as a sum of delta functions.

For objects whose linear dimensions differ by several orders of magnitude, the computational domain is divided into a number of subdomains with different steps and their stitching is performed through the values of the sought functions on the dividing surfaces. The PES thickness is magnitude smaller several orders than their width. Therefore, grid spatial steps along different directions differ significantly. A three-dimensional uniform grid is applied to the computational domain – a global grid, which is applied in such a way that the screen profile lies on its lattice. To find the distribution of magnetic induction inside the PES, this screen is divided by thickness by an additional uniform grid – a local grid, with a step N times smaller than the step of the global grid.

MONMMOPS (5) calculated from POS [20] with BPR based on HHMSOA [26, 27]. Consider MONMMOPS algorithm. When MONMMOPS calculated it is necessary VNOF $\boldsymbol{B}_R(\boldsymbol{X},\boldsymbol{\delta})$ minimum for GIMSP desired parameters vector $\boldsymbol{X}$ calculated. For this purpose VNOF $\boldsymbol{B}_R(\boldsymbol{X},\boldsymbol{\delta})$ minimum for GIMSP desired parameters vector $\boldsymbol{X}$ calculated by particle swarm optimization (PSO) algorithm in following procedure. Particle i swarm j movement described by

$$x_{ij}(t+1) = x_{ij}(t) + v_{ij}(t+1) \tag{6}$$

where

$$\begin{aligned} v_{ij}(t+1) &= w_j v_{ij}(t) + c_{1j} r_{1j}(t) H\left(p_{1j} - \varepsilon_{1j}(t)\right) * \cdots \\ \cdots &* \left[y_{ij}(t) - x_{ij}(t)\right] + c_{2j} r_{2j}(t) H\left(p_{2j} - \varepsilon_{2j}(t)\right) * \cdots \\ \cdots &* \left[y_j^*(t) - x_{ij}(t)\right] \end{aligned} \tag{7}$$

Position $x_{ij}(t)$ and velocity $v_{ij}(t)$ vectors components of swarm j particle i for VNOF $\boldsymbol{B}_R(\boldsymbol{X},\boldsymbol{\delta})$ minimum for GIMSP desired parameters vector $\boldsymbol{X}$ calculated.

PSO (6)–(7) works effectively at initial stages of iterations, when PSO movement speeds have significant values [22–24]. When entering quasi-stationary regions of VNOF $\boldsymbol{B}_R(\boldsymbol{X},\boldsymbol{\delta})$, PSO motion speeds tend to zero. To speed up VNOF $\boldsymbol{B}_R(\boldsymbol{X},\boldsymbol{\delta})$ global optima calculating process in stationary region, it is advisable second-order optimization methods (SOOM) used based on second derivatives. One of simplest and quite effective SOOM is sequential quadratic programming (SQP) algorithm. The of the initial parameters values of desired parameters vector $\boldsymbol{X}$ GIMSP obtained with PSO help are initial values for refining solutions in quasi-stationary region.

To calculate VNOF $\boldsymbol{B}_R(\boldsymbol{X},\boldsymbol{\delta})$ minimum by GIMSP desired parameters vector $\boldsymbol{X}$ formulated minimization problem with quadratic objective function (QOF)

$$\begin{aligned} &\boldsymbol{H}_r(\boldsymbol{X}_{ij}(t), \delta_{ij}(t), Q_i)\rangle + \frac{1}{2}\boldsymbol{d}_{ijx}^T(t)\boldsymbol{H}_{ijx}(t)\boldsymbol{d}_{ijx}(t) + \ldots \\ &\ldots + \nabla_{ijx}^T(t)\boldsymbol{d}_{ijx}(t) \end{aligned} \tag{8}$$

Jacobian matrices $\nabla_{ijx}(t)$ and Hessian matrices $\boldsymbol{H}_{ijx}(t)$ components along vector $\boldsymbol{X}$ calculated from particle i of swarm j movement velocities $v_{ij}(t)$ and accelerations $A_{ijx}(t)$, which calculated based on velocities $v_{ij}(t)$

$$A_{ijx}(t+1) = v_{ij}(t+1) - v_{ij}(t) \tag{9}$$

At each iteration step, in addition to VNOF $B_R(X,\delta)$ quadratic approximation (8) constraints linear approximation also used

$$\nabla g_{ijx}(x_{ij}(t), \delta_{ij}(t))^T d_{ijx}(t) + g_{ij}(x_{ij}(t), \delta_{ij}(t)) \le 0 \tag{10}$$

During SQP process (8)–(10) step size $d_{ijx}(t)$ calculated, which used to calculated VNOF $\boldsymbol{B}_R(\boldsymbol{X},\boldsymbol{\delta})$ minimum by desired parameters vector $\boldsymbol{X}$.

$$x_{ij}(t+1) = x_{ij}(t) + \alpha_{ijx}(t) d_{ijx}(t) \tag{11}$$

To calculate VNOF $\boldsymbol{B}_R(\boldsymbol{X},\boldsymbol{\delta})$ maximum by vector $\boldsymbol{\delta}$ of uncertainties formulated maximization problem with QOF by analogy (8)–(11).

4 Results

Consider CEAPS designing results. In Fig. 1.a showed initial MF distribution. MF level in SS under consideration varies from 2.0 μT to 1.3 μT, which is more than 2 times higher than 0.5 μT level for residential buildings long-term residence people safe.

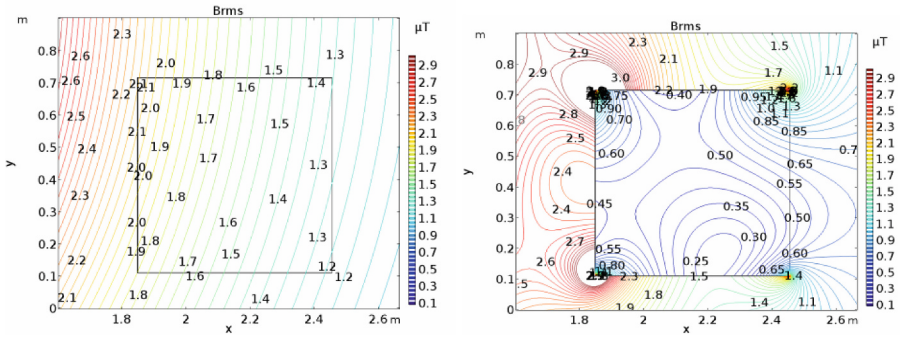

Fig. 1. Initial a) and resulting b) MF when operating PES only.

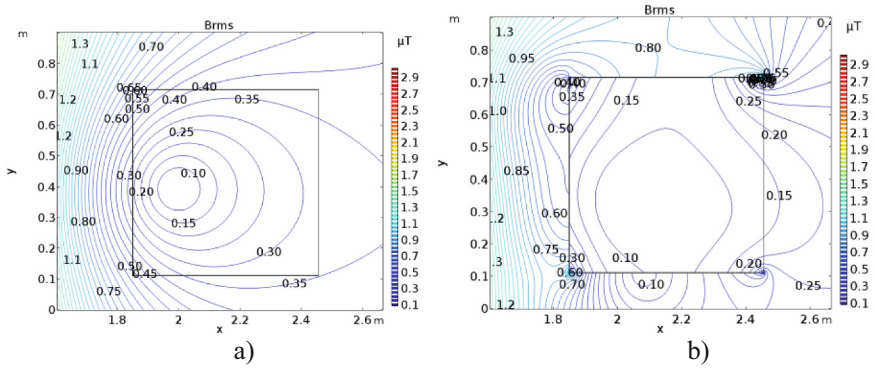

Fig. 2. Resulting MF distribution a) AES b) CEAPS.

In Fig. 1.b showed resulting MF distribution when PES using. MF level in SS center under consideration varies from 0.5 μT to 0.35 μT, but at the edges of the SS under consideration the induction level reaches 1 μT or more. The maximum calculated value of the silencing factor when PES using only is 6.8 units.

In Fig. 2.a showed resulting MF distribution when AES using. MF level in considered SS center varies from 0.1 μT to 0.3 μT, but at considered SS edges MF level reaches 1 μT or more. The maximum silencing factor value calculated when AES using is 17 units.

In Fig. 2.b showed resulting MF distribution when CEAPS using. MF level in SS under consideration center varies from 0.1 μT to 0.3 μT, but at space SS under consideration edges MF level reaches 0.5 μT or more.

The maximum silencing factor value calculated when CEAPS using is also 17 units. CEAPS advantage is that MF level value minimum of 0.1 provided in considered SS significantly larger part compared to AES using.

Consider designed CEAPS experimental studies results. In Fig. 3.a showed CEAPS experimental installation.

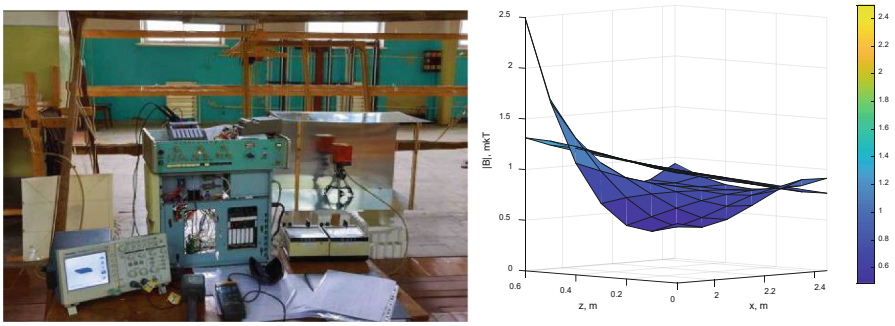

a) b)

Fig. 3. CEAPS experimental installation a) initial and resulting MF PES b) EMD.

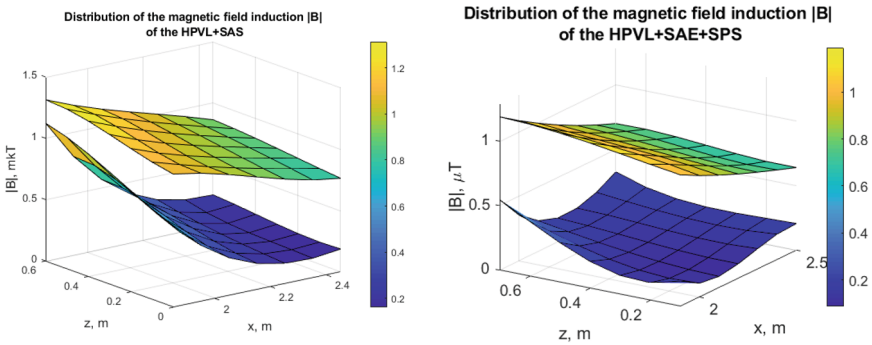

a) b)

Fig. 4. Initial and resulting MF EMD when AES using a), when CEAPS using b).

In Fig. 3.b showed initial and resulting MF experimentally measured distributions (EMD) when PES using. In SS under consideration center varies MF level from 0.5 μT to 0.35 μT, but SS under consideration edges MF level reaches 1.2 μT or more.

In Fig. 4.a showed initial and resulting MF EMD when AES using. In SS under consideration center MF level varies from 0.3 μT to 0.2 μT, but at SS under consideration edges MF level 1 μT.

In Fig. 4.b showed initial and resulting MF EMD when using CEAPS and AES. MF level in considered center SS varies from 0.3 μT to 0.2 μT, but at considered SS edges MF level reaches 0.5 μT.

5 Conclusions

CEAPS design method of OPL MF based on GIMSPS taking into account GFMSPS uncertainties developed. AES and PES spatial location geometric coordinates and AES SW currents and phases calculated during CEAPS design.

GIMSPS for CEAPS designing to compensate for initial MF reduced to MONMMOPS. VNOF calculated using COMSOL Multiphysics software. MONMMOPS calculated based on POS taking into account BPR by HHMSOA.

Based on GIMSPS developed method CEAPS of OPL MF designed. Computer modeling and EMD MF results of designed CEAPS are given.

Conflict of Interest. The authors declare that they have no conflicts of interest.

References

1. Global Cancer Statistics: GLOBOCAN Estimates of Incidence and Mortality Worldwide for 36 Cancers in 185 Countries. Enhanced Reader (2020)
2. Rozov, V.Yu., Reutskyi, S.Yu., Pelevin, D.Ye., Kundius, K.D.: Approximate method for calculating the magnetic field of 330–750 kV high-voltage power line in maintenance area under voltage. Electr. Engi. Electromech. **5**, 71–77 (2022). https://doi.org/10.20998/2074-272X.2022.5.12
3. Barsali, S., Giglioli, R., Poli, D.: Active shielding of overhead line magnetic field: design and applications. Electric Power Syst. Res. **110**, 55–63 (2014). https://doi.org/10.1016/j.epsr.2014.01.005
4. Salceanu, A., Paulet, M., Alistar, B.D., Asiminicesei, O.: Upon the contribution of image currents on the magnetic fields generated by overhead power lines. In: 2019 International Conference on Electromechanical and Energy Systems (SIELMEN). (2019). https://doi.org/10.1109/sielmen.2019.8905880
5. Ghanim, T.H., Kamil, J.A., Mutlaq, A.H.: The influence of the mixed electric line poles on the distribution of magnetic field. Indonesian J. Electr. Eng. Inform. (IJEEI) **10**(2), 292–301 (2022). https://doi.org/10.52549/ijeei.v10i2.3572
6. Mary, S.V., Sugumaran C.P.: Investigation on magneto-thermal-structural coupled field effect of nano coated 230 kV busbar. IOP Publishing Ltd., Physica Scripta, **95**(4) (2020). https://doi.org/10.1088/1402-4896/ab6524
7. Bravo-Rodríguez J., Del-Pino-López J., Cruz-Romero P.A.: Survey on optimization techniques applied to magnetic field mitigation in power systems. Energies **12**(7), 1332 (2019). https://doi.org/10.3390/en12071332
8. Canova, A., Giaccone, L., Cirimele, V.: Active and passive shield for aerial power lines. In: 25th International Conference on Electricity Distribution Madrid, 3–6 June 2019. Paper no. 1096, pp. 1–5 (2019)
9. Martynenko, G.: Analytical method of the analysis of electromagnetic circuits of active magnetic bearings for searching energy and forces taking into account control law. In: Conference Proceedings of the 2020 IEEE KhPI Week on Advanced Technology, pp. 86–91 (2020). https://doi.org/10.1109/KhPIWeek51551.2020.9250138
10. Martynenko, G., Martynenko, V.: Rotor Dynamics modeling for compressor and generator of the energy gas turbine unit with active magnetic bearings in operating modes. In: Proceedings of the 25th IEEE International Conference on Problems of Automated Electric Drive. Theory and Practice, pp. 1–4 (2020). https://doi.org/10.1109/PAEP49887.2020.9240781
11. Dergachov, K., Havrylenko, O., Pavlikov, V., Popov, A., Zhyla, S., et al.: GPS usage analysis for angular orientation practical tasks solving. In: 2022 IEEE International Conference on Problems of Infocommunications. Science and Technology, pp. 1–6. Kyiv, Ukraine (2022)

12. Popov, A., Tserne, E., Zhyla, S., Volosyuk, V., Pavlikov, V., Ruzhentsev, N.: Invariant polarization signatures for recognition of hydrometeors by airborne weather radars. In. Computational Science and Its Applications – ICCSA 2023, vol. 13956, pp. 1–14. Lecture Notes in Computer Science, Springer, Cham (2023)
13. Zhyla, S., Volosyuk, V., Pavlikov, V., Ruzhentsev, N., Tserne, E., Popov, A., et al.: Practical imaging algorithms in ultra-wideband radar systems using active aperture synthesis and stochastic probing signals. Radioelectronic Comput. Syst. **105** (1), 55–73 (2023). https://doi.org/10.32620/reks.2023.1.05
14. Rusanov, A., Chugay, M., Rusanov, R.: Advanced computer technologies in the new flow part development for reactive type HPC steam turbine of T-100 Series. In: Advances in Mechanical and Power Engineering. Selected Papers from the International Conference on Advanced Mechanical and Power Engineering (CAMPE 2021), October 18–21, 2021, pp. 55–63 (2021)
15. Tarasova, V., Kostikov, A., Kuznetsov, M.: Thermodynamic analysis and optimization of the cycle of a CHP plant power unit operating with ultra-supercritical steam parameters. advances in mechanical and power engineering. In: Selected Papers from the International Conference on Advanced Mechanical and Power Engineering (CAMPE 2021), October 18–21, 2021, pp. 44–54 (2021)
16. Ugrimov, S., Smetankina, N., Kravchenko, O.: A Study of the dynamic response of materials and multilayer structures to shock loads. advances in mechanical and power engineering. In: Selected Papers from the International Conference on Advanced Mechanical and Power Engineering (CAMPE 2021), October 18–21, 2021, pp. 304–313 (2021)
17. Solovey, V., Rusanov, A.: Integrated energy technologies when using natural gas in utility heat power engineering. In: Advances in Mechanical and Power Engineering. Selected Papers from the International Conference on Advanced Mechanical and Power Engineering (CAMPE 2021), October 18–21, 2021, pp. 78–87 (2021)
18. Shmatko, O., Volosyuk, V., Zhyla, S., Pavlikov, V., Ruzhentsev, N., Tserne, E., et al.: Synthesis of the optimal algorithm and structure of contactless optical device for estimating the parameters of statistically uneven surfaces. Radioelectronic Comput. Syst. **4**, 199–213 (2021). https://doi.org/10.32620/reks.2021.4.16
19. Volosyuk, V., Zhyla, S., Pavlikov, V., Ruzhentsev, N., Tserne, E., Popov, A., et al.: Optimal method for polarization selection of stationary objects against the background of the earth's surface. Int. J. Electr. Telecommun. **68**(1), 83–89 (2022). https://doi.org/10.24425/ijet.2022.139852
20. Sushchenko, O., et al.: Algorithms for design of robust stabilization systems. In. Computational Science and Its Applications – ICCSA 2022. Lecture Notes in Computer Science, 13375, pp. 198–213, Springer, Cham (2022). https://doi.org/10.1007/978-3-031-10522-7_15
21. Zhyla, S., Volosyuk, V., Pavlikov, V., Ruzhentsev, N., Tserne, E., Popov, A., et al.: Statistical synthesis of aerospace radars structure with optimal spatio-temporal signal processing, extended observation area and high spatial resolution. Radioelectronic Comput. Syst. **1**, 178–194 (2022). https://doi.org/10.32620/reks.2022.1.14
22. Hashim, F.A., Hussain, K., Houssein, E.H., Mabrouk, M.S., Al-Atabany, W.: Archimedes optimization algorithm: a new metaheuristic algorithm for solving optimization problems. Appl. Intell. **51**, 1531–1551 (2021). https://doi.org/10.1007/s10489-020-01893-z
23. Salameh, M.S.H.A., Nejdawi, I.M., Alani, O.A., Commission, E.R., Contracting, B.G.: Using the nonlinear particle swarm optimization (PSO) algorithm to reduce the magnetic fields from overhead high voltage transmission lines. IJRRAS **4**, 18–31 (2010)
24. Król, K., Machczyński, W.: Optimization of electric and magnetic field intensities in proximity of power lines using genetic and particle swarm algorithms. Arch. Electr. Eng. **67**, 829–843 (2018)
25. Ummels, M.: Stochastic Multiplayer Games Theory and Algorithms. Amsterdam University Press, vol. 174 (2010)

26. Ray, T., Liew, K.M.: A swarm metaphor for multiobjective design optimization. Eng. Optim. **34**(2), 141–153 (2002). https://doi.org/10.1080/03052150210915
27. Xiaohui, H.U., Eberhart, R.C., Yuhui, S.: Particle swarm with extended memory for multi-objective optimization. In: Proceedings of the 2003 IEEE Swarm Intelligence Symposium. SIS'03 (Cat. No.03EX706), pp. 193–197. Indianapolis, IN, USA (2003). https://doi.org/10.1109/sis.2003.1202267

Processes Optimisation of Coagulation, Flocculation, and Liming for Power Plant Water Treatment

Pavlo Kuznietsov(✉), Olha Biedunkova, Alla Pryshchepa, and Olesya Yaroschuk

National University of Water and Environmental Engineering, Rivne 33028, Ukraine
p.m.kuznietsov@nuwm.edu.ua

Abstract. Industrial applications often demand water quality that exceeds natural water conditions, necessitating effective multi-stage treatment. This study investigates a combined treatment approach utilizing iron (II) sulfate heptahydrate ($FeSO_4 \cdot 7H_2O$), anionic polyacrylamide (PAM), and calcium hydroxide ($Ca(OH)_2$) to remove turbidity, total suspended solids (TSS), chemical oxygen demand (COD), and phosphate ions (PO_4^{3-}). The experimental procedure employed jar tests with variable reagent dosages, pH adjustments, sedimentation times, and temperature conditions. Removal efficiencies were evaluated using standard analytical methods and correlated via the Pearson analysis. Results demonstrated that optimal removal - up to 95% for turbidity and >90% for TSS - was achieved at 2500 ppm $FeSO_4 \cdot 7H_2O$, 1.0 ppm PAM, and pH 9.0, with enhanced performance at 25 ± 5 °C and 1.4 h settling time. PO_4^{3-} removal peaked at pH 8.0, likely due to precipitation of ferric and calcium with PO_4^{3-}. Correlation analysis confirmed that coagulant dose, pH, and temperature were dominant factors in removal performance, while PAM exhibited a secondary but enhancing role. Microscopic observations indicated a transition to denser and more compact flocs during treatment. The integrated method demonstrated a synergistic effect, offering an efficient and scalable solution for improving industrial water quality.

Keywords: Turbidity Reduction · Sediment Morphology · Jar Test · Water Quality Optimization

1 Introduction

Natural waters typically do not meet industrial requirements and require multi-level water treatment to meet water quality standards for power plants [1]. In particular, turbidity and total insoluble solids (TSS) can damage equipment and cause deposits, chemical oxygen demand (COD) indicates organic contamination that is dangerous for production processes, and phosphate ions (PO_4^{3-}) contribute to scale formation, especially in heat exchangers [2]. In order to mitigate the impact of these indicators, appropriate water quality requirements are established [3]. Compliance with these requirements necessitates the implementation of water treatment methods. In the field of water treatment,

H. Altenbach et al. (Eds.): CAMPE 2025, LNME, pp. 65–74, 2026.
https://doi.org/10.1007/978-3-032-16381-3_7

considerable attention is paid to the coagulation and flocculation processes, which have been proven to be effective removing polluting solutes. In addition, liming has been shown to play a crucial role in regulating the pH of the medium [4, 5]. Each of these methods has its own strengths. Consequently, coagulation provides an effective reduction of turbidity and removal of fine insoluble impurities due to the introduction of coagulants [6]. Simultaneously, the process of flocculation is responsible for the enlargement of coagulated particles, resulting in the formation of larger flocs [7]. Furthermore, liming has been shown to correct the hydrogen pH of the medium, aid in the precipitation of carbonate and other insoluble impurities, and frequently function as an amplifier of the preceding treatment stages due to the co-precipitation phenomenon [8, 9].

The purpose of this study was to ascertain the most efficacious doses of reagents for the effective removal of contaminants (turbidity, TSS, COD, PO_4^{3-}), with the identification of factors affecting the efficiency of pollution and the study of the resulting sediment. The employment of the controlled mixing rate test method enabled the assessment of the impact of each component individually, in addition to the synergistic effect of the three-component approach. The application of the Pearson correlation analysis method enabled the identification of the interrelated dominant factors of the combined application, and the study of the sediment fraction, in particular the particle size, revealed trends in sediment formation.

2 Literature Review

Heptahydrate of ferrous sulphate ($FeSO_4 \cdot 7H_2O$) is a cost-effective inorganic coagulant with high coagulation efficiency [10]. In the context of $FeSO_4 \cdot 7H_2O$ solutions, the process of hydrolysis is known to be accelerated, resulting in the formation of a multitude of iron hydroxide compounds. The efficiency of coagulation is observed to be susceptible to alterations in pH, a phenomenon that can give rise to the generation of unstable coagulants, as well as the formation of insoluble iron hydroxides. The presence of these insoluble compounds has been found to be associated with an increase in turbidity and TSS. In order to achieve the desired outcome, it is necessary to combine the use of $FeSO_4 \cdot 7H_2O$ with other reagents, such as a flocculant and a pH adjuster. The flocculant adsorbs on the surface of coagulant-aggregated particles, forming bridges between them, which leads to the formation of larger flocs that settle more rapidly [11, 12]. Polyacrylamide (PAM) flocculant, a water-soluble polymer, is a well-known industrial water treatment agent used as a flocculant. It is widely accepted that PAMs can be categorised into three distinct groups: anionic PAMs, cationic PAMs, and nonionic PAMs. The flocculation efficiency of flocculants is contingent on the type of flocculants and their molecular weight, ionic nature and content, and TSS content. PAM has been shown to neutralise the charge of coagulant-aggregated iron hydroxide particles and has been demonstrated to affect the morphology of flocs by creating macropores for additional adsorption. It has been determined that the flocculation efficiency of a polymer chain is contingent upon its length [13]. Furthermore, quicklime (CaO or $Ca(OH)_2$) is a low-cost liming agent that increases the pH level, removing bicarbonate and carbonate ions and thus creating an additional purification effect [14].

The combined use of coagulant, flocculant and lime can significantly increase the efficiency of water treatment. However, to achieve maximum water treatment efficiency,

it is necessary to optimise the conditions for the combined use of these methods - to determine the dose of reagent [15, 16], the order of their introduction and the impact of environmental parameters (pH, time, temperature) [17]. By optimising coagulation + flocculation + liming processes, it is possible to achieve a significant reduction in reagent costs, minimise the formation of sediment, and improve the quality of treated water. The present study proposes an integrated approach to water treatment for industrial use, combining coagulation, flocculation and liming using $FeSO_4 \cdot 7H_2O$, PAM and $Ca(OH)_2$.

3 Research Methodology

The analytical methods of measurement employed in the study are enumerated in Table 1. The experiment was conducted in 1-L beakers with mechanical stirring on a six-stirrer MTOPS Jar Tester SF6. The reagents utilised in the study were as follows: The substance under investigation is $FeSO_4 \cdot 7H_2O$, with a purity of at least 97%, anionic PAM of medium molecular weight, and $Ca(OH)_2$ of technical grade, with a purity of at least 79%. Water samples were collected from the Styr River [18], the quality of which is characterised by the quality indicators shown in Fig. 1.

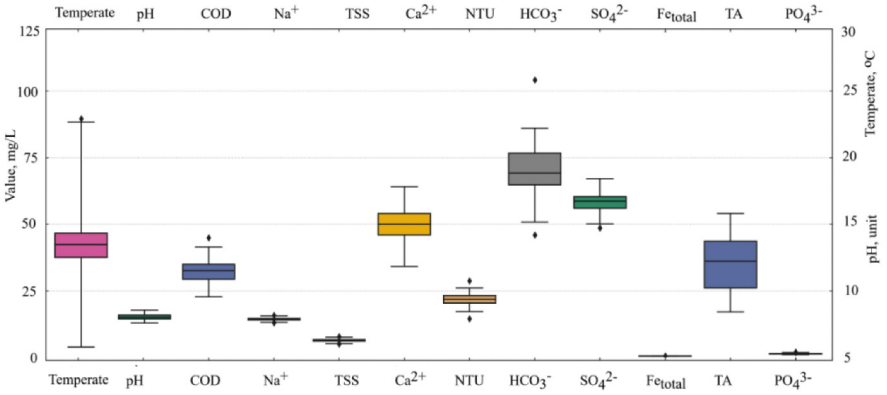

Fig. 1. The quality indicators of the input natural water used in this study.

The distribution of sediment particles by size was performed using a HIAC/ROYCO 8000A laser particle counter. Sediment morphology was determined using an XS-5520 LED binocular microscope. Temperature control was performed using a DAIHAN HP-30A analogue hotplate. Statistical processing of the research results included determining the range of the data series (min-max), the arithmetic mean (M), and the standard deviation (SD) using the BioEstar software package (Version 5.3, MLM). The analysis of the data set to assess the relationship between the variables of the control results was performed using the Pearson correlation coefficient (r) [19], using IBM SPSS, v27.

The effect of coagulation of $FeSO_4 \cdot 7H_2O$, PAM, $Ca(OH)_2$ on the excretion of substances was measured by the calculated method, the doses of $FeSO_4 \cdot 7H_2O$: 500, 1000, 1500, 2000, 2500 ppm, PAM 0.25, 0.5, 1.0, 1.5, 2.0 ppm, and $Ca(OH)_2$ to create a pH.

Table 1. List of adopted analytical procedures.

Parameter	Analytical instrument	Reference method
pH	pH/millivolt meter I-160, $\Delta = \pm 0.05$ pH*	Instruction manual for devices
Turbidity	turbidity meter Eutech TN 100, $\delta = \pm 2\%$*	
TSS	gravimetric method, balance OHAUSV12146	KND 211.1.4.039–95**
COD	permanganate titrimetric method	KND 211.1.4.021–95**
PO_4^{3-}	molybdenum method, spectrophotometer ULAB S102	MVV 081/12–0005–01**

Note: * Δ – are the absolute and δ relative measurement error; ** - are Ukrainian measurement standards

The solutions under study were analysed using the Jar test methodology at slow (20–50 rpm) and fixed rapid stirring for 3 min (200 rpm). Moreover, the study was carried out with different sedimentation times (0.6–1.6 h) and temperatures (10–30 °C). The percentage of removal efficiency (%) [20] for turbidity, TSS, COD, PO_4^{3-} was calculated using Eq. (1).

$$\text{Removal efficiency } (\%) = (\text{Ci} - \text{Ct/Ci}) \times 100 \quad (1)$$

where Ci and Ct are the concentrations parameter before treatment and after treatment, respectively.

4 Results and Discussion

Determining the optimum coagulant dosage is important for controlling the coagulation process, including the efficiency of contaminant removal. The coagulant dosage in this study of $FeSO_4{\cdot}7H_2O$ was varied from 500 to 2500 ppm under fixed agitation. Figure 2 shows the percentage removal of turbidity, TSS, COD and PO_4^{3-}. The percentage removal of turbidity (Fig. 2a), TSS (Fig. 2b), COD (Fig. 2c), and PO_4^{3-} (Fig. 2d) increased with the dosage of $FeSO_4{\cdot}7H_2O$, reaching maximum values of 83.5%, 50.7%, 59.5%, 55.8%, respectively, for turbidity, TSS, COD and PO_4^{3-} at 2500 ppm $FeSO_4{\cdot}7H_2O$. Removal of turbidity, TSS, COD achieved comparable results, taking into account the maximum values of the percentage of removal for a dose of 2000 ppm $FeSO_4{\cdot}7H_2O$. It is known from numerous studies that a higher dose helps to form larger and denser flocs that bind pollutants more effectively, facilitating their removal. However, the obtained results of comparable turbidity, TSS, COD removal efficiency for 2000 and 2500 ppm $FeSO_4{\cdot}7H_2O$ can be explained by the subsequent slowdown with the destruction of flocs formed during sedimentation at high doses of $FeSO_4{\cdot}7H_2O$ coagulant and the excess of this dose led to the reverse stabilisation of flocs due to excessive charge [21].

Adjusting the pH is important for efficient deposition, especially for hyllysing coagulants [22]. $Ca(OH)_2$ lime, when reacting with bicarbonate and carbonate ions, also

forms a precipitate of calcium carbonate, which intensifies the deposition through the co-precipitation phenomenon [23]. Therefore, using different doses of $Ca(OH)_2$ lime from 5.55 to 1105 ppm, which created a pH of 7.0 ± 0.2 to 10.0 ± 0.2 units, with fixed stirring, the percentage of turbidity, TSS, COD and PO_4^{3-} removal was determined. The percentage of removal of turbidity (Fig. 2e), TSS (Fig. 2f), COD (Fig. 2g), and PO_4^{3-} (Fig. 2h) increased, reaching maximum values at pH = 9.0 ± 0.2 units for turbidity, TSS, COD and pH = 8.0 ± 0.2 units for PO_4^{3-}. Then the removal efficiency decreased at pH = 10.0 ± 0.2 units for turbidity, TSS, COD; at pH = 9.00 ± 0.2 units and pH = 10.0 ± 0.2 units for PO_4^{3-}. The increase in the percentage of removal with pH can be explained by the presence of positively charged hydrolysed particles of iron hydroxide forms, which enhance the neutralisation capacity. At pH = 10 units and more, iron is primarily in the insoluble form of hydroxides, thus the neutralising capacity is exhausted. Removal PO_4^{3-}demonstrated moderate sensitivity to changes in pH with a slightly higher removal rate at pH = 8.00 ± 0.2. At pH > 7.5, the phosphate ion exists in the form of hydrophosphate ions (HPO_4^{2-}), which can be assumed to intensify the formation of ferrous phosphate precipitates due to the interaction between HPO_4^{2-} and positively charged iron particles. To summarise, at higher (pH > 9.0) and lower (<8.0) pH values, the removal efficiency of joint coagulation with $FeSO_4 \cdot 7H_2O$ and liming with $Ca(OH)_2$ decreases.

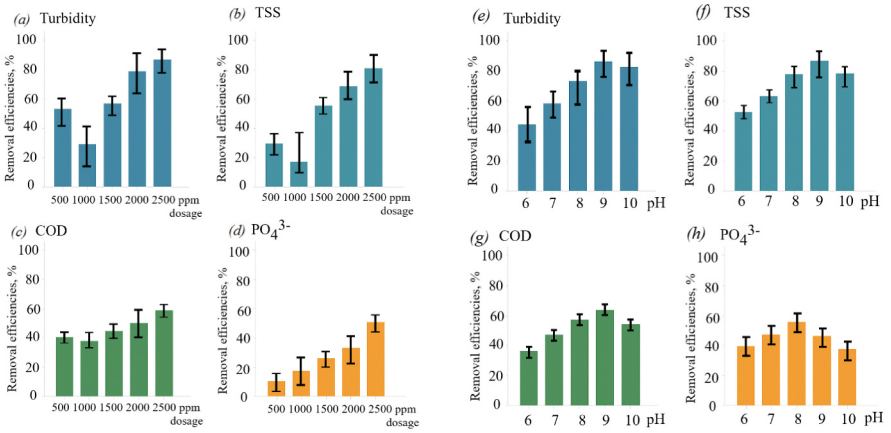

Fig. 2. The effect of $FeSO_4 \cdot 7H_2O$ coagulant dosage on the removal of turbidity (a), TSS (b), COD (c) and PO_4^{3-} (d) and the effect of pH at $Ca(OH)_2$ lime dosage and coagulation on turbidity (a), TSS (b), COD (c) and PO_4^{3-} (d) removal

The dynamics of changes in the removal efficiency of turbidity (Fig. 3a), TSS (Fig. 3b), COD (Fig. 3c), and PO_4^{3-} (Fig. 3d) in the processes of coagulation and liming with the participation of PAM flocculant shows a clear dependence between the flocculant dosage and the percentage of removal up to the PAM dose of 1.0 ppm. With an increase in the PAM dose within 0.25 ppm, a gradual increase in the removal efficiency of all studied indicators is observed. The most pronounced positive effect of PAM is demonstrated for turbidity and TSS: their removal efficiency exceeds 90% at a dose of

more than 1.0 ppm and is almost equal in the range of PAM doses of 1.5–2.0 ppm, which indicates the optimisation of aggregation and deposition of coagulated sludge. COD removal also increases with PAM dose, although the increase is less pronounced, probably due to the partial solubility of organic compounds that do not fully precipitate. A gradual increase in the efficiency of PO_4^{3-} removal from 50.2% to 73.5% may indicate the participation of the flocculant in the formation of precipitates of insoluble iron and calcium salts due to electrostatic neutralisation and complexation with ions. Flocculant PAM significantly enhances the efficiency of combined coagulation and liming, especially at an optimal dose of 1.0 ppm or more. This may be due to improved interparticle contacts and the formation of dense flocs due to the chain structure of PAM. However, the efficiency gains tend to saturate, indicating that the limiting concentration (optimal dose) is reached, after which additional flocculant addition does not provide a proportional increase in purification. In this case, it can be stated that this phenomenon is observed at a PAM dose of more than 1.0 ppm.

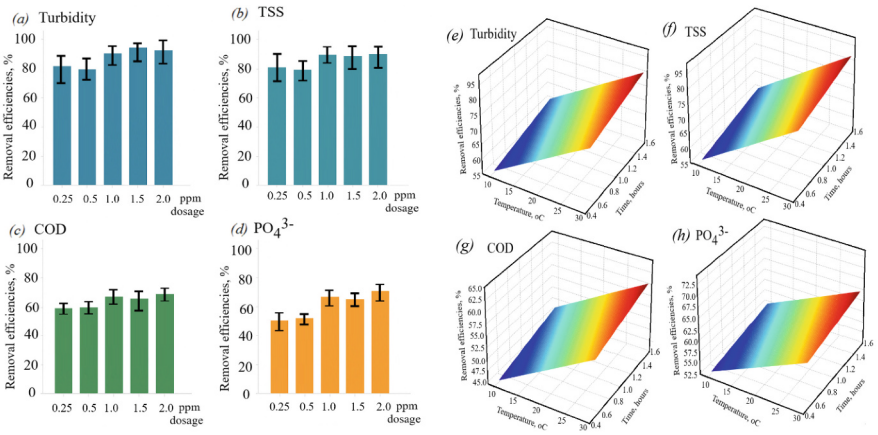

Fig. 3. The effect of flocculant dosage on the removal of turbidity (a), TSS (b), COD (c) and PO_4^{3-} (d) during coagulation and liming and the influence of temperature and settling time on the removal of turbidity (a), TSS (b), COD (c) and PO_4^{3-} (d) during coagulation - flocculation - liming.

As the temperature of the polymerisation process is increased, the movement of the molecules is also increased, leading to more efficient collisions and faster polymerisation [24]. Consequently, this results in polymers with elevated molecular weights, thereby enhancing their adsorption and bridging properties. Consequently, the removal efficiency increases with both increasing temperature and increasing deposition time (Fig. 3e, f, g, h). This trend reflects the typical behaviour of coagulation - flocculation - liming processes, where higher temperatures accelerate the hydrolysis and aggregation of the formed flocs, and longer time provides better floc stabilisation and deposition [25]. The highest efficiencies for turbidity and TSS were achieved at temperatures ranging from 20 to 30 °C and settling times of more than 1.4 h. This finding indicates that improved aggregation and sedimentation occur at elevated temperatures. For both COD

and PO_4^{3-}, the trends are analogous, yet the removal rate is lower, indicating partial chemical binding of phosphates to calcium and constrained capacity for coagulation-based organic removal. The optimal conditions for this process are a temperature of 25 ± 5 °C and a duration of 1.4 h, which ensure maximum efficiency for all four indicators without significantly increasing the process time.

The correlation analysis presented in Fig. 4a facilitates the quantification of the strength and direction of the relationship between the parameters of the water treatment process (coagulant dose, flocculant, pH, temperature, contact time) and the efficiency of pollutant removal (turbidity, TSS, COD, PO_4^{3-}). The highest correlation coefficients (r = 0.92–0.97) were found between coagulant dose, pH, temperature, settling time and turbidity, TSS, COD and PO_4^{3-} removal efficiency, indicating a strong relationship between these factors in this combined water treatment process (Fig. 7). In particular, pH (r = 0.97 for turbidity and 0.95 for COD) significantly affects the hydrolysis of $FeSO_4 \cdot 7H_2O$ coagulant and the precipitation of hydroxides, which serve as flocculation nuclei. In a similar manner, the temperature and duration of deposition have a direct impact on the kinetics of aggregation and floc growth. The coagulant dose has been demonstrated to exhibit a high degree of correlation with the purification rates (r = 0.94–0.97), thereby confirming its dominant role in the primary coagulation mechanism. Conversely, the dosage of PAM flocculant exhibited a negligible correlation with the majority of water treatment parameters, with r values ranging from 0.12 (turbidity), 0.11 (TSS), 0.25 (COD), and 0.32 (PO_4^{3-}).

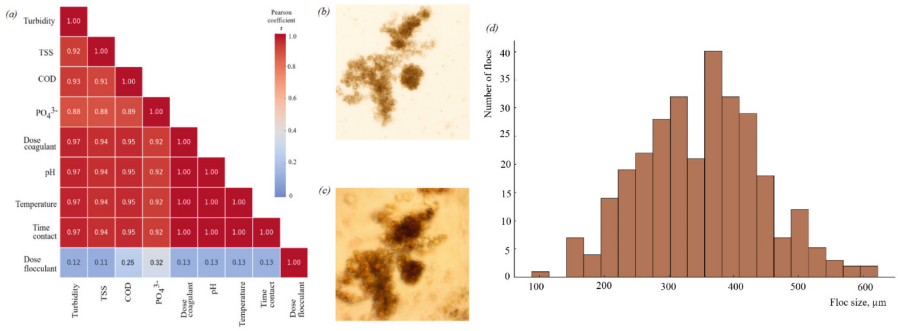

Fig. 4. Pearson correlation matrix of conditions, factors and efficiency (a), microscopic view of the formed flocs at the beginning (b) and at the end (c) and histogram of the size distribution of flocs formed after (d) the combined coagulation - flocculation - liming processes.

As a consequence of the integrated processes of coagulation, flocculation and liming, a discernible alteration in the morphology of flocs is evident (Fig. 4b,c). At the initial stage (Fig. 4b), the formed flocs exhibit a branched structure with a less dense texture, indicating an active primary aggregation of colloidal particles under the influence of the coagulant. Upon completion of the processes (Fig. 4c), the flocs become more compact, dense and darker, indicating increased particle adhesion in the presence of the flocculant and increased pH due to liming. The analysis of the histogram of the floc size distribution (Fig. 4d) shows that most flocs have a size in the range of 300–400 µm, which is

favourable for efficient sedimentation. This size ensures a high sedimentation rate and improves the conditions for subsequent treatment stages, confirming the feasibility of simultaneous use of $FeSO_4 \cdot 7H_2O$, PAM and $Ca(OH)_2$ to improve the aggregation and removal of turbidity, TSS, COD and PO_4^{3-} from water.

The implementation of the optimized coagulation - flocculation - liming processes using $FeSO_4 \cdot 7H_2O$, PAM, and $Ca(OH)_2$ contributes significantly to the environmental safety of industrial water treatment. The substantial reduction in turbidity, TSS, COD, and PO_4^{3-} ensures that the treated water meets regulatory discharge limits and is suitable for reuse in industrial operations, safe environmental discharge, or irrigation applications. Effective phosphate removal, in particular, mitigates the risk of eutrophication in receiving waters. The optimization of reagent doses and process parameters minimizes excess chemical use and reduces the potential for secondary pollution. Furthermore, the formation of dense and stable flocs facilitates efficient solid–liquid separation and reduces sludge generation, improving downstream sludge handling. This process supports a more sustainable and circular approach to water management in power plant operations by enabling internal water reuse and lowering the ecological burden of wastewater discharge.

5 Conclusions

The study demonstrated that the combined use of $FeSO_4 \cdot 7H_2O$, PAM, and $Ca(OH)_2$ is an effective method for improving industrial water quality. Optimal pollutant removal was achieved using $FeSO_4 \cdot 7H_2O$ at 2500 ppm, anionic PAM at 1.0 ppm, and $Ca(OH)_2$ sufficient to adjust the pH to 9.0 $\pm$ 0.2. These conditions ensured efficient removal of turbidity, TSS, COD, and PO_4^{3-}, particularly when applied at 25 $\pm$ 5 °C with a sedimentation time of 1.4 h. pH regulation played a key role in enhancing the hydrolysis and precipitation of iron hydroxides. Microscopic analysis confirmed the formation of denser and more compact flocs during the process. Pearson correlation analysis supported the dominant role of coagulant dose, pH, temperature, and settling time. This integrated approach offers a technically feasible and scalable solution for industrial water treatment.

References

1. Kuznietsov, P.M., Yaroschuk, O.V., Biedunkova, O.O., Pryshchepa, A.M.: Behaviour of dispersed particles in water treatment during lime softening and acid stabilisation treatment. Nanosistemi, Nanomateriali, Nanotehnologii, **22**, 1039–1052 (2024). https://doi.org/10.15407/nnn.22.04.1039
2. Kumar, A., Awasthi, M.K., Dutt, N., Singh, V.P.: Recent innovation in heat transfer enhancement techniques. Heat Trans. Enhancement Tech. **10**, 1–38 (2025). https://doi.org/10.1002/9781394270996.ch1
3. Biedunkova, O., Kuznietsov, P., Korbutiak, V.: A study of surface water quality using organic pollution indices: comparative characteristics and educational opportunities. Water Qual. Res. J. **60**, 333–347 (2025). https://doi.org/10.2166/wqrj.2025.044
4. Bandh, S.A., Mushtaq, B.: Water and Wastewater Treatment Technologies. Springer Water, Cham, pp. 67–163 (2025). https://doi.org/10.1007/978-3-031-86684-5_2

5. Randive, P., Bhagat, M.S., Bhorkar, M.P., et al.: Adaptive optimization of natural coagulants using hybrid machine learning approach for sustainable water treatment. Sci. Rep. **15**, 16096 (2025). https://doi.org/10.1038/s41598-025-96750-9
6. Kuznietsov, P., Yaroschuk, O., Biedunkova, O., Pryshchepa, A., Antonyuk, O.: Effective management of water resources cooling system discharges at nuclear power plants. In: Advances in Mechanical and Power Engineering II, CAMPE 2023, Lecture Notes in Mechanical Engineering, pp. 112–122, Springer, Cham (2025). https://doi.org/10.1007/978-3-031-82979-6_12
7. Iwuozor, K. O.: Prospects and challenges of using coagulation-flocculation method in the treatment of effluents. Adv. J. Chem. Sect. A, **2**, 105–127 (2019). https://doi.org/10.29088/SAMI/AJCA.2019.2.105127
8. Ehteshami, M., Maghsoodi, S., Yaghoobnia, E.: Optimum turbidity removal by coagulation/flocculation methods from wastewaters of natural stone processing. Desal. Water Treat. **57**, 20749–20757 (2016). https://doi.org/10.1080/19443994.2015.1110725
9. Ayoub, G.M., Hamzeh, A., Semerjian, L.: Post treatment of tannery wastewater using lime/bittern coagulation and activated carbon adsorption. Desalination **273**, 359–365 (2011). https://doi.org/10.1016/j.desal.2011.01.045
10. Mohamad, N.A., et al.: Temperature-driven pre-polymerization of copperas into poly-ferric sulphate: characteristics and coagulation behaviour in aquaculture treatment. Mater. Today Commun. **46**, 112868 (2025). https://doi.org/10.1016/j.mtcomm.2025.112868
11. Tian, Z., et al.: Synthesis and properties of starch grafted acrylamide flocculant for granite scrub tail mud. Int. J. Biol. Macromol. **319**(4), 145745 (2025). https://doi.org/10.1016/j.ijbiomac.2025.145745
12. Yang, Y., et al.: Application of flocculant and coagulant in treatment of oily pollutants: a mini review. Petrol. Sci. Technol. **43**, 913–929 (2024). https://doi.org/10.1080/10916466.2024.2307412
13. Zhao, X., et al.: In-situ formation of green rust during Fe(II) coagulation: dual reductive and adsorptive pathways for dyeing wastewater treatment. Water Res. **285**, 124174 (2025). https://doi.org/10.1016/j.watres.2025.124174
14. Kuznietsov, P., Biedunkova, O.: The role of carbonate equilibrium in scale formation of calcium carbonate in a power plant open recirculating system. Data Centric Eng. **6**, e13 (2025). https://doi.org/10.1017/dce.2025.9
15. Sahu, O.P., Chaudhari, P.K.: Review on chemical treatment of industrial wastewater. J. Appl. Sci. Environ. Manage. **17**, 241–257 (2013). https://doi.org/10.4314/jasem.v17i2.8
16. Ismail, I.M., et al.: Combined coagulation flocculation pre treatment unit for municipal wastewater. J. Adv. Res. **3**, 331–336 (2012). https://doi.org/10.1016/j.jare.2011.10.004
17. Awodiji, C., et al.: The effectiveness of hydrated lime as a flocculating agent in water treatment. Saudi J. Civ. Eng. **4**, 30–37 (2020). https://doi.org/10.36348/sjce.2020.v04i03.001
18. Biedunkova, O., Kuznietsov, P.: Liquid ion chromatographic determination of soluble ions in water: comparison of greenness and comprehensive assessment of irrigation suitability. Wat. Air Soil Pollut. **236**, 315 (2025). https://doi.org/10.1007/s11270-025-07975-3
19. Kuznietsov, P., Biedunkova, O.: Application of multivariate statistical techniques for assessing spatiotemporal variations of heavy metal pollution in freshwater ecosystems. Water Conserv. Sci. Eng. **10**, 13 (2025). https://doi.org/10.1007/s41101-025-00341-8
20. Marovic, D., et al.: The role of rapid curing on the interrelationship between temperature rise, light transmission, and polymerisation kinetics of bulk-fill composites. Int. J. Mol. Sci. **26**, 2803 (2025). https://doi.org/10.3390/ijms26062803
21. Ghernaout, D., Ghernaout, B.: Sweep flocculation as a second form of charge neutralisation - a review. Desal. Water Treat. **44**, 15–28 (2012). https://doi.org/10.1080/19443994.2012.691699

22. Feng, H., Huang, Z., Zhang, Z.: Molecular fingerprinting of dissolved organic matter during coagulation pretreatment of real textile printing and dyeing wastewater. J. Environ. Manage. **387**, 125933 (2025). https://doi.org/10.1016/j.jenvman.2025.125933
23. Jorjani, E., Sauvageau, J., Mrabet, D., Rejeb, M.: Advances in lithium extraction from spodumene: alternatives to sulfuric acid digestion. Minerals **15**, 574 (2025). https://doi.org/10.3390/min15060574
24. Bazan-Panana, G.D., Torres-Calla, M.J., Carranza-Oropeza, M.V.: Preparation of a biomedical scaffold from high-molecular-weight poly-DL-lactic acid synthesized via ring-opening polymerization. Polymers **17**, 1708 (2025). https://doi.org/10.3390/polym17121708
25. Saxena, K., Brighu, U.: Comparison of floc properties of coagulation systems: effect of particle concentration, scale and mode of flocculation. J. Environ. Chem. Eng. **8**, 104311 (2020). https://doi.org/10.1016/j.jece.2020.104311

Mathematical Model of Heat Transfer in a Roll Caliber

Viktor Lyashenko[1], Elena Kobilskaya[1(✉)], Olga Demyanchenko[2], and Michail D. Todorov[3]

[1] Kremenchuk Mykhailo Ostrohradskyi National University, Kremenchuk, Ukraine
kobilskaya1983@gmail.com
[2] Lviv Polytechnic National University, Lviv, Ukraine
[3] Technical University of Sofia, Sofia, Bulgaria

Abstract. Modern requirements for product quality in rolling production require increased accuracy of temperature control of rolls in the rolling zone. This is possible by controlling the temperature regime using a mathematical model of the thermal process in the roll caliber. Quite promising, from the point of view of reducing energy costs for strip production, is the use of continuous casting-rolling technology, which allows obtaining metal, in particular steel strip, as close in thickness as possible to the finished product. This significantly reduces the production cycle and the number of technological operations and required equipment.

The purpose of this work is to build mathematical models of the temperature field of rolls during traditional strip rolling technology and a mathematical model of the temperature field of rolls during continuous strip casting-rolling technology (technology using roll crystallizers) and to develop methods for solving model problems.

In the models presented in this paper, the authors tried to generalize and improve the mathematical models of thermal processes during rolling and continuous strip casting-rolling by setting more accurate boundary conditions. The models consider the different heat exchange between the internal and external surfaces of the roller with the strip and the outgoing roller core, as well as perfect thermal contact between the different roller layers. The constructed mathematical models, despite the fact that they describe various technological processes, make it possible to optimize and predict the cooling-heating parameters, as well as the service life of rolls in industrial conditions.

Keywords: Mathematical model · Thermal processes · Continuous casting-rolling technology · Rolling · Perfect thermal contact

1 Introduction

Rolling of strip products is accompanied by significant changes in temperature conditions along the production line. It is impossible to meet modern requirements for rolled product quality without using process control systems that must consider the maximum number of influencing parameters. One of the most important indicators of

H. Altenbach et al. (Eds.): CAMPE 2025, LNME, pp. 75–83, 2026.
https://doi.org/10.1007/978-3-032-16381-3_8

strip rolling technology is the rolling temperature, which has a significant impact on the energy parameters of the rolling process [1], the structure and mechanical properties of the resulting product. One of the important conditions for optimizing the temperature regime is clear control of the heat exchange conditions of the rolls with the environment surrounding the roll. The use of continuous roll casting of liquid metal in roll crystallizers is a promising direction in the production of metal strip, which allows to significantly reduce the energy costs for its production [1, 2]. Due to the reduction in the number of hot processing operations compared to traditional technology for producing thin strips, rolling mills achieve significant savings in energy resources, which is very relevant in our time. During the development of energy-saving technologies for the production of strip and rolled products, great importance is attached to the mathematical modeling of the technological process in the roll crystallizer. Direct observation of the processes occurring in the crystallization-deformation zone, due to its closed nature, remains practically impossible for the researcher. Therefore, simultaneously with the development of experimental studies, the question of creating physical and mathematical models describing the processes of strip rolling and strip casting-rolling remains open.

2 Literature Review

A number of mathematical models of the heat transfer process during strip rolling and during strip casting-rolling have been proposed in the scientific literature [2–9]. In most studies, mathematical models of the thermal process during strip casting-rolling involve a number of assumptions made to simplify such a complex process [3]. In [5], a finite element model was developed to simulate the thermal process during strip rolling, which took into account various strip rolling parameters and high-temperature properties of the work roll material. In [6], the construction of a finite-element model and adjustment of parameters of electromagnetic induction heating made it possible to estimate the temperature field during the rolling of titanium and aluminum. Evaluation of the effect of rolling temperature and compression speed of Ti/Al plates was carried out with the help of rolling experiments. In [9], a finite element one-dimensional model of heat transfer of a casting roller during two-roll casting of an aluminum alloy was developed. All the above studies are mainly focused on finite element models of heat transfer of individual elements of a complex system (roller-sheet). In this case, it is not taken into account that the heat exchange conditions of the inner and outer surfaces of the roll with the strip are different, since the inner surface of the roll interacts with the coolant (or other medium), and the outer surface interacts with the cooling liquid or air. The conditions of perfect thermal contact of different layers of the roll in the case of a two- or three-layer roll are not taken into account; also, in most models, there is no nonlinear component in the boundary conditions – the Stefan-Boltzmann conditions [3–8].

The aim of this work is to develop a model of the temperature field of rolls during the traditional technology of hot strip rolling and a mathematical model of the temperature field of rolls during the technology of continuous casting-rolling of strip (technology using roller crystallizers), and to develop methods for solving model problems.

3 Research Methodology

3.1 Temperature Field of Rolls During Traditional Rolling Technology

Let us consider a physical model of the temperature field of a rolling mill during traditional strip manufacturing technology. The outer surface receives heat from the deforming strip and then loses it outside the deformation zone according to Newton's and Stefan-Boltzmann's laws. Its inner surface loses heat by convection or conduction, in some cases, and also by radiation. In the zone of contact of the roll with the strip, heat from the roll surface is transferred to its axis by thermal conduction. In the other of the roll, heat is lost by radiation, convection or conduction. Such a thermophysical model of the heat exchange process during rolling leads to a mathematical model based on the homogeneous equation of heat conduction, which has the form

$$\lambda\frac{1}{r}\frac{\partial}{\partial r}(r\frac{\partial T}{\partial r})+\lambda\frac{1}{r^2}\frac{\partial^2 T}{\partial\phi^2}+\lambda\frac{\partial^2 T}{\partial z^2}-c\rho\frac{\partial T}{\partial t}=0. \tag{1}$$

During the strip rolling process, the temperature field significantly depends on the time and number of roll rotations, resulting in uncontrolled heat transfer. Therefore, a unsteady heat conduction equation is used to calculate the roll's thermal state. We further assume that the temperature of a cylindrical roll does not depend significantly on the axial coordinate, and that the bases are thermally insulated. In this case, determining the temperature distributions on the surface and in the body of the roll leads to an initial-boundary value problem for heat conductivity in the axial cross-section of a hollow cylinder $T = T(r, \phi, t)$, which rotates around its axis with an angular velocity ω. When the heat flux is orthogonal to the axis of rotation, we have the initial-boundary value problem in $\Omega \times t = \{(r, \phi)|R_1 < r < R, 0 < \phi < 2\pi, t > 0\}$

$$\lambda\frac{1}{r}\frac{\partial}{\partial r}(r\frac{\partial T}{\partial r})+\lambda\frac{1}{r^2}\frac{\partial^2 T}{\partial\phi^2}-c\rho\frac{\partial T}{\partial t}=0,$$

$$T(r,\phi,0)=T_0,\ \ T(r,\phi+2\pi,t)=T(r,\phi,t)\,,$$

$$\left.\frac{\partial T}{\partial r}\right|_{r=R_1}=-h_2(T_{c_2}-T),\,0<\phi<2\pi,\quad \left.\frac{\partial T}{\partial r}\right|_{r=R}=\overline{F}(\phi,t,T), \tag{2}$$

$$\overline{F}(\phi,t,T)=\begin{cases}h_2T_M, & \omega t<\phi<\phi_0+\omega t\\ h_1(T_c-T)+k(T_c^4-T^4), & \omega t+\phi_0<\phi<\omega t+2\pi,\end{cases}$$

where $a^2=\frac{\lambda}{c\rho}$, $h_i=\frac{\alpha_i}{\lambda}$, λ – thermal conductivity coefficient; c – heat capacity; ρ– material density; α_i – heat transfer coefficient, $T_M = T_m + T_d$, T_m temperature of the metal entering the deformation zone, T_d – average increase in temperature in the deformation zone (caused by metal deformation), T_c – temperature of the medium outside the ring, T_{c2} – temperature inside the ring.

A quasi-steady temperature distribution is established if the roll speed is sufficiently high, and the temperature is independent of time. Problem (2) reduces to the problem

of determining the temperature in the ring $\Omega = \{(r, \phi) | R_1 < r < R, 0 < \phi < 2\pi\}$. And the mathematical model for determining such a temperature is described by a stationary heat conduction equation with inhomogeneous boundary conditions and heat exchange conditions outside the ring, depending on the angular coordinate ϕ. . Problem (2) can be considered as a generalization of the one-dimensional finite element mathematical model considered in the work [9] (Fig. 1).

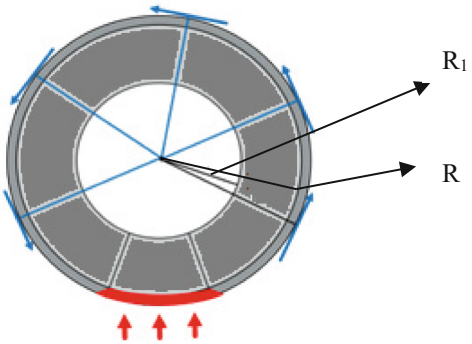

Fig. 1. Radial cross-section of a cylindrical roll

$$\frac{1}{r}\frac{\partial}{\partial r}\left(r\frac{\partial T}{\partial r}\right) + \frac{1}{r^2}\frac{\partial^2 T}{\partial \phi^2} = 0, \tag{3}$$

$$\left.\frac{\partial T}{\partial r}\right|_{r=R} = \overline{F}_1(\phi, T), \quad \overline{F}_1(\phi, T) = \begin{cases} h_2 T_M, & 0 < \phi < \phi_0 \\ h_1(T_c - T) + k(T_c^4 - T^4), & \phi_0 < \phi < 2\pi \end{cases} \tag{4}$$

$$\left.\frac{\partial T}{\partial r}\right|_{r=R_1} = -h_2(T_{c2} - T), \quad 0 < \phi < 2\pi, \tag{5}$$

$$T(r, \phi + 2\pi) = T(r, \phi). \tag{6}$$

Where $k = \frac{\varepsilon\sigma}{\lambda}$; ε – degree of blackness; σ – Stefan-Boltzmann constant. The solution to the problem is reduced to the Hammerstein integral equation, where the kernel of the equation is constructed based on the Green's function.

$$u(\xi) = u_L(\xi) - \tau \int_0^{2\pi} G_i(\phi, \xi) u^4 d\phi,$$

$$\begin{aligned} u_L(\xi) = {} & u_{21}(0) G'_\phi(0, \xi) - u_{21}(\phi_0) G'_\phi(\phi_0, \xi) + \omega_1 \int_0^{\phi_0} G_1(\phi, \xi) d\phi + \\ & + u_{22}(\phi_0) G'_\phi(\phi_0, \xi) - u_{22}(2\pi) G'_\phi(2\pi, \xi) + \omega_2 \int_0^{\phi_0} G_1(\phi, \xi) d\phi. \end{aligned} \tag{7}$$

This allows the differential equation with boundary conditions to be transformed into an integral equation, the solution of which is sought using iterations. The solution of the integral Eq. (7) was found using the modified Newton method. The iterative process was structured as follows

$$\varepsilon_{k-1}(\xi) = \tau \int_0^{2\pi} G_i(\phi, \xi) u_{k-1}^4(\phi) d\phi - u_{k-1}(\xi),$$

$$\phi_{k-1}(\xi) = \varepsilon_{k-1}(\xi) + u_L(\xi) - 4\tau \int_0^{2\pi} G_i(\phi, \xi) u_0(\xi)^3 \phi_{k-1}(\phi) d\phi,$$

The convergence of the solution was checked both by the deviation $\|\varepsilon_{k-1}\| \leq \|\varepsilon_k\|$, where < 1, and by the norm of the difference of iterations $\|u_{n-1} - u_n\| < \delta$. The number of iterations depends on the accuracy required, but does not exceed 100 in this case.

3.2 Mathematical Models of the Temperature Field of Rolls During the Production of Metal Strip Using Continuous Casting-Rolling Technology

According to the technology of manufacturing a strip in a roll crystallizer, liquid steel enters the space between the moving rolls and, upon contact with them, crystallizes, giving off its heat to the moving rolls, and then exits the space between the rolls in the form of a solid strip (Fig. 2). The thickness of the latter is determined by the distance between the rollers of the crystallizer, and the width is determined by the side walls of the roller crystallizer, which can vary. The rollers of the crystallizer are made of heat-resistant materials, for example, an alloy of copper with chromium in the form of hollow cylinders for rolling aluminum strip [9], which rotate and are intensively cooled inside by liquid [2].

The mathematical model of the heat exchange process during strip continuous casting-rolling in the roll caliber of a rolling mill includes three components: 1) a model of heat exchange of a part of the roll with the metal undergoing deformation, during which heat of deformation is released; 2) a model of heat exchange of a part of the roll with a liquid forcibly cooling it; 3) a model of heat exchange of a part of the roll with the surrounding environment according to the Newton and Stefan-Boltzmann laws.

Next, we will consider a mathematical model of the thermal process of a roll in a roller crystallizer, which has the form of a three-layer cylinder, in which one part of the outer layer is in contact with the molten metal, and the other part of the outer layer takes part in heat exchange with the surrounding environment, which has a temperature T_c. Heat is transferred to the second layer of the roll, which has perfect thermal contact with the first, by thermal conductivity, and from it to the third layer also by thermal conductivity. Determination of the temperature distribution $T_i(r, z, \phi, t)$ in a three-layer cylinder of a roller crystallizer, where part of the outer layer under conditions of perfect thermal contact perceives the heat flux from the molten metal and transfers it to the next one. The inner layer of the roll, which has a constant temperature lower than the outer layers, participates in heat exchange with the outer layers. The thermal

process is described by a boundary value problem for the homogeneous heat conduction equation in a cylindrical region with cyclically acting heat exchange conditions $\Omega \times t$: $\{0 < r < r_0,\ 0 < z < l,\ 0 < \phi < 2\pi,\ 0 < t < t_0\}$

$$\lambda_i \frac{1}{r}\frac{\partial}{\partial r}\left(r\frac{\partial T_i}{\partial r}\right) + \lambda_i \frac{\partial^2 T_i}{\partial z^2} + \lambda_i \frac{1}{r^2}\frac{\partial^2 T_i}{\partial \phi^2} - c_i \rho_i \frac{\partial T_i}{\partial t} = 0, \tag{8}$$

$$T_i(r, z, \phi, 0) = T_0, \tag{9}$$

$$T_i(r, 0, \phi, t) = T_0, \qquad T_i(r, l, \phi, t) = T_0, \tag{10}$$

$$\left.\frac{\partial T_1}{\partial r}\right|_{r=0} = 0, \quad \lambda_3 \left.\frac{\partial T_3}{\partial r}\right|_{r=r_3} = F(r, z, \phi, t, T) = \begin{cases} q, \forall, \omega t < \phi < \phi_0 + \omega t, \\ \alpha_1(T_c - T) + \varepsilon\sigma\left(T_c^4 - T_4^4\right), \end{cases} \tag{11}$$

$$T_i(r_{i-0}, z, t) = T_{i+1}(r_{i+1}, z, t), \quad i = 1...3, \tag{12}$$

$$\lambda_i \left.\frac{\partial T_i}{\partial r}\right|_{r=r_i-0} = \lambda_{i+1} \left.\frac{\partial T_{i+1}}{\partial r}\right|_{r=r_i+0}, \quad i = 1...3. \tag{13}$$

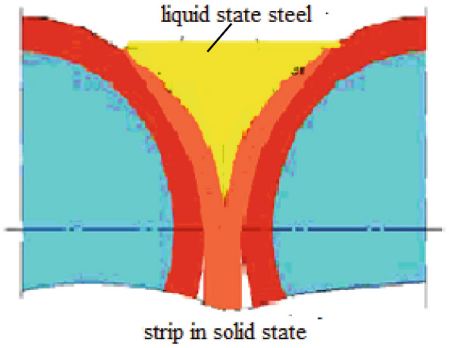

Fig. 2. The scheme of the formation of the strip in the roll crystallizer

The physical model of the problem allows for the application of a radial averaging operator to (8)–(13). This, in turn, leads to the appearance of an impedance-type boundary condition at the interface between the two media. The algorithm then proceeds from the last layer to the first using the finite element method [9].

4 Results

Numerical experiments were carried out based on the solutions of the problems. For the numerical experiment, the thermophysical characteristics of steel grade **1.2365** were taken, $T_0 = 300K$– initial temperature, $T_c = 300K$– ambient temperature $T_{M_1} =$

$900K, T_{m_1} = 615K$ – the temperature of the metal being processed and the temperature of the metal at the exit from the deformation zone, $h_i = \frac{\alpha_i}{\lambda}$ $\alpha_1 = 100\frac{W}{m^2K}, \alpha_2 = 150\frac{W}{m^2K}$, $\varepsilon = 0.7, \sigma = 6.67 \times 10^{-8}\frac{W}{m^2K^4}$ – Stefan-Boltzmann constant, $R = 0.2m$ and $R_1 = 0.1m$ – outer and inner radius of the ring.

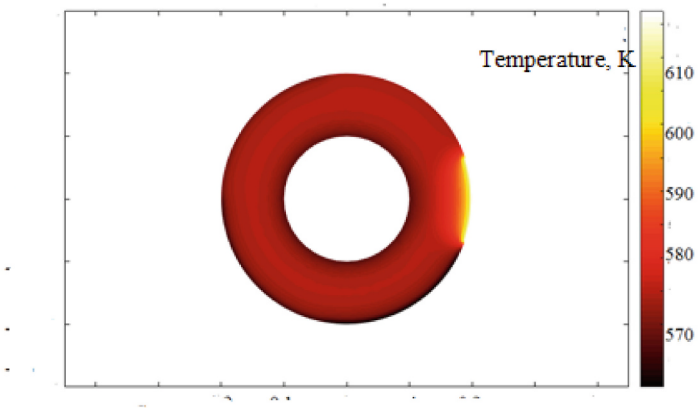

Fig. 3. Temperature distribution obtained at t = 10 s in radial cross-section of a cylindrical roll

Figure 3, 4 describes the temperature state in the cross section of a steel cylindrical roll that perceives heat within the range of the rotation angle change $0 < \phi < \phi_0$ and within $\phi_0 < \phi < 2\pi$ loses heat according to Newton's and Stefan-Boltzmann's laws 10 sec after the start of the rolling process.

Numerical calculations of the temperature distribution of the heat exchange process during rolling are given in Table 1. It contains the results of temperature measurements T_n using the AXIOMET-6520 pyrometer and the results of the computational experiment found from (3)–(6) Tm. $\Delta = |T_n - T_m|$ – the modulus of the difference between the results of temperature measurement using a pyrometer and the results of numerical modeling on the roll surface, $\delta = \frac{\Delta}{Tn}100\%$ relative calculation error.

Table 1. Comparative results between numerical and experimental analysis

ϕ, rad	Tn, K	T_m, K	Δ, K	$\delta, \%$
$\frac{\pi}{3}$	585	554	31	5.3
$\frac{2\pi}{3}$	565	540	25	7. 6
π	550	525	25	4. 5
$\frac{4\pi}{3}$	565	535	30	5. 3
$\frac{5\pi}{3}$	570	540	30	5. 3

(*continued*)

Table 1. (*continued*)

ϕ, *rad*	Tn, K	T_m, K	Δ, K	δ, %
2π	610	578	32	5. 2

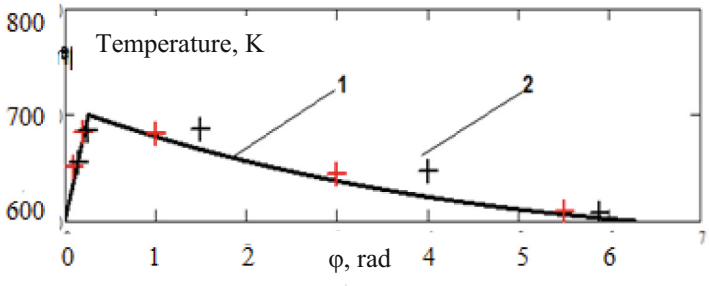

Fig. 4. Temperature distributions obtained from curve 1 are from (8)–(14) for a steel roll; curve 2 « +» – the results of the natural experiment.

5 Conclusions

A physical and mathematical model of the temperature field of a hollow roll of a rolling mill, which rotates around its axis with a constant angular velocity, has been constructed. The constructed model describes the thermal process occurring during strip rolling using traditional technology and takes into account the thermal interaction between the roll and the strip. In the case of a quasi-steady temperature distribution, the mathematical model of the thermal process in the hollow roll cross-section is described by a problem for the heat conduction equation in a ring with inhomogeneous boundary conditions and heat transfer conditions outside the ring, which depend on the angular coordinate. Integral equations were used to solve this problem. The second part of the paper is devoted to the study of the thermal process of rolls during the production of metal strip using the continuous casting-rolling technology. A mathematical model of the temperature field of a complex system – a three-layer roll crystallizer during the production of metal strip with perfect contact between roll layers with different thermophysical characteristics of the layers has been constructed. Analysis of the model, namely a comparison of a series of numerical and natural experiments, showed good agreement with the measured values. The calculation error does not exceed 7%. The constructed mathematical model and the method for constructing impedance conditions make it possible to obtain modeling results close to real conditions, which is confirmed by experiments. Further research will focus on using the data obtained from modeling the thermal behavior of the roller and the ideal shape of the cast strip to control the thermal processes during rolling. The results of this study provide a valuable theoretical basis for improving the design of roller structures in the strip rolling and strip casting-rolling processes.

References

1. Kholiavik, O., Nogovitsyn, O., Kravchuk, O., Samoilenko, R., Boris, O.: Rheological characteristics of steel in continuous roll casting-rolling. Mech. Adv. Technol. **5**(3), 381–387 (2021). https://doi.org/10.20535/2521-1943.2021.5.3.250182
2. Hui, Z., Guangming, C., Kuangdi, X.: Twin-roll strip casting and rolling. In: Xu, K., (eds) The ECPH Encyclopedia of Mining and Metallurgy. Springer, Singapore (2024)
3. Yang, R., Wang, W., Zhu, C., et al.: Tailored casting and hot rolling temperatures for the preparation of hot stamping steel thin strip. Metall Mater. Trans. B **55**, 4104–4109 (2024). https://doi.org/ https://doi.org/10.1007/s11663-024-03269-x
4. Mei, R., Chen, L., Bao, L., Li, C., Liu, X.: Numerical simulation and temperature modeling of magnesium alloy strip rolled by heated roll. Metals **13**(10), 1785 (2023). https://doi.org/10.3390/met13101785
5. Wang, J., Jiaze, C.H., Menghao, Z.H., Wei, L., Yan, P.: Analysis of fatigue damage of hot rolling work rolls coupled with wear effect. J. Manuf. Process. **131**, 1423–1436 (2024). https://doi.org/10.1016/j.jmapro.2024.09.119
6. Yu, C., He, Z., Lv, Q., et al.: Preparation of Ti/Al composite plates by differential temperature rolling with induction heating. Int. J. Adv. Manuf. Technol. **117**, 383–394 (2021). https://doi.org/10.1007/s00170-021-07775-z
7. Wang, X., Zhang, W., Ai, Y.: Influence of edge thermal spraying on the temperature field and thermal crown of work roll during cold rolling of aluminum alloy strip. Int. J. Adv. Manuf. Technol. **127**, 4331–4338 (2023). https://doi.org/10.1007/s00170-023-11830-2
8. Guo, C., Xue, Y., Yan, F., Hu, X.: Numerical simulation on flow and heat transfer in twin roll strip casting and rolling molten pool with side dams vibrating. Int. J. Adv. Manufact. Technol. **125**, 4497–4512 (2023). https://doi.org/10.1007/s00170-023-10930-3
9. Lu, J., Liu, L., Pan, W., Wang, W., Dou, K.: New model for heat transfer of copper roller in twin-roll strip casting to assist experimental and industrial process. Int. J. Therm. Sci. **213**, 109826 (2025). https://doi.org/10.1016/j.ijthermalsci.2025.109826
10. Ullmann, M., Stirl, M., Prahl, U.: Twin-roll casting defects in light metals. J. Mater. Sci. **59**, 19003–19022 (2024). https://doi.org/10.1007/s10853-024-10211-8
11. Xu, H., Zhou, L., Wang, W., et al.: A simple route for preparation of TRIP-assisted Si–Mn steel with excellent performance using direct strip casting. Int. J. Miner. Metall. Mater. **31**, 2173–2181 (2024). https://doi.org/10.1007/s12613-023-2818-z
12. Lu, C., Pan, Z., Wang, W., et al.: High-temperature simulation study of cracking mechanism during the strip casting process of P-containing weathering steel. Metall. Mater. Trans. B **55**, 2626–2637 (2024). https://doi.org/10.1007/s11663-024-03122-1
13. Guo, C., Guo, D., Li, H., et al.: Numerical and physical simulation of aluminum alloy electromagnetically twin-roll casting process. Metall. Mater. Trans. B (2025). https://doi.org/10.1007/s11663-025-03653-1
14. Biswas, P., Nayak, J., Kundu, A., et al.: A review on the development of processing techniques for the production and casting of al-alloy and metal matrix composite material. Iran J. Sci. Technol. Trans. Mech. Eng. **49**, 35–66 (2025). https://doi.org/10.1007/s40997-024-00773-y
15. Lyashenko, V., Kobilskaya, E., Zagirnyak, M., Demyanchenko, O.: Mathematical model of thermal process in an infinite cylinder heated by a moving heat source. AIP Conf. Proc. **2522**, 040003–040009. AIP Publishing, United States (2022)

Enhancement of Combustion Processes of Nonstandardized Biomass in a Jet-Vortex Heat Generator Using Numerical Methods

Oleg Kravchenko[1(✉)], Valerii Fedoreiko[2], Andrii Avramenko[1], Mykola Rutylo[2], and Vitalii Homan[1]

[1] A. Pidhornyi Institute of Power Machines and Systems of NAS of Ukraine, Komunalnykiv Street, 2/10, Kharkiv 61046, Ukraine
krav@ipmach.kharkov.ua

[2] Ternopil Volodymyr Hnatiuk National Pedagogical University, M. Kryvonosa Street, 2, Ternopil 46027, Ukraine

Abstract. A highly efficient technology for the combustion of hard-to-burn agricultural biomass with an annual regeneration cycle has been developed in Ukraine, based on jet-vortex bio-heat generators. The technology enables the combustion of sunflower, rapeseed, wheat, and corn processing residues of various dispersity and with moisture content up to 40%. These heat generators, with capacities ranging from 1.0 to 5.0 MW, have proven their efficiency and are already widely applied, particularly for grain drying and building heating. The cost of thermal energy produced in such bio-heat generators is 5–7 times lower compared to traditional hydrocarbon-based sources. The objective of this study is to improve the environmental performance of a 3 MW vortex heat generator by optimizing biomass mixing and combustion processes through the application of numerical methods.

Numerical modeling of biomass particle mixing and combustion processes in the vortex heat generator was performed using the finite volume method. The obtained results revealed shortcomings in the combustion process within the flow path of the existing generator design. The authors propose a novel structural scheme, in which secondary air is supplied at an inclination to the axis of the heat generator. Numerical investigations demonstrated that such an organization of the combustion process reduces the velocity of combustible gas release from biomass particles, enhances the mixing of combustible gases with secondary air, and decreases nitrogen monoxide emissions by 22%.

Keywords: low-reactivity biofuel · numerical modeling · jet-vortex bio-heat generator · energy and environmental performance of combustion processes

1 Introduction

The agro-technically available volume of biomass with an annual renewal cycle in Ukraine amounts to 25–30 million tons per year, which is equivalent to more than 10 billion m3 of natural gas. This refers to biomass of agricultural origin, varying in particle

H. Altenbach et al. (Eds.): CAMPE 2025, LNME, pp. 84–93, 2026.
https://doi.org/10.1007/978-3-032-16381-3_9

size and moisture content up to 40%, which accumulates annually in large quantities after the processing of corn, sunflower, wheat, rapeseed, etc., and is currently considered as waste. For regions with developed agriculture, using such non-standardized biomass as fuel is economically the most feasible.

The main problem in obtaining thermal energy from such biomass is that standard heat-generating equipment designs do not ensure its efficient combustion. This problem has been addressed through the creation and implementation of original designs of jet-vortex bioheat generators for continuous combustion of high-moisture biomass with undefined particle size, moisture, and calorific value. High-quality energy and environmental performance of the generators is achieved thanks to an automated biomass dosing and combustion system based on artificial intelligence [1]. The energy efficiency of these complexes is quite high; however, further improvement of the environmental performance of combustion remains a very relevant task.

It is proposed to solve this problem by improving both the design of the heat generator and the processes of mixture formation and biomass combustion using modern 3-D modeling technologies.

Thus, the aim of this work is to improve the environmental performance of a vortex bioheat generator by optimizing the processes of mixture formation and biomass combustion using numerical methods. To achieve this aim, the following tasks were formulated:

- Analyze existing methodologies for numerical modeling of biomass combustion in heat generators;
- Propose new design solutions and operational control approaches for heat generators that can potentially enhance their efficiency and environmental performance;
- Conduct numerical studies and a comparative analysis of combustion processes in existing and improved heat generator designs;
- Develop scientific and practical recommendations for improving the environmental performance of the vortex bioheat generator.

2 Literature Review

Modern CFD modeling methods are increasingly being applied to the study of complex thermo-physical and physico-chemical processes, including the combustion of solid dispersed fuels and biomass. Achieving the highest possible model accuracy primarily depends on the correct formulation of numerical studies and the consideration of features that most significantly influence these processes. Verification of the model is crucial, preferably through comparison with experimental results.

In [2], the authors investigated the combustion characteristics of biomass particles in an industrial circulating fluidized bed (CFB) furnace. CFD modeling of individual particles provided insight into the physical and chemical processes of granular flow in the dilute and dense regions of the CFB furnace. A multiphysics coupled model of solid-phase combustion on the grate and gas-phase combustion of biomass in small chain-grate boilers was developed in [3]. The results demonstrated the possibility of stabilizing temperature distribution in the furnace and reducing NO_x emissions through the redistribution of primary air supply. The study in [4] conducted numerical and experimental investigations of co-firing brown coal and biomass in a 300 MW boiler. The

findings showed that when biomass particles are sprayed in a fixed position at a given proportion, NO_x emissions from wheat, corn, and cotton straw are reduced.

Research on gasification of woody biomass in fluidized bed reactors is presented in [5]. A comparative analysis of 2D and 3D modeling results indicated that both models show similar behavior of the fluidized bed motion; however, the relative error is significantly lower in three-dimensional calculations.

Enhancing the efficiency of wood and agro-pellet combustion in boilers using numerical modeling methods is discussed in [6]. The results indicate that the use of a combustion intensifier can achieve a significant reduction in unburned pollutant emissions (CO > 40% – > 30%), particulate emissions (28–56 mg/m3 at 10% O_2 in dry flue gases), and improved combustion efficiency (>2.6–3.7%).

The study in [7] focused on improving existing and developing innovative burner devices for their effective integration into most existing boilers. Comparison of numerical modeling results with experimental data showed satisfactory correlation and validated the feasibility of using the chosen model for the burner–boiler system.

In [8], the thermal decomposition process of biomass was studied through numerical modeling of its combustion in heat generators. The authors proposed a procedure consisting of a static modeling phase to create algorithms (macrofunctions) and a dynamic modeling phase where the CFD model is coupled with an external biomass decomposition model in the form of a user-defined function. The proposed approach was validated on various cases and showed good agreement between calculations and experimental data.

In [9], the authors proposed scaling up the pyrolysis of a single biomass particle to particles of larger diameter and a higher number of particles. As particle size and moisture content increased, the temperature difference between the particle surface and center also increased, resulting in longer pyrolysis times.

The work in [10] utilized new experimental methods with high spatial and temporal resolution, such as laser diagnostics, in combination with numerical modeling of physical and chemical aspects of biomass conversion. The approach allowed for understanding the link between transport phenomena, chemical kinetics, and physical transformation at the single-particle scale, aiding in resolving issues related to emissions and efficiency at larger scales.

The use of computer-based numerical modeling tools to enhance the efficiency of hydrocarbon and alternative energy resource combustion is described in [11]. Equipment modifications significantly reduced harmful atmospheric emissions and saved energy resources during thermal and electrical energy production.

In [12], the biomass pyrolysis process was divided into three stages: water evaporation, volatile release, and coke combustion. The results demonstrated that the numerical model could accurately reproduce temperature, velocity, and composition variations in a hot-water boiler with an accuracy of up to 20 K.

In [13], a three-dimensional CFD model was employed to analyze co-firing of biochar and pulverized coal in blast furnaces, taking into account binary particle flow characteristics. Results showed that adding biochar effectively increases the volume fraction of high-temperature regions in the rolling channel, improves preheating, and enhances combustion efficiency.

As noted in [14], numerical modeling of biomass gasification in fluidized bed reactors faces several challenges, including accurate modeling of the physical and chemical processes involved and numerical stiffness of dense particle two-phase flow problems. It was shown that changing the steam-to-biomass ratio in the range of 0.8–2.0 had minimal impact on pyrolysis and heterogeneous reactions, whereas homogeneous reactions were significantly affected, altering the final gas composition.

A comprehensive review of various numerical models for pyrolysis, gasification, and solid fuel combustion is provided in [15]. It is highlighted that 3D CFD can provide detailed local and global information on the interaction of hydrodynamics, mixing, and heterogeneous and homogeneous chemical reactions, even for complex systems such as combustion chambers, gasifiers, or chemical reactors.

The review of available technologies and methods indicates that contemporary research predominantly focuses on combustion processes at the level of an individual biomass particle, with the possibility of further scaling to groups of solid biomass particles. Complex processes such as fuel preparation, pyrolysis, release of combustible fractions, and interactions of turbulent and convective phenomena in the combustion chamber during biomass burning are considered.

However, scaling numerical simulation results from single-particle biomass combustion to multiple particles, their interactions with each other and with gas and air flows, as well as detailed analysis of the release of individual combustible gas components and complex heat transfer processes during solid biomass combustion, remain insufficiently studied. A detailed investigation of these issues will improve the accuracy and informativeness of numerical modeling results in studying solid biomass combustion processes.

3 Materials and Methods

Considering the authors' previous research [1, 11] along with international experience, this study employs the following algorithm to perform numerical investigations of the combustion processes of annually renewable biomass (Fig. 1).

It should be noted that, in the course of numerical modeling, experimental data on the physicochemical properties and calorific value of actual biofuels were utilized. The determination of calorific value was carried out in accordance with ISO 1716:2019, while their main physicochemical properties were established in accordance with ISO 18134–3 and ISO 1928–76. The computational model employed was verified by comparing the values of the main indicators of the biomass combustion process obtained through numerical simulations with the measurements taken during industrial tests of the developed jet-vortex heat generator with capacity of a 3 MW.

For a comparative computational study using numerical methods implemented in modern CFD software packages, an investigation was conducted into the processes of mixing, combustion, and the formation of toxic components in the flow section of a vortex heat generator.

The main features of the CFD model used in this work include the consideration of the unsteady process of combustible gas release from biomass particles, taking into account their gradual heating; and the tracking of biomass particle trajectories with

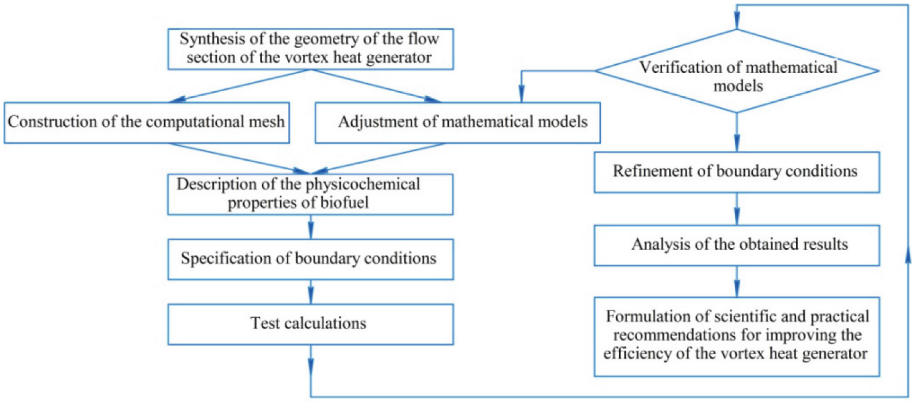

Fig. 1. Flowchart of the numerical study procedure.

respect to their size (the initial particle size was specified based on experimental data and recommendations from other authors).

The configuration (Fig. 2a) is based on a cyclone-type combustion chamber featuring a lower tangential injection of biofuel and primary air, along with an additional controllable tangential supply of secondary air. Tangential injection of the fuel–air mixture prolongs the residence time of fuel particles within the combustion zone by increasing their trajectory length, thereby significantly enhancing the completeness of biofuel combustion. The tangential supply of secondary air promotes improved mixing between fuel particles and the oxidizer and ensures the provision of sufficient oxygen for the complete and environmentally compliant combustion of low-reactivity solid fuels.

The combustion chamber of the heat generator is divided into three main zones. In Zone 1, primary air enters from below through openings in the lower horizontal wall, while the biomass–air mixture is injected tangentially. Zone 2 serves as the primary combustion zone, and Zone 3 allows for tangentially controlled injection of secondary air. This configuration enables partial oxidizer deficiency in Zone 2, promoting partial thermal decomposition of fuel components, which are then fully combusted in Zone 3. This approach is particularly effective for handling large, high-moisture particles.

The flow section of the jet–vortex heat generator, modeled in a CAD system in 3D, is shown in Fig. 2b. A computational mesh of this flow section was then generated for numerical simulation of mixture formation, combustion, and the production of combustion products, including pollutants (Fig. 2c).

Calculations were carried out using the finite volume method. To capture near-wall effects in the working fluid flow within the vortex heat generator, the computational mesh was refined in regions with abrupt geometric changes and near solid boundaries. For subsequent simulations, the third-level mesh of the computational domain was selected (Fig. 2c), containing over 3.8 million cells.

The energy and environmental performance of low-reactivity fuels, such as untreated biomass, is influenced by several factors, including combustion chamber design, the supply of air and biomass to the combustion zone, and the fuel's thermophysical properties, moisture content, and particle size distribution. The air excess ratio also affects

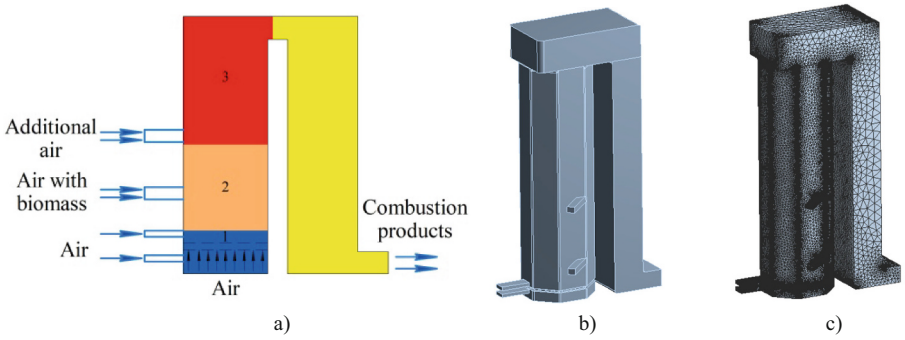

Fig. 2. Schematic (a), flow section geometry (b), and computational mesh (c) of the vortex heat generator.

combustion kinetics. These factors determine the occurrence and duration of key combustion stages—biomass drying and heating to the volatile release temperature, ignition and combustion of volatiles, char heating to ignition, and subsequent char volatile combustion—and ultimately govern overall energy and environmental performance.

Insufficient oxidizer leads to thermal decomposition and the formation of intermediate combustion products. The residual carbon after volatile release is highly porous and reactive, and moisture released during preliminary drying may promote steam or steam–oxygen conversion of carbon and hydrocarbons. For numerical modeling, averaged properties of actual biomass used in bio-heat generators were considered: lower heating value 18.5 MJ/kg, moisture 15%, and density 250 kg/m^3.

A critical factor influencing combustion efficiency and environmental performance is the density of the fuel bed. Higher fuel bed density shortens ignition time and accelerates particle combustion by reducing inter-particle distance and ensuring sufficient oxidizer, thereby increasing fuel burnout and reducing pollutant formation in the flue gases.

Assessing fuel steam density during biomass combustion requires studying individual particle motion and interactions. This enables identification of the flame shape and zones of incomplete combustion, supporting improved efficiency and environmental performance of low-reactivity biomass in vortex bio-heat generators. Numerical modeling should also consider particle size distribution, initial moisture, and the formation of residual carbon and ash.

4 Results and Discussion

Numerical analysis of biomass particle and gas trajectories in the combustion chamber suggested an improved vortex heat generator design. Two additional tangential secondary air channels, inclined slightly rather than perpendicular to the reactor axis (Fig. 3), promote higher particle trajectories, enhancing thermal decomposition and complete combustion.

All subsequent numerical simulation results and their comparisons are presented for two configurations: the existing bio-heat generator design (Fig. 2) and the improved design with additional secondary air introduced at an angle to the horizontal plane of

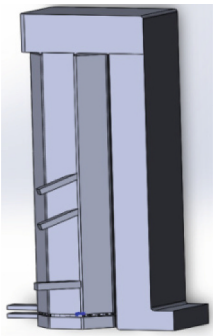

Fig. 3. Enhanced design

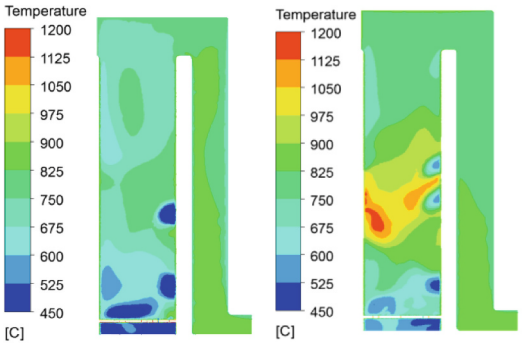

a) b)

Fig. 4. Comparative flame and gas temperature distributions.

the combustion chamber (Fig. 3). In all simulations, the air excess ratio was set at 1.5. Figure 4 shows comparative results of flame and gas temperature distributions in a vertical cross-section of the flow part for both the existing and improved bio-heat generator configurations.

For the existing design (Fig. 4a), the maximum gas and flame temperature reaches 975 °C in the central part of the vortex heat generator. This is due to excess air, where some of the heat is consumed in warming air that does not participate in combustion.

For the improved design (Fig. 4b), the maximum gas and flame temperature reaches 1200 °C in the central part of the vortex heat generator. Direct supply of secondary air to the combustion zone allows combustible gases (C_nH_m, H_2, CO) from biomass to mix more efficiently, enhancing combustion.

Figure 5 compares biomass particle size distribution and trajectories. In the improved design (Fig. 5b), particles rise only up to 2–2.5 m and release combustible gases within this region. In the existing design (Fig. 5a), particles rise higher and release gases over a longer period. This promotes higher fuel burnout and reduces tar deposition on heat-exchange surfaces.

The comparison of nitrogen monoxide (NO) mass fraction distribution is shown in Fig. 6. In the existing design (Fig. 6a), the maximum NO mass fraction occurs in the central part of the vortex heat generator, with $MF(NO) = 4.48 \times 10^{-6}$. In the improved design (Fig. 6b), the maximum NO mass fraction is observed in the upper part of the vortex heat generator, and NO emissions are significantly lower than in the existing configuration, at $MF(NO) = 2.66 \times 10^{-6}$, due to enhanced combustion and more complete fuel burnout.

Comparative of the distribution of mass fraction of combustible gases in the process of their exit from biomass is shown in Fig. 7. For the existing design (Fig. 7a) the exit of combustibles is observed in the lower part of the heat generator. Further, the combustible gases mix with air and burn at a lower speed and temperature. For the improved design (Fig. 7b) the exit of combustibles is mainly noted in the central part of the heat generator. Then the combustible gases mix with air and, evenly filling the volume of the flow part, burn at an increased speed and temperature.

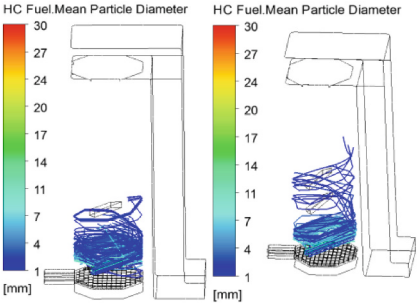

Fig. 5. Comparative biomass particle size distribution and trajectories.

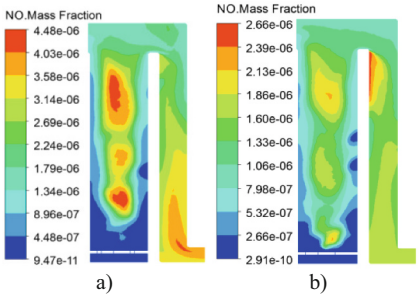

Fig. 6. Comparative NO mass fraction distribution.

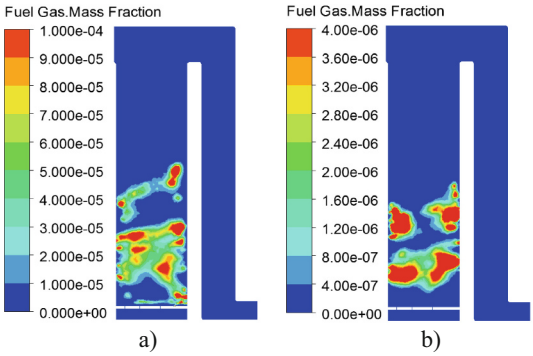

Fig. 7. Comparative of mass fraction of combustible gases

Table 1. Summary of comparative study results

Design configuration	Parameter			
	Exit temperature of heat generator, °C	Biomass particle rise height, m	Mass fraction of combustible gases	NO mass fraction
Existing design	700	1,9	1,1e-10	3,6e-10
Improved design	710	2,7	8,7e-09	2,06e-08

Table 1 summarizes the comparative study results. Modern 3-D modeling enables detailed analysis of complex processes, such as biomass mixing and combustion in the vortex heat generator. The improved design shows better environmental performance and lower unburned gas fractions, especially at higher air excess ratios.

Modifying the secondary air supply with two additional inclined channels reduces aerodynamic resistance for biomass particles and extends the height over which combustible gases are released. This improves mixing and combustion, lowering flue gas emissions. As a result, NO emissions decreased by 22%, with local values along the flow section nearly halved.

5 Conclusions

It has been proven that one of the ways to improve the results of numerical modeling of dispersed biomass combustion processes is to take into account the influence on combustion of the processes of mixture formation, movement and gasification of biomass particles during their stay in the combustion zone.

The design of the heat generator with a thermal capacity of 3 MW has been improved by changing the secondary air supply mode, which allows significantly increasing the efficiency of biomass combustion and reduces of harmful emissions into the atmosphere. Comparative analysis of the improved jet-vortex heat generator and its baseline design confirmed that modernization—particularly optimizing secondary air supply—reduces NO emissions by 22% and nearly halves local NO concentrations along the flow section.

Future studies should focus on optimizing mixing and additional air supply to enhance large-particle burnout and reduce oil-containing residues, improving heat-exchanger operation and reducing maintenance effort.

References

1. Fedoreiko, V.S., Rutylo, M.I., Iskerskyi, I.S., Zahorodnii, R.I.: Optimization of heat production processes in the biofuel vortex combustion systems. Natsional'nyi Hirnychyi Universytet. Naukovyi Visnyk. **1**(6), 83–8 (2020). https://doi.org/10.33271/nvngu/2020-6/083
2. Yang, M., et al.: CFD simulation of biomass combustion in an industrial circulating fluidized bed furnace. Combust. Sci. Technol. **195**(14), 3310–3340 (2023). https://doi.org/10.1080/00102202.2023.2260553
3. Jin, Y., et al.: Numerical simulation of combustion characteristics in a small-scale biomass chain grate furnace under different primary air conditions. ACS Omega **10**(22), 23775–23790 (2025). https://doi.org/10.1021/acsomega.5c02888
4. Li, J. Wang, Z., Ma, C.: Numerical simulation and combustion analysis of coal and biomass co-combustion. In: MATEC Web Conf. 2021 International Conference on Physics, Computing and Mathematical (ICPCM2021), vol. 355, p. 02013, p. 10 Mathematical Science and Application (2022). https://doi.org/10.1051/matecconf/202235502013
5. Mertsoy, E.Y.: Comparison of 2D and 3D numerical simulation of woody biomass combustion in fluidized bed reactor. Biomass Conv. Bioref. **15**, 21227–21246 (2025). https://doi.org/10.1007/s13399-025-06689-0
6. Horvat, I., Dović, D., Filipović, P.: Numerical and experimental methods in development of the novel biomass combustion system concept for wood and agro pellets. Energy **231**, 120929 (2021), ISSN 0360–5442, https://doi.org/10.1016/j.energy.2021.120929. (https://www.sciencedirect.com/science/article/pii/S0360544221011774)
7. Baraniuk, O., Siryi, O., Veremiichuk, H., Lysenko, O.: Simulation of pellet combustion in boilers up to 25 kW. Thermophys. Therm. Power Eng. **44**(4), 89–98 (2023). https://ihe.nas.gov.ua/index.php/journal/article/view/517

8. Ion, I.V., Popescu, F., Mahu, R., Rusu, E.A.: Numerical model of biomass combustion physical and chemical processes. Energies **2021**(14), 1978 (2021). https://doi.org/10.3390/en14071978
9. Han, F., et al.: Numerical simulation of heat transfer properties of large-sized biomass particles during pyrolysis process. Heliyon **9**(11), e21255 (2023). https://doi.org/10.1016/j.heliyon.2023.e21255
10. Fatehi, H., Weng, W., Li, Z., Bai, X.S., Alden, M.: Recent development in numerical simulations and experimental studies of biomass thermochemical conversion. Energy Fuels. **35**(9), 6940-63 (2021). https://doi.org/10.1021/acs.energyfuels.0c04139
11. Kravchenko, O., Homan, V., Suvorova, I., Baranov, I.: Using pneumo-hydrovortex nozzles for effective combustion of liquid boiler fuels engineering. In: Lecture Notes in Mechanical Engineering: Selected papers from the Int. Conference on Advanced Mechanical and Power Engineering (CAMPE-2021), pp. 67–77. Kharkiv, Ukraine, October 18–21, 2021. Cham, Switzerland: Springer (2023). https://doi.org/10.1007/978-3-031-18487-1_7
12. Yan, W., Hao, X.: CFD simulation study of a biomass pellet-fuelled boiler. J. Phys. Conf. Series **2584**(1), 012023 (2023). https://doi.org/10.1088/1742-6596/2584/1/012023
13. Zhao, P., Xu, R., Zhang, J., Yu, A., Guo, P., Hu, Z., Jia, G.: Numerical simulation research on the co-combustion of biochar and pulverized coal in the raceway of blast furnace. Energy **314**, 134310 (2025). ISSN 0360–5442, https://doi.org/10.1016/j.energy.2024.134310. (https://www.sciencedirect.com/science/article/pii/S036054422404088X)
14. Yang, M., Mousavi, S.M., Fatehi, H., Bai, X.S.: Numerical simulation of biomass gasification in fluidized bed gasifiers. Fuel **337**, 127104 (2023). ISSN 0016–2361, https://doi.org/10.1016/j.fuel.2022.127104
15. Hasse, C., Debiagi, P., Wen, X., Hildebrandt, K., Vascellari, M., Faravelli, T.: Advanced modeling approaches for CFD simulations of coal combustion and gasification. Progr. Energy Combustion Sci. **86**, 100938 (2021). ISSN 0360–1285. https://doi.org/10.1016/j.pecs.2021.100938

Modeling of a Constant Pressure Regulator for Alkaline Electrolyzers

Kotenko Dmytro(✉) and Zipunnikov Mykola

Anatolii Pidhornyi Institute of Power Machines and Systems of the NAS of Ukraine, 2/10 Kommunalnykiv Street, 61023 Kharkiv, Ukraine
dima.kotenko.96@gmail.com

Abstract. The article proposes a method for regulating the discharge of hydrogen (oxygen) from the gas separation system of an electrolyzer during continuous operation of the electrolytic cell under pressure. The hydraulic diagram of a membrane-less electrolyzer equipped with a controlled pressure regulating valve is illustrated. This method allows for the safe discharge of hydrogen and oxygen from the corresponding separators during the operation and maintenance of the electrolysis system. A valve control model is proposed to maintain constant pressure. A simulated model of deviations from ideal gas formation indicators is presented, and the feasibility of the valve control model is verified. The paper compares the efficiency and operating cycle of an electrolysis system with and without constant pressure support. Using a simulation-based model, the results demonstrate that although the average efficiency improvement is modest (from 71.3% without control to 72.8% with control), the benefits of regulation become more pronounced under higher operating pressures and larger separator sizes. These findings highlight that even incremental efficiency gains, when combined with improved stability, safety, and gas quality, can have meaningful implications for the design and scaling of electrolyzer systems.

Keywords: simulation modeling · control valve · pressure regulation · Alkaline electrolyzer

1 Introduction

Green hydrogen is one of the main renewable energy sources. It is universal and can be used across a wide range of industries, benefiting from its energy capacity, ability to be stored and transported, and the level of decarbonization that can be achieved by replacing fossil fuel resources with it.

According to the IEA report from July 2025, renewable energy sources account for the largest share of the increase in total energy supply (38%), followed by natural gas (28%), coal (15%), oil (11%), and nuclear energy (8%) [1]. Hydrogen review at the same time states that while green hydrogen market is still 1% of hydrogen demand due to costs and demand is still almost exclusively from established sectors (refining, ammonia, methanol and fossil-based direct reduced iron [DRI]), there are fast-growing

H. Altenbach et al. (Eds.): CAMPE 2025, LNME, pp. 94–101, 2026.
https://doi.org/10.1007/978-3-032-16381-3_10

market for fuel cell electric vehicles, and in shipping, the fleet of ships able to use hydrogen-based fuels is growing and offtake agreement activity has increased [2]. For this reason, optimization of green hydrogen costs is currently a highly relevant issue.

Alkaline remains the leading technology, with 60% of the additions and the global installed capacity [2]. At the same time techno-economic analysis show that efficiency could vary between 58–70% [3]. The increase in efficiency is a key objective of this research, as precise control of chamber pressure enables the electrolyzer to operate under optimal conditions.

2 Literature Review

The growing demand for renewable energy sources has positioned green hydrogen as a promising vector for achieving deep decarbonization across multiple industries [1–3].

Previous studies have examined designs, efficiency and enhancements for models of water electrolyzers [4], with particular attention to PEM electrolyzers enhancements [5] and alkaline electrolyzers enhancements using optimal operation parameters [6].

While numerous studies on alkaline systems focus on comprehensive reviews of electrochemical processes and optimal operating parameters [7, 8], as well as the cost-effectiveness of the technology in transport applications [9], integration with wind [10] and solar [11] systems, and advances in cell material design [12], other research emphasizes the superior performance [13] and responsiveness of PEM technologies under fluctuating loads [14], along with investigations into mass transfer optimization [15] and degradation mechanisms with mitigation strategies [16]. These contrasting directions highlight a persistent gap: unlike PEM systems, alkaline electrolyzers have not benefited from equivalent levels of design innovation and performance enhancement.

Despite significant usage of alkaline systems and parameter optimization works, few studies have examined alkaline degradation, design of pressure handling in alkaline systems and control tools for alkaline system as a main topic.

This gap provides the foundation for the present research, which seeks to develop a robust tool for control of optimal pressure in an electrolysis cell.

3 Research Methodology

3.1 Research Design

This study adopts a theoretical and simulation-based research design to model the process flow of hydrogen production via alkaline electrolysis with separator valve regulation that designed to maintain steady pressure needed for efficient evolution of hydrogen. The design was selected because it enables the integration of ideal laws of electrolysis and mass transfer with existing experimental data from the literature which is used in computational analysis to predict system performance under varying conditions.

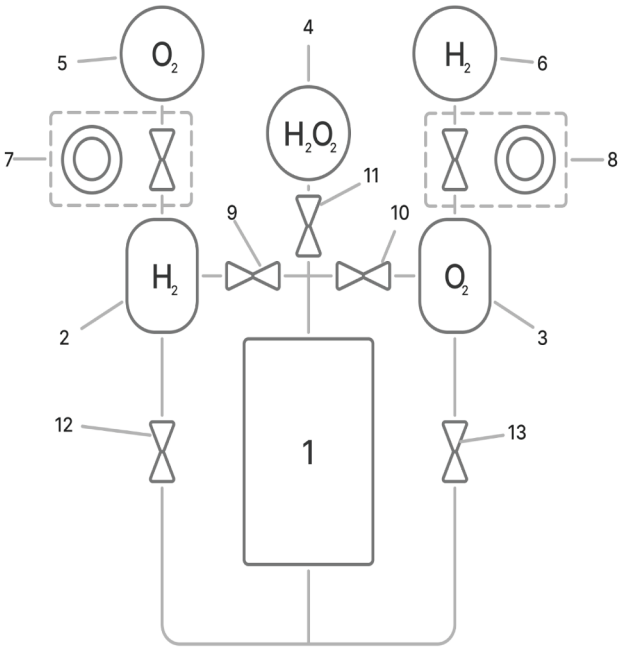

Fig. 1. Hydraulic diagram of a high-pressure membrane-less electrolyzer: 1 - electrolyzer cell; 2 - hydrogen separator; 3 - oxygen separator; 4 - residual gas separator; 5 - hydrogen storage tank; 6 - oxygen storage tank; 7,8 - electrically operated needle valve; 9 - hydrogen half-cycle solenoid valve; 10 - oxygen half-cycle solenoid valve; 11 - residual gas discharge solenoid valve; 12 - hydrogen feedback solenoid valve; 13 - oxygen feedback solenoid valve.

3.2 System Definition

To achieve optimal pressure parameters for alkaline electrolyzers and maintain them during process of gas evolution was developed a design of the system with electrically operated needle (Fig. 1) that regulates gas leak rate to gas containers.

The study was conducted by modeling a system with an electrically operated needle. The system was modeled with a fixed temperature of 300K, a half-cycle duration of 30 min, a separator volume of 0.75 L each, and a current of 2500 amperes.

3.3 Control System and Model Inputs

As noted in [7], although hydrogen evolution is theoretically defined by Faraday's law, real values deviate from the ideal. The Faraday's efficiency of an electrolyzer (the ratio of actual to theoretical productivity) is influenced by several factors, including overpotentials (where higher overpotential increases cell voltage and reduces overall efficiency), bubble coverage (slow or inefficient detachment leads to electrode surface blockage, decreasing the number of active reaction sites), and the reversible voltage (the thermodynamic decomposition voltage).

The bubble diameter and coverage rate decrease with increasing pressure, and the resistance between the electrolyte and electrode plate, which is called the ohmic overpotential, decreases. [7] demonstrated that the ohmic overpotential decreases slowly with increasing pressure and then hardly changes. At the same time reversible voltage increases when the pressure increases (but pressure has a smaller effect than temperature where high-temperature electrolysis requires lower electrical energy).

The control system for the valves is designed to maintain optimal pressure once it has been reached and sustain it until the end of gas generation during the corresponding half-cycle. The primary objective of the control procedure is to keep the pressure at the target value, which requires that the rate of gas leaving the separator chamber matches the rate of gas production. For simplicity, during activation, the controller operates based on the pressure defined by Fourier's law (2) and the valve loss law (3), while effects such as overpotential, bubble coverage, and reversible voltage are treated as errors (4) and are randomized according to correlations reported in the literature.

$$F - V_{loss} - error = 0 \tag{1}$$

$$F = \frac{dm}{dt} = \frac{I \cdot M}{n \cdot F} \tag{2}$$

$$V_{loss} = \frac{dm}{dt} = Cd \cdot A \cdot \rho \cdot v \tag{3}$$

$$error = F \cdot (1 - \eta(P)) \tag{4}$$

Thus, the regulating parameter for maintaining constant pressure is the size of the valve, which is determined as the difference between the opening required to release the produced hydrogen and the area required to handle underproduction (i.e., the size required to compensate for the underproduced gas compared to the ideal state) (5). The equations for the size of the opening for the release of produced hydrogen (6) and compensation for underproduction (7) are determined by the valve loss law (3).

$$A = A_F - A_{error} \tag{5}$$

$$A_F = \frac{F}{Cd \cdot \rho \cdot v} \tag{6}$$

$$A_{error} = \frac{error}{Cd \cdot \rho \cdot v} \tag{7}$$

3.4 Data Analysis and Validation

The efficiency of the system is simulated based on the data from Article 7 and the corresponding approximation shown in Figure 2. For the sake of experiment efficiency and its proximity to reality, the efficiency in modeling was taken with a random error of 3%, which made it possible to simulate noise and simultaneously test the regulator's performance in its presence.

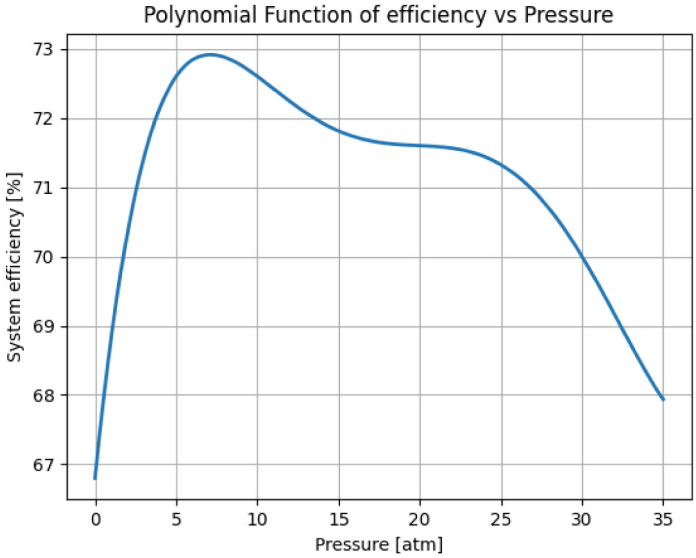

Fig. 2. Approximation of the efficiency of an electrolysis system based on the pressure in the system.

Validation is performed by comparing the pressure and efficiency of the process without a pressure maintenance system and with a system that maintains optimal pressure. An electrolyzer without pressure maintenance accumulates gas during production until the pressure in the separator reaches an acceptable level (which is significantly higher than the optimal level; in this example, a limit of 20 atmospheres is used), after which the pressure in the system is completely released. The process is repeated until the half-cycle is complete.

4 Results and Discussion

The results of the study are shown in Figs. 3 and 4, which illustrate the change in pressure in the electrolyzer and the efficiency of the system with and without a control valve. The results show that this control option can achieve the desired results. Although the average efficiency remains relatively the same—71.3% when using the model without control and 72.8% with control—the difference increases with an increase in configuration parameters such as maximum working pressure or separator size. It is also worth noting that with this type of regulation, we obtain a more stable gas flow, which reduces the likelihood of entrainment with electrolyte turbulence and, as a result, increases the quality of the gas obtained. In addition, the constant and regulated output of the gas obtained allows for predictable and safer filling of gas tanks.

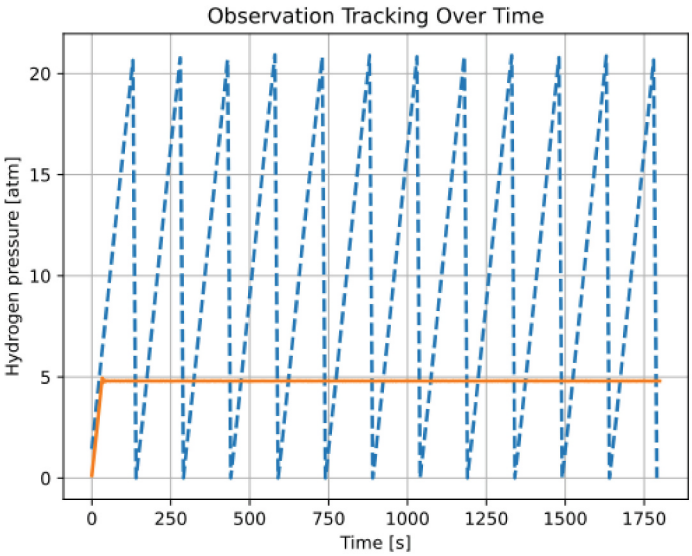

Fig. 3. Comparison of changes in the pressure of an electrolyzer with constant pressure (orange solid line) and an electrolyzer without constant pressure control (blue dotted line)

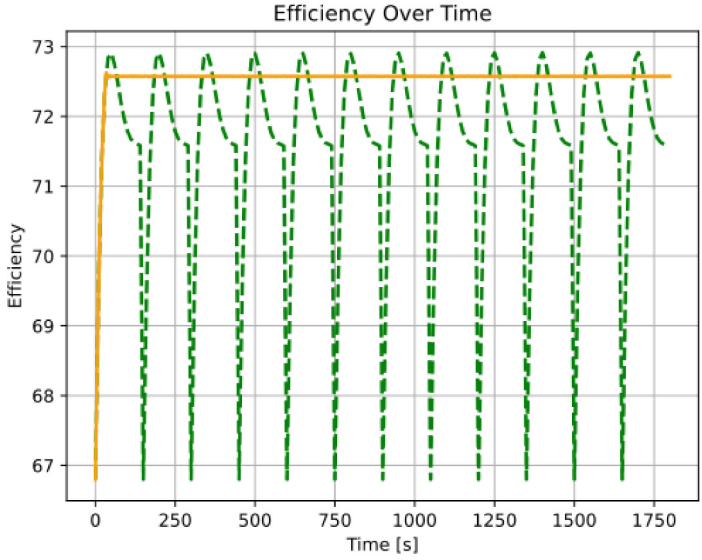

Fig. 4. Comparison of changes in the efficiency of an electrolyzer with constant pressure (yellow solid line) and an electrolyzer without constant pressure control (green dotted line)

5 Conclusions

This study examined the possible effect of incorporating a control valve into an alkaline electrolyzer system, with particular focus on pressure regulation, efficiency, and gas quality. The results obtained using imitational model demonstrate that while the average efficiency improvement is modest rising from 71.3% without control to 72.8% with control the advantages of regulation become more evident under higher operating pressures and larger separator sizes. The results of operation under noisy conditions indicate that the valve-based loss-speed adjustment approach provides a robust solution that does not require the continuous tuning and regulation typically associated with PID controllers.

In addition to efficiency, the implementation of a control valve significantly enhanced operational stability. The stabilization of gas flow reduced the likelihood of electrolyte entrainment, thereby improving the purity of the produced hydrogen. Furthermore, the consistent and predictable output achieved with regulation supports safer and more reliable hydrogen storage, especially in the filling of pressurized tanks.

Overall, the findings highlight that even small improvements in efficiency, when coupled with gains in system stability, purity, and safety, can have meaningful implications for the design and operation of electrolyzer systems. Future work should extend this analysis to larger-scale configurations and evaluate long-term operational performance to fully assess the benefits of control strategies in industrial applications.

References

1. IEA: Global Energy Review 2025. IEA, Paris (2025). https://www.iea.org/reports/global-energy-review-2025
2. IEA: Global Hydrogen Review 2025. IEA, Paris (2025). https://www.iea.org/reports/global-hydrogen-review-2025
3. ECOS: Production: techno-economic analysis of temperature influence and control. In: Proc. 36th Int. Conf. Efficiency, Cost, Optimization, Simulation and Environmental Impact of Energy Systems (ECOS), pp. 908–919 (2023). https://doi.org/10.52202/069564-0082
4. Riaz, M.A., et al.: Water electrolysis technologies: the importance of new cell designs and fundamental modelling to guide industrial-scale development. Energy Environ. Sci. **18**, 5190–5208 (2025)
5. Yang, Y., Yang, G., Chu, F.: Mass transfer enhancement and cell performance promotion of PEM electrolyzer by biomimetic lung-inspired flow field. Clean Energy Sci. Technol. **3**, 393–403 (2025). https://doi.org/10.18686/cest393
6. Xia, Y., Cheng, H., He, H., Wei, W.: Efficiency and consistency enhancement for alkaline electrolyzers driven by renewable energy sources. Commun. Eng. **2**, 70 (2023). https://doi.org/10.1038/s44172-023-00070-7
7. Hao, X., Wu, X., Pan, Q., Xiu, T., Zhang, Z., Qian, H.: Simulation of a pressurized alkaline water electrolysis electrolyzer cell and its system. ACS Omega **10**, 2476–2488 (2025). https://doi.org/10.1021/acsomega.5c02476
8. Affranchi, A., et al.: Effect of operating temperature on Ni–Fe alloy nanostructured electrodes for alkaline electrolyzer. ChemElectroChem **12**, 42 (2025). https://doi.org/10.1002/celc.202500042
9. Halder, P., et al.: Advancements in hydrogen production, storage, distribution and refuelling for a sustainable transport sector: hydrogen fuel cell vehicles. Int. J. Hydrogen Energy **52**(D), 973–1004 (2024). https://doi.org/10.1016/j.ijhydene.2023.07.204

10. Li, Z., Tu, Z., Yi, Z., Xu, Y.: Coordinated control of proton exchange membrane electrolyzers and alkaline electrolyzers for a wind-to-hydrogen islanded microgrid. Energies **17**, 2317 (2024). https://doi.org/10.3390/en17102317
11. Zhang, Y., et al.: Optimization of multiple alkaline water electrolyzers coupled with solar photovoltaic power for green hydrogen production on a large scale. Int. J. Hydrogen Energy **136**, 1–15 (2025). https://doi.org/10.1016/j.ijhydene.2025.05.056
12. Igwe, C., Achebe, C., Chinweze, A.: Design of an alkaline water electrolyzer for hydrogen production. Am. J. Mech. Ind. Eng. **7**, 89–98 (2023). https://doi.org/10.11648/j.ajmie.20220706.12
13. Bekrit, L., Seladji, C.: A multi-criteria techno-economic evaluation of PEM and alkaline electrolysers for green hydrogen production using fuzzy BWM, TOPSIS, and WASPAS. Preprint (2025). https://doi.org/10.21203/rs.3.rs-7223428/v1
14. Zerrougui, I., Li, Z., Hissel, D.: Physics-informed neural network for modeling and predicting temperature fluctuations in proton exchange membrane electrolysis. Energy AI **20**, 100474 (2025). https://doi.org/10.1016/j.egyai.2025.100474
15. Zhang, Y., Yuan, X., Yao, S., Yang, H., Wang, C.: Numerical simulation of gas–liquid flow field in PEM water electrolyzer. Energies **18**, 2773 (2025). https://doi.org/10.3390/en18112773
16. Maoulida, F., Guilbert, D., Bailo-Camara, M.: Dynamic electrical degradation of PEM electrolyzers under renewable energy intermittency: mechanisms, diagnostics, and mitigation strategies – a comprehensive review. Renew. Sustain. Energy Rev. **194**, 116170 (2025). https://doi.org/10.1016/j.rser.2025.116170

Specific Aspects of Modeling the Chill-Down Process of Cryogenic Hydrogen Systems

Illia Petukhov, Oleksii Lysytsia(✉), Taras Mykhailenko, and Artem Kovalov

National Aerospace University "Kharkiv Aviation Institute", St. Vadim Manko, 17, Kharkiv, Ukraine
a.lisitsa@khai.edu

Abstract. Correct prediction of cryogenic hydrogen system parameters during the chill-down stage plays a key role in ensuring its safety. During the chill-down process with liquid hydrogen, significant thermal loads occur on the structure, there is a risk of excessive pressure, flow instability, pulsations, and cavitation in pumps. The complexity of modeling the non-stationary cryogenic system chill-down process is associated not only with flow heterogeneity and the phase change of hydrogen from liquid through vapor–liquid to vapor, but also with the possibility of unstable flows with large-amplitude pulsations. Numerical modeling of such complex processes in the most complete formulation is hardly feasible. The paper presents quasi-stationary model of the chill-down process of cryogenic hydrogen systems and key assumptions. Based on the main equations of heterogeneous media mechanics, the corresponding thermohydraulic processes in a boiling hydrogen flow of variable structure are taken into account in this paper. The conceptual model of the chill-down process, features of modeling thermohydraulic processes, aspects of accounting for unsteady thermal conductivity are considered. Based on the calculations results, the key parameters of the hydrogen system chill-down at different moments in time were determined. The calculation results are compared with experimental data.

Keywords: Chill-Down · Hydrogen System · Modeling

1 Introduction

Filling a cryogenic system with hydrogen while cooling the structure to operating temperatures is a standard step in preparing it for operation. The significant temperature difference between the flow and the system components results in high thermal loads on structural materials, as well as the risk of excessively high pressures and flow pulsations. Eliminating such conditions during the chill-down of a cryogenic hydrogen system is critical to ensuring its safety. This, along with the need to reduce hydrogen consumption during system preparation, makes mathematical modeling of the chill-down process advisable. Solving this problem requires a reliable description not only of the set of interrelated thermohydraulic processes under varying heat transfer conditions, phase transitions, and flow structure in the two-phase state, but also of critical phenomena. Additional complications arise from the fact that the unsteady process caused by

H. Altenbach et al. (Eds.): CAMPE 2025, LNME, pp. 102–110, 2026.
https://doi.org/10.1007/978-3-032-16381-3_11

wall temperature variation often occurs in an extended cryogenic system that includes components of different designs and masses.

Numerical modeling of such processes is a complex task, and a fully comprehensive formulation is hardly practical, both due to the challenges of describing conjugate heat transfer and the substantial computational resources required. This work presents a one-dimensional quasi-stationary model of the chill-down process in cryogenic systems. The thermohydraulic processes are modeled using classical approaches of heat and mass transfer theory, as well as the mechanics of continuous and heterogeneous media. In this model, variations in the temperature of system components and in the flow parameters within the channel, resulting from hydraulic losses and unsteady heat exchange with the walls, are taken into account.

2 Literature Review

Due to its environmental friendliness and high specific calorific value, hydrogen is one of the most in-demand fuels. For aerospace systems, its storage and use in liquid form (LH2) is preferable. This applies both to rocket and space technology [1] and to aviation systems, including onboard aircraft [2] and ground-based airport facilities [3].

The filling of any cryogenic system with liquid hydrogen is an essential step in its preparation for operation and is accompanied by cooling of the structure to operating temperatures. Under unfavorable initial conditions, this process may lead to unacceptably high pressures and flow pulsations. The hazards associated with these phenomena, together with the need to minimize hydrogen consumption during chill-down within limited time constraints, have sustained research interest in this process for more than 80 years.

Despite this, due to the complexities mentioned above, a reliable and sufficiently universal method for calculating the complete chill-down process of cryogenic systems with various geometries, across a wide range of operating conditions, and for different cryogenic liquids, has not been developed yet [4]. At the same time, numerous models of varying levels of detail, often aimed at specific tasks and investigating the influence of individual factors, have been proposed. These calculations utilize both modern software and custom-developed programs. For example, in the single-liquid model presented by the authors [4], a significant effect of two-phase sound speed correlations on the chill-down process was demonstrated, while the thermal resistance of the wall material was neglected.

CFD modeling remains the traditional tool for describing heat transfer and fluid and gas dynamics in flows. For example, the authors [5] attempted to simulate the three-dimensional fluid-structural interaction and thermal analysis of a large diameter horizontal cryogenic transfer line using ANSYS Fluent. For the analysis of the chill-down process, [6] proposed the use of a VOF model coupled with the Lee model of phase change and k-ω turbulence model. The authors [7] obtained results of acceptable accuracy for nitrogen using a Mixture model with the SST k-ω turbulence model, where the effective wall heat flux was described by Chen's model. The problem was solved for a section of an insulated pipe.

In [8], the chill-down process for LCH4 was modeled using a non-equilibrium two-phase model in SINDA/FLUINT. EcosimPro software was applied for the analysis of

various experimental data on the chill-down of hydrogen cryogenic systems [9]. However, the authors noted that EcosimPro software is not able to correctly simulate the chill-down, which indicates the need to refine both the correlations and the calculation procedure.

A cryogenic system often consists of pipelines of considerable length, which allows the use of a one-dimensional chill-down model for calculations. The authors [10] proposed a one-dimensional equilibrium model for calculating the chill-down time of a hydrogen supply cryogenic system. However, it was noted in [10] that the model tends to overestimate the chill-down time in most cases compared to experimental data.

The chill-down time of any cryogenic system depends not only on the type and flow rate of the cryogenic fluid, its parameters, and the properties of system components, but also on the configuration of the pipelines. In the experimental study [7], the chill-down process was found to be highly sensitive to the orientation of the pipelines. Results of modern experiments on the chill-down of hydrogen cryogenic systems and their analysis are also presented in [9].

Due to the complexity of experiments with LH2, in some cases LN2 is used as a model fluid [11]. Results from nitrogen experiments are also used to validate chill-down models for hydrogen systems [12]. This is explained by the fact that the mechanisms and stages of chill-down for LH2 and LN2, as well as for LCH4 and LO2, are similar, and the governing equations generally differ only in the coefficients. Typically, determining these coefficients is one of the key stages of the study.

Studies of the chill-down process of cryogenic systems using LCH4 and LO2 as components of spacecraft fuel [8, 13] show the same features and challenges as those encountered with LH2. Correlations developed for other cryogenic liquids introduce additional errors, which often exceed 100% [8]; therefore, in each specific study, the coefficients and correlations must be refined. In some cases, a simulant fluid is used. For example, in the study of a two-phase cooling system on board the International Space Station, the simulant fluid PF-5060 was used [14].

Correlations for heat transfer during the boiling of cryogenic liquids remain a subject of discussion, particularly in the case of two-phase flow, as well as for the identification of flow regimes in such flows. The adequacy of the boiling heat transfer description significantly affects the accuracy of chill-down process calculations. Moreover, all stages of this heat transfer are important. In the initial stage, the chill-down of a cryogenic system occurs under film boiling of the subcooled liquid. As the wall temperature decreases, the process passes through the Leidenfrost temperature with a minimum heat flux, followed by the transition boiling regime and then nucleate boiling. In [4, 15], a review of the most well-known empirical correlations for calculating characteristic parameters on the boiling curve such as the Leidenfrost temperature, minimum heat flux, and critical heat flux was presented. However, the calculation results based on these formulas show considerable dispersion. The same conclusion is reported in [8]. For many widely used correlations, the error exceeds 100%. In [16], an attempt was made to develop a universal relation for determining the critical heat flux, applicable to various liquids and conditions. However, this has not been realized yet, partly due to the insufficient amount of experimental data.

Thus, despite numerous studies on the cryogenic systems' chill-down process, questions still exist about choosing the right mathematical model, including boiling heat transfer conditions, the critical flow regimes of variable-phase flows, the structure of two-phase flow in channels of different orientations, and unsteady heat conduction in system components, especially those with large mass such as pumps, heat exchangers, and valves. This work discusses approaches to address these issues.

3 Research Methodology

Most hydrogen cryogenic systems, especially in aerospace applications, are characterized by significant length, which allows the use of a one-dimensional model of the chill-down process with parameters varying along the channel. A hydraulic approximation is used for the flow, where its parameters are assumed to be uniform across the cross-section. Possible non-uniformity of the vapor-liquid flow due to gravity can be taken into account by using additional phase characteristics determined by the flow.

Safe chill-down modes are characterized by the absence of pressure pulsations in the system. In this case, the parameters along the channel change monotonically, and it is reasonable to use a quasi-stationary process model in which the mass flow rate is the same in each section. Within the quasi-steady-state model, the chill-down process calculation is divided into two stages. In the first steady-state stage, with a fixed temperature distribution in the cooled system and considering thermal-hydraulic processes, the flow parameters and heat flux from the inner wall of the channel in each cell are determined. The mass flow rate corresponding to the condition where the outlet pressure equals the backpressure or reaches the critical pressure is also determined. Critical conditions are determined taking into account the parameters and phase composition of the flow at the channel outlet. In the non-steady-state stage, using the calculated heat flux values in the cells, the change in the temperature of the structure in each cell over time is determined. This takes into account the non-uniformity of temperature across the wall thickness due to transient thermal conductivity. Then, taking into account the updated values of the structure temperatures, the calculation cycle is repeated.

At the steady state stage, the flow parameters are determined sequentially in each cell, taking into account hydraulic losses, including minor ones, heat fluxes from the wall, as well as changes in the phase composition and flow regime. Within the framework of the model used, the conservation of momentum of the flow is conveniently represented as a function of the pressure gradient on factors determined by hydraulic losses, gravity, changes in channel area, and the compressibility of the medium. In the general case, for a two-speed, two-temperature vapor-liquid flow, assuming vapor equilibrium, the equation has the form

$$\begin{aligned}
&\frac{dp}{dz}\left[\alpha_v U_v^2\left(\frac{d\rho_v}{dP}\right)_S + (1-\alpha_v)U_l^2\left(\frac{d\rho_l}{dP}\right)_T - 1\right] \\
&= \frac{2\dot{m}}{A}(U_v - U_l)\frac{dx}{dz} - \frac{1}{A}\left[\alpha_v\rho_v U_v^2 + a_l\rho_l U_l^2\right]\frac{dA}{dz} \\
&-\alpha_l U_l^2\left(\frac{d\rho_l}{dT}\right)_P\frac{dT_l}{dz} - \left(\rho_v U_v^2 - \rho_l U_l^2\right)\frac{d\alpha_v}{dz} + \frac{\prod\tau_w}{A} + \rho_m g sin\theta
\end{aligned} \tag{1}$$

Mixture density

$$\rho_m = \alpha_v \rho_v + (1 - \alpha_v)\rho_l \tag{2}$$

the volume vapor fraction of a flow is related to its other parameters by the equation

$$\alpha_v = \frac{1}{1 + \frac{1-x}{x}\frac{\rho_v}{\rho_l}\frac{U_v}{U_l}} \tag{3}$$

Here p is pressure, U is velocity, ρ is density, T is temperature, x is mass vapour fraction, $\dot{m}$ is mass flow rate, A is cross-sectional area of the channel, $\prod$ is perimeter of flow contact with the wall, τ_w is shear stress, θ is pipeline slope angle. Indexes l, v, s are liquid, vapor and saturation state parameters, respectively.

One of the advantages of Eq. (1) is that it provides a mathematically defined expression for the condition of the occurrence of critical phenomena in the flow. In such cases, the expression in the square brackets on the right-hand side tends to zero.

From Eq. (1), as special cases, follow the equations of motion for single-phase and homogeneous flows. For example, the equation for the pressure gradient in a single-phase steady-state flow of state j has the form

$$\frac{dP}{dz} = \left[\frac{1}{A}\left(\tau_w \pi d - \rho_j U_j^2 \frac{dA}{dz}\right) + \rho_j g sin\theta\right] \bullet \left[U_j^2 \cdot \left(d\rho_j/dp\right) - 1\right]^{-1} \tag{4}$$

The derivative of the density in the denominator is determined by the type of process. For example, for an isentropic process, it is the inverse value of the square of the equilibrium speed of sound.

For single-phase systems, classical approaches have been developed for determining the coefficients of surface friction and heat transfer depending on the flow parameters and channel geometry. In the case of a nonequilibrium multiphase flow, it can only be stated the change in its total enthalpy is equal to the heat supplied from the walls. Changes in other parameters depend not only on the conditions of interaction between the flow and the enclosing walls but also on interphase interactions, including mass transfer.

Therefore, even within the framework of a two-speed, two-temperature model of vapor-liquid flow, a rather rough schematization of the flow is required when describing the exchange processes that determine the values of the shear stress on the channel wall, as well as the corresponding derivatives $\frac{dx}{dz}$, $\frac{dT_l}{dz}$ and $\frac{d\alpha_v}{dz}$ in Eq. (1). The last derivative most fully describes the structure (flow regime) of a two-phase flow, since it explicitly contains the relationship between the volumetric and mass fractions of the phases. Its determination can be made using semi-empirical dependences of the volumetric vapor content on the influencing factors, which, unlike (3), implicitly account for the difference in phase velocities. For well-studied liquids, corresponding flow regime maps can be used. For hydrogen, such generalizations are generally lacking, and the equations are quite individual. An example is the equation

$$\alpha_v = \left[1 + K\frac{Re_{kr}^* \bullet \rho_v(1-x)}{\rho_l x^{0,25}}\right]^{-1} \tag{5}$$

where

$Re^*_{kr} = \frac{\dot{m}}{A}\frac{l_{kr}}{\mu_v}$, $l_{kr} = 2\pi\sqrt{\frac{\sigma}{(g(\rho_l - \rho_v))}}$

Here σ is surface tension, μ_v is vapor viscosity. Regardless of the approach used for nonequilibrium two-phase flow, it is necessary to consider the heat transferred to each phase. The heat supplied to the liquid during boiling is used to change its temperature and heat the mass to the saturation temperature during the phase transition. Taking this into account, the expression for the liquid's temperature gradient is

$$\frac{dT_l}{dz} = \frac{\left[\frac{q_l \prod_l}{\dot{m} C_{pl}} - (T_s - T_l)\frac{dx}{dz}\right]}{1 - x} \tag{6}$$

The remaining heat is used to increase the vapor phase

$$\frac{dx}{dz} = \frac{\pi d q_w - q_l \prod_l}{\psi \dot{m}} \tag{7}$$

Here q_w is the average heat flux density over the perimeter, taking into account heat transfer to the vapor phase; ψ is heat of phase transition, C_{pl} is the isobaric heat capacity of a liquid The proportion of the wetted perimeter depends on the volumetric vapor content and the structure of the vapor-liquid flow.

In the second stage, with the flow parameters, heat flux density, and initial temperature state of the wall known in each cell, a new temperature state is determined after time dτ. In this case, the concept of a regular thermal regime takes into account the transient thermal conductivity of the wall at a given flow temperature T_{wik} and heat transfer coefficient on the inner surface. In cell i, the average temperature T_{wik}, corresponds to the mass-averaged temperature T_{mik}, which is related to it by the relation

$$æ_{wi} = \frac{T_{wik}}{T_{mik}} \tag{8}$$

The coefficient $æ_{wi}$ is determined taking into account the shape, mass and thermophysical properties of the structure, as well as the heat transfer coefficient.

4 Validation

An analysis of the literature shows that considerable attention has been paid to the experimental study of chill-down processes in cryogenic systems [5, 7]. However, the minimum information required for validating the chill-down model, such as detailed system and component geometry, operating parameters, initial and boundary conditions, and material properties, was found only by National Bureau of Standard, report 9264, Brennan J.A. et al. Although these experiments were conducted quite a long time ago, their results are still widely used in modern research [4, 17]. A comparison between the experimental and calculated data is presented in Fig. 1.

In general, the calculation results are in good agreement with the experimental data. The total chill-down time for any section of the pipe is determined with an error of only a few seconds. The relative error in calculating the chill-down time does not exceed 10%.

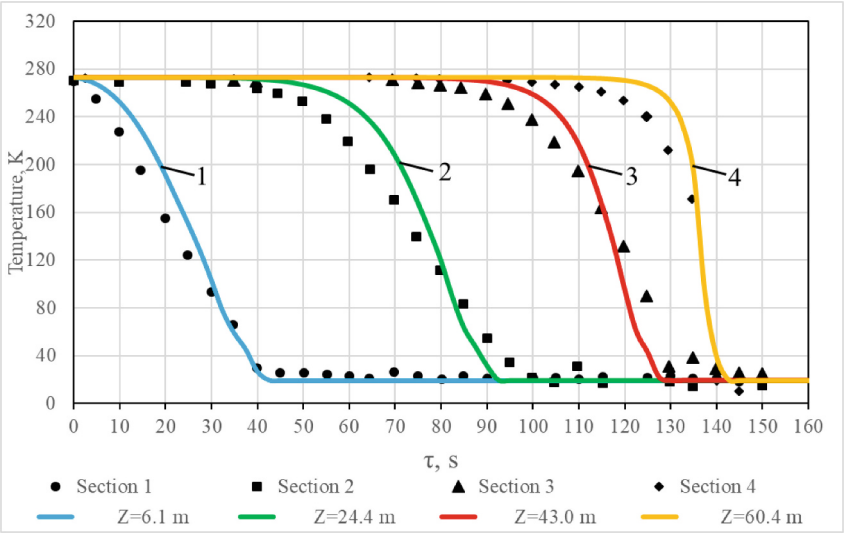

Fig. 1. Inner wall temperature: L = 61 m; D_{in} = 15.9 mm; D_{ex} = 19 mm; P_{H0} = 2.45bar. 1,●– z = 6.1 m; 2, ■□ – z=24.4 m; 3,▲ – z=43.0 m; 4, ◆ – z=60.4 m; ●,■□, ▲,◆– experimental data; 1, 2, 3, 4 – calculation results.

5 Results and Discussion

The calculations showed that chill-down completion corresponds to the stabilization of hydrogen flow through the pipe (Fig. 2).

Changing the pipe wall material to stainless steel increases the chill-down time and slightly reduces the pipe cooling rate (Fig. 3), as the thermal conductivity of stainless steel is significantly lower. The cooling rate decreases even more with increasing wall thickness, as the mass of the structure also increases.

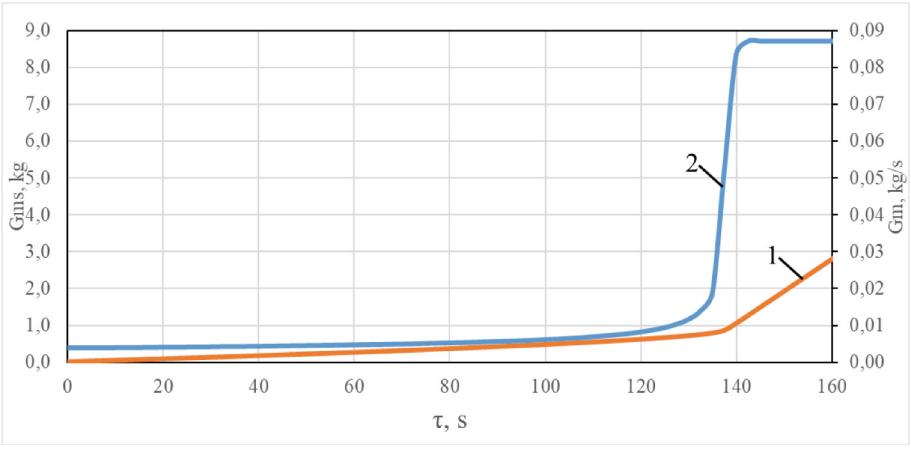

Fig. 2. Calculation results of the hydrogen mass required for chill down (1) and hydrogen mass flow rate (2). P_{H0} = 2.45bar.

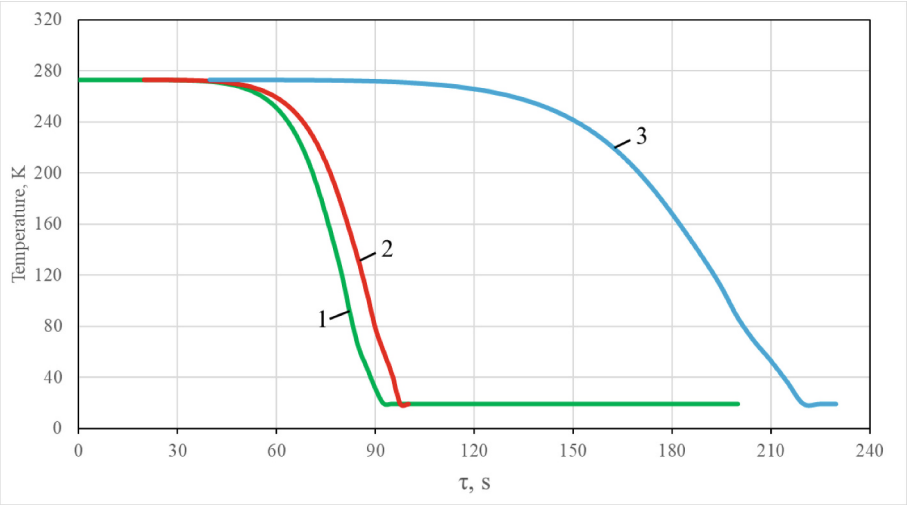

Fig. 3. Inner wall temperature calculation results, $P_{H0} = 2.45$bar; Sect. 2, z = 24.4 m; 1 – copper with a wall thickness of 1.55 mm; 2 – stainless with a wall thickness of 1.55 mm; 3 – stainless with a wall thickness 3.1mm.

6 Conclusions

A quasi-steady-state one-dimensional model of the chill-down process in a cryogenic hydrogen system is proposed. This model makes it possible to determine the temperature state of the structure and the flow parameters at any point in time and at any cross-section of the sys-tem. Fundamental equations of heterogeneous media mechanics and heat transfer theory are used to account for the main thermohydraulic processes in a variable-structure boiling hydrogen flow, including critical flow. The proposed concept of accounting for transient thermal conductivity allows the calculation of systems with elements of arbitrary shape and large mass. The calculation results are in good agreement with experimental data on the chill-down of a copper hydrogen pipeline. The proposed model does not require significant computational resources and can be used for any cryogenic fluids, as well as for analyzing static instability and modeling two-phase flow in heated pipes.

References

1. Mohammad, A.K., Sumeray, C., Richmond, M., Hinshelwood, J., Ghosh, A.: Assessing the sustainability of liquid hydrogen for future hypersonic aerospace flight. Aerospace **9**(801), 1–12 (2022). https://doi.org/10.3390/aerospace9120801
2. Mangold, J., et al.: Refueling of LH_2 aircraft—assessment of turnaround procedures and aircraft design implication. Energies **15**(2475), 1–41 (2022). https://doi.org/10.3390/en15072475
3. Krog, H.A., Jooss, Y., Fyhn, H., Nekså, P., Hjorth, I.: Large-scale LH_2 pipeline infrastructure concept for airports. Int. J. Hydrogen Energy, pp. 1–23 (2025). https://doi.org/10.1016/j.ijhydene.2025.05.123

4. Kunniyoor, K.R., Govind, R., Venkateswaran, K.S., Ghosh, P.: Liquid hydrogen pipeline chill-down: mathematical modelling and investigation. Cryogenics **118**(103324), 1–18 (2021). https://doi.org/10.1016/j.cryogenics.2021.103324
5. Lohar, K., Kunniyoor, K.R., Venkateshwaran, K.S., Ghosh, P.: Three-dimensional fluid-structural interaction and thermal analysis of a large diameter horizontal cryogenic transfer line. IOP Conf. Ser.: Mater. Sci. Eng. **1240**(012012), 1–8 (2022). https://doi.org/10.1088/1757-899X/1240/1/012012
6. Sankpal, V.U., Krishna, G.G., Ghosh, S.: Chill-down in LN_2 transfer line initially filled with air: a transient analysis. In: Proc. 10th Int. and 50th Nat. Conf. on Fluid Mechanics and Fluid Power (FMFP 2023), IIT Jodhpur, India, pp. 1–6 (2023). https://dspace.nitrkl.ac.in/dspace/bitstream/2080/4263/1/2023_FMFP_GGopalKrishna_Chill-down.pdf. Accessed 11 Sept 2025
7. Venkatesh, N., Singhal, A., Agarwal, D.K., Salih, A., Kumar, S.S.: Studies to investigate the effect of feed line orientation on chill-down performance of cryogenic feed lines. In: Proceedings of the 5th ISSE National Conference (INAC-05) on Systems Approach for Self-Reliance in Advanced Technologies (SASAT-2023), pp. 378–386. BSP Publications, Hyderabad, India (2023). https://doi.org/10.37285/bsp.sasat2023.42
8. Kunniyoor, K.R., Ghosh, P.: Numerical modelling of transient chill-down operation in liquid methane transfer line. In: ICEC28–ICMC 2022, ATSTC 70, pp. 881–888. Springer, Singapore (2023). https://doi.org/10.1007/978-981-99-6128-3_114
9. Raia, A.: Analysis and optimization of chill-down processes in cryogenic liquid propellant rocket engines. Master's thesis, Politecnico di Torino, Torino, pp. 1–153 (2023). https://webthesis.biblio.polito.it/26963/. Accessed 11 Sept 2025
10. Sandy, M., Judt, D.: Sizing and chill-down analysis of hydrogen aircraft fuel distribution systems. Centre for Aeronautics, Cranfield University, Cranfield, pp. 1–70 (2024). SSRN: https://ssrn.com/abstract=4965780. Accessed 11 Sept 2025
11. Venkatesh, N., Agarwal, D.K., Salih, A.: Effect of cryogenic feed line thermal mass distribution and orientation on chill-down performance. Cryogenics **138**(103781), 1–18 (2024). https://doi.org/10.1016/j.cryogenics.2024.103781
12. Wells, I.: Heat flux in low mass flux horizontal cryogenic flow. Master's thesis, Washington State University, School of Mechanical and Materials Engineering, Pullman, pp. 1–214 (2025). https://www.researchgate.net/publication/395024482. Accessed 11 Sept 2025
13. Zhang, J., Wang, K., Chen, L.: Fill-in and boiling transition characteristics during the liquid oxygen chill-down process in a vertical exit-contracted pipe. Int. J. Aerospace Eng. **5899199**, 1–22 (2022). https://doi.org/10.1155/2022/5899199
14. Narayanan, J.K., et al.: Line chilldown and flow boiling heat transfer characteristics of stainless steel tubes. In: Proc. ASME Summer Heat Transfer Conf. (SHTC 2023), Washington, DC, USA, July 10–12, 2023, pp. 1–8. ASME, New York (2023). https://doi.org/10.1115/HT2023-106318
15. Venkatesh, N., Agarwal, D.K., Salih, A., Kumar, S.S.: Chilldown of cryogenic feed lines—an insight into the influence of feed line orientation and mass flux. Cryogenics **130**(103644), 1–14 (2023). https://doi.org/10.1016/j.cryogenics.2023.103644
16. Meher, A.K., Venkatesh, P.H.J., Viswanath, M.S.R., Raju, J.N., Kumar, A.: Applicability of empirical correlations for critical heat flux in transfer line cool-down boiling. In: Deepak, B.B.V.L., Parhi, D.R.K., Biswal, B.B. (eds.) Advanced Manufacturing Systems and Innovative Product Design. Lecture Notes in Mechanical Engineering, pp. 457–479. Springer, Singapore (2021). https://doi.org/10.1007/978-981-15-9853-1_39
17. Majumdar, A., LeClair, A.: Nodal modeling of liquid propellant feed and pressurization system. In: Proc. 71st JANNAF Propulsion Meeting/14th Liquid Propulsion Meeting, Oklahoma City, OK, USA, May 6–10, 2024, pp. 1–20 (2024). https://ntrs.nasa.gov/citations/20240003493. Accessed 11 Sept 2025

Dynamics and Strength of Power Equipment

Numerical Assessment of Structural Integrity of Welded Absorbing Elements in VVER-1000 Control and Protection System

Oleksii Milenin(✉), Elena Velikoivanenko, Galina Rozynka, and Oleksii Makhnenko

E.O. Paton Electric Welding Institute of the NAS of Ukraine, 11, K. Malevich Street, Kyiv 03150, Ukraine
asmilenin@ukr.net

Abstract. The absorbing elements of the control and protection system in a VVER-1000 nuclear reactor are essential for maintaining operational stability and ensuring safe shutdown during emergencies. Their performance and reliability are critically dependent on the structural integrity of the enclosing shells, which are subjected to the combined effects of assembly welding and operational thermo-mechanical loading. However, these factors may introduce stress concentrations and structural weaknesses, particularly in the weld regions, posing a potential risk to the long-term reliability of the system. Using finite element modeling of the welding process and subsequent thermal–mechanical loading, the evolution of stresses in the weld area was investigated. Additionally, brittle fracture resistance was assessed through a postulated defect approach, enabling the determination of quantitative strength parameters of the absorbing elements. The analysis revealed that stress triaxiality in the weld zone results in the highest susceptibility to failure in the subsurface region. These findings provide a foundation for refining procedures for instrumental monitoring of the condition and reliability of the control and protection system.

Keywords: absorbing elements · control and protection system · VVER-1000 · welding · structural integrity · brittle strength · finite element analysis

1 Introduction

The safe and efficient operation of nuclear power plants relies heavily on the structural integrity of critical reactor components. The control and protection system (CPS) is central to this, ensuring power regulation, initiating reactor startup and shutdown, and enabling rapid termination of the fission reaction in emergency scenarios [1]. A key component of the CPS is the absorbing element (AE), which introduces neutron-absorbing materials into the reactor core to maintain reactivity control [2, 3]. AEs are subjected to complex stress states arising from residual stresses introduced during assembly welding and from thermomechanical loading during operation [4]. These stresses are particularly

H. Altenbach et al. (Eds.): CAMPE 2025, LNME, pp. 113–122, 2026.
https://doi.org/10.1007/978-3-032-16381-3_12

concentrated in welded joints connecting the shell to the tip and cone, and their interaction can significantly affect the reliability and failure resistance of AE shell (Fig. 1) [5]. Accurate prediction of these stress distributions is critical for assessing the risk of brittle or fatigue failure and ensuring structural integrity. The AE consists of a thin-walled cylindrical shell made of AISI 4340 alloy (outer diameter 8.2 mm, wall thickness 0.50–0.55 mm), hermetically sealed by arc welding of the tip and cone (Fig. 1), and filled with neutron-absorbing material (e.g., B_4C or $Dy_2O_3 + TiO_2$ in an aluminum matrix) [5]. Internal pressure (−3 MPa) develops due to swelling and evaporation of the absorber, while the reactor coolant imposes an external pressure of 16 MPa at 350 °C during normal operation. Emergency conditions may involve a rapid decrease in external pressure to atmospheric levels and cooling to room temperature. These three states, namely, post-welding, normal operation, and emergency shutdown, define the loading scenarios considered in this analysis.

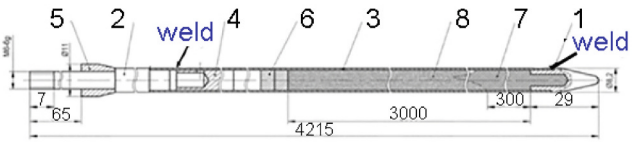

Fig. 1. Schematic design of AE of VVER-1000: 1 – cone; 2 – tip; 3 – shell; 4 – weighting component; 5 – sleeve; 6 – nickel mesh; 7 – dysprosium titanate; 8 – boron carbide [5].

Existing engineering approaches applied in the design and assessment of CPS components often rely on generalized or simplified methodologies that fail to account for the complex, nonlinear evolution of stress fields arising after welding and during operational loading [6, 7]. In many cases, these methods either assume predefined stress distributions or neglect the localized stress state near welded joints entirely, compensating instead by applying increased global safety factors [8, 9].

The objective of this work is to perform a numerical evaluation of the reliability of AE shell components in the CPS of a VVER-1000 reactor, by modeling the stress–strain evolution in assembly welding and subsequent operational loading conditions.

2 Finite-Element Procedure for Assessment of Stress-Strain and Limiting States of Welded Absorbing Elements in VVER-1000 Control and Protection System

The spatial heterogeneity and nonlinear behavior of the physical and mechanical processes governing residual and operational stresses in AE components make simplified analytical approaches insufficient. Additionally, the small size and complex geometry of AE elements in the CPS limit the applicability of direct experimental stress measurements. As a result, numerical simulation based on multiphysics mathematical modeling and finite element methods (FEM) is a rational and effective approach.

This study focuses on the numerical prediction of temperature evolution and elastic–plastic deformation using a non-stationary thermoplasticity framework [10]. The

temperature field is modeled by solving the unsteady heat conduction equation, while stress–strain evolution is addressed through a boundary value formulation of coupled thermomechanical behavior. The incremental form of the strain tensor is expressed as:

$$d\varepsilon_{ij} = d\varepsilon_{ij}^{e} + d\varepsilon_{ij}^{p} + \delta_{ij} \cdot d\varepsilon_T \tag{1}$$

where $d\varepsilon_{ij}^{e}$, $d\varepsilon_{ij}^{p}$, $\delta_{ij} \cdot d\varepsilon_T$ are the components of the increments strain tensor due to the elastic mechanism, plasticity and the temperature field kinetics, respectively.

The increments of the strain tensor can be represented in the form of a superposition of the increments of the corresponding components of the stress tensor [11]:

$$\Delta\varepsilon_{ij} = \Psi \cdot \left(\sigma_{ij} - \delta_{ij} \cdot \sigma\right) + \delta_{ij} \cdot (K \cdot \sigma + \Delta\varepsilon_T) - \frac{1}{2 \cdot G} \cdot \left(\sigma_{ij} - \delta_{ij} \cdot \sigma\right)^{*} - (K \cdot \sigma)^{*}, \tag{2}$$

where the symbol "*" refers to the corresponding variable to the previous tracing step, Ψ is the function of the material state that determines the condition of plastic flow according to the von Mises criterion, σ is the average value of the normal components of the stress tensor σ_{ij}, i.e. $\sigma = (\sigma_{rr} + \sigma_{\beta\beta} + \sigma_{zz})/3$, $K = (1\text{-}2\nu)/E$, $G = 0.5\ E/(1 + \nu)$, E is Young's modulus, ν is Poison ratio.

The determination of the function Ψ is carried out by iteration at each step of the numerical tracing by time or by load increment. The components of the stress tensor satisfy the static equation for internal FEs and boundary conditions for surface ones. The mathematical formulation of the coupled problem of temperature field evolution and stress–strain state development was implemented using finite element analysis in the 'Weld Predictions' software package [12]. Eight-node FEs were employed, with an element size of 0.5 mm in the weld region, followed by exponential mesh coarsening toward the periphery of the structure.

For proper interpretation of the calculated stress fields in the welded AEs at different stages of operation, an analytical fracture assessment approach was applied. At each node of the finite element mesh, a crack of some predefined size and geometry was postulated based on its location: for surface nodes—a surface semi-elliptical crack; for internal nodes—an embedded elliptical crack of the same size (Fig. 2).

The assessment of the limit state of the welded AE structure was carried out using a two-parameter failure assessment diagram (FAD) for brittle–ductile fracture (Fig. 3), described mathematically as follows [14]:

$$K_r = \begin{cases} (1 - 0.14 \cdot L_r^2) \cdot \left[0.3 + 0.7 \cdot \exp\left(-0.65 \cdot L_r^6\right)\right], \text{ if } L_r \le L_r^{\max} = \dfrac{\sigma_U + \sigma_Y}{2 \cdot \sigma_Y} \\ 0, \text{ if } L_r > L_r^{\max} \end{cases} \tag{3}$$

where $K_r = K_I/K_{Ic}$, $L_r = \sigma_{ref}/\sigma_Y$, K_I is the stress intensity factor at a selected point along the crack front, K_{Ic} is the fracture toughness of the material, σ_{ref} is the reference stress near the defect; σ_Y is the material yield strength, σ_U is the material ultimate strength.

For numerical evaluation of the proximity of the postulated defect state to the failure boundary, a safety factor n was introduced and defined as:

$$n \cdot K_r = \begin{cases} \left[1 - 0.14 \cdot \left(n \cdot L_r\right)^2\right] \cdot \left\{0.3 + 0.7 \cdot \exp\left[-0.65 \cdot \left(n \cdot L_r\right)^6\right]\right\}, \text{ if } L_r \le L_r^{\max} \\ 0, \text{ if } L_r > L_r^{\max} \end{cases} \tag{4}$$

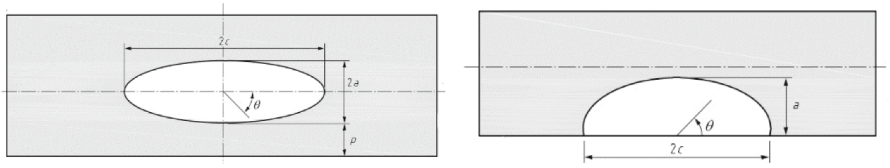

a b

Fig. 2. Schemes of embedded (a) and surface (b) cracks [13].

The safety factor n is determined as the ratio of segment OB to segment OA, where point A on the diagram (Fig. 3) corresponds to the current state of the structure with a given crack, OB intersects FAD curve and marks the boundary of the allowable state. The key parameters K_I and σ_{ref} were calculated using analytical procedures along with numerical results from FEA of spatial stress distributions in the weld zone [13]. The expression for calculating K_I is given by:

$$K_\mathrm{I} = \sigma_j \cdot \sqrt{\frac{\pi \cdot a}{Q}} \cdot F \tag{5}$$

where σ_j is the tensile stress acting normal to the crack plane along its periphery, Q is the crack shape factor, F is a correction factor accounting for boundary conditions.

Calculation of reference stresses σ_{ref} was carried out using the following relation [14]:

$$\sigma_{ref} = \frac{\sigma_b + 3 \cdot \sigma_m \cdot \alpha + \left[(\sigma_b + 3 \cdot \sigma_m \cdot \alpha)^2 + 9 \cdot \sigma_m^2 \cdot \left\{(1-\alpha)^2 + \frac{4 \cdot d \cdot \alpha}{t}\right\}\right]^{1.5}}{3 \cdot \left[(1-\alpha)^2 + \frac{4 \cdot d \cdot \alpha}{t}\right]} \tag{6}$$

where σ_b, σ_m are bending and membrane stress, respectively, d is a coefficient that reflects the position of the crack in relation to the surface, α is a dimensionless coefficient that reflects the ratio of the crack size to the wall thickness of the structure

The analytical expressions for σ_j, σ_b, σ_m, Q, F, d *and* α for surface and embedded cracks are defined in [13, 14]. For every FE, the minimum value of the safety factor n_{min} is determined, where minimization is carried out on the orientation of the crack. The proposed approach for evaluating the allowability of postulated cracks enables an analytical assessment of the brittle strength of welded AEs under design operational conditions without introducing excessive conservatism into the expert conclusions.

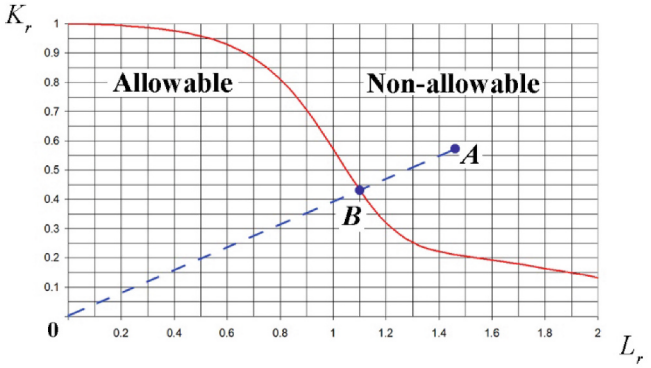

Fig. 3. Failure assessment diagram of the body with a crack

3 Results and Discussion

The developed computational model was used to analyze the stress–strain state and brittle strength of AE components during assembly welding and subsequent operation. Welding of the tip and cone to the shell was simulated using the next technological parameters (voltage U, electric current I, welding speed v_w): for the tip $U = 120$ V, $I = 20$ A, $v_w = 13$ m/h; for the cone $U = 10$ V, $I = 30$ A, $v_w = 12$ m/h.

Simulation results confirmed sufficient penetration and metallurgical bonding at the cone–shell joint. The residual stress field is characterized by high tensile stresses in the circumferential ($\sigma_{\beta\beta} = 588$ MPa, Fig. 4 a) and axial ($\sigma_{zz} = 538$ MPa, Fig. 4 a) directions, while the radial stress ($\sigma_{rr} = 153$ MPa) is significantly lower, indicating biaxial stress conditions typical for cylindrical shells with girth welds. Compressive stresses are observed on the outer surface, while the inner surface remains under tension. Under normal operating conditions ($P_{in} = 3$ MPa, $P_{out} = 16$ MPa, $T = 350$ °C), the stress magnitudes decrease slightly due to reduced yield strength at elevated temperature ($\sigma_{\beta\beta} = 526$ MPa, $\sigma_{zz} = 473$ MPa, $\sigma_{rr} = 146$ MPa), as it could be seen in Fig. 4 b. In contrast, during emergency shutdown ($P_{out} = 0$ MPa, $T = 20$ °C), the lack of external pressure compensation causes a significant stress increase in the shell wall (Fig. 4 c), making this the most critical loading condition.

At the tip–shell joint, intense local melting ensures a strong metallurgical bond as well. The residual stress field (Fig. 5 a) shows peak circumferential and axial stresses in the subsurface zone, where strength degradation is most likely. Here, the stress state becomes more triaxial ($\sigma_{rr} = 330$ MPa, $\sigma_{\beta\beta} = 458$ MPa, $\sigma_{zz} = 454$ MPa) due to geometry-induced constraint effects. As with the cone–shell region, operational stresses decrease moderately under normal conditions (Fig. 5 b) and rise sharply during emergency shutdown mode (Fig. 5 c), where the absence of external pressure and increased material strength at lower temperature elevate stress levels by over 90 MPa.

The selection of the postulated defect size is a critical factor in the quantitative analysis of the limit state of welded structures. On the one hand, the defect dimensions should not be smaller than the detection threshold of available instrumental non-destructive testing methods; on the other hand, they must be sufficiently large to ensure a conservative

assessment of structural integrity. Given that the wall thickness of AE shell is 0.5 mm, this value was adopted as the minimum linear dimension of the elliptical embedded crack along the minor axis $2a$ and the depth of the surface crack a. The corresponding major axis $2c$ was determined based on the assumed aspect ratio of $2a/2c = 0.3$ [8], resulting in defect dimensions of $2a \times 2c = 0.5 \times 1.67$ mm.

To assess the performance of the welded joints, cone-shell and tip–shell, the influence of irradiation on the material's resistance to brittle fracture was taken into account. According to [15], irradiation at a fluence of 12 dpa may reduce K_{Ic} of the chromium-nickel alloy by a factor of up to 3.66. Thus, while the initial fracture toughness of the AISI 4340 alloy was assumed to be 189 MPa·m$^{1/2}$, after irradiation, this value was reduced to 51.6 MPa·m$^{1/2}$.

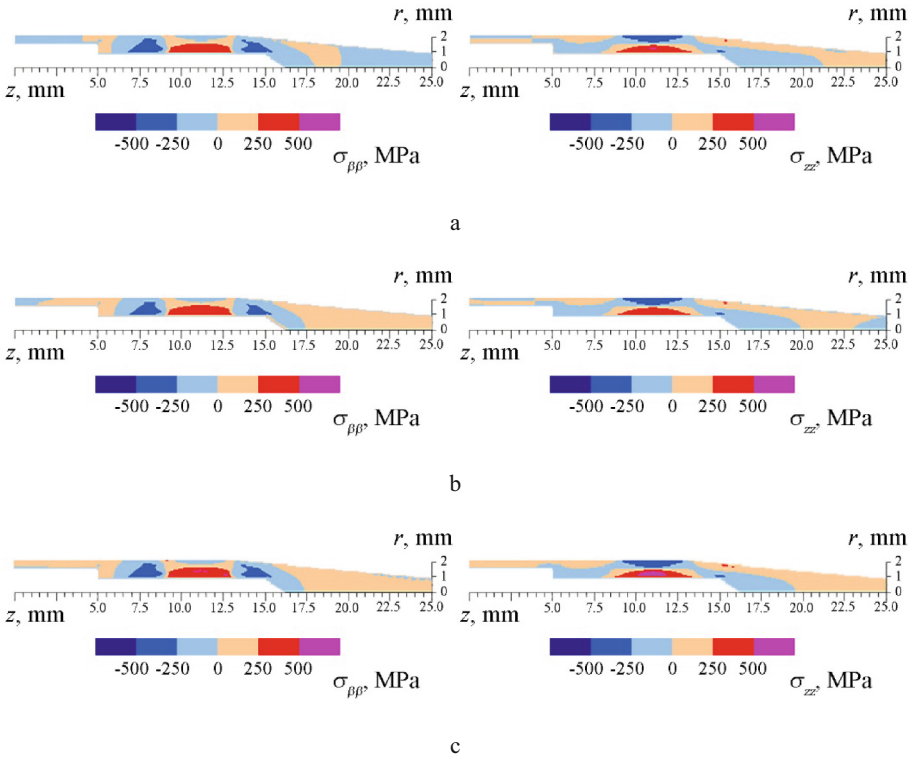

Fig. 4. Circumferential $\sigma_{\beta\beta}$ and axial σ_{zz} stresses distribution in the region of cone–shell joint: (a) – residual state after welding; (b) –normal operation conditions $P_{in} = 3$ MPa, $P_{out} = 16$ MPa, $T = 350$ °C; (c) –emergency shutdown conditions $P_{in} = 3$ MPa, $P_{out} = 0$ MPa, $T = 20$ °C.

As shown by the calculation results (Fig. 6 a, Fig. 7 a), the characteristic stress distribution in the cone–shell welded joint determines the corresponding spatial distribution of the minimum safety factor n_{min} under both normal operating conditions and emergency shutdown modes. The most critical defects are surface cracks located on the inner surface of the AE. For these, the minimum safety factor under normal operation does

not fall below $n_{min} = 3.532$, while under emergency shutdown conditions, it decreases to $n_{min} = 3.062$. Embedded cracks are less critical: for normal operation, the minimum safety factor reaches 3.663, and for emergency shutdown – 3.177.

High stress triaxiality in the region of the tip–shell welded joint results in specific features of the structure's susceptibility to brittle fracture. In particular, the relatively low or compressive stresses near the surface lead to comparatively high values of the minimum safety factor n_{min}: 6.471 under normal operational conditions and 4.789 during emergency shutdown (Fig. 6 b). In contrast, the maximum stresses, and therefore the lowest n_{min} values, are associated with embedded postulated cracks (Fig. 7 b), for which the minimum safety factor reaches 4.637 under normal operation and decreases to 3.958 under emergency shutdown.

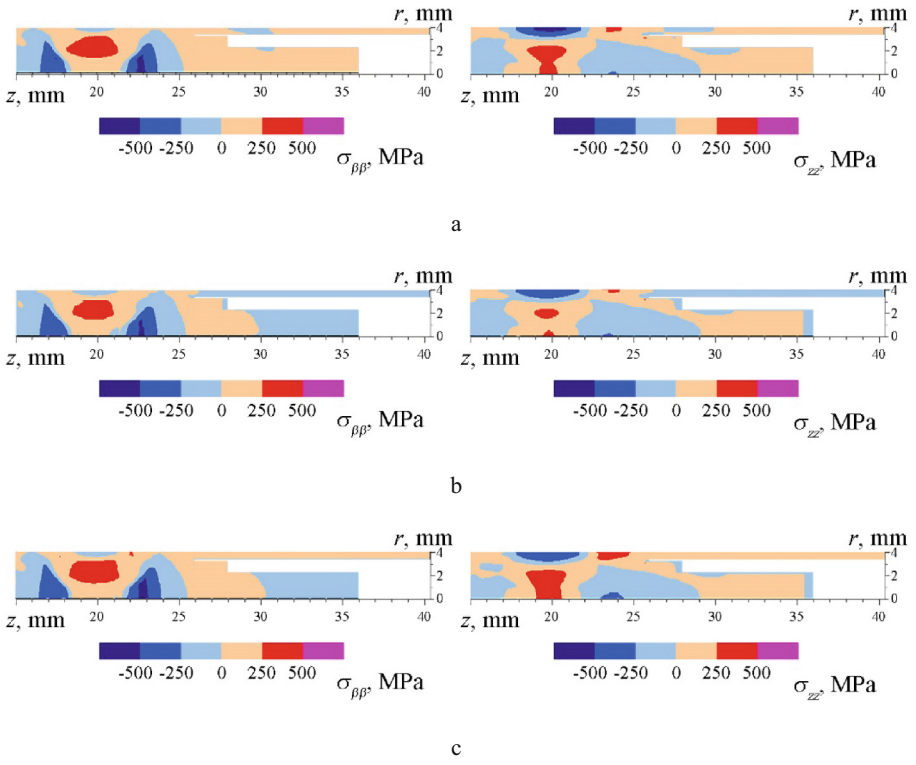

Fig. 5. Circumferential $\sigma_{\beta\beta}$ and axial σ_{zz} stresses distribution in the region of tip–shell joint: (a) – residual state after welding; (b) –normal operation conditions $P_{in} = 3$ MPa, $P_{out} = 16$ MPa, $T = 350$ °C; (c) –emergency shutdown conditions $P_{in} = 3$ MPa, $P_{out} = 0$ MPa, $T = 20$ °C.

Summarizing the results of the calculations on the brittle strength of the welded joints, it can be concluded that the cone–shell welded joint represents the most critical area in terms of potential loss of structural integrity due to brittle static fracture. This is primarily attributed to the specific design features, particularly the presence of the internal cavity in the weld region, which induces high tensile post-weld stresses along

the inner surface. As a result, a zone of reduced resistance to brittle fracture is formed in this location.

In contrast, the tip–shell welded joint, being located within the solid section of the AE structure, promotes more favorable stress distribution and is generally less susceptible to brittle fracture. In this area, embedded defects represent the most critical threat to structural integrity. These differences define specific requirements for flaw detection of these welded joints during their technical diagnostics. As the analysis has shown, the most dangerous zones are the hard-to-inspect areas of the structure, namely, the inner surface of AE and the subsurface material regions. Even small cracks in these zones can lead to a considerable reduction in load-bearing capacity under static loading and in the presence of material property degradation. Therefore, a reliable assessment of structural integrity of these elements must be based on thorough, high-resolution and accurate non-destructive evaluation in critical areas of welded AE.

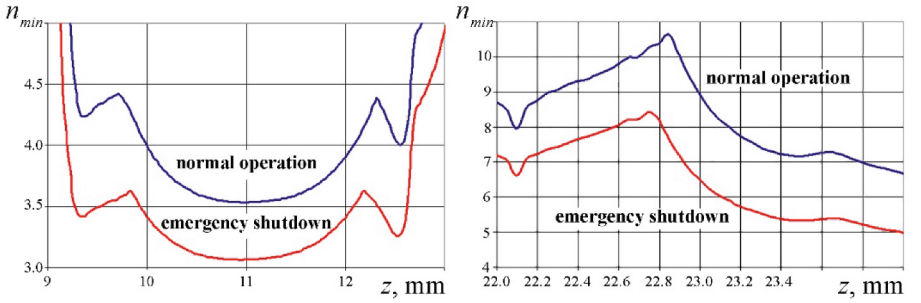

a b

Fig. 6. Distribution of the minimum brittle strength safety factor n_{min} along the surface of the AE welded joints: (a) cone–shell joint; (b) tip–shell joint.

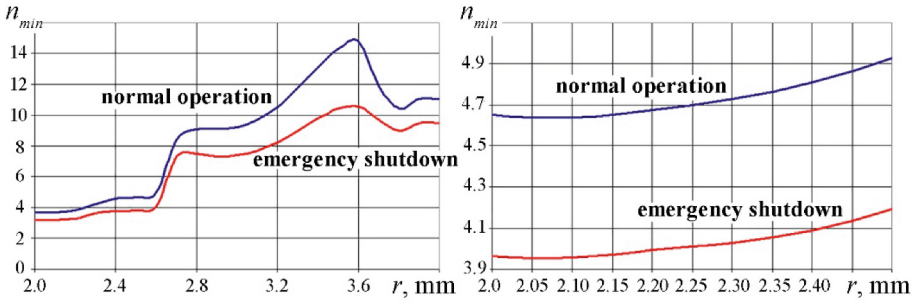

a b

Fig. 7. Distribution of the minimum brittle strength safety factor n_{min} in the critical sections of the AE welded joints: (a) cone–shell joint; (b) tip–shell joint.

4 Conclusions

1. A comprehensive computational methodology was developed and applied to assess the brittle strength of welded joints in the cross-section of AE of CRS, accounting for post-weld residual stresses, complex loading scenarios, and realistic defect configurations. The approach integrates spatial stress–strain analysis with the evaluation of local fracture resistance through the minimum safety factor, enabling a detailed comparison of defect criticality in different welded joints. This methodology ensures a reliable prediction of structural performance under both normal and emergency conditions and can be further used to support flaw tolerance assessments and inform inspection planning for safety-critical components.
2. The thermally induced stress–strain state formed during welding of the cone to the AE shell results in a biaxial stress distribution, dominated by circumferential and axial stresses, that is typical for thick-walled pipe welds. In contrast, the weld at the tip–shell joint lies within a solid section of the AE, leading to subsurface localization of high post-weld stresses. Here, the radial stress component rises to levels comparable with the axial and circumferential components, forming a triaxial stress state that increases the risk of structural degradation in this region.
3. During operation, the overall stress distribution pattern remains, but maximum stress values decrease due to material softening at the operating temperature of 350 °C. This temperature-dependent reduction in yield strength promotes localized plastic deformation and partial stress relaxation and redistribution. However, under emergency shutdown conditions, when external pressure drops sharply and temperature decreases, internal pressure becomes unbalanced, leading to a pronounced increase in stresses in the AE shell. This creates the most critical loading scenario for welded joints, heightening the risk of failure and reducing structural reliability.
4. The analysis of brittle strength in the welded joints of AE demonstrates that the most unfavorable stress and safety factor distributions occur in the cone–shell joint, especially near the inner surface. Surface cracks in this region lead to the lowest values of the minimum safety factor: $n_{min} = 3.532$ under normal operating conditions and $n_{min} = 3.062$ during emergency shutdowns. In comparison, embedded cracks in this joint are slightly less critical, with n_{min} values of 3.663 and 3.177, respectively. For the "tip–shell" welded joint, the stress state is more favorable due to its location within the solid section of the structure: surface cracks predetermine $n_{min} = 6.471$ (normal) and 4.789 (emergency), while embedded cracks result in $n_{min} = 4.637$ and 3.958. These results confirm the dominant role of design geometry and stress triaxiality in determining local resistance to brittle fracture.
5. Based on the identified areas of minimum safety factor and stress concentration, the most dangerous defects are surface and embedded cracks located on the inner surface of AE. These zones are difficult to access using conventional inspection methods but critically affect the structure's load-bearing capacity and fracture resistance. Therefore, comprehensive and reliable non-destructive evaluation techniques must be applied to monitor these hard-to-reach regions. The technical diagnostics strategy should focus on detecting small surface-breaking and embedded flaws in the cone–shell joint to ensure structural integrity under both operational and emergency conditions.

Acknowledgements. The authors of this work are grateful to the Ukrainian armed forces and the world community, which is now helping Ukraine in the struggle for freedom and independence. Thanks to the unity and unbroken spirit of the Ukrainian nation during this period of our history, it is possible carrying out scientific researches for our peaceful and successful future.

References

1. Wang, H., Li, M., Sun, P., Wei, X.: Research on protection control strategy of pressurized water reactor nuclear power units for typical power system faults. Ann. Nucl. Energy **201**, 11041415 (2024)
2. Zhang, R., Qiu, L., Sun, P., Wei, X.: Research on nuclear reactor power control system of VVER-1000 with thermal energy supply system. Energy **294**, 130813 (2024)
3. Jeong, H.S., Choo, K.N., Park, S.J., Yang, S.W.: Analysis of nuclear reactions and material damage on neutron absorbers using the HANARO research reactor. Ann. Nucl. Energy **208**, 110785 (2024)
4. Makarenko, A, Chaikovskyi, M., Mazurok, O., Zuyok, V., Mykhaylenko, O.: Calculation analysis of VVER-1000 RCCA elements to justify lifetime extension. Nuclear Radiat. Safety **3**(103), 26–35 (2024)
5. Kushtym, A., et al.: Characteristics of weld joints in absorbing rods made of 42CrNiMo alloy for VVER-1000 RCCA. Nuclear Radiat. Safety **4**(100), 38–48 (2023)
6. REGDOC-2.5.2, Design of Reactor Facilities, Version 2 (2023)
7. SSG-53. Design of the Reactor Containment and Associated Systems for Nuclear Power Plants. Specific Safety Guide. Vienna, International Atomic Energy Agency (2019)
8. Brumovsky, M., Martin, O.: VERLIFE Guidelines for Integrity and Lifetime Assessment of Components and Piping in WWER Nuclear Power Plants. Publications Office of the European Union, Luxembourg (2024)
9. RCC-MRx. Construction Rules for Mechanical Components of Nuclear Installations: high temperature, research and fusion reactors (2022)
10. Golubiatnikov, K., Ghimire, A., Wald, F., Vild, M., Stancik, V.: Stress and strain distributions in fillet welded joints. J. Constr. Steel Res. **226**, 109314 (2025)
11. Milenin, A., Velikoivanenko, E., Rozynka, G., Pivtorak, N.: Probabilistic assessment of the state of welded pipeline elements and pressure vessels with detected corrosion-erosion defects. Struct. Integrity **5**, 178–183 (2019)
12. Milenin, A., Velikoivanenko, E., Rozynka, G., Pivtorak, N.: Novel approach for numerical evaluation of limiting state and reliability of corroded pipelines under in-service repair welding. Welding World **67**(10), 373–379 (2023)
13. BS 7910:2019. Guide to methods for assessing the acceptability of flaws in metallic structures (2019)
14. API 579–1/ASME FFS-1. (2021). Fitness-For-Service. Washington, D.C., American Petroleum Institute / American Society of Mechanical Engineers (2021)
15. Mills, W.J.: Fracture toughness of two Ni-Fe-Cr alloys. Eng. Fract. Mech. **2**(26), 223–238 (1987)

Effect of Fibre Bridging on Delamination Resistance of Hybrid Carbon–Glass/Epoxy Laminates

Francisco Maciel Monticeli(✉)

Department of Aerospace Structures and Materials, Faculty of Aerospace Engineering, Delft University of Technology, Kluyverweg 1, 2629 HS Delft, The Netherlands
F.M.Monticeli@tudelft.nl, francisco_monticelli@hotmail.com

Abstract. Hybrid laminates combining carbon and glass fibres offer an attractive balance of mechanical performance and cost, particularly in sectors such as automotive and wind energy. However, incorporating multiple fibre types gives rise to complex interfacial behaviours that must be thoroughly understood before these materials can be used in structural applications. This study investigates the mode I delamination behaviour of unidirectional carbon fibre laminate (CFL) composite, glass fibre laminate (GFL) composite and hybrid carbon–glass (HCG) fibre-reinforced laminates. To isolate the contribution of fibre bridging, a fracture model based on the Sørensen approach was employed to quantify the bridging zone by fitting energy release rates and opening displacements. Despite their intermediate stiffness, the hybrid laminates exhibited the greatest resistance to crack propagation. This enhanced performance is attributed to the synergistic effect between the rigid carbon fibres and the more flexible glass fibres, which increases both the bridging stress and the end-opening of the bridging zone. The results emphasise the importance of fibre bridging as a primary toughening mechanism in hybrid systems and demonstrate that hybridisation can be employed strategically to enhance delamination resistance.

Keywords: Hybrid composite · Fibre bridging stress · Mode I delamination

1 Introduction

Fibre-reinforced polymer (FRP) laminates are widely used in industries requiring a combination of high structural performance and low weight, such as aerospace, automotive, and wind energy [1, 2]. While carbon fibre-reinforced composites (CFRPs) offer exceptional stiffness and strength, the high cost of the material and its processing can be limiting, particularly for applications where cost is a key factor, such as the manufacture of automotive structures and turbine blades [3–5]. Hybrid laminates combining carbon and glass fibres have therefore been proposed as a cost-effective alternative, offering a promising balance between mechanical performance and economic viability [6, 7].

However, using different types of reinforcement makes the mechanical response of the laminate more complex, particularly with regard to failure modes such as delamination [7, 8]. One of the most critical limitations of laminated composites is their

H. Altenbach et al. (Eds.): CAMPE 2025, LNME, pp. 123–132, 2026.
https://doi.org/10.1007/978-3-032-16381-3_13

low interlaminar toughness, caused by a lack of reinforcement throughout the material thickness [9, 10]. This issue is further intensified at hybrid interfaces, where different fibre/matrix interfacial strengths and stiffness mismatches can result in unpredictable fracture behaviour. Although previous studies have demonstrated that hybridisation can enhance delamination resistance via methods such as differential fibre surface treatments and interfacial energy dissipation, some failure mechanisms remain unclear [11].

In mode I delamination, fibre bridging often forms behind the crack tip [12, 13]. This can lead to an apparent increase in fracture toughness. However, this effect can obscure the material intrinsic fracture resistance, as the energy absorbed by the bridging fibres does not accurately reflect crack-tip toughness [14]. Therefore, accurate characterisation requires that the contribution of bridging be distinguished from the baseline resistance [15–17].

Due to the limited amount of literature addressing the mode I delamination behaviour of hybrid carbon/glass laminates, particularly with regard to bridging mechanisms, this study aims to model and quantify the effect of fibre bridging in hybrid composite systems. By comparing the delamination behaviour of hybrid and non-hybrid laminates, this study sheds light on the contribution of bridging to energy dissipation and the influence of hybrid reinforcement strategies on crack propagation and interfacial performance.

2 Research Methodology

2.1 Materials

The laminates were manufactured using resin infusion in a rigid mould, resulting in a final thickness of 3 mm. The epoxy matrix used was RTM6® (Hexcel), infused at 120 °C and cured at 180 °C for 240 min, in accordance with the manufacturer specifications. The reinforcement consisted of unidirectional carbon and glass fibres, also supplied by Hexcel. Carbon fibre laminates (CFL) were composed of carbon fibre/epoxy, glass fibre laminates (GFL) were manufactured with glass fibre/epoxy, and hybrid carbon–glass fibre (HCG) composites were made from a 50% combination of both fibres, i.e., carbon–glass fibre/epoxy. To introduce a predefined delamination, a 13 μm thick fluoropolymer film was embedded during layup to create an artificial crack front with a length of 50 mm.

The specimens were cut to final dimensions of $150 \times 22 \times 3\ mm^3$ using a high-speed diamond cutting disc. Piano hinges were bonded on both specimen surfaces at the insert region to enable the application of opening loads, following the double cantilever beam (DCB) configuration described in ASTM D5528 [18].

2.2 Test Procedure

The tests were carried out using a universal MTS 810 servo hydraulic testing machine, as illustrated in Fig. 1. The mode I crack opening configuration was applied using a 500 N load cell and a constant crosshead displacement rate of 1 mm/min.

A camera was positioned to capture side-view images of the specimen every 5 s, enabling crack length measurement and correlation with force and displacement data.

All testing and post-processing procedures were conducted in accordance with ASTM D5528 [18].

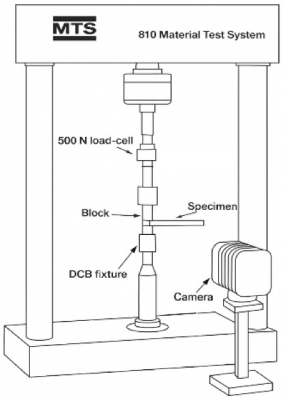

Fig. 1. Illustration of test set-up.

3 Results and Discussions

3.1 Experimental R-curve

The load versus displacement and crack propagation curves are presented in Fig. 2, which shows the average response from four repetitions for illustration purposes. As can be seen, the carbon fibre laminate (CFL) exhibits greater stiffness, resulting in increased instability during propagation. In contrast, the glass fibre laminate (GFL) showed lower stiffness, requiring greater bending displacement of the arm to initiate crack growth. This resulted in more stable propagation behaviour, eliminating the zig-zag instability observed in the CFL specimens.

As expected, the hybrid laminate (HCG) exhibited intermediate behaviour, balancing the stiffness profile between the pure carbon and glass fibre laminates due to its combination of reinforcement types.

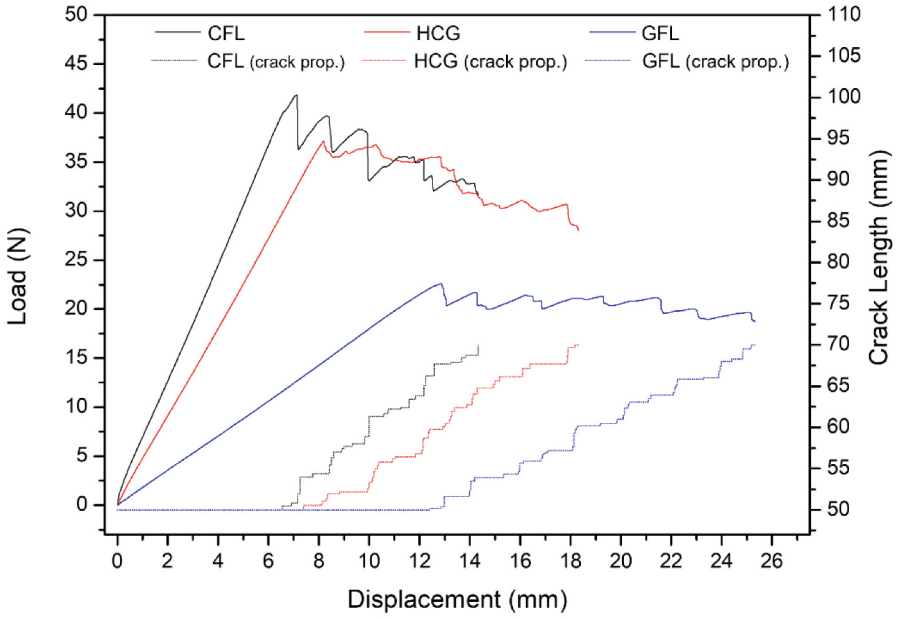

Fig. 2. Load vs displacement and crack propagation of mode I delamination test.

The modified beam theory (MBT) was carried out to calculate the strain energy release required to propagate the crack in each laminate case. Figure 3 illustrates the change in fracture toughness (G_{IC}) with crack growth (a–a_0) across all three laminate configurations. The results from the four repetitions for each condition overlap, indicating a high level of repeatability.

A general trend across all curves is an increase in G_{IC} values along the crack length, which is directly linked to fibre bridging formation. This phenomenon enhances the material resistance to delamination until a saturation plateau is reached, which relates to fibre bridging saturation [19, 20]. Further details on the fibre bridging effect are discussed in the following section.

Unlike the intermediate behaviour observed in the load/displacement curves (Fig. 2) results in Fig. 3 demonstrate that hybrid laminates (HCG) exhibit higher energy release levels than carbon (CFL) and glass (GFL) fibre laminates. This behaviour is attributed to the synergistic effect of the higher stiffness of carbon fibres combined with the greater compliance of glass fibres, which results in an increased energy requirement for crack propagation. The enhanced delamination resistance is also associated with the higher interfacial strength of the carbon fibre/epoxy interface, as well as the improved ductility promoted by organosilane treatments at the glass fibre/epoxy interface. This has been detailed reported in previous work [21].

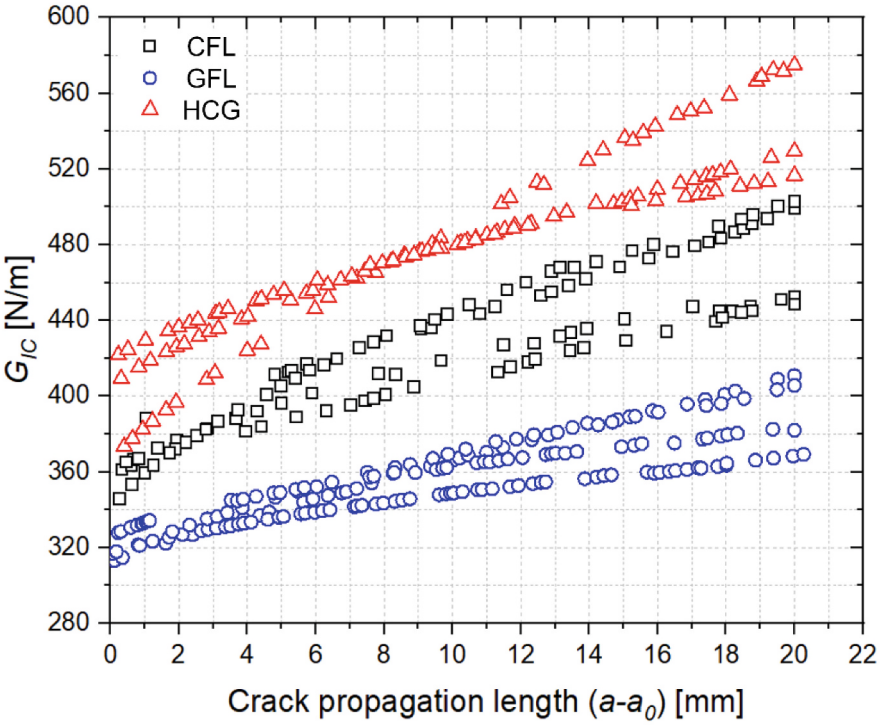

Fig. 3. R-curve for all laminates.

3.2 Fibre Bridging Stress Modelling

In order to better understand whether the observed increase in strain energy in the hybrid laminate is indeed associated with enhanced delamination resistance, considering the previously discussed factors, and to evaluate the contribution of fibre bridging to this effect, the model proposed by Sørensen [22], was applied. This model estimates strain energy using the J-integral method, as expressed in Eq. (1).

$$G_r = G_0 + \int_0^{\delta^*} \sigma(\delta^*) d\delta^* \tag{1}$$

where, G_r is the fracture toughness (resistance curve), G_0 is the zero-bridging strain energy release, δ^* is the end-opening in the fibre bridging zone.

By simplifying Eq. (1) and expressing it in terms of crack opening in the fibre-bridging region, the experimental data were fitted using Eq. (2). In this case, the increase in G_r is related to the progressive opening displacement caused by crack extension. Equation (3) defines the homogenised bridging stress function across the fracture surface, quantifying the total bridging energy as the integral of the bridging stress as a function of end-opening displacement curve [23].

$$G_r = G_0 + (G_s - G_0)\left(\frac{\delta_i}{\delta^*}\right)^{1/2} \tag{2}$$

$$\sigma(\delta^*) = \frac{G_s - G_0}{2\sqrt{\delta^* \delta_i}} \tag{3}$$

where, G_s is the saturation level of G and δ_i is the end-opening along the fibre bridging zone (until maximal value of δ^*).

Figure 4 shows the average fitted curves alongside the experimental variability, considering a 95% reliable interval based on Weibull formulation. The increase in strain energy is attributed to the development of fibre bridging up to the saturation level. The model fits the experimental data well, accurately capturing the expected trends in the R-curve: the GFL laminate exhibits the lowest resistance, followed by the CFL laminate, and the hybrid laminate (HCG) shows the greatest delamination resistance.

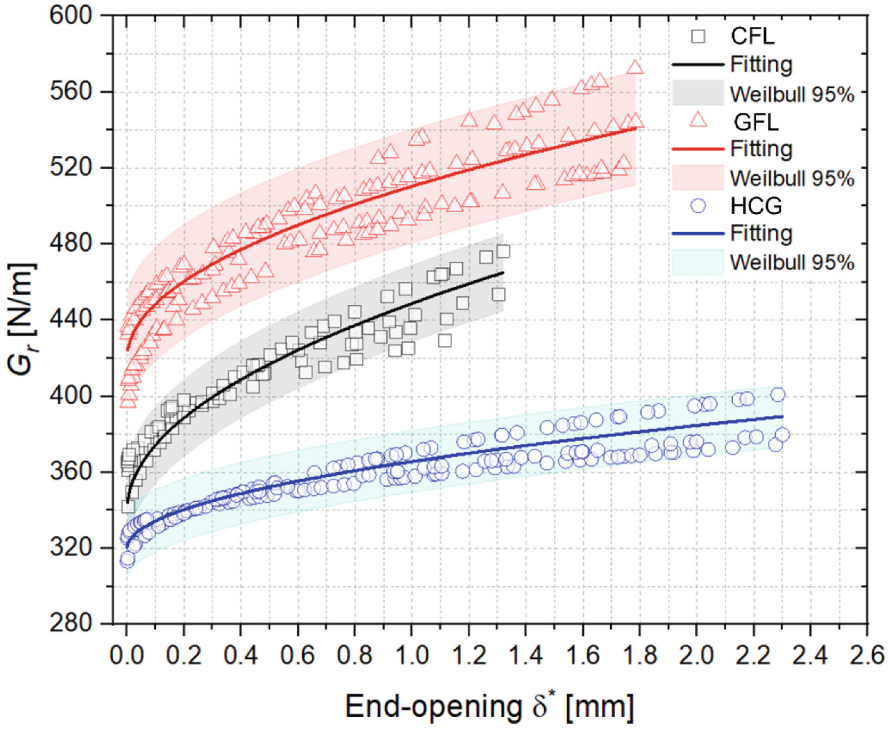

Fig. 4. Crack growth resistance as a function of end-opening.

The fitted parameters extracted from Fig. 4 are summarised in Table 1. These include: the strain energy release rate at zero bridging (G_0); the saturation energy level (G_s); the maximum end-opening displacement (δ^*).

It is noteworthy that the G_0 values for the non-hybrid laminates overlap within the experimental variability. However, there are more pronounced differences in G_s, indicating that fibre bridging plays a significant role in enhancing delamination resistance for non-hybrid composites. Similarly, distinct maximum end-opening values (δ_0) are

observed between the CFL and GFL laminates: carbon fibres tend to fracture at smaller openings due to their higher stiffness, whereas glass fibres can tolerate larger openings before failing.

Table 1. Parameters used to determine the fibre bridging stress curve

Laminate	G_0 [N/m]	G_s [N/m]	δ^* [mm]
CFL	340 ± 20.172	460 ± 20.172	1.215 ± 0.112
GFL	320 ± 16.146	390 ± 16.146	2.343 ± 0.056
HCG	420 ± 29.734	540 ± 29.734	1.758 ± 0.028

Even when accounting for sample variability, the hybrid laminate exhibited significantly higher G_0 and G_s values, confirming its superior delamination resistance. Interestingly, the maximum bridging opening (δ^*) in the hybrid case was intermediate. This suggests that while the carbon fibres probably fractured at similar opening levels to those of the CFL laminate, the glass fibres permitted additional deformation, resulting in an increase of fibre bridging zone compared with CFL, and an intermediate value between both non-hybrids.

These findings confirm that the fibre bridging behaviour in the hybrid laminate is indeed intermediate – Fig. 5. This is evident in the peak bridging stress (highlight 1), the maximum end-opening (highlight 2), and the overall shape of the bridging stress curve. As fibre bridging is characterised by the difference between the maximum and minimum values of the resistance curve ($G_s - G_0$), the position of the R-curve is irrelevant; only the difference in maximum and minimum energy is significant.

The results suggest that, in the hybrid laminate, bridging involves contributions from both types of reinforcement: the carbon fibres increase resistance to crack opening, and the glass fibres enlarge the bridging zone due to their greater allowable opening displacement compared to the CFL laminate. As a final result, this increases the area under the FB stress curve, which is related to the increase in the G values.

Fibre bridging arises from nesting effect, whereby unidirectional fibres are arranged irregularly in the delamination region. This prevents clean separation and leaves some fibres connected across the fractured interface. Given the presented bridging curves and the higher stiffness of carbon fibres, their smaller diameter may promote denser nesting and thereby increase their contribution to bridging. In contrast, the larger-diameter glass fibres are less prone to nesting. The hybrid configuration may increase the likelihood of smaller carbon fibres intercalating between the glass fibres, producing an intermediate amount of bridging and, as a consequence, intermediate stress response with improved bridging and delamination resistance.

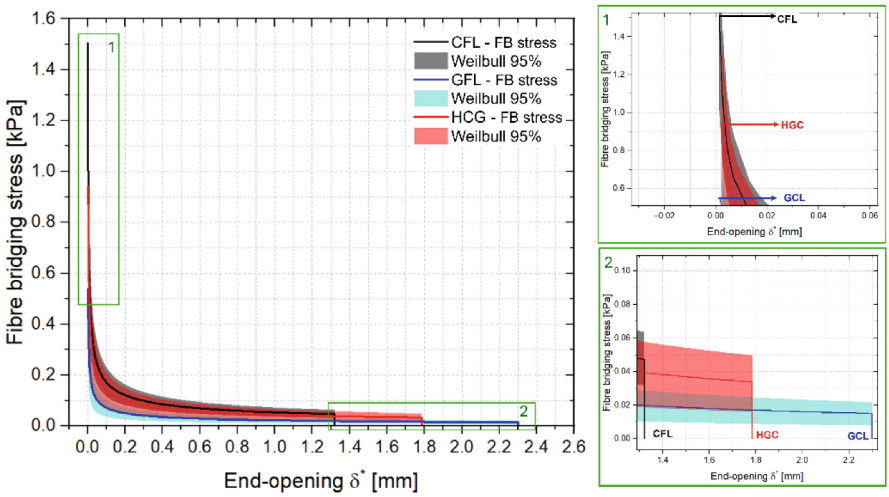

Fig. 5. Fibre bridging stress curve.

4 Conclusions

This study investigated the mode I delamination behaviour of carbon (CFL), glass (GFL) and hybrid carbon-glass (HCG) fibre-reinforced epoxy laminates. The experimental results revealed that, although CFL laminates exhibited high stiffness, they demonstrated unstable crack growth. In contrast, GFL exhibited lower stiffness and more stable propagation. The hybrid laminate showed an intermediate mechanical stiffness and superior delamination resistance, as evidenced by its higher fracture toughness and shift of the R-curve to higher values. This performance was attributed to the combined effects of the higher interfacial strength of the carbon fibre/epoxy interface and the improved ductility promoted by organosilane treatments at the glass fibre/epoxy.

Using the Sørensen bridging model, the study quantified the contribution of fibre bridging through key R-curve parameters. HCG laminates were found to consistently exhibit increased bridging energy and a broader bridging zone, indicating a synergistic interaction between the two fibre types. These results confirm that fibre bridging is a key mechanism for energy dissipation, particularly in hybrid configurations, and that tailoring the fibre architecture can significantly enhance the interlaminar toughness of composite materials.

References

1. Swolfs, Y.: Perspective for fibre-hybrid composites in wind energy applications. Materials **10**(11), 1281 (2017)
2. Li, X., Monticeli, F., Pascoe, J.A., Mosleh, Y.: Interlaminar fracture behaviour of emerging laminated-pultruded CFRP plates for wind turbine blades. Eng. Fract. Mech. **308**, 110353 (2024)

3. Swolfs, Y., Gorbatikh, L., Verpoest, I.: Fibre hybridisation in polymer composites: a review. Compos. Part A Appl. Sci. Manuf. **67**, 181–200 (2014)
4. Suriani, M.J., Rapi, H.Z., Ilyas, R.A., Petrů, M., Petrů, P., Sapuan, S.M., et al.: Polymers delamination and manufacturing defects in natural fiber-reinforced hybrid composite: a review. Polymers (Basel) **13**, 1323 (2021)
5. Kistaiah, N., Kiran, C.U., Reddy, G.R., Rao, M.S.: Mechanical characterization of hybrid composites: a review. J. Reinf. Plast. Compos. **33**, 1364–1372 (2014)
6. Zachariah, S.A., Pai, K.D., Shenoy, B.S.: Multi-level hybridization in mitigating impact damages in advanced composites – a review on recent trends. Mater. Today Proc. **46**, 9059–66 (2021)
7. Wu, W., Wang, Q., Ichenihi, A., Shen, Y., Li, W.: The effects of hybridization on the flexural performances of Carbon/Glass interlayer and intralayer composites. Polymers (Basel) **10**, 549 (2018)
8. Swolfs, Y., Verpoest, I., Gorbatikh, L.: Recent advances in fibre-hybrid composites: materials selection, opportunities and applications. Int. Mater. Rev. **64**, 181–215 (2019)
9. Hu, P., Tao, R., Li, X., Lubineau, G.: Decomposing the coupling damage in mode I multidirectional delamination. Compos. Sci. Technol. **229**, 109684 (2022)
10. Yao, L., Wang, J., He, Y., Zhao, X., Chen, X., Liu, J., et al.: Hygrothermal effects on fatigue delamination behavior in composite laminates. Compos. Struct. **330**, 117830 (2024)
11. Monticeli, F.M., Voorwald, H.J.C., Cioffi, M.O.H.: The influence of carbon-glass/epoxy hybrid composite under mode I fatigue loading: physical-based characterization. Compos. Struct. **286**, 115291 (2022)
12. Erives, R., Sørensen, B.F., Goutianos, S.: Extraction of mix-mode cohesive laws of a unidirectional composite undergoing delamination with large-scale fibre bridging. Compos. Part A Appl. Sci. Manuf. **165**, 107346 (2023)
13. Yao, L., Sun, Y., Alderliesten, R.C., Benedictus, R., Zhao, M.: Fibre bridging effect on the Paris relation for mode I fatigue delamination growth in composites with consideration of interface configuration. Compos. Struct. **159**, 741–748 (2017)
14. Jensen, S.M., Bak, B.L.V., Bender, J.J., Carreras, L., Lindgaard, E.: Transient delamination growth in GFRP laminates with fibre bridging under variable amplitude loading in G-control. Compos. B Eng. **225**, 109296 (2021)
15. Riccio, A., Russo, A., Sellitto, A., Toscano, C., Alfano, D., Zarrelli, M.: Experimental and numerical assessment of fibre bridging toughening effects on the compressive behaviour of delaminated composite plates. Polymers (Basel) **12**, 1–20 (2020)
16. Yao, L., Sun, Y., Zhao, M., Alderliesten, R.C., Benedictus, R.: Stress ratio dependence of fibre bridging significance in mode I fatigue delamination growth of composite laminates. Compos. Part A Appl. Sci. Manuf. **95**, 65–74 (2017)
17. Khan, R., Alderliesten, R., Yao, L., Benedictus, R.: Crack closure and fibre bridging during delamination growth in carbon fibre/epoxy laminates under mode I fatigue loading. Compos. A **67**, 201–211 (2014)
18. Standard ASTM D5528–01. Standard Test Method for Mode I Interlaminar Fracture Toughness of Unidirectional Fiber-Reinforced Polymer Matrix Composites. American Society for Testing and Materials 1, 1–13 (2014)
19. Yao, L., Cui, H., Sun, Y., Guo, L., Chen, X., Zhao, M., et al.: Fibre-bridged fatigue delamination in multidirectional composite laminates. Compos. Part A Appl. Sci. Manuf. **115**, 175–186 (2018)
20. Riccio, A., Russo, A., Sellitto, A., Toscano, C., Alfano, D.: Experimental and numerical assessment of fibre bridging toughening effects on the compressive behaviour of delaminated composite plates. Polymers **12**(3), 554 (2020)

21. Monticeli, F.M., Shiino, M.Y., Voorwald, H., Cioffi, M.O.: The synergy effect of carbon/glass/epoxy hybrid laminate in Mode I delamination: a physical microfracture analysis. Eng. Fract. Mech. **239**, 107295 (2020)
22. Sørensen, B.F., Jacobsen, T.K.: Large-scale bridging in composites: R-curves and bridging laws. Compos. Part A Appl. Sci. Manuf. **29**, 1443–1451 (1998)
23. Monticeli, F.M., Biagini, D., Mosleh, Y., Pascoe, J.A.: A novel analytical model to characterise the monotonic and cyclic contribution of fibre bridging during Mode I fatigue delamination in (C)FRPs. Composites part B Eng **297**, 112319 (2025)
24. Author, F.: Article title. Journal **2**(5), 99–110 (2016)

Advanced Means for Computer Simulation of Aerodynamic Control of High-Voltage Glow Discharge Electron Gun Current

Igor Melnyk[1(✉)], Serhii Tuhai[1], Olga Demyanchenko[2], and Andriy Luntovskyy[3]

[1] Department of Electronic Devices and Systems, Electronic Faculty, National Technical University of Ukraine "Igor Sikorsky Kyiv Polytechnic Institute", Beresteiskyi Ave., 37, Building 12, Kyiv 03056, Ukraine
imelnik@phbme.kpi.ua

[2] Institute of Applied Mathematics and Fundamental Sciences of the National University "Lviv Polytechnic", 5 Mytropolyta Andreia St., Building 4, Lviv, Ukraine
olgademyanchenko@gmail.com

[3] DHSN Dual University in Dresden, Saxon Study Academy, Hans-Grundig-Str. 25, 01062 Dresden, Germany
Andriy.Luntovskyy@dhsn.de

Abstract. In this chapter the advanced mathematical means for computer simulation of aerodynamic control systems of High Voltage Glow Discharge Electron Guns (HVGDEG) current are described and analyzed. The structure of electromagnetic valve for automatic changing the gas pressure in discharge chamber is presented and basic mathematical relations for simulation process of High Voltage Glow Discharge (HVGD) current are given. The mechanical structure of electromagnetic valve (EV) is also presented and analyze if the gas flow has been provided. Also advanced mathematical approach for analyzing such kind of aerodynamic control systems with using Finite Sequence Machines (FSM) Theory and Fuzzy Logic (FL) are described and analyzed. Corresponding practical recommendation for designing and exploitation of such kind control systems are also given.

Keywords: Electron Beam Technologies · High-Voltage Glow Discharge (HVGD) · Aerodynamic Control System (ACS) · Electromagnetic Valve (EV) · Finite Sequence Machines (FSM) Theory · Fuzzy-Logic (FL) · Membership Function · Root-Polynomial Function (RPF)

1 Introduction

High Voltage Glow Discharge Electron Guns (HVGDEG) are widely used in industry today for realizing different technological operations with direct heating of metals and dielectrics in vacuum, including welding [1], deposition of ceramic films in mechanical industry [2–8] and microelectronics [9, 10], refining of refractory metals and ceramics

H. Altenbach et al. (Eds.): CAMPE 2025, LNME, pp. 133–159, 2026.
https://doi.org/10.1007/978-3-032-16381-3_14

[11–14], as well as three-dimensional printing by the metal in soft vacuum [15–18]. The basic advantages of such kind of Electron Guns (EG) are simplicity of construction, operation in the soft vacuum, range of 0.1–10 Pa, relative simplicity of repairing and put into operation [19–32], as well as simplicity of control of EG current both aerodynamically, by changing operation pressure [33–36], and electrically, by lighting in the guns' volume additional low-voltage discharges [37–40].

Clear, that precision control of discharge current is really very important for providing stable operation of HVGDEG as a part of technological equipment [33, 34]. Therefore, further development of mathematical theory on this aspect is, really, very important today. Today advanced researches in the field of elaboration and industrial application of HVGDEG are provided in Scientific and Educational Laboratory of Electron Beam Technological Devices of National Technical University of Ukraine "Igor Sikorsky Kyiv Polytechnical Institute" [1–3, 19–21] and in AVIC Manufacturing Technology Institute, Beijing, China [22–32].

Therefore, the aim of this chapter is considering the basic principles of simulation technique for aerodynamic HVGDEG current control system. The Electromagnetic Valve (EV), as the part of this system is considered both as separate element and as the necessary part of aerodynamic control system (ACS) [33–36].

2 Statement of Problem

It is known fact, that the current-voltage characteristic of HVGDEG is described by following relation:

$$I_{EG} = a p_{EG}^{m} U_{ac}^{n}, \tag{1}$$

where I_{EG} – the current of EG, U_{ac} – acceleration voltage, p_{EG} – the pressure in the discharge chamber, and a, m, n – are the semiempirical constant, depended on the sort of gas, cathode material and the geometry of electrodes' system. The coefficients m and n in the relation (1) are lies in the range from 1 to 2 [41, 42].

Generally, it is clear that the aerodynamic method of controlling the current of HVGDEG is based on changing the current by the automatic or manual regulating of the incoming gas flow into the EG chamber under the condition of its continuous pumping [33, 34]. From the point of view of the physics of the system operation, this method is due to the stepwise dependence of the discharge current on the gas pressure, which is determined by the relationship (1).

Controlled gas flow into the EG chamber is carried out using an Electromagnetic Valve (EV), which can operate both in manual and automatic modes of operation [33, 34]. However, the requirements for the stability of most technological processes of Electron-Beam Technologies (EBT) require the use of automatic control systems with a small control time constant [33, 34]. Therefore, in such conditions, automatic control systems are really preferable [33, 34].

3 Scheme of Analyzed Control System and Basic Construction of Electromagnetic Valve

The functional model of a typical ACS of the HVGD current with EV is shown in Fig. 1 [33–36].

From the diagram, presented in Fig. 1, it is clear that the EG current sensor is a low-impedance resistor 3, which is connected in series to the low-voltage power supply section. The electromagnetic injector has a linear electromagnetic drive, which is rigidly connected to the moving part of the dosing device. The injector operates in analog mode, which ensures high stability and reliability of its operation. The electron gun is pumped out, together with the technological chamber, continuously. The basic construction of electromagnetic valve is presented in Fig. 2, and the structural diagram of the injector dosing device is shown in Fig. 3 [35, 36].

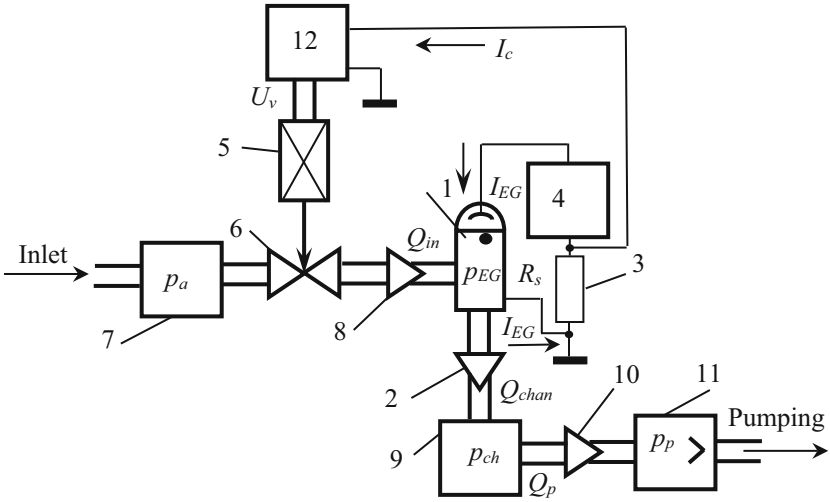

Fig. 1. Functional model of the aerodynamic automatic control system of the HVGDEG current. 1 – EG, 2 – beam guiding system, 3 – gun current sensor, 4 – high voltage power source, 5 – gas injector with electromagnetic drive, 6 – injector dosing device, 7 – injector gas chamber, 8 – channel for gas supply to the electron gun, 9 – vacuum chamber, 10 – vacuum line, 11 – vacuum pump, 12 – electronic block of EV driving

The principle of operation of the presented in Fig. 1 ACS of EG current is as follows. During the operation of the EG, the signal from the current sensor 3 is supplied to the electronic control unit 4. Here, the input signal is compared with the specified reference voltage, amplified, and the formed difference signal is supplied to the winding of the electromagnetic injector. Thus, depending on the magnitude of the control signal, the injector changes the gas flow into the electron gun chamber, which is continuously pumped out. That is, as a result of the operation of the gas-dynamic control system, a pressure is established in the electron gun chamber that corresponds to the set value of the gun current.

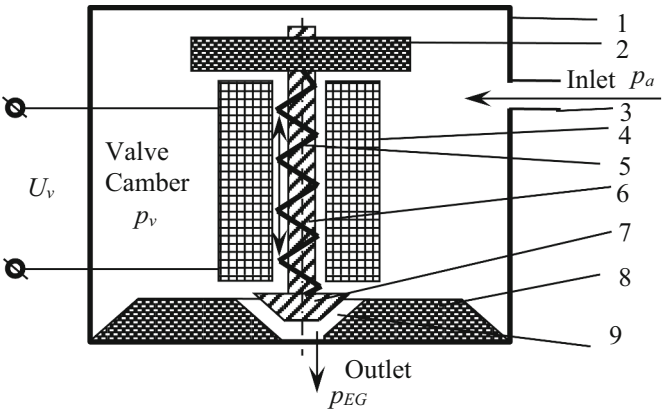

Fig. 2. Scheme of construction of EV. 1 – capsule, 2 – basis, 3 – inlet channel, 4 – electromagnetic coil, 5 – elastic spring, 6 – rod, 7 – anchor, 8 – gate valve seat, 9 – controlled gap between anchor and seat

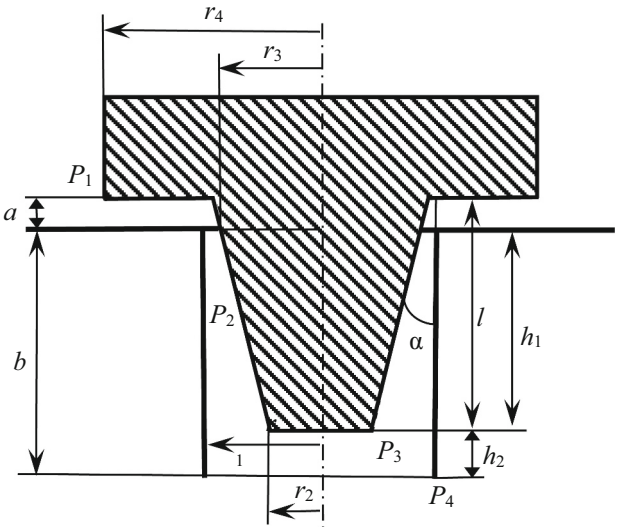

Fig. 3. Detailed scheme of construction of dosed item of EV and its' constructive parameters

Main notifications in the Fig. 1 are as follows [33, 34]: p_a – atmospheric pressure, p_{ch} – pressure in the technological chamber, p_p – pressure in the pumping means, Q_{in} – input gas flow into EG, Q_{chan} – gas flow in the channel of guiding of EB, Q_p – gas flow in the pumping system, I_c – control current for electronic block of driving EV, U_v – the voltage on EV. This notes will be used later in the mathematical model of control system.

Despite the apparent simplicity of the considered control method, the inertia of gas-dynamic processes of gas flow, as well as the inertia of actuators used, significantly

worsens the quality of discharge current regulation, which limits the dynamic characteristics of the control system and increases the control time constant [33, 34]. The complexity of developing effective control systems significantly hinders the introduction into industry of promising HVGDEG, despite their significant advantages over traditional EG with heated cathodes, as indicated above. The characteristics of ACS can be significantly improved by selecting the optimal values of the parameters of the gas pumping, gas supply system, and the settings of the electronic regulator, and also by developing electromagnetic valves with appropriate gas-dynamic and electromechanical characteristics. The solution of this complex scientific and technical problem is significantly simplified with the use of computer modeling tools [33, 34]. The accurate search for such dependencies is the subject of research in this work.

4 Generalized Mathematical Model of the Aerodynamic Current Control Process for a High-Voltage Glow Discharge Electron Gun

4.1 Basic Conception

During the formation of the mathematical model of the control system, shown in Fig. 1, the gas-dynamic system of pumping out and letting in the gas has been considered as a system with lumped parameters, and the volumes of the beam pipes and the release of gas from the working surfaces were not taken into account. It was also assumed that the speed of the vacuum pump 11 is a constant value in a wide range of operating pressures, which is generally characteristic of the vacuum equipment used in modern electron-beam equipment. The generalized mathematical model of the ACS for HVGDEG current stabilization can be written in the form of a system of the following algebraic-differential equations, including such important relations [33, 34, 43–45].

1. Electrical engineering equations that describe the current balance in the inductor winding [46–48].
2. Equations of mechanics that describe the dynamics of the actuator [44, 45, 49].
3. Gas dynamics equations that describe the gas dynamic properties of the injector dosing device depending on its geometric constructive parameters, which are shown in Fig. 3 [50].
4. Vacuum engineering equations that describe the balance of gas flows in the considered vacuum system [51, 52].

For the differential equations system that is being formed, the input parameter of the model should be the control voltage on the inductor U_v, and the output parameter should be the gun current I_{EG}, corresponding to structure diagram of ACS, presented in Fig. 1.

4.2 Simulation the Moving of Electromagnetic Valve Rod Using the Laws of Classical Mechanics by Considering Forces Equilibrium

The dynamic of the electromagnetic drive of the direct-motion actuator is determined by a set of two algebraic-differential equations, namely: the voltage balance equation

in the electromagnet power supply circuit and the condition of mechanical equilibrium of the actuator rod on the stress of the elastic spring 5. Under the condition of small deviations, these equations are written by the laws of mechanics as follows [43–47]:

$$R_v \Delta I_v + L_v \frac{d\Delta I_v}{dt} = \Delta U_v; \tag{2}$$

$$m_v \frac{d^2 \Delta l_v}{dt^2} = \sum_{i=1}^{n} \Delta F_i = \Delta F_e - \Delta F_s - \Delta F_f,$$

where R_v, L_v, – active resistance and inductance of the inductor winding, I_v and U_v – current and voltage on its winding, m_v – mass of the moving part of the inductor rod, l_v – coordinate that determines the position of the armature with the rod relative to the valve seat, corresponding to Fig. 3, F_e – traction force of the electromagnet, F_s – spring elasticity force, F_f – friction force.

The quantities ΔF_e, ΔF_s, and ΔF_f are calculated by the well-known relations [49]:

$$\Delta F_e = C_e \Delta I_c, \ \Delta F_s =_s \Delta l_v, \tag{3}$$

$$\Delta F_f = C_{ch} \frac{dl_v}{dt},$$

where C_e is the slope of the traction characteristic of the electromagnet, C_s is the stiffness coefficient of the spring, C_{ch} is the friction coefficient of the rod in the channel where it moves.

4.3 Forming of Mathematical Model of Gas-Dynamic Pumping System

As can be seen from Fig. 3, the dosing device of the injector is a valve, the throughput of which depends on the position of the anchor l_v and on the values of the pressure at the inlet of the dosing device elements P_1, P_2, P_3 and P_4. The corresponding mathematical model is grounded on the basis of vacuum engineering equations [51, 52] and will be given in the next subsection of the work. The mathematical model of the gas-dynamic system of a EG with a pumping system can be written as a system of differential equations that describe the conditions of the balance of gas flows in the discharge chamber of the gun and in the technological chamber of the electron beam equipment. As can be seen from Fig. 1, the main flows that determine the pressure in the discharge chamber of the gun are the regulated gas flow Q_{EG}, which enters the gun through the injector and the vacuum line, and the gas flow Q_{chan}, which is pumped out of the gun through the beam line. Accordingly, the equation of the balance of gas flows in the discharge chamber of the gun can be written in the form [51, 52]:

$$V_{EG} \frac{dp_{EG}}{dt} = Q_{EG} - Q_{chan}, \tag{4}$$

where V_{EG} – volume of the gun discharge chamber, p_{EG} – pressure in the discharge chamber.

The regulated gas flow into the discharge chamber Q_{EG} is determined according to the basic equation of vacuum technology through the vacuum conductivity of the channel through which the gas S_g enters and through the pressure difference P_1 and P_4, according to Fig. 3, i.e. [51, 52]:

$$Q_{EG} = S_{EG}(P_1 - P_4) = S_{EG}(p_a - p_{EG}). \tag{5}$$

Accordingly, the gas flow pumped out of the gun through the beam guiding pipe is determined by the conductivity of the pipe and the pressure difference in the EG and in the vacuum chamber of the EB installation, namely [51, 52]:

$$Q_{chan} = S_{chan}(p_{EG} - p_{ch}). \tag{6}$$

Let one now consider the main gas flows that are components of Eqs. (5, 6) and through which the pressure in the vacuum chamber of the EB technological installation is determined. According to Fig. 1, such flows are the flow that comes from the gun to the vacuum chamber Q_{chan} and the flow Q_p, which corresponds to the pumping of gas from the chamber using a vacuum pump. According to this, the equation of the balance of gas flows in the vacuum chamber of the technological installation can be written as follows [51, 52]:

$$V_{ch}\frac{dp_{ch}}{dt} = Q_{chan} - Q_p, \tag{7}$$

where V_{ch} – the volume of vacuum chamber.

The gas flow Q_p, which corresponds to the pumping of gas from the technological chamber, is proportional to the pumping speed S_p and the pressure in the chamber p_p [51, 52]:

$$Q_p = S_p p_{ch}, \tag{8}$$

and the pumping speed S_p is determined by the speed of the vacuum pump S_n and the conductivity S_v of the vacuum pipe connecting the pumping means to the vacuum chamber through the corresponding relationship [51, 52]:

$$\frac{1}{S_p} = \frac{1}{S_n} + \frac{1}{S_v}. \tag{9}$$

In the turn, the speed of the vacuum pump S_n is determined from the following ratio [51, 52]:

$$S_n = S_n\left(1 - \frac{p_p}{p_{ch}}\right), \tag{10}$$

where S_p is the calculated value of the pump speed, p_p is the maximum possible pressure in the pump. Usually, the parameters S_p and p_p are given in the technical passport for vacuum equipment or in the relevant vacuum technology reference books [51, 52]. Taking into account the written relations (9, 10), formula (8) is rewritten as [51, 52]:

$$Q_p = \frac{S_v S_p}{S_v + S_p}(p_{ch} - p_p). \tag{11}$$

4.4 The Complete System of Algebraic-Differential Equations

Taking into account Eqs. (1 – 11), one can write the complete system of algebraic-differential system for process of aerodynamic control of HVDGEH as follows [33, 34]:

$$\begin{cases} R_v I_v + L_v \dfrac{dI_v}{dt} = U_v, \\ m_v \dfrac{d^2 l_v}{dt^2} = C_e I_v - C_s l_v - C_{ch} \dfrac{dl_v}{dt}, \\ V_{EG} \dfrac{dp_{EG}}{dt} = S_{EG} \cdot (_a - _{EG}) - S_{ch}(_{EG} - _{ch}), \\ V_{ch} \dfrac{dp_{ch}}{dt} = S_{ch} \cdot (_{EG} - _{ch}) - \dfrac{S_v S_p}{S_v + S_p} \cdot \left(p_{ch} - p_p\right), \\ I_{EG} = \cdot^m_{EG} U^n_{ac}. \end{cases} \tag{12}$$

In the case of numerical solving the set of Eqs. (12), the output parameter of the control object is the gun discharge current I_{EG}. The main feature of this solving, from a mathematical point of view, is the equation of the input gas flow $S_g = S_g(t)$, which describes the transient characteristic of the EV as a control element of the system. In the works [33, 34], generalized methods of numerical solution of the system (12) in a linear approximation were considered. To solve this problem, the Runge-Kutta method has been used [53–59].

However, the main problems of the functioning of gas-dynamic current control systems due to pressure changes are caused precisely by the nonlinear nature of the system (12). In particular, the selection of EV parameters and a stable control algorithm is associated with the nonlinear nature of this dependence [35, 36]. The study of the generalized dependence in the static mode for an open control system was considered in the works [35, 36].

Corresponded graphic dependences, has been obtained by solving relations (12) for different parameters of evacuation system and EV, are presented in the Fig. 4. It is clear from this dependences, that in the case of unsuitable choosing of evacuation system parameters and their discrepancy with the parameters of the electromagnetic valve, an overshoot effect is observed with an increase in the HVGDEG current by 1.5 – 2 times. It has been shown in the papers [33, 34], that such regimes with overshoot can't provide the stable EG operation in the complex vacuum conditions of technological installations by the reason of appearance and stimulation the arc breakdowns in HVGD in such physical conditions. Obtained dependence of HVGDEG current on the time for different EG volume are given in Fig. 4, a, and corresponding dependence for different vacuum conductivity of the guiding channel S_g in Fig. 4, b. Corresponding parameters of EV for these simulation task are also given.

Finding the pressure values in the different parts of EV dose element construction, which are presented in Fig. 3, is the subject of next part of the chapter. The numerical methods of solving optimization tasks are also used in this aspect [60, 61]. Other method of electronic programable control of energetic parameters of intensive electron beams in high-voltage accelerators, based on dosimetry microcomputer system, have been proposed recently in the papers [62–65].

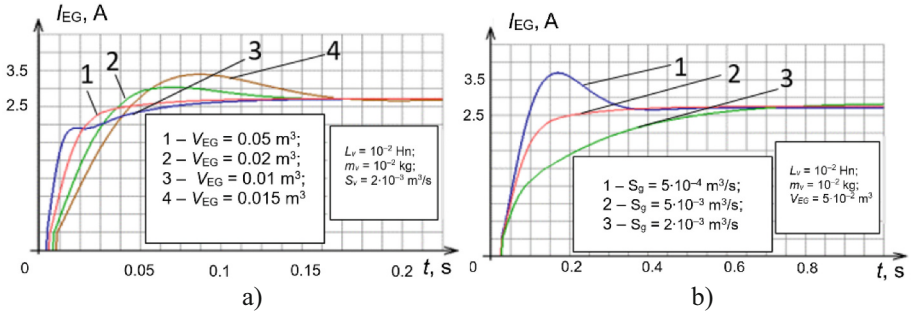

Fig. 4. Dependences of gun current on the time for different gun volume (a) and vacuum conductivity of the guiding channel (b), has been obtained directly by numerical solving the set of algebraic-differential Eqs. (12)

5 Simplified Analysis of the Operation of the Electron Gun Current Control System Without Feedback in Static Mode

5.1 Basic Mathematical Relations

According to the above-considered generalized system of Eqs. (11), the operation of an electromagnetic actuator in static mode can be described by the following simplified system of equations, which is also based on the fundamental laws of mechanics [44, 45, 49] and electrodynamics [46–48]:

$$\begin{cases} R_v I_v = U_v; \\ C_e I_v - l_v C_s = 0. \end{cases} \tag{13}$$

For the design of the EV injector dosing device, the constructive diagram of which is shown in Fig. 3, one can easy to write in mathematical form the relationship between the geometric design parameters as the following algebraical relations [35, 36]:

$$h_1 = l_v - a;\ b = h_1 + h_2;\ r_3 = r_1 - \alpha\, a;\ \alpha = arctg\left(\frac{r_1 - r_2}{l_v}\right);\ r_m = \frac{r_3 + r_2}{2}. \tag{14}$$

On the other hand, taking into account the set of Eqs. (12), one can write the following analytical expression [35, 36]:

$$a = b - \frac{U_v C_e}{R_v C_s}. \tag{15}$$

On the basis of the general equations of vacuum technology, for calculating the vacuum conductivity of the dosing device of the electromagnetic valve, the structural diagram of which is shown in Fig. 3, the following analytical expressions have been obtained in the works [35, 36]:

$$G_1 = \frac{1,445 \cdot 10^4 K_d(a) a^3}{\ln(r_4) - \ln(\alpha a)}, K_d(a) = \frac{a^2}{a^2 + 0,001}, G_3 = 1,088 \cdot 10^4 \frac{r_1^4}{h_2},$$

$$G_2 = \frac{2,72 \cdot 10^3}{h_1}\left(4\left(r_1^4 - r_m^4\right) - \frac{\left(r_1^2 - r_m^2\right)}{\ln(r_1) - \ln(r_m)}\right). \tag{16}$$

Taking into account the given relations (16), the pressure on the constructive elements of the dosing device can be directly determined as follows [35, 36]:

$$P_2 = \sqrt{\frac{G_1 p_a^2 + \frac{G_2\left(p_{EG}^2 G_3 + \frac{p_a^2 G_1 G_2}{G_1+G_2}\right)}{\left(G_3+G_2-\frac{G_2^2}{G_1+G_2}\right)}}{G_1+G_2}}, \; P_3 = \sqrt{\frac{\left(p_{EG}^2 G_3 + \frac{P_a^2 G_1 G_2}{G_1+G_2}\right)}{\left(G_3+G_2-\frac{G_2^2}{G_1+G_2}\right)}}. \tag{17}$$

According to these transformations, and taking into account the given relations (16, 17), the vacuum conductivity of the dosing device design of EV, given in Fig. 3, can be determined using the basic equation of vacuum technology [51, 52]:

$$P_1 = p_a; \; U_1 = G_1(P_1 - P_2); \; U_2 = G_2(P_2 - P_3); \; U_3 = G_3(P_3 - p_{EG});$$

$$S_v = \frac{U_1 U_2 U_3}{U_1 + U_2 + U_3}. \tag{18}$$

Simulation of operation HVGDEG as a part of gas-dynamic control system with electromagnetic valve as a control element has been provided using advanced mathematical and graphic means of MATLAB system for scientific and technical calculations [53–56]. Corresponded graphic dependences $I_g(U_v)$ for different acceleration voltage U_{ac} and operation pressure p_g, have been obtained using relations (13 – 18), are presented at Fig. 5. For obtaining simulation results such parameters of electromagnetic valve as control element have been choose.

Resistor for current, sensor: $R_v = 10$ O;

Slope of the electromagnet push: $C_e = 1.2$ kg/A;

Stiff coefficient of the spring: $C_s = 0.9$ N/m;

Geometry parameters of dosed items, presented at Fig. 3:

$l = 4.5$ mm, $r_1 = 0.8$ mm, r_2, $= 2.3$ mm, $r_4 = 1.6$ mm.

Semiempirical coefficients in relation (1) have been chosen from experimental researches and solving approximation task. Corresponded values are as follows: $a_g = 1{\cdot}10^{-6}$ A/kV, $m = 1.3$, $n = 1.7$.

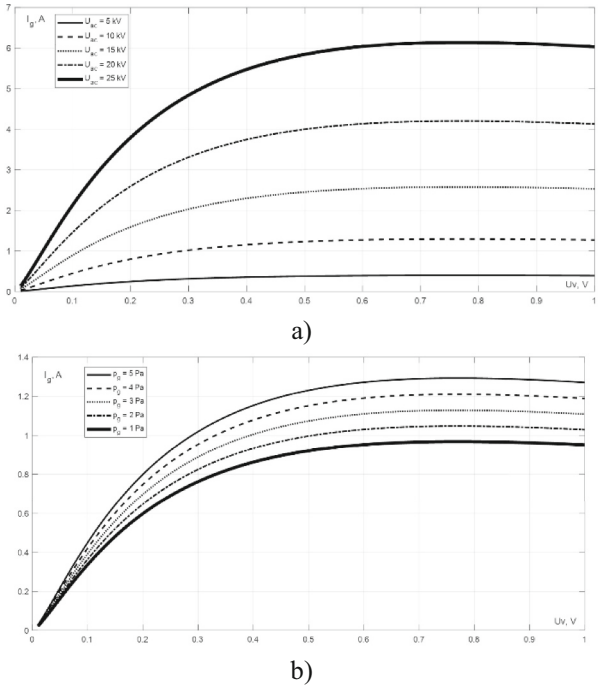

Fig. 5. Obtained graphic dependences of EG current on the voltage in the coil of EV for different values of acceleration voltage U_{ac} (a) and operation pressure in the chamber of EG (b): a – p_{EG} = 4 Pa, b – U_{ac} = 10 kV

5.2 Discussion of Obtained Simulation Results

Basic Recommendations.

From the obtained computer simulation results presented in Fig. 4, it is clear that the gas-dynamic control system can transmit into saturation mode. Therefore, when the threshold voltage value on the solenoid of the control element U_v is reached, the system always transmits automatically to this mode, and, in this case, the rate of rise of the electron gun current $\frac{dI_g}{dU_v}$ is significantly reduced. Of course, when the control system operates in this mode, gas-dynamic automatic control of the gun current by changing the pressure becomes ineffective.

But, in any case, this type of control is very effective for regime of small and average value of HVGD current, when the voltage on valve's solenoid is in range of 0.1 – 0.5 V. Generally, it is caused by the fact, that relation (1), which is described dependence of HVGD current I_g on operation pressure p_g is power with small exponent value m. Namely by that reason dependence $I_g(U_v)$, presented at Fig. 5, are generally slight and haven't outliers.

In work [33, 34] has been pointed out, that main disadvantage of ACS is high values of time regulation constant. By this reason considered control systems with electromagnetic valve can't track short-time bursts of current in automatic mode of operation [33, 34]. In this aspect electric control of beam power with firing additional low-voltage discharge

and changing it current is more effective [33, 34] and mostly correspond to general requirement to advanced electron beam technological equipment [33, 34]. But, in any case, control of pressure in the HVGDEG chamber is always necessary, even in case of using more precision electric control of beam power [38–40].

The obtained simulation results by the quality fully correspond to the experimental parameters of the developed aerodynamic control systems, and the quantitative discrepancy between the calculated and experimental data did not exceed 15–20%. Corresponding experimental data will be considered in the next section of this chapter.

Approximation of Transmission Characteristic of Control System in Static Mode of Operation

For simplifying calculation of EG current different approaches for approximation for approximation of experimental characteristics of gas-dynamic control systems has been proposed and applied. For example, in the works [35, 36] has been proposed using of Gauss error function [66, 67] for approximation the dependences with saturation, like presented in Fig. 3. In such case corresponding analytical relation is written as follows [35, 36]:

$$I_{EG} = \beta_1 \Phi\left((\beta_2 U)^2\right) = \frac{2\beta_1}{\sqrt{\pi}} \int_0^{U_v} \exp\left(-(\beta_2 U)^2\right) dU, \tag{19}$$

where β_1 and β_2 are the function parameters.

Also function (19) can be successfully used for approximation numerical data obtained using relations (13 – 18) for acceleration the process of numerical solving of sophisticated set of Eqs. (12). Really, using approximation (19) except of multiple calculations by the relations (13 – 18) give the significant improving for this numerical algorithm.

Let consider the example of using approximation function (19) for such parameters of control system of HVGDEG current: $b = 0.02$ m, $l_v = 0.03$ m, $r_4 = 0.02$ m, $r_1 = 1 \cdot 10^{-3}$ m, $r_2 = 2 \cdot 10^{-4}$ m, $\alpha = 10^{-3}$ rad, $R_v = 10$ O, $U_{ac} = 15$ kV, $C_e = 1.8$ kg/A. Corresponding dependence of HVGDEG current on voltage on the EV, as regulated element, as well as its approximation by the function (19), are presented in Fig. 6. The values of β_1 and β_2 parameters in function (19) have been defined using the advanced means of MATLAB software and obtained result is: $\beta_1 = 1.5$, $\beta_2 = 0.03$. Clear, that obtained interpolation error does not exceed 5% of the total electron gun current.

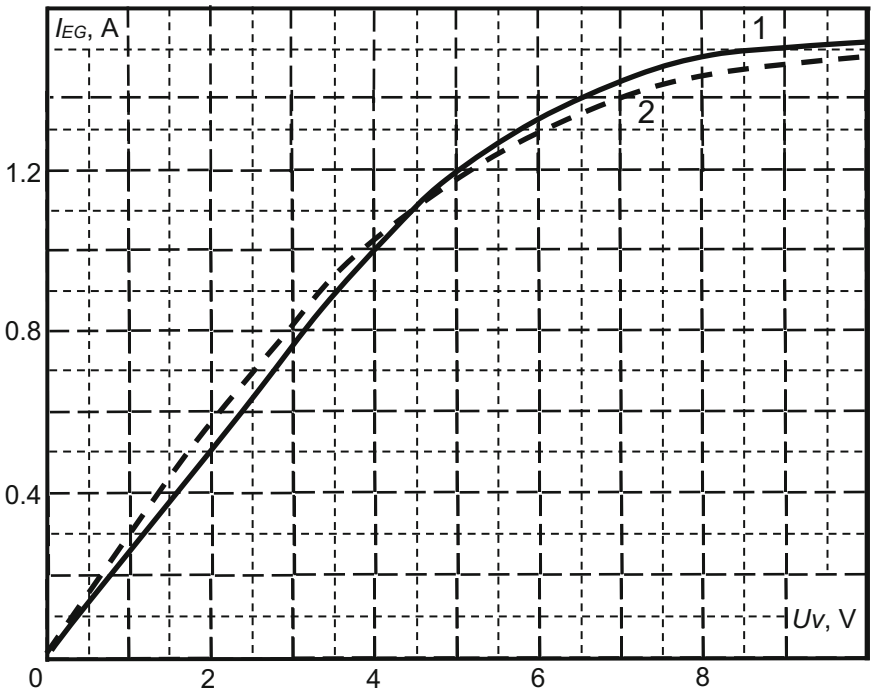

Fig. 6. Transmission characteristic of simulated aerodynamic control system (1) and its approximation by the function (19) (2)

Other advanced approaches for simulation aerodynamic control systems for stabilization of HVGDEG current will be considered in the next section of the chapter.

6 Advanced Approaches for Simulation Aerodynamic Control Systems for Stabilization of Electron Gun Current

6.1 Finite Sequence Machine Theory

Basic ideas of this approach have been developed and verified in the paper [68]. Generally, it is based on the theory of arithmetic-logic relations [69, 70], which has been directly for the discrete sequence of digital control system. Following relation is written as follows [68]:

$$S_i = (i \le k_s) \cdot \left((S_0 - W_i) \cdot \left(1 - \frac{i}{N} \right) \right) + (i > k_s) \cdot \left(\left(S_0 - \frac{\sum_{j=1}^{k_s} W_{i-j}}{k_s} \right) \cdot \left(1 - \frac{i}{N} \right) \right), \quad (20)$$

where S_i – considered states of control system, and W_i is random disturbing effect. Corresponding scheme of Moore FSM for such process is given in Fig. 7.

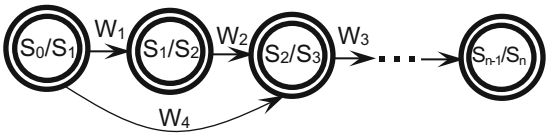

Fig. 7. Moore FSM for operation of aerodynamic control system

This approach has been carefully analyzed theoretically in the paper [68]. Provided researches shown, that there is only slight difference between using simple relation (20) and numerical solving sophisticated set of Eqs. (12). Therefore, now namely the approach, based on using relation (20) consist the theoretical base for further development of engineering elaboration of aerodynamic control systems for HVGDEG current. For approximation transmission characteristic of control system, the relation (19) is used usually. Corresponding experimental results will be given in the next section of the chapter.

6.2 Fuzzy Logic Theory and Root-Polynomial Membership Functions

This approach also has been proposed recently [71, 72], and it is, generally, more sophisticated for realizing in digital programmable microcontrollers, than simple approach, based on FSM theory and has been described before [68]. Generally, it is based on fuzzy logic theory with including such important definition, as "MIDDLE CURRENT", "LOW CURRENT", "HIGH CURRENT" for the current of HVGDEG as output value, and "MIDDLE VOLTAGE", "LOW VOLTAGE", "HIGH VOLTAGE" for the EV voltage as input value [71]. After that, for such defined variables the fuzzy rules formed. Generally, such rules are also based on the arithmetic-logic relations (20) [71]. Examples of these rules are as follows [71]:

$$\text{IF}(I = \text{EG and } DI = \text{SN})\text{THEN}(DU = \text{SN}), \tag{21}$$

where "EG" mean Extra Great, "SN" – Slow Negative. The full set of corresponding 25 rules is given in the work [71].

In the work [72] has been proposed using of root-polynomial functions for describing the membership functions of described variables. For example, in the classic approach, a Z membership function is defined as [73–80]:

$$f_Z(x; a, b) = \begin{cases} 1, & x \le a; \\ 1 - 2 \cdot \left(\frac{x-a}{b-a}\right)^2 & a < x \le \frac{a+b}{2}; \\ 2 \cdot \left(\frac{b-x}{b-a}\right)^2 & \frac{a+b}{2} < x < b; \\ 0, & x \ge b, \end{cases} \tag{22}$$

S – function, as [73–80]:

$$f_S(x;a,b)=\begin{cases}0, & x\le a;\\ 2\cdot\left(\frac{x-a}{b-a}\right)^2 & a<x\le\frac{a+b}{2};\\ 1-2\cdot\left(\frac{b-x}{b-a}\right)^2 & \frac{a+b}{2}<x<b;\\ 1, & x\ge b.\end{cases} \tag{23}$$

and Π – function, from relations (22, 23), as [73–80]:

$$f_\Pi(x;a,b,c,d)=f_S(x;a,b)\cdot f_Z(x;c,d)\,,\ a\le b<c\le d\,. \tag{24}$$

Clear, that relations (22 – 24) can be simply rewritten in the form of arithmetic-logic relations for solving the programming tasks in microcontrollers control systems, but it perfect analyze in computer simulation software is seriously limited by the fact, that derivative of memberships functions in the critical point a, b, c, and d are undefined. Therefore, using of complex advantage numerical methods, which are generally, not critical to this singularity of functions, is necessary.

But in the paper [72] has been shown and proof, that such type of stiff functions with strong changing in the $[a; b]$ and $[c; d]$ ranges, which are usually very small, and mostly unchangeable the function value in the largest range $[b; c]$, are always can be described by the advanced mathematical approach of Root-Polynomial Functions (RPF) [72]. In the generalized form, corresponding analytical relation for RPF written as follows [72]:

$$r(z)=\sqrt[n]{C_nz^n+C_{n-1}z^{n-1}+\ldots+C_1z+C_0}-\delta, \tag{25}$$

where z is the argument, r is the value of the function, and $C_0 - C_n$ are the values of the polynomial coefficients, δ – value of deviation of function (25) corresponding to numerical data. Deviation is usually used for providing stable convergence of interpolation procedure, when near the minimum the values of interpolation numerical set are close to zero [72]. Generally clear, that interpolative relation (25) is suitable only for positive values of argument r.

For example, fuzzyficated variable for the relative value of HVGDEG current, defined as $N=\frac{I_{cur}}{I_{nom}}$, I_{cur} – current value of HVGDEG current, I_{nom} – established nominal value of HVGDEG current, with using RPF relation is defined as follows:

$$F_{\mathrm{FUZ}}(I_g)=\sqrt[4]{\begin{array}{c}2.9\cdot10^{10}N^8-2,67\cdot10^{11}N^7+1.0754\cdot10^{12}N^6-\\ -2.471\cdot10^{12}N^5+3.5511\cdot10^{12}N^4-3.2655\cdot10^{12}N^3+\\ +1.8766\cdot10^{12}N^2-6.161\cdot10^{11}N-8.85\cdot10^{10}.\end{array}} \tag{26}$$

Corresponded graphic dependence for function (26) is presented in the Fig. 8.

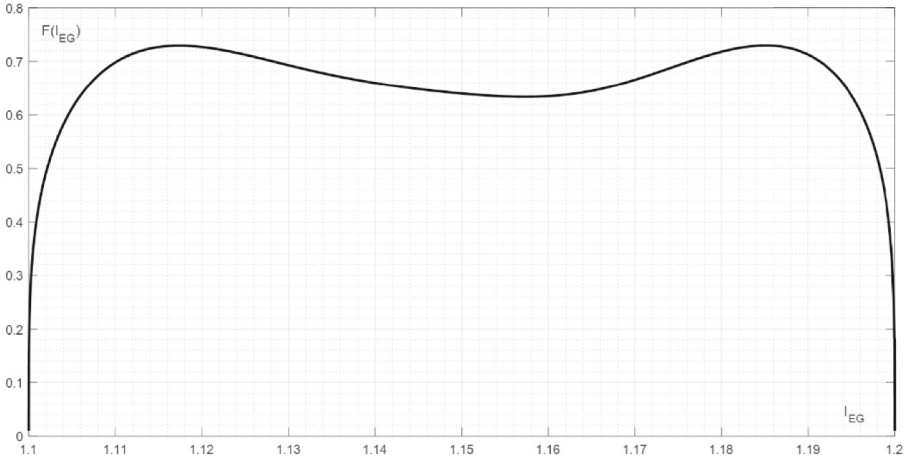

Fig. 8. Fuzzyficated function for HVGDEG current, defined as RPF by the relation (26)

Fuzzyficated variable for the deviation of HVGDEG current defined as follows:

$$F_{\mathrm{FUZ}}(dI_g) = \sqrt[4]{\begin{array}{c} 7.48 \cdot 10^8 dI_g^8 - 4.2335 \cdot 10^8 dI_g^7 + 9.8473 \cdot 10^7 dI_g^6 - \\ -1.1123 \cdot 10^7 dI_g^5 + 7.9761 \cdot 10^5 I_g^4 + 1.9234 \cdot 10^4 I_g^3 - \\ -6.6723 \cdot 10^2 dI_g^2 + 4.45195 \cdot 10 dI_g + 6.225 \cdot 10^{-10}. \end{array}} \qquad (27)$$

Corresponding graphic dependence for function (27) is presented in the Fig. 9.

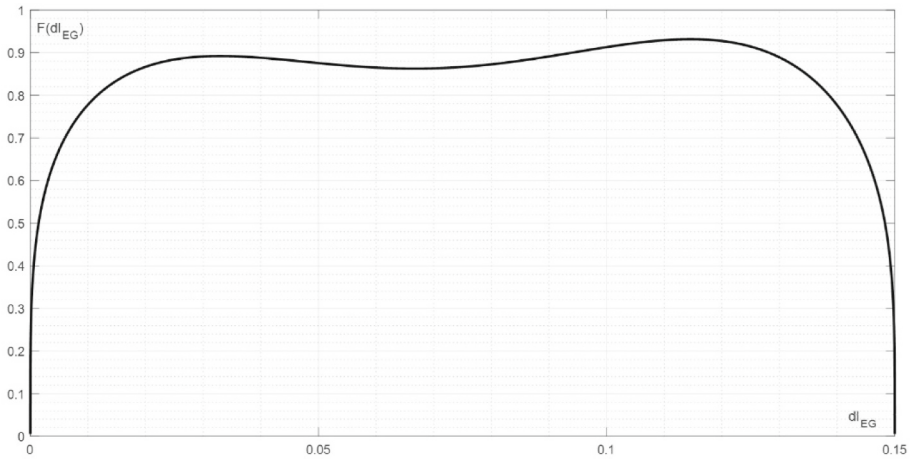

Fig. 9. Fuzzyficated function for changing of HVGDEG current, defined as RPF by the relation (27)

Really, presented standard arithmetical relations (22 – 24) are simpler for providing computer calculations, than RPF (26, 27), because calculation of RPF is always

included multiple use of power function [81–83]. But, in contrary, RPFs always have the derivatives on the whole range of its' using, therefore, this approach is very suitable for complex study the singularities of control system operation.

7 Engineering Realization and Experimental Results

Clear, that main necessary elements of ACS are as follows.

1. Electromagnetic valve.
2. Microcontroller for realizing ACS functions.
3. Valve driver with digital-analogue signal transformer.

Corresponding assembled construction of EV, elaborated in Educational and Scientific Laboratory of Electron-Beam Technological Devices, is presented in Fig. 10. Generally, this construction is fully corresponded to the basic scheme of EV as control element, presented in Fig. 10.

Fig. 10. Electromagnetic valve

For realizing control of EG current on the level of programming the advanced microcontroller SIMATIC S7 1200 with central processor unit 1217 C have been used [81]. For solving programming task in this microcontroller advanced original software with suitable graphic interface for solving the tasks of control systems designing, has been used [81]. Generally, this software is based on the principle of visual connection the necessary functional blocks of control system and defining the blocks parameters, and, after that, microcontroller generated the correct executable code simultaneously by using existed libraries of control functions. Such approach of system design firstly has been realized in MATLAB in Simulink software [54–56], and now it is, in fact, recognized as the standard for software designed to support the development of complex technical

systems. The advantage of this approach is the simplicity of engineering design of control systems, but the created program code is not always optimal in terms of the speed of solving problems of control of mechanical and electrical devices. In most cases, this disadvantage in modern microcontrollers is compensated by the high clock frequency of the central processor. From a theoretical point of view, this approach is associated with the FSM theory and, generally, corresponds to the modern trend of development of artificial intelligence systems. Solving of control task for EG current using EV has been realized, generally, has been realized by the arithmetic-logic relation (20) and Moore FSM diagram, presented in Fig. 7 [68]. The photo of microcontroller SIMATIC S7 1200 is presented in Fig. 11. Correspondingly, photo of assembled ACS with electromagnetic valve, connected to microcontroller by USB interface, is presented in Fig. 12.

Fig. 11. SIEMENS microcontroller SIMATIC S7 1200 for ACS

It should be noted that the solution of ACS problems using the fuzzy logic functions described in Subsect. 6.2 is also possible using visual programming at the circuit level. It is only necessary to implement the corresponding libraries [81]. In this case, the speed of solving the control problem is always somewhat lower due to more complex calculations; however, on the other hand, with this approach, current overshoots of the EG are usually completely eliminated. Therefore, in general, fuzzy logic algorithms, from the point of view of the quality of solving the control problems, are considered as more optimal, although they have a lower speed of object regulation.

As for practical realizing the approach of using RPF (25) as membership functions, considered in Subsect. 6.2, generally it is possible, but only though creation the separates users' libraries for calculation RPF coefficients. Really, this approach is appearing quite recently, therefore, it has still been studied only at the theoretical level for solving a narrow, separate class of applied problems. From a technical point of view, there are two possibilities for connecting such libraries to a microcontroller: writing software directly for the microcontroller using an appropriate compiler or connecting the microcontroller to a personal computer with the ability to parallelize calculations in a computer network.

However, as noted in Subsect. 6.2, the use of RPF for solving fuzzy logic problems mainly makes sense at the stage of preliminary analysis of control systems and finding optimal parameters of system elements.

Fig. 12. Electromagnetic valve, connected to microcontroller by USB interface

The photo valve driver with digital-analogue transformer control signal and liquid crystal monitor is presented in Fig. 13. Generally, this component is always included in the basic set of necessary microcontroller elements, which is supplied by the manufacturer to the customer of electronic equipment. This block also has on the monitor suitable interface for changing ACS parameters [81].

Oscilogramm of changing EG current with abrupt change of acceleration voltage is presented in Fig. 14. This result corresponds to such ACS parameters: $L_v = 10^{-2}$ Hn, $m_v = 10^{-2}$ kg, $V_{EG} = 5{\cdot}10^{-2}$ m^3, and $S_g = 5{\cdot}10^{-2}$ m^3/s. Clear, that 30% overshoot of EG current is fully corresponds to simulation results, presented in Fig. 4, b. In the case of reducing of pumping productivity to $S_g = 5{\cdot}10^{-3}$ m^3/s overshoot of EG current is not observed. Generally, simulation results, obtained by numerical solving the set of Eq. (12), are similar to the corresponding experiments, and the discrepancy between theoretical and experimental data is usually smaller than 15%. The measurements have been provided using digital oscilloscope SIGLENT SDS1042D [82]. Measurement accuracy of this electronic device, pointed out by the manufacturer, is range of 3% [82].

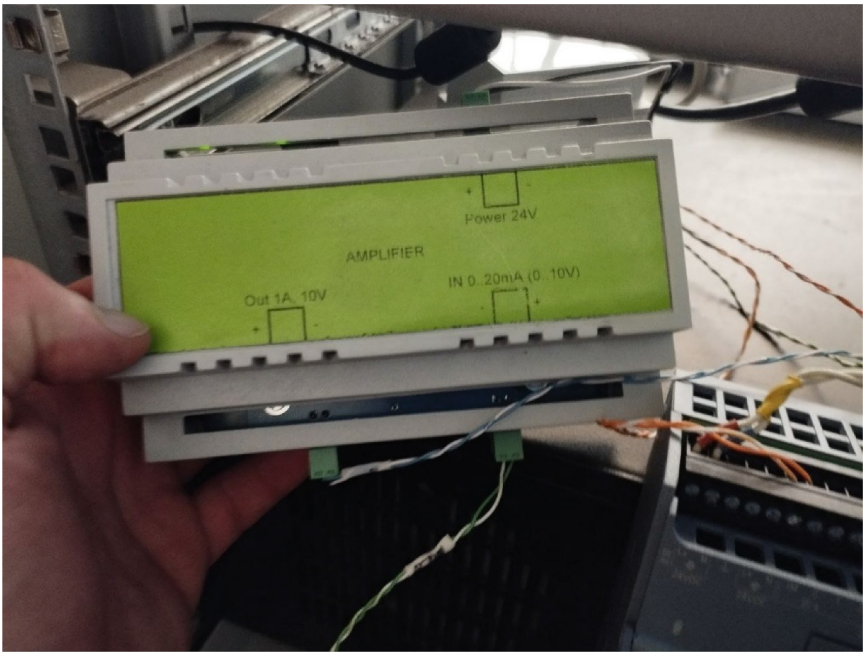

Fig. 13. Valve driver with digital-analogue signal transformer and liquid crystal monitor

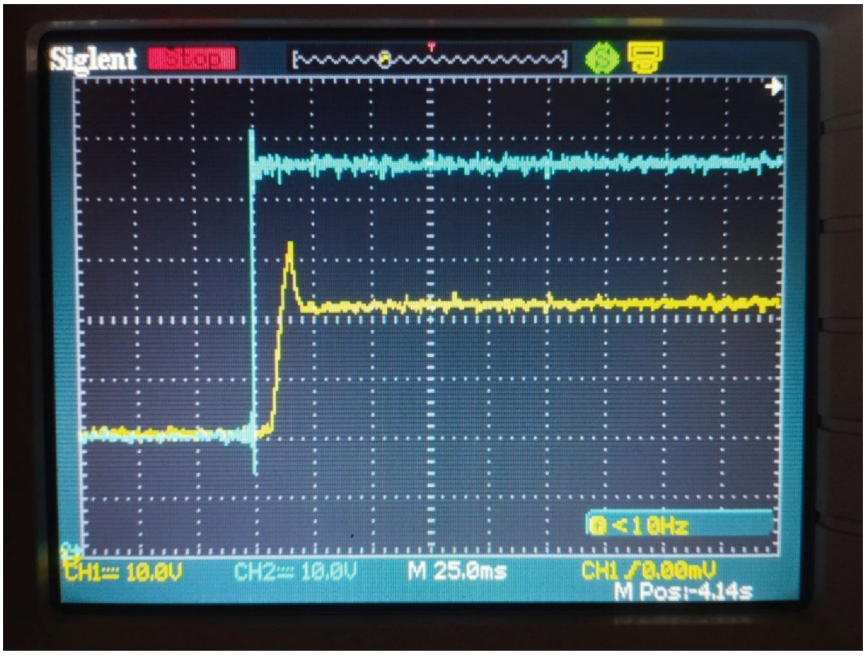

Fig. 14. Obtained experimental dependences of changing acceleration voltage (blue line) and gun current (yellow line) on the time

8 Conclusion

Results of numerical simulation and experimental data, presented un this chapter, shown, that numerical simulation the regimes of operation aerodynamic control systems of HVGDEG current give the advanced possibilities to improve the stability of operation of HVGDEG in a real technological equipment, taking into account the particularities of realizing technological operation, including operation pressure in technological chamber. Particularities of using described methods of simulation are as follows.

In the level of preliminary simulation of HVGDEG current control system, designed by the customer requirement, solving the complete set of Eqs. (12) for estimated values of necessary HVGDEG current and operation pressure in technological chamber is provided. The geometrical parameters of EV are changed in this simulation process for obtaining the optimal, smallest value of time regulation constant without overshoot of current. The approximative relation (19) in this step of simulation control system is also used effectively.

On the second step, when the optimal parameters of HVGDEG current aerodynamic control system are choose, engineering designing of digital control systems, is provided. In this step, the suitable microcontroller, which can provide the necessary time of calculation in the regime of small deviation of gun current, is choose. The corresponding calculation algorithm in this step of control system designing is realized by using FSM theory, taking into account arithmetic-logic relation (20). Corresponding rough estimations of microcontroller operation time can be realized taking into account the basic conceptions of theory of operation [83–85]. In this case, it is also necessary to consider the set of elementary commands executed by the microcontroller, as well as the time required to perform them.

The approach, based of fuzzy logic algorithm, described in the Sect. 6.2, is also possible to realizing on the hardware level of control system in microcontroller device, but it has to be taking into account, that such approach is more sophisticated by the necessary calculations. Therefore, speed of performing the elementary arithmetic and logic hove to be significantly greater. In contrary, for correct choose of membership functions, fuzzy logic approach always allows to perform the control with grater accuracy and without overshoots. Generally, using of arithmetic-logic functions, formed by the relations (22 – 24) is the best way for effective solving of this programming task on high-speed microcontrollers. But using RPF (25) give the advanced possibilities for finding optimal time regimes for control system operation.

The accuracy of numerical simulation ACS using the set of Eqs. (12) relatively to experimental data is very high. Usually, the discrepancy between theoretical and experimental data is smaller than 15%.

The results of researches, presented in this chapter, are very interesting and important for the expert in the designing and exploitation of EB technological equipment, as well as for expert on the basic theory of control systems, which included electromechanical control elements.

Acknowledgements. All scientific research, described in this paper, has been provided in the Scientific and Educational Laboratory of Electron Beam Technological Devices of National Technical University of Ukraine “Igor Sikorsky Kyiv Polytechnical Institute” within the framework of

the implementation of the state order of the Ministry of Education and Science of Ukraine No. 0124U001525.

References

1. Melnyk, I., Tuhai, S., Surzhykov, M., Shved, I., Melnyk, V., Kovalchuk, D.: Analytical estimation of the deep of seam penetration for the electron-beam welding technologies with application of glow discharge electron guns. In: 2022 IEEE 41st International Conference on Electronics and Nanotechnology (ELNANO), pp. 1–5. (2022). https://doi.org/10.1109/ELNANO54667.2022.9927071. https://ieeexplore.ieee.org/document/9927071
2. Denbnovetsky, S.V., Melnyk, V.I., Melnyk, I.V., Porytskyy, P.V.: Experimental and theoretical investigation of technological process of obtaining of metals oxide and nitride coatings by using high-voltage gas-discharge electron beam evaporator. In: 19th International Symposium on Discharges and Electrical Insulation in Vacuum, ISDEIV, vol. 2, pp. 552–555. (2000). https://doi.org/10.1109/DEIV.2000.879048. https://ieeexplore.ieee.org/document/879048
3. Denbnovetsky S.V., Melnyk V.I., Melnyk I.V., Porytskyy P.V.: Investigation of metal evaporation and film deposition with a high voltage glow-discharge electron gun under middle vacuum. In: 21th International Symposium on Discharges and Electrical Insulation in Vacuum, ISDEIV, vol. 2, pp. 575–578, 2E-01 (2004). https://doi.org/10.1109/DEIV.2004.1422681. https://ieeexplore.ieee.org/document/1422681
4. Prikhna, T.O., et al.: Electron-beam and plasma oxidation-resistant and thermal-barrier coatings deposited on turbine blades using cast and powder Ni(Co)CrALY(Si) Alloys I. fundamentals of the production technology, structure, and phase composition of cast NiCrAlY alloys. Powder Metall. Metal Ceramics, **61**(1 – 2), 70–76. (2022). https://doi.org/10.1007/s11106-022-00296-8, https://link.springer.com/article/
5. Prikhna, T.O., et al.: Electron-beam and plasma oxidation-resistant and thermal-barrier coatings deposited on turbine blades using cast and powder Ni(Co)CrAlY(Si) alloys produced by electron-beam melting ii. structure and chemical and phase composition of cast CoCrAlY alloys. Powder Metall. Metal Ceramic, **61**(3–4), 230–237 (2022). http://www.materials.kiev.ua/issue/212/article/3403
6. Grechanyuk, I.M., et al.: Electron-beam and plasma oxidation-resistant and thermal-barrier coatings deposited on turbine blades using cast and powder Ni(Co)CrAlY(Si) alloys produced by electron beam melting IV. chemical and phase composition and structure of cocralysi powder alloys and their use. Powder Metall. Metal Ceramics, **61**(7–8), 459–464 (2022). http://www.materials.kiev.ua/issue/215/article/3461
7. Grechanyuk, M.I., et al.: Electron-beam and plasma oxidation-resistant and thermal-barrier coatings deposited on turbine blades using cast and powder Ni (Co)CrAlY (Si) alloys produced by electron beam melting III. formation, structure, and chemical and phase composition of thermal-barrier Ni(Co)CrAlY/ZrO_2–Y_2O_3 coatings produced by physical vapor deposition in one process cycle. Powder Metall. Metal Ceramics, **61**(5–6), 328–336 (2022). http://www.materials.kiev.ua/issue/214/article/3439
8. Grechanyuk, V.G., Grechanyuk, N.I., Chornovol, V.O., Grabina, T.D., Kozyreva, Y.I.: Copper and molybdenum-based nanocrystalline materials. Progress Phys. Metals, **44**(7), 927–942. (2022). https://mfint.imp.kiev.ua/f/issues/Metallofiz.%20Noveishie%20Tekhnol.%202022,%20vol. %2044,%20No.%207.pdf
9. Zakharov, A., Litvintsev, S., and Ilchenko, M.: Trisection bandpass filters with all mixed couplings. IEEE Microwave Wireless Components Lett. **29**(9), 592–594. (2019). https://doi.org/10.1109/LMWC.2019.2929650. https://ieeexplore.ieee.org/abstract/document/8782802

10. Zakharov, A., Rozenko, S., Ilchenko, M.: Varactor-tuned microstrip bandpass filter with loop hairpin and combline resonators. IEEE Trans. Circ. Syst. II, Exp. Briefs. **66**(6), 953 – 957. (2019). https://doi.org/10.1109/TCSII.2018.2873227, https://ieeexplore.ieee.org/document/8477112
11. Sasaki, H., Kobashi, Y., Nagai, T., Maeda, M.: Application of electron beam melting to the removal of phosphorous form silicon: toward production of solar-grade silicon by metallurgical process. Adv. Mater. Sci. Eng. 857196 (2013). https://cyberleninka.org/article/n/299910/viewer
12. Kemmotsu, T., Nagai, T., Maeda, M.: Removal rate of phosphorous form melting silicon. High Temperature Mater. Processes **30**(1–2), 17–22 (2011). https://doi.org/10.1515/htmp.2011.002 https://www.degruyter.com/journal/key/htmp/30/1-2/html
13. Pires, J.C.S., Barga, A.F.B., May, P.R.: The purification of metallurgically grade silicon by electron beam melting. J. Mater. Process. Technol. **169**(1), 347–355 (2005)
14. Luo, D., Liu, N., Lu, Y., Zhang, G., Li, T.: Removal of impurities from metallurgically grade silicon by electron beam melting. J. Semiconductors **32**(3), 033003 (2011). http://www.jos.ac.cn/en/article/doi/https://doi.org/10.1088/1674-4926/32/3/033003
15. Kovalchuk, D., Melnyk, V., Melnyk, I.: A coaxial wire-feed additive manufacturing of metal components using a profile electron beam in space application. J. Mater. Eng. Perform. **31**(8), 6069–6082 (2023). https://doi.org/10.1007/s11665-022-06994-z
16. Kovalchuk, D., Ivasishin, O.: Profile electron beam 3D metal printing. In: Additive Manufacturing for the Aerospace Industry. Book chapter, pp. 213–233 (2029). https://doi.org/10.1016/B978-0-12-814062-8.00012-1
17. Markovsky, P.E., et al.: Ballistic resistance of layered titanium armour made using powder metallurgy and additive 3D printing. Metallofiz. Noveishie Tekhnol. **44**(10), 1361–1375 (2021). https://doi.org/10.15407/mfint.43.12.1573
18. Markovsky, P.E., et al.: Titanium-based layered armour elements manufacture with 3D-printing approach. Metallofiz. Noveishie Tekhnol. **44**(10), 1361–1375 (2022). https://doi.org/10.15407/mfint.44.10.1361
19. Denbnovetsky, S.V., Melnyk, V.I., Melnyk, I.V.: High voltage glow discharge electron sources and possibilities of its technological application. In: 20th International Symposium on Discharges and Electrical Insulation in Vacuum, Tours, France, pp. 111–114 (2002). https://doi.org/10.1109/ISDEIV.2002.1027321. https://ieeexplore.ieee.org/document/1027321
20. Denbnovetsky, S.V., Melnyk, V.G., Melnyk, I.V., Tugay, B.A.: Obtaining of powerful electron beams in high voltage glow discharges with cold cathodes. In: 21-th International Symposium on Discharges and Electrical Insulation in Vacuum (ISDEIV), vol. 2., pp. 533–536, 2D-01. (2004). https://doi.org/10.1109/DEIV.2004.1422668. https://ieeexplore.ieee.org/document/1422668
21. Denbnovetsky, S.V., Melnyk, I.V., Melnyk, V.G., Tugai, B.A., Tuhai, S.B.: High voltage glow discharge electron guns and its advanced application examples in electronic industry. In: 2016 International Conference Radio Electronics & Info Communications (UkrMiCo), pp. 255–258. Kyiv, Ukraine (2016). https://doi.org/10.1109/UkrMiCo.2016.7739615, https://ieeexplore.ieee.org/document/7739615
22. Haiying, X., Xinghua, S., Bo, Y., Peng, Y., Jikang, F.: Development of novel cold-cathode gas-discharge electron beam gun: an instrumentation study. Chin. J. Vacuum Sci. Technol. **41**(3), 284–290 (2021). http://cjvst.cvs.org.cn/en/article/doi.org/10.13922/j.cnki.cjvst.202005028?viewType=citedby-info
23. Jiawei, C., Shengbo, L., Zhishu, L., Fengmin, B., Guozheng, L., Zongzheng, B.A.: Characterization of magnetic focusing of electron gun based on structural parameters of magnetic lens. Chin. J. Vacuum Sci. Technol. **44**(5), 463–469. https://doi.org/10.13922/j.cnki.cjvst.202401009 (2024). http://cjvst.cvs.org.cn/en/article/doi/

24. Liang, G., Jie, Y., Hua, Z., Wei, T., Jinrong, L.: Simulation analysis of factors affecting penning discharge in high current pulsed electron beam. Chin. J. Vacuum Sci. Technol. **44**(2), 184–190 (2024). https://doi.org/10.13922/j.cnki.cjvst.202306003, http://cjvst.cvs.org.cn/en/article/doi/
25. Yufan, Q., Shengbo, L., Xinjian, Z., Shengping, F., Fengmin, B.: Electrostatic focusing characteristic of electron gun with multi-parameter coupling. Chin. J. Vacuum Sci. Technol. **41**(11), 1094–1100 (2021). https://doi.org/10.13922/j.cnki.cjvst.202101027. http://cjvst.cvs.org.cn/en/article/doi/
26. Deng, C., Wang, Y., Liu, J., Han, L.: Property characterization of electron flood gun with self-developed test platform. Chin. J. Vacuum Sci. Technol. **40**(9), 847–852 (2020). https://doi.org/10.13922/j.cnki.cjovst.2020.09.09, http://cjvst.cvs.org.cn/en/article/doi/
27. Wang, J.: Applications of resistance spot welding in assembling electron gun for travelling wave tube: a review study. Chin. J. Vacuum Sci. Technol. **40**(4), 381–388 (2020). https://doi.org/10.13922/j.cnki.cjovst.2020.04.17, http://cjvst.cvs.org.cn/en/article/doi/
28. Yidong, X., Zhao, D., Xue, Q., Xiaofei, L.: Design optimization of planar sheet beam magnetron injection gun: a simulation study. Chin. J. Vacuum Sci. Technol. **40**(3), 226–232 (2020). https://doi.org/10.13922/j.cnki.cjovst.2020.03.08, http://cjvst.cvs.org.cn/en/article/doi/
29. Yan, W., Weixia, Z., Chenhui, D., Liu, J., Han, L.: Design optimization of low energy electron gun: a simulation study with hybrid mesh model. Chin. J. Vacuum Sci. Technol. **40**(1), 1–6 (2020). https://doi.org/10.13922/j.cnki.cjovst.2020.01.01, http://cjvst.cvs.org.cn/en/article/doi/
30. Yunting, G., et al.: Design of new electron gun capable of generating uniform electron-beam with large width. Chinese J. Vacuum Sci. Technol. **39**(12), 1109–1113 (2019). https://doi.org/10.13922/j.cnki.cjovst.2019.12.11, http://cjvst.cvs.org.cn/en/article/doi/
31. Huo, W., Hu, J., Cao, X., Fu, Y., Zhao, W.: Design and properties of Cu-based lab_6 photocathode for pseudospark discharge in electron beam source: an experimental study. Chin. J. Vacuum Sci. Technol. **39**(8), 631–636 (2019). https://doi.org/10.13922/j.cnki.cjovst.2019.08.03, http://cjvst.cvs.org.cn/en/article/doi/
32. Fu., Xuecheng, Ying, W., Ju., Quan Xueling, Minni, W.F.: Mechanism for black particle formation on gold coatings deposited by electron beam evaporation: a theoretical and experimental study. Chinese J. Vacuum Sci. Technol. **39**(5), 396–400 (2019). https://doi.org/10.13922/j.cnki.cjovst.2019.05.07
33. Denbnovetsky, S.V., Melnyk, V.I., Melnyk, I.V., Tugay, B.A.: System of automatic control of glow discharge electron gun current and it's computer simulation. In: International Symposium on Discharges and Electrical Insulation in Vacuum, ISDEIV, Proceedings, vol. 2, pp. 633–636 (2000). https://doi.org/10.1109/DEIV.2000.879069, https://ieeexplore.ieee.org/document/879069
34. Denbnovetsky, S.V., Melnyk, V.I., Melnyk, I.V., Tugay, B.A.: Model of control of glow discharge electron gun current for microelectronics production applications. In: Proceedings SPIE 5065, Sixth International Conference on Material Science and Material Properties for Infrared Optoelectronics, (14 April 2003). https://doi.org/10.1117/12.502174
35. Denbnovetsky, S.V., Melnyk, I.V., Melnyk, V.G., Tugai, B.A., Tuhai, S.B.: Simulation of dependences of discharge current of high voltage glow discharge electron guns from parameters of electromagnetic valve. In: IEEE 37th International Conference on Electronics and Nanotechnology, 2017, pp. 369–374 (2017). https://doi.org/10.1109/ELNANO.2017.7939781. https://ieeexplore.ieee.org/document/7939781
36. Melnyk, I.V., Melnyk, V.G., Tugai, B.A., Tuhai, S.B.: Investigation of complex control system for high voltage glow discharge electron sources. In: The Second IEEE International Conference on Information-Communication Technologies and Radioelectronics UkrMiCo'2017. Collections of Proceedings of the Scientific and Technical Conference, pp. 295 – 299. 11–15

September, Odesa, Ukraine (2017). https://doi.org/10.1109/UkrMiCo.2017.8095394. https://ieeexplore.ieee.org/document/8095394
37. Denbnovetsky, S.V., Melnik, V.I., Melnik, I.V., Tugay, B.A.: Investigation of forming of electron beam in glow discharge electron guns with additional electrode. In: International Symposium on Discharges and Electrical Insulation in Vacuum, ISDEIV, vol. 2, pp. 637–640. (1998). https://doi.org/10.1109/DEIV.1998.738530, https://ieeexplore.ieee.org/stamp/stamp.jsp?tp=&arnumber=738530
38. Melnyk, I.V.: Estimating of current rise time of glow discharge in triode electrode system in case of control pulsing. Radioelectronics Commun. Syst. **56**(12), 592–599 (2013). https://doi.org/10.3103/S0735272713120066, https://radioelektronika.org/article/view/S0735272713120066
39. Melnik, I.V., Tugay, S.B.: Analytical calculations of anode plasma position in high-voltage discharge range in case of auxiliary discharge firing. Radioelectronics Commun. Syst. **55**(11), 514–521 (2012). https://doi.org/10.3103/S0735272712110064, https://radioelektronika.org/article/view/S0735272712110064
40. Melnyk, I.V.: Simulation of energetic efficiency of triode high voltage glow discharge electron sources with account of temperature of electrons and its mobility in anode plasma. Radioelectronics Commun. Syst. **60**(7), 319–329 (2017). https://doi.org/10.3103/S0735272717007056, https://radioelektronika.org/article/view/S0735272717070056
41. Melnyk, I., Tuhai, S., Pochynok, A.: Universal complex model for estimation the beam current density of high voltage glow discharge electron guns. In: Ilchenko M., Uryvsky L., Globa L., (eds.) Lecture Notes in Networks and Systems, vol. 152, pp. 319–341. Springer (2021). ISBN 97–3–030–58358–03, https://doi.org/10.1007/978-3-030-58359-0_18, https://link.springer.com/chapter/https://link.springer.com/chapter/
42. Melnyk, I.V.: Numerical simulation of distribution of electric field and particle trajectories in electron sources based on high-voltage glow discharge. Radioelectronics Commun. Syst. **48**(6), 41–48 (2005). https://doi.org/10.3103/S0735272705060087, http://radioelektronika.org/article/view/S0735272705060087
43. Friedland, B.: Control System Design: An Introduction to State-Space Methods, p. 528. Dover Publications (2005)
44. Flux, J: Dynamics And Control Systems (Mechanical Engineering Essentials with Python). Kindle Edition (2024)
45. Flux, J: Fluid Mechanics and Hydraulic Systems (Mechanical Engineering Essentials with Python). Kindle Edition (2024)
46. Gonen, T.: Electric Power Distribution Engineering, p. 1061. CRC Press (2014)
47. Haynes, G.: Step-by-Step Electrical Engineering: Learn and Apply Core Concepts Quickly. Build Your Knowledge with Practical Examples, p. 174. Independent Publisher (2024)
48. Short, T.A.: Electric Power Distribution Handbook, 2nd Edition, p. 898. CRC Press (2014)
49. Budynas, R., Nisbett, K.: Shigley's Mechanical Engineering Design. 10th Edition, p. 1104 McGraw Hill (2014)
50. Anderson J.D.: Fundamentals of Aerodynamics. 6th Edition, p. 1152. McGraw Hill (2016)
51. Rao, V.V., Gosh, T.B., Chorpa, K.L.: Vacuum Science and Technology, p. 202. Alliedm Publisher PVT Ltd. (2008)
52. Hoffman, D., Singh, B., Thomas, J.H.: Handbook of Vacuum Science and Technology, p. 873. Academic Press (1997)
53. Mathews, J.H., Fink, K.D.: Numerical Methods. Using MATLAB, p. 689. Prentice Hall (1998)
54. Gilat, A.: MATLAB: An Introduction with Applications, p. 384. Wiley (2008)
55. Attaway, S.: MATLAB: A Practical Introduction to Programming and Problem Solving, p. 560. Butterworth-Heinemann (2013)
56. Kattan, P.: MATLAB for Beginners: A Gentle Approach: Revised Edition, p. 290. Self-published (2009)

57. Jain, M.K., Iengar, S.R.K., Jain, R.K.: Numerical Methods for Scientific & Engineering Computation. New Age International Pvt. Ltd., p. 733 (2010). ISBN: 978–81–224–2707–3
58. Chapra, S.C., Canale, R.P.: Numerical Methods for Engineers. 7th Edition, p. 992. McGraw Hill (2020). ISBN: 978–0073397924
59. Phillips, G.M.: Interpolation and Approximation by Polynomials, p. 312. Springer (2023). ISBN: 978–0387002156
60. Draper N., Smith H.: Applied Regression Analysis. 3 Edition, p. 706. Wiley Series, (1998). ISBN: 978–0–471–17082–2
61. Mohan, C., Deep, K.: Optimization Techniques. New Age Science, p. 628 (2009). ISBN: 978–1906574215
62. Tseluyko, A.F., et al.: Influence of plasma nucleus form on radiation orientation in high-current pulse plasma diode. Problems Atomic Sci. Technol. (6), pp. 176–178 (2010)
63. Lazurik, V.M., Lazurik, V.T., Popov, G., Zimek, Z.: Two-parametric model of electron beam in computational dosimetry for radiation processing. Radiat. Phys. Chem. **124**, 230–234 (2016)
64. Tseluyko, A.F., et al.: Influence of plasma nucleus form on radiation orientation in high-current pulse plasma diode. Prob. Atomic Sci. Technol. (6), pp. 176–178 (2010)
65. Kaluska, I., Lazurik, V.T., Lazurik, V.M., Popov, G., Yu., Rogov, Zimek, Z.: The features of electron dose distributions in circular objects: comparison of Monte Carlo calculation predictions with dosimetry. Radiat. Phys. Chem. **76**(11–12), 1815–1819 (2007). https://doi.org/10.1016/j.radphyschem.2007.03.018
66. Grudskii, M.Y., Roldugin, N.N., Smirnov, V.V., Adadurov A.F., Lazurik V.T.: Experimental investigation and Monte Carlo calculation of photon-induced electron emission from solids. A, **227**(1), 126–134 (1984). https://doi.org/10.1016/0168-9002(84)90110-4
67. Handbook on Mathematical Functions with Formulas, Graphs and Mathematical Tables. Edited by Milton Abramovich and Irene Stegun, National Bureau of Standards, Applied Mathmatic Series, 55, p. 1046. Washington (1964)
68. Bronshtein, I.N., Semendyayev, K.A., Musiol, G., Meuhlig, H.: Handbook of Mathematics. 5th Edition, p. 1164. Springer (2007)
69. Melnyk, I., Tuhai, S., Surzhykov, M., Shved, I.: Discrete vehicle automation algorithm based on the theory of finite state machine. In: Klymash, M., Luntovskyy, A., Beshley, M., Melnyk, I., Schill, A.: Editors. Emerging Networking in the Digital Transformation Age. TCSET 2022. Lecture Notes in Electrical Engineering, vol. 965, pp. 231-245. Springer. Cham (2023). https://doi.org/10.1007/978-3-031-24963-1_13. https://link.springer.com/chapter/
70. Melnyk, I., Luntovskyy A.: Estimation of energy efficiency and quality of service in cloud realizations of parallel computing algorithms for IBN. future intent-based networking. In: Klymash, M., Beshley, M., Luntovskyy, A., (eds.) On the QoS Robust and Energy Efficient Heterogeneous Software Defined Networks. Lecture Notes in Electrical Engineering, vol. 831, Chapter 20,pp. 339–379 (2022). ISBN 978–3–030–92433–1, https://doi.org/10.1007/978-3-030-92435-5_20, https://link.springer.com/chapter/

71. Melnyk, I., Luntovskyy, A.: Networked simulation with compact visualization of complex graphics and interpolation results. In: Klymash, M., Luntovskyy, A., Beshley, M., Melnyk, I., Schill, A., (eds.) Emerging Networking in the Digital Transformation Age. TCSET 2022. Lecture Notes in Electrical Engineering, vol. 965, pp. 175–196. Springer, Cham (2023). https://doi.org/10.1007/978-3-031-24963-1_10, https://link.springer.com/chapter/
72. Melnyk, I., Tuhai, S., Skrypka, M., Shved, I.: Fuzzy logic models for technological and communication electronic control systems. In: Klymash, M., Luntovskyy, A., Beshley, M., Melnyk, I., Schill, A.: Editors. Lecture Notes in Electrical Engineering 1198, Digital Ecosystems: Interconnecting Advanced Networks with AI Applications, pp. 337 – 363. Springer (2024). ISBN 978–3–031–61220–6. https://doi.org/10.1007/978-3-031-61221-3_17; https://link.springer.com/book/https://link.springer.com/book/
73. Melnyk, I., Tuhai, S., Skrypka, M., Pochynok, A.: Membership root-polynomial functions. In: Klymash, M., Luntovskyy, A., Beshley, M., Melnyk, I., Schill, A (eds.) Lecture Notes in Electrical Engineering 1198, Digital Ecosystems: Interconnecting Advanced Networks with AI Applications, pp. 364–390. Springer (2024). ISBN 978–3–031–61220–6. https://doi.org/10.1007/978-3-031-61221-3 https://link.springer.com/chapter/
74. Zadeh, L.A, Aliev, R.A.: Fuzzy Logic Theory and Applications: Part I and Part II. WSPC, p. 610 (2018)
75. Belohlavek, R., Dauben, J.W., Klir, G.J.: Fuzzy Logic and Mathematics: A Historical Perspective 1st Edition, p. 544. Oxford University Press (2017)
76. Trillas, E., Eciolaza, L.: Fuzzy Logic: An Introductory Course for Engineering Students, p. 204. Springer (2015)
77. Mendel, J.M., Hagras, H., Tan, W.W., Melek, W.W., Ying, H.: Introduction to Type-2 Fuzzy Logic Control: Theory and Applications, p. 256. John Wiley & Sons (2014). https://ieeexplore.ieee.org/book/6852062
78. Klir, G.J., Yuan, B.: Fuzzy Sets and Fuzzy Logic: Theory and Applications. 1st Edition. Pearson College Div, p. 592 (1995)
79. Nguyen, H.T., Walker, E.A.: A First Course in Fuzzy Logic (Textbooks in Mathematics). 3rd Edition. Chapman and Hall/CRC, p. 440 (2005)
80. Zadeh, L.A.: Fuzzy Sets. Inf. Control **8**, 338–353 (1965)
81. Mamdani, E.H.: Application of fuzzy algorithms for control of simple dynamic plant. In: Proceedings of the Institution of Electrical Engineers, vol. 121, no. 12, pp. 1585–1588 (1974)
82. https://mall.industry.siemens.com/mall/en/WW/Catalog/Products/10205320?tree=CatalogTree
83. https://doc.tipa.eu/datasheet/07730090-datasheet-en.pdf
84. Monks, J.G.: Operations Management: Theory and Problems (MCGRAW HILL Series in Management), p.800. Subsequent Edition. Subsequent Edition (1998)
85. Holweg, M., Davies, J., de Meyer, A., Lawson, B., Schmenner, R.W.: Process Theory: The Principles of Operations Management, p. 254. Oxford University Press (2018)
86. Mahadevan, B.: Operation Management: Theory and Practice. Pearson Education India, p. 612 (2009)

Dynamic of Ring- Stiffened Conical Thin-Walled Structure Interacting with Supersonic Flow

Maryna Chernobryvko[1] and Konstantin Avramov[1,2,3](✉)

[1] Anatolii Pidhornyi Institute of Power Machines and Systems of National Academy of Science of Ukraine, St. Komunalnykiv 2/10, Kharkiv 61046, Ukraine
kvavramov@gmail.com

[2] Department of Aircraft Strength, National Aerospace University N.Ye. Zhukovsky "KhAI", St. Chkalov 17, Kharkiv 61070, Ukraine

[3] Department of Technical Systems, Kharkiv National University of Radio Electronics, Kharkov, Ukraine

Abstract. Dynamical behavior of conical thin-walled structure with rings is analyzed semi-analytically. Kirchhoff- Love theory of shell is used to simulate the conical thin-walled structure. The beam theory of Euler-Bernoulli is applied to simulate rings flexural-flexural-torsional-longitudinal oscillations. Rayleigh- Ritz technique is used to study thin-walled structure linear vibrations. The dynamical instability of the structure is simulated by ordinary differential equations, which are obtained by the assumed-mode method.

In order to analyze the dynamic instability, the eigenvalue problem is used to obtain characteristic exponents. From these characteristic exponents, the critical frequency of flutter is obtained.

Keywords: thin-walled structure · Kirchhoff- Love theory of shell · Euler-Bernoulli beam theory · critical eigenfrequency

1 Introduction

The thin-walled fairing is protected pay-loads when ones are carried into orbit. Mostly, this thin-walled structure is conical shell. Significant aerodynamic loads act on firing during launch vehicle operation. Therefore, rings are used to reinforce the thin-walled fairings. Interactions of the shell with gas flow leads to structure instability and flutter. These nonlinear phenomena lead to pay-load fracture. These phenomena are very dangerous and must be analyzed.

Therefore, many efforts were made to study properties of dynamical instability and supersonic flutter. Ritz method [1] is applied to study conical shell free oscillations. Conical shell and angular plate are parts of thin-walled structure [2]. The dynamic of this structure is studied by transfer matrix method. The forced oscillations of conical thin-walled structure are studied in [3] by Hamiltonian's principle. Irie et al. used transfer matrix method to study conical thin-walled structure dynamics [4]. Rayleigh- Ritz

H. Altenbach et al. (Eds.): CAMPE 2025, LNME, pp. 160–168, 2026.
https://doi.org/10.1007/978-3-032-16381-3_15

approach is applied to analyze the linear oscillations of conical panel [5]. Composite doubly curved shell is considered in [6].

Dynamics of cylindrical shell with reinforcements are considered in [7] by applying Fourier series. Rings and stringers are used to reinforce conical shell in [8]. Smeared technique is applied to obtain the equations of stiffened functionally graded cylindrical thin-walled structure in [9]. Oscillations of conical thin-walled structure with rings and stringers reinforcements are analyzed numerically in [10].

2 Problem Formulation

Dynamics of launch vehicle fairing is analyzed. The fairing is conical thin-walled structure with rings reinforcement. This structure interacts with supersonic gas flow. Structure dynamic instability occurs due to gas/ structure interactions, which leads to flutter of the structure. Such phenomenon is very dangerous. The dynamical instability of the structure is the subject of this article. Isotropic conical thin-walled structure with geometrical parameters, which are shown on Fig. 1a, are considered. The thickness of the structure h is constant. The bottom edge of the structure is clamped.

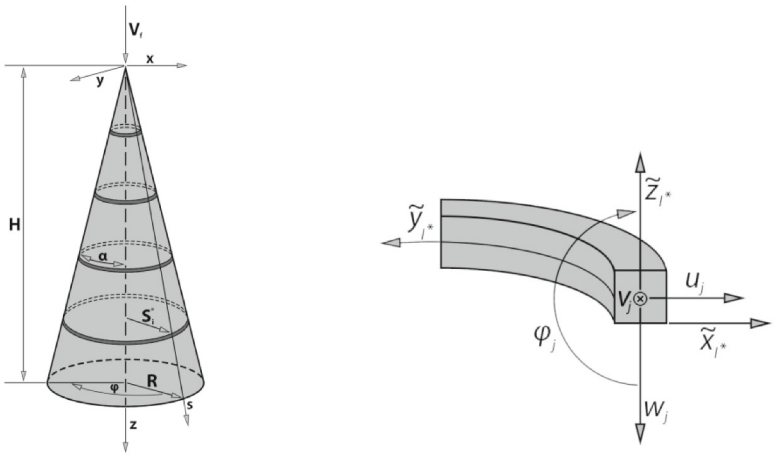

a. b.

Fig. 1. a. thin-walled structure; b. ring

N rings reinforcement is applied inside the thin-walled structure. The rings are located at the same distance between each other in cone longitudinal direction. All rings are identical. The rings perform vibrations jointly with the conical structure. The rings perform bending vibrations in two perpendicular surfaces, torsional and longitudinal oscillations. The middle surface of the cone describes by two coordinate s and ϕ. The radiuses of the curvatures are the following: $R_s = \infty$, $R_\phi = \frac{R}{\cos\alpha} - \left(\frac{H}{\cos\alpha} - s\right)\tan\alpha$,

where $0 < R_\phi \le \frac{R}{\cos\alpha}$. The shell structure is studied in the coordinates system (s, ϕ, ξ). Axis ξ is normal to the middle surface. The longitudinal coordinates of the rings are $s_l^*;\ l = 1, ..., N$; $s_l^* = \frac{l\,H}{(N+1)\cos\alpha}$. The shell response satisfies Kirchhoff- Love theory [11]. The material of the beam is isotropic and elastic. Thus, the Hooke's law is satisfied. The coordinate axes (s, ϕ, ξ) is used for displacements projections $u(s, \phi, t)$, $v(s, \phi, t)$, $w(s, \phi, t)$.

The ordinary differential equations are derived to study the shell structure. These differential equations are obtained from assumed-mode method [11].

The strain energy of the structure has the form:

$$\Pi = \Pi_1 + \sum_{i=1}^{N} \Pi_2^{(i)} \tag{1}$$

where Π_1 is conical shell potential energy; $\Pi_2^{(l)}; l = 1, ..., N$ are rings potential energy. The strain energy of the conical thin-walled structure is

$$\Pi_1 = \frac{1}{2}\int\limits_{-\frac{h}{2}}^{\frac{h}{2}}\int\limits_{0}^{2\pi}\int\limits_{0+}^{L}(\sigma_{11}\varepsilon_{11} + \sigma_{22}\varepsilon_{22} + \sigma_{12}\varepsilon_{12})\left[R - \left(\frac{H}{\cos\alpha} - s\right)\sin\alpha\right] ds\, d\phi\, d\xi\,, \tag{2}$$

where $L = \frac{H}{\cos\alpha}$ is generatrix line; h is thickness of the structure skin.

The thin-walled structure displacements and strain tensor elements satisfies the equations:

$$\begin{aligned}
&\varepsilon_{11} = \frac{\partial u}{\partial s} - \xi\frac{\partial^2 w}{\partial s^2},\ \varepsilon_{12} = \frac{\partial v}{\partial s} - \frac{v}{s} + \frac{\partial u}{\partial \varphi}\frac{1}{s\tan\alpha} + 2\xi\left(\frac{1}{s\tan\alpha}\left[\frac{\partial^2 w}{\partial s\partial\varphi} - \frac{\partial w}{s\partial\varphi} + \frac{\partial v}{\partial s} - \frac{v}{s}\right]\right),\\
&\varepsilon_{22} = \frac{1}{s\tan\alpha}\left(\frac{\partial v}{\partial\varphi} + u\cdot\tan\alpha + w\right) + \zeta\left(\frac{1}{s^2\tan^2\alpha}\left[\frac{\partial v}{\partial\varphi} - \frac{\partial^2 w}{\partial\varphi^2}\right] - \frac{\partial w}{s\partial s}\right)
\end{aligned} \tag{3}$$

The strain energy of the skin has the form:

$$\begin{aligned}
&\Pi_1 = \frac{Eh}{2(1-\nu^2)}\int_0^{2\pi}\int_{0+}^{L}\left[(E_1+E_2)^2 - 2(1-\nu)\left(E_1E_2 - \frac{1}{4}\Omega^2\right)\right]\left\{R - \left(\frac{H}{\cos\alpha} - s\right)\sin\alpha\right\} ds\, d\varphi\\
&+\frac{Eh^3}{24(1-\nu^2)}\int_0^{2\pi}\int_{0+}^{L}\left[(K_1+K_2)^2 - 2(1-\nu)\left(K_1K_2 - \Omega^2\right)\right]\left\{R - \left(\frac{H}{\cos\alpha} - s\right)\sin\alpha\right\} ds\, d\varphi,\\
&E_1 = \frac{\partial u}{\partial s},\ E_2 = \frac{1}{s\tan\alpha}\left(\frac{\partial v}{\partial\varphi} + u\tan\alpha + w\right);\ K_2 = \left(\frac{1}{s^2\tan^2\alpha}\left[\frac{\partial v}{\partial\varphi} - \frac{\partial^2 w}{\partial\varphi^2}\right] - \frac{\partial w}{s\partial s}\right),\\
&\Omega_1 = \frac{\partial v}{\partial s} - \frac{v}{s} + \frac{\partial u}{\partial\varphi}\cdot\frac{1}{s\tan\alpha},\ \Omega_2 = \frac{1}{s\tan\alpha}\left[\frac{\partial^2 w}{\partial s\partial\varphi} - \frac{\partial w}{s\partial\varphi} + \frac{\partial v}{\partial s} - \frac{v}{s}\right],\ K_1 = -\frac{\partial^2 w}{\partial s}
\end{aligned} \tag{4}$$

where, ν is ratio of Poisson; E is modulus of Young.

The j th ring strain energy is considered. Figure 1b shows this ring. Rings are attached inside of the conical shell. The coordinate system of the j th ring is denoted by

$\left(\tilde{x}_j, \tilde{y}_j, \tilde{z}_j\right)$. The beam performs bending, displacements of which are denoted by $u_j(\tilde{y}_j, t)$ and $w_j(\tilde{y}_j, t)$. The ring tension and compression are denoted by $v_j(\tilde{y}_j, t)$ and $\phi_j(\tilde{y}_j, t)$ describes twist angle of torsion. Figure 1b shows all components of deformations. The generalized coordinates and strains satisfy the following equations [12]:

$$\varepsilon = \frac{\partial v_j}{\partial \tilde{y}_j} - \frac{w_j}{R_j}, \tau = \frac{\partial u_j}{R_j \partial \tilde{y}_j} - \frac{\partial \varphi_j}{\partial \tilde{y}_j}, \chi_1 = \frac{\partial^2 u_j}{\partial y_j^2} + \frac{\varphi_j}{R_j}, \chi_2 = \frac{\partial^2 w_j}{\partial \tilde{y}_j^2} + \frac{w_j}{R_j^2}, \tag{5}$$

where τ is twist; ε is hoop strain; χ_1, χ_2 are ring middle curve curvature.

The ring strain energy is:

$$\Pi_2^{(j)} = \frac{1}{2} \oint \left\{ E_j F_j \left(\frac{\partial v_j}{\partial \tilde{y}_j} - \frac{w_j}{R_j} \right)^2 + E_j J_{Z_j} \left(\frac{\partial^2 u_j}{\partial \tilde{y}_j^2} + \frac{\phi_j}{R_j} \right)^2 + \right.$$
$$\left. + E_j J_{X_j} \left(\frac{\partial^2 w_j}{\partial \tilde{y}_j^2} + \frac{w_j}{R_j^2} \right)^2 + G_j J_j \left(\frac{\partial u_j}{R_j \partial \tilde{y}_j} - \frac{\partial \phi_j}{\partial \tilde{y}_j} \right)^2 \right\} d\tilde{y}_j, \tag{6}$$

where F_j is cross section area; J_{Z_j}, J_{X_j}, J_j are cross section inertia moments.

Displacements compatibility of the rings and skin of the structure takes the form:

$$u_j(\tilde{y}_j, t) = u(s_j^*; \varphi, t) - \tilde{h}_j \varphi_1(s_j^*; \varphi, t),\ v_j(\tilde{V}_j, t) = -v(s_j^*, \varphi, t) - \tilde{h}_j \varphi_2(s_j^*, \varphi, t),$$
$$w_j(\tilde{v}_j, t) = -w(s_j^*, \varphi, t),\ \varphi_j(\tilde{V}_j, t) = \varphi_1(S_j^*, \varphi, t) \tag{7}$$

where $\tilde{h}_j = \tilde{H}_j + \frac{h}{2}$; $\tilde{H}_j$ are distances from the ring section center to shell inside surface. The relations (7) are substituted into (6) and the relations (4) are applied in (1). The structure strain energy is obtained in the suitable form.

The thin-walled structure kinetic energy is:

$$T = T_1 + \sum_{j=1}^{N} T_2^{(j)}, \tag{8}$$

where $T_2^{(j)}$ is j th ring kinetic energy; T_1 is kinetic energy of the skin. The skin kinetic energy is the following:

$$T_1 = \frac{\rho h}{2} \int_0^{2\pi} \int_{0^+}^{L} \left[\left(\frac{\partial u}{\partial t} \right)^2 + \left(\frac{\partial v}{\partial t} \right)^2 + \left(\frac{\partial w}{\partial t} \right)^2 \right] \left[R - \left(\frac{H}{\cos \alpha} - s \right) \sin \alpha \right] ds\, d\phi, \tag{9}$$

where ρ is thin-walled structure density. The j th ring kinetic energy has the form:

$$T_2^{(j)} = \frac{\rho_1 F_j}{2} \oint \left(\dot{u}_j^2 + \dot{v}_j^2 + \dot{w}_j^2 \right) d\,\tilde{y}_j + \frac{\rho_1 J_j}{2} \oint \dot{\phi}_j^2 d\,\tilde{y}_j, \tag{10}$$

where J_j is cross section inertia moments; ρ_1 is material density. If the relations (7) are substituted into (10), the ring kinetic energy is obtained in simple for analysis form.

The interactions of supersonic gas flow with shell structure are taken place. The gas/structure interactions are described by the piston theory. The piston theory takes the following form [13, 14]:

$$p = -\frac{\rho_f V_f^2}{\beta}\left[\frac{\partial w}{\partial s} + \frac{(M^2-2)}{V_f \beta^2}\frac{\partial w}{\partial t}\right], \tag{11}$$

where $\beta = \sqrt{M^2-1}$; ρ_f is gas density; M is Mach number.

3 Linear Dynamical System

The assumed-mode method [11] is used to derive dynamical system with finite-degrees-of-freedom, which describes the considered thin-walled structure. The shell displacements are represented as:

$$u(s,\varphi,t) = \sum_{n=1}^{N_u} q_n^{(u)}(t) U_n(s,\varphi);\ v(s,\varphi,t) = \sum_{n=1}^{N_v} q_n^{(v)} V_n(s,\varphi) : w(s,\varphi,t) = \sum_{n=1}^{N_w} q_n^{(w)} W_n(s,\varphi); \tag{12}$$

where $U_n(s,\phi)$, $V_n(s,\phi)$, $W_n(s,\phi)$ are structure eigenmodes.

In order to calculate the structure eigenmode, the Rayleigh-Ritz method is implemented [11]. The structure eigenmodes take the form:

$$\begin{aligned} U_n(s,\varphi) &= \sum_{l=1}^{N_1}\sum_{j=1}^{N_2} A_{lj}^{(n)} \psi_l^{(l)}(s)\cos j\varphi,\ V_n(s,\varphi) = \sum_{l=1}^{N_1}\sum_{j=1}^{N_2} B_{lj}^{(n)} \psi_l^{(v)}(s)\sin j\varphi\$, \\ W_n(s,\varphi) &= \sum_{l=1}^{N_1}\sum_{j=1}^{N_2} C_{ij}^{(n)} \psi_l^{(w)}(s)\cos j\varphi \end{aligned} \tag{13}$$

The unknown values $A_{lj}^{(n)}$, $B_{lj}^{(n)}$, $C_{lj}^{(n)}$ are obtained by using Rayleigh-Ritz technique.

The generalized force of the aerodynamic pressure can be presented in the following matrix form:

$$\mathbf{Q^{(w)}} = \mathbf{K^{(w)}}\mathbf{q^{(w)}} + \mathbf{C^{(w)}}\dot{\mathbf{q}}^{\mathbf{(w)}}, \tag{14}$$

where $\mathbf{K^{(w)}}$, $\mathbf{C^{(w)}}$ are matrices of aerodynamic stiffness and aerodynamic damping.

The truncated series (12) are used in the structure kinetic energy (8) and the structure potential energy (6). These energies take the following quadratic forms: $\Pi = \Pi\left(q_1, ..., q_{N_G}\right)$, $T = T\left(\dot{q}_1, ..., \dot{q}_{N_G}\right)$. Then the structure motions matrix equations are represented as

$$\begin{aligned} &\mathbf{M}_{11}\ddot{q}^{(n)} + \mathbf{K}_{11}q^{(n)} + \mathbf{K}_{12}q^{(r)} + \mathbf{K}_{13}q^{(w)} = 0;\ \mathbf{M}_{22}\ddot{q}^{(v)} + \mathbf{K}_{21}q^{(n)} + \mathbf{K}_{22}q^{(v)} + \mathbf{K}_{23}q^{(w)} = 0; \\ &\mathbf{M}_{33}\ddot{q}^{(w)} + \mathbf{K}_{31}q^{(n)} + \mathbf{K}_{32}q^{(v)} + \mathbf{K}_{33}q^{(w)} + \mathbf{K}^{(w)}q^{(w)} + \mathbf{C}^{(w)}\dot{q}^{(w)} = 0. \end{aligned} \tag{15}$$

The eigenfrequencies of torsional and longitudinal vibrations are considerably higher, than the flexural oscillations eigenfrequencies. Therefore, the terms

$\mathbf{M_{11}}\ddot{\mathbf{q}}^{(\mathbf{u})}$,$\mathbf{M_{22}}\ddot{\mathbf{q}}^{(\mathbf{v})}$ can be removed from the analysis. Then the first two matrices equations of the system (15) take the following matrix form:

$$\mathbf{q}^{(\mathbf{u})} = \mathbf{K}_{\mathbf{u},\mathbf{w}}\,\mathbf{q}^{(\mathbf{w})}\,;\ \mathbf{q}^{(\mathbf{v})} = \mathbf{K}_{\mathbf{v},\mathbf{w}}\,\mathbf{q}^{(\mathbf{w})}\,. \tag{16}$$

The matrices relations (16) are used in the third matrix differential Eq. (15). Thus, the following ordinary differential equations matrix system is derived as:

$$\mathbf{M_{33}}\ \ddot{\mathbf{q}}^{(\mathbf{w})} + \mathbf{K}_{*}\,\mathbf{q}^{(\mathbf{w})} + \tilde{\mathbf{C}}^{(\mathbf{w})}\dot{\mathbf{q}}^{(\mathbf{w})} = 0\,. \tag{17}$$

The dynamical system trivial equilibrium (17) instability is analyzed in the phase variables $\mathbf{y} = \left(q_1^{(w)}, ..., q_{N_w}^{(w)}, \dot{q}_1^{(w)}, ..., \dot{q}_{N_w}^{(w)}\right)$ are used. Then the dynamical system (17) is rewritten in the following form:

$$\dot{\mathbf{y}} = \mathbf{G}\mathbf{y}. \tag{18}$$

The linear dynamical system (18) has the solution in the following form: $\mathbf{y} = \mathbf{A_l}\exp(\lambda_l\, t)$, $l = 1, ..., 2N_w$, where $\mathbf{A_i}$ is vector; λ_l are characteristic exponents. These values are obtained from the eigenvalue problem. These characteristic exponents are represented as [15, 16]: $\lambda_{2j-1} = \alpha_j + i\Omega_j\,;\ \lambda_{2j} = \alpha_j - i\Omega_j\,;\ j = 1, ..., N_w$. If $\alpha_j < 0\,; j = 1, ..., N_w$, the trivial equilibrium is stable. If $\lambda_{1,2} = \pm i\,\Omega_1$, the Hopf bifurcation is observed.

4 Numerical Study of Linear Oscillations

The thin-walled structure (Fig. 1) has thickness $h = 2 \cdot 10^{-3}\ m$; radius of the base $R = 1.95\ \boldsymbol{m}$; $H = 5.24$ m. The structure materials characteristics are: $E = 72 \cdot 10^9\ Pa$; $\rho = 2770$ kg/m^3, $\nu = 0.3$. Two thin-walled structures (conical shell without rings; conical shell with five rings) are considered. The areas of the sections of the rings are $F_j = 5.7 \cdot 10^{-4}\ m^2$. The distance between rings and structure edges are the same. The distances between the rings of thin walled structure with five rings are $d_5 = 0.932\ \boldsymbol{m}$.

The eigenfrequencies of shell structures are obtained by The Rayleigh-Ritz method. The eigenfrequencies, which are calculated by the Rayleigh- Ritz technique, are presented in Table 1. The data of ANSYS calculations are shown in Table 1. These calculations are performed to verify the data, which are gotten by the Rayleigh-Ritz technique.

The numerical analysis of the critical frequencies of flutter is carried out with $N_u = N_v = N_w$ of the truncated series (12). The dynamical system (17) with 9, 12, 15, 18, 21 degrees-of-freedom is analyzed in order to perform converge analysis of critical frequency. The critical frequencies of the shell with three, five, seven ribs are published in Table 2. The unstable trivial equilibrium is taken place in the Mach number range $M \in [1; 1.414]$.

Table 1. Eigenfrequencies (in Hz) of thin-walled structure

The structure without rings						
The numbers of frequencies	1	2	3	4	5	6
Frequencies obtained by RRM	27.088	27.465	27.973	28.671	30.474	31.230
Frequencies obtained by FEM	27.1	27.5	28.0	28.7	30.8	31.5
Relative error, %	0.04	0.13	0.1	0.1	1.07	0.86
The structure with five rings						
The number of frequency	1	2	3	4	5	6
Frequencies obtained by RRM	69.674	75.105	77.557	85.804	86.024	86.306
Frequencies obtained by FEM	69.5	75.0	77.8	85.9	86.2	86.4
Relative error, %	0.25	0.14	0.31	0.11	0.2	0.11

Table 2. The critical frequencies Ω_1 of the flutter

N_w	9	12	15	18
The structure without rings	63.180	57.113	56.657	56.392
The structure with 3 rings	65.623	58.938	60.007	60.319
The structure with 5 rings	57.841	60.113	60.532	61.096
The structure with 7 rings	58.256	60.147	60.734	61.045

5 Conclusions

Numerical analysis of oscillations conical thin-walled structures with reinforced rings shows, that the reinforcement leads to essentially eigenfrequencies increase. Moreover, the first three eigenfrequencies are not changed essentially, if the ribs numbers are

increased from five to seven. When rings numbers are changed from three to five, the eigenmode nodes numbers are not changed along the circumferential coordinate.

As follows from converge analysis of conical thin-walled structure/ gas stream interactions, the mechanical model with $9 \div 21$ degrees of freedom gives closed results for critical Mach numbers. But, the convergence of critical eigenfrequency of flutter is observed in 15 degrees of freedom model.

Acknowledgment. This study was particularly funded by National Research Foundation of Ukraine (grant number 2023.04/0001).

References

1. Zhao, X., Li, Q., Liew, K.M., Ng, T.Y.: The element-free kp-Ritz method for free vibration analysis of conical shell panels. J. Sound Vib. **295**, 906–922 (2006). https://doi.org/10.1016/j.jsv.2006.01.045
2. Liang, S., Chen, H.L.: The natural vibration of a conical shell with an annular end plate. J. Sound Vib. **294**, 927–943 (2006). https://doi.org/10.1016/j.jsv.2005.12.033
3. Li, F.-M., Kishimoto, K., Huang, W.-H.: The calculations of natural frequencies and forced vibration responses of conical shell using the Rayleigh-Ritz method. Mech. Res. Commun. **36**, 595–602 (2009). https://doi.org/10.1016/j.mechrescom.2009.02.003
4. Irie, T., Yamada, G., Kaneko, Y.: Free vibration of a conical shell with variable thickness. J. Sound Vib. **82**, 83–94 (1982). https://doi.org/10.1016/0022-460X(82)90544-2
5. Lim, C.W., Kitipornchai, S.: Effects of subtended and vertex angles on the free vibration of open conical shell panels: a conical co-ordinate approach. J. Sound Vib. **219**, 813–835 (1999). https://doi.org/10.1006/jsvi.1998.1890
6. Lim, CW., Liew, K.M.: Vibration of cantilevered laminated composite shallow conical shells. Int. J. Solids Struct. **35**, 1695–1707 (1998). https://doi.org/10.1016/S0020-7683(97)00157-1
7. Stanley, A.J., Ganesan, N.: Free vibration characteristics of stiffened cylindrical shells. Comput. Struct. **65**, 33–45 (1997). https://doi.org/10.1016/S0045-7949(96)00115-0
8. Srinivasan, R.S., Krishnan, P.A.: Dynamic analysis of stiffened conical shell panels. Comput. Struct. **33**, 831–837 (1989). https://doi.org/10.1016/0045-7949(89)90257-5
9. Bich, D.H., Dung, D.V., Nam, V.H.: Nonlinear dynamical analysis of eccentrically stiffened functionally graded cylindrical panels. Compos. Struct. **94**, 2465–2473 (2012). https://doi.org/10.1016/j.compstruct.2012.03.012
10. Rao, S.S., Reddy, E.S.: Optimum design of stiffened conical shell with natural frequency constraints. Comput. Struct. **14**, 103–110 (1981). https://doi.org/10.1016/0045-7949(81)90089-4
11. Amabili, M.: Nonlinear Vibrations and Stability of Shells and Plates. Cambridge University Press, Cambridge (2008). https://doi.org/10.1017/CBO9780511619694
12. Vlasov, V.Z.: Thin-Walled Elastic Beams. Oldbourne Press, London (1961)
13. Krumharr, H.: The accuracy of linear piston theory when applied to cylindrical shells. AIAA J. **1**, 1448–1449 (1963). https://doi.org/10.2514/3.1832
14. Bolotin, V.V.: Nonconservative Problems of the Theory of Elastic Stability. Pergamon, London (1963)

15. Avramov, K., Strel'nikova, E., Pierre, C.: Resonant many-mode periodic and chaotic self-sustained aeroelastic vibrations of cantilever plates with geometrical non-linearities in incompressible flow. Nonlin. Dyn. **70**, 1335–1354 (2012). https://doi.org/10.1007/s11071-012-0537-5
16. Uspensky, B., Avramov, K., Liubarskyi, B., Andrieiev, Y., Nikonov, O.: Nonlinear torsional vibrations of electromechanical coupling of diesel engine gear system and electric generator. J. Sound Vib. **460**, 114877 (2019). https://doi.org/10.1016/j.jsv.2019.114877

Creep-Damage Modeling of Turbine Blades with Consideration of Wear and Stress Corrosion Cracking

Holm Altenbach[1], Dmytro Breslavsky[2(✉)], Andrii Khoroshun[2], Alyona Senko[2], and Oksana Tatarinova[2]

[1] Otto-Von-Guericke-Universität Magdeburg, Magdeburg, Germany
[2] National Technical University "Kharkiv Polytechnic Institute", Kharkiv, Ukraine
Dmytro.Breslavsky@khpi.edu.ua

Abstract. An approach for the analysis of high-temperature creep and damage accumulation in turbomachine blades, taking into account wear of the part of surface due to contacts with the casing and stress corrosion cracking is proposed. The calculation method and algorithms built on the basis of the proposed approach and the Finite Element Method are described. An updated form of evolution equations is proposed for assessing damage accumulation due to the action of creep and corrosion mechanisms. In the considered example of numerical analysis, the results of modeling the cases of purely static loading, consideration the effects of interaction with the casing surface and corrosion of parts of the blade with a destroyed coating are analyzed. It is emphasized that these factors have a significant influence on the total time before the emergence of the macroscopic defect and its intensive development. The developed approach and calculation method can be further applied to the numerical analysis of real blade models.

Keywords: Creep · Damage · Wear · Stress Corrosion Cracking · Fracture · Blade

1 Introduction and Literature Review

The problems of ensuring the long-term strength of turbomachine blades operating at high temperatures remain relevant and attract the attention of researchers and engineers. The requirements for the operating conditions of these structural elements are constantly changing in the direction of increasing temperatures and loads. Calculation methods for assessing the influence of such factors, including taking into account their cyclicity, have been fruitfully developed recently [1–3].

The real operating conditions of blades in turbines and gas turbine engines at high temperatures are characterized by additional influences of external objects and influences, among which we will highlight two. The first is the influence of an external aggressive environment, which leads to surface corrosion [4]. The second is the interaction of the upper parts of the blades with other structural elements, for example, the

H. Altenbach et al. (Eds.): CAMPE 2025, LNME, pp. 169–178, 2026.
https://doi.org/10.1007/978-3-032-16381-3_16

casing, in which surface fretting wear occurs [5, 6]. Such influences, additional to the high-temperature creep of the material, both by themselves and due to the synergy of action, can significantly limit the resource of the blades [4, 6, 7].

It is emphasized in [8] that fretting wear negatively affects the fatigue life of turbine blades. The authors experimentally analyzed the wear of surfaces of nickel superalloys. It is noted that even for a polished surface under conditions of increased load, cracks, delamination and peeling of materials occur; the wear mechanism changes from severe oxidative wear to fatigue wear.

Due to the difficulty and cost of conducting experimental studies, computational approaches to the analysis of the influence of the above factors on the deformation and strength of turbomachinery elements have been developed recently. Thus, in [9], a Finite Element (FE) model of the creep wear process of the turbine blade root made of Inconel 718 alloy is presented, taking into account the redistribution of energy, material properties, geometry and non-uniform temperature field. It is noted in [10] that turbine blades during creep are constantly exposed to various forms of damage and destruction, including hot corrosion, oxidation, erosion, fatigue, damage by external objects and cracking. The authors used the Finite Element Method in the ABAQUS software to conduct a numerical analysis of the first-row turbine blade of the C20–250 engine, including its heat-shielding coatings. Also, it is important to consider the cyclicity of loading. The effect of creep on nonlinear vibrations of frictionally connected blades was numerically investigated in [11]. The time-dependent creep behavior under centrifugal load and high temperatures is determined, and for different values of the holding time, the deformed configuration and conditions in the contact surfaces are determined. Then, an analysis of nonlinear blade vibrations is performed. The aim of [12] was to determine the region of a gas turbine blade that is most susceptible to failure due to various wear mechanisms. A methodology using numerical analysis by the Finite Element Method for modeling the creep of turbine blades is proposed in [13]. A review of possible damage to blade surfaces and methods for their analysis can be found in [4].

An important factor limiting the resource of turbine and gas turbine engines blades is the corrosion of their surfaces and subsequent corrosion cracking [4, 7]. The results of experimental analysis of spent nickel alloy blades indicate [14] that their surfaces show signs of corrosion and erosion. A large number of cracks were found in different parts of the blades due to operation at high temperatures and stresses for a long period of time. An intergranular crack was found on the coating of the destroyed blade; there were some microvoids on the fracture surface, which caused the mechanism of fracture due to creep. Also, as in the case of surface wear analysis, recently there have been results of studies devoted to the computational assessment of the joint development of such processes, but the consideration in numerical analysis the material creep is practically absent. The cause of corrosion at the tip of an internally cooled blade of a high-pressure turbine of a turbofan engine is analyzed in [15]. The FEM analysis was used to determine the temperature and pressure distribution. It was shown that the pressure distribution at the blade tip could cause erosion in this area in the presence of impurities in the inlet air and that high temperatures also caused a phase transformation, which increased the presence of corrosion and led to the formation of cracks in the blade. The authors of [16] noted that in practice, two adjacent blades of a condensing industrial turbine rotor had

failed. The computational analysis was performed using the Finite Element Method. It was concluded that the blade destroyed due to corrosion fatigue.

The aim of this paper is to present an approach and method for comprehensive assessment of long-term high-temperature behaviour of turbomachine blades, taking into account creep processes, associated hidden damage accumulation, possible wear fracture due to the interaction of the blade tip with the casing and subsequent corrosion cracking. To demonstrate the capabilities of the method, a simplified model of the blade was used, but a real alloy used in Ukrainian turbomachinery was used as its material.

2 Problem Statement and Constitutive Equations

Let us consider the mathematical formulation of the problem, which describes the approach to its solution. It is based on the statement about the possibility of a comprehensive assessment in a structural element the creep and damage caused by it, also taking into account damage to other types, primarily caused by the action of an external aggressive environment, as well as the influence of impacts by contacts with turbine casing, which is called as fretting wear in some approaches [6].

In this research, we will limit ourselves to considering a two-dimensional formulation of the problem in the form of a plane stress state, which will allow us to clearly demonstrate the obtained distributions of unknowns, primarily of the damage parameter [1]. Considering that the planned goal of the investigations is the computational analysis of the model of a turbomachine blade, the distribution of bending stresses caused by the action of pressure on the blade will also be taken into account. Let us consider the two-dimensional object V. We use Cartesian coordinate system $\mathbf{x} = (x_1,x_2)$. Within the framework of the Lagrangian approach, the stress-strain state will be described by a displacement vector $\mathbf{u}$ with components u_i, stress $\boldsymbol{\sigma}$ ($\sigma_{ij} = \sigma_{ji}$) and strain tensors $\boldsymbol{\varepsilon}$ ($\varepsilon_{ij} = \varepsilon_{ji}$), ($i,j = 1,2$), which are the functions of coordinates $\mathbf{x}$ and time t. Creep strains are presented by tensor $\boldsymbol{\varepsilon}^{\mathbf{c}}$ with components $\varepsilon_{ij}^{\mathrm{c}}$, as well as elastic strains by tensor $\boldsymbol{\varepsilon}^{\mathbf{e}}$ with components $\varepsilon_{ij}^{\mathrm{e}}$. The hypothesis of the strain additivity will be used. The tensor connection for creep strain with the stress tensor and time will be determined by the adopted constitutive equations. The considered solid V can be subjected to volume forces $\mathbf{f}(\mathbf{x},t)$, which are centrifugal in this approach. Tractions $\mathbf{p}(\mathbf{x},t)$ may act on part of the object surface S_1, known displacements $\overline{u}_i$ are given on the other part S_2.

Under the assumptions formulated above, the mathematical formulation of the boundary – initial value problem of deformation of solid in time can be represented by a system of Eqs. (1) with boundary and initial conditions (2)-(4) [1, 3]:

$$\sigma_{ij,j} = f(\mathrm{x}, t),\ \varepsilon_{ij} = \frac{1}{2}\left(u_{i,j} + u_{j,i} + u_{k,i}u_{k,j}\right),\ \varepsilon_{ij} = \varepsilon_{ij}^{\mathrm{e}} + \varepsilon_{ij},\ \sigma_{ij} = D_{ijkl}(\varepsilon_{kl} - \varepsilon_{kl}^{\mathrm{c}}),\ x_i \in V; \tag{1}$$

$$\sigma_{ij}n_j = p_i(\boldsymbol{x}, t),\ x_i \in S_1;\ u_i| = \overline{u}_i\, x_i \in S_2, \tag{2}$$

$$\varepsilon_{ij}^{\mathrm{c}}(\boldsymbol{x}, 0) = 0,\ \sigma_{ij}(\boldsymbol{x}, 0) = \sigma_{ij}^{\mathrm{2D}}(\boldsymbol{x}, 0) + \sigma_{ij}^{\mathrm{bend}}(\boldsymbol{x}, 0). \tag{3}$$

$$\sigma_{ij}(\boldsymbol{x}, t^{\mathrm{ext}}) = \sigma_{ij}^{\mathrm{c}}(\boldsymbol{x}, t^{\mathrm{ext}}) + \sigma_{ij}^{\mathrm{ic}}(\boldsymbol{x}, t^{\mathrm{ext}}),\ x_i \in V_{\mathrm{ic}}; \tag{4}$$

Here **n** is the vector of the unit normal to the solid's boundary, its components are n_i, D_{ijkl} are the components of the tensor **D** of the material elastic properties, $i, j, k, l = 1,2$. The initial conditions (3) for the creep problem, which are determined by the action of forces in the plane of the solid V, are supplemented by conditions for the added bending stresses $\boldsymbol{\sigma}^{\text{bend}}$. Also, in this formulation, it is assumed that when the current length of the upper edge of the blade model reaches a given value, starting from the moment t^{ext} in the general stressed state in the V_{ic} region, the stresses $\boldsymbol{\sigma}^{\text{ic}}$, caused by the contact impact interaction with another surface (in this case, with the turbine casing), begin to be considered jointly with current stress state $\boldsymbol{\sigma}^{\text{c}}$. The *LS Dyna* software [17] was used to determine the stresses $\boldsymbol{\sigma}^{\text{ic}}$.

We will use the creep theory with the hardening law in the modeling, which allows us to consider processes with additional loading [1]. The equation of state, accompanied by the evolution equations for the scalar damage parameter ω, to describe the creep process together with other degradation phenomena, are presented as follows:

$$\dot{\varepsilon}_{ij}^{\text{c}}\left(\varepsilon_{\text{vM}}^{\text{c}}\right)^{\alpha} = \frac{3}{2}B\frac{\left(\sigma_{\text{vM}}\right)^{n-1}}{(1-\omega)^{k}}s_{ij},\ \dot{\omega}^{\text{c}} = D\frac{\left(\sigma_{eq}\right)^{m}}{(1-\omega)^{l}},\ x_i \in V;$$
$$\dot{\omega}^{\text{scc}} = C\left(t^{\text{scc}}\right)^{s},\ \omega^{\text{scc}}(\boldsymbol{x}, t^{\text{scc}}) = 0,\ t^{\text{scc}} = t - t_{*} \tag{5}$$
$$\mathrm{d}\omega = \mathrm{d}\omega^{\text{c}} + \mathrm{d}\omega^{\text{scc}},\ \omega(\boldsymbol{x}, 0) = 0,\ \omega(\boldsymbol{x}, t_{*}) = \omega_{*}.$$

The following notations are adopted here: **s** is the deviator of the stress tensor with components s_{ij}; σ_{vM},ε_{vM}: are von Mises equivalent stress and strain; σ_{eq} is the equivalent stress, the expression of which is formulated using the high-temperature strength criterion obtained for a given material; ω is a scalar parameter that describes the total accumulation of damage; ω^{c} is a scalar parameter that describes damage accumulation caused by the creep process; ω^{scc} is a scalar parameter that describes the accumulation of damage due to the stress corrosion cracking; t_* is the value of time in which the process of hidden damage accumulation finishes; ω_* is a critical value of the damage parameter, upon reaching which at a point of the body at time t_*, the process of hidden damage accumulation finishes and the seed of a macroscopic defect appears; *B, D, n, k, m, l*, α are the constants that describe creep and the resulting damage accumulation, *C, s* are the constants describing the corrosion cracking process in the region V_{scc} adjacent to the surface S_{scc}, which arose as a result of the destruction of the surface layer; t^{scc} is the variable describing the time of corrosion cracking. We assume that the blade is covered with a protective coating that does not allow the corrosion process to develop, and it begins in the main material only after the destruction of a certain part of the blade during its interaction with the casing.

As it was emphasized, the impact interaction of the blade tip with the inner surface of the casing begins only after its length reaches a certain value. Starting from this moment, cyclic loading of the blade occurs. The number of cycles of such loading is determined by the turbine rotation frequency ϖ and can be large. Direct solution of the problem taking into account the load on each cycle is associated with great computational difficulties. In this regard, to obtain an effective method for solving the problem, as in [3] we apply methods of many time scales and averaging over the cycle period.

Let us suppose that the contact interaction occurs for a certain part of the rotation cycle period $T_r = \frac{2\pi}{\varpi}$ during the time interval $t_f - t_b$ (Fig. 1), which may be possible due to the oscillating motion of the rotor. Corrosion damage is not yet presented.

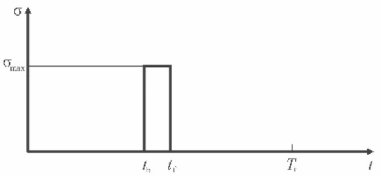

Fig. 1. Schematic representation of the process of cyclic loading

Let us explain the method using the case of a uniaxial stress state in the form of the specimen's extension by stress σ. We will expand the stress acting in the cycle into a trigonometric Fourier series:

$$\sigma(t) = \sigma_{\max}\left(\frac{A_0}{2} + \sum\nolimits_{k=1}^{\infty}[A_k \cos(k\varpi t) + B_k \sin(k\varpi t)]\right) \tag{6}$$

Coefficients in expansion are:

$$A_0 = \frac{2}{T_r}\int_{t_b}^{t_f} \mathrm{d}t = \frac{2(t_f - t_b)}{T_r},\ A_k = \frac{2}{T_r}\int_{t_b}^{t_f} \cos(k\varpi t)\mathrm{d}t = \frac{1}{\pi k}[\sin(k\varpi t_f) - \sin(k\varpi t_b)], \tag{7}$$

$$B_k = \frac{2}{T_r}\int_{t_b}^{t_f} \sin(k\varpi t)\mathrm{d}t = \frac{1}{\pi k}[\cos(k\varpi t_b) - \cos(k\varpi t_f)].$$

Then the law of stress varying in a cycle can be represented as follows:

$$\sigma(t) = \sigma_{\max} g(t), \tag{8}$$

$$g(t) = \frac{t_f - t_b}{T_r} + \sum_{k=1}^{\infty}\left\{\frac{1}{\pi k}[\sin(k\varpi t_f) - \sin(k\varpi t_b)]\cos(k\varpi t) + \right.$$
$$\left. + \frac{1}{\pi k}[\cos(k\varpi t_b) - \cos(k\varpi t_f)]\sin(k\varpi t)\right\}.$$

Since the deformation process lasts much longer than one loading cycle, we introduce a small parameter $\mu = \frac{T_r}{t_*} \ll 1$ and two independent time scales: 'slow' t and 'fast' $\xi = t/T$, $(0 \le \xi < 1)$.

Expanding the functions of creep strain and the damage parameter into asymptotic series gives:

$$\varepsilon^c(t,\xi) = \varepsilon_0^c(t) + \mu\varepsilon_1^c(t,\xi) + O(\mu^2),\ \omega^c(t,\xi) = \omega_0^c(t) + \mu\omega_1^c(t,\xi) + O(\mu^2). \tag{9}$$

Let us average these expansions over a period with scaled time from 0 to 1. Let us limit ourselves, as in [3], to two terms in expansions (9), as well as to consider that

$$\left(\varepsilon_0^{\mathrm{c}}(t)+\mu\varepsilon_1^{\mathrm{c}}(t,\xi)\right)^{\alpha}\approx\left(\varepsilon_0^{\mathrm{c}}\right)^{\alpha}\left(1+\mu\alpha\frac{\varepsilon_1^{\mathrm{c}}}{\varepsilon_0^{\mathrm{c}}}\right)\cong\left(\varepsilon_0^{\mathrm{c}}\right)^{\alpha}. \tag{10}$$

Let us consider that the terms $\varepsilon_1^{\mathrm{c}}$ and ω_1 are single-periodic functions in ξ and have zero mean value:

$$\int_0^1\varepsilon_1^{\mathrm{c}}(t,\xi)\mathrm{d}\xi=0,\qquad\int_0^1\omega_1^{\mathrm{c}}(t,\xi)\mathrm{d}\xi=0.$$

After that, we substitute the obtained expression into the equations for creep strain rates and the damage parameter from (2). Therefore, the averaged equations take the form:

$$\dot{\varepsilon}_0^{\mathrm{c}}\left(\varepsilon_0^{\mathrm{c}}\right)^{\alpha}=B\langle g^n\rangle\frac{\sigma^n}{\left(1-\omega_0^{\mathrm{c}}\right)^k},\ \dot{\omega}_0^{\mathrm{c}}=D\langle g^m\rangle\frac{\sigma^m}{\left(1-\omega_0^{\mathrm{c}}\right)^l}\ \omega_0(0)=0,\ \omega(t_*)=\omega_*, \tag{11}$$

where

$$\langle g^p\rangle=\int_0^1 g^p(T_r\xi)\mathrm{d}\xi, \tag{12}$$

and

$$\langle g^p\rangle=\int_0^1\left(\frac{A_0}{2}+\sum_{k=1}^{\infty}[A_k\cos(2\pi k\xi)+B_k\sin(2\pi k\xi)]\right)^p\mathrm{d}\xi. \tag{13}$$

Here in (12)-(13) $p=n$ in the case of the equation for creep strain rates and $p=m$ for the damage evolution equation.

Generalizing Eqs. (11) for the case of a complex stress state and neglecting, as in [3], the index "0" when describing the 'slow' process of creep and damage accumulation, we obtain:

$$\dot{\varepsilon}_{ij}^{\mathrm{c}}\left(\varepsilon_{vM}^{\mathrm{c}}\right)^{\alpha}=\frac{3}{2}B\langle g^n\rangle\frac{\sigma_{\mathrm{vM}}^{n-1}}{(1-\omega)^k}s_{ij},\ \dot{\omega}^{\mathrm{c}}=D\langle g^m\rangle\frac{\sigma_{eq}^m}{(1-\omega)^l} \tag{14}$$

$$\dot{\omega}^{\mathrm{scc}}=C\left(t^{\mathrm{scc}}\right)^s,\ \omega^{\mathrm{scc}}(\boldsymbol{x},t^{\mathrm{scc}})=0,\ t^{\mathrm{scc}}=t-t_*x_i\in V_{\mathrm{scc}};$$

$$\mathrm{d}\omega=\mathrm{d}\omega^{\mathrm{c}}+\mathrm{d}\omega^{\mathrm{scc}},\ \omega(\boldsymbol{x},0)=0,\ \omega(\boldsymbol{x},t_*)=\omega_*.$$

Here we considered that in the surfaces under corrosion action both creep and creep damage is affected by the total accumulated damage values, in other areas the classical creep-damage equations operate.

In the considered loading process, the cyclic deformation of the blade surface takes place [18], which is often called fretting fatigue [6]. Under creep conditions, such degradation of the surface of the structural element can be described by taking into account

local creep deformation at the contact points. This will be done in this approach, but if experimental data on separate deformation during surface friction are obtained for real calculations, it will be possible to take them into account in the calculations, for example, using the Archard model [6].

After the completion of hidden damage accumulation in a certain area adjacent to the surface S, mathematical modeling of damage accumulation processes in other points of the solid continues, and the analysis of corrosion processes on a certain surface S_{scc} begins. The completion of the hidden damage accumulation in some region ΔV means that it is excluded from the object V. Also, often the parts of the boundary S_1 and S_2, where the boundary conditions in stresses and displacements are given, will also change to the values ΔS_1 and ΔS_2 due to the possible fracture of the fixed and loaded boundaries. This algorithm can be described as follows:

$$S_1 = S_1 + \Delta S_1; S_2 = S_2 + \Delta S_2.; \; V = V + \Delta V; S = S + \Delta S. \tag{15}$$

In expressions (15) the operator + is understood in an algebraic sense, and the operator = is an assignment operation. Therefore, for further analysis of the fracture process, it is necessary to reformulate the boundary-initial value problem with the obtained new boundary and initial conditions. The last ones are determined by the distribution of the components of the stress-strain state and the damage parameter obtained at this time.

The *FEM Creep Damage Fracture* software developed at NTU "KhPI" is used for the numerical modeling, the used algorithms are described in [19].

3 Numerical Modeling Results

As an example of using the proposed approach and the discussed constitutive equations, let us consider a 2D model of a turbomachine blade (Fig. 2b a). The model can be described by a rectangle 0.15 × 0.05 m, the upper part of which is an arc of a circle with a maximum deviation from the side of the rectangle of 0.0015 m. Centrifugal forces act on the blade with a frequency $\varpi = 50\ s^{-1}$. The additional distribution of bending stresses from the pressure on the blade with a value of 0.3 MPa is also taken into account.

The blade material is high-chromium foundry heat-resistant nickel-based alloy (Ni 57%, Cr 16%, Co 11%,W 5%). Blade is heated evenly to temperature 950 °C. Constants for the creep-damage equations are: $B = 5.26\ 10^{-27}$ MPa^{-n}/ h, $n = 5.508$, $\alpha = 4.678$, $D = 1.18\ 10^{-17}$ MPa^{-n}/ h, $m = k = l = 5.569$.

The constants for the stress corrosion cracking equation were determined using the experimental data presented for this alloy at a given temperature in [20] using data on material loss during corrosion over a certain period of time. The constants for the equation for the parameter ω_{scc} in (14) were equal to $C = 2.\ 10^{-5}$ h^{-s}, $s = 2$.

The order of the model was determined using numerical experiments, and a mesh of 15,000 elements was used in the calculations. The initial stress state in the blade model is presented in Fig. 2b), where the distribution of von Mises equivalent stress is given.

Initially, a numerical analysis was performed for the case of purely static loading. As always in the case of cantilever objects, the completion of hidden damage accumulation occurred in the area adjacent to the fixed side at $t_* = 15267.3$ h. The distribution of the

damage parameter for this time is shown in Fig. 3 b). The von Misses stress relaxation in the element where the damage accumulation finishes is presented in Fig. 3 a).

Next, the cyclic action of stresses arising from the contact of the upper part of the blade with the casing, which was considered rigid, was taken into account. The value of the displacement of the upper points of the blade in 0.0005 m, at which contact with the casing already occurs, was reached in $t^{\text{ext}} = 7502$ h. The simulation results showed that in this case the time to the completion of the hidden damage accumulation was reduced almost by half and was $t_* = 8472.4$ h. At the same time, the location of the failure changed, it corresponds to the area at the edge of the blade. The distribution of the damage parameter for this case is given in Fig. 3 c).

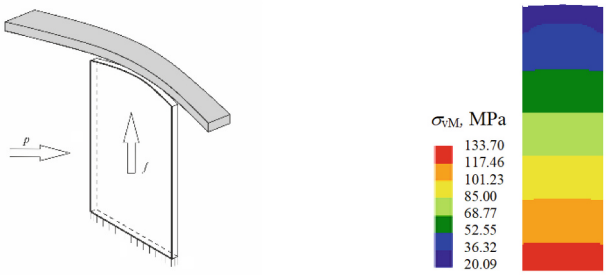

Fig. 2. a) the sketch of the blade; b) distribution of the von Mises stress, blade model, $t = 0$.

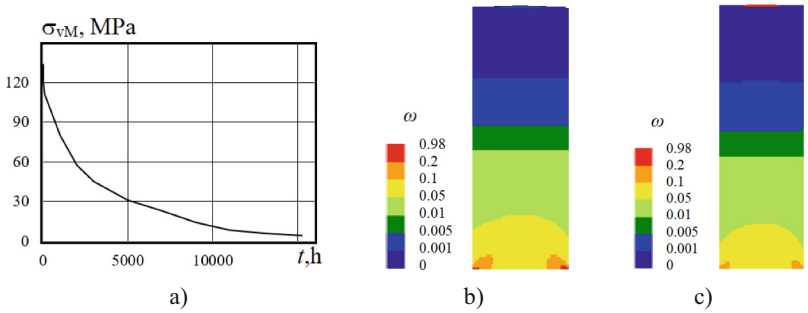

Fig. 3. a) von Mises stress versus time; Distribution of the damage parameter through the blade model before the completion of the damage accumulation b) Static loading, $t_* = 15267.3$ h; c) Consideration of the loading in the blade tip, $t_* = 8472.4$ h.

'Element corrosion' is employed when the damage parameter reaches the critical value of 0.98. As the calculations showed, a number of elements along the upper edge were removed. Then the algorithm, which detected the presence of finite elements that were internal in the original model, but now became external, started. This means that starting from this time $t_* = 8472.4$ h, the total value of the damage parameter began to

be determined additionally by the corrosion effect. The calculations showed that over the next approximately 200 h, the process of intensive corrosion began in the area of the initial macroscopic defect. The current view of the blade fragment in the area of intensive damage accumulation and corrosion at $t = 8652$ h is presented in Fig. 4. After this moment, the simulation was stopped.

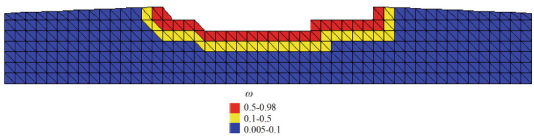

Fig. 4. Distribution of the damage parameter in the upper fragment of the blade model, stress corrosion cracking after the destruction of the upper zone, $t* = 8652$ h.

4 Conclusions

This paper proposes an approach for a comprehensive analysis of high-temperature deformation and failure of turbomachine blades during creep, taking into account surface wear due to contacts with the casing and stress corrosion cracking. To implement the assessment of deformation and long-term strength of blades, an updated form of evolution equations, combining creep and corrosion effects, is proposed. As an example of numerical modeling using this approach and software with new analysis capabilities, the problem of creep of a turbomachine blade model was considered. Various variants of creep and fracture modeling were analyzed with the sequential addition to the analysis the effects of interaction with the casing and corrosion of blade parts with a destroyed coating. It was demonstrated that the latter factors have a significant impact on the total time to the appearance of a macroscopic defect, which is reduced almost by half, and its intensive growth. The developed approach can be further applied to the numerical analysis of real blade models taking into account their complex geometry, the presence of cooling and non-uniform temperature distributions, etc. This will require generalization of existing algorithms for three-dimensional analysis.

References

1. Lemaitre, J., Chaboche, J.L.: Mechanics of Solid Materials. Cambridge University Press, New York (1994)
2. Huda, Z.: Mechanical Behavior of Materials. Springer International Publishing, Cham (2022)
3. Breslavsky, D., Morachkovsky, O., Tatarinova, O.: Creep and damage in shells of revolution under cyclic loading and heating. Int. J. Non-Linear Mech. **66**, 87–95 (2014). https://doi.org/10.1016/j.ijnonlinmec.2014.02.005
4. Singh, S., Kharub, M., Singh, J., Singh, J., Jangid, V.: Brief survey on mechanical failure and preventive mechanism of turbine blades. Mater. Today Proc. **38**, 2515–2524 (2021). https://doi.org/10.1016/j.matpr.2020.07.546
5. Hills, D.A., Andresen, H.N.: Mechanics of Fretting and Fretting Fatigue. Solid Mechanics and Its Applications, vol. 266. Springer, Berlin/Heidelberg (2021). https://doi.org/10.1007/978-3-030-70746-0

6. Araújo, J.A., Nowell D., de Castro, F.C.: Fretting Fatigue. Comprehensive Structural Integrity (Second Edition), 249–282 (2023). https://doi.org/10.1016/B978-0-12-822944-6.00004-9
7. Schofield, J., Nowell D.: Aero Engines. Fretting Wear and Fretting Fatigue. Elsevier, 441–471 (2023)
8. Kuang, W., et al.: Fretting wear behaviour of machined layer of nickel-based superalloy produced by creep-feed profile grinding. Chin. J. Aeronaut. **35**(10), 401–411 (2022). https://doi.org/10.1016/j.cja.2021.10.007
9. Miao, Q., et al.: Creep-feed grinding of single crystal nickel-base turbine blade fir-tree roots: tool wear, grinding force, temperature, and surface integrity. Int. J. Adv. Manufact. Technol. **126**(3), 1453–1470 (2023). https://doi.org/10.1007/s00170-023-11188-5
10. Livani, M., Zarei, H. R., Kamali, S. M.: Investigating the effect of wear on the creepage life of jet engine turbine blades model 250-C20. J. Technol. Aerospace Eng. **9**(1), 1–14 (2025). https://doi.org/10.22034/jtae.2025.9.1.1
11. Gross, J., Buhl, P., Weber, U., Schuler, X., Krack, M.: Effect of creep on the nonlinear vibration characteristics of blades with interlocked shrouds. Int. J. Non-Linear Mech. **99**, 240–246 (2018). https://doi.org/10.1016/j.ijnonlinmec.2017.12.002
12. Villagrán-Villegas, L.Y., Hernández-Gómez, L.H., Martínez-Cruz, M.Á., Rojas-Ramírez, J.A.: The numerical characterization of the gas turbine blade with static stress analysis applying finite element method. J. Mech. Eng. **5**(15), 16–23 (2021)
13. Forghani, M., Ariafar, K.: Investigation of creep behavior of a gas turbine blade with a visco plastic FEM model to estimate the blade life. Trans. Mach. Intell. **7**(3), 194–207 (2024). https://doi.org/10.47176/TMI.2024.194
14. Naeem, M. T., Jazayeri, S. A., Rezamahdi, N., & Toosi, K. N.: Failure analysis of gas turbine blades. In: Proceedings of the 2008 IAJC-IJME International Conference (2008). ISBN 978–1–60643–379–9
15. Khushbash, S., Hameed, A., Mumtaz, A., Khan, H.A., Shahzad, A.: Investigation of temperature assisted corrosion failure of an aircraft turbine blade. Eng. Fail. Anal. **167**, 108909 (2025). https://doi.org/10.1016/j.engfailanal.2024.108909
16. Katinić, M., Kozak, D., Gelo, I., Damjanović, D.: Corrosion fatigue failure of steam turbine moving blades: a case study. Eng. Fail. Anal. **106**, 104136 (2019). https://doi.org/10.1016/j.engfailanal.2019.08.002
17. Hallquist, J.: LS–Dyna Theory Manual: LSTC (Livermore Software Technology Corporation) (2018)
18. Legrand, M., Pierre, C., Cartraud, P., Lombard, J.: Two-dimensional modeling of an aircraft engine structural bladed disk-casing modal interaction. J. Sound Vib. **319**(1–2), 366–391 (2009). https://doi.org/10.1016/j.jsv.2008.06.019
19. Breslavsky, D., Senko, A., Tatarinova, O.: Creep damage and fracture of notched specimens under static and fast periodic loading. Int. J. Damage Mech **30**(6), 964–983 (2021). https://doi.org/10.1177/1056789521991207
20. Kvasnytska, Y.H., Ivaskevych, L.M, Balytskyi, OI, Maksyuta, II, Myalnitsa, H.P.: High-temperature salt corrosion of a heat-resistant nickel alloy. Mater. Sci. **56**(3), 432–440 (2020). https://doi.org/10.1007/s11003-020-00447-5

Identification of Early Degradation Mechanisms in Zinc Coating on Cold-Formed Steel Sections Through Analysis of the Production–Storage Chain

Volodymyr V. Kukhar[1(✉)], Khrystyna V. Malii[1], Sergiu G. Mazuru[2], Natalia S. Hrudkina[1], and Eleonora O. Butenko[3]

[1] Technical University "Metinvest Polytechnic" LLC, 80 Pivdenne Highway, Zaporizhzhia 69008, Ukraine
kvv.mariupol@gmail.com

[2] Technical University of Moldova, 168 Stefan Cel Mare Avenue, Chişinău MD-2004, Republic of Moldova

[3] Pryazovskyi State Technical University, 29 Gogolya Street, Dnipro 49000, Ukraine

Abstract. Cold-formed steel hollow sections (CFS) with hot-dip galvanized coatings (e.g., DX51D + Z140) are widely used in window and façade systems, especially in urgent restoration contexts. However, premature degradation—despite conformity to EN 10346—raises concerns about long-term performance. This study examines early-stage corrosion risks of such sections, integrating coating thickness measurements, chemical surface analysis, and production history. Specimens were extracted from strip blanks and finished CFS. Coating thickness was measured using electromagnetic and gravimetric methods, while chloride, sulphate, and chromate residues were assessed via ISO-based chemical tests. Variability in coating thickness and the presence of chlorides and iron oxides were linked to sharp bending radii, excessive roll pressure, and lack of post-forming passivation. Key findings show that compliance with nominal Z140 specifications is insufficient to prevent early white rust or undercoating corrosion. A structured risk map was developed to identify root causes of degradation in sections with non-uniform coating, microcracks, and surface contamination, enabling targeted preventive measures. The study emphasizes the need for integrated process–logistics control: optimized forming parameters, systematic passivation, and ventilated packaging. These actions are critical to ensuring reliable corrosion protection in CFS, especially under accelerated post-conflict recovery conditions.

Keywords: Cold-Formed Steel · Galvanized Coating · White Rust · Coating Thickness · Passivation · Corrosion Resistance · Storage Conditions

1 Introduction

Cold-formed steel hollow sections (CFS) with hot-dip galvanized coatings (e.g., DX51D+Z140) are widely used in window and façade systems, greenhouse and agricultural frames, and other lightweight structures [1], where they offer stiffness, dimensional

H. Altenbach et al. (Eds.): CAMPE 2025, LNME, pp. 179–189, 2026.
https://doi.org/10.1007/978-3-032-16381-3_17

stability, and ease of installation (see Fig. 1). Among these, Rectangular Hollow Sections (RHS) — a common type of CFS with rectangular cross-section —are particularly favored for their optimal strength-to-weight ratio and aesthetic integration in façade designs. However, premature degradation of galvanized coatings may still occur and should be considered at both the design and manufacturing stages.

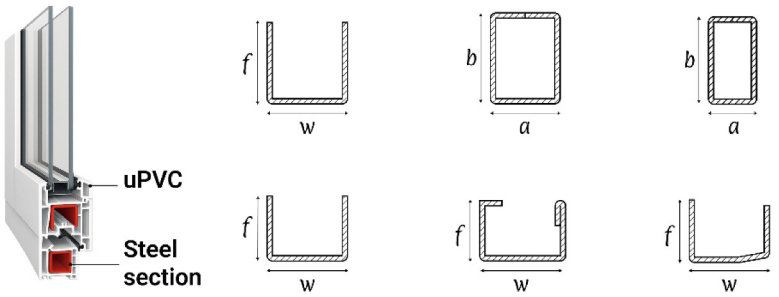

Fig. 1. CFS in window design: left – cross-section of a typical window frame with inserted elements (red); right – schematic geometry with dimensions w and f – width and flange height; a and b – RHS width and height. Original drawing prepared by the authors.

In practice, Z140 is treated as a baseline protection level; guidance specifies a nominal coating thickness of −10 μm per side and a working range of 7–15 μm for conformity under EN 10346 [2]. While such conformity is necessary, long-term performance also depends on coating uniformity [3], surface integrity after forming [4], adequacy of passivation/oiling, and proper transport/storage [5]. A common field issue is white rust—early atmospheric corrosion caused by humidity, poor ventilation, and inadequate passivation, compromising protection before carbonate film stabilizes [5, 6].

The broader context underscores the need for material-efficient, rapid structural solutions in building rehabilitation. In Ukraine this is acute—windows and façade elements require constant replacement after shelling and will intensify post-war; hence buffer stocks of standardized cold-formed sections (CFS) are critical. Risks include microcracking and local thinning of the zinc layer at small bending radii or excessive roll pressure/misaligned guides, as well as corrosion from poor storage. These require integrated process controls (radius/pressure/guide settings, passivation/oiling) and handling protocols (ventilated, dry packaging; controlled logistics), not isolated checks.

Practice shows that CFS from coils of the same grade but different production histories suffered coating damage after routine transport and short storage, confirming that vulnerability results from both forming technology and logistics. This underlines the need for research to mitigate degradation risks along the production–logistics chain.

Against this backdrop, the present work addresses durable corrosion protection for CFS beyond nominal compliance. Within EN 10346 [2] (delivery of hot-dip coated flat products) and EN 10143 [7] (dimensional/surface tolerances and responsibilities during transport/storage), the study examines how forming routes, passivation, and packaging conditions influence early degradation—and how these risks can be reduced by process-integrated controls and logistical best practices.

2 Literature Review

Corrosion of metal structures is a large-scale problem, leading to loss of material, reduced structural strength, and shortened service life. According to the World Corrosion Organization, global direct corrosion costs amount to 1.3–1.4 trillion EUR annually, corresponding to 3.1–3.5% of GDP [8, 9]. This multifactorial process depends on material properties, environmental conditions, and operational factors [10, 11]. Difficulties in accurately predicting corrosion losses often result in the application of excessive safety factors, which in turn leads to overuse of structural materials [6]. For cold-forming technologies, product quality and durability are sensitive to both manufacturing-induced damage and environmental exposure. Research has shown that optimizing deformation parameters in preliminary forming passes can reduce energy and force requirements more than fourfold and lower trim loss to 22% [10].

White rust, a common form of atmospheric corrosion on galvanized products, develops under high humidity, aggressive aerosols, and insufficient passivation [11]. It gradually destroys the zinc layer, exposes the steel substrate, and reduces in-service reliability. These risks are intensified by climate change, which is accompanied by abrupt temperature fluctuations, increased humidity, and more aggressive atmospheric conditions [12].

Beyond compliance with nominal zinc coating mass, long-term performance is influenced by the residual stress, microcrack formation, and the presence or absence of effective passivation layers [13, 14]. While many studies address these factors individually, fewer works consider them in an integrated framework combining process monitoring with logistics controls under variable climate conditions—an approach directly relevant to improving the reliability of cold-formed galvanized sections in service.

The study aims to determine the key technological and environmental factors that cause degradation of zinc coatings on cold-formed steel sections made from DX51D + Z140. This is achieved through an integrated assessment of production processes, coating thickness measurements, chemical surface analysis, and statistical evaluation, with the goal of developing targeted measures to prevent premature corrosion.

3 Research Methodology

3.1 General Concept

The research methodology was developed to enable a comprehensive analysis of the technological process for manufacturing cold-formed sections from galvanized steel. It focused on identifying critical production stages, selecting representative specimens, and applying physicochemical and instrumental methods to evaluate the zinc coating.

The logical and structural framework of the study is presented in Fig. 2.

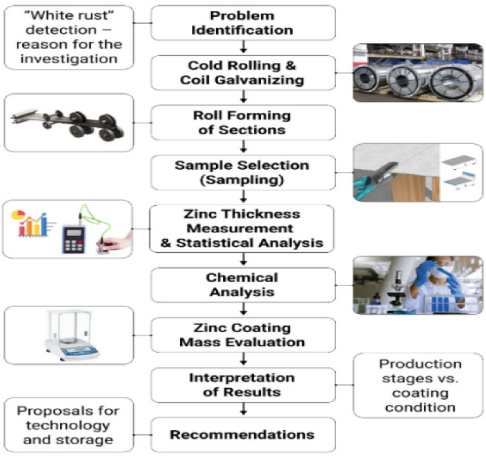

Fig. 2. Logical and structural framework of the research methodology.

3.2 Materials and Methods

Sampling and Specimen Preparation. Specimens (30 × 20 mm) were obtained from both strip blanks and finished CFS made from DX51D + Z140 galvanized coils (see Fig. 3 for sampling). The set included three strip and three CFS series, with dimensions and strip/wall thickness (t) recorded. Strip specimens (Fig. 4): (I) t = 1.03 mm (Poland), (II) t = 1.35 mm and (III) t = 1.5 mm (same Ukrainian supplier, certified separately). CFS specimens (Fig. 5) were cut with preserved bend and corner geometry: (IV) 30 × 50 mm, t = 1.48–1.5 mm; (V) 30 × 50 mm, t = 1.5 mm; (VI) 35 × 49.5 mm, t = 1.5 mm. Each specimen was marked by location (web, edge, or bend).

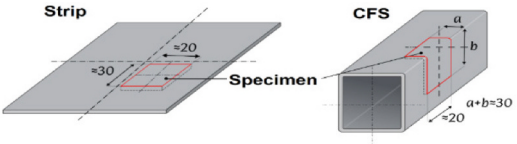

Fig. 3. Diagram of specimen extraction from strip (a) and CFS (b).

Coating Thickness Measurement. Zinc coating thickness was measured using a NOVOTEST TP-1 electromagnetic thickness gauge, calibrated with certified standards. For each specimen, multiple measurements were taken in predefined zones to evaluate local variation. Data processing included calculation of mean values, measurement errors, variance, and relative error. Statistical evaluation of homogeneity and variance equality between series was performed using Cochran's criterion, and significance of differences between means was assessed using Fisher's criterion at a 95% confidence level.

Chemical Surface Analysis. Chemical tests were conducted to detect corrosion-related surface contaminants and passivation indicators:

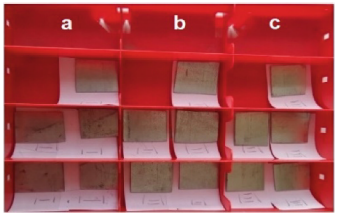

Fig. 4. Test specimens from strip blanks: (a) "Poland" (I); (b), (c) strips (II), (III) from same Ukrainian supplier, separately certified.

Fig. 5. Specimens from the CFS: (a) 30 × 50 mm, t = 1.48–1.5 mm (IV); (b) 30 × 50 mm, t = 1.5 mm (V); (c) 35 × 49.5 mm, t = 1.5 mm (VI); t – strip/wall thickness.

- chloride ions (Cl^-): $AgNO_3$ test (white precipitate of AgCl) following
- ISO 8502–5 [15];
- sulphate ions (SO_42^-): $BaCl_2$ test (white precipitate of $BaSO_4$);
- hexavalent chromium (Cr(VI)): Diphenylcarbazide colorimetric test (violet coloration) to identify chromate passivation layers;
- iron oxides (Fe_xO^y): optical microscopy at × 50 magnification for corrosion products beneath the zinc layer;
- residual rolling emulsions: visual inspection and solvent test for organic films.

Gravimetric Determination of Coating Mass. Coating mass was evaluated according to EN ISO 1460 [16], involving chemical stripping of zinc using inhibited acid solutions, followed by gravimetric mass difference calculation. Results were converted to coating thickness assuming a zinc density of 7.14 g/cm^3.

Data Integration and Compliance Assessment. All measurement and test results were compiled and assessed for compliance with EN 10346:2015 [2] requirements for Z140 coating class. Coating uniformity, defect occurrence, and chemical contamination were analyzed in correlation with production stage and coil origin to identify high-risk process steps.

4 Results and Discussion

4.1 Main Results and Interpretation

Coating Thickness and Uniformity. The measured coating thickness (h) values for strip blanks and cold-formed sections are summarized in Table 1 and graphically illustrated in Fig. 6 and Fig. 7. Strip I (h = 10.8 ± 2.3 µm) and Strip II (h = 12.4 ± 1.5 µm) fully complied with the EN 10346:2015 Z140 requirement of 7–15 µm, with relative errors of 7.7% and 4.4%, respectively. In contrast, Strip III (h = 21.4 ± 3.2 µm) exceeded the upper limit, indicating excessive coating application, which may reflect deviations in bath chemistry or withdrawal speed during galvanizing.

For the CFS, average coating thickness falls within the normative range, but series CFS 30 × 50 × (1.48–1.50) mm exhibited the lowest value (h = 8.6 ± 3.7 µm) and the

highest relative error (15.6%), highlighting reduced uniformity and increased variability. CFS 30 × 50 × 1.50 mm and CFS 35 × 49.5 × 1.50 mm achieved averages of h = 10.4 ± 3.7 μm and h = 11.0 ± 3.4 μm, respectively, both within the acceptable interval. Statistical evaluation confirmed significant variance inhomogeneity between strip and CFS series (Cochran's criterion, $C_{calc} < C_{tab} = 0.544$) and notable differences in mean values (Fisher's criterion, $F_{calc} < F_{cr} = 14.02$), pointing to induced thickness variations.

Table 1. Coating thickness measurement results.

Series	h ± Δh, μm	Relative error, %	Variance (S^2)	Cochran's criterion, C_{calc}	Fisher's criterion, F_{calc}	Compliance with Z140 standard (EN 10346:2015)	
						Nominal h = 10 μm	Range 7–15 μm
Strip (I)	10.8 ± 2.3	7.7	3.50	0.315	2.31	Yes	Yes
Strip (II)	12.4 ± 1.5	4.4	1.50	0.399	3.06	Yes	Yes
Strip (III)	21.4 ± 3.2	7.6	3.96	0.327	3.17	Yes	No
CFS (IV)	8.6 ± 3.7	15.6	13.69	0.538	3.291	No	Yes
CFS (V)	10.4 ± 3.7	12.1	13.69	0.538	3.29	Yes	Yes
CFS (VI)	11.0 ± 3.4	10.2	11.56	0.487	3.232	Yes	Yes

Table 2. Chemical surface analysis results (' +' – detected; '–' – not detected; numerator – on surface, denominator – beneath zinc coating).

Series	Cl^-	SO_4^{2-}	Cr(VI)	Fe-oxides under Zn	Organics (emulsion)
Strip (I)	–/–	–/–	–/+	–	+
Strip (II)	–/–	–/–	–/+	–	+
Strip (III)	–/–	–/–	–/+	–	+
CFS (IV)	+/–	–/–	–/+	+	+
CFS (V)	+/–	–/–	–/+	+	+
CFS (VI)	+/–	–/–	–/+	+	+

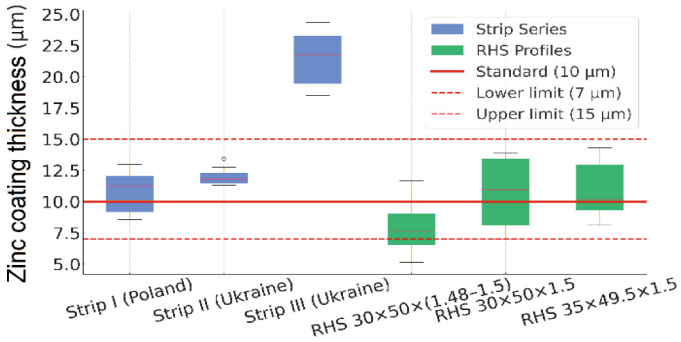

Fig. 6. Boxplot of mean and spread of zinc coating thickness for strip and CFS specimens.

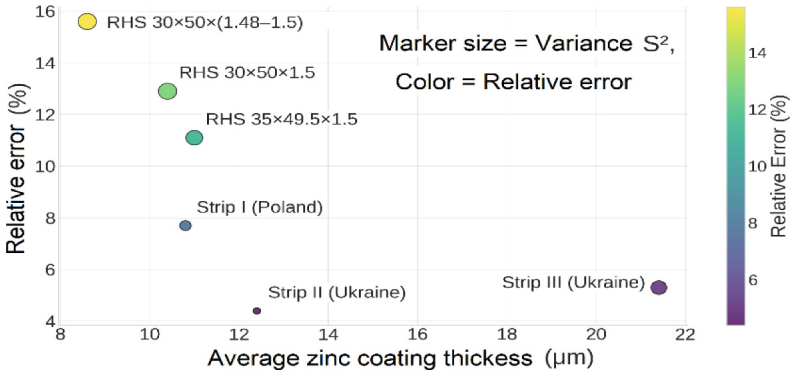

Fig. 7. Assessment of zinc coating stability using thickness–error bubble chart.

Chemical Surface Analysis. The results of chemical testing are presented in Table 2. Chloride contamination (Cl^-) was detected on the external surfaces of all CFS but was absent on strip blanks, indicating contamination introduced during forming or post-forming handling. Sulphates (SO_42^-) were not found in significant concentrations. Hexavalent chromium (Cr(VI))—a marker of chromate passivation—was detected only beneath the zinc layer, implying the absence of external passivation, which would otherwise enhance short-term atmospheric resistance.

Optical microscopy revealed localized Fe-oxide formation beneath the zinc layer in CFS specimens, particularly in bends, suggesting microcrack penetration, though local thinning, roll-forming stresses or contamination could also contribute to undercoating corrosion. Residual rolling emulsions were occasionally observed in concave areas, potentially promoting localized corrosion under humid storage.

Gravimetric Coating Mass Determination. Gravimetric analysis according to EN ISO 1460 yielded coating masses consistent with thickness measurements. Strip I and II corresponded to calculated thicknesses of 10–12 µm per side, while CFS 30 × 50

× (1.48–1.50) mm approached the lower conformity limit (≈8 μm). Excessive coating mass in Strip III confirmed the over-thickness observed in direct measurements. This convergence of methods (electromagnetic gauge and gravimetry) reinforces the reliability of the measurement dataset (Table 1).

Correlation of Technological Deviations with Observed Defects. Analysis of thickness and chemical data shows that reduced coating uniformity in certain CFS correlates with roll-forming geometry and parameters. Sharp bending radii and high roll pressure can cause microcracks, enabling chloride ingress and undercoating oxidation during storage. Lack of external passivation increases susceptibility to white rust under tight, humid packaging.

The industrial case behind this study confirms these patterns: sections with non-uniform coating and activated surfaces developed white rust and brown corrosion after short-term storage, despite meeting Z140 thickness specifications. This demonstrates that coating conformity alone does not ensure durability.

Implications for Production and Logistics. Maintaining uniform zinc coating after forming requires precise control of roll-forming parameters—particularly bending radius, roll alignment, and contact pressure. In-line monitoring (e.g., NOVOTEST TP-1) could detect deviations in real time. Logistically, immediate passivation or light oiling, along with ventilated, moisture-resistant packaging, is essential to prevent early atmospheric corrosion. The findings confirm that both technological and logistical factors significantly affect protective layer performance.

4.2 Discussion

Table 3 summarizes the risk map linking each process stage to its dominant degradation mechanism and corresponding countermeasures, derived from the experimental results of coating thickness (Table 1), chemical surface analysis (Table 2), and microscopic observations (Sect. 4.1).

Table 3. Risk map and corresponding technological interventions.

Zone/Stage	Defect	Cause	Risk	Mitigation
Section bend zone	Microcracks in the coating	Low-plasticity Zn + tight bends	High	Larger radius + ZnAlMg coating
Roller stands	Contact damage to the coating	Impurities / contamination / high pressure	Medium	Roll cleaning & auto pressure control
Coil surface	Residual acids / emulsions	Poor cleaning and drying	High	Control drying, degreasing & pickling
Section edges	Local thinning of zinc coating	Storage humidity and low ventilation	Medium	Perforated/open-end packaging
Strip width	Uneven coating thickness	Unbalanced air knives, spot cooling	Medium	Control air knives and cooling

(*continued*)

Table 3. (*continued*)

Zone/Stage	Defect	Cause	Risk	Mitigation
Outer surface	Lack of passivation, moisture	Missing passivation	High	EN 10346 passivation/oil; side check
Storage/ logistics	White rust, no protective ability	Humidity and confined packaging	High	Ventilation + sloped packing + spacers
Post-forming surface	Local zinc layer loss	Forming-induced wear	Medium	Reduce friction + optimize lube + control strain zones
Section surface	Cl^-/Fe-oxide inclusions	Deposition, pickling defects, poor storage	High	Controlled transport & packaging

The results show that coating thickness conformity alone does not guarantee corrosion resistance in galvanized CFS. Although strip blanks retain uniform Z140 coatings, forming causes localized thinning—especially at tight bends and under high roll pressure—leading to microcracks and early corrosion initiation. Chloride ions were detected only on finished CFS, confirming contamination during post-forming handling and storage. This is aggravated in coastal or industrial environments and by the absence of chromate passivation, leaving zinc active until natural passivation occurs. Even short-term exposure to humid, poorly ventilated packaging can trigger white rust. Fe-oxides beneath the zinc in bend areas confirm subsurface breaches undetectable visually. This hidden corrosion may begin during storage and transport, shortening service life. Effective mitigation includes non-destructive testing and thorough washing and drying to remove emulsions.

A dual strategy is needed: (i) process control—optimizing bend geometry, roll pressure, and tooling finish; (ii) logistics control—preventing contamination and moisture ingress before installation. Table 3 links microcracks at bends to excessive deformation and rough tooling, which can be mitigated by controlled forming pressure and guided rollers. Chlorides and emulsions—confirmed via $AgNO_3$ and diphenylcarbazide tests—indicate insufficient drying and highlight the need for ventilated packaging. Especially vulnerable zones include section ends and internal corners, where stress and moisture accumulate. These showed greater coating variation and more frequent corrosion. Countermeasures include local inhibitors or improved coil passivation.

The risk map underscores the gap between nominal EN 10346 compliance and actual performance. Even within-spec coatings may fail under uncontrolled conditions. Diagnostic data structured into a risk matrix enables targeted corrective and preventive actions aligned with service demands.

5 Conclusions

This study examined early-stage degradation risks of hot-dip galvanized coatings on cold-formed steel sections, emphasizing both technological and logistical factors influencing corrosion resistance. Despite conformity to Z140 specs, measurements and chemical analyses revealed that such compliance alone does not ensure reliable performance. Key issues included microcracks and thinning at bends, oxidation from residual emulsions, and early white rust due to insufficient packaging and lack of passivation. These problems often stem not from steel quality but from uncontrolled forming, handling, and storage conditions.

To address these risks, the following measures are recommended: (a) forming control: use appropriate bending radii, optimize roll pressure and alignment, regularly clean tooling surfaces; (b) surface protection: apply passivation or light oiling after forming to stabilize the zinc layer and delay corrosion; (c) packaging/logistics: use ventilated, moisture-resistant packaging; avoid tight bundling without airflow gaps; (d) quality control: perform coil acceptance checks and monitor coating thickness and uniformity using portable gauges; (e) integrated strategy: merge technological and logistical measures into a unified protocol covering production, delivery, and installation stages.

These measures define a "risk-to-action" framework that guides future research and supports practical implementation, particularly under demanding conditions of preparing and restoring window and façade systems.

References

1. Al Zand, A.W., Alghaaeb, M.F., Liejy, M.C., Mutalib, A.A., Al-Ameri, R.: Stiffening performance of cold-formed C-section beam filled with lightweight-recycled concrete mixture. Materials **15**(9), 2982 (2022)
2. EN 10346:2015: Continuously hot-dip coated steel flat products for cold forming – Technical delivery conditions. European Committee for Standardization (CEN), Brussels (2015)
3. Artiukh, V., Mazur, V., Kukhar, V., Vershinin, V., Shulzhenko, N.: Study of polymer adhesion to steel. In: E3S Web of Conferences, vol. 110, p. 01048 (2019)
4. Savchenko, I., Kozechko, V., Shapoval, A.: Method for accelerating diffusion processes when borating structural steels. Lecture Notes in Mechanical Engineering, pp. 793–800 (2022)
5. Wu, B.-R., Yao, J.-T., Dong, H., Chen, Z.-L., Liu, X.-G.: Enhancing the corrosion resistance of passivation films via the synergistic effects of graphene oxide and epoxy resin. Coatings **15**(4), 444 (2025)
6. Ning, P.D., Xiao, L.Y., Wang, J., Wang, D.Y., Fu, Y.F., Shi, L.X.: Corrosion mechanism of Zn–Al–Mg-coated steel in simulated polluted marine atmosphere. J. Iron. Steel Res. Int. **31**, 2294–2307 (2024)
7. EN 10143:2006: Continuously hot-dip coated steel sheet and strip—Tolerances on dimensions and shape. European Committee for Standardization (CEN), Brussels (2006)
8. Zehra, S., Aslam, R., Mobin, M., Verma, C., (eds.): Industrial Corrosion: Fundamentals, Failure, Analysis and Prevention. 1st edn. Wiley-Scrivener, Hoboken (2025)
9. Du, C., et al.: Corrosion behavior and mechanism of 921 a high-strength low-alloy steel in harsh marine atmospheric environments. Int. J. Electrochem. Sci. **19**(9), 100755 (2024)
10. Kukhar, V., Balalayeva, E., Hurkovska, S., Sahirov, Y., Markov, O., Prysiazhnyi, A., Anishchenko, O.: The selection of options for closed-die forging of complex parts using computer simulation by the criteria of material savings and minimum forging force. In: Advances in Intelligent Systems and Computing, vol. 989, pp. 325–331. Springer, Singapore (2020)

11. Manu, K.C., Madhushree, C., Chandini, M.S., Nudi, S., Siri, H., Jeevan, T.P.: Corrosion in steel structures: a review. J. Mines Metals Fuels **73**(1), 189 (2025)
12. Kopiika, N., Robery, P., Ninic, J., Mitoulis, S.-A.: Remaining life of ageing RC infrastructure for sustainable development: deterioration under climate change. Case Stud. Constr. Mater. **22**, e04757 (2025)
13. Maleki, K., Pallisco, D.M., McDermid, J.R., Bassim, N.D.: On the origin of micro-cracking in zinc-coated press hardened steels. Surf. Coat. Technol. **437**, 128360 (2022)
14. Huang, F., Liu, Y., Tao, X., Wang, H., Wang, J., Zhang, D.: Cracking behavior of zinc coating on pre-cracked hot-dip galvanized steel plate under static tension. Structures **61**, 106019 (2024)
15. ISO 8502–5:2025: Preparation of steel substrates before application of paints and related products — Tests for the assessment of surface cleanliness. Part 5: Measurement of chloride on steel surfaces prepared for painting (ion detection tube method). International Organization for Standardization, Geneva (2025)
16. ISO 1460:2020: Metallic coatings—Hot dip galvanized coatings on ferrous materials—Gravimetric determination of the mass per unit area. International Organization for Standardization, Geneva (2020)

Fatigue Life Assessment of Power Machinery Components via Finite and Boundary Element Methods

Kyryl Degtyariov[1], Konstantin Vandyshev[2], Denis Kriutchenko[1(✉)], and Marina Chugay[1]

[1] Pidhornyi Institute of Power Machines and Systems NAS of Ukraine, Kharkiv, Ukraine
wollydenis@gmail.com
[2] Delft University of Technology, Delft, Netherlands

Abstract. The objective of this study is to propose a robust methodology for predicting the fatigue life of structural components subjected to cyclic tension–compression loading. The stress–strain distribution is determined using a coupled finite and boundary element approach, enabling accurate identification of critical high-stress regions where model cracks are introduced for subsequent analysis. Crack propagation is evaluated by computing stress intensity factors within a hypersingular integral equation framework. The proposed methodology is validated by benchmark problems involving flat cracks of elliptical and rectangular geometries, demonstrating both accuracy and effectiveness. The novelty of this research is in the application of hypersingular integral formulations to fatigue assessment in both simplified test cases and practical engineering problems, including a steam turbine blade. The results indicate that crack-free structures exhibit high resistance to cyclic loading, whereas the presence of cracks in stress-critical regions sufficiently reduces fatigue life. The cycles number to failure is quantified for the cracked turbine blade, providing a reliable computational tool for evaluating the residual life of structural components under cyclic loading conditions.

Keywords: Crack Propagation · Hypersingular Integral Equations · Boundary and Finite Element Methods

1 Introduction

Modern engineering materials invariably contain microdefects that may propagate under service loading, potentially resulting in component failure or catastrophic structural collapse. In Ukraine's petrochemical and energy sectors, a significant part of the equipment has exceeded its design service life or has incurred damage from military actions, underscoring the urgent need for reliable residual life assessment methodologies. A critical component of such evaluations is the estimation of structural durability in the presence and evolution of fatigue cracks under cyclic loading. As incipient cracks are typically too small for visual detection, representative model cracks are introduced at areas of maximum stress concentration. Since the actual crack geometry is generally unknown,

H. Altenbach et al. (Eds.): CAMPE 2025, LNME, pp. 190–199, 2026.
https://doi.org/10.1007/978-3-032-16381-3_18

systematic analysis of different crack configurations under identical loading conditions enables identification of the most critical cases, thereby supporting targeted durability assessments. Accordingly, the evaluation of structural integrity and the prediction of safe service life remain pressing and technically significant challenges in contemporary engineering practice.

2 Literature Review

Experimental studies of dynamic processes in structural components are often limited by cost, safety, and hazard concerns, particularly in crack initiation and propagation. As a result, computational modeling has become essential for assessing structural durability. Theoretical and numerical methods for crack growth have been well documented in [1–3]. Fatigue crack growth is crucial for the safety and durability of structures such as steam turbines [4], hydro-turbines [5], wind turbine blades [6], and aerospace components [7]. Various predictive approaches under cyclic loading have been proposed, identifying regions of maximum stress concentration [8]. Advanced numerical methods, including Finite Element Method (FEM) [9], Boundary Element Method ([10]), coupled FEM and BEM [11], Finite volume method (FVM) [12], and the Immersed Boundary Method [13], have been employed to characterize local stress fields and predict fatigue crack initiation and growth. Model cracks are introduced at regions of maximum stress concentration, where the stress intensity factors (SIFs) serve as the principal parameters governing crack behavior and structural response. Extensive research has addressed SIFs in plates with cracks and holes [14], welded beams [15], 3D structure elements [16], and brittle rock under complex loading [17], with hypersingular integral equations (HIEs) applied for SIF evaluation [18]. Crack propagation and fatigue life assessment have been further studied in [19, 20]. Despite this research, accurate prediction of crack growth and fatigue life remains challenging, requiring advanced, robust numerical techniques. The present study develops an efficient approach integrating BEM and FEM with hypersingular integral equations to provide reliable predictions of both crack propagation and structural fatigue life.

3 Research Methodology

3.1 Basic Equations for Crack Propagation Analysis

Stress concentrations can initiate cracks in highly loaded regions of a structural element. A two-stage methodology is employed to assess their effects. First, the stress–strain state of the intact structure is estimated to identify regions of peak stress. Next, cracks of various geometries, such as circular or rectangular, are introduced at these critical zones, with equivalent boundary conditions derived from the undamaged stress distribution applied to the crack faces. This procedure enables rigorous evaluation of the influence of localized defects on structural integrity, strength, and stability [1, 8].

The displacement vector $\mathbf{U}(\mathbf{x})$ of the cracked element is then expressed as a sum.

$$\mathbf{U}(\mathbf{x}) = \mathbf{u}_0(\mathbf{x}) + \mathbf{u}(\mathbf{x}), \tag{1}$$

where $\mathbf{u}_0(\mathbf{x})$ denotes the displacement field that would arise in a crack-free structural element subjected to the same external loads. This field is obtained by solving the following mixed boundary value problem:

$$\nabla \cdot \sigma(\boldsymbol{u}_0(\mathbf{x})) + \mathbf{f}(\mathbf{x}) = 0, \mathbf{x} \in \Omega, \mathbf{u}_0(\mathbf{x}) = \mathbf{u}_1(\mathbf{x}), \mathbf{x} \in \Gamma_1, \ \sigma(\mathbf{u}_0(\mathbf{x})) \cdot \mathbf{n} = \mathbf{t}_2(\mathbf{x}), \mathbf{x} \in \Gamma_2, \tag{2}$$

where Ω is the crack-free body, Γ_1 and Γ_2 are the displacement- and traction-prescribed parts of the boundary $\Gamma = \Gamma_1 \cup \Gamma_2, \Gamma_1 \cap \Gamma_2 = \varnothing$, $\mathbf{f}(\mathbf{x})$ is the body force density, $\mathbf{u}_1(\mathbf{x})$ and $\mathbf{t}_2(\mathbf{x})$, are the prescribed boundary data, and $\mathbf{n}$ is the unit outward normal vector. In (2), $\mathbf{s}(\mathbf{u}_0(\mathbf{x}))$ is the stress tensor, defined for the displacement field $\mathbf{u}_0(\mathbf{x})$ via Hooke's law.

$$\sigma(\mathbf{u}_0(\mathbf{x})) = \mathbf{C} \cdot \varepsilon(\mathbf{u}_0(\mathbf{x})), \ \varepsilon(\mathbf{u}_0(\mathbf{x})) = \frac{1}{2}\Big(\nabla \mathbf{u}_0(\mathbf{x}) + (\nabla \mathbf{u}_0(\mathbf{x}))^{\mathrm{T}}\Big), \tag{3}$$

where $\mathbf{C}$ is the fourth-order elasticity tensor, and $+(\mathbf{u}_0(\mathbf{x}))$ is the deformation tensor.

Similarly, the perturbation displacement field $\mathbf{u}(\mathbf{x})$, induced by the crack presence, satisfies the equilibrium equations

$$\nabla \cdot \sigma(\mathbf{u}(\mathbf{x})) = 0, \ \mathbf{x} \in \Omega \backslash \Gamma_{\mathrm{c}}, \tag{4}$$

where Γ_{c} denotes the crack surface. No body forces are considered in this auxiliary problem. The associated boundary conditions are following:

$$\mathbf{u}(\mathbf{x}) = 0, \mathbf{x} \in \Gamma_1, \ \sigma(\mathbf{u}(\mathbf{x})) \cdot \mathbf{n} = 0, \mathbf{x} \in \Gamma_2, \ \sigma(\mathbf{u}(\mathbf{x})) \cdot \mathbf{n} = -\sigma(\mathbf{u}_0(\mathbf{x})) \cdot \mathbf{n}, \ \mathbf{x} \in \Gamma_{\mathrm{c}}. \tag{5}$$

The last condition in (5) enforces the application of the corrective tractions $-\mathbf{s}(\mathbf{u}_0(\mathbf{x})) \cdot \mathbf{n}$·along the crack faces, which precisely cancel the stresses that would have existed there in the crack-free solution. So, the resulting total displacement $\mathbf{U}(\mathbf{x}) = \mathbf{u}_0(\mathbf{x}) + \mathbf{u}(\mathbf{x})$ satisfies the traction-free condition on the crack surfaces while preserving equilibrium throughout the remaining domain.

3.2 Hypersingular Integral Equations in Model Crack Analysis

For an unbounded body, the boundary value problem defined by Eqs. (4–5), can be reformulated as a hypersingular boundary integral equation [18], expressed as.

$$\frac{1}{4\pi}\mathbf{T}^{\mathbf{n}(\mathbf{x})} \iint\limits_{\Gamma_c} \mathbf{T}^{\mathbf{n}(\xi)}(\Gamma_1(\mathbf{x}-\mathbf{y}))\alpha(\xi)dS_{\mathrm{y}} = -\sigma(\mathbf{u}_0(\mathbf{x})) \cdot \mathbf{n}, \ \mathbf{x} \in \Gamma_{\mathrm{c}}. \tag{6}$$

Here $\mathbf{a}(\mathbf{x})$ denotes the unknown density function representing the discontinuity in the normal component of the displacement field across the crack surface,

$$\Gamma_1(\mathbf{x}-\mathbf{y}) = [\mathbf{T}^{\mathbf{n}(\xi)}\Gamma(\mathbf{y}-\mathbf{x})]', \ \Gamma_{ij}(\mathbf{x}-\mathbf{y}) = \frac{\lambda+\mu}{8\pi\mu(\lambda+2\mu)}\Big[\frac{\lambda+3\mu}{\lambda+\mu}\frac{\delta_{ij}}{|\mathbf{x}-\mathbf{y}|} + \frac{(x_i-\mathrm{y}_i)\Big(x_j-\mathrm{y}_j\Big)}{|\mathbf{x}-\mathbf{y}|^3}\Big],$$

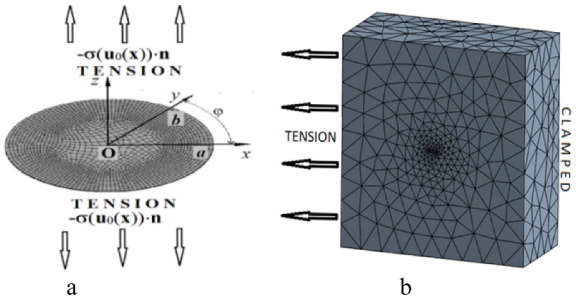

Fig. 1. Model elliptic crack in 3D body: a) BEM discretization, b) FEM discretization.

λ and μ are the Lame coefficients. Figure 1 shows a model elliptical crack.

For a planar isolated crack, subjected to normal separation, the traction operator $\mathbf{T}^{\mathbf{n}(\mathbf{x})}\mathbf{U}$ reduces to differentiation in the normal direction to the crack surface, and Eq. (6) accordingly takes the form

$$\iint_{\Gamma_c} \alpha_3(\mathbf{y}) \frac{\partial^2}{\partial \mathbf{n}_\mathbf{x} \partial \mathbf{n}_\xi} \frac{1}{|\mathbf{x}-\mathbf{y}|} dS_y = -\boldsymbol{\sigma}(\mathbf{u}_0(\mathbf{x})) \cdot \mathbf{n} = Mq(\mathbf{x}), M = \frac{1-\nu}{\mu} \tag{7}$$

where ν denotes Poisson's ratio, and $q(\mathbf{x})$ represents the applied load. Integrals in Eqs. (6) and (7) are interpreted in the sense of the following limiting value [18]

$$\lim_{\varepsilon_1 \to 0} \iint_{\Gamma_c} \alpha_3(\mathbf{y}) \frac{\partial^2}{\partial \mathbf{n}_\mathbf{x} \partial \mathbf{n}_\xi} \frac{1}{|\mathbf{x}'-\mathbf{y}|} dS_y, \tag{8}$$

where $\mathbf{x}' = \mathbf{x} + \varepsilon_1 \mathbf{n}$.

In fracture mechanics, stress intensity factors are describing stress and displacement fields near a crack tip. They are essential for predicting crack propagation and structural failure. For mode I (opening) cracks, only the stress intensity factor K_1 is relevant. Its determination reduces to evaluating the displacement discontinuity $u_3(\mathbf{y})$ as follows:

$$K_1(\mathbf{x}) = \lim_{r \to 0} \sqrt{\pi/2r} \frac{\mu}{1-\nu} u_3(\mathbf{y}). \tag{9}$$

Here $r = |\mathbf{x} - \mathbf{y}|$ denotes the distance between the point $\mathbf{y}$, located in the vicinity of the crack, and the point $\mathbf{x}$ on the crack contour. Within the BEM framework, we have $\lim_{\mathbf{y} \to \mathbf{x}} u_3(\mathbf{y}) = \alpha_3(\mathbf{x})/2$, with $\alpha_3(\mathbf{x})$ defined as the solution of Eq. (7).

Let the domain Γ_c be an ellipse $x_1^2/a_1^2 + x_2^2/a_2^2 = 1$, Fig. 1a). An analytical solution is obtained below for the hypersingular integral Eq. (7) with unit right-hand side. As shown in [21], if the density vanishes at the boundary of the integration domain and its derivatives satisfy the Hölder condition throughout the domain Γ_c, Eq. (7) can be rewritten in the following form:

$$I(\mathbf{x}) = \frac{1}{4\pi} \iint_{\Gamma_c} \frac{(\nabla \alpha_3(\mathbf{y}) \cdot \mathbf{r})}{r^3} dS_y = 1, \mathbf{r} = \mathbf{x} - \mathbf{y}, r = |\mathbf{r}| \tag{10}$$

The solution to Eq. (10) will be sought as

$$\alpha_3(\mathbf{y}) = Cg(y_1, y_2)g(y_1, y_2) = \sqrt{1 - \frac{y_1^2}{a_1^2} - \frac{y_2^2}{a_2^2}} \tag{11}$$

with partial derivatives obtained as $\frac{\partial \alpha_3(\mathbf{y})}{\partial y_i} = -C/g((y_1, y_2)$. Substituting these expressions into Eq. (10) and transforming to the polar coordinate system $y_1 - x_1 = \rho cos\varphi$, $y_1 - x_1 = \rho sin\varphi$, we receive

$\alpha_3(\rho, \varphi) = C\sqrt{K}\sqrt{\tau_0^2 + M - (\rho + \tau_0)^2}, r = \rho, \tau_0 = P/K,$

$P = \frac{x_1}{a_1^2} cos\varphi + \frac{x_2}{a_2^2} sin\varphi$, $K = \frac{\cos^2\varphi}{a_1^2} + \frac{\sin^2\varphi}{a_2^2}$, $M = \left(1 - \frac{x_1^2}{a_1^2} - \frac{x_2^2}{a_2^2}\right)/K.$

Note that $K > 0 \forall \varphi$, and $M > 0$ inside the ellipse. Introduce the following notation $l = \sqrt{\tau_0^2 + M}$. Since $P(\varphi) = -P(\varphi + \pi)$; $K(\varphi) = K(\varphi + \pi)$, $\tau_0(\varphi) = -\tau_0(\varphi + \pi)$ we obtain.

$$\mathrm{I}(\tau_0) = -\frac{C}{4\pi}\left[\int_0^{\pi} \frac{Pd\varphi}{\sqrt{K}} \int_{-l}^{l} \frac{1}{(u-\tau_0)\sqrt{l^2-u^2}} du + \int_0^{\pi} Pd\varphi \int_{-l}^{l} \frac{\sqrt{K}}{\sqrt{l^2-u^2}} du\right].$$

Using the Cauchy principal value integral with Chebyshev's weight [22], we arrive at.

$\mathrm{I}(\tau_0) = -\frac{C}{2a_1a_2}\int_0^{\pi/2} \sqrt{a_2^2 \sin^2\varphi + a_1^2 \cos^2\varphi} d\varphi.$

Determining the constant C, the analytical solution to Eq. (10) is obtained as

$$\alpha_3(\mathbf{x}) = -\frac{2a_2}{E(k)} g(x_1, x_2), k = \sqrt{1 - a_2^2/a_1^2}, a_1 > a_2 \tag{12}$$

where $E(k)$ is second kind complete elliptic integral.

After evaluating the limit and performing the necessary algebraic transformations, and using (9) with $\mathrm{q}(\mathbf{x}) = \sigma$, together with (12), the following expression for the stress intensity factor was obtained

$$\mathrm{K}_1(\varphi) = \frac{\sigma\sqrt{\pi a_2}}{\mathrm{E(k)}} \left(\frac{a_2^2}{a_1^2} \cos^2\varphi + \sin^2\varphi\right)^{\frac{1}{4}} \tag{13}$$

This analytical value will be used below at benchmark testing evaluations.

4 Numerical Results and Discussion

4.1 Benchmark Tests

After determining the zones of maximum stress concentration from the stress–strain analysis of the structural element, representative model cracks are introduced into these regions. In this study, the planar cracks with elliptical and rectangular shapes are adopted as model cracks.

An elliptical crack in 3D body, shown in Fig. 1, subjected to uniaxial tensile stress σ, is analyzed first. Both BEM and FEM are employed for the SIF numerical estimation.

In the FEM analysis, the crack is modeled in a prismatic specimen of characteristic dimension L, with semi-axes $a_1 = 3$ mm, and $a_2 = 1$ mm, where $a_2/L = 0.005$. In the BEM analysis, the elliptical crack is considered in an unbounded body. Table 1 presents a comparative overview of the stress intensity factor (SIF) data obtained using the BEM and FEM with the analytical solution given by Eq. (13). For the FEM analysis, 45600 finite elements were used, whereas the BEM employed 4450 and 9450 boundary elements. The corresponding meshes are schematically shown in Figs. 1a) and 1b).

Table 1. Comparison of dimensionless $K_1/(2\sigma\sqrt{a_2})$ numerical evaluations.

Degrees φ	Analytical value, (13)	BEM, HIE, (7), 4450 elements	BEM, HIE, (7), 9450 elements)	FEM
0	0.918819	0.9194332	0.918820	0.919006
30	1.2092340	1.2100740	1.20925631	1.2100023
60	1.4945297	1.4947027	1.49453001	1.4947897
90	1.5914415	1.5915562	1.59144230	1.5914547

The findings are of notable practical importance, offering a quantitative basis for selecting the appropriate number of finite elements and defining the optimal mesh density in both BEM and FEM.

We now turn to the case of an infinite body containing a flat crack shaped as a square region S (Fig. 2a).

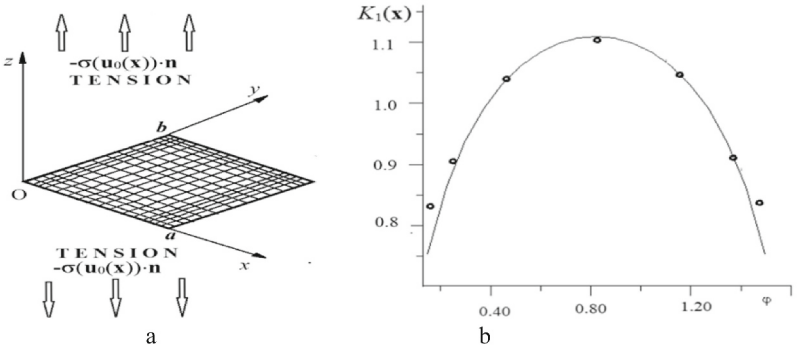

Fig. 2. Modal rectangular crack: a) BEM discretization, b) comparison of the computed $K_1(x)$ with data from [2].

The determination of the SIF is reduced to solving the hypersingular integral Eq. (7). This problem was earlier addressed in [2], where an affine transformation was used to map the domain S onto the interior of a unit circle. The square crack was defined as $S = \{0 \le x_1 \le 1;\ 0 \le x_2 \le 1\}$. It was assumed that $q(\mathbf{x}) = \sigma$. Figure 2b presents

$K_1(\mathbf{x})$ computed using the proposed BEM, with the rectangular domain discretized into 9409 boundary elements based on prior elliptical crack results. The solid curve shows $K_1(\mathbf{x})$ from [2], while points represent the present BEM results, demonstrating good agreement.

For the rectangular crack, the maximum dimensionless SIF is 1.091, varying along the crack front, whereas for the elliptical crack it reaches 1.591. Therefore, the elliptical crack is used in subsequent fatigue life evaluations.

4.2 Crack Propagation in Power Machine Units

This analysis focuses on evaluating the structural strength and remaining service life of a steam turbine engine blade operating under steady rotational conditions at 3450 RPM. The blade is subjected to substantial centrifugal loading resulting from high-speed rotation. It is rigidly secured to a disk of 1 m radius via a precision locking mechanism, as depicted in Fig. 3a.

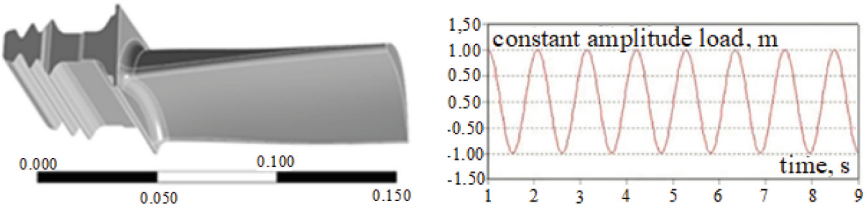

a) b)

Fig. 3. Stream turbine blade: a) geometrical model, b) loading distribution

Figure 3a presents a simplified model of a steam turbine blade with a locking mechanism and a root fillet. The blade, made of 12X13 steel ($\rho = 7720$ kg/m3, $E = 209$ GPa, $\nu = 0.3$, yield strength 580–620 MPa), has a height of 120 mm, length of 50 mm, maximum thickness of 10 mm, and with a total height of 175 mm including the locking mechanism. Rotating at 3450 RPM, it is rigidly attached to a 1 m radius disk, producing centrifugal forces. A stationary cyclic load (Fig. 3b) was applied, and the stress–strain state of the uncracked blade was analyzed using FEM with a tetrahedral mesh comprising approximately 124000 elements (Fig. 4a). The maximum stress, 206 MPa, occurred at the blade root near the fillet (Fig. 4b), remaining below the yield strength and indicating long service life and sufficient strength. Fatigue analysis under cyclic loading (stress ratio –1 to 1) predicted a life exceeding 10^6 cycles.

To assess the reliability of the results, a model crack in the form of a flat elliptical flaw, with radii of 0.0001 mm and 0.0003 mm, was introduced in the region of maximum stress. This results in the boundary value problem described by Eqs. (4)-(5), corresponding to the crack analysis in an infinite body. The HIE (7), was then employed, with the right-hand side defined as $q(\mathbf{x}) = 206.0$. Subsequently, after determining the stress intensity factors, Paris' law was applied to calculate the number of cycles to failure

$$N = \frac{1}{C}(\Delta K - \Delta K_{th})^{-n} da_2, \; \Delta K_{th} < \Delta K < K_{1C} \tag{14}$$

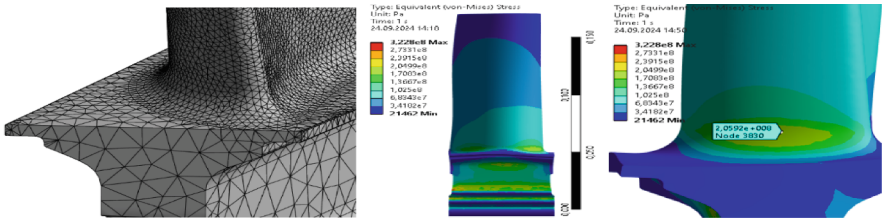

a) b)

Fig. 4. Finite element mesh (a) and equivalent stress distribution (b)

Here, $\Delta K = 2\max K_1(\mathbf{x})$, $C = 3.2 \cdot 10^{11}$ MPa $\sqrt{m}$, $n = 3.09$, K_{1C}= 31MPa $\sqrt{m}$, ΔK_{th}= 7.4MPa $\sqrt{m}$. We integrate Eq. (14), supposing $\frac{a_2}{a_2} = 3$, from the initial crack radius a_2=0.0003 mm to the final value a_2=3 mm, which is considered unacceptable according to standard inspection criteria. Accordingly, the number of cycles to failure was found to be $N = 5\ 10^6$.

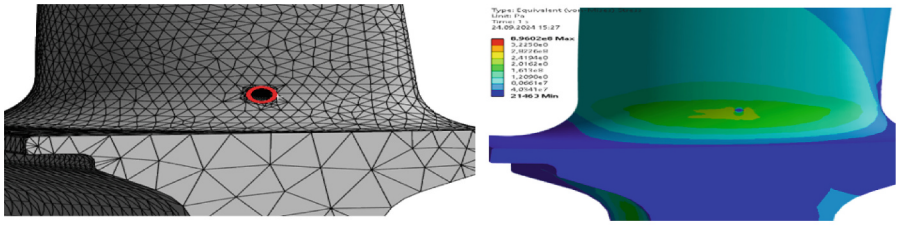

a b

Fig. 5. Finite element mesh of gas turbine blade with the elliptical crack (a) and von Mises equivalent stress distribution (b).

Next, an elliptical crack with semi-axes $a_1 = 3$ mm and $a_2 = 1$ mm is introduced into the region of near-maximum stresses using FEM (Fig. 5a), and the corresponding blade response is analyzed (Fig. 5b). The computed von Mises equivalent stress field in the cracked model closely resembles that of the intact blade. However, a pronounced local stress concentration develops near the crack, reaching a maximum of 896 MPa, while the minimum stress preserves both its magnitude and location (Fig. 5b).

Under cyclic loading with an amplitude of –1 to 1, fatigue analysis showed that the blade material outside the crack maintained a service life exceeding 10^6 cycles. In contrast, a pronounced reduction in fatigue life was observed within the crack-affected zone (Fig. 6). The minimum number of cycles to failure, as few as 315, occurred in the regions of highest stress concentration along the crack front. Although the applied loading was uniform and cyclic, real non-stationary loads can exert an even stronger influence on residual strength and fatigue life. A single overload may cause significant damage, whereas operation under realistic conditions with smaller load fluctuations can help preserve structural integrity.

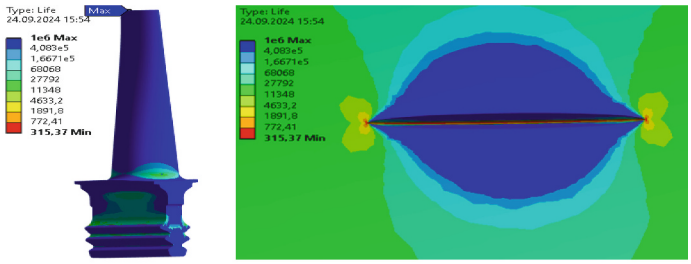

a b

Fig. 6. Fatigue life distribution across the blade: (a) entire blade, (b) crack vicinity.

5 Conclusion and Future Research

The methodology for predicting the fatigue life of structures with stress concentrators has been developed and validated through benchmark simulations of planar cracks. Test calculations established the necessary number of both boundary and finite elements to ensure accurate evaluation of stress intensity factors and the stress–strain state. Application to the turbine blade demonstrated a pronounced reduction in fatigue life in highly stressed regions with cracks. The approach will be further extended to a wider range of structural components and more complex crack geometries.

Acknowledgments. The authors are very thankful to professor Alexander Cheng (Wessex Institute of technology for his constant collaboration.

References

1. Guz, A.N., Bogdanov, V.L., Nazarenko, V.M.: Fracture of Materials Under Compression Along Cracks, Springer, Advanced Structured Materials, Cham, vol. 138 (2020). https://doi.org/10.1007/978-3-030-51814-1
2. Zhang, L., et al.: Methods for fatigue-life estimation: a review of the current status and future trends. Nanotechnol. Precis. Eng. **6**, 025001 (2023). https://doi.org/10.1063/10.0017255
3. Li, T., Li, S., Cao, B., Zhao, X., Kang, Y., Li, H.: Review of fatigue life. In: 2022 3rd International Conference on Advanced Electrical and Energy Systems (AEES), pp. 207–212. Lanzhou, China (2022). https://doi.org/10.1109/AEES56284.2022.10079522
4. Rusanov, R., Subotin, V., Rusanov, A., Shvetsov, V., Palkov, S., Palkov, I., Chugay, M.: Application of innovative solutions to improve the efficiency of the low-pressure cylinder flow part of a 1000 MW steam turbine for nuclear power plant. Arch. Thermodynamics, **45**(4), 141−152 (2024). https://doi.org/10.24425/ather.2024.152003
5. Khoryev, O., Korotaiev, P., Agibalov, Y., Bykov, Y., Maksymenko-Sheiko, K.: Experimental Studies of Pump-Turbine Flow Part Models at Heads of 80–120 m. Lecture Notes in Mechanical Engineering, pp. 24−33 (2023). https://doi.org/10.1007/978-3-031-18487-1_3
6. Sierikova, O., Strelnikova, E., Degtyariov, K.: Numerical simulation of strength and aerodynamic characteristics of small wind turbine blades. In: Nechyporuk, M., Pavlikov, V., Kritskiy, D. (eds.) Integrated Computer Technologies in Mechanical Engineering - 2022. ICTM 2022. Lecture Notes in Networks and Systems, vol. 657. (2023). Springer, Cham. https://doi.org/10.1007/978-3-031-36201-9_31

7. Zaitsev, B.P., Protasova, T.V., Smetankina, N.V., Klymenko, D.V., Larionov, I.F., Akimov, D.V.: Oscillations of the payload fairing body of the cyclone-4M launch vehicle during separation. Strength Mater. **52**, 849–863 (2020). https://doi.org/10.1007/s11223-021-00239-5
8. Moskalenko, R., Zaydenvarg, O., Strelnikova, O., Gnitko V.: Software development for the computational analysis of crack propagation and durability of structures. In: 2020 IEEE KhPI Week on Advanced Technology (KhPIWeek), pp. 509–514 (2020). https://doi.org/10.1109/KhPIWeek51551.2020.9250089
9. Fageehi, Y.A.:Prediction of fatigue crack growth rate and stress intensity factors using the finite element method. Adv. Mater. Sci. Eng. Wiley (2022). https://doi.org/10.1155/2022/2705240
10. Karaiev, A., Strelnikova, E.: Axisymmetric polyharmonic spline approximation in the dual reciprocity method. Z. Angew. Math. Mech. **101**(4), e201800339 (2021). https://doi.org/10.1002/zamm.201800339
11. Sierikova O., Strelnikova, E., Gnitko, V.V., Degtyarev, K.: Boundary calculation models for elastic properties clarification of three-dimensional nanocomposites based on the combination of finite and boundary element methods. In: 2021 IEEE 2nd KhPI Week on Advanced Technology (KhPIWeek), pp. 351–356. Kharkiv, Ukraine (2021), https://doi.org/10.1109/KhPIWeek53812.2021.9570086
12. Rusanov, A., Rusanov, R., Klonowicz, P., Lampart, P., Żywica, G., Borsukiewicz, A.: Development and experimental validation of real fluid models for CFD calculation of ORC and steam turbine flows. Mater. (Basel). **14**(22), 68–79 (2021). https://doi.org/10.3390/ma14226879
13. Kurennov, S., Smetankina, N. Stress-Strain State of a Double Lap Joint of Circular Form. Axisymmetric Model. Lecture Notes in Networks and Systems, vol. 367, pp. 36–46. Springer, Cham (2022). https://doi.org/10.1007/978-3-030-94259-5_4
14. Wysmulski, P.: Numerical and experimental study of crack propagation in the tensile composite plate with the open hole. Adv. Sci. Technol. Res. J. **17**(4), 249–261 (2023). https://doi.org/10.12913/22998624/169970
15. Zong, L., Shi, G.: Three-dimensional fatigue crack propagation analysis of welded steel beam based on global-local numerical model. Adv. Bridge Eng. **2**(4), 1–17 (2021)
16. Yi, W., Rao, Q., Li, Z., Chun-Lin, C.: A new method for predicting the crack propagation process of brittle rock under thermo-hydro-mechanical loading conditions. IEEE Access **9** (2021). https://doi.org/10.1109/ACCESS.2021.3076001
17. Zhang, J., Xu, R., He, Y., Yang, W.: Direct computation of 3-d stress intensity factors of straight and curved planar cracks with the P-version finite element method and contour integral method. Materials **14**(14), 3949 (2021). https://doi.org/10.3390/ma14143949
18. Strelnikova, E., Choudhary, N., Degtyariov, K., Kriutchenko, D., Vierushkin, I.: Boundary element method for hypersingular integral equations: Implementation and applications in potential theory. Eng. Anal. Boundary Elements, **169**, Part B, 105999 (2024), https://doi.org/10.1016/j.enganabound.2024.105999
19. Ren, Y., Dong, Y., Liu, B., Zhao, S., Yang, R.: Research on low stress high temperature precision shear separation process of metal bars. Heavy Mach. **05**, 37–41 (2021). https://doi.org/10.1016/j.tafmec.2021.103017
20. Braun, M., Claas Fischer, C., Baumgartner J., Hecht, M., Varfolomeev, I.: Fatigue crack initiation and propagation relation of notched specimens with welded joint characteristics. Metals **12**, 615, 1–24, (2022). 10.3390/ met12040615
21. Qin, X., Yan, Y., Li, H., Lei, W.: A direct method for solving singular integrals in three-dimensional time-domain boundary element method for elastodynamics. Mathematics **10**(2), 286 (2022). https://doi.org/10.3390/math10020286
22. Li, C.: On the evaluation of oscillatory kind with cauchy principal value. J. Appl. Math. Phys. **9**, 976–981 (2021). https://doi.org/10.4236/jamp.2021.95067

Sloshing Dynamics and Stability of Fuel Tanks Under Short-Duration High-Intensity Loads

Neelam Choudhary[1], Vasyl Gnitko[2], Andry Kolodiazhnyi[2], Denis Kriutchenko[2(✉)], and Elena Strelnikova[2,3,4]

[1] School of Artificial Intelligence, Bennett University, Greater Noida 201310, Uttar Pradesh, India

[2] A. Pidhornyi Institute of Power Machines and Systems NAS of Ukraine, Kharkiv, Ukraine
wollydenis@gmail.com

[3] V.N. Karazin Kharkiv National University, Svobody sq., 4, Kharkov 61022, Ukraine

[4] Kharkiv National University of Radio Electronics, Nauky Ave, 14, Kharkiv 61166, Ukraine

Abstract. This study investigates the stability of liquid movement in tanks subjected to combined horizontal and vertical periodic loads, with particular emphasis on damping effects. The liquid is modeled as incompressible, inviscid, and irrotational, reducing the governing equations to the Laplace formulation with kinematic and dynamic free-surface conditions. By exploiting rotational symmetry, the problem is simplified to one-dimensional singular equations, which are solved using a boundary element method combined with the normal mode approach. Spectral analysis yields natural frequencies and vibration modes of the liquid in a rigid shell, forming the basis for equations that describe free-surface dynamics. Since in-flight loads cannot be precisely defined, fuzzy logic is employed to capture uncertainty, and stability regimes are determined under vertical and combined excitations. The modeling approach neglects the influence of internal baffles, compressibility of the gas above the liquid, and capillary effects, which are left for future research. Rayleigh damping is incorporated, demonstrating that even minor damping coefficients significantly reduce surface oscillations. The analysis underlines that damping plays a decisive role in suppressing sloshing instabilities and ensuring the structural reliability of launch vehicle fuel tanks.

Keywords: Sloshing · Stability · Damping Effects · Internal Liquid

1 Introduction and Literature Review

Fuel tanks in aerospace structures are usually subjected to impact loads from collisions or rapid acceleration. Owing to their stochastic nature, these loads are better modeled with probabilistic methods than with purely deterministic approaches [1]. Since full-scale testing is costly and hazardous, computational simulations have become the primary tool for analyzing tanks, typically designed as shells of rotation partially filled with liquids [2, 3]. Numerical methods such as the finite element method [4], boundary element method (BEM) [5], *R*-functions [6], mesh-free methods [7], and series expansions [8]

H. Altenbach et al. (Eds.): CAMPE 2025, LNME, pp. 200–210, 2026.
https://doi.org/10.1007/978-3-032-16381-3_19

are widely used to study sloshing and fluid-structure interaction, providing essential insights into vibrational characteristics that affect structural integrity and flight stability. Mitigation strategies, including baffles, partitions, and covers, have been explored extensively, with numerical and analytical methods presented in [9–11]. Sloshing in prismatic tanks was investigated in [12], elliptical geometries were examined in [5], and the effectiveness of baffles in suppressing sloshing-induced instabilities was evaluated in [7]. Experimental insights into liquid damping effects under vertical excitation are provided in [13], which studied a single-degree-of-freedom (SDOF) vertical sloshing tank, highlighting the role of damping in stabilizing dynamic responses. Additionally, [14] employed δ-SPH with pressure correction algorithms to simulate intense sloshing flows in rectangular tanks, offering a robust numerical approach for modeling nonlinear sloshing under high-intensity loads. Broader investigations into shell stability, combining theoretical and experimental approaches, are detailed in [15]. A comprehensive analysis of linear dynamics in elastic containers filled with compressible (acoustic) liquids, including sloshing and capillary effects at the free surface, was presented in [16]. A pivotal contribution to the field comes from Roger Ohayon, whose works have significantly advanced the understanding of fluid-structure interactions under high-intensity loads. In [16], a groundbreaking framework for reduced-order modeling of vibroacoustic systems was introduced, providing efficient computational strategies for analyzing sloshing in fuel tanks subjected to short-duration, high-intensity loads. This work emphasized the coupling between liquid sloshing and structural vibrations, offering robust methodologies for aerospace applications. Further, in [17] this framework was extended to incorporate uncertainty quantification, addressing variability in loading conditions through advanced numerical techniques, which aligns closely with the fuzzy logic approach adopted in the present study. These contributions provide a foundation for modeling complex sloshing dynamics while highlighting the need for computational efficiency in practical engineering scenarios.

The present study builds upon these advancements by analyzing liquid oscillations in fuel tanks with Rayleigh damping incorporated, a factor underexplored in prior works. By demonstrating that even small damping coefficients can stabilize regimes near parametric resonance, this work introduces a novel perspective on achieving stability under dynamic loading. Furthermore, the study integrates fuzzy logic to assess the probability of instability when uncertainties in initial conditions and loading parameters are considered, extending the uncertainty quantification approaches of [18]. This finding underscores the critical role of damping devices, such as baffles and floating covers, in enhancing tank stability, offering a practical contribution to fuel tank design that complements and extends the previous foundational works in the area.

2 Research Methodology

2.1 Crisp Boundary Value Problem Formulation

An analysis is conducted for rigid rotational shells partially occupied by liquid (Fig. 1). Let S_1 denote the shell wetted surfaces, and S_0 is the liquid free surface. It is assumed that the liquid behaves as an inviscid, incompressible fluid, with irrotational movement inside the shell. Surface tension effects are neglected, as confirmed by the Bond number Bo

$= \rho_l g L^2/\sigma$. For $L \approx 1$ m, $\rho_l \approx 1000$ kg/m^3, g $= 9.81$ m/s^2, and $\sigma \approx 0.07$ N/m, taken here as representative values, Bo $\approx 10^5$ is obtained, indicating that gravity overwhelmingly governs the free-surface dynamics. Low-gravity effects are beyond the scope of this study. Owing to the absence of vorticity, a scalar velocity potential Φ exists such that $\mathbf{V} = \nabla\Phi$. This potential satisfies the Laplace equation within the domain Ω containing the liquid. The liquid pressure p is then determined as [10]:

$$\frac{p}{\rho_l} = -\frac{\partial \Phi}{\partial t} - (g + a_v(t))z + a_h(t)x + \frac{p_0}{\rho_l}. \tag{1}$$

Here, x and z coordinates of a point within the liquid domain Ω. The functions $a_h(t)$ and $a_v(t)$ represent the lateral and longitudinal terms of the external forcing acceleration, typically defined with inherent uncertainties, their characterization requires the application of fuzzy mathematical concepts. An important aspect of the problem is the interaction between vertical and horizontal loading.

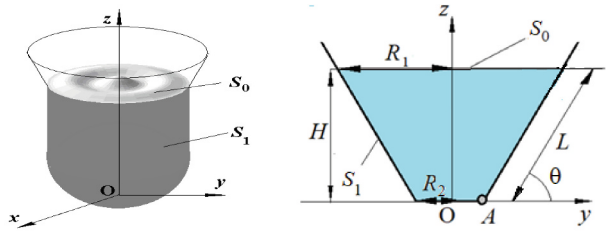

Fig. 1. Fluid-filled shell of rotation (a) and its draft (b)

The conditions prescribed on the boundary of Ω for Laplace's equation are specified as detailed below: on the wetted surface S_1, the no-slip condition is imposed, while on the free surface S_0, conditions of a kinematic as well as a dynamic nature need to be met.

Under these assumptions, the following problem is expressed as a boundary value problem (BVP) governed by the Laplace's equation for the velocity potential Φ, which is coupled with the elevation function ζ through the kinematic boundary condition:

$$\nabla^2\Phi = 0, \left.\frac{\partial \Phi}{\partial \mathbf{n}}\right|_{S_1} = 0, \left.\frac{\partial \Phi}{\partial \mathbf{n}}\right|_{S_0} = \frac{\partial \zeta}{\partial t}, p - p_0|_{S_0} = 0. \tag{2}$$

Here, p_0 is the atmospheric pressure, and $\mathbf{n}$ is the unit outward normal to the corresponding surface. The function $\zeta = \zeta(t, x, y)$, which is to be determined, characterizes the time-dependent displacement and shape of the free surface.

2.2 The Method of Defined Normal Modes

Within the framework of the normal mode method, the unknown functions Φ and ζ for shells of revolution are represented in the cylindrical system (r, θ, z), as

$$\Phi(r, \theta, z, t) = \sum_{k=1}^{n} \sum_{j=0}^{m} \dot{d}_{kj}(t)\varphi_{kj}(r, z)\cos(j\theta), \tag{3}$$

$$\zeta(r,\theta,t)=\sum\nolimits_{k=1}^{n}\sum\nolimits_{j=0}^{m}d_{kj}(t)\zeta_{kj}(r)\cos(j\theta). \tag{4}$$

Here, j denotes the wave number, and the time-dependent coefficients $d_{kj}(t)$ remain unknown. The basis functions $\zeta_{kj}(r)$ and $\varphi_{kj}(r,z)$ are obtained as results of solving the linear spectral BVP, as described in [18]

$$\nabla^2\varphi_{kj}=0,\frac{\partial\varphi_{jk}}{\partial\mathbf{n}}=0\Big|_{S_1},\frac{\partial\varphi_{kj}}{\partial\mathbf{n}}=\frac{\partial\zeta_{kj}}{\partial t}\Big|_{S_0}. \tag{5}$$

In the linear formulation, one obtains

$$\zeta_{kJ}(r)=\frac{\partial_{\varphi kJ}(r,z)}{\partial z}\Big|_{S_0}=\frac{\chi_{kj}^2}{g}\varphi kj(r,H), \tag{6}$$

where χ_{kj} are the fundamental frequencies, and H denotes the equilibrium free-surface level. Consequently, the function $\zeta(r,\theta,t)$ can be represented as follows:

$$\zeta(r,\theta,t)=\frac{1}{g}\sum\nolimits_{k=1}^{n}\sum\nolimits_{j=1}^{m}\cos(j\theta)\chi_{kj}^2\varphi kj(r,H)d_{kj}(t). \tag{7}$$

Thus, problem (5) is reduced to the basis functions $\varphi_{kJ}(r,z)$ calculation.

Green's third identity is used to represent the potentials φ_{kj}. For brevity, the indices kl are omitted. In combination with the boundary conditions of the Laplace Eq. (5), this results in a system of singular integral equations [18]

$$2\pi\varphi(z_0)+\int_\Gamma\varphi(z)\Theta(z,z_0)r(z)d\Gamma-\frac{\chi^2}{g}\int_0^R\varphi(\rho)\Xi(P,P_0)\rho d\rho=0,P_0\in S_1, \tag{8}$$

$$2\pi\varphi(\rho_0)+\int_\Gamma\varphi(z)\Theta(z,z_0)r(z)d\Gamma-\frac{\chi^2}{g}\int_0^R\varphi(\rho)\Xi(P,P_0)\rho d\rho=0,P_0\in S_0.$$

$$\Theta(z,z_0)=4/\sqrt{a+b}\left\{\frac{1}{2r}\left[\frac{r^2-r_0^2+(z_0-z)^2}{a-b}E_l(k)-F_l(k)\right]n_r+\frac{z_0-z}{a-b}E_l(k)n_z\right\},$$

$$\Xi(P,P_0)=4/\sqrt{a+b}\,F_l(k),a=r^2+r_0^2+(z-z_0)^2,b=2rr_0.$$

For the numerical evaluation of the generalized elliptic integrals $E_l(k)$, $F_l(k)$ in Eqs. (8), an efficient computational procedure is employed [18].

Let the basis functions $\varphi_{kJ}(r,z)$ be determined. Substituting them into expressions (3) and (4) and subsequently into the dynamic condition on S_0, yields the following system of second-order ordinary differential equations, supposing that an artificial damping, as proposed in [19], is incorporated

$$\ddot{d}_{k0}(t)+2\omega_{k0}c\dot{d}_{k0}(t)+\omega_{k0}^2\left(1+\frac{a_v(t)}{g}\right)d_{k0}(t)=0, \tag{9}$$

$$\ddot{d}_{k1}(t)+2\omega_k1c\dot{d}_{k1}(t)+\omega_{k1}^2\left(1+\frac{a_v(t)}{g}\right)d_{k1}(t)+a_h(t)F_{k1}=0,$$

$$\ddot{d}_{kl}(t) + 2\omega_{kl} c \dot{d}_{kl}(t) + \omega_{kl}^2 \left(1 + \frac{a_v(t)}{g}\right) d_{kl}(t) = 0, l = \overline{2, m}.$$

In Eqs. (9), $k = \overline{1, n}$, the parameter c denotes the damping coefficient, and $F_{k1} = (r, \varphi_{k1})/(\varphi_{k1}, \varphi_{k1})$. In this study, c is chosen to represent a low damping regime [20].

To ensure a unique solution of system (9), the initial conditions are specified as

$$d_{kl}(t) = d_{kl}^0, \dot{d}_{kl}(t) = d_{kl}^1 = q_1, k = \overline{1, n}, l = \overline{0, m}. \tag{10}$$

Following [18], the accelerations, $a_h(t)$ and $a_v(t)$, are expressed as $a_x(t) = a_0 \cos(\omega_h)$, $a_z(t) = a_1 \cos(\omega_v t)$. In the fuzzy formulation, we assume $\omega_h = \omega_v = f_0$. Consequently, the deterministic problem is reformulated as the system of differential Eqs. (9) subject to boundary conditions (10), parameterized by $f_0, q_1, a_0, \overline{a_1}$, $(\overline{a_1} = a_1/g)$, and the damping coefficient c.

2.3 Simulation of Liquid Vibrations in Reservoirs by Fuzzy Techniques

To move from a crisp to a deterministic formulation for rigid shells with liquid under horizontal and vertical loading, exact values are assigned to all governing parameters: load magnitudes, frequencies, and boundary conditions, eliminating uncertainty. In this crisp formulation, parameters are fixed and precisely known, and the system's response is obtained from deterministic Eqs. (9). In contrast, the fuzzy formulation treats the loading parameters as fuzzy sets with triangular membership functions, introducing uncertainty and requiring fuzzy arithmetic and interval analysis [18, 21]. Instead of a single deterministic result, this approach yields a bounded range of possible responses. The deterministic parameters $f_0, q_1, a_0, \overline{a_1}, \overline{a_1}$ and c are fuzzified and represented as triangular fuzzy numbers $D = (d_1, d_2, d_3)$ with non-axisymmetric membership functions $\mu_D(x)$ defined as

$$\mu_D(x) = \begin{cases} (x - d_1)/(d_2 - d_1), & d_1 < x \le d_2 \\ (d_3 - x)/(d_3 - d_2), & d_2 < x \le d_3 \\ 0, & x < d_1, \quad x > d_3 \end{cases}$$

The corresponding crisp intervals B_α, obtained via the α-cut operation, are expressed as $D_\alpha = \left[d_1^{(\alpha)}, d_3^{(\alpha)}\right]$, $d_1^{(\alpha)} = (d_2 - d_1)\alpha + d_1, d_3^{(\alpha)} = (d_2 - d_3)\alpha + d_3$. This formulation enables the fuzzification of the crisp parameters as follows:

$$f_0 \leftrightarrow F_0 = (f_{01}, f_{02}, f_{03}), \; q_1 \leftrightarrow Q_1 = (q_{11}, q_{12}, q_{13}), \; c \leftrightarrow C = (c_1, c_2, c_3), \tag{11}$$

$$a_0 \leftrightarrow A_0 = (a_{01}, a_{02}, a_{03}), \quad \overline{a_1} \leftrightarrow A_1 = (a_{11}, a_{12}, a_{13}).$$

Using these fuzzified parameters, system (9) is solved numerically as in [21]. Consequently, the α-cut intervals of the function ζ are computed for various α values, facilitating the analysis of uncertainties in estimating the free surface elevation.

3 Numerical Results and Discussion

3.1 Spectral Boundary Value Problem

The spectral BVP for a truncated conical rigid shell (Fig. 1b) is solved using BEM [18] to obtain fundamental mode shapes and frequencies of the contained liquid. The liquid domain is characterized by a cone angle $\theta = \pi/6$, a top radius $R_1 = 1$, and various base radii R_2 (see Table 1), with liquid height defined as $H = (R_1 - R_2)\cot(\theta)$, (Fig. 1b). Numerical results are validated against reference data from [22] (Table 1).

Table 1. Frequency parameter $\omega_k^2 = \chi_k^2/g$

	Frequency parameter $\omega_k^2 = \chi_k^2/g$			
R_2	0.2	0.6	0.8	0.9
$j = 0, k = 1$				
[22]	3.3868	3.3821	3.1392	2.1871
BEM	3.3871	3.3870	3.1411	2.1832
$j = 1, k = 1$				
[22]	1.3042	1.2546	0.9342	0.5429
BEM	1.3051	1.2581	0.9413	0.5641
$j = 2, k = 1$				
[22]	2.2639	2.2558	2.0157	1.3613
BEM	2.2651	2.2592	2.0280	1.3950

Numerical simulations used 150 boundary elements on the conical surface and 120 on the free surface and bottom radii. Further refinement had negligible effect, confirming convergence. Simulations for vibration modes $j = 0, 1, 2$ across various R_2 values showed close agreement with reference data, validating the method. These modes, corresponding to the lowest natural frequencies, dominate the dynamic response under forced excitation [22].

3.2 Forced Vibrations of Liquid: Deterministic Formulation

The free-surface response was computed for a range of parameters a_h, a_v and ω_h, ω_v. The analysis first addresses vertical excitation with $R_2 = 0.6$ m, and with the damping ratio $c = 0$. The resulting phase trajectories in the $(\zeta, \zeta^{\cdot})$ plane are depicted in Fig. 2. Figure 2a corresponds to the case $a_0 = 0, a_1 = 1\,\mathrm{m/sec^2}$, $\omega_v = 1$ Hz. Figures 2b and 2c illustrate the response for $a_0 = 0, a_1 = 1\,\mathrm{m/sec^2}$ with $\omega_v = 1.254$ Hz and $\omega_v = 2.508$ Hz, respectively. The results demonstrate that the motion remains stable in the first two cases; however, at $\omega_v = 2.508$ Hz, the system exhibits unbounded growth in amplitude, denoting the initiation of parametric resonance, when the excitation frequency is twice the liquid fundamental frequency.

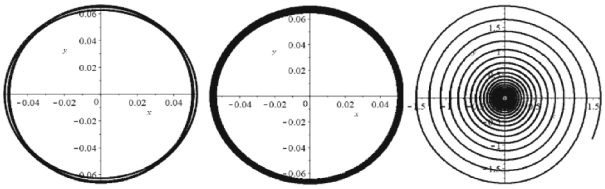

a b c

Fig. 2. Phase portraits of the free-surface elevation response to vertical excitation

We then extend the analysis to the case of combined vertical and horizontal excitation. The corresponding phase portraits are presented in Fig. 3 in the $(\zeta, \dot{\zeta})$ phase space.

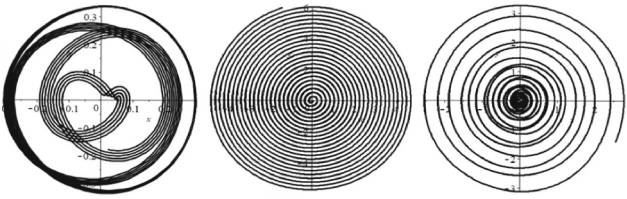

a b c

Fig. 3. Phase portraits of liquid motion subjected to lateral and longitudinal excitations

The parameters of the combined load corresponding to the phase portraits in Fig. 3 are as follows: (a) $a_0 = 0.1\,\mathrm{m/sec^2}, a_1 = 1\,\mathrm{m/sec^2}, \omega_h = \omega_v = 1\,\mathrm{Hz}$, (b) $a_0 = 0.1\,\mathrm{m/sec^2}, a_1 = 1\,\mathrm{m/sec^2}, \omega_h = \omega_v = 1.254\,\mathrm{Hz}$, and (c) $a_0 = 0.1, a_1 = 1, \omega_h = \omega_v = 2.508\,\mathrm{Hz}$. Notably, in these cases an additional resonance phenomenon emerges, caused by the horizontal excitation.

3.3 Damping Effects

Next, we analyze the fluid motion under combined vertical and horizontal loads with non-zero damping.

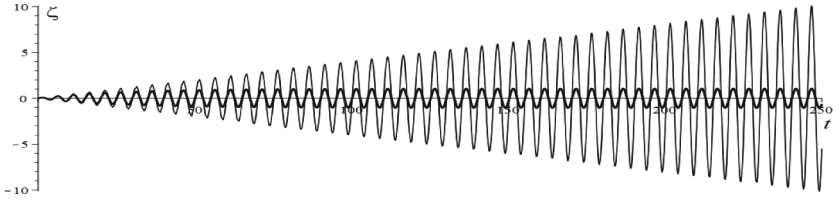

Fig. 4. Time history of the free-surface elevation for case (b)

System (9) is solved under the following initial conditions: $d_{kl}(t) = 0, \dot{d}_{kl}(t) = 0, k = \overline{2,n}, l \neq 1, \dot{d}_{11}(t) = 0.05$. The damping coefficient is specified as $c = 0.075$.

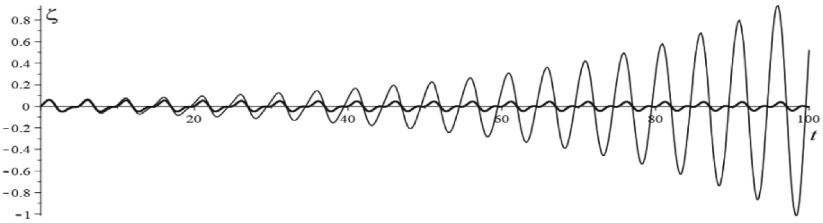

Fig. 5. Time history of the free-surface elevation for case (c)

Figures 4 and 5 present the temporal variations of the free surface at the point ($\theta = 0$, $r = R$). The gray curves correspond to solutions of the undamped system of differential Eqs. (9), whereas the black curves represent solutions of the damped system with Rayleigh damping $c = 0.075$. Although this damping coefficient corresponds to a low damping level, a pronounced reduction in oscillation amplitude is observed in all cases.

3.4 Numerical Solution of Fuzzy Initial Value Problem

Let the fuzzy numbers corresponding to the parameters f_0, q_1, a_0, and, $\overline{a_1}$ be defined as following triangular numbers:

$$f_0 \leftrightarrow F_0 = (1, 2.5, 3), \qquad c \leftrightarrow C = (0.05, 0.075, 0.1),$$

$$a_0 \leftrightarrow A_0 = (0.05, 0.1, 0.5), \qquad \overline{a_1} \leftrightarrow A_1 = (0.05, 0.1, 1.0).$$

Here, short-term loads are considered in the form:

$$a_h(t) = \begin{cases} a_0 \cos(\omega_h), & t \le T \\ 0, & t > T \end{cases}, \quad a_v(t) = \begin{cases} a_1 \cos(\omega_v), & t \le T \\ 0, & t > T \end{cases}.$$

In the numerical simulations, the load duration was set to $T = 10$ s.

The choice of triangular fuzzy numbers is motivated by the following considerations. The driving-force frequency becomes particularly critical when it approaches the first natural frequency or its double. Moreover, the amplitudes of the driving force are increased by an order of magnitude relative to those used in standard calculations, allowing for an assessment of the most hazardous conditions during flight. Additionally, the initial velocity q_1 is considered. In most cases, the free-surface motion is assumed to start from rest. However, since small disturbances are always possible, the initial velocity q_1 is represented as a fuzzy number, defined as $Q_1 = (0.01, 0.05, 0.075)$.

To account for uncertainties in loading, system (9) is modeled with fuzzy parameters in its right-hand side, representing the forcing terms, and fuzzy initial conditions, reflecting imprecise initial states. These fuzzy parameters are expressed as fuzzy sets, capturing the range of possible values with associated membership degrees. The system is solved using advanced numerical methods, including finite difference schemes and iterative solvers, as developed in [18, 21], which are adapted to handle interval arithmetic

for α-cut representations. These methods ensure robust convergence and high accuracy despite the system's nonlinearities and uncertainties. This procedure yields the α-cut intervals for the function ζ at different α levels, enabling a comprehensive assessment of the uncertainties introduced by wind loading in estimating the free-surface rise.

The analysis shows that the most critical sloshing occurs at a probability level of 0.5 ($\alpha = 0.5$), even with substantial artificial damping. This hazardous behavior arises at an external load frequency of 2.55 Hz, roughly twice the first natural frequency.

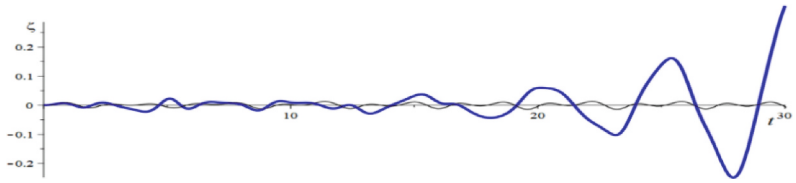

Fig. 6. Lower and upper time-dependent α-cut bounds for the function ζ

While damping reduces oscillation amplitude, increased load amplitudes can still induce abrupt, unstable free-surface dynamics. As illustrated in Fig. 6, the upper bound of the elevation at $\alpha = 0.5$ remains unsteady, highlighting the need to account for loading uncertainties. To suppress such vibrations in launch vehicle fuel tanks, damping strategies like baffles, floating covers, or advanced materials should be explored.

4 Conclusion and Future Research

This study presented a computational technique for modeling free-surface disturbances in containers under horizontal and vertical external loads, incorporating fuzzy logic to capture uncertainties in load parameters and initial conditions. Rayleigh damping was examined in detail, demonstrating its influence on the system's dynamic response. The study of fuzzy load parameters and initial conditions, utilizing α-cuts, provided valuable interval-based results that reflect the range of possible system behaviors under uncertainty, thereby enhancing the robustness and reliability of the proposed model. Future work will extend the analysis to include baffles, floating covers, and other damping devices, as well as the role of capillary effects, particularly under low gravity. Overall, the findings advance the understanding of liquid sloshing dynamics and support the development of strategies to mitigate hazardous responses in engineering applications.

Acknowledgments. We are deeply grateful to our foreign colleagues, Professors Alexander Cheng and Juri Ravnick, for their ongoing assistance and support.

References

1. Ohayon, R., Schotté, J.-S.: Advanced Computational Vibroacoustics: Reduced-Order Models and Uncertainty Quantification. Cambridge University Press, Cambridge (2019)

2. Dolgopolov, S., Nikolayev, O.: Features of mathematical modeling of nonlinear Pogo oscillations of launch vehicles. CEAS Space J. **16**(2), 32–48 (2024). https://doi.org/10.1007/s12567-024-00541-3
3. Rusanov, A., Khoryev, O., Agibalov, Y., Bykov, Y., Korotaiev, P.: Experimental research of Francis pump-turbines with splitters in a pump mode. In: 2020 IEEE KhPI Week on Advanced Technology, KhPI Week 2020 - Conference Proceedings, 9250157, pp. 183–187 (2020). https://doi.org/10.1109/KhPIWeek51551.2020.9250157
4. Bykov, Y., Kolodyazhna, L., Kostin, M., Petrov, O.: Modeling of coupled auto-oscillations of aircraft engine fan blades. In: Lytvynov, O., Pavlikov, V., Krytskyi, D. (eds.) Integrated Computer Technologies in Mechanical Engineering - 2024, ICTM 2024. LNNS, vol. 1474, pp. 553–564. Springer, Cham (2025). https://doi.org/10.1007/978-3-031-94852-7_47
5. Liu, L., Li, J.: Dynamic deformation and perforation of ellipsoidal thin shell impacted by flat-nose projectile. Materials **15**(12), 4124 (2022). https://doi.org/10.3390/ma15124124
6. Lamtiuhova, S.M.: Mathematical modeling of steady flow past circular cylinder with splitter plates by R-functions method. Int. J. Math. Phys. (2025). https://doi.org/10.26577/ijmph.202516110
7. Li, D., Xiao, H., Jin, Y.C.: Design optimization of sloshing tank using weakly compressible mesh free model. Ocean Eng. **284**, 115218 (2023). https://doi.org/10.1016/j.oceaneng.2023.115218
8. Gontarovskyi, P., Smetankina, N., Garmash, N., Melezhyk, I.: Numerical analysis of stress-strain state of fuel tanks of launch vehicles in 3D formulation. In: Nechyporuk, M., Pavlikov, V., Kritskiy, D. (eds.) Integrated Computer Technologies in Mechanical Engineering – 2020, ICTM 2020. LNNS, vol. 188, pp. 609–619. Springer, Cham (2021). https://doi.org/10.1007/978-3-030-66717-7_52
9. Liu, D., Chang, F., Wang, J.: Three-dimensional resonant sloshing in an upright cylindrical container with a ring baffle. Phys. Fluids **36**(10) (2024). https://doi.org/10.1063/5.0238525
10. Choudhary, N., Kumar, N., Strelnikova, E., Gnitko, V., Kriutchenko, D., Degtyariov, K.: Liquid vibrations in cylindrical tanks with flexible membranes. J. King Saud Univ. Sci. **33**(8), 101589 (2021). https://doi.org/10.1016/j.jksus.2021.101589
11. Liu, J., Zang, Q., Ye, W., Lin, G.: High performance of sloshing problem in cylindrical tank with various barrels by isogeometric boundary element method. Eng. Anal. Boundary Elem. **114**, 148–165 (2021). https://doi.org/10.1016/j.enganabound.2020.02.014
12. Balas, O.-M., Doicin, C.V., Cipu, E.C.: Analytical and numerical model of sloshing in a rectangular tank subjected to a braking. Mathematics **11**, 949–955 (2023). https://doi.org/10.3390/math11040949
13. Martinez-Carrascal, J., González-Gutiérrez, L.: Experimental study of the liquid damping effects on a SDOF vertical sloshing tank. J. Fluids Struct. **100**, 103172 (2021). https://doi.org/10.1016/j.jfluidstructs.2020.103172
14. Yang, H.: Numerical simulation of intense sloshing flows in a rectangular tank using δ-SPH with pressure correction algorithms. J. Fluids Struct. **108**, 103456 (2022). https://doi.org/10.1016/j.jfluidstructs.2021.103456
15. Gani, E., Öztürk, S., Sari, A., Cengiz, T.M.: Effects of liquid sloshing in storage tanks: an overview of analytical, numerical, and experimental studies. Int. J. Steel Struct. **25**, 544–556 (2025). https://doi.org/10.1007/s13296-025-00946-8
16. Ohayon, R., Soize, C., Akkaoui, Q., Capiez-Lernout, E.: Novel formulation for the effects of sloshing with capillarity on elastic structures in linear dynamics. Int. J. Numer. Meth. Eng. **122**(19), 5169–5481 (2019). https://doi.org/10.1002/nme.6290
17. Ohayon, R., Schotté, J.-S., Morand, H.: Uncertainty quantification in fluid-structure interactions for aerospace fuel tanks under dynamic loading. J. Aerosp. Eng. **36**(4), 04023045 (2023). https://doi.org/10.1061/JAEEEZ.ASENG-4567

18. Degtyariov, K., Gnitko, V., Kononenko, Y., Kriutchenko, D., Sierikova, O., Strelnikova, E.: Fuzzy methods for modelling earthquake induced sloshing in rigid reservoirs. In: 2022 IEEE 3rd KhPI Week on Advanced Technology (KhPIWeek), pp. 297–302 (2022). https://doi.org/10.1109/KhPIWeek57572.2022.9916466
19. Zhang, C., Zhu, Y., Yu, Y., Rezavand, M., Hua, X.: A simple artificial damping method for total Lagrangian smoothed particle hydrodynamics. Computational Engineering, Finance, and Science, 25 P. (2021) https://doi.org/10.48550/arXiv.2102.04898
20. Flis, L., Szwoch, G., Krawczyk, P.: Determining a damping coefficient by using a micro-electromechanical systems accelerometer for finite element method simulation purposes on a discrete damper example. Adv. Sci. Technol. Res. J. **19**(6), 275–290 (2025). https://doi.org/10.12913/22998624/202753
21. Gazi, K., Biswas, A., Singh, P.: A comprehensive literature review of fuzzy differential equations with applications. J. Fuzzy Ext. Appl. **6**(1), 134–161 (2025). https://doi.org/10.22105/jfea.2024.449970.1426
22. Raynovskyy, I.A., Timokha, A.N.: Sloshing in Upright Circular Containers: Theory, Analytical Solutions, and Applications. CRC Press/Taylor and Francis Group (2020). https://doi.org/10.1201/9780429356711

Packing of Cylindrical Nanostructures with Orientation Constraints: A Unified Geometric Model

Andrii Chuhai[1,2(✉)], Yuriy Stoyan[1], Georgiy Yaskov[1,3], Tatyana Romanova[1,3,4], and Carlos Gustavo Martínez Gomez[5]

[1] Anatolii Pidhorniy Institute of Power Machines and Systems, Str. Komunalnykiv, 2/10, Kharkiv 61046, Ukraine
Chugay.andrey80@ipmach.kharkov.ua
[2] Simon Kuznets Kharkiv National University of Economics, Nauky Ave. 9A, Kharkiv 61166, Ukraine
[3] Kharkiv National University of Radio Electronics, Nauky Ave. 14, Kharkiv 61166, Ukraine
[4] University of Leeds, Maurice Keyworth Building, Leeds LS2 9JT, UK
[5] Faculty of Mechanical and Electrical Engineering, Autonomous University of Nuevo Leon, 66455 Monterrey, Mexico

Abstract. This paper deals with the problem of packing elongated cylindrical nanostructures, such as carbon nanotubes (CNTs), into a bounded three-dimensional domain, taking into account their spatial positions and orientations. The motivation is forced by experiments that demonstrate that the orientation of carbon nanotubes influences the material's mechanical, electrical, and thermal properties. To consider these peculiarities, we introduce a geometric mathematical model that extends standard non-overlap conditions by adding angular constraints depending on orientation. The formulation is a mixed-integer nonlinear programming (MINLP) problem, where continuous and binary variables are used. It makes it possible to adjust the number of cylinders and rotation angles with respect to axis directions and manage how cylinders are oriented to each other. The solving approach uses decomposition into subsets, starts with block-coordinate initialization, and then applies continuous optimization using the IPOPT solver. Two numerical examples are given, one considering almost parallel alignment, which is essential for conductive composites, and another showing random orientations, typical for porous or entangled structures.

Keywords: cylinder · carbon nanotube · orientation angle · mixed-integer optimization · porous media · anisotropic materials

1 Introduction

Packing problems involving geometric objects within bounded domains have broad applications in materials science [1], biophysics [2], chemistry [3], and nanotechnology [4]. Problems involving the packing of cylindrical objects are of particular interest,

H. Altenbach et al. (Eds.): CAMPE 2025, LNME, pp. 211–220, 2026.
https://doi.org/10.1007/978-3-032-16381-3_20

which arise in the modeling of carbon nanotubes (CNTs), fibers, nanowires, and other elongated nanostructures [5]. In such problems, not only are the size and position of the objects important, but also their spatial orientation, which can significantly affect the physical properties of the system, from mechanical strength to electrical conductivity.

The last papers have emphasized the importance of controlling the orientation of nanostructured systems. For instance, research has demonstrated that the mechanical behavior of carbon nanotube arrays is heavily influenced by the angle between neighboring tubes, impacting both adhesion and mechanical coupling [6]. This is important for the stability of CNT arrays, especially under mechanical stress. Even in the absence of an explicit packing formulation, the physical model implies that very small angles between tubes are undesirable, which can be formalized as a minimum allowable angle in a mathematical model.

In [7], the behavior of CNT bundles is modeled using molecular mechanics. The model takes into account the relative position, length, and orientation of the tubes, as well as the forces described by the Lennard-Jones potential. The results show that the orientation of the tubes within the bundle significantly affects the mechanical response of the system.

Paper [8] emphasizes the importance of orientation control in composites. Random orientation can reduce electrical and thermal conductivity, whereas alignment at specific angles to the substrate or to each other enables desirable anisotropic properties.

Further evidence of the importance of orientation control comes from studies in nanoelectromechanical systems, particularly nano-oscillators used in high-frequency sensing, energy conversion, and actuation. For example, orientation-dependent van der Waals interactions and geometric configurations have been shown to influence oscillation stability and frequency tuning [9]. In such systems, the angle between adjacent nanotubes or between a nanotube and the substrate directly affects the mechanical and dynamic behavior, reinforcing the need for angular constraints in modeling.

In the context of composite materials, the orientation of carbon nanotubes (CNTs) in the matrix has been shown to have a significant impact on mechanical properties such as tensile strength and elastic modulus. Load transfer occurs most efficiently along the nanotube axis, making the angle between the tube and the load direction a key factor influencing mechanical properties. This has been demonstrated in recent studies on carbon nanotube (CNT)-reinforced composites and mechanical metamaterials [10].

These examples show that orientation control of CNTs is a key factor determining the performance of nanomaterials and devices. Accordingly, mathematical models that take into account angular constraints in packing problems can serve as universal tools for describing and optimizing such systems.

These problems come from different fields, but they all share a common geometric setup where elongated cylinders interact inside a confined space with constraints based on their orientation. This means they can be studied using a single mathematical model focused on cylinder packing with orientation restrictions. This approach is valuable because it covers many physical situations within one framework. It is also adaptable, so it can handle specific conditions like preventing cylinders from being parallel, limiting how much they tilt, or maintaining a minimum distance between them. Additionally, the

model can be used to find the best configurations, such as maximizing packing density, minimizing interaction energy, or optimizing orientation for a particular purpose.

Depending on the target application, either nearly parallel or random (isotropic) orientation of the nanotubes may be optimal. For example, to achieve high electrical or thermal conductivity in a specific direction, dense alignment of the tubes with minimal angular deviation (2.5–10°) is required [11]. In contrast, in applications where isotropy, porosity, or maximum surface area are important (such as in filters, sensors, or supercapacitors), a random orientation with a wide range of angles is preferred [12].

In the context of cylinder packing, two recent studies are particularly relevant. The first, paper [13] proposes an algorithm for packing cylinders into a cylindrical domain with a focus on global optimization. While the approach is mathematically rigorous and efficient, it is limited to cylinders without rotational degrees of freedom, i.e., fixed orientations. This restricts its applicability to systems where orientation plays a critical role, such as CNT arrays or fibrous composites.

The second study [14] investigates packing behavior using adaptive shrinking cell (ASC) and inverse Monte Carlo methods. It provides valuable insights into the relationship between packing density, aspect ratio, and structural order.

2 Problem Statement and Mathematical Model

We consider a collection of cylinders C_i, each with radius r_i and height $2h_i$, $i \in I_N = \{1, 2, ..., N\}$. Let $\mathbf{u} = (\mathbf{u}_1, \mathbf{u}_2, ..., \mathbf{u}_N)$ where $\mathbf{u}_i = (\mathbf{v}_i, \mathbf{\Theta}_i)$ consists of the center coordinates $\mathbf{v}_i = (x_i, y_i, z_i)$ and orientation angles $\mathbf{\Theta}_i = (\varphi_i, \omega_i)$ of cylinder C_i. Here, $\varphi_i \in [0, 2\pi)$ denotes the azimuthal angle and $\omega_i = [0, \pi/2]$ is the inclination angle.

The direction of the axis of each cylinder is represented by a unit vector $\mathbf{n}_i \in \mathbf{R}^3$, derived from its orientation angles as follows:

$$\mathbf{n}_i = \begin{bmatrix} \sin(\omega_i)\cos(\varphi_i) \\ \sin(\omega_i)\sin(\varphi_i) \\ \cos(\omega_i) \end{bmatrix}.$$

A cuboidal container C with specified dimensions $W \times L \times H$ is given. The objective is to pack a given set of cylinders into this container in such a way that no cylinders overlap, the angles between the axes of the cylinders as well as between each cylinder axis and the vertical direction ($\mathbf{e}_z = (0, 0, 1)$ aligned with the z-axis) satisfy prescribed constraints, and the packing density is maximized.

The mathematical model of the problem has the following form:

$$\max 2\pi \sum_{i=1}^{N} b_i r_i^2 h_i \quad \text{subject to } \mathbf{U} = (\mathbf{u}, \mathbf{b}) \in W \subset \boldsymbol{R}^m \times \boldsymbol{B}^N, \tag{1}$$

where $\boldsymbol{R}^m$ is the Euclidean space, $m = 5n + 1.5n(n-1)$, $\boldsymbol{B}^n$ is the binary space, $\mathbf{b} = (b_1, b_2, ..., b_N) \in \boldsymbol{B}^n$, $b_i \in \{0, 1\}$.

The feasible set W is described by the following system of inequalities:

$$b_i \Phi_i(\mathbf{u}_i) \geq 0, i \in I_N, \tag{2}$$

$$b_i b_j \Phi_{ij}(\mathbf{u}_i, \mathbf{u}_j) \geq 0, i, j \in I_N,\ i < j, \tag{3}$$

$$b_i \alpha_{\min} \leq b_i \arccos \frac{\mathbf{n}_i \cdot \mathbf{e}_z}{|\mathbf{n}_i|} \leq b_i \alpha_{\max}, i \in I_N, \tag{4}$$

$$b_i b_j \beta_{\min} \leq b_i b_j \arccos \frac{\mathbf{n}_i \cdot \mathbf{n}_j}{|\mathbf{n}_i| \cdot |\mathbf{n}_j|} \leq b_i b_j \beta_{\max}. \tag{5}$$

The model is MINLP [15] and aims to maximize the total volume of selected cylinders placed within the cuboidal container C. Each cylinder is defined by its radius and height, and its inclusion in the packing is controlled by a binary variable. If $b_i = 1$ then cylinder C_i is included in the packing.

If $b_i = 0$, then cylinder C_i is excluded, and all constraints related to it are deactivated.

The objective function maximizes the sum of the volumes of the included cylinders.

The decision variables include the spatial coordinates and orientation angles of each cylinder, as well as binary variables indicating whether a cylinder is included. The feasible set W is defined by the system of constraints:

1. Each cylinder must be fully contained within the container. This is enforced by a geometric constraint $\Phi_i(\mathbf{u}_i)$ (see (2)), based on Φ-functions.
2. No two cylinders may overlap. This is ensured by pairwise non-overlap constraints $\Phi_{ij}(\mathbf{u}_i, \mathbf{u}_j) \geq 0$ (see (3)), activated only when both cylinders are included.
3. The orientation of each cylinder must satisfy angular constraints (4) with respect to the vertical axis (aligned with the z-axis). The angle between the cylinder axis and the vertical must lie within a specified segment $[\alpha_{\min}, \alpha_{\max}]$. This constraint is enforced only when $b_i = 1$.
4. The angle between the axes of any two included cylinders must also lie within a prescribed segment $[\beta_{\min}, \beta_{\max}]$, ensuring controlled mutual orientation (see (5)). This constraint is active only when both $b_i = 1$ and $b_j = 1$.

The total number of variables in the model is given by the expression $m = 5n + 1.5n(n-1)$, which reflects the geometric and combinatorial complexity of the packing problem. Each of the N cylinders is described by five continuous variables: three coordinates for the center of the cylinder and two angles that define its orientation in space. In addition, for every pair of cylinders, the model introduces three auxiliary variables that define a separating plane between the two cylinders. These planes are used to construct the Φ-functions, which are known from the literature and are used to model non-overlap conditions between convex polyhedral. Since cylinders can be approximated with arbitrary precision by convex polyhedra, this approach allows the model to enforce non-overlapping constraints with high geometric accuracy. The number of such pairs is $n(n-1)/2$, and with three variables per pair, this gives additional $1.5n(n-1)$ variables.

In the context of modeling nanotube packing, the orientation of each nanotube (represented as a cylinder) plays a critical role in determining the physical properties of the resulting material, such as anisotropy, conductivity, or mechanical strength. The angular constraints in the model serve to control and regulate this orientation:

Constraint (4) limits the angle between the axis of a nanotube and the vertical direction (typically aligned with the z-axis). By bounding this angle within a specified range, the model can:

- simulate vertically aligned nanotube arrays (e.g., forests or brushes) when the angle is close to 0;
- allow tilted or randomly oriented nanotubes when the range is wider;
- enforce fabrication constraints where nanotubes must grow or be deposited within a certain angular tolerance.

Constraint (5) bounds the angle between the axes of any two included cylinders. It helps:

- prevent entanglement or excessive misalignment,
- promote parallel alignment for applications requiring directional properties (e.g., thermal or electrical conductivity),
- model inter-nanotube interactions that depend on relative orientation.

3 Solution Method

3.1 Construction of a Starting Point

Once a subset of cylinders has been selected (that is the binary variables have been fixed) the next step is to construct a feasible starting point. For this purpose, we employ a block-coordinate descent method (see, e.g., [17]). According to this method, we sequentially optimize the position of each cylinder C_k such that $b_k = 1$.

At each step, a group of variables corresponding to the position of a single cylinder C_k (with $b_k = 1$) is selected for optimization, while all other variables remain fixed. The height of the cuboidal container along the z-axis is chosen to be significantly larger than the original height $H^0 \gg H$, allowing more flexibility in vertical placement.

To simplify the optimization problem, we treat only the z_k coordinate as a variable. Its initial value is chosen as $H^0 - \sqrt{r_k^2 + h_k^2}$, ensuring that the cylinder is placed below the top boundary of the container. Angles φ_k, ω_k are set so that $\alpha_{\min} = \arccos \frac{\mathbf{n}_k \cdot \mathbf{e}_z}{|\mathbf{n}_k|}$. The remaining variables (x_k, y_k) are initialized randomly, but in such a way that constraints (2)–(4) are satisfied.

This simplified approach is intentionally coarse, as the primary goal at this stage is not to find an optimal configuration, but rather to quickly obtain a feasible point that satisfies all geometric and angular constraints.

We then solve a one-dimensional optimization problem of the form:

$$\min z_k \quad \text{subject to } z_k \in D_k \subset \boldsymbol{R}^1, \tag{6}$$

where the feasible set D_k is defined by the following system of inequalities:

$$b_i \Phi_i(z_k) \geq 0, i \in I_N, \tag{7}$$

$$b_j \Phi_{kj}(z_k) \geq 0, j \in I_N, \tag{8}$$

$$b_i b_j \beta_{\min} \leq b_i b_j \arccos \frac{\mathbf{n}_i \cdot \mathbf{n}_j}{|\mathbf{n}_i| \cdot |\mathbf{n}_j|} \leq b_i b_j \beta_{\max}. \tag{9}$$

The minimum of problem (6)–(9) can be efficiently found using the bisection method, which iteratively halves the search interval for the variable z_k until convergence.

Once such a point is found, a full optimization over all variables is performed in the next stage.

3.2 Iterative Improvement via Subset-Based Height Optimization

Now we solve the following problem based on the problem (1)–(5):

$$\min h \quad \text{subject to } (u, h) \in G \subset \boldsymbol{R}^{m+1} \times \boldsymbol{B}^N \tag{10}$$

where the feasible set G is described by the inequalities:

$$b_i \Phi_i(\mathbf{u}_i, h) \geq 0, i \in I_N, \tag{11}$$

$$b_i b_j \Phi_{ij}(\mathbf{u}_i, \mathbf{u}_j) \geq 0, i, j \in I_N, \ i < j, \tag{12}$$

$$b_i \alpha_{\min} \leq b_i \arccos \frac{\mathbf{n}_i \cdot \mathbf{e}_z}{|\mathbf{n}_i|} \leq b_i \alpha_{\max}, i \in I_N, \tag{13}$$

$$b_i b_j \beta_{\min} \leq b_i b_j \arccos \frac{\mathbf{n}_i \cdot \mathbf{n}_j}{|\mathbf{n}_i| \cdot |\mathbf{n}_j|} \leq b_i b_j \beta_{\max}. \tag{14}$$

If the result of the height minimization yields a value $h^* \leq H$, this indicates that the selected subset of cylinders can be successfully packed within the original container dimensions. In this case, the corresponding configuration is considered feasible and valid for the original cuboid. Moreover, if the value of the objective function from the initial problem (1), i.e., the total packed volume, is improved compared to the best previously found configuration, it is updated and used as a reference for evaluating future subsets.

This process is embedded within a broader iterative framework, where multiple subsets of cylinders are explored. The selection of subsets is guided by a tree strategy inspired by the approach of [14, 15], which prioritizes combinations with high estimated packing potential.

It is worth noting that in the case where all cylinders are identical, the subsets are selected by gradually increasing the number of cylinders.

The solution scheme involves some basic steps:

- select a promising subset of cylinders based on estimated density or geometric compatibility;
- construct a feasible starting point using the block-coordinate descent method;
- perform full nonlinear optimization, including orientation angles and container height;
- evaluate the result, namely if the configuration fits within the original container and improves the objective, update the best-known solution;
- repeat the process for other subsets until a target packing density is achieved, or all relevant subsets have been exhausted.

An iterative algorithm combines combinatorial subset selection with continuous nonlinear optimization. The goal is to efficiently explore the space of feasible cylinder configurations while satisfying all geometric and orientation constraints.

Decomposition approaches can significantly reduce computational time and permit considering large-scale problems. See, e.g.l [16].

General solution algorithm.

Step 1. Set $count := 0$, $V_{best} := 0$ (initialize the subset counter and best total volume).
Step 2. Set $count := count + 1$ and select a subset of n_{count} cylinders according to the method proposed by [15].
Step 3. Set $k := 1$;
Step 4. Solve the one-dimensional placement problem (6) – (9) for the k-th cylinder.
Step 5. If $k := n_{count}$, then go to Step 7.
Step 6. Set $k := k + 1$ and go to Step 4.
Step 7. Solve the full optimization problem (9)–(13), and compute the resulting height h^* and $\mathbf{u}*$.
Step 8. If $h^* > H^0$, then go to Step 2. Otherwise go to Step 9.
Step 9. If $V^* > V_{best}$, then set $V_{best} = V^*$, $\mathbf{u}_{best} = \mathbf{u}^*$.
Step 10. Go to Step 2.

4 Numerical Experiments and Discussion

4.1 Modeling Nearly Parallel Cylinders with Small Tilt Angles

This specific arrangement is crucial for uses that emphasize directionality, specifically in areas like electrical behavior, heat transfer, and structural strengthening. Take aligned Carbon Nanotube (CNT) arrangements, for example; they demonstrate electron movement capabilities significantly exceeding randomly organized networks. This advantage is especially beneficial in advanced nanoelectronics and biosensing technologies. Research into vertically aligned CNT formations created using chemical vapor deposition reveals that this orientation can be managed with external electric fields or strategic catalyst placement [10]. These systems typically impose angular constraints such that the angle between adjacent CNTs lies within 2°–15°, and the tilt angle relative to the substrate normal (Z-axis) is limited to 2°–10°.

To simulate such conditions, we consider a representative test case involving the packing of 30 cylinders within a cuboidal domain with base 7x7. Angular constraints are as follows: $\alpha_{\min} = \beta_{\min} = 2°, \alpha_{\max} = 10°, \beta_{\max} = 15°$. An illustration of placement is shown in Fig. 1a. A local optimum is $h^* = 39.7721$. As seen in Fig. 1, the resulting configuration exhibits nearly parallel alignment of the cylinders, oriented along the Z-axis.

4.2 Statistically Random or Semi-Random Orientations

Random or isotropic orientation of CNTs is particularly true for systems where porosity, surface area, or isotropic mechanical response is desired, such as in filters, supercapacitors, and catalytic supports. In these cases, a wide distribution of orientations enhances the accessible surface area and promotes uniform interaction with surrounding media [12].

Rather than enforcing strict pairwise angular constraints, which may be geometrically infeasible in dense packings, random orientations are modeled using angular distributions centered around a mean direction (typically the z-axis), with a standard deviation of 15°–20°. This approach reflects the statistical nature of orientation in real materials and

is supported by modeling studies of CNT-reinforced composites and fibrous networks [5].

Based on experimental and modeling data, a realistic tilt angle range for such systems is from 20° to 60° relative to the Z-axis. This avoids both near-vertical alignment (which would resemble aligned arrays) and extreme horizontal orientations (which are difficult to pack densely and may lead to mechanical instability). A practical test case, each of cylinders with a tilt angle being within the 20°–60° range. This configuration mimics the structure of porous or entangled CNT networks used in energy storage, sensing, and filtration applications. To this end, we generate a test case with 30 identical cylinders ($r_i = 0.5, h_i = 4$) in a container with a square base and angular constraints: $\alpha_{\min} = 20°$ and $\alpha_{\max} = 60°$. An illustration of the obtained configuration is shown in Fig. 1b.

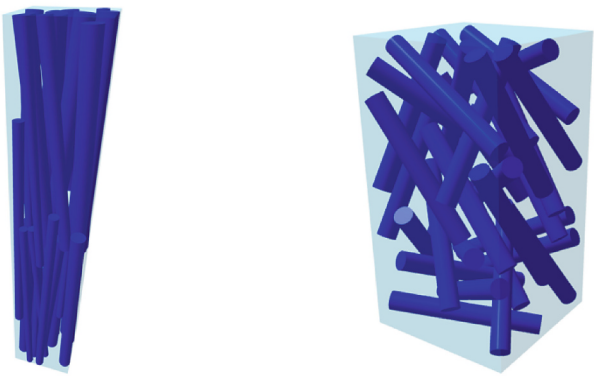

a b

Fig. 1. Packing cylinders with different limitations. a) modeling of packing nearly parallel cylinders with small tilt angles; b) modeling of packing semi-random orientations of cylinders.

For both configurations, the model employs an iterative optimization approach that combines subset selection with nonlinear programming. For each subset, a feasible starting point is constructed using a block-coordinate descent method [16, 17], followed by full optimization using the IPOPT solver [20].

5 Conclusion

This study introduces a singular geometric model, designed for the arrangement of cylindrical nanostructures, accommodating orientation limitations. This model encompasses a wide spectrum of applications pertinent to nanotechnology, materials science, and the creation of devices. The presented method builds upon established packing models, enhancing them with angular constraints. These constraints are both grounded in physical principles and supported by experimental observations. These constraints are essential for accurately modeling systems in which the spatial orientation of elongated objects (for example, carbon nanotubes (CNTs), nanowires, or fibers) directly influences key functional properties, including mechanical strength, electrical conductivity,

and thermal transport. The model is formulated as a nonlinear optimization problem that combines geometric non-overlap conditions with orientation-dependent constraints. It allows for the inclusion or exclusion of individual cylinders via binary variables and supports a wide range of angular configurations, from highly aligned arrays to statistically disordered networks. The mathematical formulation is general and flexible, enabling adaptation to various physical scenarios by adjusting the angular bounds and container geometry. To solve the problem efficiently, a two-stage algorithm is proposed. It combines subset-based decomposition with continuous nonlinear programming. For each selected subset of cylinders, a feasible initial configuration is constructed using a block-coordinate descent method, followed by full optimization using the IPOPT solver. This approach enables the exploration of high-quality packing configurations without exhaustive enumeration, which would be computationally infeasible due to the combinatorial nature of the problem. Two representative case studies are presented to illustrate the model's capabilities: one involving nearly parallel alignment with small tilt angles, and another with statistically random orientations. The suggested model offers a flexible and physics-based means to simulate and refine the spatial arrangement of cylindrical nanostructures. It acts as a starting point for advanced theoretical investigations, computational tests, and real-world applications focused on designing sophisticated nanomaterials and technological components.

Acknowledgments. This work has been supported by the British Academy (grant #100072) and Grant of the President of Ukraine for Early Career Researchers and Doctors of Science.

References

1. Wang, Y., Li, J., Zhang, H., Chen, X.: Progress in multiscale research on calcium-looping for thermochemical energy storage: from materials to systems. Prog. Energy Combust. Sci. **94**, 101194 (2025). https://doi.org/10.1016/j.pecs.2024.101194
2. Imran Alsous, J., Villoutreix, P., Stoop, N., et al.: Entropic effects in cell lineage tree packings. Nat. Phys. **14**, 1016–1021 (2018). https://doi.org/10.1038/s41567-018-0202-0
3. Deng, Z., Zou, G., Du, R., et al.: Particle size effects of nano-Ag films on the interface sintered bonding for die attachment. J. Electron. Mater. **53**, 473–488 (2024). https://doi.org/10.1007/s11664-023-10786-z
4. Wen, H., Yao, J., Li, Y., et al.: Length-dependent alignment of large-area semiconducting carbon nanotubes self-assembly on a liquid-liquid interface. Nano Res. **16**, 1568–1575 (2023). https://doi.org/10.1007/s12274-022-4782-8
5. Gupta, N., Gupta, S.M., Sharma, S.K.: Carbon nanotubes: synthesis, properties and engineering applications. Carbon Lett. **29**, 419–447 (2019). https://doi.org/10.1007/s42823-019-00068-2
6. Adhikari, B.C., Ketan, B., Patil, R., et al.: Optimization of vertically aligned carbon nanotube beam trajectory with the help of focusing electrode in the microchannel plate. Sci. Rep. **13**, 15630 (2023). https://doi.org/10.1038/s41598-023-42554-8
7. Mählich, D., Eberhardt, O., Wallmersperger, T.: Numerical simulation of the mechanical behavior of a carbon nanotube bundle. Acta Mech. **232**, 483–494 (2021). https://doi.org/10.1007/s00707-020-02874-6

8. Sivaganga, K.C., Varughese, T.: Physical properties of carbon nanotubes. In: Abraham, J., Thomas, S., Kalarikkal, N. (eds.) Handbook of Carbon Nanotubes, pp. 283–297. Springer, Cham (2022). https://doi.org/10.1007/978-3-030-91346-5_62
9. Huang, J., Han, Q.: Strain effects on rotational property in nanoscale rotation system. Sci. Rep. **8**, 432 (2018). https://doi.org/10.1038/s41598-017-18903-9
10. Paupst, T., Pagliocca, N., Youssef, G., et al.: Experimental characterization of nonlinear mechanical behavior and auxeticity in 3D-printed rotating-square auxetics with spatially variable materials. Prog. Addit. Manuf. (2025). https://doi.org/10.1007/s40964-025-01260-9
11. Sabet, M.: Advanced developments in carbon nanotube polymer composites for structural applications. Iran. Polym. J. **34**, 917–946 (2025). https://doi.org/10.1007/s13726-024-01419-1
12. Ayanda, O.S., Mmuoegbulam, A.O., Okezie, O., et al.: Recent progress in carbon-based nanomaterials: critical review. J. Nanopart. Res. **26**, 106 (2024). https://doi.org/10.1007/s11051-024-06006-2
13. Moqa, R., Zheng, J., He, K.: Online and offline packing cylinders in a cylindrical container. Discrete Appl. Math. **375**, 85–104 (2025). https://doi.org/10.1016/j.dam.2025.05.039
14. Liu, L., Yuan, Y., Deng, W., Li, S.: Evolutions of packing properties of perfect cylinders under densification and crystallization. J. Chem. Phys. **149**(10), 104503 (2018). https://doi.org/10.1063/1.5049562
15. Stoyan, Y., Yaskov, G.: Optimized packing unequal spheres into a multiconnected domain: mixed-integer non-linear programming approach. Int. J. Comput. Math. Comput. Syst. Theory **6**(1), 94–111 (2020). https://doi.org/10.1080/23799927.2020.1861105
16. Litvinchev, I., Rangel, S., Saucedo, J.: A Lagrangian bound for many-to-many assignment problems. J. Comb. Optim. **19**(3), 241–257 (2010). https://doi.org/10.1007/s10878-008-9196-3
17. Yaskov, H., Chuhay, A.: Packing equal spheres by means of the block coordinate descent method. Comput. Methods Inf. Sci., CEUR Workshop Proc. 2608, Paper 13 (2020). https://doi.org/10.32782/cmis/2608-13
18. Romanova, T., et al.: Optimized packing soft ellipses. In: Manshahia, M.S., Litvinchev, I., Thomas, J.J., Vasant, P., Weber, W.G. (eds.) Human-Assisted Intelligent Computing: Modeling, Simulations and Applications, Chap. 9, pp. 1–16. IOP Publishing (2023). https://doi.org/10.1088/978-0-7503-4801-0ch9
19. Urniaieva, I., Pankratov, A., Romanova, T., Grebennik, I., Dupas, I., Shekhovtsov, S.: Balance packing problem of cuboids in an optimized cylindrical container. In: 9th International Conference on Advanced Computer Information Technologies (ACIT), Ceske Budejovice, Czech Republic, pp. 133–136 (2019). https://doi.org/10.1109/ACITT.2019.8780049
20. Wächter, A., Biegler, L.T.: On the implementation of an interior-point filter line-search algorithm for large-scale nonlinear programming. Math. Program. **106**(1), 25–57 (2006). https://doi.org/10.1007/s10107-004-0559-y

Tuned Liquid Damper for Mitigation of Structural Vibrations

Vasyl Gnitko[1], Kyryl Degtyariov[1(✉)], Marina Chugay[1], and Alexander Steinwolf[2]

[1] A. Pidhornyi Institute of Power Machines and Systems NAS of Ukraine, Kharkiv, Ukraine
kdegt@gmail.com
[2] AST Consulting Ltd., Auckland, New Zealand

Abstract. This research explores the effectiveness of tuned liquid dampers (TLDs) in mitigating structural vibrations under dynamic loading. The dampers are modeled as rigid shells of rotation, partially filled with liquid and rigidly attached to an elastic structure. These damper geometries are of particular interest because their sloshing dynamics differ from those of conventional rectangular containers, offering potential advantages for energy dissipation. The elastic structure is represented as a single-degree-of-freedom oscillator (SDOF), with explicit inclusion of its interaction with the TLD. Fundamental sloshing frequencies are evaluated using the reduced boundary element method, which ensures both computational efficiency and accuracy in fluid-structure interaction analysis. The novelty of this work lies in demonstrating the applicability of arbitrary shells of revolution as TLDs, enabling a more realistic assessment of vibration mitigation performance. The results show that cylindrical shell-type dampers can markedly enhance structural resilience against intensive dynamic excitations. These findings offer important guidance for designing and optimizing TLDs in engineering contexts.

Keywords: Fluid-Structure Interaction · Vibration Control · Shells of Revolution

1 Introduction and Literature Review

In recent years, accidents at critical infrastructure facilities caused by seismic activity and other emergency situations have become increasingly frequent. This trend has stimulated intensive research into vibration damping of elastic structures. Among the various passive and semi-active vibration control devices, TLDs have proven to be particularly effective for high-rise structures exposed to dynamic loads. These devices consist of rigid, thin-walled containers partially filled with liquid and rigidly attached to the structure. Controlling the sloshing response by preventing coincidence with the natural frequency of the structure, TLDs can significantly reduce vibrations induced by wind, earthquakes, and other dynamic excitations. This study focuses on cylindrical and conical rigid shells employed as liquid dampers. These geometries are of particular interest because they exhibit sloshing dynamics and energy dissipation mechanisms distinct from those of conventional rectangular or prismatic containers. The objective of the paper is to analyze the efficiency of such shell-type TLDs in mitigating structural vibrations.

H. Altenbach et al. (Eds.): CAMPE 2025, LNME, pp. 221–231, 2026.
https://doi.org/10.1007/978-3-032-16381-3_21

A wide variety of damping devices have been developed to reduce structural vibrations [1]. These include membranes [2] and baffles [3] in fuel tanks, along with shock-absorbing suspensions in vehicles [4]. The concept of TLDs in civil engineering was introduced in [5], where single- and multi-story buildings were analyzed. Subsequent studies have extensively advanced vibration-control strategies for tall buildings [6, 7], and for vehicle suspensions [4]. In addition to conventional cylindrical and conical tanks, more complex TLD geometries have recently been investigated, including coaxial, toroidal [8], and elliptical reservoirs [9], which provide alternative sloshing characteristics and broaden the design space. Significant progress has also been achieved in numerical modeling of fluid sloshing [10, 11] and in studies of structural stability [12]. Both finite element and finite volume methods [13], as well as boundary element method (BEM) [14], have proven to be highly effective for addressing fluid-structure interaction problems. Furthermore, the performance of TLDs equipped with baffles has been studied in detail [15, 16], highlighting the role of lateral and longitudinal baffles in modifying sloshing frequencies. TLDs are widely recognized as effective devices for suppressing vibrations induced by earthquakes [17], wind loads [18], and other intensive dynamic excitations [19]. The widespread adoption of TLDs highlights their versatility and cost-effectiveness compared to traditional Tuned Mass Dampers (TMDs). Companies such as Flow Engineering and SDEA Solutions have been instrumental in advancing these technologies and providing innovative solutions for global infrastructure projects. Ongoing developments, including the use of smart materials and optimization algorithms, are expected to further improve TLD performance and broaden their applications across engineering fields [20].

2 Research Methodology

The algorithm for analyzing the influence of TLDs is implemented in several stages. First, structural vibration modes and their associated frequencies without TLD are determined, while the spectral boundary value problem (BVP) for the liquid damper is analyzed. The resulting modes are subsequently employed as basis functions in the analysis of forced vibrations. Finally, the vibration response of the elastic structure equipped with a TLD is formulated, and the effectiveness of vibration mitigation is evaluated.

2.1 Boundary Value Problem for Liquid Motion in Rigid Shells

Consider a SDOF elastic system equipped with a TLD designed to mitigate oscillations induced by external dynamic load, Fig. 1.

The formulation is based on standard modelling assumptions. The container is filled with water (density 997 kg/m^3), while the upper part is occupied by air at constant atmospheric pressure. Surface tension is neglected, as the wavelengths and amplitudes considered exceed the capillary length. The free surface is assumed idealized, without phase change; evaporation and condensation are disregarded.

Dynamic gas effects (compressibility, internal flows, variable pressure) are neglected. The liquid is assumed isothermal, with thermal and buoyancy effects ignored, an acceptable approximation for short-term dynamics without heat sources. For water at room

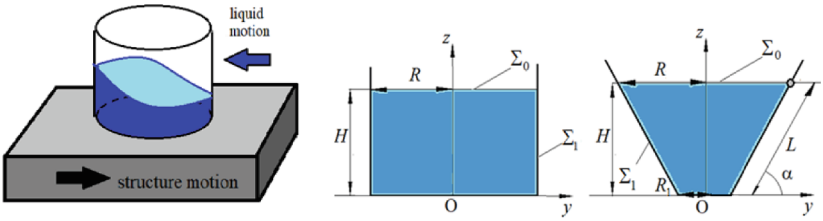

Fig. 1. Elastic structure with an attached tuned liquid damper

temperature ($\rho_l \approx 1000$ kg/m^3, $g = 9.81$ m/s^2, $\sigma \approx 0.072$ N/m, $L = 0.5$ m), the Bond number is $\mathrm{Bo} = \rho_l g L^2/\sigma \approx 3.5 \times 10^4$. Viscous effects are limited to thin boundary layers and have negligible impact on natural frequencies or modes, supporting the use of a potential-flow model standard in first-order TLD analyses [22]. Thus, the tank liquid is treated as inviscid and incompressible. Let $S_0(t)$ denote the time-varying free surface of the fluid, and $S_1(t)$ is the shell wetted surface. At the initial time, we set $S_0(t) = \Sigma_0$, and $S_1(t) = \Sigma_1$, where the free surface Σ_0 lies in the plane $z = 0$ when the system is at rest.

The liquid domain $Q(t)$ in the cylindrical system is defined as follows

$$Q(t) = \{0 \le \theta \le 2\pi, 0 \le r \le r(z), -H \le z \le \zeta(r, \theta, t)\}. \tag{1}$$

Here, $r = r(z)$ defines the shell meridian, while the unknown function $\zeta = \zeta(\theta, r, t)$ represents the change in free surface level over time.

The continuity equation is expressed as $\nabla \cdot \mathbf{V} = 0$, where $\mathbf{V}$ denotes the liquid velocity. In the absence of vorticity, a scalar velocity potential $\Phi = \Phi(x, y, z, t)$ exists, reducing the continuity condition to Laplace's equation, $\nabla^2 \Phi = 0$. When the fluid-filled shell is subjected to an external horizontal force $\mathbf{F}_Q$, producing an acceleration $\mathbf{a} = a_x(t)\mathbf{i}$, together with gravity acting in the vertical direction, the governing equation of fluid motion is obtained from the principle of momentum conservation as follows:

$$p - p_0 = -\rho_l \left[\frac{\partial \Phi}{\partial t} + gz + a_x(t)x + \frac{1}{2}(\nabla\Phi, \nabla\Phi) \right]. \tag{2}$$

where p is the liquid pressure, p_0 is the atmospheric pressure, ρ_l is the liquid density, and g is the gravitational acceleration. The BVP for the Laplace equation in the time-varying fluid domain $Q(t)$ is then formulated. On the wetted surface S_1, the impermeability condition is imposed as

$$\partial\Phi/\partial\mathbf{n}|_{S_1} = 0. \tag{3}$$

Here, $\mathbf{n}$ is the outward unit normal to the surface S_1. In addition to the no-slip condition (3) on S_1, the kinematic as well as dynamic boundary conditions are imposed on S_0:

$$\frac{\partial \Phi}{\partial \mathbf{n}} = \left. \frac{\partial \zeta/\partial t}{\sqrt{1 + |\nabla \zeta|^2}} \right|_{S_0}, \quad \frac{\partial \Phi}{\partial t} + gz + a_x(t)x + \frac{1}{2}(\nabla\Phi, \nabla\Phi) = 0. \tag{4}$$

The solvability requirement for the Neumann problem (3)–(4) is used [22].
The initial data for the BVP (3)–(4) are as follows:

$$\zeta(x, y, 0) = \zeta_0(x, y) = 0, \quad \left.\frac{\partial \Phi}{\partial \mathbf{n}}\right|_{\Sigma_0} = \varphi(x, y, 0). \tag{5}$$

The estimation of pressure is thereby reduced to evaluating the unknown functions Φ and ζ, subject to the boundary conditions (3)–(4) of Laplace's equation and the initial data (5). To address this problem, series expansions based on the eigenfunctions of the spectral BVP outlined in [19] are employed. Consequently, the task requires identifying the fundamental frequencies and modes of the fluid confined within the rigid shell.

2.2 Spectral Boundary-Value Problem for a Shell of Revolution

The spectral BVP involves determining the fundamental modes and frequencies of a liquid, partially filling a rigid reservoir. In this study, the reservoir is modeled as a rigid shell (Fig. 1). Following the approach presented in [22], the unknowns ζ and Φ are given in cylindrical coordinates (r, θ, z) as the following series expansions:

$$\zeta(r, \theta, t) = \sum\nolimits_{k=1}^{n} d_k(t)\zeta_k(r, \theta), \quad \Phi(r, \theta, z, t) = \sum\nolimits_{k=1}^{n} \dot{d}_k(t)\varphi_k(r, \theta, z). \tag{6}$$

Here, $\zeta_k(r, \theta)$ and $\varphi_k(r, \theta, z)$ denote the fundamental basis functions, while $d_k(t)$ are the unknown generalized coordinates. The determination of these basis functions in (6) is reduced to solving the corresponding linear BVP, formulated in accordance with [19]

$$\nabla^2\varphi_k = 0, \mathbf{P} \in Q(0), \left.\frac{\partial \varphi_k}{\partial \mathbf{n}} = 0\right|_{\Sigma_1}, \left.\frac{\partial \varphi_k(r,\theta,z)}{\partial \mathbf{n}}\right|_{\Sigma_0} = \frac{\chi_k^2}{g}\varphi_k(r,\theta,H), \tag{7}$$

where $\mathbf{P}$ is a point within the liquid domain $Q(0)$, and χ_k denote the fundamental frequencies. To solve the BVPs (7), Green's third identity was applied to derive one-dimensional equations describing the liquid sloshing dynamics within the TLD, modeled as a shell of revolution. The axisymmetric cross-sectional geometry permits reduction of the three-dimensional problem to a one-dimensional formulation via integration over the azimuthal coordinate. The validity of Green's third identity does not require the cross-section to be convex; it holds for any connected domain with a piecewise-smooth boundary, ensuring applicability to both convex and non-convex geometries. In the present model, the cross-section is assumed sufficiently regular to satisfy the conditions of Green's identity, while numerical simulations incorporate the specific geometry of the TLD. For non-convex cross-sections, the integration may be more complex, but this does not compromise the correctness of the derived equations [22]. By applying the boundary conditions (3)–(4) of the spectral BVP (7), the following set of one-dimensional singular integral equations is derived:

$$2\pi\varphi(r_0, z_0) + \int_\Gamma r(z)\varphi(r(z), z)\Theta(z, z_0)d\Gamma - \frac{\chi^2}{g}\int_0^R \varphi(\rho, H)\,\Xi(\mathbf{P}, \mathbf{P}_0)\rho d\rho = 0, \tag{8}$$

$$2\pi\varphi(r_0, H) + \int_\Gamma r(z)\varphi(r(z), z)\Theta(z, z_0)d\Gamma - \frac{\chi^2}{g}\int_0^R \varphi(\rho, H)(\mathbf{P}, \mathbf{P}_0)\rho d\rho = 0,$$

$$\Theta(z, z_0) = \frac{4}{\sqrt{a+b}}\left\{\frac{1}{2r}\left[\frac{r^2 - r_0^2 + (z_0 - z)^2}{a-b}E_l(k) - F_l(k)\right]n_r + + \frac{z_0 - z}{a-b}E_l(k)n_z\right\},$$

$$\Xi(P, P_0) = \frac{4}{\sqrt{a+b}}F_l(k),\ \ a = r^2 + r_0^2 + (z - z_0)^2,\ \ b = 2rr_0.$$

The numerical solution of Eqs. (8) was carried out using the BEM described in [19], while the evaluation of the elliptic integrals employed the approach developed in [23]. After determining the basic functions and fundamental vibration frequencies, substitute them into series (6) and then into the dynamic condition on the surface S_0, and derive differential equations for unknowns $d_k(t)$. The acceleration **a,** appearing in the dynamic boundary condition, represents the acceleration of the elastic body, the vibrations of which need to be reduced using the TLD.

2.3 Governing Differential Equations

In the first stage, the own frequencies and modes of the elastic structure are determined without accounting for the influence of the TLD. Neglecting damping effects, the governing equations take the form:

$$[\boldsymbol{M}_S]\left\{\ddot{\mathbf{u}}^s\right\} + [\boldsymbol{K}_S]\left\{\mathbf{u}^s\right\} = 0, \tag{9}$$

Here, $[\mathbf{M}_S]$ and $[\mathbf{K}_S]$ represent the mass and stiffness matrices, $\{\mathbf{u}^s\}$ is the unknown vector of structure displacements. The solution of problem (9) results in the natural vibration frequencies Ω_k and the corresponding modes $\boldsymbol{u}_k(r, \theta, z)$, which are subsequently adopted as the basis functions. Accordingly, displacements in the fluid–structure interaction problem are expanded in series form

$$\boldsymbol{u}^s(x, y, z, t) = \sum\nolimits_{k=1}^{N} c_k(t)\boldsymbol{u}_k(x, y, z), \tag{10}$$

where $c_k(t)$ are the unknown time-dependent coefficients. The coupled problem formulation for the vibration damping of an elastic structure equipped with a TLD is presented below:

$$[\mathbf{M}_S]\left\{\ddot{\mathbf{u}}^s\right\} + [\mathbf{K}_S]\left\{\mathbf{u}^s\right\} = \{\mathbf{f}_S\} + \left\{\mathbf{f}_{pr}\right\}. \tag{11}$$

Here, $\{\mathbf{f}_S\}$ represents the external force vector applied to the elastic structure, and $\left\{\mathbf{f}_{pr}\right\}$ corresponds to the force vector arising from fluid pressure in the TLD. To evaluate the vector $\left\{\mathbf{f}_{pr}\right\}$, the pressure distribution p is determined using the following relations:

$$\mathbf{p} = p\mathbf{n},\ \ p = \rho_l\left(\frac{\partial \Phi}{\partial t} + gz\right),\ \ p = \rho_l\left[\sum\nolimits_{k=1}^{n} \ddot{d}_k(t)\varphi_k(r, z)\right] + \sum\nolimits_{k=1}^{n} d_k(t)\zeta_k(r))]. \tag{12}$$

The vector $\left\{\mathbf{f}_{pr}\right\}$, is evaluated by integrating the product of the pressure, given by Eq. (12), with the eigenmodes of elastic shell vibrations $\boldsymbol{u}_k(r, \theta, z)$ over the shell wetted

surfaces. The dynamic boundary condition on the surface S_0 is employed to estimate the unknown coefficients $d_k(t)$, which in linear formulation leads to the following differential equations [19]:

$$\left[M_f\right]\{\ddot{\mathbf{d}}\} + \left[K_f\right]\{\mathbf{d}\} + \rho_l\{\mathbf{a}\} = 0 \tag{13}$$

where the free-surface mass and stiffness matrices are denoted by $\left[\mathbf{M}_f\right]$ and $\left[\mathbf{K}_f\right]$, and $\{\mathbf{a}\}$ is the acceleration vector induced by the motion of the elastic structure.

Next, the spectral BVP for liquid vibrations in the rigid tank is solved, and by introducing $c_k(t)$ and $d_k(t)$ as generalized coordinates, the reduced coupled system of ODEs is obtained for each wave number l

$$[\mathbf{M}][\ddot{\mathbf{c}}] + [\mathbf{K}][\mathbf{c}] + [\mathbf{R}]\left[\ddot{\mathbf{d}}\right] = \left\{\tilde{\mathbf{f}}_{\mathrm{s}}\right\}, \;\; [\mathbf{M}_{\mathrm{f}}]\left\{\ddot{\mathbf{d}}\right\} + [\mathbf{K}_{\mathrm{f}}]\{\mathbf{d}\} + \rho_l\{\ddot{\mathbf{c}}\} = 0. \tag{14}$$

Here, $[\mathbf{M}] = \left\{\mathbf{M}_S\mathbf{u}_k, \mathbf{u}_j\right\}$, $[\mathbf{C}] = \{\boldsymbol{C}_S\mathbf{u}_k, \mathbf{u}_i\}$, $[\mathbf{K}] = \left\{\mathbf{K}_S\mathbf{u}_k, \mathbf{u}_j\right\}$, $[\mathbf{R}] = \left\{\mathbf{f}_{\mathbf{pr}}, \mathbf{u}_j\right\}$, and $\left\{\tilde{\mathbf{f}}_{\mathrm{s}}\right\} = \left\{\mathbf{f}_{\mathbf{s}}, \mathbf{u}_j\right\}$. In this study, only horizontal external excitation is considered, with the analysis restricted to the first wave mode, $l = 1$.

3 Numerical Results and Discussion

3.1 Benchmark Tests

The fundamental frequencies are calculated according to [19, 22] using the reduced BEM in a linear statement. For both cylindrical and conical shells, the total number of boundary elements (BEs) along the shell meridians and free-surface radii is 240. Table 1 shows the numerical results alongside analytical results from [22] for $l = 0$ (axisymmetric shapes) for different mode numbers k.

Table 1. Comparison of axisymmetric sloshing frequencies, Hz

k	Conus		Cylinder		
	Numerical solution, 120 BEs	Numerical solution, 240 BEs	Numerical solution,	Analytical solution [22],	Relative Error, %
1	5.3528	5.3534	5.9969	5.9965	0.0066
2	7.8092	7.8068	8.2851	8.2842	0.0108
3	9.6046	9.6034	9.9937	9.9932	0.0050
4	11.1065	11.1044	11.4313	11.4261	0.0455
5	12.4257	12.4246	12.7127	12.7051	0.0598
6	13.6173	13.6180	13.8696	13.8656	0.0288

Rigid cylindrical and conical shells exhibit different sloshing frequencies, despite both having equal height $H = 0.5$ m, and radius $R = 1$ m; for the cone, $R_1 = 1$ m. The results demonstrate the accuracy of the proposed method (relative error ≈0.05%). Although the frequencies are distinct, their discrepancy decreases with higher modes.

3.2 Analysis of Tuned Liquid Damper Effects

The influence of a liquid damper on the vibration response of a square elastic plate under periodic loading is investigated. The plate is assumed to be made of steel, with side length $a = 4$ m, Young's modulus $E = 210$ GPa, Poisson's ratio $\nu = 0.3$, and the material density $\rho_s = 7950$ kg/m^3.

Two types of dampers are examined: a cylindrical and a conical one, both having the same height and fabricated from the same steel as the plate. Their geometric parameters are specified as follows: $R = 0.5$ m, $R_1 = 0.25$ m, and $H = 0.5$ m (Figs. 1b, 1c).

The external load is represented as a time-dependent function $a_x(t) = a_0 \cos(f_0 t)$. In this study, the elastic structure is simulated as a SDOF system. Using the method developed in [24], the free vibration modes of the plate are obtained, and the lowest frequency is estimated as $\Omega_1 = \frac{\pi^2 h}{a^2}\sqrt{EF/6\rho_s(1-\nu^2)} = 10.38$ Hz, $F = 22.52$. First, the rigid cylindrical damper (Fig. 1b) was represented as a cylinder partially filled with an ideal incompressible liquid. Figures 2, 3 and 4 illustrate its effectiveness in reducing the vibration response of the elastic plate.

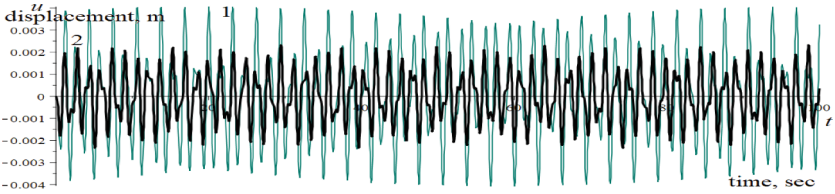

Fig. 2. Time -history of plate displacement under periodic loading ($f_0 = 4$ Hz, $a_0 = 0.01$ m)

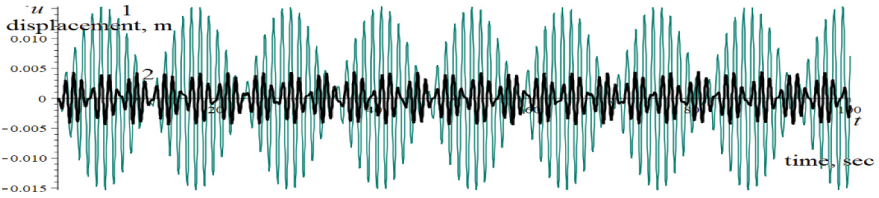

Fig. 3. Time -history of plate displacement under periodic loading ($f_0 = 8.0$ Hz, $a_0 = 0.05$ m)

In Figs. 2, 3 and 4, the gray curves (labeled 1) represent the plate displacements in the absence of a damper, whereas the black curves (labeled 2) correspond to the displacements accounting for damping effects. The results demonstrate that, despite detuning from the fundamental frequency of the plate vibrations, both a beat-type response (Fig. 3) and a linear growth in amplitude (Fig. 5) are observed. It should be emphasized that the plate vibrations were analyzed without incorporating the damping matrix. Nevertheless, the installation of the TLD led to a pronounced reduction in vibration amplitudes across all cases considered. Figure 5 corresponds to the most critical loading case. It presents a comparison of the performance of cylindrical and conical liquid dampers characterized

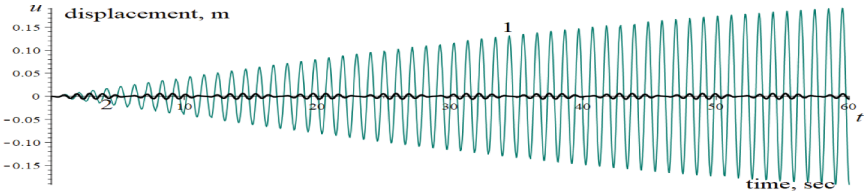

Fig. 4. Time -history of plate displacement under periodic loading ($f_0 = 9.7$ Hz, $a_0 = 0.1$ m)

by the parameters $H = 1$ m, $R = R_2 = 1$ m, $R_1 = 0.5$ m. Curves 1, 2, and 3 denote the vibration amplitudes of the plate without a damper (labeled1), with a conical damper (labeled 2), and with a cylindrical damper (labeled 3), respectively.

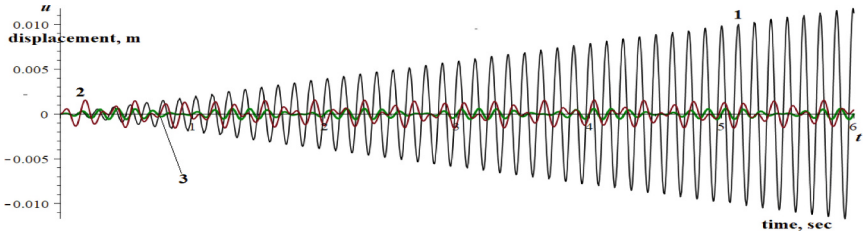

Fig. 5. Time -history of plate displacements for different TLD under periodic loading ($f_0 = 9.7$ Hz, $a_0 = 0.1$ m)

The results indicate that both dampers significantly reduce the vibration amplitude of the plate, however, the cylindrical damper achieves a greater reduction.

To assess the relative mass contribution of the dampers, the ratios of damper mass to the structure mass (12,720 kg) were determined, Table 2.

Table 2. Mass contribution of dampers relative to the structure

Damper Type	Without Liquid		With Liquid	
	Mass, kg	Ratio, %	Mass, kg	Ratio, %
Cylindrical	37.20	0.29%	429.93	3.37
Conical	31.20	0.25%	260.92	2.05%

Both dampers fall within or slightly above the typical 1–3% range for TLDs. The conical damper reaches 2.05% and the cylindrical 3.37%, consistent with optimized designs [25].

4 Conclusion and Future Research

The methodology developed to investigate the influence of a TLD on vibration mitigation in elastic structures provides a robust framework for analyzing TLD performance. A system of differential equations is formulated to describe the vibration response of a multi-degree-of-freedom structure equipped with a liquid damper. For numerical implementation, the formulation is reduced to a SDOF case. The approach relies on singular integral equations to determine the natural frequencies and vibration modes of the TLD. It has been demonstrated that the proposed liquid damper achieves a substantial reduction in the vibration amplitude of the elastic element across the entire load range considered. Notably, the methodology is versatile, accommodating not only conical and cylindrical geometries but also other axisymmetrical geometries, thereby broadening its applicability to diverse structural configurations. Future research will focus on extending the analysis to multi-dimensional systems with multiple degrees of freedom and on investigating the oscillatory behavior of the TLD within a nonlinear framework.

Acknowledgments. The authors express their sincere gratitude to Dr. Neelam Choudhary (Bennett University, India) for her continuous support and collaboration.

References

1. Yuan, J.: Recent advance of vibration control techniques in structures. In: Li, D., Zhang, Y. (eds.) Advances in Frontier Research on Engineering Structures II. LNCE, vol. 535, pp. 13–23. Springer, Singapore (2025). https://doi.org/10.1007/978-981-97-6238-5_2
2. Choudhary, N., Kumar, N., Strelnikova, E., Gnitko, V., Kriutchenko, D., Degtyariov, K.: Liquid vibrations in cylindrical tanks with flexible membranes. J. King Saud Univ. Sci. **33**(8), 101589 (2021). https://doi.org/10.1016/j.jksus.2021.101589
3. Zhang, Z.L., Khalid, M.S.U., Long, T., Chang, J.Z., Liu, M.B.: Investigations on sloshing mitigation using elastic baffles by coupling smoothed finite element method and decoupled finite particle method. J. Fluids Struct. **94**, 102942 (2020). https://doi.org/10.1016/j.jfluidstructs.2020.102942
4. Yi, M., et al.: The nexus of sustainability and damping: a quasi-zero stiffness and pseudo-piecewise inerter damper for vehicle suspension. Sustain. Mater. Technol. **40**, e00909 (2024). https://doi.org/10.1016/j.susmat.2024.e00909
5. Ocak, A., Bekda, G., Nigdeli, S.M., Kim, S., Geem, Z.W.: Optimization of tuned liquid damper including different liquids for lateral displacement control of single and multi-story structures. Buildings **12**, 377 (2022). https://doi.org/10.3390/buildings12030377
6. Wang, H., Gao, H., Li, J., Wang, Z., Ni, Y., Liang, R.: Optimum design and performance evaluation of the tuned inerter-negative-stiffness damper for seismic protection of single-degree-of-freedom structures. Int. J. Mech. Sci. **212**, 106805 (2021). https://doi.org/10.1016/j.ijmecsci.2021.106805
7. Wang, M., Liu, C., Zhao, M., Sun, F.-F., Nagarajaiah, S.: Damping dissipation analysis of damped outrigger tall buildings with inerter and negative stiffness considering soil-structure-interaction. J. Build. Eng. **88**, 109225 (2024). https://doi.org/10.1016/j.jobe.2024.109225
8. Karaiev, A., Strelnikova, E.: Liquid sloshing in circular toroidal and coaxial cylindrical shells. In: Ivanov, V., Pavlenko, I., Liaposhchenko, O., Machado, J., Edl, M. (eds.) Advances in Design, Simulation and Manufacturing III, DSMIE 2020. LNME, pp. 3–13. Springer, Cham (2020). https://doi.org/10.1007/978-3-030-50491-5_1

9. Liu, L., Li, J.: Dynamic deformation and perforation of ellipsoidal thin shell impacted by flat-nose projectile. Materials **15**(12), 4124 (2022). https://doi.org/10.3390/ma15124124
10. Zheng, J.H., Xue, M.A., Dou, P., He, Y.M.: A review on liquid sloshing hydrodynamics. J. Hydrodyn. **33**(6), 1089–1104 (2021). https://doi.org/10.1007/s42241-022-0111-7
11. Smetankina, N., Pak, A., Oksana Mandrazhy, Usatova, O., Vasiliev, A.: Modelling of free axisymmetric vibrations of the fluid-filled shells with non-classical boundary interface conditions. In: Arsenyeva, O., Romanova, T., Sukhonos, M., Biletskyi, I., Tsegelnyk, Y. (eds.) Smart Technologies in Urban Engineering, STUE 2023. LNNS, vol. 807, pp. 185–196. Springer, Cham (2023). https://doi.org/10.1007/978-3-031-46874-2_17
12. Bykov, Y., Kolodyazhna, L., Kostin, M., Petrov, O.: Modeling of coupled auto-oscillations of aircraft engine fan blades. In: Lytvynov, O., Pavlikov, V., Krytskyi, D. (eds.) Integrated Computer Technologies in Mechanical Engineering – 2024, ICTM 2024. LNNS, vol. 1474, pp. 553–564. Springer, Cham (2025). https://doi.org/10.1007/978-3-031-94852-7_47
13. Konar, T., Ghosh, A.D.: Deep-tuned sloshing damper with multiple horizontal baffles for structural vibration control. In: Shrikhande, M., Agarwal, P., Kumar, P.C.A. (eds.) Proceedings of 17th Symposium on Earthquake Engineering (Vol. 1), SEE 2022. LNCE, vol. 329, pp. 33–42. Springer, Singapore (2023). https://doi.org/10.1007/978-981-99-1608-5_3
14. Sierikova, O., Strelnikova, E., Kriutchenko, D., Degtyarev, K., Gnitko, V., Doroshenko, V.: Aeolian liquid vibrations in conical tanks with baffles under wind loading with fuzzy parameters. WSEAS Trans. Fluid Mech. **18**, 295–300 (2023). https://doi.org/10.37394/232013.2023.18.28
15. Konar, T.: Design of intermediate-depth tuned liquid damper with horizontal baffles for seismic control and carbon footprint reduction of buildings. J. Vib. Eng. Technol. **12**, 2641–2658 (2024). https://doi.org/10.1007/s42417-023-01005-4
16. Lu, J., Jin, H., Xue, M.-A., Shen, J., Li, S.: Experimental investigation of the effect of the floating damping baffle on liquid tank sloshing under vertical excitation. Appl. Ocean Res. **147**, 103976 (2024). https://doi.org/10.1016/j.apor.2024.103976
17. Ramya, Y., Rekha, K.: Analysis and design of wind and earthquake loads on tall buildings. Int. J. Techno-Eng. **XIII**(IV), 149–156 (2022). ISSN: 2057-5688
18. Liu, J., Yan, B., Mou, Z., Gao, Y., Niu, G., Li, X.: Numerical study of aeolian vibration characteristics and fatigue life estimation of transmission conductors. PLoS ONE **17**(1), e0263163 (2022). https://doi.org/10.1371/journal.pone.0263163
19. Degtyariov, K., Gnitko, V., Kononenko, Y., Kriutchenko, D., Sierikova, O., Strelnikova, E.: Fuzzy methods for modelling earthquake induced sloshing in rigid reservoirs. In: 2022 IEEE 3rd KhPI Week on Advanced Technology (KhPIWeek), pp. 297–302 (2022). https://doi.org/10.1109/KhPIWeek57572.2022.9916466
20. Love, J.S., Tait, M.J.: Advances in the design and optimization of tuned liquid dampers for seismic vibration control. J. Sound Vib. **498**, 115962 (2021). https://doi.org/10.1016/j.jsv.2021.115962
21. Çengel, Y.A., Cimbala, J.M.: Fluid Mechanics: Fundamentals and Applications. McGraw-Hill Education (2021). ISBN 978-0-07-338032-2
22. Faltinsen, O.M., Timokha, A.N.: Multimodal method for liquid sloshing in a tank with complex geometry. J. Fluid Mech. **926**, A25 (2021). https://doi.org/10.1017/jfm.2021.682
23. Karaiev, A., Strelnikova, E.: Axisymmetric polyharmonic spline approximation in the dual reciprocity method. ZAMM-J. Appl. Math. Mech./Zeitschrift für Angewandte Mathematik und Mechanik **101**(1), e201800339 (2021). https://doi.org/10.1002/zamm.201800339

24. Nguyen, D.T.A., Li, L., Ji, H.: Stable and accurate numerical methods for generalized Kirchhoff-Love plates. Numer. Anal. **1**, 1–26 (2020). https://doi.org/10.48550/arXiv.2008.01693
25. Ghaemmaghami, A.R., Kianoush, M.R.: Optimization of tuned liquid damper including different liquids for lateral displacement control of single and multi-story structures. Appl. Sci. **12**(6), 2977 (2022). https://doi.org/10.3390/app12062977

Numerical Simulation of a Mine Explosion Impact on the Gas-Detonation Demining Device

Denys Tkachenko, Vadym Garin(✉), Oleksiy Pavlenko, Olga Shypul, and Vitalii Myntiuk

National Aerospace University "Kharkiv Aviation Institute", 17 Vadyma Manka Street, Kharkiv 61070, Ukraine
v.garin@khai.edu

Abstract. This study investigates the dynamic response of a gas-detonation demining device's structure to shock waves from mine detonations. The Arbitrary Lagrangian-Eulerian method, implemented in LS-DYNA, was selected as the most suitable computational approach for simulating the coupled system "soil-air-mine-structure". To accurately reproduce cratering and capture the formation of secondary reflected waves, the soil was explicitly represented in the model as a deformable medium. The simulation results revealed the complex dynamics of shock wave propagation, allowing for a detailed analysis of the interaction between the primary and reflected waves with the demining device's structure. The developed numerical model made it possible to determine the pressure loads generated by both primary and secondary shock waves acting on structural elements of the demining device. The obtained results demonstrated that these loads are of destructive magnitude, leading to stresses exceeding the critical strength of the current design. Based on the numerical assessment, engineering recommendations were formulated to improve the structural resistance, including reinforcement of the main tube and supporting frame as well as the use of energy-dissipating attachments.

Keywords: mine detonation · shock wave · soil modeling · gas-detonation demining device

1 Introduction

The ongoing military aggression in Ukraine has led to unprecedented levels of land contamination from mines and explosive ordnance, necessitating extensive mine clearance efforts. According to current estimates, the area requiring clearance exceeds 150,000 km^2. Given the significant risks to human life, national and international security strategies are increasingly prioritizing the use of remotely operated technologies.

Various robotic platforms, including unmanned ground-based and aerial devices, have been developed with different mine neutralization subsystems. These platforms are typically divided into two categories: contact and non-contact. Contact platforms, such as flails, rollers, or tillers, detonate mines mechanically. Although effective, these

H. Altenbach et al. (Eds.): CAMPE 2025, LNME, pp. 232–241, 2026.
https://doi.org/10.1007/978-3-032-16381-3_22

methods expose the devices to high blast loads and fragmentation, which leads to a need for heavy armour, reinforced components, and complex repairs. This negatively affects operational reliability and economic viability.

Non-contact demining platforms represent a vital alternative. Their operation is based on the remote initiation of explosive devices using low-power impulse charges, directed cumulative jets, or gas-dynamic systems. The main advantage of this approach is that the critical subsystems of the device remain outside the blast zone, which minimizes structural damage, enhances the survivability of onboard electronics, and reduces maintenance costs. This approach significantly improves operator safety and clearance efficiency.

Of particular interest are systems that utilize gas detonation. A prototype demining complex employing directed gas-detonation jets was previously developed for detonating mines from a safe standoff distance [1]. While experimentally validated, the approach's effectiveness is heavily influenced by environmental factors, especially the condition of the upper soil layer.

Therefore, the objective of the present research is to enhance the structural design of the demining device based on numerical simulations of its response to both incident and reflected blast waves resulting from the detonation of a neutralized mine.

To achieve this objective, the following tasks must be addressed:

1. Select and implement the most appropriate numerical model for the coupled system of "soil-air-mine-demining device" in order to determine the dynamic loading effects of shock waves on the structural elements of the demining system.
2. Evaluate the stress-strain state of the principal structural components of the demining device resulting from the combined action of incident and reflected blast waves. Develop engineering recommendations to ensure the strength, integrity, and functional operability of the system.

2 Numerical Modeling for Structural Integrity: Methods and Application

Numerical simulation of detonation and its impact on structures is one of the most complex problems in computational mechanics. The challenge lies in simultaneously modelling the interaction of distinct physical continua explosives, air, soil, and structural materials under extreme pressures. Modern computational environments like LS-DYNA [2] offer several specialized techniques, including the Arbitrary Lagrangian-Eulerian (ALE) method [3–6], Smoothed Particle Hydrodynamics (SPH) method [7–9], and simpler Load Blast Enhanced (LBE) method [10, 11], as well as more recent particle-based approaches such as the Discrete Element Method (DEM) [12], which are actively being explored for blast-soil interaction problems.

The ALE method is a hybrid framework where compressible fluids (air, soil and detonation products) are modelled in a Eulerian reference frame, while the deminer structure uses a Lagrangian description. This coupling effectively reproduces shock wave propagation and impulse transfer to the structure. While robust across a wide pressure range, ALE is computationally demanding and requires stable schemes at material interfaces. In

contrast, the mesh-free SPH method excels at large deformations and material fragmentation but is sensitive to discretization parameters and prone to instabilities at interfaces with Lagrangian solids. Particle-based DEM, on the other hand, represent soil as assemblies of discrete particles and can capture granular effects with high fidelity; however, they are computationally intensive, still under validation, and therefore were not adopted in this study.

For structural analysis, where the primary objective is not the detonation dynamics itself, a simplified procedure like LBE method is used. These methods prescribe the load directly as time-dependent pressure functions, eliminating the need to model air, mine and soil as physical continua. This approach significantly reduces computational costs, enabling rapid parametric studies and structural optimization. However, this simplification precludes analysis of soil-structure interaction and reflected waves, limiting its use to engineering assessments.

The primary objective of the present study was to analyse the loading of the demining device structure induced by shock waves generated by mine detonation, encompassing both the primary wave and the secondary wave formed as a result of their reflection from the surface of the soil with the crater. Therefore, a hybrid ALE formulation was adopted as the primary computational strategy.

For a detailed analysis, a three-dimensional finite element model was created (Fig. 1). At its core was a Multi-Material Arbitrary Lagrangian-Eulerian [13] mesh, which allowed multiple continua (air, mine and soil) to coexist within a single computational domain. This ensured a physically consistent representation of interfacial phenomena like shock wave reflection and material mixing. Each medium was defined as a separate material group with its own properties and constitutive laws.

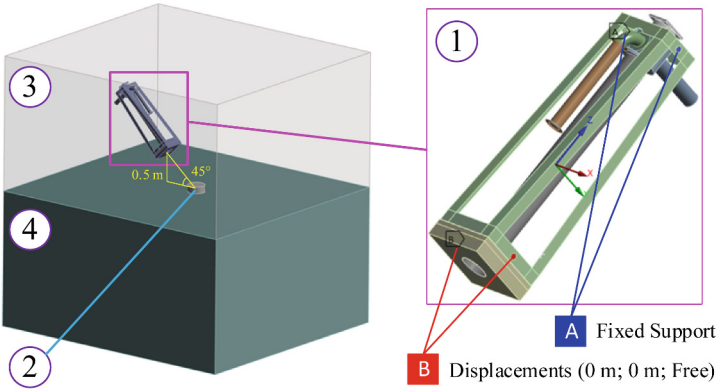

Fig. 1. Structure of the computational model: 1. Deminer (see [1]); 2. Mine; 3. Air; 4. Ground.

The deminer's structural elements were modelled as deformable Lagrangian bodies, with solid elements for protective plates and case's components, and shell elements for tubes, flanges, and frame members. The interaction between the Eulerian continua and Lagrangian bodies was implemented using the *CONSTRAINED_LAGRANGE_IN_SOLID algorithm [3, 4], as a standard LS-DYNA

scheme for fluid-structure interaction. This penalty-based method ensured physically consistent momentum transfer, and the use of the LEAKAGE_CONTROL = STRONG option guaranteed robust resolution of sharp pressure gradients at material interfaces.

The simulations were performed on a computer with 48 processing cores. The computational model comprised approximately 10 million elements. An automatic time step without mass scaling was employed. The estimated computational time for a single calculation point was approximately 6 h.

In conclusion, the chosen numerical approach provides a detailed and physically consistent description of the entire detonation process. This not only allows for the evaluation of the demining device's structural strength but also facilitates the development of reliable design criteria that account for real-world geotechnical conditions.

3 Material Properties of the Computational Model Elements

In constructing the finite element model of the demining device, accurately describing material properties is crucial, as they influence the reliability of the structure's dynamic response to blast loading. The elements of the computational model can be divided into four main groups: metallic structural elements, the air medium, the explosive charge, and the soil foundation. For each group, specialised LS-DYNA material cards were applied to define their mechanical and physical properties under detonation loading.

The elements of the gas-detonation demining system consist of two principal types of steels. The housing, working tubes, connecting nodes, and supporting struts of the protective casing are manufactured from structural steel. In contrast, the screen section of the casing comprises two plates: the inner plate is constructed from Rolled Homogeneous Armour (RHA), and the outer plate is also made of structural steel. The armour plate provides stiffness to the protective plate enabling it to withstand the detonation wave generated by the mine explosion. The outer plate is a replaceable component: after being damaged, it can be dismantled and replaced without compromising the overall durability of the system. To describe the physico-mechanical characteristics of steels, following the recommendations of [14], a unified LS-DYNA card *MAT_POWER_LAW_PLASTICITY [15] was employed. Examples of this card filled out for structural steel and RHA are shown in Fig. 2a and Fig. 2b, respectively. All values in the material cards are given in the unit system "kg, m, s, N, Pa".

The specified cards implement a model of isotropic elastoplastic material behaviour with power-law hardening and account for the influence of strain rate through the Cowper–Symonds relation. The yield stress (σ_y) in the model is described by the expression:

$$\sigma_y = k\left(\varepsilon_{yp} + \overline{\varepsilon}^p\right)^n, \tag{1}$$

where ε_{yp} is the elastic strain to yield, $\overline{\varepsilon}^p$ is the effective (logarithmic) plastic strain, k and n are power-law constants. The influence of strain rate is accounted for by an additional scaling factor: $1 + \left(\frac{\dot{\varepsilon}}{C}\right)^{1/p}$, in which C and p are user-defined strain-rate sensitivity parameters, and $\dot{\varepsilon}$ is the current strain rate.

In the computational model, the charge was represented as a cylinder with a diameter of 250 mm and a height of 100 mm, corresponding to a mass of 7.85 kg based on a trinitrotoluene density of 1630 kg/m^3. This configuration was used as an analogue for the TM-62T combat mine, which is extensively deployed and regarded as the most powerful within the category of ground anti-tank mines. The behaviour of the charge in LS-DYNA was described using a combination of the *MAT_HIGH_EXPLOSIVE_BURN and *EOS_JWL cards [14, 15], which allowed for the consideration of both detonation front propagation and the pressure of the explosion products. The Jones-Wilkins-Lee equation of state, which determines the behaviour of detonation products, has the following form:

$$p = A\left(1 - \frac{\omega}{R_1 v}\right)exp(-R_1 v) + B\left(1 - \frac{\omega}{R_2 v}\right)exp(-R_2 v) + \frac{\omega E_1}{v}, \qquad (2)$$

where p – pressure, v – relative volume, E_1 – specific internal energy and A, B, R_1, R_2, ω are material constants that characterize the behavior of detonation products across a wide pressure range from peak conditions to hydrodynamic equilibrium.

The parameters for trinitrotoluene and the coefficients of the equation of state, as described by these two cards, are shown in Fig. 2c.

*MAT_POWER_LAW_PLASTICITY

$#	mid	ro	e	pr	k	n	src	srp
	1	7850.0	2.1E11	0.28	5.57E8	0.119	40.4	5.0
$#	sigy	vp	epsf					
	2.5E8	0.0	0.0					

a)

*MAT_POWER_LAW_PLASTICITY

$#	mid	ro	e	pr	k	n	src	srp
	2	7850.0	2.1E11	0.28	1.56E9	0.0918	3200.0	5.0
$#	sigy	vp	epsf					
	9.5E8	0.0	0.0					

b)

*MAT_HIGH_EXPLOSIVE_BURN

$#	mid	ro	d	pcj	beta	k	g	sigy
	3	1630.0	6930.0	2.1E10	0.0	0.0	0.0	0.0

*EOS_JWL

$#	eosid	a	b	r1	r2	omeg	e0	vo
	3	3.712E11	3.231E9	4.15	0.95	0.3	7.0E9	1.0

c)

*MAT_NULL

$#	mid	ro	pc	mu	terod	cerod	ym	pr
	4	1.2255	0.0	0.0	0.0	0.0	0.0	0.0

*EOS_LINEAR_POLYNOMIAL

$#	eosid	c0	c1	c2	c3	c4	c5	c6
	4	0.0	0.0	0.0	0.0	0.4	0.4	0.0
$#	e0		v0					
	253312.5		1.0					

d)

*MAT_PSEUDO_TENSOR

$#	mid	ro	g	pr				
	5	2094.63	23028498	0.0				
$#	sigf	a0	a1	a2	a0f	a1f	b1	per
	-6895	0.0	0.0	0.0	0.0	0.0	0.0	0.0
$#	er	prr	sigy	etan	lcp	lcr		
	0.0	0.0	0.0	0.0	0	0		
$#	x1	x2	x3	x4	x5	x6	x7	x8
	0.0	13790	34474	68948	137895	344738	379212	413686
$#	x9	x10	x11	x12	x13	x14	x15	x16
	448159	482633	517107	551581	620528	689476	827371	1034214
$#	ys1	ys2	ys3	ys4	ys5	ys6	ys7	ys8
	30034	47643	74057	118080	206126	470264	514287	558310
$#	ys9	ys10	ys11	ys12	ys13	ys14	ys15	ys16
	602333	646356	690379	734402	822448	910494	1086587	1350725

*EOS_TABULATED_COMPACTION

$#	eosid	gama	e0	v0	lcc	lct	lck	lcid
	5	0.0	0.0	1.0	0	0	0	0
$#	ev1	ev2		ev3		ev4		ev5
	0.0	-0.00252		-0.00479		-0.00703		-0.00917
$#	ev6		ev7		ev8		ev9	ev10
	-0.0103		-0.01143		-0.01254		-0.01362	-0.01599
$#	c1	c2		c3		c4		c5
	0.0	68948		137895		206843		275790
$#	c6		c7		c8		c9	c10
	310264		344738		379212		413686	490562
$#	t1	t2	t3	t4	t5			
	0.0	0.0	0.0	0.0	0.0			
$#	t6	t7	t8	t9	t10			
	0.0	0.0	0.0	0.0	0.0			
$#	k1		k2		k3		k4	k5
	1.33552e+08		1.33552e+08		1.33552e+08		1.33552e+08	1.33552e+08
$#	k6		k7		k8		k9	k10
	1.33552e+08		1.33552e+08		1.33552e+08		1.33552e+08	1.33552e+08

e)

Fig. 2. Description of the physical and mechanical properties of the computational model elements using LS-DYNA cards (designations adopted in accordance with [15]).

In the computational model, the air medium was described using a combination of the *MAT_NULL and *EOS_LINEAR_POLYNOMIAL cards [14, 15]. The dynamic

viscosity of air in the model was taken as zero, which is a justified assumption, since its influence on the formation of the shock wave and, consequently, on the loading of the structure near the blast epicentre, is negligibly small. Thus, we arrive at an ideal gas model, which is a generally accepted approach for modelling high-intensity, short-period shock-wave processes. The pressure in such a medium is determined by the formula:

$$p = (\gamma - 1)\frac{\rho}{\rho_0}E_2, \tag{3}$$

here $\gamma = 1.4$ s the adiabatic index of air, ρ/ρ_0 is the ratio of the current density to the initial density, E_2 is the specific internal energy. All air medium parameters used in the calculation are shown in Fig. 2d.

In the numerical simulation of the blast loading on the structure of the demining device, we considered both the direct impact of the primary shock wave from the mine's detonation and the secondary impact of the reflected wave forming on the soil surface. The explosion process is accompanied by cratering, which alters the surface configuration and, consequently, affects the geometry of the shock wave front. This leads to a change in the direction of wave propagation and the generation of additional impulsive loads acting on the structure. Therefore, a correct description of soil mechanics is a key condition for an adequate assessment of the system's dynamic response during a mine detonation.

Among the geological material models implemented in LS-DYNA, a combination of the *MAT_PSEUDO_TENSOR and *EOS_TABULATED_COMPACTION cards [15] were used to describe the properties of porous sandy soil, in accordance with the recommendations from [16, 17]. The first card defines strength characteristics through a Mohr–Coulomb yield surface with a Tresca cutoff. The diagram is plotted in "principal stress difference ($\sigma_1 - \sigma_3$) vs. mean pressure p" coordinates and reflects the increase in shear strength with increasing confining pressure. The second card defines the volumetric behaviour of the material through a tabulated pressure-volumetric strain relationship, which allows for the reproduction of compaction and decompaction processes.

Unwashed sand [17] was used as the computational soil. Its characteristics were specified using the LS-DYNA cards shown in Fig. 2e.

4 Results of Numerical Experiments

Figure 3 illustrates the evolution of shock-wave propagation over the time interval (τ) from 0.1 to 10 ms. This visualization allows us to track the dynamics of interaction between the primary shock wave and the reflected shock wave as they interact with the structure of the demining device. Analysing the frames presented demonstrates the effectiveness of the protective plate, which absorbs the primary impact of a mine explosion and redistributes the energy of the initial detonation wave. This redistribution significantly reduces the loading on the critical structural elements of the device.

During this design stage of the demining device's protective plate, we observed that the shock wave imposes a considerable dynamic impact on the inner walls of the tube. The visualization further confirms that damage to the structure is solely due to the shock wave, as soil particles do not reach the device's surface. This indicates that the protective

system is functioning effectively. Figure 4 presents the calculated impulse pressure values generated by the incident and reflected shock waves acting on the protective plate (made of structural steel) and the main tube of the demining device.

In Fig. 5, the computed stress fields for the adopted structural dimensions of the demining device are presented. The principal dynamic loading is concentrated on the protective plate (Fig. 5a); however, the stresses induced in this component remain within the admissible limits. A stress surge at the tube inlet of the demining device (Fig. 5b) is associated with the direct penetration of the detonation wave into the tube. Within a distance of up to 100 mm from the tube edge, the resulting stresses exceed the allowable values. The response of the frame struts (Fig. 5c) to the loading transmitted through the protective plate under shock-wave impact demonstrates stress levels surpassing the critical buckling load, which indicates a potential loss of structural stability in these elements.

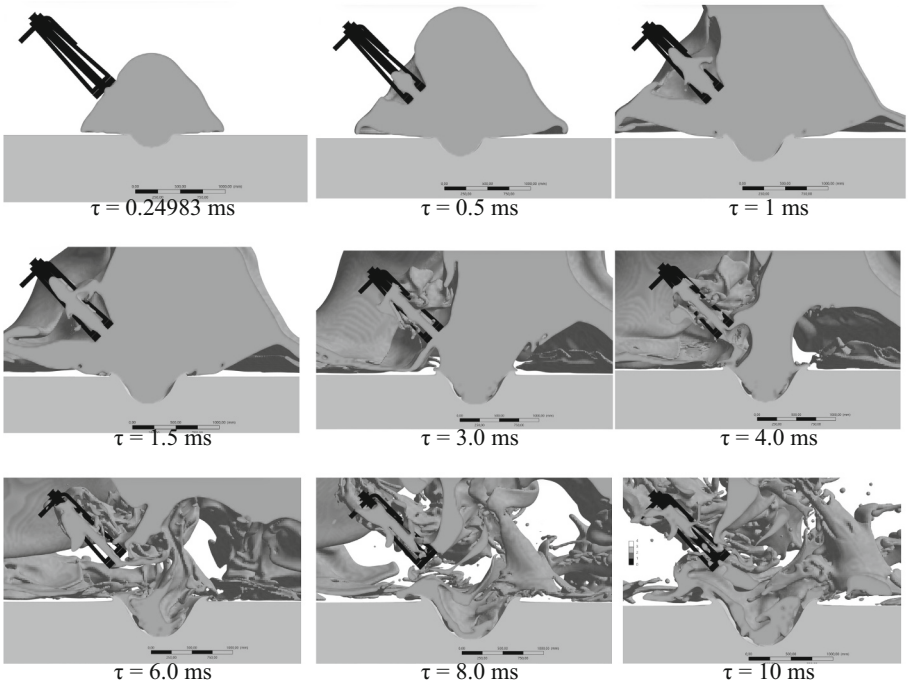

Fig. 3. Distribution of the detonation wave and explosive products.

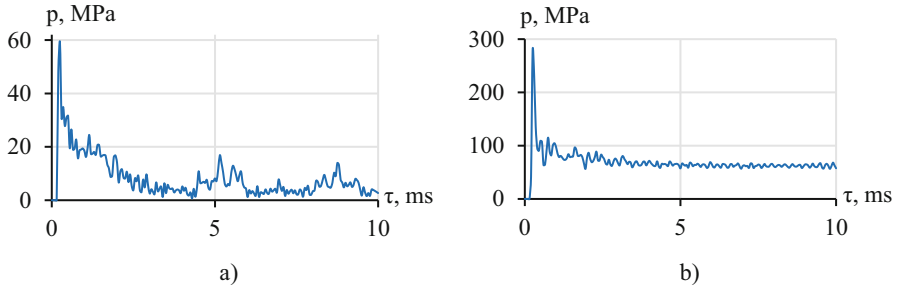

Fig. 4. Pressure on: a) protective plate (structural steel) and b) main tube.

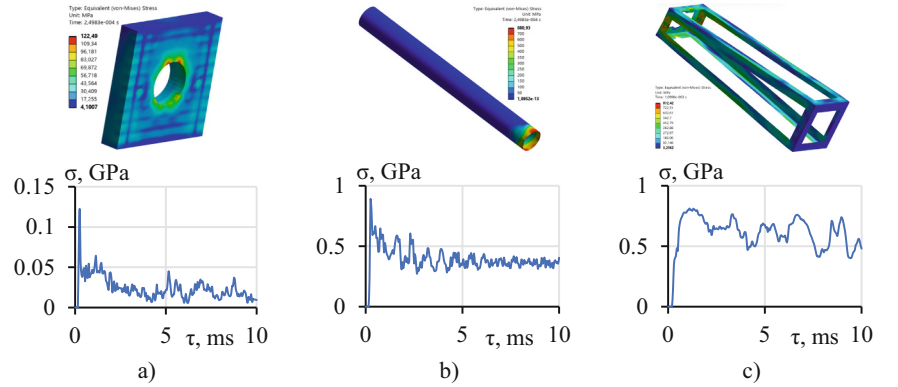

Fig. 5. Von Mises equivalent stresses in the main load-bearing elements of the demining device structure.

5 Conclusions

1. The adopted ALE numerical model of the "soil-air-mine-demining device" system, which accounts for crater formation and reflections of detonation waves from the soil surface, enabled the determination of dynamic loads acting on the demining device structure.
2. The dimensions and strength of the protective plate, located at the frontal end of the main tube, are sufficient to withstand both the incident and reflected detonation waves generated by the explosion of the targeted mine.
3. The calculated stress levels in the main tube of the demining device, caused by the action of incident and reflected detonation waves, exceed the critical limits. To ensure operability, either the tube material should be replaced with a higher-strength alloy, or, if the same material is retained, the wall thickness must be increased by 170%. Since the stresses at the frontal end of the main tube exceed those along the rest of its length, the output section of the tube should be reinforced by installing an outer sleeve under interference fit with a length of 1.5–2 tube diameters.

4. The analysis revealed that the designed longitudinal frame struts of the demining device do not possess sufficient strength to withstand the applied loads. Instead of the angle-section profile, a square tube with a cross-sectional area increased by a factor of 4.2 should be used to satisfy the strength and stability requirements.
5. To partially compensate for the intensity of loading on the structural elements of the demining device by incident and reflected detonation waves, a sliding mounting system with damping devices should be developed.

References

1. Pavlenko, O., Shypul, O., Myntiuk, V., Tkachenko, D., Brega D., Garin V.: Development of a conceptual model for a gas detonation deminer. Aerosp. Technic Technol. **6**(200), 70–79 (2024). https://doi.org/10.32620/aktt.2024.6.07
2. LS-DYNA Homepage. https://lsdyna.ansys.com. Accessed 1 Aug 2025
3. Barsotti, M., Sammarco, E., Stevens, D.: Comparison of strategies for landmine modeling in LS-DYNA with sandy soil material model development. In: 11th European LS-DYNA Conference, Detroit, USA, 12–14 June 2016 (2016)
4. Trajkovski, J.: Comparison of MM-ALE and SPH methods for modelling blast wave reflections of flat and shaped surfaces. In: 11th European LS-DYNA Conference, Salzburg, Austria (2017)
5. Gong, C., Qiu, Y., Long, Z., Liu, L., Xu, G., Yang, L.: Study on the earth-covered magazine models under the internal explosion. Shock. Vib. **2024**, 20 (2024). https://doi.org/10.1155/2024/6626486
6. Wang, D., Xu, S., Wang, Z., Zhou, Z., Gao, N.: Research on physical explosion crater model of high-pressure natural gas tubeline. Pet. Res. **9**(2024), 432–438 (2024)
7. Cui, Y., Li, Z., Fang, J., Zhao, B.: Crater effects of shallow burial explosions in soil based on SPH-FEM analysis. Front. Earth Sci., 9 (2023). https://doi.org/10.3389/feart.2022.1114178
8. Jindra, D., Hradil, P., Kala, J.: Finite element analysis of concrete slab exposed to high velocity pressure wave – simplified vs. smoothed-particle hydrodynamics (SPH) method. In: MATEC Web of Conferences, vol. 396, p. 13 (2024). https://doi.org/10.1051/matecconf/202439605005
9. Espinoza-Garcés, C., Aguilar-Pérez, L., Rueda-Arreguin, J., Pérez-Martínez, I., Torres-Ariza, J., Torres SanMiguel, C.: Head injuries evaluation during a tubeline explosion. Results Eng. **21** (2024). https://doi.org/10.1016/j.rineng.2023.101655
10. Mihali, A., Rebelo, H.B., Cismaşiu, C., Shaker, N.H.: Impact of building model complexity on predicting external explosion consequences. Eng. Struct. **339**, 14 (2025). https://doi.org/10.1016/j.engstruct.2025.120534
11. Li, W., Wang, P., Feng, G., Lu, Y., Yue, J., Li, H.: The deformation and failure mechanism of cylindrical shell and square plate with pre-formed holes under blast loading. Def. Technol. **17**(4), 1143–1159 (2021). https://doi.org/10.1016/j.dt.2020.06.014
12. Faergestad, R.M., Holmen, J.K., Berstad, T., Cardone, T., Ford, K.A., Børvik, T.: Coupled finite element-discrete element method (FEM/DEM) for modelling hypervelocity impacts. Acta Astronaut. **203**, 296–307 (2023). https://doi.org/10.1016/j.actaastro.2022.11.026
13. LS-DYNA Keyword User's Manual, Volume I (2025)
14. Myntiuk, V., Tkachenko, D., Pavlenko, O., Shypul, O.: simulating the effect of mine explosion on a remote gas detonation deminer. In: Lytvynov, O., Pavlikov, V., Krytskyi, D. (eds.) Integrated Computer Technologies in Mechanical Engineering – 2024, ICTM 2024. LNNS, vol. 1474, pp. 443–454. Springer, Cham (2025). https://doi.org/10.1007/978-3-031-94852-7_37

15. LS-DYNA Keyword User's Manual, Volume II, Material Models (2025)
16. Rokhy, H., Nasouri, R., Montaya, A., Matamoros, A., Bakzadeh, R.: Calibration of six constitutive material models for geomaterial. In: 13th European LS-DYNA Conference, Ulm, Germany (2021)
17. Thomas, M.A., Chitty, D.E., Gildea, M.L., T'Kindt, M.C.: NASA/CR-2008-215334. Constitutive Soil Properties for Unwashed Sand and Kennedy Space Center. National Aeronautics and Space Administration Langley Research Center, Hampton, Virginia (2008)

Effect of Nanodiamond and Nanographite Fillers on the Dielectric Characteristics of Polymer Composites

Maryna Shevtsova[1], Oleksii Vambol[2], Tetyana Nabokina[3], and Andrii Kondratiev[4](✉)

[1] Vilnius Gediminas Technical University, 11, Saul˙etekio Al., 10223 Vilnius, Lithuania
[2] Lviv Polytechnic National University, 12, Stepan Bandera St., Lviv 79013, Ukraine
[3] National Aerospace University "Kharkiv Aviation Institute", 17, Vadym Manko St., Kharkiv 61070, Ukraine
[4] O.M. Beketov National University of Urban Economy in Kharkiv, 17, Chornohlazivska St., Kharkiv 61002, Ukraine
andrii.kondratiev@kname.edu.ua

Abstract. This study investigates the effect of nanodiamond and nanographite fillers on the dielectric properties of epoxy resin composites. Cylindrical specimens based on epoxy resin EPICOTE 828 with an anhydride curing agent were fabricated in neat form and with the addition of 0.6 wt.% nanodiamonds or nanographite. The dielectric response was measured using a resonant Q-meter method in the frequency range of 0.1–100 kHz. The developed experimental setup, combining the Q-meter with a digital voltmeter and a frequency counter, enabled reliable determination of dielectric permittivity and dielectric loss tangent. The results demonstrate that the incorporation of nanodiamonds reduces the dielectric permittivity compared with the neat epoxy binder. This decrease indicates a reduction in the number of polar groups and an increase in the structural ordering of the polymer matrix. In contrast, the addition of nanographite leads to a slight increase in dielectric permittivity, which suggests the formation of additional polarization pathways and a more disordered polymer structure. The scientific novelty of the study lies in providing a comparative analysis of nanodiamond and nanographite fillers in epoxy composites using resonant dielectric spectroscopy. The findings highlight the different mechanisms by which carbon-based nanofillers alter the dielectric behavior of polymers, offering practical guidance for tailoring epoxy-based composites for electrical insulation and related engineering applications.

Keywords: Resonant Method · Dielectric Spectroscopy · Polarization

1 Introduction

Polymer-based dielectric materials play a pivotal role in modern technology, being widely used in electrical insulation, sensors, and high-frequency electronic devices [1]. Among them, epoxy resins represent one of the most versatile classes due to their strong

H. Altenbach et al. (Eds.): CAMPE 2025, LNME, pp. 242–251, 2026.
https://doi.org/10.1007/978-3-032-16381-3_23

adhesion, chemical resistance, and good mechanical performance [2]. These characteristics have secured their position in critical applications ranging. Advanced epoxy resins with tailored dielectric performance are increasingly required in aerospace and transportation industries [3–5], where multifunctional polymer structures must serve not only as lightweight load-bearing elements [6, 7] but also as effective insulators in environments involving high electrical, thermal [8, 9], and mechanical stresses. In recent decades, the increasing demand for higher operating voltages, reduced component size, and improved energy efficiency has revealed the limitations of neat epoxies, such as relatively low dielectric constant, limited thermal stability, and susceptibility to dielectric breakdown under harsh operating conditions. A widely adopted strategy to overcome these limitations is the modification of epoxy with nanofillers [10]. The incorporation of nanoscale reinforcements provides the opportunity to tailor dielectric, thermal, and mechanical performance simultaneously [11]. Carbon-based nanofillers are particularly attractive due to their abundance, stability, and unique electronic properties [12]. However, their impact strongly depends on the nature of the filler: while conductive carbons such as graphene and nanographite can increase the dielectric permittivity through interfacial polarization, insulating carbons such as nanodiamond contribute to dielectric strength and stability by suppressing charge transport and reducing the number of active polar groups in the polymer matrix.

This duality highlights the scientific and practical importance of exploring carbon nanofillers with contrasting electrical characteristics. Nanodiamonds, consisting of sp3-carbon with a wide band gap, act as electrical insulators capable of trapping high-energy electrons, thereby reducing dielectric losses and improving breakdown resistance. Nanographite, on the other hand, with its sp2-carbon structure, promotes interfacial charge accumulation and enhances Maxwell-Wagner polarization, which leads to increased dielectric permittivity but may also raise dielectric loss if the filler concentration approaches the percolation threshold. Direct comparative analysis of these two fillers within the same epoxy system can therefore provide valuable insights into the mechanisms by which nanofillers influence dielectric response.

2 Literature Review

Carbon nanofillers have shown considerable potential for enhancing dielectric properties of epoxy composites. In [10], fluorinated graphene improved permittivity to about 8.23 at 1 wt.% while keeping dielectric loss very low ($tg\delta < 0.015$). This confirmed that chemical modification can suppress intrinsic conductivity and improve insulation reliability. Yet, the work was limited to fluorinated derivatives and did not compare insulating nanodiamonds with conductive carbons such as nanographite.

Graphene-based systems have also been investigated in other forms. In [13], small amounts of graphene enhanced partial discharge resistance and charge decay, indicating improved insulation, though frequency-dependent dielectric behavior was not examined. A more systematic study [14] used broadband dielectric spectroscopy of epoxy with functionalized graphene oxide, revealing strong interfacial polarization and β-relaxation while maintaining insulation. Similarly, [15] reviewed epoxy/graphene oxide systems, emphasizing their potential for improving dielectric constant and interfacial polarization in energy storage, but focusing only on conductive fillers.

Insulating carbon nanofillers have attracted less attention. Polyimide/nanodiamond composites in [16] showed a 37.5% increase in permittivity ($\varepsilon' = 4.4$) and high breakdown strength with only 0.4 vol.% filler, demonstrating the strong interfacial polarization of nanodiamonds. However, the results were limited to polyimide matrices, leaving their role in epoxy and comparison with conductive fillers unresolved.

Conductive fillers other than graphene have been tested. Epoxy with multi-walled carbon nanotubes and carbon-coated copper nanoparticles [17] showed reduced percolation thresholds and higher conductivity, but dielectric stability was not evaluated. Epoxy with polyaniline nanorods [18] achieved permittivity values around 15 at 100 Hz, yet exhibited high dielectric losses at low frequencies. A multilayer design in [19] using reduced graphene oxide and boron nitride nanosheets provided $\varepsilon' = 24.1$ with low losses (0.01–0.05), but did not consider insulating carbons such as nanodiamonds.

Overall, graphene and related conductive carbons generally increase permittivity but often lead to higher dielectric losses, whereas nanodiamonds can improve breakdown strength and stability but are scarcely explored in epoxy matrices. Direct comparisons of insulating and conductive carbons within the same epoxy host are almost absent.

The aim of this study is therefore to investigate the influence of nanodiamond and nanographite fillers on the dielectric properties of epoxy resin composites using a resonant Q-meter method. Particular attention is given to the frequency dependence of dielectric permittivity and dielectric loss tangent, in order to clarify how nanofillers with different electronic structures affect structural ordering and polarization mechanisms in the polymer matrix.

3 Research Methodology

To evaluate the influence of gamma irradiation on the dielectric properties of the polymer, cylindrical specimens with a thickness of 2–3 mm were prepared (Fig. 1).

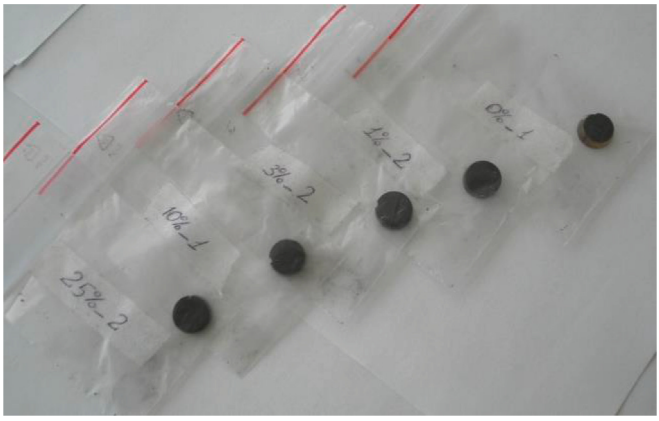

Fig. 1. Specimens for determining dielectric permittivity

The samples were fabricated from epoxy resin EPICOTE 828 (Westlake Epoxy/Hexion, USA) cured with the anhydride hardener EPICURE (Westlake Epoxy/Hexion, USA) [20, 21], as well as from modified formulations containing 0.6 wt.% nanodiamonds and nanographite (Fig. 2).

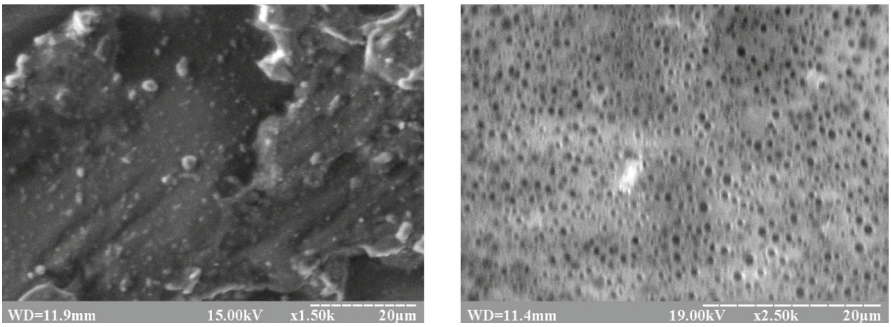

a b

Fig. 2. Micrographs of epoxy resin specimens reinforced with nanodiamond (a) and nanographite (b) fillers

Measurements of the dielectric properties were carried out using a Q-meter, which enabled the determination of both the dielectric loss tangent ($tg\delta$) and the equivalent capacitance of the measuring cell. Based on the capacitance values, the real part of the dielectric permittivity (ε') was calculated, while the quality factor of the resonant circuit was used to determine the dielectric loss tangent.

To determine the dielectric constants of the polymer, a resonant measurement method was employed [22]. The principle of the method consists in placing the polymer specimen into the measuring cell, which acts as a capacitor C_x connected in parallel with the variable capacitor C_v (control capacitor) of the series resonant circuit of the Q-meter, as illustrated in Fig. 3.

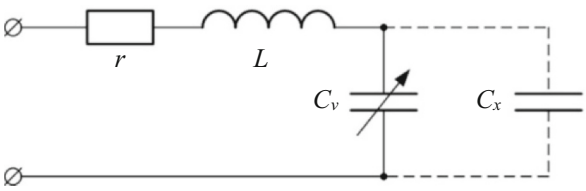

Fig. 3. Schematic diagram of the series resonant circuit of the Q-meter

During the measurements, the capacitance C_v was gradually varied at the frequency f_r to tune the series resonant circuit of the Q-meter into resonance. Using the instrument indicator, the quality factor Q_1 of the resonant circuit was determined, where the total capacitance of the circuit is given by $C_1 = C_x + C_v$.

The quality factor is proportional to the maximum voltage U_{max} across the capacitor C_x. Knowing the quality factor Q_0 of the circuit and its capacitance without the test

specimen C_x at the resonance frequency f_r, the quality factor of the measuring cell with the investigated material as the dielectric can be determined:

$$Q_{cx} = \frac{(C_0 - C_1)Q_0Q_1}{(Q_0 - Q_1)(C_0 + C_{ic})}, \tag{1}$$

where C_{ic} – the self-capacitance of the inductor coil of the Q-meter resonant circuit.

It should be noted that the accuracy of determining the dielectric constants using a Q-meter depends on the precision in measuring the capacitance of the resonant circuit, the resonance voltage, as well as the accuracy of tuning the alternating current resonance frequency. Compared to digital measuring instruments, the accuracy of these quantities, which are read from the analog scales of the Q-meter, is relatively low. To improve the accuracy of measuring the frequency dependence of the dielectric constants with the Q-meter (VM-560), a measurement setup was employed, the block diagram of which is shown in Fig. 4. In this setup, a digital voltmeter (V7–21) and a digital frequency counter (Ch3–34) were used to measure the voltage across the resonant circuit at resonance and to monitor its frequency, respectively.

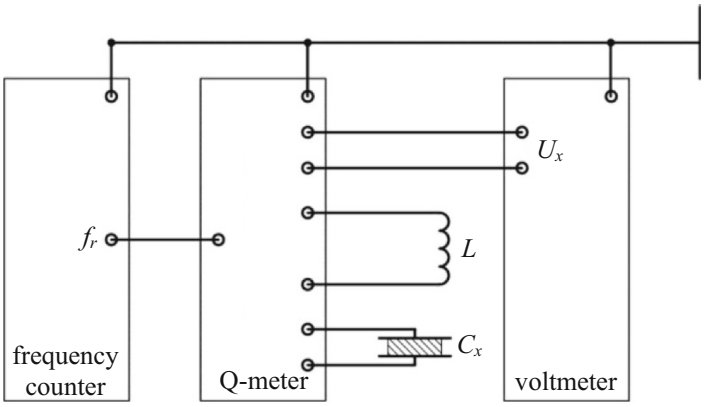

Fig. 4. Block diagram of the setup for measuring the frequency dependence of the dielectric parameters of the polymer

Let us consider the equivalent circuit of the Q-meter with the specimen (Fig. 5).

The measured value of the intrinsic quality factor Q_0 of the circuit with the specimen disconnected is mainly determined by the losses in the coil:

$$Q_0 = \frac{2\pi f_0 L}{r} = \frac{1}{2\pi f_0 C_0 r} = \frac{1}{d_0}, \tag{2}$$

where d_0 – the damping of the circuit without the specimen at resonance; C_0 – the capacitance of the variable capacitor C_v.

When the specimen with parameters R and C_x is connected, the complex equivalent impedance of the circuit is determined by the following relation:

$$Z_{eq} = r + j2\pi fL + \frac{R\left[1 - j2\pi fR(C_x + C_1)\right]}{\left[1 + 4\pi^2 f^2 R^2 (C_x + C_1)^2\right]}, \tag{3}$$

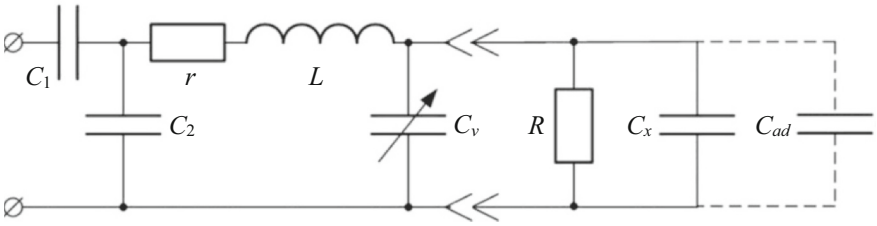

Fig. 5. Equivalent circuit of the Q-meter with the specimen

where C_1 – the new value of the capacitance measured at resonance.

From Eq. (1), the active equivalent resistance of the Q-meter circuit at resonance can be written as:

$$r_{eq} = r + \frac{R}{1 + 4\pi^2 f_0^2 R^2 (C_x + C_1)^2}, \tag{4}$$

Let $Q_{eq} = 2\pi f_0 R(C_x + C_1)$ denote the equivalent quality factor of the entire capacitive branch of the Q-meter circuit. Transforming Eq. (4), we obtain:

$$r_{eq} \approx r + \frac{1}{4\pi^2 f_0^2 R(C_x + C_1)C_1} = r + \frac{1}{2\pi f_0 C_1 Q_{eq}}, \tag{5}$$

Hence, the quality factor of the Q-meter circuit with the connected specimen at resonance is determined as:

$$Q = \frac{2\pi f_0 L}{r_{eq}} = r + \frac{2\pi f_0 L}{r + \frac{1}{2\pi f_0 Q_{eq} C_1}} = \frac{Q_0 Q_{eq}}{Q_0 + Q_{eq}}, \tag{6}$$

Knowing that the equivalent dielectric loss tangent $tg\delta_{eq}$ of the entire capacitive branch of the circuit with the specimen is the reciprocal of Q_{eq}, it can be expressed as:

$$tg\delta_{eq} \approx \frac{1}{2\pi f_0 C_1 R} = \frac{C_x tg\delta}{C_1},$$

where $tg\delta = \frac{1}{2\pi f_0 C_x R}$ – the dielectric loss tangent of the specimen.

The attenuation $d_c = 1/Q_c$ can be expressed as

$$d_c = d_0 + tg\delta_{eq} = d_0 + \frac{C_c tg\delta}{C_1}, \tag{7}$$

from which it follows that

$$tg\delta = \frac{(d_c - d_0)C_0}{C_x}, \tag{8}$$

i.e., the range of measurable values of $tg\delta$ can be extended by increasing the capacitance C_0.

The described method makes it possible to measure the frequency dependences of the dielectric parameters of the specimens for $tg\delta$ values up to 16. The specimens were tested at frequencies of 0.1 kHz, 1 kHz, 10 kHz, and 100 kHz.

4 Results and Discussion

Although the Q-meter allows simultaneous acquisition of the frequency dependences of ε' and $tg\delta$, only the graphs of dielectric permittivity ε' are presented below for analysis. This is due to the fact that variations in ε' more clearly reflect the influence of nanofillers on the polymer structure, whereas $tg\delta$ was mainly used for intermediate calculations. After processing the experimental data, the following frequency dependences of dielectric permittivity were plotted for the neat binder and the binder modified with nanodiamonds and nanographite (Figs. 6, 7).

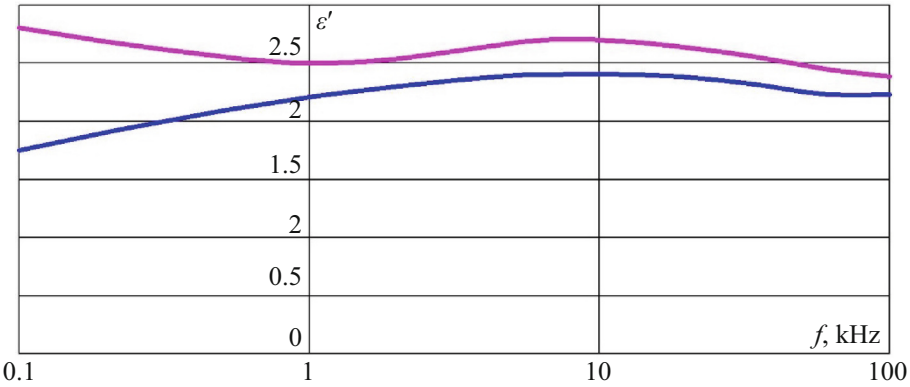

Fig. 6. Frequency dependence of dielectric permittivity for the neat binder (▬) and the binder modified with nanodiamonds (▬)

As shown in Fig. 6, the dielectric permittivity of the epoxy resin decreases upon the addition of nanodiamonds. This reduction indicates a decrease in the concentration of polar groups and suggests that nanodiamonds promote a more ordered polymer structure. The observed behavior is consistent with previous reports that insulating nanocarbon fillers, such as nanodiamonds, act as electron traps and suppress interfacial polarization, thereby reducing the effective dielectric constant while improving structural stability and breakdown performance.

In contrast, Fig. 7 demonstrates that the addition of nanographite leads to a slight increase in dielectric permittivity compared to the neat epoxy. This behavior is attributed to the sp^2-carbon structure of nanographite, which facilitates interfacial charge accumulation and enhances Maxwell-Wagner polarization at the filler-matrix interface.

Similar trends have been reported for graphene- and graphite-filled epoxy nanocomposites, where small additions of conductive fillers significantly enhance ε', particularly at low frequencies. However, this enhancement is accompanied by a risk of increased dielectric loss if the filler loading approaches the percolation threshold.

A key finding of this study is the contrasting role of the two nanocarbon fillers: nanodiamonds act as dielectric stabilizers that reduce permittivity but may improve breakdown strength and reduce losses, while nanographite acts as a permittivity booster that increases ε' but can potentially compromise insulation integrity if not carefully

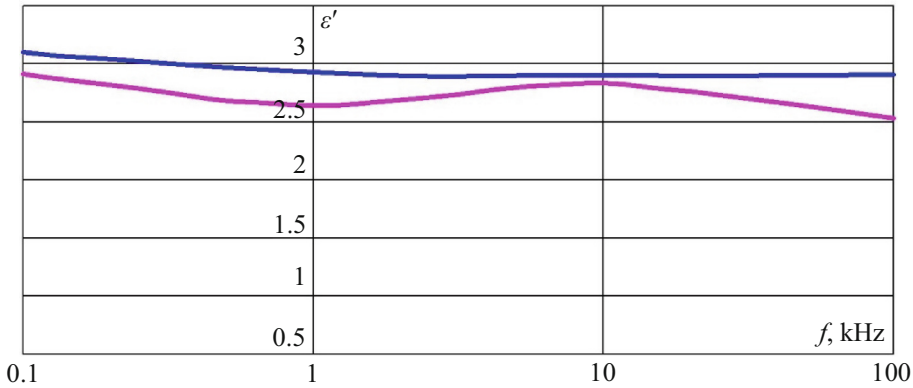

Fig. 7. Frequency dependence of dielectric permittivity for the neat binder (▬) and the binder modified with nanographene (▬)

controlled. This dual behavior highlights the importance of tailoring filler type and concentration depending on the target application. For example, nanodiamond-modified epoxies are promising for high-voltage insulation systems, where low loss and high reliability are critical. Nanographite-modified epoxies may be suitable for capacitive or sensing applications, where enhanced polarization and permittivity are desirable.

The frequency-dependent measurements further reveal that the differences induced by nanodiamond and nanographite are more pronounced at low frequencies (0.1–1 kHz), where interfacial polarization dominates. At higher frequencies (10–100 kHz), the permittivity values of all composites converge, suggesting that the contribution of interfacial polarization diminishes as the relaxation processes cannot keep pace with the alternating electric field. This frequency-dependent behavior corroborates the general understanding of dielectric relaxation phenomena in polymer nanocomposites.

Overall, the results confirm literature findings and provide direct comparative evidence that two nanocarbon fillers with fundamentally different electronic structures – insulating nanodiamonds and conductive nanographite – produce opposite effects on the dielectric characteristics of epoxy composites. The findings demonstrate the feasibility of using selective nanofiller strategies to engineer polymer composites with application-specific dielectric performance.

5 Conclusions

A resonant Q-meter method, supported by digital instrumentation, was applied to epoxy resins with nanodiamond and nanographite fillers in the frequency range 0.1–100 kHz. The technique enabled reliable evaluation of dielectric permittivity and loss tangent.

The incorporation of nanodiamonds reduced permittivity, reflecting fewer polar groups and greater structural order, while nanographite caused a slight increase, indicating additional polarization pathways and a more disordered matrix. Overall, the

results show that insulating nanodiamonds improve dielectric stability, whereas conductive nanographite enhances permittivity but reduces structural order, confirming the contrasting roles of these nanofillers in tailoring epoxy dielectric behavior.

References

1. Xie, B., Cai, J., Wang, T., Liu, Z., Jiang, S., Zhang, H.: Research progress of polymer-based multilayer composite dielectrics with high energy storage density. J. Inorg. Mater. **38**(2), 137–147 (2023). https://doi.org/10.15541/jim20220343
2. Kurennov, S., Barakhov, K., Polyakov, O., Taranenko, I.: Application of genetic algorithm for double-lap adhesive joint design. Arch. Mech. Eng. **70**(1), 27–42 (2023). https://doi.org/10.24425/ame.2022.144074
3. Miroshnikov, V., Savin, O., Younis, B., Nikichanov, V.: Solution of the problem of the theory of elasticity and analysis of the stress state of a fibrous composite layer under the action of transverse compressive forces. East.-Eur. J. Enterp. Technol. **4**(7(118)), 23–30 (2022). https://doi.org/10.15587/1729-4061.2022.263460
4. Sagin, S., et al.: Ensuring the environmental friendliness of drillships during their operation in special ecological regions of Northern Europe. J. Mar. Sci. Eng. **10**(9), 1331 (2022). https://doi.org/10.3390/jmse10091331
5. Gerlici, J., Lovska, A., Pavliuchenkov, M.: Study of the dynamics and strength of the detachable module for long cargoes under asymmetric loading diagrams. Appl. Sci. **14**, 3211 (2024). https://doi.org/10.3390/app14083211
6. Kurennov, S., Smetankina, N., Pavlikov, V., Dvoretskaya, D., Radchenko, V.: Mathematical model of the stress state of the antenna radome joint with the load-bearing edging of the skin cutout. In: Cioboată, D.D. (ed.) International Conference on Reliable Systems Engineering (ICoRSE) - 2021, ICoRSE 2021. LNNS, vol. 305, pp. 287–295. Springer, Cham (2022). https://doi.org/10.1007/978-3-030-83368-8_28
7. Kondratiev, A., et al.: Effect of ply orientation on the mechanical performance of carbon fibre honeycomb cores. Polymers **15**(11), 2503 (2023). https://doi.org/10.3390/polym15112503
8. Akkalamattam Maitheenkunju, R., Gopalakrishnan, J.: Reduced graphene oxide/epoxy nanocomposites with enhanced dielectric, mechanical, thermomechanical and thermal properties. J. Elastomers Plast. **54**(3), 407–428 (2021). https://doi.org/10.1177/00952443211054196
9. Tkachenko, D., Tsegelnyk, Y., Myntiuk, S., Myntiuk, V.: Spectral methods application in problems of the thin-walled structures deformation. J. Appl. Comput. Mech. **8**(2), 641–654 (2022). https://doi.org/10.22055/jacm.2021.38346.3207
10. Zhang, J., Wang, Z., Jiang, G., Wei, H., Zhang, Z., Ren, J.: Enhanced thermal conductivity and dielectric properties of epoxy composites with fluorinated graphene nanofillers. Nanomaterials **13**, 2322 (2023). https://doi.org/10.3390/nano13162322
11. Wang, J., Khan, M., Li, T., et al.: Preparation and structural investigations of the graphite and nanodiamonds dispersed epoxy hybrid composites for enhanced mechanical and thermal properties. Bull. Mater. Sci. **45**, 160 (2022). https://doi.org/10.1007/s12034-022-02729-x
12. Kumar, A.M., Selvaraj, S.K., Kanniyappan, S., Karthikeyan, B., Chadha, U.: Effects of adding nanodiamonds in mechanical properties of jute and ramie fiber reinforced epoxy composites. Polym. Compos. **45**, 11872–11882 (2024). https://doi.org/10.1002/pc.28605
13. Zhang, J., et al.: Improvement in anti-static property and thermal conductivity of epoxy resin by doping graphene. IEEE Trans. Dielectr. Electr. Insul. **27**(2), 542–548 (2020). https://doi.org/10.1109/TDEI.2020.008620

14. Rehim, M.A., Turky, G.: Epoxy resin reinforced with graphene derivatives: physical and dielectric properties. J. Polym. Res. **29**, 120 (2022). https://doi.org/10.1007/s10965-022-02971-1
15. Luo, X., Du, B., Ding, J.: Study on the effect of diamond on the dielectric properties of epoxy resin composites during aging. In: Yang, Q., Li, Z., Luo, A. (eds.) The Proceedings of the 18th Annual Conference of China Electrotechnical Society, ACCES 2023. LNEE, vol. 1180, pp. 26–33. Springer, Singapore (2024). https://doi.org/10.1007/978-981-97-1420-9_4
16. Wang, C., Cao, X., Tian, J., et al.: Significantly enhanced energy density of nanodiamond/polyimide composites at high temperatures with ultralow nanodiamond contents. SCIENCE CHINA Technol. Sci. **66**, 956–965 (2023). https://doi.org/10.1007/s11431-022-2251-1
17. Tsyhanok, D., et al.: Dielectric spectroscopy and synergistic effects in epoxy composites filled with multi-walled carbon nanotubes and carbon-coated copper nanoparticles. Polym. Compos. **46**(7), 5994–6007 (2025). https://doi.org/10.1002/pc.29337
18. Rahnamol, A.M., Gopalakrishnan, J.: Improved dielectric and dynamic mechanical properties of epoxy/polyaniline nanorod/in situ reduced graphene oxide hybrid nanocomposites. Polym. Compos. **41**, 2998–3013 (2020). https://doi.org/10.1002/pc.25592
19. Lu, T., Lu, T., Wang, Z., Li, W., Song, S., Gan, W.: Enhanced dielectric properties of epoxy-based multilayer composite with highly controlled distribution of 2D nanomaterials. J. Alloy. Compd. **1027**, 180611 (2025). https://doi.org/10.1016/j.jallcom.2025.180611
20. Kondratiev, A., Píštěk, V., Vambol, O., Kučera, P.: Effect of heating conditions during moulding on residual stress–strain behaviour of a composite panel. Polymers **14**, 1660 (2022). https://doi.org/10.3390/polym14091660
21. Miroshnikov, V., Savin, O., Sobol, V., Nikichanov, V.: Solving the problem of elasticity for a layer with N cylindrical embedded supports. Computation **11**, 172 (2023). https://doi.org/10.3390/computation11090172
22. Zable, M.A.-H., Khan, Z.I., Rashid, N.E., Zakaria, N.A.Z., Ibrahim, I.P., Ab Rahim, S.A., Mahmood, M.K.A.: Dielectric material measurement method: a review. J. Electr. Electron. Syst. Res. **22**(1), 19–28 (2023). https://doi.org/10.24191/jeesr.v22i1.003

Analysis of the Accuracy of Estimating the Dynamic Parameters of Gas Turbine Engines from Experimental Data

Sergiy Yepifanov(✉) and Oleksii Bondarenko

National Aerospace University "Kharkiv Aviation Institute", 17, Vul. Vadyma Manka, Kharkiv 61070, Ukraine
s.yepifanov@khai.edu

Abstract. To solve a number of problems of control and diagnostics of gas turbine engines, dynamic models are used, the coefficients of which in a number of practically important cases must be determined from real information obtained experimentally or during operation. The paper proposes a method for analyzing errors in estimating the dynamic parameters of engines, the main concepts of which consist in using a linear dynamic model, considering influencing errors as independent normally distributed random variables, using dimensionless parameters and the corresponding transformation of equations that describe the relationship between estimation errors and influencing factors, which makes these equations universal, suitable for analyzing any parameters of the engine operating process and any control actions. It is established that, depending on the formation of errors in the initial data, they can be divided into two categories: parameters distributed over a set of experiments, and in each experiment – over a set of local measurements, as well as parameters distributed only over a set of experiments, the values of which are fixed over a set of local measurements. Using analytical and numerical methods, universal dependencies have been obtained that make it possible to determine the errors in estimating the time constant of a single-shaft gas generator with a sudden change in fuel consumption and with a linear change with stabilization depending on the time and frequency of observation, the expected value of the time constant, as well as the root-mean-square errors of the initial data: measurements of the rotor speed and fuel consumption, as well as the gain factor for fuel supply.

Keywords: Gas turbine engine · Mathematical model · Dynamic parameters · Estimation · Error

1 Introduction

One of the most promising areas in the advancement of aircraft engine is the development of adaptive automatic control systems [1, 2]. The key component of such systems is a dynamic mathematical model of the engine that can self-adjust based on the measured parameters of its operating process. Under the initiative of NASA, a concept for creating

H. Altenbach et al. (Eds.): CAMPE 2025, LNME, pp. 252–261, 2026.
https://doi.org/10.1007/978-3-032-16381-3_24

such models, known as STORM (Self-Tuned On-board Real-time Model), was proposed [3, 4]. However, existing studies devote insufficient attention to the crucial issue of verifying whether the collected data are adequate to achieve the required model accuracy. Such verification must be performed both a priori - to predict engine operating modes and determine the required data volume - and a posteriori, after obtaining the experimental results.

2 Literature Review

2.1 Identification of Engine Static Performances

Static models of gas turbine engines (GTE) underlie their development and are used at all stages of their life cycle, from preliminary design to operation and maintenance.

The component-based static model of the engine has the form [1]

$$\vec{Y} = F\left(\vec{U}_{\mathrm{m}},\ \vec{U}_{\mathrm{f}},\ \vec{\theta}\right) \tag{1}$$

where $\vec{Y}$ are simulated workflow parameters; $\vec{U}_{\mathrm{m}}$ are parameters that determine the engine operating mode; $\vec{U}_f$ are parameters that determine flight conditions; $\vec{\theta}$ are parameters of components characteristics.

These models accompany the development of the engine design, therefore their coordination with experimental data is a relevant task, the solution of which is developed inextricably with the methods of calculating static characteristics [1, 2]. The latest advances in this field are published in the works of Y. Li [5], Tsoutsanis et al. [6], S. Li et al. [7], Kim et al. [8].

The approaches used are based on the Least Squares method. To ensure the stability of the solution, regularization of the estimation algorithm is used [1, 9].

Therefore, we will consider the problem of identifying static characteristics of a gas turbine engine to be sufficiently studied and will focus further on dynamic models.

2.2 Identification of Engine Dynamic Characteristics Using a Nonlinear Component-Level Thermodynamic Model

The most common approach to identifying the dynamic performances of engines is associated with the estimation of the parameters of nonlinear component-level thermodynamic models. In 2015, Tsoutsanis et al. [10] presented a method for identifying characteristics to use the results of measuring parameters in transient modes for engine diagnostics. In 2016, Asgari et al. [11] used machine learning methods and improved the modeling of temperature in transient modes. In 2018, Mehrpanahi et al. [12] proposed a procedure for correcting the dynamic model of an industrial gas turbine using operational information. They also showed that this method has a drawback, because it does not provide modeling with acceptable accuracy outside the operating range in which the data used for identification were obtained. In 2019, Pang et al. [13] showed that the accuracy of the model improves if data obtained in transient modes is used to adapt the characteristics of the compressor and turbine. In 2020, S. Kim et al. [14] proposed a

method for adapting the dynamic model of the F100-PW-229 turbofan engine taking into account the dynamic characteristics of the temperature gage. In [15], in contrast to previous works that used a bench set of measured parameters, they proposed a method that provides adaptation of the model to the parameters measured on a regular basis. Not only are the characteristics of the components adjusted, but also the characteristics of the sensors.

However, on the one hand, the problem of estimating the parameters of nonlinear component-level thermodynamic models is currently clearly insufficiently studied; on the other hand, the use of these models as on-board real-time models as part of control and diagnostic algorithms requires the appropriate development of the hardware and algorithmic means of ensuring software reliability, which may become the subject of a special study, but goes beyond the scope of this work. Therefore, we will consider the use of dynamic models that have a linear structure in the future.

2.3 Identification of Engine Dynamic Characteristics Using Linear Dynamic Models

The linear dynamic model of the engine has the form [16]

$$\dot{\vec{X}} = A\Delta\vec{X} + B\Delta\vec{U}; \tag{2}$$

$$\vec{Y} = C\Delta\vec{X} + D\Delta\vec{U}, \tag{3}$$

where $\vec{X}$ is the state vector; $\vec{U}$ is the control vector; A, B, C, D are matrices; Δ is the deviation of parameters from values that correspond to the established engine operating mode. In the vicinity of the engine operating mode, the matrix coefficients are constant. Such a model is called a single-mode model. It is known that the dynamic properties of the engine significantly depend on its mode and flight operating conditions [16]. This can be taken into account if the dependence of the matrix coefficients on the parameters $\vec{U}_{\mathrm{m}}$ and $\vec{U}_{\mathrm{f}}$ is taken into account. Such a model is called quasilinear. It takes into account nonlinear relationships, but is linear in structure. The task of identifying this model is to determine the coefficients of the specified matrices based on the values of the parameters measured in transient processes caused by changes in the elements of the control vector (i.e., the mode or external conditions).

The most famous monograph on the problem of forming linear dynamic models of gas turbine engines was published by Kulikov and Thompson [17]. It considers the problem of identifying the dynamic characteristics of gas turbine engines based on experimental information. The main attention is paid to identification in the frequency domain. Unfortunately, the practical significance of such a method is small, because for its implementation it is necessary to ensure a harmonic or random change in the influence (fuel consumption). From the analysis of the problem, it becomes clear that practical identifiability consists in the possibility of forming a model of the object based on experimental data with the required accuracy. Therefore, a method of analyzing the accuracy of identification is needed. However, unfortunately, quantitative assessments of the accuracy of identification are not considered in this monograph.

Castiglione et al. [18] stated that to ensure the required control accuracy the model used should take into account the degradation of the engine. However, in this work only the degradation of the compressor characteristics was considered, the influence of measurement errors was not analyzed, and the identification algorithm was not given at all – only a reference was made to the fact that standard MATLAB tools were used. In the work of Tavakolpour-Saleh et al. [19], two approaches to the identification of the dynamic properties of a turbojet engine were considered: parametric and nonparametric. Neural networks were used for nonparametric identification.

Wei and his co-authors from Beijing Beihang University and Cranfield University presented a comprehensive review of the development of onboard GTE models [20].

The application of piecewise linear dynamic models of GTE was initiated in the work of Teren, published in a NASA report [21] and dedicated to the control of the F100 engine. The parameters of such a model are set on a finite set of points of the engine throttle performance. Therefore, when modeling transient characteristics, the model parameters are interpolated by the values of the parameter that sets the operating mode – the rotor speed. The corresponding modeling algorithm is presented by Kulikov, Thompson [17]. A nonlinear component-based engine model or an experimental throttle performance can be used as a static model. Frequency identification methods for piecewise linear engine models were reviewed in 1998 in the works of Borell et al. [22], as well as Arkov et al. [23].

In 2019, Jafari and Nikolaidis [24] considered three types of engine models: 1) Hammerstein model; 2) Wiener model; 3) mixed Wiener-Hammerstein and Hammerstein-Wiener models. As a result of the analysis, they recommended the Wiener model for practical application and compared it with the piecewise linear model and the neural network model. All models were tuned on the same data set. It was shown that the neural network model is unsuitable because it accumulates static error.

As a result of the analysis of the on-board models development, Wei et al. [20] noted that they have not yet found a wide practical application. According to the authors, this is due to the need to solve two problems: 1) reliable modeling of the most important unmeasured parameters during a sudden change in the engine state; 2) ensuring sufficient accuracy of tuning the on-board model taking into account the characteristics of the engine. The second problem is the subject of further research in this work.

Thus, tuning dynamic models based on measurement information is an important task that is solved at different stages of using the models.

Among all the works on the identification of engine characteristics, works related to dynamic characteristics constitute a small number. They mainly consider the determination of the coefficients of a single-mode dynamic model by the Least Squares method. However, the problem of analyzing the accuracy of estimating the parameters of dynamic models using real data has clearly not been studied enough, and the problem of planning experiments has not been considered.

The goal of the work is to develop a method for analyzing the accuracy of estimating the parameters of dynamic models of gas turbine engines and their practical implementation using the example of testing a single-shaft gas generator under conditions of sudden changes in fuel consumption.

3 Research Methodology

The duration of the transient process in a gas turbine engine is determined by the combined influence of several phenomena: mechanical inertia, quantitatively characterized by the rotor moment of inertia, and the dynamic stability of the gas generator during transient modes, which depends on the difference in the slopes of the torque characteristics of the compressor and turbine. Since both components jointly determine the engine time constant, it is not necessary to evaluate them separately. Therefore, the main objective is to estimate the resulting time constant, which reflects the combined effect of these factors.

To form a methodology, let us consider the simplest problem: determining the time constant τ of a single-shaft gas generator or engine using a step change in fuel consumption by the value G_0. The mathematical model (2), which describes the change in the rotor speed n for a given change in fuel consumption G, has the form

$$\tau \frac{dn}{dt} + \Delta n = K \Delta G, \tag{4}$$

where τ is the rotor time constant; K is the rotor gain factor for fuel consumption.

According to the analysis, the gain factor K should be regarded as a static rather than a dynamic parameter, as it defines the slope of the steady-state characteristic – that is, the relationship between rotor speed and fuel consumption under established operating conditions. Hence, K can be determined beforehand from the static dependence $n = f(G)$.

The transient characteristic of the engine under the specified influence has the form

$$\Delta n(t) = KG_0\left(1 - e^{-\frac{t}{\tau}}\right). \tag{5}$$

The total uncertainty in evaluating the time constant is influenced by several factors: measurement errors σ_n (rotational speed) and σ_G (fuel consumption); model-related inaccuracies σ_K (error in parameter K) and ΔS (error due to the assumption of constant coefficients K and τ K and τ); the sampling period Δt.

It is further assumed that Δt is selected sufficiently large to suppress the effects of signal autocorrelation, while the amplitude of the fuel flow variation G_0 is chosen small enough to minimize the impact of model nonlinearity.

Then the instrumental error of the estimate is the sum of the partial errors, and its variance is the sum of the partial variances:

$$\Delta\tau = (\Delta\tau)_n + (\Delta\tau)_G + (\Delta\tau)_K; \sigma_\tau^2 = \sigma_{\tau\,\mathrm{n}}^2 + \sigma_{\tau\,\mathrm{G}}^2 + \sigma_{\tau\,\mathrm{K}}^2. \tag{6}$$

To determine these components, let us assume that the structure of the dynamic model is correct, and the estimate is determined by the Least Squares method (LSM), i.e., it minimizes the functional

$$\Phi(\Delta\tau) = \sum_{\mathrm{j}=1}^{\mathrm{N}} \left[n_{\mathrm{j}} - KG\left(1 - e^{-\frac{\mathrm{t}}{\tau}}\right)\right]^2 = \sum_{\mathrm{j}=1}^{\mathrm{N}} \left[\Delta n_{\mathrm{j}} - \left(\frac{\partial n}{\partial \tau}\right)_{\mathrm{j}} \Delta\tau - \left(\frac{\partial n}{\partial G}\right)_{\mathrm{j}} \Delta G - \left(\frac{\partial n}{\partial K}\right)_{\mathrm{j}} \Delta K \right]^2,$$

whence $\Delta\hat{\tau} = \dfrac{\sum\limits_{j=1}^{N}\left[\left(\frac{\partial n}{\partial \tau}\right)_j \Delta n_j - \left(\frac{\partial n}{\partial \tau}\right)_j \left(\frac{\partial n}{\partial G}\right)_j \Delta G - \left(\frac{\partial n}{\partial \tau}\right)_j \left(\frac{\partial n}{\partial K}\right)_j \Delta K\right]}{\sum\limits_{j=1}^{N}\left(\frac{\partial n}{\partial \tau}\right)_j^2}$.

We obtain expressions for the variance components (6), taking into account the significant difference between the influence of measurement errors $\sigma_n{}^2$ and errors in specifying the amplitude of the fuel consumption step and model coefficients $\sigma_G{}^2$, $\sigma_K{}^2$: both are random variables, but the errors of the coefficients change only over a set of repeated experiments, while the errors of measurement change over both the set of experiments and the set of measurements in each experiment. Therefore, the errors of the fuel consumption step and gain factor can be carried out behind the signs of the sum in the numerator of the expression to estimate $\Delta\hat{\tau}$.

To obtain a universal characteristic of the error, we introduce dimensionless variables $\bar{n} = \frac{n}{K^0 G_0^0}$; $\bar{t} = \frac{t}{\tau^0}$; $\Delta\bar{t} = \frac{\Delta t}{\tau^0}$; $\bar{\sigma}_n = \frac{\sigma_n}{K^0 G_0^0}$; $\bar{\sigma}_G = \frac{\sigma_G}{G_0^0}$; $\bar{\sigma}_K = \frac{\sigma_K}{K^0}$, where τ^0, ${G_0}^0$, K^0 are true values of the engine time constant, fuel step and boost factor. For the same purpose, we convert the expressions to continuous form using the transformation $\sum\limits_{j=1}^{N} x_j \approx \frac{1}{\Delta t}\int\limits_0^{t_N} x(t)dt$, assuming that measurements are made over time t_N evenly spaced Δt. Then

$$\bar{\sigma}^2_{\tau\, n} = \frac{\Delta\bar{t}^2\bar{\sigma}_n^2}{\int\limits_0^{t_N}\left(\frac{\partial\bar{n}}{\partial\tau}\right)^2 dt};\ \bar{\sigma}^2_{\tau\, G} = \frac{\left[\int\limits_{j=1}^{N}\left(\frac{\partial\bar{n}}{\partial\tau}\frac{\partial\bar{n}}{\partial\bar{G}}\right)dt\right]^2}{\left[\int\limits_{j=1}^{N}\left(\frac{\partial\bar{n}}{\partial\tau}\right)^2 dt\right]^2}\bar{\sigma}_G^2;\ \bar{\sigma}^2_{\tau\, K} = \frac{\left[\int\limits_{j=1}^{N}\left(\frac{\partial\bar{n}}{\partial\tau}\frac{\partial\bar{n}}{\partial\bar{K}}\right)dt\right]^2}{\left[\int\limits_{j=1}^{N}\left(\frac{\partial\bar{n}}{\partial\tau}\right)^2 dt\right]^2}\bar{\sigma}_K^2. \tag{7}$$

4 Results

Differentiating the solution (5), we transform (7):

$$\bar{\sigma}^2_{\tau\, n} = \sigma^2_{\bar{n}}\cdot\Delta\bar{t}\cdot f_n(\bar{t}_N),\ \text{where}\ f_n(\bar{t}_N) = \frac{2}{\frac{1}{2} - e^{-2\bar{t}_N}\left[\bar{t}_N^2 + \bar{t}_N + \frac{1}{2}\right]}. \tag{8}$$

$$\bar{\sigma}^2_{\tau G} = \bar{\sigma}^2_G f_1(\bar{t}_N);\ \bar{\sigma}^2_{\tau K} = \bar{\sigma}^2_K f_1(\bar{t}_N)\ \text{where}\ f_1(\bar{t}_N) = \left\{\frac{3 - 4(\bar{t}_N+1)e^{-\bar{t}_N} + (2\bar{t}_N+1)e^{-2\bar{t}_N}}{1 - \left[2\bar{t}_N^2 + 2\bar{t}_N + 1\right]e^{-2\bar{t}_N}}\right\}^2. \tag{9}$$

Function $f_n(\bar{t}_N)$ is presented in Fig. 1, *a*. As the observation duration increases, its value converges to a finite limit equal to 4. This indicates that after the transient process is completed, subsequent measurements no longer carry information about the desired time constant. Function $f_1(\bar{t}_N)$ is presented in Fig. 1, *b*. With an increase in observation time, the influence of additional measurements on the total error diminishes, and the function approaches not zero but a finite limit equal to 9.

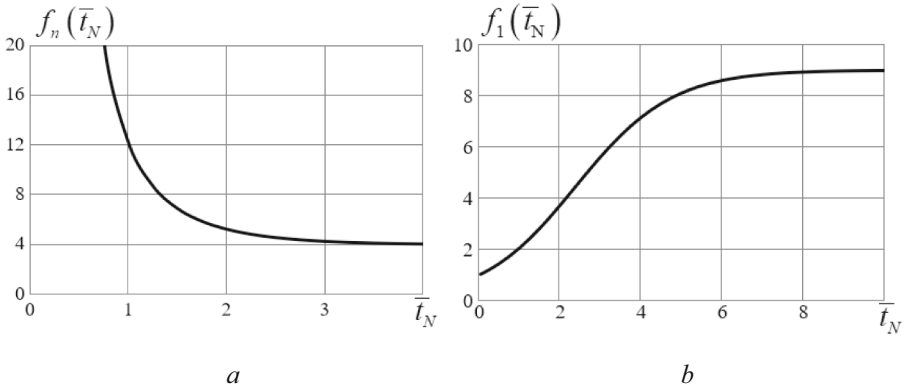

a *b*

Fig. 1. Influence functions of errors in measuring the rotational speed and setting the fuel consumption and gain coefficient on the error in estimating the engine time constant: $a - f_n$; $b - f_1$

Using the derived Eqs. (8), (9) for the specific variance, along with the corresponding graphs, one can estimate the error for any engine, chosen time interval, amplitude of the step input, and measurement inaccuracy. This formulation of the error model also serves as a foundation for designing experiments aimed at determining the engine time constant, effectively addressing the inverse modeling problem.

The characteristic obtained from the analysis of a sudden change in fuel consumption represents the minimum achievable error, as the rotor's response to alternative forms of input occurs more slowly, thereby increasing the estimation error.

Let us consider examples of determining the errors in estimating the time constant of a single-shaft gas generator with the following parameters: $\tau^0 = 1$ s; $K^0 = 10$ (rpm)/(kg/h); $G^0 = 100$ kg/h; $\Delta t = 0.2$ s; $\sigma_n = 15$ rpm; $\sigma_G = 0.5$ kg/h; $\sigma_K = 0.1$ (rpm)/(kg/h). The corresponding dependences on the relative observation time of individual components and the total root mean square deviation (RSMD) of the time constant estimation error are presented in Fig. 2. Analysis of the obtained results shows that the opposite effect of the observation time on the change in the components of the total time constant estimation error under certain conditions determines the presence of a minimum of the total error, which means the existence of a limited optimal duration of the experiment.

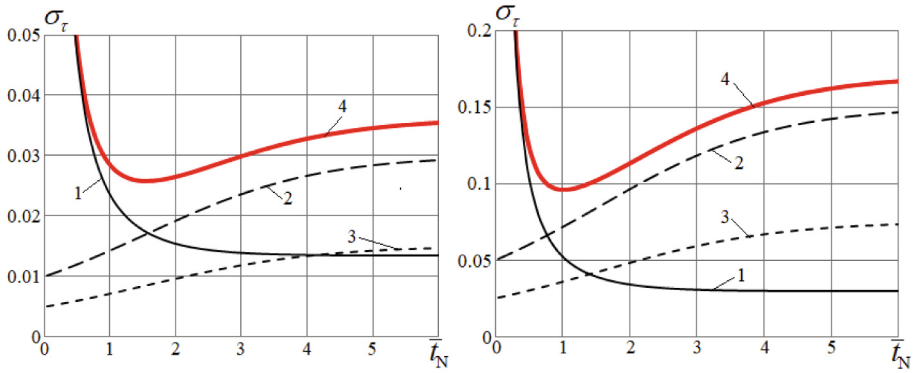

a *b*

Fig. 2. Dependences of the RMSD of the errors of the time constant estimates on the observation interval: 1 - $\sigma_{\tau n}$; 2 - $\sigma_{\tau G}$; 3 - $\sigma_{\tau K}$; 4 - σ_τ; *a* – $\tau_0 = 1$ s; *b* – $\tau_0 = 5$ s

5 Conclusions

In the course of investigating the problem, a generalized method for analyzing the errors arising during GTE model adaptation was developed. The main ideas of this method can be summarized as follows: 1) application of a linear approximation of the engine's dynamic model in the region corresponding to the actual values of the parameters to be identified; 2) assessment of the impact of all measurement inaccuracies and model-related parameter deviations – including rotor speed and fuel flow errors, inaccuracies in the sensitivity coefficient, the form and parameters of the control signal, and the interval between recorded data points; 3) assumption that the influencing errors are statistically independent and normally distributed random quantities; 4) utilization of normalized parameters and appropriate transformations of the equations that connect estimation inaccuracies with influencing factors, which makes these relationships universal and suitable for any set of engine parameters and operating conditions.

Instrumental errors in determining the time constants of the engine have a lower theoretical limit, which arises from the finite duration of transient processes. Once the transient has ended and output parameters become steady, the system's response ceases to depend on dynamic parameters such as the time constant. Therefore, additional data obtained after stabilization do not improve the accuracy of the estimate.

Based on the analysis of the transient response of the engine to a step change in fuel supply, the minimum achievable estimation error was determined. In practical situations, the rate of fuel change is restricted by the mechanical limits of the metering unit and control algorithms, which in turn slows down the rotor's acceleration and reduces the amount of useful information contained in experimental data.

For the first time, the possibility of the existence of an optimal observation duration has been established, which must be taken into account when designing experiments and developing algorithms for adapting dynamic engine models.

The proposed method for calculating the error in estimating the time constant can be applied not only to a single-shaft engine. To implement the described approach, it

is necessary to use the solution of the differential equation that represents the system under study (for example, a twin-shaft engine) for the corresponding input action. By performing the appropriate transformations, it becomes possible to obtain universal relationships expressed in dimensionless parameters.

References

1. Yepifanov, S., Kuznetsov, B., Bogayenko, V., et al.: Synthesis of automatic control and diagnostic systems for gas turbine engines. Tekhnika, Kyiv (1998). (Rus)
2. Stamatis, A., Mathioudakis, K., Papailiou, K.D.: Adaptive simulation of gas turbine performance. J. Eng. Gas Turbines Power **112**(2), 168–176 (1990). https://doi.org/10.1115/1.2906157
3. Luppold, R., Roman, J., Gallops, G., et al.: Estimating in-flight engine performance variations using Kalman filter concepts. In: 25th Joint Propulsion Conference; 1989 Jul 12–16; Monterey, CA. Reston: AIAA (1989). https://doi.org/10.2514/6.1989-2584
4. Brotherton, T., Volponi, A., Luppold, R., et al.: eSTORM: Enhanced self-tuning on-board real-time engine model. In: 2003 IEEE Aerospace Conference Proceedings; Big Sky, MT, USA, pp. 3075–3086. Piscataway: IEEE (2003). https://doi.org/10.1109/AERO.2003.1234150
5. Li, Y.G.: Aero gas turbine flight performance estimation using engine gas path measurements. J. Propul. Power **31**(3), 851–860 (2015). https://doi.org/10.2514/1.B35381
6. Tsoutsanis, E., Li, Y., Pilidis, P.: Nonlinear model-based adaptation for off-design performance prediction of gas turbines. ISABE Paper ISABE-2017–21436, p. 17 (2017)
7. Li, S., Li, Z., Li, S.: Improved method for gas-turbine off-design performance adaptation based on field data. J. Eng. Gas Turbines Power **142**(4), 12 (2020). https://doi.org/10.1115/1.4044470
8. Kim, S., Kim, K., Son, C.: Adaptation method for overall and local performances of gas turbine engine model. Int. J. Aeronaut. Space Sci. **19**, 250–261 (2019). https://doi.org/10.1007/s42405-018-0016-4
9. Khustochka, O., Yepifanov, S., Zelenskyi, R., Przysowa, R.: Estimation of performance parameters of turbine engine components using experimental data in parametric uncertainty conditions. Aerospace **7**(1), 17 (2020). https://doi.org/10.3390/aerospace7010006
10. Tsoutsanis, E., Meskin, N., Benammar, M, Khorasani, K.: Transient gas turbine performance diagnostics through nonlinear adaptation of compressor and turbine maps. J. Eng. Gas Turbines Power **137**(9), 12 (2015). https://doi.org/10.1115/1.4029710
11. Asgari, H., Chen, X., Morini, M., et al.: NARX models for simulation of the start-up operation of a single-shaft gas turbine. Appl. Therm. Eng. **93**, 368–376 (2016). https://doi.org/10.1016/j.applthermaleng.2015.09.074
12. Mehrpanahi, A., Hamidavi, A., Ghorbanifar, A.: A novel dynamic modeling of an industrial gas turbine using condition monitoring data. Appl. Therm. Eng. **143**, 507–520 (2018). https://doi.org/10.1016/j.applthermaleng.2018.07.081
13. Pang, S., Li, Q., Feng, H., Zhang, H.: Joint steady state and transient performance adaptation for aero engine mathematical model. IEEE Access, 10 (2019). https://doi.org/10.1109/ACCESS.2019.2905865
14. Kim, S. Kim, K., Son, C.: A new transient performance adaptation method for an aero gas turbine engine. Energy, Elsevier **193**(10) (2020). https://doi.org/10.1016/j.energy.2019.116752
15. Kim, S., Lee, C-R., Yang, W., Kim, Y.: Suitability of performance adaptation methods for updating the thermodynamic cycle model of a turboprop engine. Appl. Therm. Eng. **242**, 122408, 32 (2024). https://doi.org/10.1016/j.applthermaleng.2024.122408

16. Jaw, L., Mattingly, J.: Aircraft Engine Controls: Design, System Analysis, and Health Monitoring. American Institute of Aeronautics and Astronautics Inc, Reston, USA (2009)
17. Kulikov, G., Thompson, H.: Dynamic Modelling of Gas Turbines. Identification, Simulation, Condition Monitoring and Optimal Control. Springer-Verlag, London (2004)
18. Castiglione, T., Perrone, D., Strafella, L., et al.: Linear model of a turboshaft aero-engine including components degradation for control-oriented applications. Energies **16**, 18 (2023). https://doi.org/10.3390/en16062634
19. Tavakolpour-Saleh, A., Nasib, A., Sepasyan, A., Hashemi, S.: Parametric and nonparametric system identification of an experimental turbojet engine. Aerosp. Sci. Technol. **43**, 21–29 (2015). https://doi.org/10.1016/j.ast.2015.02.013
20. Wei, Z., Zhang, S., Jafari, S., Nikolaidis, T.: Gas turbine aero-engines real time on-board modelling: a review, research challenges, and exploring the future. Progress Aerospace Sci. **121**, 16 (2020). https://doi.org/10.1016/j.paerosci.2020.100693
21. Teren, F.: Minimum time acceleration of aircraft turbofan engine. Report No.: NASA-TM-X-73624, Lewis Research Center, National Aeronautics and Space Administration, Cleveland, Ohio, p. 13 (1977)
22. Borrell, A., Evans, C., Rees, D.: Identification of aircraft gas turbine dynamics using frequency-domain techniques. In: Control '98, UKACC International Conference on (Conf. Publ. No. 455), pp. 1372–1378 (1998)
23. Arkov, V., Kulikov, G., Breikin, T., Fleming, P.: Dynamic model identification of gas turbines. In: Control '98, UKACC International Conference on (Conf. Publ. No. 455), pp. 1367–1371 (1998). https://doi.org/10.1016/j.proeng.2017.02.339
24. Jafari, S., Nikolaidis, T.: Meta-heuristic global optimization algorithms for aircraft engines modelling and controller design; a review, research challenges, and exploring the future. Prog. Aero. Sci. **104**, 40–53 (2019). https://doi.org/10.1016/j.paerosci.2018.11.003

Free Vibration Analysis of an Auxetic Honeycomb Sandwich Shallow Shell with an Arbitrary Planform Resting on Pasternak Elastic Foundation

Lidiya Kurpa[1(✉)], Tetyana Shmatko[2], and Jan Awrejcewicz[3]

[1] Department of Applied Mathematics, National Polytechnic University "KhPI", Kharkov, Ukraine
kurpalidia@gmail.com

[2] Department of Higher Mathematics, National Polytechnic University "KhPI", Kharkov, Ukraine
ktv_ua@yahoo.com

[3] Department of Automation, Biomechanics and Mechatronics, Lodz University of Technology, Lodz, Poland
jan.awrejcewicz@p.lodz.pl

Abstract. This paper proposes an approach for analyzing the free vibrations of sandwich shallow shells with an auxetic core exhibiting a negative Poisson's ratio. The face sheets are made of functionally graded materials (FGMs). The method allows to consider the panels with arbitrary planform geometries. The shell is assumed to be resting on a Pasternak elastic foundation. Mathematical formulation is based on the first order shear deformation theory (FSDT). The core's unit cell is modeled with a hexagonal configuration, and established analytical relations are used to determine its material properties. Power law distribution is applied to characterize the effective properties of the FGM face sheets. To address shells with arbitrary planforms, the R-functions theory is integrated with the variational Ritz method. The accuracy and efficiency of the proposed methodology are demonstrated through comparison with existing results as well as new results obtained for auxetic shells of complex geometries.

Keywords: arbitrary shape · R-functions theory · sandwich shallow shells with auxetic core · FGM · first order shear deformation theory · elastic foundation

1 Introduction

Sandwich structures are widely recognized in engineering due to their ability to combine lightweight characteristics with high stiffness and strength. The performance of sandwich structures is highly influenced by the choice of materials for both face sheets and the core. Face sheets can include functionally graded materials (FGMs), which are attractive for different applications. In recent years auxetic honeycomb core materials have

H. Altenbach et al. (Eds.): CAMPE 2025, LNME, pp. 262–272, 2026.
https://doi.org/10.1007/978-3-032-16381-3_25

gained significant attention due to their negative Poisson's ratio, which leads to effective energy absorption, impact resistance, and enhanced strength capacity compared to conventional core architectures. This class of materials is deformed in a counterintuitive manner, becoming thicker perpendicular to an applied stretch, making them ideal for advanced core designs in highly productive sandwich structures. Note that such structures can serve as protective armor, reducing overall weight while improving acoustic insulation, thermal resistance, and impact mitigation against collisions or shock waves from explosions [7]. Extensive studies have been explored the modeling and performance of sandwich panels within the frameworks of classical plate theory (CPT), first order shear deformation theory (FSDT), and higher-order shear deformation theories (HSDT). A recent comprehensive review [1] has highlighted the progress in research on sandwich structures with auxetic cores. That work offers an in-depth discussion of design strategies, classifications of auxetic geometries, and material choices for both the core and the face sheets. A wide range of studies has been focused on problems such as static bending, buckling loads, dynamic response plates, and both linear and nonlinear vibrations [2–14]. Free vibration analyses of auxetic plates were presented in [2–4], while works [5–8] examined auxetic sandwich plates resting on elastic foundations. Further investigations [9–11] were addressed the vibration behavior of FGM shells with auxetic cores. The questions of the design of doubly curved sandwich panels with honeycomb cores were considered in [12, 13].

Although significant progress has been made in the study of sandwich structures with FGM face sheets and auxetic cores, relatively little attention has been devoted to shallow sandwich shells with complex planforms. To address this gap, the present work introduces a semi-analytical approach based on the variational Ritz method in combination with the R-functions theory [14, 15].

2 Mathematical Model for Vibration Analysis of Sandwich Panels with Auxetic Core on Elastic Foundation Using FSDT

The study focuses on sandwich shallow shells (panels) with an auxetic honeycomb core and FGM face sheets supported by an elastic foundation (Fig. 1). The three-layer configuration includes a core of thickness $h_c = h_2 - h_1$ and two FGM face sheets placed on the top (T) and bottom (B), each with thickness h_f. The total shell thickness h is defined by $h = 2h_f + h_c$. Planform can take complex shapes with different boundary conditions. The effective properties of the FGM sheets, made of ceramic and metal, vary along the thickness following a power law function.

$$E^{(i)}(z) = (E_c - E_m)V^{(i)} + E_m,\ \rho^{(i)}(z) = (\rho_c - \rho_m)V^{(i)} + \rho_m,\ i = T, B, \qquad (1)$$

where

$$V^{(T)}(z) = \left(\frac{z - h_2}{h/2 - h_2}\right)^p,\ V^{(B)}(z) = \left(\frac{h_1 - z}{h_1 + h/2}\right)^p. \qquad (2)$$

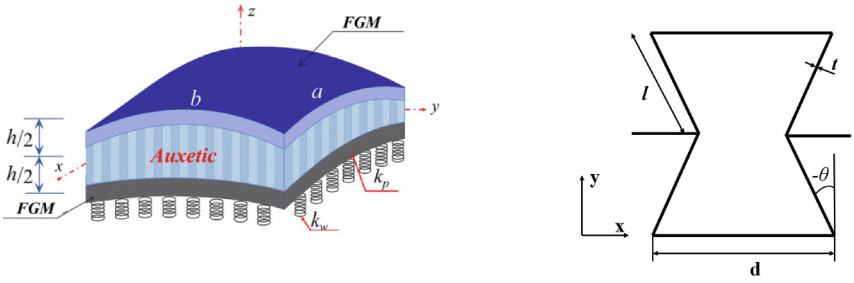

Fig. 1. Sandwich FGM shallow shell with honeycomb core

In formulas (1) and (2) z represents the distance from the current point to the midsurface of the shell, while $z = h_1$ and $z = h_2$ correspond to the bottom and top surfaces of the core layer, respectively. The index p ($0 \le p < \infty$) denotes the ceramic volume fraction exponent, which is related to the metal volume fraction V_m by expression $V_c + V_m = 1$. The subscripts c and m stand for "ceramic" and "metal," respectively, E_m, E_c and ρ_m, ρ_c denote the Young's modulus and mass density of the constituent materials.

Suppose that unit cell of an auxetic honeycomb core has form of the hexagonal shown in Fig. 1. Geometrical parameters d, l define length of the horizontal and inclined sides respectively, parameter t defines thickness of hexagonal rib and parameter θ corresponds to inclined angle of the rib. Then core's material properties for negative θ are adopted from [11]:

$$E_1^{(c)} = E\eta_3^3 \frac{\gamma}{cos\theta\left[cos^2\theta + \left(sin^2\theta + \eta_1\right)\eta_3^2\right]},\ \gamma = \eta_1 + sin\theta,\ \eta_1 = \frac{d}{l},\ \eta_3 = \frac{t}{l},$$

$$E_2^{(c)} = \frac{E\eta_3^3}{\gamma cos\theta\left(tan^2\theta + \eta_3^2\right)},\ G_{12}^{(c)} = \frac{E\eta_3^3}{\eta_1 cos\theta(1+2\eta_1)},\ G_{23}^{(c)} = \frac{G\eta_3 cos\vartheta}{\gamma},$$

$$G_{13}^{(c)} = \frac{G\eta_3}{2cos\theta}\left(\frac{\gamma}{1+2\eta_1} + \frac{\eta_1 + 2sin^2\theta}{2\gamma}\right),\ \rho^{(c)} = \rho\frac{\eta_3(\eta_1+2)}{2\gamma cos\theta}, \tag{3}$$

$$\nu_{12}^{(c)} = \frac{\gamma sin\theta\left(1-\eta_3^2\right)}{cos^2\theta + \left(sin^2\theta + \eta_1\right)\eta_3^2},\ \nu_{21}^{(c)} = \frac{sin\theta\left(1-\eta_3^2\right)}{\gamma\left(tan^2\theta + \eta_3^2\right)},$$

where E, G are modulus of elasticity and shear, ρ is a mass density of original core material. By FSDT the strain components $\{\varepsilon\} = \{\varepsilon_{11}, \varepsilon_{22}, \varepsilon_{12}\}^T$ for moderately large deformations can be expressed as $\{\varepsilon\} = \left\{\varepsilon^{(0)}\right\} + z\{\chi\}$, where

$$\left\{\varepsilon^{(0)}\right\} = \left\{u_{0,x} + w_0/R_x, \quad v_{0,y} + w_0/R_y, \quad u_{0,y} + v_{0,x} \quad \right\}^T,$$

$$\{\chi\} = \left\{\psi_{x,x}, \quad \psi_{y,y} \quad \psi_{x,y} + \psi_{y,x}\right\}^T,\ \varepsilon_{13} = \psi_x + w_{0,x} - \frac{u_0}{R_x},\ \varepsilon_{23} = \psi_y + w_{0,y} - \frac{v_0}{R_y}, \tag{4}$$

here (u_0, v_0, w_0) denote displacements of a point at the mid-plane to x, y, z directions, ψ_x, ψ_y are rotation angles of the transverse normal in yz and xz planes respectively, R_x, R_y are radii of principal curvatures in x and y directions.

Note that we consider shallow shells of small curvature, the equations of which are described by quadratic functions that do not contain the product xy. In this case, the curvatures are constant. Thus, it is approximately assumed that the intrinsic geometry of the middle surface does not differ from the Euclidean geometry of the plane. The principal directions of curvature do not change and coincide with the directions of the Ox and Oy-axes. The expressions for the in-plane force resultants $N = (N_{11}, N_{22}, N_{12})^T$, bending moment resultants $M = (M_{11}, M_{22}, M_{12})^T$ and transverse shear force resultants $Q = \left(Q_x, Q_y\right)$ can be written in matrix form as:

$$\{N\} = [A]\{\varepsilon\} + [B]\{\chi\}, \quad \{M\} = [B]\{\varepsilon\} + [D]\{\chi\}, \ \{Q\} = \begin{bmatrix} D_{44}0 \\ 0D_{55} \end{bmatrix} \begin{Bmatrix} \varepsilon_{13} \\ \varepsilon_{23} \end{Bmatrix}, \tag{5}$$

$$[A] = \begin{bmatrix} A_{11} & A_{12} & 0 \\ A_{12} & A_{22} & 0 \\ 0 & 0 & A_{66} \end{bmatrix}, [B] = \begin{bmatrix} B_{11} & B_{12} & 0 \\ B_{12} & B_{22} & 0 \\ 0 & 0 & B_{66} \end{bmatrix}, [D] = \begin{bmatrix} D_{11} & D_{12} & 0 \\ D_{12} & D_{22} & 0 \\ 0 & 0 & D_{66} \end{bmatrix}.$$

Note that elements $A_{ij},\ B_{ij},\ D_{ij}, (i, j = 1{,}2, 6)$ of the matrices $[A]$, $[B]$ and $[D]$ in relations (5) are calculated by formulas:

$$\left(A_{ij}, B_{ij}, D_{ij}\right) = \int_{-\frac{h}{2}}^{h_1} Q_{ij}^{(B)}\left(1, z, z^2\right)dz + \int_{h_1}^{h_2} Q_{ij}^{(C)}\left(1, z, z^2\right)dz + \int_{h_2}^{\frac{h}{2}} Q_{ij}^{(T)}\left(1, z, z^2\right)dz. \tag{6}$$

Elements D_{ij} $(i, j = 4{,}5)$ are defined as.

$$D_{ij} = K_s^2\left(\int_{-\frac{h}{2}}^{h_1} Q_{ij}^{(B)}dz + \int_{h_1}^{h_2} Q_{ij}^{(C)}dz + \int_{h_2}^{\frac{h}{2}} Q_{ij}^{(T)}dz\right),$$

where K_s^2 is a shear correction factor (it is assumed to be $K_s^2 = 5/6$ in the work). Values $Q_{ij}^{(B,T)}$ and $Q_{ij}^{(C)}$ $(i, j = 11, 22, 12, 66, 44, 55)$ are defined by the following expressions:

$$Q_{11}^{(i)} = Q_{22}^{(i)} = \frac{E^{(i)}(z)}{1-\nu^2}, Q_{12}^{(i)} = \nu Q_{11}^{(i)}, Q_{66}^{(i)} = Q_{44}^{(i)} = Q_{55}^{(i)} = \frac{E^{(i)}(z)}{2(1+\nu)},\ i = T, B, \tag{7}$$

$$Q_{11}^{(C)} = \frac{E_1^{(C)}}{1-\nu_{12}^{(C)}\nu_{21}^{(C)}}, Q_{22}^{(C)} = \frac{E_2^{(C)}}{1-\nu_{12}^{(C)}\nu_{21}^{(C)}}, Q_{12}^{(C)} = \frac{\nu_{12}^{(C)}E_2^{(C)}}{1-\nu_{12}^{(C)}\nu_{21}^{(C)}} Q_{66}^{(C)} = G_{12}^{(C)},$$

$$Q_{44}^{(C)} = G_{23}^{(C)}, Q_{55}^{(C)} = G_{13}^{(C)}.$$

Here $E^{(i)}(z), \nu,$ are effective Young's modulus, Poisson's ratio of the corresponding FGM layers $(i = T, B)$. For core (C) values $E_1^{(C)}, E_2^{(C)}, \nu_{12}^{(C)}, \nu_{21}^{(C)}, G_{12}^{(C)}, G_{23}^{(C)}, G_{13}^{(C)}$ are calculated by formulas (3).

The governing equations of the sandwich shallow shells with auxetic core are obtained by applying Hamilton's principle [11]:

$$N_{11,x} + N_{12,y} + \frac{Q_x}{R_x} = I_0\ddot{u}_0 + I_1\ddot{\psi}_x,$$

$$N_{12,x} + N_{22,y} + \frac{Q_y}{R_y} = I_0\ddot{v}_0 + I_1\ddot{\psi}_y,$$

$$Q_{x,x} + Q_{y,y} - \frac{N_{11}}{R_x} - \frac{N_{22}}{R_y} - k_w w_0 + k_p\vec{\nabla}^2 w_0 = I_0\ddot{w}_0, \tag{8}$$

$$M_{11,x} + M_{12,y} - Q_x = I_1\ddot{u}_0 + I_2\ddot{\psi}_x,$$

$$M_{12,x} + M_{22,y} - Q_y = I_1\ddot{v}_0 + I_2\ddot{\psi}_y,$$

where cofactors I_0, I_1, I_2 in system (8) are defined as:

$$(I_0, I_1, I_2) = \int\limits_{-\frac{h}{2}}^{h_1} \rho^{(B)}\left(1, z, z^2\right)dz + \int\limits_{h_1}^{h_2} \rho^{(C)}\left(1, z, z^2\right)dz + \int\limits_{h_2}^{\frac{h}{2}} \rho^{(T)}\left(1, z, z^2\right)dz.$$

Here $\rho^{(r)}$ $(r = B, C, T)$ is a mass density of the r-th layer for bottom (B), top (T), and for auxetic core (C), k_w, k_P are the parameters of elastic foundations.

3 Solution Method

To analyze the linear vibrations of FGM shallow shells with arbitrary planforms and various boundary conditions, the variational Ritz method is used. Assuming that the shell vibrations are harmonic, the problem can be formulated in variational form, which reduces to finding the stationary point of the following functional:

$$J = U\left(u, v, w, \psi_x, \psi_y\right) + V_e(w) - \lambda^2 T\left(u, v, w, \psi_x, \psi_y\right), \tag{9}$$

where λ is a natural frequency, U, T and V_e are strain, kinetic and potential energies, which are defined by the expressions:

$$U = \int_\Omega \left(N_{11}\varepsilon_{11}^{(0)} + N_{22}\varepsilon_{22}^{(0)} + N_{12}\varepsilon_{12}^{(0)} + M_{11}\chi_{11} + M_{22}\chi_{22} + M_{12}\chi_{12} + Q_x\varepsilon_{13} + Q_y\varepsilon_{23}\right)d\Omega,$$

$$V_e = \frac{1}{2}\int_\Omega \left(k_w w_0^2 + k_p\left(\overrightarrow{\nabla w_0}\right)^2\right)d\Omega,$$

$$T = \int_\Omega \left(I_0\left(u_0^2 + v_0^2 + w_0^2\right) + I_1\left(\psi_x u_0 + \psi_y v_0\right) + I_2\left(\psi_x^2 + \psi_y^2\right)\right)d\Omega.$$

Despite the effectiveness of the Ritz method as a tool for solving vibration problems of plates and shells, a key challenge arises when dealing with complex geometries and varied boundary conditions connected with the construction of admissible functions. This difficulty can be addressed using the R-functions theory [14, 15], which allows sequences of admissible functions to be systematically constructed for arbitrary geometries and boundary conditions. Importantly, these functions exactly satisfy the necessary prescribed boundary conditions. Consequently, the solution can be expressed in analytical form, representing a significant advantage of the R-functions method (RFM) over conventional numerical approaches.

Suppose that admissible functions $\{u_i\}, \{v_i\}, \{w_i\}, \{\psi_{xi}\}, \{\psi_{yi}\}$ have been constructed. Then according to the Ritz method, unknown functions $u(x, y), v(x, y), w(x, y), \psi_x(x, y), \psi_y(x, y)$ are presented as follows:

$$u = \sum_{i=1}^{N_1} a_i u_i,\ v = \sum_{i=N_1+1}^{N_2} a_i v_i,\ w = \sum_{i=N_2+1}^{N_3} a_i w_i,$$

$$\psi_x = \sum_{i=N_3+1}^{N_4} a_i \psi_{xi},\ \psi_y = \sum_{i=N_4+1}^{N_5} a_i \psi_{yi}. \tag{10}$$

Coefficients of expansion $\{a_i\}\ i = 1,2, \ldots, N_5$ in (10) are solution of the Ritz system:

$$\frac{\partial J}{\partial a_i} = 0, i = 1, 2, \ldots, N_5.$$

4 Results and Discussion

4.1 Shells of Rectangular Shape of Plan

Problem 1. Sandwich plates as well as cylindrical, spherical, and hyperbolic paraboloidal panels with auxetic core are examined. Each structure has a square planform with sides of length $a = b = 2$m and thickness $h = 0.1$m [11]. The shell edges are assumed to be simply supported and movable. The structural configuration includes two FGM face sheets composed of Al/Al_2O_3 and an auxetic honeycomb core layer made of *Al*. The material properties of the FGM mixture constituents are:

$$\text{Al} : E = 69GPa,\ \rho = 2700kg/m,\ \nu = 0.33;$$

$$Al_2O_3 : E = 380GPa,\ \rho = 3800kg/m,\ \nu = 0.33.$$

Table 1 shows fundamental frequencies computed by the approach proposed (RFM) and using Navier's form for analytical solution from work [11]. Comparison is carried out for shallow shells with the following parameters: $h = 0{,}1m$, $a = b = 20h$, $\eta_1 = \frac{d}{l} = 2$, $\eta_3 = \frac{t}{l} = 0.013857$, $\frac{h_c}{h_f} = 2$, angle $\theta = -55^0$ and different values $p = 0.5, 1, 5, 10$.

Problem 2. The second comparison was done for an auxetic honeycomb core sandwich square plate with isotropic face sheets *(Al)* and the same material of the core layer, but in this case the plate is resting on elastic foundation ($k_w = 0.1kN/m^3$, $k_P = 0.05kN/m$), inclined angle θ and ratio $\eta_1 = \frac{d}{l}$ vary. Comparison of results (Table 2) is presented for two works: [5], where authors used FEM and FSDT, and [8], where researchers employed HSDT theory and solved the problem analytically using the Navier solution.

Table 1. Comparison of fundamental frequencies (Hz) for auxetic sandwich shallow shells with square planform

$R_x(m)$	$R_y(m)$	Method	$p = 0.5$	$p = 1$	$p = 5$	$p = 10$	Pure metal
∞	∞	[11]	288.580	273.369	217,785	194.966	155.052
		RFM	288.554	273.345	217.744	194.919	154.933
∞	10	[11]	296.045	280.085	222.851	199.673	159.411
		RFM	296.013	280.056	222.803	199.618	159.348
10	10	[11]	319.520	301.356	239.022	214.613	173.206
		RFM	319.476	301.321	238.967	214.550	173.047
–10	10	[11]	286.209	271.122	215.992	193.363	153.781
		RFM	286.183	271.095	215.950	193.314	153.663

Table 2. Comparison of the fundamental frequency (Hz) of the square simply supported FGM auxetic plate on elastic foundation

η_1	Method	$\theta = -10^0$	$\theta = -35^0$	$\theta = -55^0$	$\theta = -80^0$
0.5	RFM	276.72	318.29	292.71	306.69
	[8]	276.542	317.795	292.415	306.313
	[5]	277.622	319.212	293.616	307.568
2	RFM	280.601	279.74	278.000	267.00
	[8]	280.387	279.537	277.803	266.875
	[5]	281.512	280.656	278.910	267.903
4	RFM	281.05	280.66	279.845	274.24
	[8]	280.836	280.454	279.645	274.095
	[5]	281.946	281.572	280.750	275.114

4.2 Shells of a Complex Planform

To illustrate the capabilities of the method proposed, a shallow shell with the complex planform shown in Fig. 2 is analyzed. As in the previous cases, the face sheets are assumed to be made of an FGM mixture Al/Al_2O_3, while the core consists of an auxetic aluminum (Al) honeycomb structure. It should be noted that the manufacturing process of curved cores for double-curved sandwich panels is a highly complex task. This problem is discussed in [12], and in [13] with respect to flexible honeycomb cores. In the present work, we assume that the cell geometry is designed in such a way that the mechanical properties of the core are preserved.

The shell is assumed to be clamped along its entire boundary. Accordingly, the boundary conditions are specified as:

$$w(x, y) = 0, u(x, y) = 0, v(x, y) = 0, \psi_x(x, y) = 0, \psi_y(x, y) = 0, \forall(x, y).$$

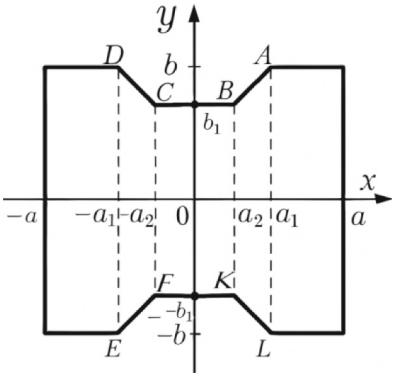

Fig. 2. Planform of the shallow shell

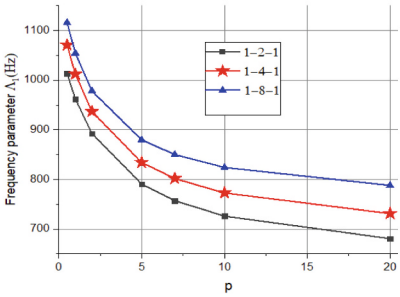

Fig. 3. Effect of gradient index on frequency

The solution structure [14, 15] for a fully clamped shell can be expressed in the form:

$$w = \omega\Phi_1, u = \omega\Phi_2, v = \omega\Phi_3, \psi_x = \omega\Phi_4, \psi_y = \omega\Phi_5, \tag{11}$$

where indefinite components $\Phi_i,\ i = \overline{1,5}$ are expanded in the form of an appropriate complete system such as polynomials, trigonometric functions, splines, etc. Function $\omega(x, y)$ constructed using the R-functions theory vanishes exactly on the shell boundary. In the present case this function is given by the following equation:

$$\omega(x, y) = (f_1 \wedge_0 f_2) \wedge_0 ((f_{AB} \vee_0 f_{CD}) \wedge_0 (f_{EF} \vee_0 f_{KL}) \vee_0 f_3),$$

symbols $\wedge_0,\ \vee_0$ denote the R-operations [14]. Functions $f_i,\ i = \overline{1,3}$ are defined as:

$$f_1 = \frac{(a^2 - x^2)}{2a} \geq 0, f_2 = \frac{(b^2 - y^2)}{2b} \geq 0, f_3 = \frac{(b_1^2 - y^2)}{2b_1} \geq 0.$$

Functions $f_{AB}, f_{CD}, f_{EF}, f_{KL}$ are defined by the expressions of the oriented [14] straight lines (AB, CD, EF, KL).

$$f_{AB} = ((b - b_1)(x - a_1) - (a_2 - a_1)(y - b))/\sqrt{(b - b_1)^2 + (a_2 - a_1)^2} \geq 0,$$

$$f_{CD} = ((b_1 - b)(x + a_2) + (a_2 - a_1)(y - b_1))/\sqrt{(b - b_1)^2 + (a_2 - a_1)^2} \geq 0,$$

$$f_{EF} = ((b - b_1)(x + a_1) + (a_2 - a_1)(y + b))/\sqrt{(b - b_1)^2 + (a_2 - a_1)^2} \geq 0,$$

$$f_{KL} = ((b - b_1)(x - a_2) + (a_1 - a_2)(y + b_1))/\sqrt{(b - b_1)^2 + (a_2 - a_1)^2} \geq 0.$$

Functions $\Phi_i,\ i = \overline{1,5}$ in (11) were expanded in a power series upon consideration of the problem symmetry [14, 15]. To approximate Φ_1 twenty eight terms of the polynomial's series were retained, and the remaining components were approximated

by fifteen terms. Figure 3 illustrates influence of fraction index p and thickness of layers on fundamental natural frequency Λ of the FGM auxetic sandwich spherical shells $\left(R_x = R_y = 10m\right)$ on elastic foundation ($k_w = 0.1kN/m^3$, $k_P = 0.05kN/m$). Values of geometric parameters were taken as: $h = 0{,}1m$; $2a = 2b = 20h$; $2a_1 = 1{,}4m$; $2a_2 = 0.6m$; $2b_1 = 1.2m$; $\theta = -55^0$, $\eta_3 = \frac{t}{l} = 0.013857$; $\eta_1 = \frac{d}{l} = 2$; $\frac{h_c}{h_f} = 2, 4, 8$. As shown in Fig. 3, an increase in the gradient index p results in a higher metal content in the FGMs, which, in turn, reduces the overall stiffness of the shell and consequently leads to lower fundamental frequencies. However, increasing the thickness of the core layer contributes to a rise in these frequencies.

The effect of the inclined angle θ of the auxetic honeycomb unit cell core on the fundamental frequency of the shell is shown in Fig. 4. The results are presented for a spherical shell with the same geometric and mechanical parameters as for Problem 2. The volume fraction index p and thickness ratio $\frac{h_c}{h_f}$ between the face sheets and the core are kept constant: $p = 2$; $\frac{h_c}{h_f} = 8(1-8-1)$.

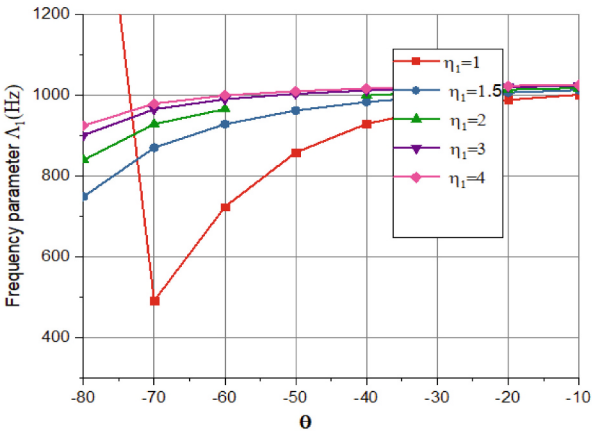

Fig. 4. Effect of the inclined angle on fundamental frequency of the clamped spherical shell

As shown in Fig. 4 for values of inclined angle from –80° to –50°, the fundamental frequency increases significantly for $\eta_1 = 1.5, 2, 3, 4$. But for $\eta_1 = 1$ frequency behavior is extraordinary. This phenomenon should be taken into account when using metamaterials in practical applications.

5 Conclusions

This study presents the first application of the R-functions theory combined with the variational Ritz method to analyze the free vibrations of sandwich shallow shells with auxetic cores and functionally graded face sheets. The validity and efficiency of the proposed approach have been confirmed through comparisons with previously published

results. As a novel contribution, the work investigates the vibration response of a clamped spherical shallow square shell with trapezoidal cutouts on two opposite edges, resting on an elastic foundation.

Acknowledgment. The research was carried out within the NATO project "Composite Metamaterials for Aerospace Structures CoMetA", grant number G6176, under the framework of the Science for Peace and Security (SPS) Programme.

References

1. Bohara, R. P., Linforth, S., Nguyen, T., Ghazlan, A., Ngo, T.: Anti-blast and -impact performances of auxetic structures: a review of structures, materials, methods, and fabrications. Eng. Struct. **276**. 115377 (2023). https://doi.org/10.1016/j/engstruct.2022.115377
2. Singh, S.J., Harsha, S.P.: Free vibration analysis of sandwich plate with honeycomb core and FGM face sheets. In: Saran, V.H., Misra, R.K. (eds.) Advances in Systems Engineering. LNME, pp. 905–917. Springer, Singapore (2021). https://doi.org/10.1007/978-981-15-8025-3_85
3. Sadiq, E., Sadeq, H.B., Munsin, J.J.: Optimum vibration characteristics for honeycomb sandwich panel used in aircraft structure. J. Eng. Sci. Technol. **16**(2), 1463–1479 (2021)
4. Quoc, T.H., Tu, T.M., Tham,V.V: Free vibration and dynamic response of sandwich composite plates with auxetic honeycomb core. J. Sci. Technol. Civ. Eng. HUCE (NUCE) **15**(4), 1–14 (2021). https://doi.org/10.31814/stce.huce(nuce)2021-15(4)-01
5. Tran, T.T., Pham, Q.H., Thoi, T.N., Tran, V.T.: Dynamic analysis of sandwich auxetic honeycomb plates subjected to moving oscillator load on elastic foundation. Adv. Mater. Sci. Eng. (2020). https://doi.org/10.1155/2020/6309130
6. Thang, N.T., Van Long, N., Tu, T.M., Nam, N.H., Anh, M.C.: Navier solution for static and free vibration analysis of sandwich plate with auxetic honeycomb core resting on Pasternak elastic foundation. J. Sci. Technol. Civ. Eng. HUCE (NUCE) **16**(3), 18–28 (2022). https://doi.org/10.31814/stce.huce(nuce)2022-16(3)-02
7. Ghazwani, M.H., Alnujaie, A., Vinh, P.V.: A general viscoelastic foundation model for vibration analysis of functionally graded sandwich plate with auxetic core. Defence Technol. **46**, 40–58 (2024). https://doi.org/10.1016/j.dt.2024.12.008
8. Binh, D.C., Huan, D.T., Hai, N.T., Le V.Q., Chau, L.T-M., Anh, H.X.: Free vibration analysis of sandwich plates with auxetic core and porous FGM faces resting on winkler/pasternak/kerr elastic foundations. Vietnam J. Agric. Sci. **8**(2), 2493–2508 (2025). https://doi.org/10.31817/vjas.2025.8.2.06
9. Shariyat, M., Alipour, M.M.: Analytical bending and stress analysis of variable thickness FGM auxetic conical/cylindrical shells with general tractions. Latin Am. J. Solids Struct. **14**, 805–843 (2017). https://doi.org/10.1590/1679–78253413
10. Cong, P.H., Long, P.T., Nguyen Van Nhat, N.V., Duc, N.D.: Geometrically nonlinear dynamic response of eccentrically stiffened circular cylindrical shells with negative Poisson's ratio in auxetic honeycombs core layer. Int. J. Mech. Sci. **152**, 443–453 (2019). https://doi.org/10.1016/j.ijmecsci.2018.12.052
11. Pham, H.-A., Tran, H.-Q., Tran, M.-T., Nguyen, V.-L., Huong, Q.-T.: Free vibration analysis and optimization of doubly-curved stiffened sandwich shells with functionally graded skins and auxetic honeycomb core layer. Thin-Walled Struct. **179**, 109571 (2022). https://doi.org/10.1016/j.tws.2022.109571

12. Evans, K.E.: The design of doubly curved sandwich panels with honeycomb cores. Compos. Struct. **17**(2), 95–111 (1991)
13. Avramov, K., Uspensky, B.: Nonlinear vibrations of doubly curved composite sandwich shells with FDM additively manufactured flexible honeycomb core. Acta Mech. **234**, 1183–1210 (2023). https://doi.org/10.1007/s00707-022-03426-w
14. Rvachev, V.L.: The R-functions Theory and Its Some Application. Naukova Dumka, Kiev (in Russian) (1982)
15. Kurpa, L., Pellicano, F., Shmatko, T., Zippo, A.: Free vibration analysis of porous functionally graded material plates with variable thickness on an elastic foundation using the R-functions method. Math. Comput. Appl. **29**(1), 10 (2024). https://doi.org/10.3390/mca29010010

Development of Extended-Life Lance Tips: Symmetrical Cooling of Zones Behind the Nozzles

Sergei Panteikov(✉) and Elena Leshchenko

Dniprovsky State Technical University, Dniprobudivska Str., 2, Kamianske 51918, Ukraine
ser_pant_in@ukr.net, lescha_helen@meta.ua

Abstract. This research aims to design highly durable mechanical structures intended for delivering oxygen into the working cavity of 250-ton converters at the Dniprovsky Metallurgical Combine OJSC (Kamianske, Ukraine). Drawing on the performed industrial experiments, the hypothesis suggesting a notable extension in lance tip lifespan while providing symmetrical cooling to the behind-nozzle zones of their copper bowls was verified; this method's significant efficiency was established for the first time. Two versions of the innovative lance tip design (protected by Ukrainian patent No. 40428) with six shortened Laval nozzles have been designed, which, owing to improved coolant distribution within them, made it possible to increase its life by 1.2 and 1.168 times compared to similar designs of 6-nozzle tips without guiding blades (characterized by a 2.33 times greater life compared to standard 5-nozzle tips), by 2.8 and 2.72 times compared to standard 5-nozzle tips. It was established that the external welding zones surrounding the Laval nozzles are the limiting link that does not allow achieving high life of welded lance tip designs. All of this supports the use of forged and stamped and/or solid-cast designs, which possess a significantly longer life – one that can be further extended through cooling of the behind-nozzle space. The results of experimental assessments of the effectiveness of various versions of the developed lance tip design, as presented in this study, indicate the potential for effectively addressing the issue of low life of this type of lance tip in operating converter shops.

Keywords: converter process · top oxygen lance · cooler · copper bowl · water velocity · behind-nozzle space · blowing device · welding seam · water-cooling tract · top lance barrel

1 Introduction

Modern technologies of converter steel production [1] require high efficiency at each stage of the technological process. Efficiency is ensured mainly by the reliability of the power equipment available in the converter shop, including the designs of the top blowing lances, which are one of its key elements and determine the quality and speed of metal refining. These mechanical devices are used to supply technical oxygen to the molten converter bath at high (supersonic) speeds and play a crucial role in activating and

H. Altenbach et al. (Eds.): CAMPE 2025, LNME, pp. 273–282, 2026.
https://doi.org/10.1007/978-3-032-16381-3_26

intensifying the oxidation of impurities, affecting the rate of lime dissolution, promoting intensive stirring of the liquid bath, increasing the productivity of the units in the converter shop, and more [2].

The lance tip is one of the most loaded and vulnerable elements of the top lance, located in the zone of extreme temperatures, aggressive chemical effects of the melt, and shock loads from reactive blowing flows. Overheating and wear of the tip remain key problems, since their damage directly affects the stability of the technology and the quality of steel. Imperfect tip designs complicate the operation of top lances, disrupt the workflow, and reduce the shop productivity.

All conventional lance tip designs share a common disadvantage – the occurrence of stagnant coolant regions located behind each blowing nozzle. This fact leads to local film boiling of water in the behind-nozzle zones, significantly increasing the temperature of these sections of the lower bowl. The heterogeneity of its temperature field leads to overheating and melting of copper in the zones behind the nozzles, which leads to the failure of the lances. In the tips of welded structures, the outer copper welds around the nozzles fall into the overheating zone, which sharply reduces the life of the tips. An increased number of nozzles results in a larger number and greater area of stagnant zones, which explains the inversely proportional dependence of the life of the tips on the number of nozzles in them. Eliminating stagnant coolant zones behind the nozzles in tip cooling systems will greatly enhance cooling efficiency and extend lance life, allowing them not to be limited by the number of nozzles when designing blowing devices.

Therefore, particular attention should be directed toward improving the tip designs: primarily their cooling systems, as well as optimizing the tip geometry to eliminate local overheating zones of the lower bowls, using highly resistant structural materials. These are urgent tasks of metallurgy aimed at reducing the wear of power equipment, improving the quality of steel, and increasing energy efficiency and productivity.

The work aims to develop an innovative lance tip design with shortened Laval nozzles, based on the developed theoretical provisions, with a subsequent evaluation of the effectiveness of the proposed symmetrical cooling methods applied to the behind-nozzle zones of the lower bowl, aimed at addressing the issue of low life of this tip type in converter shops conditions.

2 Literature Review

In order to improve the technical and economic characteristics of converter shops and increase the operational performance of shop power equipment (including top–blowing devices), the use of multi–nozzle (6 or more) top oxygen lances is proposed.

High temperatures in the working space, the oxidation of carbon, and the splashing of metal with slag during oxygen blowing create an aggressive atmosphere in the converter [3], which has a destructive effect on the lance device, especially lance tip [4]. This fact can lead to changes in the microstructure of its materials with subsequent destruction of the welds, especially copper [3].

To prevent these phenomena, it is necessary to organize effective cooling of the lance tip. However, an increased number of blowing nozzles worsens the cooling of copper bowls due to stagnant water zones arising behind the nozzles. The behind–nozzle

sections of the external copper welds connecting the lower bowl with the nozzles are very vulnerable due to their low strength and smaller thickness. An increase in the number of nozzles reduces the life of the tip (by 22% when the number of nozzles increases from 5 to 6). In this regard, lances with several nozzles up to 5 are used in practice, which improves the life of the tips, but leads to deterioration of the process parameters poor slag formation, metal removal, reduced steel output, increased content of harmful impurities in it, and other technological problems.

Modern developments of lances are aimed at increasing the resource–saving efficiency of the converter process due to their reserves. Designs of lance tips for the afterburning of CO to CO_2 are being developed, which allows improving the heat balance of the melt, accelerating the mixing of the melt, reducing the blowing time, increasing the dephosphorization rate, and reducing defects [5]. An analysis of the blowing processes with and without afterburning of CO has been performed [6]. It has been established [7] that under $P_{CO_2}/P_{CO} = 1$ the temperature of the exhaust gases increases from 1800 to 2000 K.

In order to enhance the mass transfer rate between the melt and the slag by more than 30%, a gas-jet-actuated self-rotating lance was developed [8].

The influence of the cross-sectional area of the central blow-through channel and the gas flow rate on jet characteristics was investigated, enabling the design and optimization of the central nozzle in the top oxygen lance for injecting an O_2–CO_2 gas mixture into the converter [9]. The influence of preheating temperature and gas mixture flow rate (90% O_2 + 10% CO_2) on the jet characteristics during its injection through a swirling nozzle was also studied [1].

To optimize the design of the top lance nozzle, the influence of outlet section wear on the parameters of the supersonic gas jet was investigated. It was established [10] that increased wear leads to a more rapid decline in jet velocity and results in an earlier jet convergence point. However, no measures to eliminate or reduce wear were proposed.

When designing an oxygen lance with a high (2.15) Mach number at different oxygen pressures, the jet characteristics and their effect on the bath were studied [11]. The process of blowing with a dynamic oxygen lance was also studied – the effect of its design, including the rotation speed and twist angle, on melt dephosphorization was established [12]. To develop top submersible lances, studies were conducted on the dynamics of gas penetration into the bath [13], the formation and floating of bubbles in the melt [14], including using X-ray visualization [15], and the rotation of splashing waves in liquid metal [16]. The effect of interphase forces and melt viscosity on the bath hydrodynamics was analyzed [17].

To apply a protective slag to the lining of the converters, the effect of the top blowing on the foaming of slag was investigated [18], and heat flows to the slag-splashing lance were calculated [19].

The conducted analysis of the literature showed the absence of works on the study and improvement of lance tip cooling systems. However, this is an important problem for all converter shops, especially when using outdated welded tips. Thus, the need for work to improve the service life of lance tips, including designs with shortened Laval nozzles, remains relevant and requires an effective solution.

3 Research Methodology

The impact of different symmetrical cooling configurations in the behind-nozzle space of copper bowls on the durability of welded lance tips was investigated – with a partition (without collision of coolant flows) and without a partition (with collision of water flows). The subject of the study is an innovative 6-nozzle lance tip design with shortened Laval nozzles, whose profile and positioning were defined through high-temperature modeling of the converter process. Experiments were conducted on industrial 250-ton converters, utilizing structured observation. The causes of failure of lance tips were recorded through photography. The MS Excel 2015 program processed the results.

4 Results and Discussion

To once again test the previously proposed hypothesis regarding the influence of the cooling intensity in the behind–nozzle zones of the copper bowl on the life of the lance tip, an innovative design (Patent 40428 UA, C 21 C 5/48. Lance tip with symmetrical cooling of nozzles) of a 6-nozzle tip with shortened Laval nozzles for the top lances of 250-ton converters at Dniprovsky Metallurgical Combine OJSC (currently KAMET–STAL' PrJSC, Kamianske, Ukraine) was developed, manufactured and tested. Due to the improvement of the cooling system, it ensures intensive cooling of the behind-nozzle zones of the inner surface of the copper bowl, where stagnant water zones are formed in classical designs (Fig. 1, a). That is, an increase in the life of the tips was achieved by eliminating stagnant coolant zones in their nozzle zones according to the options proposed by the authors (Fig. 1, b, c).

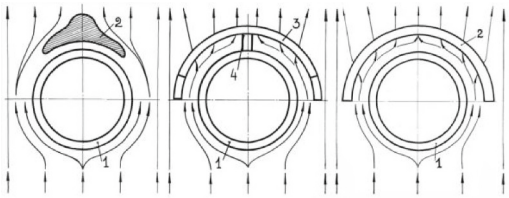

Fig. 1. Scheme of coolant flow in the behind-nozzle zones of lance tips: a – in the classic design; b – in the design with symmetrical nozzle cooling and a partition (see Fig. 2, a, b); c – in the design with symmetrical nozzle cooling and without a partition (see Fig. 2, c, d); 1 – nozzle; 2 – stagnant zone of coolant; 3 – guide blade; 4 – partition.

Two versions (Fig. 2, a–d) of the new design were developed with an improved cooling system, which provided for symmetrical cooling of the zones behind the nozzle space of the lower bowls. These results were achieved by symmetrically installing special guiding blades in the form of a semicircle (Fig. 2, e) with a gap positioned behind each nozzle in the direction the water moves, which allowed for an intensive supply of coolant behind the nozzles, thereby ensuring highly efficient cooling of the behind–nozzle zones of the copper bowls.

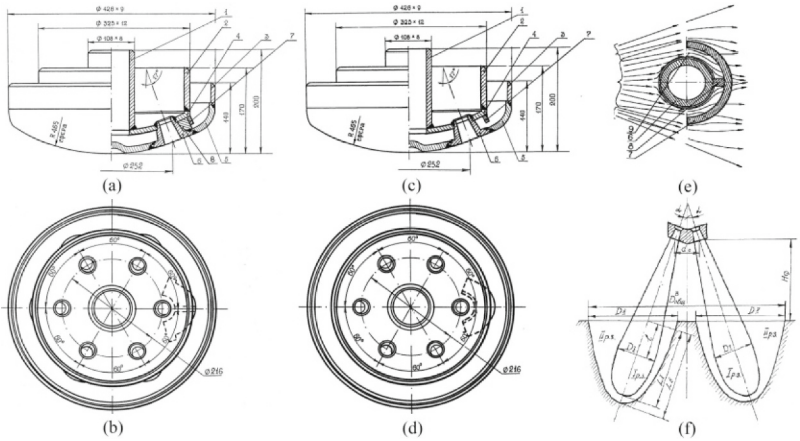

Fig. 2. Designs of a 6-nozzle tip with symmetrical cooling of the zones of the behind-nozzle space of the copper bowl by separate flows (a, b) and without isolation of the water flows (c, d), schemes for cooling the behind–nozzle space according to the 1st variant (e) and the reaction zone when oxygen is blown onto the converter bath from above (f), see the text for designations.

The previously designed and successfully tested 6-nozzle design with shortened Laval nozzles and a distance between the bowls reduced to 25 mm was taken as a prototype for the specified variants of the innovative lance tip design. While it did not include cooling of the copper bowl in the areas behind the nozzles, it was characterized by 2.27–2.41 (on average 2.33) times greater life, which amounted to 114–143 melts (with an average durability of 126.67 melts) compared to standard 5-nozzle tips, the life of which amounted to 49–63 (on average 54.33) melts.

The arrangement of Laval nozzles in the lance tip – specifically, their inclination angles relative to the vertical axis of the lance (α, degrees), the angular spacing between adjacent nozzle axes in the horizontal plane (φ, degrees), and the diameter of the circumference along which their outlets are positioned (d_o, m) – was determined through high-temperature modeling of top-blowing processes. This modeling accounted for the number of nozzles and the distance from the lance to the bath surface at rest ($H_ф$, m), aiming to ensure a stable blowing process without causing metal splashing onto the oxygen lance barrel or the converter neck. Optimal nozzle positioning was designed to maintain appropriate diameters and depths (D, D_I, D_{II}, L_I, L_{II}) of the reaction zone developed under elevated temperatures (Fig. 2, f), thereby preventing premature localized wear of the converter's lining on its walls and bottom.

The developed variants of the lance tip design (Fig. 2, a–d) consist of central water pipes 1, intermediate oxygen supply pipes 2, and external water discharge pipes 3. The top (steel) bowl 4 and lower (copper) bowl 5 accommodate inserts 6 fitted with Laval nozzles, which are welded into pre-drilled holes. These nozzles are evenly spaced along the circumference at an inclination angle of 17° relative to the vertical axis of the top lance.

Behind each nozzle insert 6, in the direction of water flow, a semicircular guiding blade 7 is installed. In the first design variant of the lance tip, a partition 8 is provided.

Blade 7 is mounted with a coaxial annular gap 9 relative to insert 6, allowing symmetrical coolant supply from both sides behind the nozzle. The size of this coaxial annular gap 9 acts as a control parameter regulating water flow into the behind-nozzle zones of the lower bowl 5, thereby achieving the desired cooling intensity.

The lance tips (Fig. 3, a–c) are cooled in the following manner. Water is introduced at the inlet of the discharge channel (between bowls 4 and 5) through branch pipe 1 (Fig. 2, a–d). In front of nozzles 6, the continuous coolant flow is divided by guide blades 7 into two separate flow groups (Fig. 2, e) – I (the main) and II (the additional). Group I (water consumption 59% of the total) continues moving, passes between blades 7, and, slightly bending around them, goes into the discharge tract of the lance between branch pipes 2 and 3; at the same time, it does not cool the zones behind nozzles 6 and blades 7. For this purpose, group II is provided (water consumption 41% of the total), which, bending around nozzles 6, passes into gaps 9 between nozzles 6 and blades 7, cools behind–nozzle zones and exits under blades 7 through gaps between them and the lower bowl 5, cooling the zones behind blades 7. At the outlet of the discharge channel behind blades 7, water flows I and II are mixed and directed as a common flow into the discharge tract of the lance. This approach ensures highly efficient heat removal from the entire inner surface of the lower bowl 5, thereby eliminating the formation of behind–nozzle areas that could lead to overheating.

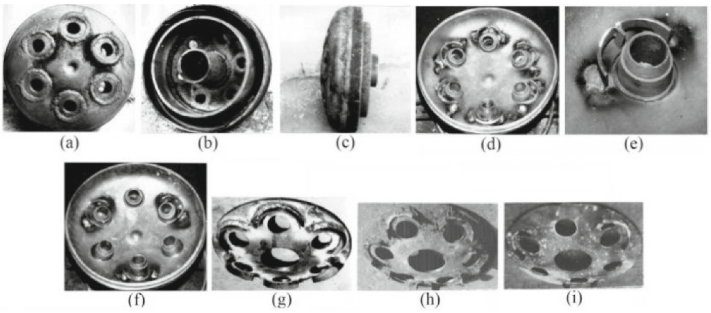

Fig. 3. External appearance (a–c) of the developed variants of a 6-nozzle tip and its components with symmetrical cooling by separate flows (d–f) and without isolation of water flows (g–i): see the text for designations.

In the first variant of the tip design (see Fig. 2, a, b), the guiding blades had a symmetrical cutout at the lower end over 70% of its surface, while the extreme sections of the blade (each 15% of its length, on which each blade rests on the inner surface of the lower bowl and is welded to it (Fig. 3, d)) did not have such a cutout (Fig. 3, e). Due to these sections, water, when entering the annular gaps between the nozzles and blades, acquires a rotational motion, due to which the surface of the lower bowl is cooled more effectively. This variant, in addition, provides for the installation of a partition in the middle of the blade between the latter and the nozzle (Fig. 3, e). In the second variant (see Fig. 2, c, d) the partition was absent. The blades, in order to simplify the manufacture and assembly of the tip, initially had the shape of a semicircle without a symmetrical cutout at the lower end and were attached to the top bowl by welding (Fig. 3, g). At the

same time, a gap for the passage of water was formed between the entire lower end of the blade and the inner surface of the lower bowl.

Figure 4 shows calculated water velocities (flow rate $U_B = 300–340$ m^3/h) in various sections (A–A; B–B; C–C; D–D; E–E, left to right) of the water-cooling tract for 5- and 6-nozzle tips. Optimal coolant flow rates were 340 m^3/h and 300 m^3/h, with temperature differences between lance input and output of 11–16 °C and 10–15 °C (depending on blowdown time), respectively. Data in Fig. 4 indicate a marked increase in water velocity at the inlet (B–B) of the 6-nozzle tip (see Fig. 2, a–d; Fig. 3, a–c) and in the inter-nozzle region (C–C). A slightly lower increase is seen at the outlet (D–D), while the most significant rise – up to 10.1 m/s – is recorded behind the nozzles, compared to the 5-nozzle tip, despite a lower overall coolant flow rate. At the inlet (A–A) and outlet (E–E) sections, water velocity decreased somewhat, which should be noted for future consideration.

In terms of life, the lance tips showed the following results (Fig. 5).

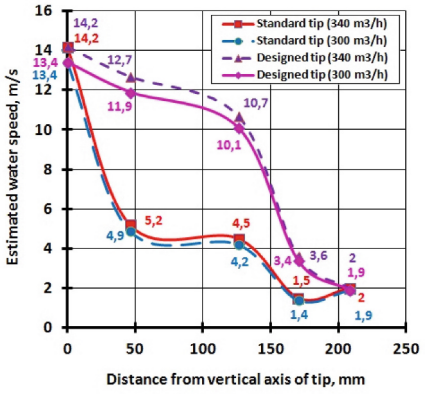

Fig. 4. Dependence of the average water velocity in different sections of the studied lance tips.

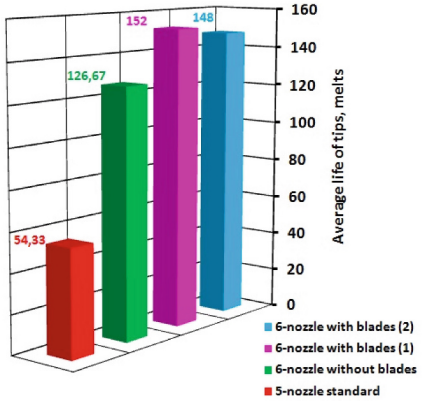

Fig. 5. Average lifespan of the studied tip designs for top converter lances.

The average life (152 melts) of the 1st variant (Fig. 2, a, b) increased by 1.2 times compared to the designs of 6-nozzle tips without blades and by 2.8 times compared to the standard 5-nozzle tips (see above).

Tests of the 2nd design variant (Fig. 2, c, d) were initially unsuccessful, as simplifying the guiding blade design reduced the tip outlet tract's capacity to 270 m^3/h due to the formation of reverse braking water flows behind the nozzles. After its modernization (Fig. 3, h) according to the example of the 1st variant, the water consumption was normalized, and the life of the tip increased by 1.168 times (average life of 148 melts, Fig. 5) in comparison with 6-nozzle tips without guiding blades and by 2.72 times in comparison with standard 5-nozzle tips.

The installation of a partition between the nozzle and the blade improves the cooling of the behind–nozzle zones, preventing a decrease in the water velocity, eliminating the collision of oncoming and the formation of reverse flows in the upper layers of

the behind–nozzle zones (above the gap) in the annular gap. This fact also provides an additional support point for the blade. The longer service life (152 melts versus 148) of the 1st tip design (Fig. 2, a, b) compared to the 2nd (Fig. 2, c, d) confirms the positive effect of the presence of a partition on the life of lances.

Figure 6 shows tested samples of various lance tip designs, including those with cooling of the behind–nozzle zones of the copper bowl.

Fig. 6. Tested samples of various designs of lance tips.

As expected, the behind-nozzle areas of the external welds surrounding the nozzles do not withstand the thermomechanical stresses caused by high temperatures. This fact leads to their cracking in the 5- (Fig. 6, a, 54 melts) and 6-nozzle bladeless (Fig. 6, b, 115 melts) tips, causing water leakage and the need for urgent replacement of the tip to prevent an accident, which repeatedly occurred in practice.

To test the effect of cooling the behind–nozzle areas on the life, the 1st and 2nd tip variants were manufactured with alternating nozzles with and without blades (Fig. 3, f and Fig. 3, i), which, respectively, failed after 127 (Fig. 6, c) and 125 melts due to burnout of the weld behind one of the uncooled nozzles. The tips with cooling of all nozzles retained the integrity of weld seams for 152 melts and more (Fig. 6, d). These results confirmed that symmetrical supply of coolant increases the life of tips, especially welded structures.

Work continues on further optimization of lance tip designs: use of asymmetrical cooling of behind–nozzle zones, change of the outer diameter of the intermediate pipe from 325 to 377 mm, manufacture of cast tips [20] with quality control [21], strengthening of the design, and ensuring uniform cooling of the copper bowl of the tip.

5 Conclusions

In the work, based on the series of industrial trials conducted on 250-ton converters of the Dniprovsky Metallurgical Combine OJSC (now KAMET–STAL' PrJSC, Kamianske, Ukraine), the hypothesis regarding a substantial increase in the life of lance tips through the cooling of the inner surfaces in the behind-nozzle zones of their copper bowls has been reaffirmed. For the first time, the high efficiency of the implemented approach was demonstrated – achieving symmetrical cooling of the copper bowl's behind-nozzle zones with enhanced cooling intensity, which represents the most effective and essential method for extending the life of lance tips equipped with shortened Laval nozzles.

The use of two variants of the innovative design of the 6-nozzle lance tip increased its life by 1.2 and 1.168 times compared to similar 6-nozzle tips without cooling the

zones behind the nozzles, by 2.8 and 2.72 times compared to standard 5-nozzle tips. It was found that the main limitation of the life of welded lance tips is external copper welds around the Laval nozzles. This result indicates the feasibility of using forged, stamped, and/or solid-cast copper bowls, which have higher life, and effective cooling of the behind-nozzle zones, as shown by the study data, will additionally increase the life of such structures.

The experimental assessment results regarding the efficiency of the developed lance tip design variants with shortened Laval nozzles, as presented in this study, confirm the potential for a more effective solution to the persistent issue of limited life of this lance type, commonly encountered in operating converter shops.

References

1. Feng, C., Chen, S., Dong, J., et al.: Influence of preheating temperature on the characteristics of $O_2 + CO_2$ jet by mixed injection with a swirling oxygen nozzle. JOM **73**, 2985–2994 (2021). https://doi.org/10.1007/s11837-021-04836-2
2. Singha, P.: Contribution of emulsion zone in refining of basic oxygen steelmaking converter. Metall. Mater. Trans. B **55**, 2580–2590 (2024). https://doi.org/10.1007/s11663-024-03117-y
3. Wang, J., Cao, Z., Liu, J., et al.: Structure design and optimization of a 150t converter oxygen lance under high oxygen supply intensity. JOM **77**, 5882–5891 (2025). https://doi.org/10.1007/s11837-025-07469-x
4. Lim, S.M., Park, S.S., Yi, K.W.: Extension of lance life by change of height of lances in the smelting furnace of Mitsubishi process. Met. Mater. Int. **27**, 3721–3729 (2021). https://doi.org/10.1007/s12540-020-00712-x
5. Dong, P., Zheng, S., Zhu, M.: Numerical study on gas-metal-slag interaction with single-flow postcombustion oxygen lance in the steelmaking process of a top-blown converter. JOM **74**, 1509–1520 (2022). https://doi.org/10.1007/s11837-021-05147-2
6. Liu, F., Wei, G., Zhu, R., et al.: Flow field characteristic of postcombustion oxygen lance formed by various secondary nozzle arrangements. Metall. Mater. Trans. B **55**, 935–949 (2024). https://doi.org/10.1007/s11663-024-03006-4
7. Protopopov, E.V., Temlyantsev, M.V., Yakushevich, N.F., et al.: Peculiarities of exhaust gases afterburning in converter with application of two-tier oxygen lance blowing. Steel Transl. **51**, 872–878 (2021). https://doi.org/10.3103/S0967091221120093
8. Gao, Q., Wu, W., Zhi, J., et al.: Effect of a self-rotating oxygen lance system on mass transfer between slag and molten steel. J. Iron Steel Res. Int. **28**, 152–159 (2021). https://doi.org/10.1007/s42243-020-00515-9
9. Feng, C., Zhu, R., Dong, K., et al.: Effects of nozzle layout and parameters on the jet characteristics of a $CO_2 + O_2$ mixed oxygen lance. Metall. Mater. Trans. B **52**, 425–439 (2021). https://doi.org/10.1007/s11663-020-02048-8
10. Panteikov, S.P.: Stages of improvement for welded structures with five-nozzle lance heads in the converter shop of public joint stock company "Dneprovsky Metallurgical Combine." Steel Transl. **50**, 756–761 (2020). https://doi.org/10.3103/S0967091220110108
11. Zhang, Y., Zhang, C., Han, Y., et al.: Jet characteristics of a high-mach-number oxygen-lance nozzle under high oxygen pressure. Metall. Mater. Trans. B **52**, 4070–4081 (2021). https://doi.org/10.1007/s11663-021-02325-0
12. Li, M., Shao, L., Li, Q., et al.: A numerical study on blowing characteristics of a dynamic free oxygen lance converter for hot metal dephosphorization technology using a coupled VOF-SMM method. Metall. Mater. Trans. B **52**, 2026–2037 (2021). https://doi.org/10.1007/s11663-021-02155-0

13. Obiso, D., Reuter, M., Richter, A.: CFD investigations of bath dynamics in a pilot-scale TSL furnace. Metall. Mater. Trans. B **52**, 3064–3077 (2021). https://doi.org/10.1007/s11663-021-02233-3
14. Kandalam, A., Stelter, M., Reinmöller, M., Reuter, M.A., Charitos, A.: Determining the bubble dynamics of a top submerged lance smelter. In: Lazou, A., Daehn, K., Fleuriault, C., Gökelma, M., Olivetti, E., Meskers, C. (eds.) REWAS 2022: Developing Tomorrow's Technical Cycles (Volume I). The Minerals, Metals & Materials Series. Springer, Cham (2022). https://doi.org/10.1007/978-3-030-92563-5_57
15. Lappan, T., et al.: X-ray and neutron radiographic experiments on particle-laden molten metal flows. In: Lee, J., Wagstaff, S., Anderson, A., Tesfaye, F., Lambotte, G., Allanore, A. (eds.) Materials Processing Fundamentals 2021. The Minerals, Metals & Materials Series. Springer, Cham (2021). https://doi.org/10.1007/978-3-030-65253-1_2
16. Obiso, D., Reuter, M., Richter, A.: CFD investigation of rotational sloshing waves in a top-submerged-lance metal bath. Metall. Mater. Trans. B **52**, 2386–2394 (2021). https://doi.org/10.1007/s11663-021-02182-x
17. Cao, L., Wang, Y., Cheng, Z., et al.: Bubble formation and surface sloshing in the TSL flow with a viscous liquid. JOM **74**, 4920–4929 (2022). https://doi.org/10.1007/s11837-022-05539-y
18. Wang, R., Zhang, B., Hu, C., et al.: Physical modeling of slag foaming in combined top and bottom blowing converter. JOM **74**, 151–158 (2022). https://doi.org/10.1007/s11837-021-04984-5
19. Zhulkovskyi, O., Panteikov, S., Zhulkovska, I., Kashcheev, M., Leshchenko, E.: Heat transfer calculation for numerical simulation of thermal mode of slag–splashing lance in the forecasting system. In: Kazymyr, V., et al. (eds.) Mathematical Modeling and Simulation of Systems. MODS 2023. Lecture Notes in Networks and Systems, vol. 1091. Springer, Cham (2024). https://doi.org/10.1007/978-3-031-67348-1_6
20. Stalnichenko, O., Lysenko, T., Ponomarenko, O., Kreitser, K., Kozishkurt, E.: Vacuum technology for magnesium alloys during die casting of radiators. In: Tonkonogyi, V., Ivanov, V., Trojanowska, J., Oborskyi, G. (eds.) Advanced Manufacturing Processes VI. Interpartner 2024. Lecture Notes in Mechanical Engineering. Springer, Cham (2025). https://doi.org/10.1007/978-3-031-82746-4_20
21. Ponomarenko, O., Yevtushenko, N., Akimov, O., Vasilets, V., Lopes, H.: Study of the laws of random fluctuations in the parameters of foundry processes and the quality of castings. In: Machado, J., Trojanowska, J., Ottaviano, E., Xavior, M.A., Valášek, P., Basova, Y. (eds.) Innovations in Mechanical Engineering IV. ICIENG 2025. Lecture Notes in Mechanical Engineering. Springer, Cham (2025). https://doi.org/10.1007/978-3-031-93554-1_36

Improving the Operational Safety of Tip Structures for Top-Blown Converter Lances

Elena Panteikova[1](✉), Sergei Panteikov[2], and Elena Leshchenko[2]

[1] Private Joint–Stock Company "KAMET–STAL'", Soborna Str., 18B, Kamianske 51925, Ukraine
hel_pant_in@ukr.net

[2] Dniprovsky State Technical University, Dniprobudivska Str., 2, Kamianske 51918, Ukraine
ser_pant_in@ukr.net, lescha_helen@meta.ua

Abstract. This paper aims to develop mechanical devices for feeding various process gases (such as oxygen and nitrogen) into the working space of 250-ton converters during steel smelting, ensuring significant production safety during operation and achieving higher durability. Based on a comprehensive analysis of various literary materials, patent searches, and the results of industrial testing of different tip designs (both standard and previously developed) for top oxygen lances, a new, safe lance tip design was developed and proposed, protected by Patent UA 78112. The results of the study have, for the first time, demonstrated a high level of efficiency in unloading the outer copper weld seam due to the installation of special reinforcing pins in the lance tip design, which is the most effective and necessary measure to increase operational safety and durability of any tip design for the top lance. The necessary technical documentation was transferred to the converter shop of OJSC "Dniprovsky Metallurgical Combine" (Kamianske, Ukraine) for the manufacture and implementation of this design of top blowing devices in the production process. The use of a safe design of a mechanical blowing device to the top converter lances, described in this work, will significantly secure the converter steel production, as well as increase the resistance of the tips to the top oxygen lances in comparison with known designs, which will lead to the complete elimination of the possibility of major accidents in the shop due to the destruction of the outer copper weld seam of the lance tip and the cost of huge funds for its elimination, as well as to obtaining a tangible economic effect due to the high degree of efficiency of solving the above problems, which are always present in operating converter shops.

Keywords: melt blowing · durability · emergency situation · converter shop · reinforcing pin · weld seam · blowing device · cooling water · economic effect

1 Introduction

A long service life of the top-blown oxygen lance contributes to the regular and cost-effective operation of the basic oxygen furnace. To maintain the long service life of the top lance, its cooling water flow rate is critically important, and it should not be

H. Altenbach et al. (Eds.): CAMPE 2025, LNME, pp. 283–292, 2026.
https://doi.org/10.1007/978-3-032-16381-3_27

lower than the design level. The cooling water temperature at the lance outlet must not exceed 60–65 °C. The quality of the coolant is also an important parameter. If the water is contaminated with oxides or dirt, deposits usually form on the inner surfaces of the tubes and the lance tip. This fact harms heat transfer and reduces the service life of the top lance, which varies depending on the operating conditions in each specific converter shop and ranges from 50 to 1000 melts, and sometimes more.

The most vulnerable part of the top lance is the so-called lance tip, which is exposed to extremely high temperatures during operation, exceeding 2000 °C. At the same time, the height of the lance tip above the liquid bath is crucial to ensure the deep penetration of the oxygen jet into the iron-carbon melt. However, if the lance height is too small, there is a high probability of melting of certain areas of the lance tip surface experiencing severe overheating. Therefore, the outer end surface (lower bowl) of the top lance tip should be made of copper, which has a high degree of thermal conductivity, due to which the heat from the heated lance tip is quickly transferred to the lance water cooling. This fact can only be ensured by forged and chemically pure copper.

In this case, a lance tip of any design (welded, solid-turned, cast, forged and stamped) necessarily has an external copper weld, which connects the copper part of the tip (usually the lower bowl) with a steel external connecting ring, which is necessary for the rapid replacement of the tip on the top lance by attaching the ring to the barrel (outer pipe) of the top lance using a steel weld. However, during the operation of the top lance, this copper weld is subjected to cracking and, in many cases, breaks, which leads to the separation of the connecting steel ring from the copper part of the lance tip.

Cracking and subsequent rupture of the outer welded joint of the steel ring with the copper part of the tip on the top converter lances is a serious problem that can lead to serious emergencies in the converter shop – the top lance, like a rocket, flies out of the converter, tearing off the metal hoses supplying oxygen and coolant to it, which can lead to an explosion of the converter as a result of a significant amount of water entering the high-temperature working cavity of the unit.

The causes of cracking in the specified external copper weld may be different, including metal defects, technological violations, incorrect welding modes, shrinkage stresses during seam cooling, and corrosion.

There are four types of cracks: hot, cold, hydrogen, and stress cracks. Hot cracks usually occur before the weld is complete and are longitudinal. Cold cracks form after the welding process is complete, during cooling below the temperature range of 100–150 °C, or the subsequent period; they are among the most dangerous defects and are unacceptable according to all current regulatory and technological documents. Hydrogen cracks are related to the presence of hydrogen in the weld metal, which contributes to the embrittlement of the metal. Stress cracks occur due to mechanical (thermomechanical, temperature) effects on the weld material during the operation of the blowing device.

To prevent the formation of the first three types of cracks, it is necessary to strictly comply with the technology and welding modes, as well as to maintain quality control of the metal and welds. Additionally, the use of welding materials with low hydrogen content, heat treatment of welds, and the application of anti-corrosion protective coatings to welds are crucial.

The use of all the above measures should almost eliminate the risk of cracking of welds on the top oxygen lances and ensure reliable and safe operation of the equipment.

However, even if all the above requirements are met (which is almost impossible in production conditions), the risk of cracks in welds is very high because the top lances are subjected to significant thermal loads and vibrations during their operation, working in an aggressive high-temperature environment (and this applies to both top-blown lances and slag-splashing lances of oxygen converters). These reasons contribute to the inevitable occurrence (accumulation) of stresses in the structure of the top lances during its heating as a result of temperature elongation of the outer pipe (barrel) of the top lances and the imperfection of its compensation devices, which leads to the appearance of stress cracks in the welds due to their smaller thickness and lower strength in comparison with other areas of the welded parts of the top lances.

This study aims to develop a new and safe lance tip design in order to eliminate potential accident risks and increase the durability of top blowing devices in operating converter shops.

2 Literature Review

Enhancing the technical and economic efficiency of converter shops, as well as the operational characteristics of their process equipment (including top oxygen lances), necessitates the design and use of multi-nozzle top-blowing devices.

High temperature of the liquid bath, formation of flame torches due to oxidation of carbon during blowing of the melt with technical oxygen, splashing of molten slag and metal, as well as the presence of torches of afterburning of CO of the exhaust gas to CO_2 create an atmosphere with high temperatures in the working space of the converter [1]. The top lance is subjected to intense thermal and oxidative stresses that significantly affect the integrity of its materials and components, particularly its tip [2]. Operation of the top blow-out device under the described unfavorable conditions typically leads to changes in the microstructure of the original materials (copper, steel), from which the components of the lance (nozzle, bowl, pipe) are made, which over time causes metal fatigue. All this also leads to softening of the welds (both copper and steel), which in turn leads to destruction, usually of the external welds and sometimes of the internal welds, especially in copper [1].

To prevent these phenomena, lance tip designs were developed to maintain a sufficient coolant flow rate within the cooling channels, thereby ensuring effective cooling across the entire top-blowing device [3]. This became possible due to the use of information-modeling systems for forecasting the thermal regime of top lances during their design and development (both oxygen [3] and slag-splashing [4] lances), as well as methods for calculating heat transfer during numerical modeling of the lances' thermal regime within these forecasting systems.

When developing top lance designs, the primary focus is currently on enhancing the resource-saving efficiency of the steelmaking process in converters by utilizing the internal reserves of the process. In this regard, various top lance tip designs are continuously being developed to support the afterburning of CO to CO_2, which improves the thermal balance of the melt, increases the degree of melt mixing, reduces the blow-down time, accelerates the dephosphorization process, and reduces the level of defects

[5]. It has been established that under conditions promoting CO afterburning, when $P_{CO_2}/P_{CO} = 1$, the temperature of the converter exhaust gases increases from 1800 to 2000 K [6].

A self-rotating lance, powered by a gas jet, was developed to enhance mass transfer between the liquid slag and the molten metal. This advancement led to an increase in the mass transfer rate of over 30% [7].

A study on how the blow hole's cross-sectional area and blast flow rate affect the characteristics of the jet penetrating the melt facilitated the design and optimization of the central nozzle of the top oxygen lance for delivering the $O_2 + CO_2$ gas mixture into the converter cavity [8]. Additionally, the effect of the flow rate of the 80% O_2 and 20% CO_2 gas mixture on the dispersion patterns of jets carrying powdered lime was also investigated [9].

For the design and development of the top lance nozzle profile, a study was conducted to assess the influence of outlet wear in the Laval nozzle on the characteristics of the resulting supersonic jet. Reference [10] demonstrated that increased wear of the blowing nozzles leads to a more rapid decline in gas jet velocity and an earlier convergence point. However, the causes of melting at the nozzle exit edges, as well as potential measures for its prevention, were not addressed.

To design and produce a top oxygen lance capable of achieving a high Mach number (oxygen pressure of 1.01 MPa and a nozzle exit Mach number of 2.15), the jet characteristics under varying oxygen supply pressures and their impact on the melting bath dynamics were thoroughly investigated and analyzed [11].

The parameters of blowing using a dynamic oxygen lance in the converter were also studied. The effect of lance design parameters, specifically the twist angle and rotation speed, on the efficiency of melt dephosphorization was determined [12].

As part of the design of top submersible lances, studies were conducted aimed at studying the dynamics of the following processes: gas injection into the melt [13]; the formation and ascent of bubbles in the metal bath [14], incorporating X-ray imaging techniques [15]; rotational dynamics of splash waves in the melt [16]. It was found that viscous and interphase forces substantially influence the hydrodynamic behavior of the bath [17].

Recently, in connection with the widespread use of technology that applies a protective skull to the refractory lining of converters, interest in studying the processes of blowing and foaming of the liquid final slag using a top (blowing or special skull) lance has increased significantly. In particular, in work [18], the influence of the impact action of the top lance blowing on the process of foaming of converter slag under conditions of combined (top and bottom) blowing was studied.

As can be seen from the literature review conducted on this issue, work on improving the designs of top converter lances from the perspective of increasing their safety has not been carried out, and the subject has yet to be documented in the literature. However, this remains one of the most critical challenges consistently encountered in converter shops. Thus, the relevance of work in this area is beyond doubt, requiring the fastest and most effective solution to this issue.

3 Research Methodology

The effect of modifying the lance tip design by strengthening the outer copper weld seam, which connects the copper lower bowl to the steel outer transition ring, on the operational safety of lance tip and their durability was studied. The subject of this study is the improved design of the tip for top blowdown lances, protected by Patent UA 78112. The experiments were conducted on 250-ton converters using structured observation; lance tip failures were documented photographically. MS Excel 2015 was used to graphically present the results.

4 Results and Discussion

It is known that during operation of top converter lances, significant stresses arise in their structures (usually caused by repeated thermal expansion and subsequent cooling of the outer pipe in top-blowing devices), which are attempted to be reduced by various designs of compensation devices (packing, plate, metal hose, telescopic, including rubber rings, etc.) installed on the pipes of the top lances.

However, despite this, all top lances are characterized by a low strength of the outer copper weld at the tip, which connects the copper tip to the steel outer transition ring. As a result of the impact of significant force loads on the lance from the supplied oxygen and cooling water, especially at the moments of their supply, thermal elongation and return to the original position of the outer lance pipe, its deformation and the effect of torque and bending moments on the pipe, the outer pipe will break in a weaker place, i.e. along the outer copper weld seam on the lance tip, which connects two dissimilar materials (copper and steel) and, in addition, has low strength and is not additionally reinforced.

Poor fusion of dissimilar materials – a copper bowl and a steel ring with a copper weld, low quality of its execution (low density and high porosity of copper) and a smaller thickness of the weld compared to the thickness of the joint of the lower bowl (tip) with the ring itself fully explain the low strength of the said external copper weld. Additionally, the external copper weld softens due to exposure to a high-temperature environment. A high-temperature aggressive gas-slag-metal environment can partially wash it out. The destruction of this external weld can lead to the lower bowl tearing off or the entire lance tip separating from the outer pipe of the top oxygen lance, resulting in a significant accident in the shop, which has repeatedly occurred in the practice of operating converter shops.

The elongation of the outer tube of the top lance when it is heated during blowing in the converter can be calculated using the formula for linear thermal expansion taken from classical literary sources on the resistance of materials:

$$\Delta L = \alpha \cdot L_0 \cdot \Delta T,$$

where α – the coefficient of linear thermal expansion of the tube material (steel), $^{\circ}C^{-1}$; L_0 – the length of the outer tube of the lance that is subject to heating, m; ΔT – the temperature gradient, $^{\circ}C$.

Figure 1 shows the dependence of the elongation value of the outer pipe of the top lance (in mm) on the length (in m) of the section of the top-blown lance barrel (outer pipe), which is heated during the blowdown of the iron-carbon melt in the converter, and on the average temperature of this heating (in ºC), studied by the authors.

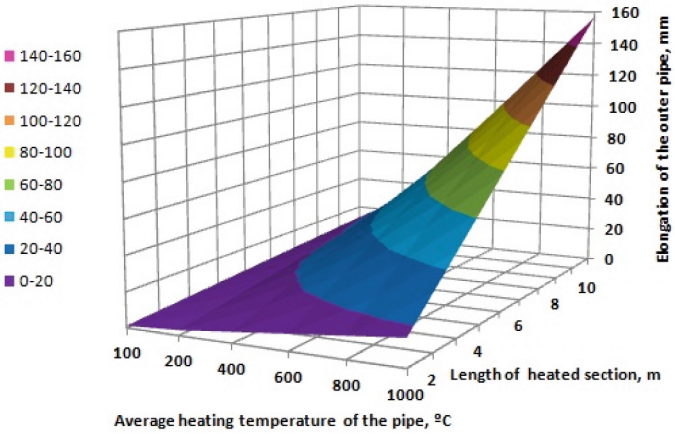

Fig. 1. Elongation (ΔL) of the outer pipe of the top lance (outer diameter 426 mm, 250-ton converter) depending on the length of the section of the lance barrel that is subject to heating, and on the average temperature of this heating.

In order to improve the safety of operation of top oxygen lances and increase their durability, the Department of Ferrous Metallurgy of the Dniprodzerzhynsk State Technical University (now the Department of Metallurgy of the Dniprovsky State Technical University, Kamianske, Ukraine) together with the workers of the converter shop of OJSC "Dniprovsky Metallurgical Combine" (now PrJSC "KAMET–STAL'", Kamianske, Ukraine) for 250-ton converters have developed new safe designs (Patent UA 78112) of the lance tip, in which the reinforcement of the outer copper weld is carried out through the use of special reinforcing pins.

Figure 2 shows the developed versions of tips with different versions (I–IV) of reinforcing pin designs (see Fig. 3) for lances with central oxygen supply (Fig. 2, a) and with central water supply (Fig. 2, b), respectively. Lance tips (Fig. 2, a – with five nozzles and pin designs I, II; Fig. 2, b – with six nozzles and pin designs III, IV) consist of a tip (copper bowl) 1, central 2, intermediate 3 and outer 4 transition rings, nozzles 5, collector 6, pins 7 (for connecting tip 1 and outer transition ring 4), inserted into through holes made in the mating parts and held from falling out via a weld 8 (Fig. 3, I). Additionally, the copper tip 1 and the steel outer ring 4 are connected via a copper weld 9. The pins 7 can be made elongated and with their inner ends inserted into a through (Fig. 3, II) or blind (Fig. 3, III) hole made in the intermediate transition ring 3 or in special overlay parts 10 (Fig. 3, IV) attached by means of a weld 11 to the outer surface of the intermediate transition ring 3. To achieve maximum efficiency of the proposed designs, the number of pins 7 in each tip should be at least three.

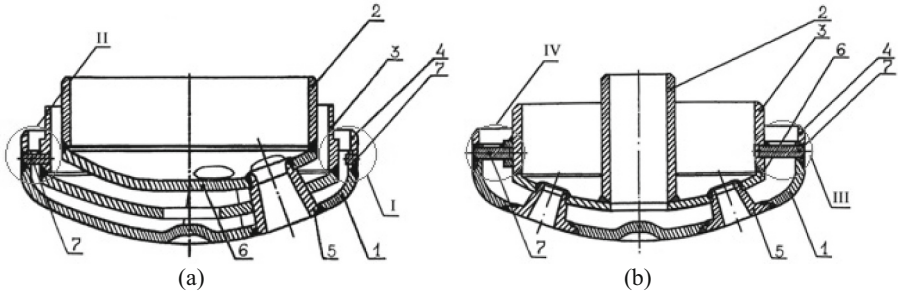

Fig. 2. Designs of tips for top oxygen lances with central oxygen supply (a) and with central water supply (b) with pin reinforcement of the outer copper weld seam (here and in Fig. 3 see text of the article for designations).

When the lance tip is in operation, the blowing and coolant pressure is exerted on the inner surface of the tip 1, as well as the outer lance tube as a result of its thermal elongation on the outer copper weld 9, connecting the outer transition ring 4 with the tip 1, which leads to deformation, cracking and destruction of the outer copper weld 9. The presence of pins 7 in the telescopic connection of the tip 1 with the outer transition ring 4 (Fig. 3, I) enables the outer weld 9 to be unloaded, as the main load is taken by pins 7 in this case. Weld 9 will only seal the gap between the mating parts to prevent water from entering the converter cavity through the lance.

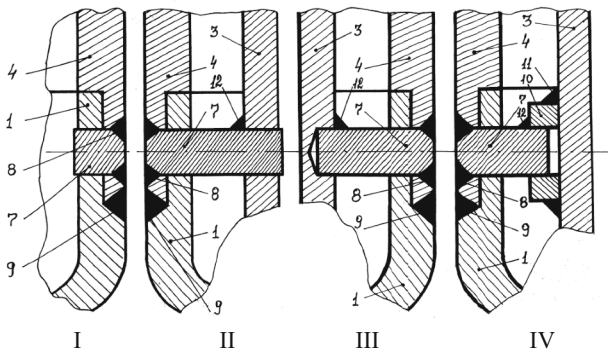

Fig. 3. Variants for installing reinforcing pins in lance tips.

A more preferable design variant is shown in Fig. 3, II, in which pin 7 is made elongated and inserted with its inner end into a through hole made in the intermediate transition ring 3. However, this variant is acceptable only for designs of tips with a central oxygen supply (Fig. 2, a), since in tips with a central water supply (Fig. 2, b) there will be a possibility of water getting into the oxygen tract as a result of its leakage from the through hole, which is in no way acceptable, since it will lead to an accident due to water getting into the lance nozzles. For tips with a central water supply (Fig. 2, b), it is advisable to use variants with elongated pins 7 (see Fig. 3, III, IV).

Figure 3, III shows a variant where pin 7 is inserted with its inner end into a blind hole made on the outer surface of intermediate transition ring 3. This variant allows for the use of thick-walled intermediate transition rings 3, as the strength of intermediate transition ring 3 decreases at the locations where pins 7 are inserted due to the decrease in wall thickness of intermediate transition ring 4 when creating the hole. This fact can lead to a violation of the integrity of intermediate transition ring 3 at the locations of the holes. The use of thin-walled intermediate transition rings 3 is unacceptable with this design variant.

A safer variant, which allows the use of the intermediate transition ring 3 with any wall thickness and avoids its damage, is shown in Fig. 3, IV. It proposes using special overlay parts 10 with a hole (through or blind), into which the pin 7 is inserted with its inner end. The overlay parts, in turn, are fixed to the outer surface of the intermediate transition ring 3 by means of a weld 11. In this case, in order to increase the rigidity of the lance tip structure, pin 7 can be additionally attached by means of a weld 12 to the outer surface (see Fig. 3, II, III) of the intermediate transition ring 3 or to the body of the special overlay parts 10 (Fig. 3, IV).

Thus, a sufficiently complete unloading of the external copper weld 9 from thermomechanical loads in the lance tip design is achieved, which ultimately increases its safety and durability. In this case, the last three variants with extended pins 7, in addition, increase the rigidity of the entire tip design due to the fastening of the tip components to each other, thereby unloading and protecting the welds around the nozzles 5 from destruction (both external, connecting the nozzles 5 with the tip 1, and internal, fixing the nozzles 5 in the collector 6), which will increase the durability of the lance tips to an even greater extent.

Figure 4 shows cases of cracking after a certain number of converter melts (indicated below) of the external copper weld, resulting in the failure of the top blowdown lances, which were subsequently removed for repair. Calculations have shown that the tensile strength of this weld is 40–100 MPa (with the strength of pure copper being 210–250 MPa). Such a weld is practically unreliable for critical mechanical structures, which include the top oxygen lance.

(a) (b) (c)

Fig. 4. Cracking of the outer copper weld (top lance durability: (a) – 45; (b) – 62; (c) – 8 melts).

The use of variant I (see Fig. 3, I) for installing reinforcing pins in the lance tips made it possible to strengthen the external copper weld (the calculated tensile strength of this welded joint was 400 MPa) and eliminate its cracking significantly. In contrast, the top lances failed exclusively for other reasons, namely: cracking of the external welds around the nozzle inserts, the melting of the outlet edges of the Laval blowing nozzles, damage to the tip as a result of the top lance fit on scrap metal, cracking of the internal

welds around the nozzle inserts, the need to replace metal hose compensators due to their damage.

Work continues on further optimizing the safe designs of lance tips to increase their operational safety and durability, including the provision of their manufacture through injection molding [19] with proper quality control of castings [20].

5 Conclusions

In this paper, based on the analysis of literary sources, patent search and industrial testing results of various (both standard and previously developed) designs of tips for top oxygen lances on 250-ton converters of OJSC "Dniprovsky Metallurgical Combine" (now PrJSC "KAMET–STAL'", Kamianske, Ukraine), a new safe design of a lance tip was developed and proposed, protected by Patent UA 78112.

For the first time, high unloading efficiency of the outer copper weld seam in the lance tip has been proven by installing reinforcing pins in its design, which is the only practical and extremely necessary measure for effectively solving the problems of operating safety of top converter lances, as well as the low durability of their tips, which are always present in operating converter shops.

The use of these designs eliminates the likelihood of major accidents in the shop, allowing for secure production, avoiding personnel injuries and huge costs of eliminating the consequences of an accident, and obtaining an economic effect.

References

1. Wang, J., Cao, Z., Liu, J., et al.: Structure design and optimization of a 150t converter oxygen lance under high oxygen supply intensity. JOM **77**, 5882–5891 (2025). https://doi.org/10.1007/s11837-025-07469-x
2. Lim, S.M., Park, S.S., Yi, K.W.: Extension of lance life by change of height of lances in the smelting furnace of Mitsubishi process. Met. Mater. Int. **27**, 3721–3729 (2021). https://doi.org/10.1007/s12540-020-00712-x
3. Panteikov, S.P.: Stages of improvement for welded structures with five-nozzle lance heads in the converter shop of public joint stock company "Dneprovsky Metallurgical Combine. Steel Transl. **50**, 756–761 (2020). https://doi.org/10.3103/S0967091220110108
4. Panteikova, E., Panteikov, S., Zhulkovskyi, O., Zhulkovska, I., Pieieva, I.: Development of the slag-splashing lance for slag skull coating the converter lining. In: Altenbach, H., Gao, X.W., Syngellakis, S., Cheng, A.H.D., Lampart, P., Tkachuk, A. (eds.) Advances in Mechanical and Power Engineering II. CAMPE 2023. Lecture Notes in Mechanical Engineering. Springer, Cham (2025). https://doi.org/10.1007/978-3-031-82979-6_15
5. Dong, P., Zheng, S., Zhu, M.: Numerical study on gas-metal-slag interaction with single-flow postcombustion oxygen lance in the steelmaking process of a top-blown converter. JOM **74**, 1509–1520 (2022). https://doi.org/10.1007/s11837-021-05147-2
6. Protopopov, E.V., Temlyantsev, M.V., Yakushevich, N.F., et al.: Peculiarities of exhaust gases afterburning in converter with application of two-tier oxygen lance blowing. Steel Transl. **51**, 872–878 (2021). https://doi.org/10.3103/S0967091221120093
7. Gao, Q., Wu, W., Zhi, Jg., et al.: Effect of a self-rotating oxygen lance system on mass transfer between slag and molten steel. J. Iron Steel Res. Int. **28**, 152–159 (2021). https://doi.org/10.1007/s42243-020-00515-9

8. Feng, C., Zhu, R., Dong, K., et al.: Effects of nozzle layout and parameters on the jet characteristics of a $CO_2 + O_2$ mixed oxygen lance. Metall. Mater. Trans. B **52**, 425–439 (2021). https://doi.org/10.1007/s11663-020-02048-8
9. Li, W., Zhu, R., Feng, C., et al.: Influence of carrier gas of converter oxygen lance on smooth distribution of O_2-CO_2-CaO mixed jet. Trans. Indian Inst. Met. **73**, 3027–3035 (2020). https://doi.org/10.1007/s12666-020-02105-5
10. Feng, C., Zhu, R., Han, B., et al.: Effect of nozzle exit wear on the fluid flow characteristics of supersonic oxygen lance. Metall. Mater. Trans. B **51**, 187–199 (2020). https://doi.org/10.1007/s11663-019-01722-w
11. Zhang, Y., Zhang, C., Han, Y., et al.: Jet characteristics of a high-mach-number oxygen-lance nozzle under high oxygen pressure. Metall. Mater. Trans. B **52**, 4070–4081 (2021). https://doi.org/10.1007/s11663-021-02325-0
12. Li, M., Shao, L., Li, Q., et al.: A numerical study on blowing characteristics of a dynamic free oxygen lance converter for hot metal dephosphorization technology using a coupled VOF-SMM method. Metall. Mater. Trans. B **52**, 2026–2037 (2021). https://doi.org/10.1007/s11663-021-02155-0
13. Obiso, D., Reuter, M., Richter, A.: CFD investigations of bath dynamics in a pilot-scale TSL furnace. Metall. Mater. Trans. B **52**, 3064–3077 (2021). https://doi.org/10.1007/s11663-021-02233-3
14. Kandalam, A., Stelter, M., Reinmöller, M., Reuter, M.A., Charitos, A.: Determining the bubble dynamics of a top submerged lance smelter. In: Lazou, A., Daehn, K., Fleuriault, C., Gökelma, M., Olivetti, E., Meskers, C. (eds.) REWAS 2022: Developing Tomorrow's Technical Cycles (Volume I). The Minerals, Metals & Materials Series. Springer, Cham (2022). https://doi.org/10.1007/978-3-030-92563-5_57
15. Akashi, M., Keplinger, O., Shevchenko, N., et al.: X-ray radioscopic visualization of bubbly flows injected through a top submerged lance into a liquid metal. Metall. Mater. Trans. B **51**, 124–139 (2020). https://doi.org/10.1007/s11663-019-01720-y
16. Obiso, D., Reuter, M., Richter, A.: CFD investigation of rotational sloshing waves in a top-submerged-lance metal bath. Metall. Mater. Trans. B **52**, 2386–2394 (2021). https://doi.org/10.1007/s11663-021-02182-x
17. Cao, L., Wang, Y., Cheng, Z., et al.: Bubble formation and surface sloshing in the TSL flow with a viscous liquid. JOM **74**, 4920–4929 (2022). https://doi.org/10.1007/s11837-022-05539-y
18. Wang, R., Zhang, B., Hu, C., et al.: Physical modeling of slag foaming in combined top and bottom blowing converter. JOM **74**, 151–158 (2022). https://doi.org/10.1007/s11837-021-04984-5
19. Stalnichenko, O., Lysenko, T., Ponomarenko, O., Kreitser, K., Kozishkurt, E.: Vacuum technology for magnesium alloys during die casting of radiators. In: Tonkonogyi, V., Ivanov, V., Trojanowska, J., Oborskyi, G. (eds.) Advanced Manufacturing Processes VI. Interpartner 2024. Lecture Notes in Mechanical Engineering. Springer, Cham (2025). https://doi.org/10.1007/978-3-031-82746-4_20
20. Ponomarenko, O., Yevtushenko, N., Akimov, O., Vasilets, V., Lopes, H.: Study of the laws of random fluctuations in the parameters of foundry processes and the quality of castings. In: Machado, J., Trojanowska, J., Ottaviano, E., Xavior, M.A., Valášek, P., Basova, Y. (eds.) Innovations in Mechanical Engineering IV. ICIENG 2025. Lecture Notes in Mechanical Engineering. Springer, Cham (2025). https://doi.org/10.1007/978-3-031-93554-1_36

Modified Kalker Principle for Contact Analysis Between Complex-Profile Bodies with Non-linear Surface Layers

Mykola M. Tkachuk[1,2(✉)], Andriy Grabovskiy[1], Oleh Loznyi[1], and Mykola A. Tkachuk[1,2]

[1] National Technical University "Kharkiv Polytechnic Institute", Kyrpychova St., 2, Kharkiv 61002, Ukraine
m.tkachuk@tmm-sapr.org
[2] Örebro University, Fakultetsgatan 1, 701 82 Örebro, Sweden

Abstract. The aim of this study is to develop a new approach for analyzing the influence of various factors on the distribution of contact pressure and the shape of the contact area between complex-profile bodies. This need arises from the increasing use of components with intricate geometries in modern mechanical systems. These complex-profile bodies facilitate the transfer of motion trajectories and dynamic forces or momentum. Both are determined by the initial gap between the bodies that cannot generally be described accurately using a quadratic form of the coordinates of the tangent plane. Additionally, the surfaces of the contacting bodies may include material layers that are not adequately represented by traditional Winkler-type models. The proposed approach is based on a modification of the Kalker's variational principle. The formulation can include arbitrary geometry of the contact surfaces and incorporate various types of mechanical behavior of the intermediate surface layers. Both factors affect the distribution of the contact pressure and the shape of the contact area, which is illustrated by several representative examples. Various nontrivial shapes of the contact area other than elliptic are retrieved, including dumbbell-shaped and multiply connected domains with various localizations of maximum contact pressure. These findings are crucial for the rational design of new mechanisms and machines that involve contact between complex-profile components.

Keywords: First Keyword · Second Keyword · Third Keyword

1 Introduction

A common trend in modern mechanical engineering is the pursuit of implementing complex relative motions between individual contacting components. These include gears, cams, elements of hydraulic volumetric transmissions, and others. As a result, two key criteria emerge in the justification of technical solutions.

On the one hand, a kinematic criterion arises, necessitating the formation of bodies with complex geometries to satisfy specific motion requirements. Typically, the initial

H. Altenbach et al. (Eds.): CAMPE 2025, LNME, pp. 293–302, 2026.
https://doi.org/10.1007/978-3-032-16381-3_28

contact between such bodies occurs at a single point. On the other hand, a strength criterion must be considered. This criterion aims to maximize the contact area in the actual (deformed) state while minimizing the peak contact pressure. Thus, a dual-criterion scenario emerges, involving both kinematic and strength considerations. In such cases, the initial gap between contacting bodies may not be analytically defined but instead represented as two envelopes of paired conjugate points.

However, this is not the only challenge in analyzing the contact interaction of such complex-profiled bodies (CPBs). Due to the proximity of the contacting surfaces, displacements caused by the compression of surface layers such as roughness, coatings, and films begin to play an increasingly significant role. Moreover, the elastic properties of these surface layers may exhibit nonlinear behavior.

Consequently, existing analytical and numerical methods for contact analysis are not directly applicable to such bodies. A new approach is required – one that accounts for both the geometry of CPB surfaces and the properties of their surface layers. To address this, variational formulations are employed. Based on this framework, it becomes possible to investigate the contact interactions of elements in both existing and proposed designs.

2 Literature Review

Numerous publications have been dedicated to the study of contact interactions between elastic bodies. For instance, in [1], the authors examine a unilateral contact problem involving a nonlinear Winkler-type surface layer between a massive elastic body and a composite structure. The latter consists of a thin coating modeled as a Timoshenko-type shell and a massive elastic substrate, which is connected to the coating via another nonlinear Winkler layer. A parallel Robin-type domain decomposition method is applied to reduce the original contact problem to the iterative solution of independent linear variational equations. The analysis explores the dependence of contact pressure and stresses on the coating thickness and the parameters of the layer.

A similar methodology is employed in [2] for the contact problem between two elastic bodies, one of which features a discontinuous thin elastic coating modeled as a Timoshenko-type shell. The study analyzes the dependence of surface and equivalent stresses on both the thickness and stiffness of the coating.

The conditions of weak convergence of the methods used in [1, 2] are established in an earlier work [3]. As it was discovered, the speed of numerical converge can differ significantly depending on the height and Young's modulus of the thin intermediate body. This can somehow limit the numerical feasibility of the method despite the benefits of the domain decomposition approach.

In [4], the contact interaction problem involving multiple elastic bodies with nonlinear Winkler-type surface layers is investigated. To solve the associated nonlinear variational equation, which includes a non-differentiable operator characteristic of this contact problem, the authors propose the use of implicit two-point combined differential-difference parallel iterative domain decomposition algorithms of the Robin type. The two-point scheme offers broader admissible ranges for the iterative parameter and, beyond a certain threshold of this parameter, ensures the desired accuracy with fewer iterations.

Thermal effects play a significant role in contact interactions. In [5], the thermomechanical behavior of a heterogeneous bimaterial with an interfacial crack is investigated. The crack faces are in contact at their tips under compressive forces and a uniform thermal flux.

The expansion of the modeling scope from normal contact towards tangential interaction and deformations increases dramatically the complexity of the problem. The paper [6] introduces a Fast Fourier Transform (FFT)-based Boundary Element Method (BEM) for tangential contact between a rigid body and an elastic half-space coated with a layer of different elastic properties. The tangential stress applied at the surface is modeled as a plane wave. The coating alters the surface displacement response to tangential loads, depending on its thickness and material properties. The effect is more pronounced for thicker coating.

General variational inequalities (GVI) [7] have application potential for nonconvex contact problems. GVIs provide a framework to model these using generalized convexity (like log-convex or kg-convex functions). This enables the use of well-developed projection methods, penalty techniques, and auxiliary principle approaches for solving such problems.

A numerical algorithm for solving a frictional contact problem involving the interaction between a deformable layer and dies of complex geometry is presented in [8]. The contact problem, characterized by an unknown interaction domain, is expressed through Signorini-type integral inequality equations. It is subsequently reduced to a quadratic programming problem by applying cubature formulas.

Contact interaction plays important role in the dynamics of various systems. This aspect is addressed in [9] for railway vehicle dynamics simulations. The wheel–rail contact is modeled using Kalker's variational principle. The solutions for contact area and contact pressure are used as input for real-time and large-scale simulations.

Creep understood as undesired micro-slip between two surfaces in contact is another phenomenon related to the wheel and rail interaction. A review in [10] covers recent advances in modeling wheel–rail creep forces, with a focus on tribological effects such as surface roughness, lubrication layers, and plastic deformation.

Thus, the works [1–10] primarily address contact interaction at the macroscopic scale. One of the principal approaches used in analyzing contact phenomena is the variational method. However, these and other works do not offer a comprehensive solution to the contact interaction problem for CPBs. Modeling the highly nonlinear response in normal and tangent direction, anisotropy and adhesive properties of various coatings and surface roughness remains a critical issue.

The paper [11] investigates how surface anisotropy and non-Gaussian height distributions affect elastic contact mechanics, using numerical simulations based on the Boundary Element Method. It demonstrates that both anisotropic and non-Gaussian surfaces influence the real contact area and load-separation behavior in similar ways. A key contribution is the identification of a single scaling parameter, derived from Persson's theory, that captures these effects across different surface types. Previously the same authors investigated in [12] how surface anisotropy and fractal roughness dimensionality (1D vs 2D) affect adhesion in elastic contacts. It shows that adhesion is strongly reduced in 2D fractal surfaces compared to 1D, contradicting predictions from the Persson–Tosatti

criterion. An extended version of the Bearing Area Model (BAM) is proposed to better capture these anisotropic effects.

Adhesive properties of two types of surface structures are examined in [13] and [14]. In [13], a soft elastic layer is shown to enhance contact between rough surfaces but may reduce overall adhesion depending on its thickness and stiffness. Numerical simulations using a boundary element method reveal how variations in modulus and thickness affect contact area and pull-off force. In [14], fibrillar adhesive structures are studied, showing that softer fibrils improve surface conformity and adhesion, while stiffer ones enhance load distribution.

The influence of electrolysis parameters on microarc oxidation coatings for magnesium alloys is investigated in [15]. Coating composition varies with electrolyte, typically including MgO, Mg_2SiO_4, $MgAl_2O_4$, and amorphous silicates. In [16], ceramic coatings on aluminum alloys are formed using alkaline-silicate electrolytes; adding $Na_6P_6O_{18}$ significantly increases thickness without changing phase composition, while $NaAlO_2$ alters phase structure but has minimal effect on thickness. Study [17] develops epoxy-silicone rubber composites with boron particles, forming ablation-resistant coatings containing B_4C, borosiloxane, SiO_2, and SiC. Adding 2.5 wt% boron raises decomposition temperature by over 12% and reduces ablation rates by 30%.

Thus, the initial data required for further investigation of CPBs with coatings is now available. The next challenge lies in identifying suitable methods for solving such contact interaction problems. For instance, work [18] presents several exact solutions to contact problems; however, a comprehensive solution for the contact interaction of complex 3D profiles – especially with consideration of surface layer properties – remains unavailable. This highlights the need to develop a new approach for solving problems of this type. Such research is particularly relevant for analyzing the interaction of spherical pistons in radial hydrostatic transmissions [19, 20].

3 Goal

The objective of this study is to develop a novel approach for analyzing the influence of various factors on the distribution of contact pressure and the geometry of the contact area between complex-shaped bodies. This research builds upon the foundational work presented in [21–23]. While previous studies have provided exact solutions for certain contact problems, a comprehensive solution for the interaction of complex 3D bodies – particularly those with surface layers – remains unavailable in the general case. Consequently, there is a need to establish a new methodological framework for addressing such problems. This line of inquiry is especially relevant for understanding the contact behavior of spherical pistons in radial hydrostatic transmissions [19, 20].

4 Research Methodology

The contact of two bodies Ω_1 та Ω_2 with surfaces S_1 and S_2 is considered in presence of exterior thin layers Ω'_1 and Ω'_2 with interface surfaces S'_1 end S'_2 (Fig. 1).

Contact loads are transmitted over the interface surfaces S'_1 та S'_2. Due to the small thickness of the exterior layers Ω'_1 and Ω'_2 we can disregard their load distributing

capacity. Hence, we do not distinguish any further the surfaces S'_1 and S'_2 from S_1 and S_2. The identical normal traction is transmitted through the mutually correspondent points from the two opposite sides of the exterior layers.

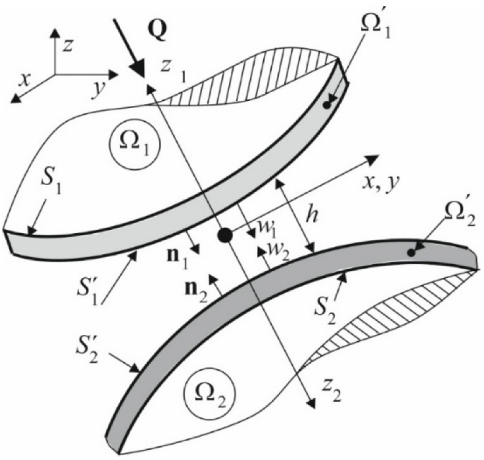

Fig. 1. Normal contact of two bodies with exterior intermediate layers.

The normal displacements $w_{1,2}$ at the contact surfaces $S_{1,2}$ are superposition of w_i^G – "global" displacements due to elastic deformations of the entire bodies Ω_i, w_i^L – "local" displacements caused by normal compression of the layers Ω_i.

$$w_i = w_i^G + w_i^L; i = 1, 2. \tag{1}$$

Given the large size of the bodies Ω_i compared to the size of the contact areas, the "global" displacements w_i^G can be determined as the depression of the half-space due to the distributed normal load (Fig. 2):

$$w_i^G(x, y) = \frac{1 - \nu_i^2}{\pi E_i} \iint\limits_{(S)} \frac{q(\xi, \eta)}{\rho} d\xi d\eta, \ \rho = \sqrt{(x - \xi)^2 + (y - \eta)^2}, \tag{2}$$

where E_i – modulus of elasticity of material for Ω_i, ν_i – Poisson's ratio,q – contact pressure, x, y, ξ, η – point coordinates in the tangent plane S that is shared between the two contact surfaces S_1 та S_2.

As for w_i^L, the general relations that holds for them can be given in the form

$$w_i^L = f_i(q); i = 1, 2, \tag{3}$$

where f_i – some functions of the contact pressure q with parameters specific to the contact layer. These functions capture the elastic or quasi-elastic response of the material and/or the layer structure to the compression. These relations can either be derived from a physically motivated model or be of a generic nature as an approximation fit. For example, it can be a power function.

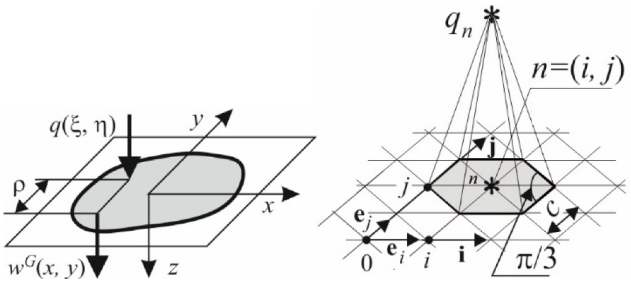

Fig. 2. Normal displacement of a half-space due to the contact pressure (left) and its approximation by pyramidal basis functions on a regular triangular mesh (right).

By modifying Kalker's variational principle, the contact interaction problem can be reformulated as a minimization problem for a functional

$$\left.\begin{array}{c} \Pi(q) = \Pi^G(q) + \Pi^L(q); \quad \Pi^G = \Pi_1^G + \Pi_2^G; \quad \Pi^L = \Pi_1^L + \Pi_2^L \\ \Pi(q) \to min; \quad q \geq 0 \end{array}\right\}, \tag{4}$$

where G^L – complementary energy components corresponding to the "global" (2) and "local" (3) response of the elastic bodies and the exterior layers:

$$\left.\begin{array}{l} {}^G_i = \frac{1}{2}\iint\limits_{(S)} q w_i^G dS + \iint\limits_{(S)} q(h-\delta)dS; \quad i = 1,\ 2; \\ {}^L_i = \iint\limits_{(S)} \left[\int\limits_0^q w_i^L(q)dq\right] dS; \quad i = 1,\ 2. \end{array}\right\} \tag{5}$$

Taking into account dependencies (2), (3), we come to the problem of finding the minimum of convex functional $\Pi(q)$ on a convex set of constraints in the form of the non-negativity of the contact pressure q (x, y). Approximating the unknown contact pressure q with basis functions φ_n built on a regular triangular mesh (Fig. 2) the problem (4) can be reduced to a minimization problem for a function of several variables:

$$\Pi(q_n) \to min; q_n \geq 0, \tag{6}$$

where n – index set of nodes where the discrete values of the unknown non-negative contact pressure values q_n are defined.

Various methods can be employed to solve Eq. (6), including the method of auxiliary gaps [21–23]. This approach transforms the original problem into a sequence of quadratic minimization tasks. At each iteration, the nonlinear functional defined in Eq. (6) is approximated by a quadratic function, incorporating an adjusted distribution of fictitious gaps to refine the solution. Otherwise, in the case of linear relation (6) as is in the case of linear elastic Winkler foundation, the problem (6) is just a quadratic programming problem and can be solved as is just in one step.

If we turn to the factors that are introduced above for consideration, then:

1) the macrogeometric shape is given by the distribution of the initial gap between the bodies $h = h(x, y)$; this distribution is determined by the above-mentioned "kinematic" criterion, i.e. the conditions of mutual motion of the contacting bodies; this

distribution may be a variable factor for the design depending on the kinematic and strength requirements; since this distribution h is included in the functional (5), then, accordingly, a parametric dependence is realized $q = q(h)$;

2) microgeometric properties, which are regulated by dependencies (3), are also included in functionals (5); so, similarly, another parametric dependence is implemented $q = q(f_i)$.

By varying the geometry of the contacting surfaces and the material properties of the surface layers, one can systematically assess their influence on the size and shape of the contact area, as well as on the distribution and magnitude of contact pressure.

5 Research Results

As an illustration of the capacities of the developed approach, the analysis of the contact interaction of the ball piston of a hydraulic radial-volumetric transmission with the running track of its stator ring [19] (Fig. 3). Here the piston I is a ball with a radius R_p, running track II is a torus with a transverse profile Γ. The profile Γ is a combination of circular arcs with radius R_{sp}. The opening angle of the central arc is θ.

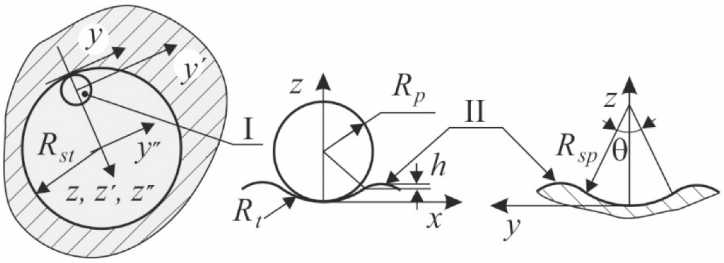

Fig. 3. Diagram of the interaction of ball pistons I with the running track II of the stator ring of hydraulic transmission.

For certainty, the radius of the treadmill of the stator ring $R_{st} = 0.128$ m; piston radius $R_p = 0.03175$ m; the transverse profile of the treadmill of the stator ring in the zy plane is formed by arcs of circles with radii R_{sp} with opening angle $\theta = \pi/12$. The identical moduli of elasticity $E = 2{\cdot}10^{11}$ Pa and Poisson's ratios $\nu = 0.3$ are taken for the steel piston and the stator ring. Contact force was fixed at the value $P_r = 120$ kN.

The following design parameter combinations for the contact geometry were studied: radius R_{sp}; $k = 1, 2, 3$; $R_{sp} = R_1 = 1.05{\cdot}R_p$; $R_{sp} = R_2 = 1.01{\cdot}R_p$; $R_{sp} = R_3 = 0.99{\cdot}R_p$.

These were paired with three different stiffness characteristics of the exterior layers shown in Fig. 4. The first one is just a linear response f_I with the given compliance. The other two functions f_I and f_{II} capture elastic-rigid response, when the layer has a constant compliance α up to a threshold pressure limits $p_{II} = 100$ MPa and $p_{III} = 1000$ MPa after which it loses compressibility and become rigid.

As shown in Fig. 5, the presence of a linearly elastic intermediate layer (Case I) between the contacting bodies results in a larger contact area compared to the elastically

rigid configurations (Cases II and III). Moreover, the stiffer the intermediate layer, the smaller the resulting contact area.

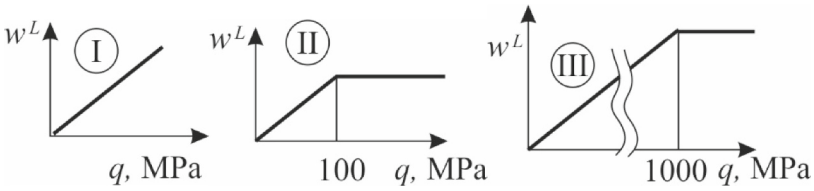

Fig. 4. The three types of surface layers response to compression.

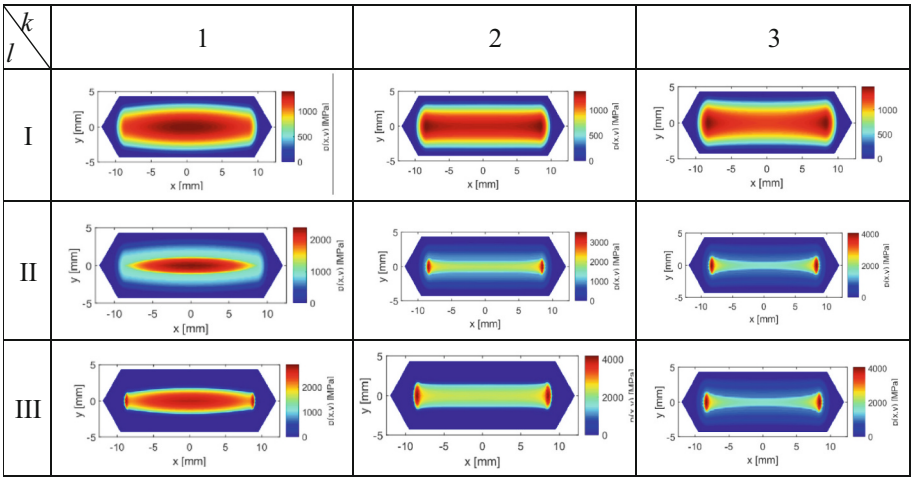

Fig. 5. Distributions of contact pressure (MPa) between the ball and the toroidal running track for geometry variants $k = 1, 2, 3$ and layer response types $l =$ I, II, III.

Additionally, the geometry of the contact area is significantly influenced by the radius of the central portion of the toroidal profile Γ. A smaller radius leads to more pronounced changes in the shape of the contact zone. For instance, in Case 1, the contact area resembles an oval or a curvilinear quadrilateral, whereas in Case 3, it takes on a dumbbell-like shape, which may become multiply connected under elevated loading conditions. Regarding contact pressure, there is a tendency for its reduction in regions where the arc radius of the toroidal profile exceeds the radius of the spherical counterpart by approximately 5%. Conversely, the stiffer the intermediate layer between the bodies, the higher the level of contact pressure observed.

6 Conclusions

The developed approach for analyzing the distribution of contact pressure and the geometry of the contact area between complex-shaped bodies is based on a modified variational formulation. This formulation overcomes many limitations inherent in traditional methods. Moreover, it incorporates the ability to vary both the geometry of the contacting bodies and the material properties of intermediate surface layers, enabling a more rigorous and flexible framework for contact interaction analysis.

Unlike conventional approaches, the proposed method is specifically adapted to describe contact between bodies with arbitrarily shaped surfaces, including those formed through kinematic constraints. This allows for the modeling of a broader range of realistic contact scenarios.

The established patterns of contact pressure distribution in the case of sphere–torus interaction indicate that when the difference in surface geometry is significant, the qualitative behavior of pressure distribution and contact area shape aligns with traditional models. However, as the surface geometries become more conforming, the observed patterns increasingly deviate from classical predictions. The developed approach can be applied to the study of contact interaction between complex-shaped bodies and to the justification of optimal engineering solutions in machine design.

References

1. Dyyak, I.I., Prokopyshyn, I.I., Prokopyshyn, I.A., Styahar, A.O.: Numerical analysis of contact between elastic bodies in the presence of thin coating and nonlinear winkler surface layers. In: Altenbach, H., Bogdanov, V., Grigorenko, A.Y., Kushnir, R.M., Nazarenko, V.M., Eremeyev, V.A. (eds.) Selected Problems of Solid Mechanics and Solving Methods. Advanced Structured Materials, vol. 204, pp. 123–140. Springer, Cham (2024)
2. Prokopyshyn, I.I., Styahar, A.O.: Numerical analysis of contact of the elastic bodies one of which has a discontinuous thin coating. Mater. Sci. **57**, 734–744 (2022)
3. Prokopyshyn, II, Styahar, AO: Investigation of contact between elastic bodies one of which has a thin coating connected with the body through a nonlinear winkler layer by the domain decomposition methods. J. Math. Sci. **258**, 477–506 (2021)
4. Prokopyshyn, II, Shakhno, S.M.: Differential-difference iterative domain decomposition methods for the problems of contact of elastic bodies with nonlinear winkler surface layers. J. Math. Sci. **261**, 41–58 (2022)
5. Serednytska, K.I., Martynyak, R.M.: Contact of the faces of an interface thermally insulated crack under thermomechanical loading. Mater. Sci. **57**, 173–179 (2021)
6. Burger, H., Forsbach, F., Popov, V.L.: Boundary element method for tangential contact of a coated elastic half-space. Machines **11**(7), 694 (2023)
7. Noor, M.A., Noor, K.I., Rassias, M.T.: General variational inequalities and optimization. In: Pardalos, P.M., Rassias, T.M. (eds.) Geometry and Non-Convex Optimization. Springer Optimization and Its Applications, vol. 223, pp. 301–320. Springer, Cham (2025)
8. Solyar, T.Ya., Solyar, O.I.: Axisymmetric contact problem for half-space with nonspecified areas of interaction. Mat. Met. Fiz. Mekh. Polya **65**(3–4), 178–187 (2022) (in Ukrainian). https://doi.org/10.15407/mmpmf2022.65.3-4.178-187; English translation: Solyar, T.Y., Soliar, O.I.: Axisymmetric Contact Problem for a Half Space with Nonspecified Zones of Interaction. J. Math. Sci. **287**(2), 321–333 (2025)

9. Yao, J., Ren, G.: Embedding Kalker's variational theory into railway vehicle system dynamics and its efficiency improvement. Veh. Syst. Dyn. **62**(4), 932–954 (2023)
10. Vollebregt, E., Six, K., Polach, O.: Challenges and progress in the understanding and modelling of the wheel-rail creep forces. Veh. Syst. Dyn. **59**(7), 1026–1068 (2021). https://doi.org/10.1080/00423114.2021.1912367
11. Pérez-Ràfols, F., Ciavarella, M.: Towards a universal scaling for the elastic contact between anisotropic and non-gaussian surfaces. Tribol. Lett. **73**, 62 (2025)
12. Ciavarella, M., Pérez-Ràfols, F.: Strongly different adhesion reduction for 1D or 2D random fractal roughness, and an extension of the BAM model to anisotropic surfaces. Tribol. Lett. **72**, 119 (2024)
13. Li, Q., Lyashenko, I.A., Pohrt, R., Popov, V.L.: Influence of a soft elastic layer on adhesion of rough surfaces. In: Borodich, F.M., Jin, X. (eds.) Contact Problems for Soft, Biological and Bioinspired Materials. Biologically-Inspired Systems, vol. 15, pp. 85–102. Springer, Cham (2022)
14. He, X., Li, Q., Popov, V.L.: Strength of adhesive contact between a rough fibrillar structure and an elastic body: influence of fibrillar stiffness. J. Adhes. **98**(12), 1820–1833 (2021)
15. Subbotina, V., Bilozerov, V., Subbotin, O., Kniaziev, S., Volkov, O., Lazorko, O.: New features of surface modification of magnesium alloys by microarc oxidation (MAO). Funct. Mater. **30**(4), 590–596 (2023)
16. Subbotina, V., Bilozerov, V., Subbotin, O., Barmin, O., Hryhorieva, S., Pysarska, N.: Investigation of the influence of electrolyte composition on the structure and properties of coatings obtained by microarc oxidation. Phys. Chem. Solid State **23**(2), 380–386 (2022)
17. Kniaziev, S., Kniazieva, H., Subbotina, V., Volkov, O., Riaboshtan, V.: Improving the technology of producing boron and siliconized layers and comparing their properties. Phys. Chem. Solid State **26**(2), 436–441 (2025)
18. Popov, V.L., Heß, M., Willert, E.: Handbook of Plane Contact Mechanics. Exact Solutions of Plane Contact Problems. Springer, Berlin, Heidelberg (2025)
19. Samorodov, V., Avrunin, G.: Solution of the problem of calculating the leakage working fluid in eccentric gap of the ball piston pair hydraulic fluid power machine. Bull. Natl. Tech. Univ. KhPI. Ser.: Hydraul. Mach. Hydraul. Units **1**, 81–87 (2021)
20. Marchenko, D.D., Matvyeyeva, K.S.: Study of the stress-strain state of the surface layer during the strengthening treatment of parts. Probl. Tribol. **27**(3/105), 82–88 (2022)
21. Tkachuk, M.M., Skripchenko, N., Tkachuk, M.A., Grabovskiy, A.: Numerical methods for contact analysis of complex-shaped bodies with account for non-linear interface layers. East.-Eur. J. Enterp. Technol. **5**(7), 22–31 (2018)
22. Tkachuk, M., Grabovskiy, A., Tkachuk, M., Hrechka, I., Sierykov, V.: Contact interaction of a ball piston and a running track in a hydrovolumetric transmission. In: Ivanov, V., Pavlenko, I., Liaposhchenko, O., Machado, J., Edl, M. (eds.) Advances in Design, Simulation and Manufacturing IV. Lecture Notes in Mechanical Engineering, pp. 210–218. Springer, Cham (2021). https://doi.org/10.1007/978-3-030-77823-1_20
23. Tkachuk, M., Grabovskiy, A., Tkachuk, M., Hrechka, I., Tkachuk, H.: Contact interaction of a ball with a toroidal running track with a closely shaped power law profile. In: Tonkonogyi, V., Ivanov, V., Trojanowska, J., Oborskyi, G. (eds.) Advanced Manufacturing Processes VI. Lecture Notes in Mechanical Engineering, pp. 512–520. Springer, Cham (2025). https://doi.org/10.1007/978-3-031-82746-4_56

Model Analysis of Metal Degradation Processes in Tubing Pipes in Service

Oksana Klochko[1(✉)], Oleg Trishevskiy[1], Mariia Bilinska[2], Ivan Rybalko[1], and Evgeniya Deryabkina[1]

[1] State Biotechnological University, 44, Alchevskih Street, Kharkiv 61002, Ukraine
klochko.hntysh@gmail.com
[2] Jagiellonian University, 171, Orla Street, 30-244, Kraków, Poland

Abstract. The corrosive-aggressive downhole environment and cyclic loads are among the most common factors that affect running condition and service life of tubing pipes. Long-term operation in these settings causes aging processes, accompanied by metal degradation and a decrease in the level of its properties. In our present study we investigate microstructure of low-carbon steel AISI 1020 which is widely used in tubing pipes manufacture and establish the influence of plastic deformation (stretching) on a significant change in coercive force. The scientific novelty of our paper consists in the way the degradation of the pipe steel is investigated: we experimentally model the development of diffusion processes in the structure under cyclic stretching similar to that in operation under the load of an entire column. We use both optical-mathematical and EDS structure analyses in order to identify the degradation. The observed structural changes determine the level of coercive force, which can be effectively used to evaluate the degradation degree of the pipe material in operation. The surface extrusion zones have been detected, which include carbide-type phases with different carbon content, solid non-metallic inclusions, oxides, and, presumably, areas where spontaneous transformation of metal into powder occurred. Such zones appear due to plastic deformation in the original and deformed samples. In the near surface region post deformation, a quasi-homogeneous structure without pearlite is observed with an equal amount (~7.0%) of point carbides and a transition phase of the ferrite type that is maximally saturated with carbon (colour 155). Carbon content within the main ferrite (86%) varies. Based on the obtained results, for the effective use of pipe material in operation, we discuss the importance of taking into account both the initial state of the material and the degree of its initial deformation when developing further technological processes, which brings additional practical value to our study.

Keywords: low-carbon steel · structural changes · deformation · tubing pipes · coercive force level

H. Altenbach et al. (Eds.): CAMPE 2025, LNME, pp. 303–312, 2026.
https://doi.org/10.1007/978-3-032-16381-3_29

1 Introduction

Low-carbon steels are widely used in mechanical engineering and metallurgy, in particular in pipe production. During the long-term operation of pump and compressor pipes (tubing pipes), the aging processes accompanied by degradation of mechanical properties of pipe steels occur inevitably. The state change in metal depends on a number of operational factors, primarily on a long-term combined effect of mechanical loads and a corrosive environment. It is imperative to study the contribution of each of these factors in order to predict the impact of degradation processes on the durability of such products. In order to investigate the development of structural degradation, we have carried out a modeling experiment of the metal stretching process that occurs in the tubing pipes subjected to a load of an entire column. The effect of plastic deformation is studied on AISI 1020 low-carbon structural steel. Due to its strength vs. ductility optimal combination, this steel grade is widely used in rolled sheets, structural shapes, both rolled tubular and rolled section products, which includes using it in the tubing manufacture.

2 Literature Review

Wear and tear of pipeline and drill pipe steels result in deterioration of their mechanical and electrochemical properties, thus reducing resistance of such steels to cracking under environmental exposure effects. The reduce of brittle fracture resistance and stress corrosion cracking resistance occurs most intensively under stresses associated with the development of volumetric scattered microdamage inside the material [1]. It has been established that cold plastic deformation is accompanied by the formation of new dislocations [2], grain fragmentation (subgrains formation), and the emergence of structural heterogeneity [3]. Microhardness anisotropy of the structural components of an alloy is a sensitive indicator of the change in the state of material as a result of degradation. It is possible to assess the degree of pipeline steels degradation non-destructively by changing the level of coercive force. The formation of microstructure in AISI 1020 low-carbon steel after stretching (cold plastic deformation) and its influence on the level of physical [4] and mechanical [5] properties have been studied using optical metallography methods. The influence of deformation has been evaluated by the change of coercive force and by anisotropy of the ferrite microhardness values [6]. Metallographic analysis has revealed the following structural changes: additional deformation of pearlite grains and, to a greater extent, ferrite (on average by 10%, as estimated via microhardness method) in relation to the original rolled product; deformation structure buildup (additional stretching of grains); presence of stresses from non-metallic inclusions; pore formation; cementite inclusions. Microdamage buildup inside the steel is confirmed [7] by the tendency toward selective etching of the boundaries between adjacent bands of ferrite and pearlite, as well as via fractography: by detection of brittle fracture elements on the fracture surfaces (delaminations and chips that indicate areas of weakened adhesion between the bands of ferrite and pearlite) [8]. The aforementioned studies show that residual microscopic stresses localize in the structure of low-carbon steel under tensile deformation. This is confirmed by an increase in the level of coercive force and magnetic anisotropy, as well as by the anisotropy of the ferrite microhardness.

The above-mentioned factors determine a partial change in the level of the coercive force of the post-deformation sample. However, the set of identified factors does not fully explain a significant increase in the coercive force level (~3 times) after deformation [9]. It is evident that such difference cannot be present due to the deformation-driven change in dislocation structure alone. More in-depth studies are needed to obtain a complete picture of the influence of deformation on such changes in coercive force.

The aim of our work is to conduct microstructural studies of low-carbon steel to evaluate the effect of plastic deformation (stretching) on a significant change in the level of coercive force. To do so, we use EDS analysis and mathematical evaluation of SEM images that trace changes in the microstructure. The quality of the original alloy has been taken into account.

3 Research Methodology

We conduct our studies on samples of AISI 1020 sheet steel (0.18–0.23% C; 0.30–0.60% Mn), 5 mm thick before and after stretching. The samples have been analysed after 12.8% cyclic deformation and cut along and across the deformation within the destruction zone. The samples of original metal in hot-rolled condition and those cut from the grip zone and near it have been comparatively examined. All of the etched deformed samples cut from the grip, as well as along and across the deformation in the destruction zone, are characterized by the deformation of pearlite grains greater than that of the original metal. The greatest deformation degree has been found within the transverse samples near the destruction zone, which we have further investigated.

For a detailed analysis of fragments of SEM images of metal structures, we use our own analytical research technique based on hydrodynamic analogies and making use of the Navier-Stokes equations [10] occurring during the formation of phases (energy dissipation, diffusion transfer, change in the density of the dislocation structure) [11]. The mathematical basis is an optical–structural analysis method that evaluates images differing in their statistical characteristics (distribution of image elements, pixels, and their density) [12]. Each pixel coordinate of a digital image in.pgm format has been assigned with a code value of a conditional colour. Using these values, an absolute value of Laplacian has been calculated at each point of the image, which describes a heterogeneity of chemical elements due to energy dissipation during structural transformations. Integral distribution histograms for the analysed parameters have then been constructed. These distributions allow the alloy phases and their degree of local heterogeneity to be evaluated. By comparing the histograms, the quantity and quality of phases have been determined. Histograms have been plotted across eleven groups of conditional colours (in %) that reflect differences in component content. Carbon saturation of the studied region increases from lower to higher colour numbers, where the following intervals are defined [13]: 0–10 (colours 0–163): ferrite phases (dark shades), α-phase with different lattice perfection levels and chemical compositions; 10 (colours 147–163): ferrite phases with higher carbon saturation (dark gray shades); 11–16 (colours 164–255): carbide phases (shades of white).

The microstructure has been examined using a scanning electron microscope (SEM) JEOL JSM-6390LV equipped with microprobe analyser Link AN10/85S EDS system.

The chemical composition of the carbides is determined using energy dispersive X-ray spectroscopy (EDS).

4 Results and Discussion

Samples cut from the as-delivered steel show coercive force (Hc) of 3.3 A/cm longitudinally and 3.9 A/cm transversely, with anisotropy coefficient of A = 0.87. After transverse deformation, coercive force increases up to 9.3 A/cm. The steel structure then consists of ferrite and pearlite.

Analysis of pearlite and ferrite structures (Fig. 1) shows changes in the distribution of phases. Histograms of structural components according to conditional colours (Table 1) reveal that deformation reduces pearlite fraction and destroys cementite lamellae (Fig. 1b). In some regions, pearlite grain boundaries get blurred even though the lamellar relief remains the same (Fig. 1c). As presented in Table 1, the cementite fraction (colour 255) decreases by half post-deformation (1.61% → 0.78%) at general view images with × 2000 magnification. At the same time, carbon redistribution occurs in the vicinity of ferrite: carbon-rich zones (colors 82 and 91) increase 2–3 times, and the structures of color No. 155 (intermediate phase between carbon-saturated deformation induced ferrite and cementite) increase fourfold. At the same time, the proportion of the carbide phase with a reduced carbon content increases (colours 164 and 246). Image analysis at 5000 × magnification (local regions) reveals a nearly similar phase ratio (see Table 1 and Fig. 1c).

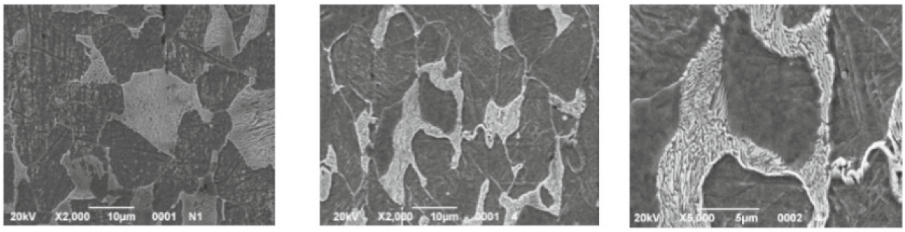

Fig. 1. SEM images of AISI 1020 steel microstructure in the initial state (a), after deformation: general view (b), × 2000; local area (c), × 5000

EDS analysis confirms higher carbon content in ferrite as compared to pearlite in the initial sample. Up to 0.21% Si has been identified in pearlite (compared to the overall alloy content of 0.15%). In the deformed sample, an elevated carbon content remains in the ferrite regions compared to pearlite (~1.1 times higher). In pearlite, a reduction in manganese concentration by 1.6 has been observed (from 0.42% to 0.27%).

Based on the obtained structural changes and EDS analysis, histograms of the distribution of regions with increased carbon content are constructed (Fig. 2). Depending on the proportion of such structures (%) within a 10 × 10 pixel image fragment, a colour has been assigned in accordance with Table 2.

Table 1. Histogram of the conditional colour distribution (%) in the studied SEM images (see Fig. 1) of the AISI 1020 steel microstructure

0	8	9	73	82	92	155	164	246	247	255	Image
0.0	0.0	0.0	63.66	20.02	14.30	0.41	0.0	0.0	0.0	1.61	a
0.0	0.0	0.0	2.35	44.13	46.23	04.81	0.52	0.18	0.0	0.78	b
0.11	5.54	0.98	0.01	14.74	44.43	15.22	11.37	0.72	5.99	0.89	c

Table 2. Image colour depending on the amount of structural components with increased carbon content (x, %)

x, %	$x = 0$	$0 < x \leq 5$	$5 < x \leq 10$	$10 < x \leq 15$	$15 < x \leq 20$	$x > 20$
Colour	-	black	blue	green	yellow	red

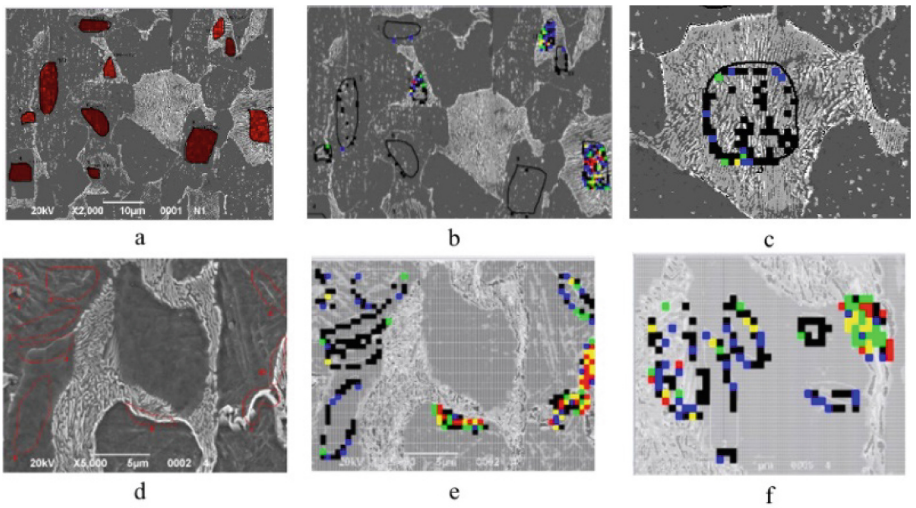

Fig. 2. Distribution of structural constituents with increased carbon content: original SEM images before (a) and after (d) deformation (red - analysed zones); evaluated histograms of regions with increased carbon content: before (b), (c) and after deformation (e), (f).

It has been established that the amount of post-deformation structures with increased carbon content increases in the ferrite region compared to the undeformed sample, and distinct, close to cementite areas with phases and carbon-depleted carbides are observed. The mechanism of cementite decomposition under deformation in the studied steel is associated with the fragmentation of cementite lamellae.

The investigation of the carbon elemental distribution map (EDS) using two-dimensional mapping of C concentration in the structure of AISI 1020 steel clearly confirms the redistribution of carbon atoms as a result of deformation (Fig. 3).

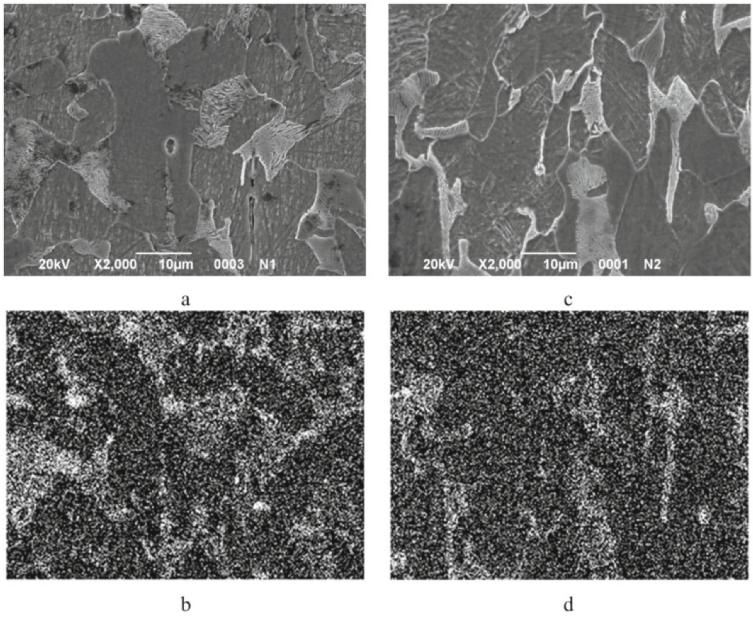

Fig. 3. Elemental distribution analysis of carbon (EDS) in the structure of AISI 1020 steel. SEM microstructure images: initial (a) and deformed (c) samples. Elemental maps: initial (b) and deformed (d) samples.

In the process of cementite decomposition, carbon atoms are released and retained along dislocation walls at grain boundaries, where their density increases [14]. They may also form fullerenes and fullerene complexes with iron [15]. As a result, a supersaturated phase is formed which itself is an intermediate (transitional) state between ferrite and cementite. In terms of carbon concentration it is close to austenite (colour No. 155 [12]). Consequently, an increase in carbon concentration in ferrite is observed. In some cases, it may even exceed that in pearlite. Moreover, this effect is also present in the initial sample. Therefore, when studying the influence of cold plastic deformation on the structure of low-carbon steel, it is essential to account for the quality of the initial material and the fraction of the pearlitic constituent.

Microstructure analysis of SEM images has shown extrusion zones on the sample surface (Fig. 4), formed as a result of plastic deformation both in the initial state (after rolling, Fig. 4a) and in the deformed sample (Fig. 4d). Using EDS analysis, the surface structure of these zones and the adjacent areas have been examined in detail (Fig. 4b, e). Two distinct regions have been identified within the extrusion zone. The first region (spectrum 10 in Fig. 4b, and spectrum 1 in Fig. 4e) has revealed an increased concentration of C (36.44% and 38.13%) and O (12.58% and 26.16%), with a simultaneously reduced fraction of Fe (49.38% and 25.14%). In addition, small amounts of Na (1.06% and 0.92%), Si (0.22% and 2.75%), Mn (0.32% in spectrum 10), and in spectrum 1: Zn (2.11%), Al (0.6%), Cl and Ca (1.02% each), Cr (0.59%), K (0.93%), and S (0.55%) have been detected. The observed phenomena (see Fig. 4a and d) can be explained both

by the diffusion of elements resulting from plastic deformation and the extrusion of hard non-metallic inclusions to the specimen edge (in particular, the increase of silicon in post-deformation extrusion zone by ~3 times, with a significant reduction in its concentration in pearlite). The second region (spectrum 2 in Fig. 4e) corresponds to SiO_2 silicon oxides (rounded inclusions 4–6 μm in size, which do not deform during rolling but are being pushed to the surface if located near it under tension). These contain 57.41% O with a minimal fraction of Fe (1.27%). SEM analysis has shown such grains to be surrounded by ferritic interlayers.

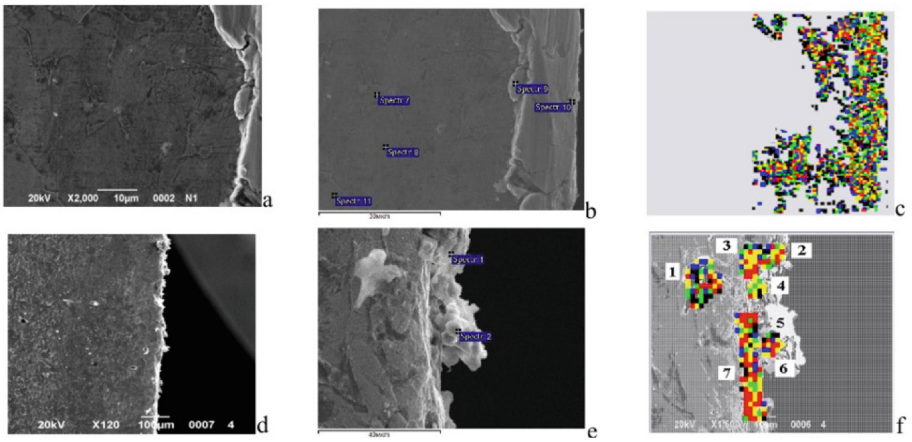

Fig. 4. Investigation of surface microstructure of AISI 1020 steel specimens: SEM images of the initial structure (a) and after cyclic tensile deformation (d); EDS analysis zones: in the initial sample (b) and after deformation in the extrusion area (e); histogram of structural constituents with increased carbon content (colours according to Table 2): initial sample (c) and extrusion area (f)

The subsurface zones have been studied in the post-rolling initial sample (spectra 7, 8, 9, 11 in Fig. 4b). The carbon content in these zones ranges from 16.25–20.49%, Fe: 79.09–83.17%, and Mn: 0.42–0.58%. Evidently, these zones contain a fraction of cementite formed at the surface during hot rolling deformation.

The obtained spectral X-ray microanalysis data provide results only for the depths no more than 3 μm, whereas the extrusion zone extends up to 160 μm which makes selective indicators insufficient for a full assessment by EDS alone. Moreover, the phases that form within the extrusion zone and their spatial distribution remain unclear. To evaluate this, we have carried out mathematical analysis of the formed structures on the surface of the post-deformation specimen. As a result, histograms of conditional colour distributions have been constructed. To do this, we have used a methodology of assessment the distribution of structural constituents (presented in Table 3) and areas with increased carbon content (see Fig. 4f).

Our analysis has shown the first extrusion zone (Fig. 4f, region 2) to be consisting of 31.8% ferrite (with the maximum fraction corresponding to colour 8: 15.5%, and colour 92: 8.4%), 54.6% cementite, and 13.7% transition phase enriched in carbon (colour 155).

Table 3. Histogram of conditional colour distribution (%) in the extrusion zone

0	8	9	73	82	92	155	164	246	247	255	Region
00,0	42,6	13,0	00,4	02,4	01,8	02,0	03,9	09,4	10,2	14,1	1
00,1	15,5	01,0	00,9	05,9	08,4	13,7	28,1	00,2	21,4	04,9	2
02,3	26,9	06,9	03,4	05,5	03,6	05,4	15,3	05,5	19,9	05,5	3
02,2	16,3	11,4	02,6	03,2	02,4	03,4	19,5	18,9	10,6	09,4	4
00,0	30,8	14,1	00,0	01,3	00,2	00,0	21,9	10,4	21,0	00,2	5
00,0	15,9	04,4	00,6	10,5	12,3	10,0	18,1	03,9	11,6	12,7	6
00,6	20,7	07,6	00,3	01,6	03,0	03,7	15,3	11,9	13,6	21,7	7

The second extrusion zone (Fig. 4f, region 5) demonstrates a decrease in carbide phases (53.5%) with lower carbon content and the presence of 46.4% ferrite (maximum fractions: colour 8: 30.8%, and colour 9: 14.1%). Mathematical and X-ray spectral analyses in this zone have revealed significant discrepancies in ferrite content (46.4% and 1.27%, respectively). This difference may be explained by lattice distortion of Fe at high carbon saturation under severe deformation, leading to spontaneous metal-to-powder transformation [16]. Phase of the colour 155 is absent. Free carbides structurally identified in the extrusion zones under comparison display a wide colour range from 164 to 255, indicating varying carbon content within different inclusions. The minimum carbon fraction corresponds to colour 246 in the first zone and to colour 255 in the second zone (0.2% each). Maximum distributions reaches 28.1% in the first case (colour 164) and 21.9% and 21.0% (colours 164 and 247) in the second one. We have conducted further investigation in the areas adjacent to the surface layer (Fig. 4c). In these regions, deformation causes a sharp reduction in pearlite content, with isolated cementite inclusions appearing. In regions 1 and 7, a pronounced ferritic structure enriched in carbon has been formed, with 60.2% in region 1 (maximum value of colour 8 is 42.6%) and 33.6% in region 7 (maximum for colour 8: 20.7%), along with 37.6% (maximum for colour 255: 14.1%) and 62.5% (maximum for colour 255: 21.7%) cementite, respectively, and 2–3.7% of the transition phase (colour 155). Region 6 closely resembles region 2, while regions 3 and 4 are also carbide inclusions with varying carbon content (Fig. 4f). Near the sample surface (Fig. 4c), the structure is quasi-homogeneous (pearlite is absent), with discrete carbides (7.0%) and an equal amount of ferrite highly saturated with carbon (colour 155). The main ferrite fraction accounts for 86%. However, this kind of ferrite varied in carbon content, as indicated by the histogram of colours: 23.5% in colour 0 ferrite; 0.7% in colour 9; 0.2% in colour 8; 4.8% in colour 73; 41.3% in colour 82; and 15.5% in colour 92. The higher the ferrite colour index, the greater is its carbon content.

5 Conclusion

The obtained results demonstrate that tensile deformation induces pronounced microstructural changes, which govern the evolution of the coercive force in low-carbon steel. A decrease in the pearlite fraction accompanied by the fragmentation of cementite

lamellae has been observed, with blurring the pearlite grain boundaries while retaining the lamellar relief. After cyclic tensile deformation, both pearlite and ferrite exhibit a similar carbon concentration (~10% higher in ferrite). This can be attributed to carbon atom diffusion along dislocation walls, their trapping within dislocations at grain boundaries, and the possible formation of fullerene-type complexes with iron. Consequently, an oversaturated ferrite-like phase is formed, which is intermediate between ferrite and cementite, in some cases approaching the carbon content of austenite. Notably, traces of this intermediate phase have also been identified in the initial sample. These findings emphasize the necessity of accounting for the initial microstructural condition and deformation degree when evaluating the effects of cold plastic deformation on the structural and functional response of low-carbon steels, thereby ensuring accurate process design and reliable in-service performance.

References

1. Nykyforchyn, H.: In-service degradation of pipeline steels. In: Bolzon, G., Gabetta, G., Nykyforchyn, H. (eds.) Degradation Assessment and Failure Prevention of Pipeline Systems. Lecture Notes in Civil Engineering, vol. 102. Springer, Cham (2021). https://doi.org/10.1007/978-3-030-58073-5_2
2. Zhang, C., Juul Jensen, D., Yu, T.: Microstructure and texture evolution during cold rolling of 316L stainless steel. Metall. Mater. Trans. A **52**(9), 4100–4111 (2021). https://doi.org/10.1007/s11661-021-06367-6
3. Volokitin, A.V., Panin, E.A., Lavrinyuk, D.N.: Mechanisms of structure formation under severe plastic deformation: a review, metallofiz. Noveishie Tekhnol. **45**(11), 1311–1335 (2023). https://doi.org/ https://doi.org/10.15407/mfint.45.11.1311
4. Mushnikov, A.N., Zadvorkin, S.M., et al.: Effect of biaxial tension on the coercive force of low-alloy steel. J. Nondestructive Eval. **42**. Article number 94 (2023). https://doi.org/10.1007/s10921-023-01012-1
5. Dewangan, S., Mainwal, N., Khandelwal, M., et al.: Performance analysis of heat treated AISI 1020 steel samples on the basis of various destructive mechanical testing and microstructural behaviour. Aust. J. Mech. Eng. **20**(1), 74–87 (2022). https://doi.org/10.1080/14484846.2019.1664212
6. Putilova, E.A., Mushnikov, A.N., et al.: Effect of tensile elastic deformations on magnetic properties of preliminarily deformed structural steel operating under pressure. Met. Sci. Heat Treat. **64**, 410–414 (2022). https://doi.org/10.1007/s11041-022-00822-w
7. Nykyforchyn, H., Zvirko, O., Dzioba, I., et al.: Assessment of operational degradation of pipeline steels. Materials **14**(12), 3247 (2021). https://doi.org/10.3390/ma14123247
8. Vakhrusheva, V.S., Volchuk, V.M., et al.: Fractal model of estimating quality of cold worked fuel cladding tubes. Prob. Atomic Sci. Technol. **5**(135), 57–63 (2021). https://doi.org/10.46813/2021-135-057
9. Hasičić, M., Angelopoulos, S., Ktena, A., et al.: A study on the effect of plastic strain on magnetic phenomenology and microstructure. Magnetism **5**(1), 1 (2025). https://doi.org/10.3390/magnetism5010001
10. Temam, R.: Navier–Stokes equations: theory and numerical analysis. Am. Math. Soc. **343**, 408 (2024)
11. Skoblo, T., Romaniuk, S., Belkin, E., et al.: Structure and wear-resistance of hardened thin-blade knives with PVD coating. In: Altenbach, H., et al. Advances in Mechanical and Power Engineering. CAMPE 2021. Lecture Notes in Mechanical Engineering. Springer, Cham (2023). https://doi.org/10.1007/978-3-031-18487-1_12

12. Skoblo, T.S., Klochko, O.Y., Belkin, E.L., et al.: Features of the carbide phase degradation under heating and deformation. Lett. Mater. **11**(1), 22–27 (2021). https://doi.org/10.22226/2410-3535-2021-1-22-27
13. Skoblo, T.S., Sidashenko, O.I., Saichuk, O.V., et al.: Influence of stresses on structural changes in gray cast iron. Mater. Sci. **56**, 347–358 (2020). https://doi.org/10.1007/s11003-020-00436-8
14. Dong, Q., Lu, H., Wang, Y., et al.: The influence of strain aging at different temperatures on the mechanical properties of cold-drawn 10B21 steel combined with an electron microscope study of the structures. Materials (Basel). **17**(4), 826 (2024). https://doi.org/10.3390/ma17040826
15. Larionova, N.S., et al.: Structural-phase composition of iron-containing high carbon composites with fullerite and graphite obtained by mechanosynthesis. J. Alloy. Compd. **909**, 164749 (2022). https://doi.org/10.1016/j.jallcom.2022.164749
16. Galetz, M.C., Schlereth, C., White, E.M.H., et al.: An expanded model for the pressure effect in metal dusting of Mn-containing alloy 600 based on advanced scale characterization. High Temp. Corrosion Mater. **100**, 541–555 (2023). https://doi.org/10.1007/s11085-023-10201-2

Determinative Approach to Analysis of the Influence of Thermomechanical Phenomena on the Quality of Working Surfaces of Parts in Finishing Operations

Maksym Kunitsyn(✉), Anatoly Usov, Yuriy Zaychyk, and Yulia Sikirash

Odessa Polytechnic National University, 1, Shevchenko Ave, Odessa 65044, Ukraine
{m.v.kunitsyn,usov-a-v,zaichyk.y.i,u.e.sikirash}@op.edu.ua

Abstract. This study aims to model thermomechanical processes in grinding, accounting for material heterogeneity and technological heredity. A deterministic model was developed linking the crack resistance criterion (K_{Ic}) to key technological parameters and hereditary defects, allowing the determination of limit values for heat flux. These operations generate substantial heat, resulting in structural defects such as burn marks on the machined surface. These defects decrease the initial surface hardness, induce tensile residual stresses, and lower the parts' contact endurance and fatigue strength. For many metals and alloys not susceptible to structural transformations during grinding, cracks are a notable defect type that severely impacts the operational properties of the products. The intensity of crack formation largely depends on various inhomogeneities that develop in the surface layer during manufacturing. Based on these criteria, an algorithm was developed to ensure technological capabilities for defect-free processing of products made of materials prone to loss of quality of the surface layer of parts, taking into account maximum processing productivity.

Keywords: Grinding · Surface integrity · Technological inheritance · Cracks

1 Introduction

Insufficient control at stage finishing operations can lead to severe economic consequences (cost increase and scrap [1]) and production losses (quality reduction [2, 3], reliability decline, productivity decrease) [4].

Grinding, as one of the most critical finishing processes, inevitably involves thermomechanical phenomena such as heat and stress, which strongly affect surface integrity [4, 5]. The most dangerous defects in high-loaded parts include fatigue and corrosion cracks [6, 7], tensile residual stresses [6, 8], and various microstructural damages [5–7, 9, 10]. These defects initiate and accelerate failure, significantly reducing the performance of the product. Moreover, technological heredity plays a key role: defects formed in earlier stages of production (e.g., inclusions, flakes, microcracks) may act as concentrators for

H. Altenbach et al. (Eds.): CAMPE 2025, LNME, pp. 313–322, 2026.
https://doi.org/10.1007/978-3-032-16381-3_30

stresses arising during grinding [11–14]. Their interaction with thermomechanical fields leads to cracks, burns, and further degradation of performance [5, 13, 14].

Existing models of thermal and mechanical processes in grinding provide valuable insights [5, 13, 14], but they are often restricted by simplifying assumptions such as material homogeneity, neglect of hereditary defects, or insufficient consideration of microstructural features.

This study aims to model thermomechanical processes in grinding, accounting for material heterogeneity and technological heredity.

2 Literature Review

Thermal and mechanical modeling of grinding processes has been widely studied, as heat generation and stress distribution directly determine surface quality [5, 13, 14]. Thermoelasticity theory allows treating the surface layer as a thermoelastic body, providing a framework for predicting conditions of burns and cracks [13, 14]. However, most models assume material homogeneity and do not adequately represent microstructural variability or defects.

The concept of technological heredity emphasizes that defects formed in earlier operations influence the quality of subsequent stages [11, 12]. For grinding, this means that inclusions, flakes, or microcracks can interact with residual tensile stresses, acting as crack initiators [13, 14]. Despite its importance, technological heredity is often considered qualitatively rather than quantitatively. Existing recommendations for crack prevention usually focus on single process parameters and rarely integrate heredity effects into comprehensive models [5, 10, 13]. This demonstrates a lack of systemic approaches that connect inherited defects with grinding conditions in a predictive manner.

Fracture mechanics provides valuable tools for analyzing crack formation, especially through the concept of the stress intensity factor (SIF) [9, 13, 15]. SIF enables a detailed assessment of stress concentration at defects and has been applied to explain crack initiation in grinding [13, 14]. Nevertheless, while these methods capture local stress conditions, they often fail to establish a robust link with grinding parameters and material heterogeneity. The “weak link” hypothesis further underscores the stochastic nature of failure in heterogeneous materials, in which overall strength is determined by the weakest defect rather than by average properties [13, 16].

Experimental approaches provide qualitative descriptions of defects and their evolution, but they often lack quantitative relationships between process parameters and material response [6, 11–13]. Furthermore, recommendations for crack prevention remain material-specific, reducing their universality and transferability [5, 10, 13].

The literature demonstrates significant achievements in modeling thermal processes, analyzing defects, and applying fracture mechanics to grinding. However, these efforts remain fragmented. There is no integrated approach that quantitatively links technological heredity, thermomechanical fields, and process parameters.

3 Research Methodology

The assumption is that the workpiece surface can be modeled as a heterogeneity with distinct properties embedded within the principal matrix material. This conceptualization facilitates the examination of thermomechanical processes occurring during the grinding of components whose working surfaces exhibit the specified technological inhomogeneities characterized by linear dimensions. L_{ks} [17, 18].

The investigation focused on the impact of inhomogeneities arising from phase transitions of metastable structures, such as intergranular films, hereditary austenite grain boundaries, carbide networks, non-metallic inclusions, as well as defects including shells and flakes, within the surface layer. These were analyzed in the context of induced conditional cracks. The model analyzes a semi-infinite body containing subsurface irregularities with arbitrary orientations, which are exposed to a moving heat source on the surface, simulating the grinding wheel.

The mathematical framework relies on a set of equations that characterize the transient thermal and stress-strain conditions of the surface layer. It includes the Fourier equation of unsteady heat conduction and Lamé's elasticity equations in displacements with corresponding initial and boundary conditions that account for the moving heat source from the grinding wheel [17].

In a surface layer characterized by structural and technological irregularities, the conditions leading to solution discontinuity will vary according to the nature of the defect: for inclusions, the conditions are $\langle \overline{u} \rangle = 0$, $\langle \sigma_x \rangle \neq 0$ and $\langle \overline{v} \rangle = 0$, $\langle \tau_{xy} \rangle \neq 0$, while for crack-like defects, $\langle \sigma_x \rangle = 0$, $\langle \overline{u} \rangle \neq 0$ and $\langle \tau_{xy} \rangle = 0$, $\langle \overline{v} \rangle \neq 0$.

4 Results and Discussion

Among the existing failure criteria that consider the local physical and mechanical properties of heterogeneous materials, the force-based criteria, which utilize the concept of the stress intensity factor (SIF), are deemed most suitable for this situation [19–21]. When the applied load results in a stress intensity factor, K_I, that reaches the critical threshold, K_{Ic}, the defect resembling a crack transitions into a primary crack.

The resolution to the problem is accomplished through the application of the method of discontinuous solutions [18, 22]. As one traverses the boundary of an inhomogeneity, the displacement and stress fields experience first-order discontinuities, represented as jumps. This discontinuity of a quantity f is denoted by $\langle f \rangle$, resulting in noticeable jumps such as $\langle u \rangle$, $\langle v \rangle$, $\langle \sigma_x \rangle$, and $\langle \tau_{xy} \rangle$.

Applying generalized Fourier transforms yields singular integral equations that provide recursive relations linking stresses and displacements at defects with those on the machined surface.

When subjected to uneven heating, the surface layer experiences thermal deformations, leading to the development of thermal stresses. These stresses, which are concentrated at defect sites, result in the formation of grinding cracks.

The primary focus is on the stress behavior near defect peaks, including cracks, sharp inclusions, and structural imperfections, which represent stress characteristics in these regions $y \to \pm L_{ks}$.

The characteristics of the stress field near the defect's tip, as analyzed through classical elasticity theory, are often described using a complex stress intensity factor K, which combines Mode I and Mode II contributions as $K = K_I + iK_{II}$ [21].

The investigation into the stress intensity at the vertices of a defect, characterized by a length of $2L_{ks}$, situated at a depth of R_i, under the application of a heat flux q to the body's surface ($x = 0$, $|y| \leq a^*$) facilitated the determination of the critical value of this flux, q^*, at which the defect begins to propagate into a significant crack [22]:

$$q^* = \frac{2\sqrt{3}\lambda(1-\nu)K_{Ic}}{\alpha_2 El\sqrt{\pi l}\sigma^*} \tag{1}$$

The interaction between defects affecting stress intensity becomes evident when they are separated by a distance slightly exceeding $\sigma^* = 1/3$. Simultaneously, the material exhibits its minimum crack resistance when the defects are aligned at an angle of $\phi = \pi/6 + \pi/4$ relative to one another. The geometry and characteristics of inclusions can establish conditions that either prevent or promote the formation of grinding cracks. When the heat flow is oriented parallel to the major axis of both the elliptical inclusion and the linearly insulated crack, and the inclusion's linear thermal expansion coefficient, α_t^B, surpasses that of the base material, α_t^M (i.e., $\alpha_t^B > \alpha_t^M$), a resultant increase in stiffness is noted, culminating in an enhancement of K_I. This observation is contingent upon the varying ratios of the thermal conductivity coefficients of the material components.

This results in a reduction of the crack resistance in the surface layer. For crack-type defects in a layer characterized by a lower coefficient, α_t, the defect's orientation significantly affects the SIF value.

To ensure defect-free processing of steels and alloys that possess crack-like defects and inclusions, it is crucial to consider the threshold values of the heat flow generated during grinding when selecting processing modes and tool characteristics, thereby preventing hereditary defects from being disturbed from their equilibrium state.

The randomness of micro-inhomogeneities plays a crucial role in these alloys, cemented steels, and diverse coatings. Here, the weakest link hypothesis is applied, focusing on the defect with the largest geometric dimension [23, 24].

The impact of tool design parameters on the thermomechanical condition of the surface layer was investigated utilizing the model problem and boundary conditions expressed as follows:

$$q(y,\tau) = \frac{c\sqrt{\tau}}{\lambda}\left[H(y) - H\left(y - 2a^*\right)\right]\sum\nolimits_{k=0}^{n}\sigma\left(y + kl - v_{kp}\tau\right) \tag{2}$$

where $H(y)$ is the Heaviside function; $\sigma(y)$ is the Dirac delta function; n is the number of grains passing through the contact zone during the time $\tau = \sqrt{\pi t_{gr}}/v_{kp}$; λ is the thermal conductivity of the product material; $c\sqrt{\tau}$ is the heat flux from a single grain; v_g, v_{kp}, t_{gr} are grinding modes, $2a^*$ is the length of the arc of contact between the tool and the workpiece; l^* is the distance between cutting grains.

The maximum instantaneous temperature values, T_M, ranging from individual grains to the steady state component, T_K, were both theoretically derived and experimentally validated. These values are utilized as criteria for predicting the conditions under which burn-in defects form and their respective depths.

Figure 1 illustrates the spatial distribution of temperature within the contact zone, highlighting the concentration of the maximum temperature just beneath the surface and its progressive diminution with both depth and extent of the contact zone. The three-dimensional temperature field shown in Fig. 1 is an illustrative model based on an analytical function commonly used to approximate the heat source in grinding. This approach allows for a clear visualization of the temperature gradient without the complexity of a full numerical simulation. The temperature distribution T as a function of contact length x and depth z was described by the equation: $T(x, z) = T_0 \cdot \exp(-z/\delta_z) \cdot \exp\left(-(x - x_0)^2/\delta_x^2\right)$. The following parameters were used: maximum surface temperature $T_0 = 800$ °C; characteristic depth decay constant $\delta_z = 0.5$ mm; central position of the heat source $x_0 = 2.5$ mm; and characteristic length decay constant $\delta_x = \sqrt{2}$ mm. These values are representative of the conditions during the grinding of hardened steel.

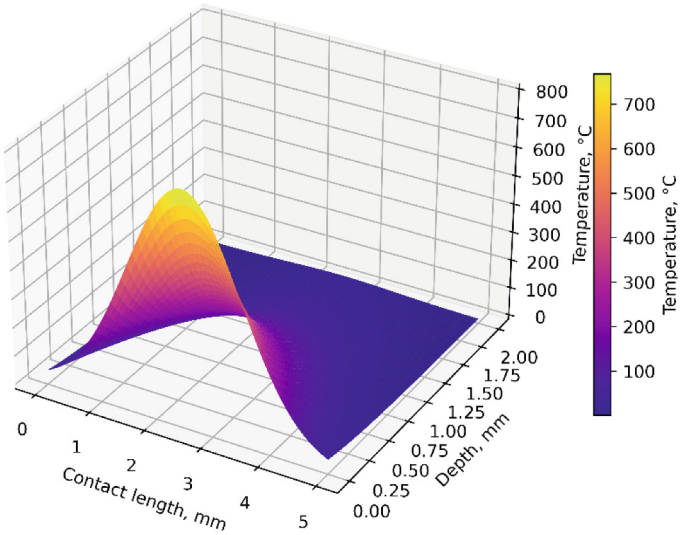

Fig. 1. Three-dimensional distribution of the temperature field in the contact zone of the grinding wheel with the workpiece

The impact of technological inheritance on the crack resistance of metals during grinding was evaluated using the fracture mechanics parameter, K_{Ic}, which considers the relationship between the stress-strain condition and the structural elements of the surface layer.

The fracture mechanics parameter K_{Ic} is highly sensitive to the material's technological heredity. For steels, K_{Ic} decreases with higher carbon content but is improved by tempering, grain refinement, and reducing impurities like sulfur, which cause micro-destruction. For instance, cyclic electrothermal treatment can increase K_{Ic} by up to 50%. These examples underscore the necessity of incorporating material-specific

microstructural properties and their history into predictive models for defect-free grinding.

Quantitative assessments of the crack resistance of magneto-hard alloys were carried out depending on the methods of obtaining blanks and their subsequent heat treatment to the γ-phase, thermomagnetic treatment to the $a + a'$ phase at different tempering modes and cooling rates. The controlled parameters were the values of the bending stress σ_b, tensile stress σ_t, coefficient K_{Ic}, and magnetic properties—coercive force of the material h_C according to magnetization and residual induction B_r. Experimental data show that the values of K_{Ic} are different for monocrystals and polycrystals of the studied alloy in the blank stage. This is because the percentage content of non-metallic inclusions in alloys obtained by different methods varies widely. The phase composition of these alloys changes the coefficient value of K_{Ic}. Thus, for polycrystals in the initial state, $K_{Ic} = 30\text{MPa}\sqrt{m}$, while the presence of the γ-phase increases K_{Ic} to 97 $\text{MPa}\sqrt{m}$. It has been established that the γ-phase, being more plastic than the main matrix of this alloy, contributes to the inhibition of microcracks [25].

Blank permanent magnets made of certain magneto-hard alloys are mainly obtained by casting. Currently, the following casting methods are used: open and vacuum. The most common open casting method is melting [13, 14].

Fractographic analysis is a critical tool for understanding such failure modes, as it can reveal how thermomechanical loads lead to specific fracture characteristics, such as intercrystalline cracking [26]. However, the presence of this phase in the the studied alloy reduces the coercive force by 40%, the residual magnetic induction by 15–20%, and the maximum magnetic energy by more than 60%. Therefore, these alloys are subjected to further thermomagnetic treatment. A distinctive feature of the structure of the high coercivity state of the alloys under consideration is the periodic alternation of elliptical-shaped particles of the α'-phase surrounded by a matrix of the α-phase. Further processing of these alloys by grinding causes the formation of crack-like defects in the surface layer. Moreover, the intensity of crack formation is related to heat treatment modes, which, in turn, affect the size of the α'-phase particles and the direction of thermomechanical processing relative to the longitudinal feed during grinding. The dominant technological parameters affecting crack resistance and contact temperature are the grinding depth and the characteristics of the wheel. Thus, in the case of grinding with different depths of diamond wheels, the crack resistance changes insignificantly, in contrast to the range of change of K_{Ic} when machining with wheels white Al_2O_3 (white fused alumina), grain size F60 / P60, ceramic bond. The contact temperature in the first case is significantly lower than in the second.

Based on a deterministic analysis of the thermomechanical phenomena accompanying the finishing methods of parts, the mechanism of the occurrence of grinding cracks was studied from the point of view of the influence of the geometry and physical properties of the α'-phase and its orientation relative to the direction of grinding of magnets in a high coercivity state. In this case, the conditions of equilibrium of the structural components of the α'-phase, depending on the dominant factors of the grinding process and the fracture toughness K_{Ic} of the magnet, were also used; the fulfillment of which does not lead to the formation of cracks on the machined surface.

The formulation of technological criteria for ensuring a defect-free grinding process can be achieved by utilizing established functional relationships between the physical and mechanical properties of the materials under processing and the primary technological parameters.

The assurance of processed surface quality is achieved by selecting technological conditions, such as processing modes, lubricating and cooling media, and tool characteristics, guided by control technological parameters. This selection ensures that the current values of grinding temperature $T(x, y, \tau)$, heat flow $q(y, \tau)$, stresses $\sigma(M)$, and the fracture toughness coefficient K_{Ic} remain within their permissible limits.

The establishment of a framework of constraints on the temperature values and the extent of its penetration can be expressed as follows:

$$T(x, y, \tau) = \frac{C}{2\pi\lambda} \sum_{k=0}^{n} H\left(\tau - \frac{kl}{v_{kp}}\right) \times H\left(\frac{L + kl}{v_{kp}}\right) \int_{\gamma_1}^{\gamma_2} f\left(x, y, \tau, \tau'\right) d\tau' \leq [T]_M \tag{3}$$

Similar criteria were established to limit the temperature at specific depths and locations within the contact zone.

To prevent grinding cracks during the processing of materials and alloys, it is essential to restrict the stress levels generated within the intensive cooling stress zone:

$$\sigma_{max}(x, \tau) = 2G \frac{1 + \nu}{1 - \nu} \alpha_t T_k erf\left(\frac{x}{2\sqrt{\alpha\tau}}\right) \leq [\sigma_i] \tag{4}$$

When hereditary heterogeneity significantly impacts the severity of grinding crack development, it is essential to apply criteria that incorporate deterministic relationships between technological parameters and the characteristics of the heterogeneities. Accordingly, for this purpose, one can identify restrictions on the stress intensity factor in the following form:

$$K_I = \frac{1}{\pi\sqrt{l}} \int_{-l}^{l} \sqrt{\frac{l + t}{l - t}} \sigma_n(t) dt \leq K_{Ic} \tag{5}$$

In this equation, $\sigma_n(t)$ represents the normal stress component acting on the defect face, $\tau(t)$ represents the shear stress component for Mode II analysis, and the integral is taken over the defect length l. Thus, by regulating technological control parameters, guarantee a threshold for heat flow that sustains the equilibrium of structural defects:

$$q^* = \frac{P_z v_{kp} \alpha_s}{\sqrt{D t_{gr}}} \leq \frac{\sqrt{3}\lambda K_{Ic}}{Hl\sqrt{\pi l}\sigma} \tag{6}$$

Figure 2 shows the change in the stress intensity factor depending on the crack length L for different depths of its location. It can be seen that with increasing depth h, the effect of the defect on the stress state decreases, which corresponds to the equilibrium conditions (5)–(6). The relationship between the stress intensity factor (K_I), crack length (L), and its depth (h) presented in Fig. 2 was calculated for a scenario representative of hardened carbon steel. The model assumes a crack-like defect is present in a semi-infinite

body subjected to a uniform remote tensile stress, which simulates the residual thermal stresses from grinding. The calculation assumes a remote stress value of $\sigma = 200$ MPa. The curves illustrate the behavior of the stress intensity factor for three distinct defect depths: a surface defect (h) and two subsurface defects ($h = 1.0$ mm and $h = 3.0$ mm).

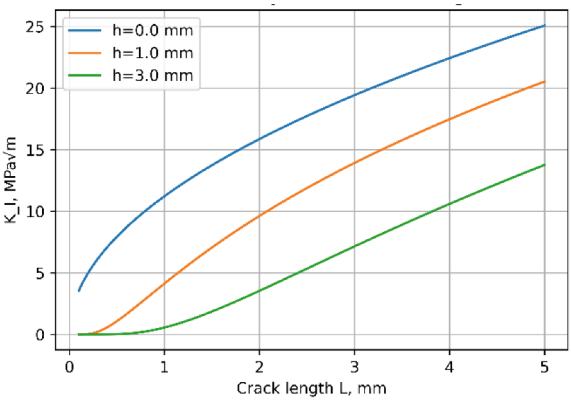

Fig. 2. Dependence of the stress intensity factor on the crack length at different depths of its occurrence

Achieving defect-free grinding conditions can be facilitated by understanding the material's structural characteristics. Specifically, when structural imperfections are primarily characterized by a length of $2l$ and are systematically aligned with the contact zone between the tool and the workpiece, the defect equilibrium condition is expressed as:

$$l_0 < \frac{K_C^2}{x[GT_k(1+\nu)\alpha_t]^2} \tag{7}$$

Based on the obtained criteria, an algorithm was developed to ensure surface quality. It uses the physical properties of the material, equipment characteristics, and processing modes as inputs to model the process and optimize control parameters for defect-free machining with maximum productivity.

5 Conclusions

This study lays the groundwork for defect-free processing of materials susceptible to cracking by elucidating the relationship between hereditary defects and the crack resistance of the surface layer in grinding processes. Technological parameters for processing have been determined, considering the accumulated damage and material inhomogeneities, especially in alloys prone to cracking during grinding. This is crucial for reducing defects in finishing operations and enhancing the operational properties of machine components:

1. Grinding cracks were found to be thermal in nature, thus requiring thermal criteria for defect-free processing.
2. A deterministic model was developed linking the crack resistance criterion (K_{Ic}) to key technological parameters and hereditary defects, allowing the determination of limit values for heat flux.
3. Based on these criteria, an algorithm was developed to optimize processing parameters for maximum productivity while ensuring surface quality.

References

1. Muratkin, G.V., Sarafanova, V.A.: The effect of the technological heredity of the stress-strain state on the accuracy of Nonrigid parts. J. Mach. Manuf. Reliab. **49**, 45–50 (2020). https://doi.org/10.3103/S1052618820010094
2. Yakimov, O., Zadorozhko, G., Bovnegra, L., Beznos, S., Balan, V.: Possible ways to reduce the cost of grinding process of products with intermittent circles. Pratsi OPU **1**, 36–45 (2018). https://doi.org/10.15276/opu.1.54.2018.05
3. Yakimov, O., Bovnegra, L., Tonkonogyi, V., Vaysman, V., Strelbitskyi, V., Sinko, I.: Influence of the geometric characteristics of the discontinuous profile working surfaces of abrasive wheels for precision and temperature when grinding. Cutt. Tools, 115–125 (2021). https://doi.org/10.20998/2078-7405.2021.94.13
4. Shin, Y.C., Joo, Y.S.: Optimization of machining conditions with practical constraints. Int. J. Prod. Res. **30**, 2907–2919 (1992). https://doi.org/10.1080/00207549208948198
5. Yang, M., et al.: Temperature field model in surface grinding: a comparative assessment. Int. J. Extrem. Manuf. **5**, 042011 (2023). https://doi.org/10.1088/2631-7990/acf4d4
6. La Monaca, A., et al.: Surface integrity in metal machining - part ii: functional performance. Int. J. Mach. Tools Manuf. **164**, 103718 (2021). https://doi.org/10.1016/j.ijmachtools.2021.103718
7. Hiew Sze Kei, S., Van Haaften, W.M., Britton, T.B., Pedrazzini, S.: A review of the factors that can increase the risk of Sulfide stress cracking in thermomechanical controlled processed pipeline steels. Adv. Eng. Mater. **25**, 2300406 (2023). https://doi.org/10.1002/adem.202300406
8. Stupnytskyy, V., Pasternak, S., Prodanchuk, O.: Increase productivity of hard-to-machine materials by preventive heating of the workpiece. UJMEMS **10**, 66–80 (2024). https://doi.org/10.23939/ujmems2024.02.066
9. Chen, J., Fang, Q., Du, J., Xie, C., Liu, F.: Impact of process parameters on subsurface crack growth in brittle materials grinding. Arch. Appl. Mech. **87**, 201–217 (2017). https://doi.org/10.1007/s00419-016-1187-8
10. Nadot, Y.: Fatigue from defect: influence of size, type, position, morphology and loading. Int. J. Fatigue **154**, 106531 (2022). https://doi.org/10.1016/j.ijfatigue.2021.106531
11. Kheifetz, M.L., Vasilyev, A.S., Klimenko, S.A.: Technological control of the heredity of operational quality parameters for machine parts. AM&T, 008–018 (2019). https://doi.org/10.17277/amt.2019.02.pp.008-018
12. Kolmakov, A.G., Kheifetz, M.L., Gretskiy, N.L., Prement, G.B.: Technological control on the heredity of operational quality parameters. In: Thanapalan, K. (ed.) Engineering Failure Analysis. IntechOpen (2020). https://doi.org/10.5772/intechopen.89471
13. Usov, A.V., Kunitsyn, M.V., Zaychyk, Y.I.: An information model concept for a thermomechanical process in grinding. HAIT **6**, 250–262 (2023). https://doi.org/10.15276/hait.06.2023.17

14. Usov, A., Zaychyk, Y., Kunitsyn, M., Sikirash, Y.: Levereging technological heredity to increase production efficiency of ferrocerramic products during final machining. Cutting & Tools, 168–185 (2024). https://doi.org/10.20998/2078-7405.2024.100.12
15. Hutchinson, J.W.: Fundamentals of the phenomenological theory of nonlinear fracture mechanics. J. Appl. Mech. **50**, 1042–1051 (1983). https://doi.org/10.1115/1.3167187
16. Slatcher, S., Evandt, Ø.: Practical application of the weakest-link model to fracture toughness problems. Eng. Fract. Mech. **24**, 495–508 (1986). https://doi.org/10.1016/0013-7944(86)90223-7
17. Kheir, N.: Systems Modeling and Computer Simulation. Routledge, Milton Park (2018)
18. Trukhanska, O.: Technological methods of increasing wear resistance and durability of details. Eng., Energy, Transp. AIC **4**, 109–115 (2020). https://doi.org/10.37128/2520-6168-2020-4-12
19. Bergheau, J.M.: Thermomechanical Industrial Processes: Modeling and Numerical Simulation. Wiley, Hoboken (2014)
20. Lebedev, V., Chumachenko, T., Klymenko, N., Frolenkova, O., Yevtifieiev, S.: Penetration depth of the critical temperature into the workpiece material during grinding. In: Ivanov, V., Trojanowska, J., Pavlenko, I., Zajac, J., and Peraković, D. (eds.) Advances in Design, Simulation and Manufacturing IV, pp. 453–462. Springer International Publishing, Cham (2021). https://doi.org/10.1007/978-3-030-77719-7_45
21. Anlas, G., Santare, M.H., Lambros, J.: Numerical calculation of stress intensity factors in functionally graded materials. Int. J. Fract. **104**, 131–143 (2000). https://doi.org/10.1023/A:1007652711735
22. Freiman, S.W., Mecholsky, J.J., Jr.: The Fracture of Brittle Materials: Testing and Analysis. John Wiley & Sons, Hoboken (2019)
23. Babich, D.V.: A statistical strength criterion for brittle materials. Strength Mater. **43**, 573–582 (2011). https://doi.org/10.1007/s11223-011-9330-9
24. Lajtai, E.Z.: Brittle fracture in compression. Int. J. Fract. **10**, 525–536 (1974). https://doi.org/10.1007/BF00155255
25. Popov, V.: Two-dimensional dynamic problems of the theory of elasticity reduced to singular integral equations with immobile singularities. J. Math. Sci. **270**, 107–122 (2023). https://doi.org/10.1007/s10958-023-06335-y
26. Yildirim, B., Dag, S., Erdogan, F.: Three dimensional fracture analysis of FGM coatings under thermomechanical loading. Int. J. Fract. **132**, 371–397 (2005). https://doi.org/10.1007/s10704-005-2527-9

Efficient Geometric Modeling and Visualization of Heat Transfer Domains Using R-functions and JavaScript

Roman Uvarov(✉)

Anatolii Pidhornyi Institute of Power Machines and Systems of the National Academy of Sciences, Vul. Komunalnykiv 2/10, Kharkiv 61046, Ukraine
rqa0001@gmail.com

Abstract. The behavior of heat transfer processes in engineering and physical systems is profoundly influenced by domain geometry and the internal structure of temperature fields. As modern applications, such as compact heat exchangers, microelectronics, and additive manufacturing, require increasingly complex geometries and fine control over thermal behavior, traditional numerical methods often struggle with domain definition, boundary enforcement, and visualization. The theory of R-functions, developed by V.L. Rvachev, provides a powerful analytical tool for representing complex domains through logical combinations of implicit functions. This paper explores the integration of R-functions with lightweight browser-based computation, using JavaScript to model and visualize heat transfer domains in two dimensions. The proposed method supports the analytical construction of geometric domains and exact boundary conditions through R-operations, implemented in a modular and computationally efficient manner. The function visualization pipeline is structured in three main stages: domain pre-processing with extrema detection, annotation and level curve configuration, and real-time pixel-based rendering. Optimization through minimal-index R-operations allows fast computation, enabling interactive visualization directly in a web browser with sub-second response times. As a case study, the level curves of a heat transfer problem involving a porous square cavity with four heated cylinders are rendered in real time, demonstrating the method's speed and flexibility. The framework supports interactive manipulation of geometric parameters, making it valuable for parametric studies, design optimization, and educational purposes. The approach is accessible, platform-independent, and requires no specialized software, offering a powerful alternative to traditional simulation workflows in heat transfer and related fields.

Keywords: R-functions · heat transfer · JavaScript

1 Introduction

Heat transfer remains a central topic in engineering, materials science, and applied physics, driven by needs in electronics cooling, energy systems, additive manufacturing, environmental control, and more. In the late five years, several challenges and trends have

H. Altenbach et al. (Eds.): CAMPE 2025, LNME, pp. 323–332, 2026.
https://doi.org/10.1007/978-3-032-16381-3_31

emerged that underscore how geometry of the domain and spatial/temporal structure of the temperature field significantly affect heat-transfer behavior, modelling, and design.

Advanced technologies such as compact heat exchangers, micro-electronics, and additive manufacturing demand fine control over thermal gradients, hotspots, temperature uniformity, and transient responses. Geometric complexity (e.g. fins, cavities, inclusions, porous media, curved boundaries) increasingly becomes unavoidable.

Non-uniform temperature fields within domains cause nonlinear behavior: material properties (thermal conductivity, heat capacity) often depend on temperature, internal heat generation may vary spatially, and phase change or moving boundaries may arise. Accurate prediction of the temperature distribution, both steady and transient, in realistic geometries is needed for reliability, energy efficiency, minimization of thermal stresses, and prevention of failure. Thus, studying geometry (shape, layout, size, orientation) and how it molds the temperature field within the domain is central to both modeling and optimization.

The heat transfer field increasingly recognizes that domain geometry is not just a boundary condition or external factor, but an active design variable that shapes the internal temperature field**,** which in turn governs performance, reliability, and efficiency. Advances in numerical methods, optimization, and materials allow ever more complex geometries to be exploited. Yet, balancing fidelity, cost, and manufacturability remains a central challenge. The future appears to lie in integrated geometry-temperature optimization, transient and multiphysics models, and better experimental tools to validate internal thermal fields.

The theory of R-functions originated by academician Rvachev V.L. provides a powerful framework for representing complex geometric domains via logical combinations (Boolean operations) of simpler implicitly defined shapes, enabling analytic or semi-analytic boundary representations. One of its major strengths is enforcing boundary conditions exactly on complicated geometries while maintaining smoothness and flexibility in domain definition. This makes R-functions potentially very well matched to heat transfer problems where domain shape has strong effect on internal temperature fields and boundary behavior.

R-functions theory offers strong advantages for modeling heat transfer in geometrically complex domains, particularly for exact boundary enforcement and flexible domain definitions. Given the surge in interest in precise geometry (new isogeometric methods, metamaterials, etc.), R-functions are well placed to play a larger role. Leveraging them for transient, convective, or optimization-driven heat transfer problems is a promising frontier.

2 Literature Review

Several recent works illustrate heat transfer problem researches, especially with respect to geometry and internal temperature fields.

In [1], a method combining the adjoint lattice Boltzmann approach with level set techniques was developed to optimize 2D/3D convection, accounting for porosity, diffusivity, and flow restrictions. A density-based topology optimization strategy for two-fluid heat exchangers is introduced in [2], handling internal channel design and interface control to balance fluid separation and thermal performance.

Additive manufacturing has enabled complex geometries, such as triply periodic minimal surfaces and porous frameworks, that improve heat transfer by enhancing internal surface area and flow interaction [3]. These structures have shown gains in Nusselt number and convective efficiency.

Phase change systems, as reviewed in [4], are highly sensitive to both container geometry and heat application strategies. Melting/solidification behavior depends not only on shape and orientation but also on convection and transient thermal loads. Dynamic heat sources, such as in laser melting, further influence thermal behavior.

Numerical approaches like the isogeometric finite volume method [5] help resolve curved boundaries precisely, improving simulation accuracy near complex surfaces. Similarly, geometric modifications in microchannel designs such as fins, ribs, porous inserts studied in [6], affect internal temperature fields by enhancing mixing or boundary layer control, though often at the cost of increased pressure drop and fabrication complexity.

In [7] the unsteady natural convection in a porous square enclosure with four diagonally aligned heated cylinders is numerically studied. Effects of cylinder spacing, Rayleigh, and Darcy numbers on heat transfer and flow symmetry are analyzed with the results that convective behavior intensifies at higher Ra and Da.

Over the past five years, R-functions have seen notable applications and demonstrate strong potential for broader adoption in future research and engineering practice. One significant example is mathematical and computational modeling of convective heat transfer in fuel element cartridges with varying rod geometries and packing configurations [8]. It uses R-functions to represent different packings of fuel rods in reactor cartridges and to model convective heat transfer, exploring how packing geometry (shape, arrangement) influences temperature and velocity distributions. It reduces the number of R-operations needed.

Another usage of R-functions is in structural/mechanical problems with complex planforms or shells [9]. The application of R-functions theory (together with high-order shell theory) studies free vibration of functionally graded shallow shells of arbitrary planform shapes. In that case, R-functions help define the geometric boundary and domain shape, enabling the variational Ritz method to handle arbitrary shell outlines.

In [10] free vibrations of porous functionally graded material plates with variable thickness resting on Winkler-Pasternak elastic foundations are analyzed via the R-functions method and Ritz procedure. Effects of porosity distribution, material gradient, thickness taper, foundation stiffness, boundary conditions, and plate geometry on natural frequencies are studied.

The study [11] presents a robust combination of R-functions and Ritz method for static and free vibration analysis of plates with arbitrary geometry, boundary conditions, and varying stiffness. A novel sub-cell integration approach improves accuracy, domain representation, and computational efficiency over conventional Ritz methods.

Made in [12] geometrically nonlinear analysis of variable-stiffness laminates via R-functions and Ritz method uses first-order shear deformation theory and asymptotic-numerical method. It handles complex plate shapes and arbitrary supports. Meshfree, efficient, accurate, and validated against finite element method it is useful for preliminary nonlinear design with reduced modeling effort.

Works [13] and [14] propose novel methods for defining feasible design and operational regions using R-functions and closed-form constraint approximations. These approaches avoid complex optimization and require minimal model evaluations. Work [13] focuses on feasibility analysis, validated through benchmark cases, while [14] introduces the R-DS identifier, which efficiently maps process design spaces, demonstrated on a batch reactor model, with improved performance over traditional sampling methods.

These works demonstrate how R-functions can aid heat-transfer-adjacent problems: i.e. geometry definition, boundary enforcement, coupling with other numerical methods (Galerkin, Ritz etc.), for improved modeling of fields that depend strongly on domain shape (temperature, flux, normals etc.).

Nikos Chamakos [15] introduced FEAScript, a lightweight, open-source JavaScript library for finite element analysis, aimed at making FEA more accessible for education and experimentation. Running directly in modern browsers, it supports both linear and non-linear heat transfer problems, allowing quick model testing before using larger solvers.

Several open-source projects focus primarily on applications related to 3D printing, such as ImpliSolid [16], a geometric modeling library for solid modeling using implicit surfaces, developed mainly in C++ and Python with minimal use of JavaScript (approximately 6.8%), and ImplicitCAD [17], a programmatic CAD tool written entirely in the Haskell programming language.

3 Research Methodology

Mathematical models of physical and mechanical fields are typically formulated as partial differential equations subject to specific boundary and initial conditions. A distinctive feature of these fields is that their behavior depends not only on the underlying physical laws encoded in the equations but also on the geometry and relative arrangement of the domains in which the fields exist. This dual nature, combining analytical (equational) and geometrical information, presents a central challenge in developing effective methods and algorithms for solving boundary value problems.

The wide variety, complexity, and uniqueness of geometric forms underscore the importance of an inverse problem in analytical geometry, originally posed by René Descartes: given a geometric object, determine its defining equation. This challenge is addressed by the theory of R-functions, developed by academician Rvachev V.L. The theory enables the representation of geometric objects using functions whose values encode boundary conditions, interior domains, and other geometric properties.

To construct such equations, the researcher must define appropriate support functions and a logical formula. By selecting suitable R-operations, it is possible to generate an analytical expression for the object's boundary. In general, a specific set of R-operations is employed to build these defining functions.

$$x \wedge_\alpha y = \frac{1}{1+\alpha}\left(x + y - \sqrt{x^2 + y^2 - 2\alpha xy}\right),$$
$$x \vee_\alpha y = \frac{1}{1+\alpha}\left(x + y + \sqrt{x^2 + y^2 - 2\alpha xy}\right), \quad (1)$$

$$\overline{x} = -x,$$

where $\alpha = \alpha(x, y)$, $-1 < \alpha \leq 1$.

Also, the property of function's normalization may be implemented

$$\left.\frac{\partial \omega_i}{\partial \nu_i}\right|_{\omega_i=0} = \pm 1 \tag{2}$$

where ν_i is a normal vector to $\partial\Omega_i$.

With the rapid development of modern information technologies, automating the visualization of mathematical functions has become increasingly accessible. This task can be approached in various ways, ranging from resource-intensive solutions that rely on complex software and hardware ecosystems, to more streamlined methods requiring only a basic understanding of programming. Among the latter, object-oriented programming has established itself as a dominant paradigm for implementing computational algorithms due to its modularity, reusability, and clarity.

One of the most versatile and lightweight object-oriented programming languages today is JavaScript**.** It offers a high-level syntax, is easily extensible for domain-specific applications, and, importantly, requires minimal system resources. Its wide accessibility is largely due to the fact that modern web browsers include built-in JavaScript engines capable of interpreting and executing code without the need for separate compilers or integrated development environments.

These JavaScript engines are continually updated alongside browser releases, incorporating support for the evolving features of the language. While HTML is used to structure the content of a web page and CSS defines its appearance, JavaScript brings dynamic behavior, allowing real-time interaction between the user and page elements. Together, these technologies provide a complete platform for interactive computational tools directly within the browser.

For researchers and educators, this means that developing, testing, and visualizing computational algorithms can be done using just a standard web browser and basic knowledge of JavaScript, HTML, and CSS. This browser-based environment eliminates the need for platform-specific software installations or heavy development frameworks. Moreover, since JavaScript code is interpreted at runtime and not compiled into binaries, it remains open and easily modifiable, enabling quick iteration and adaptation of computational models as research evolves.

Thus, implementing numerical algorithms and function visualizations using JavaScript presents a practical, accessible, and flexible approach. Its simplicity in deployment, cross-platform compatibility, and capacity for real-time interaction make it especially suitable for studying and solving a wide range of applied problems in science and engineering. This methodology not only accelerates the research process but also enhances transparency and collaboration through the use of openly readable and shareable code.

4 Results and Discussion

The construction of computational domains is performed using a set of R-operations, specifically, the R-conjunction, R-disjunction, and R-negation operations (1), (2), implemented in the JavaScript programming language. The method for constructing and visualizing arbitrary two-dimensional functions is divided into several sequential stages, each addressing a specific aspect of the overall process.

The first stage is preprocessing and parameter initialization that involves creating a subroutine that determines the global minimum and maximum values of the function within the defined domain. These extrema are essential for calculating the spacing between level curves. The uniform spacing is computed as the ratio of the maximum function value to the number of desired level curves or equivalently, the number of color gradations used to represent them visually. This ensures consistent and inter pretable contour intervals across the visualization.

Next, at legend and curve value annotation stage, a subroutine is implemented to display the numerical values corresponding to each level curve. These values are rendered in the upper-right corner of the canvas element, serving as a legend. This allows researchers to easily associate color-coded regions in the plot with their corresponding function values, enhancing interpretability.

The final stage is function visualization and plot rendering. It is dedicated to the core plotting routine. The visualization is constructed by scanning the canvas pixel-by-pixel, from top to bottom and left to right. At each pixel, which corresponds to a point in the domain, the value of the function is evaluated and mapped to the corresponding color level, based on the intervals determined in first stage. If the function value at a given point falls within a specific interval, it is assigned the corresponding color from the pre-defined palette, effectively producing a color-coded map of the function's level curves.

There is also optimization using R-function operators. To ensure computational efficiency, R-operations, specifically R-conjunction and R-disjunction, are implemented using index 1, which corresponds to the most computationally efficient form of these operations. This choice minimizes overhead and accelerates rendering, which is especially important when working with high-resolution visualizations or real-time interactive plotting.

As a demonstration of the method's efficiency, a two-dimensional plot (see Fig. 1) representing the level curves of a complete analytical function, describing a cross-section of a square-shaped porous enclosure containing four heated cylinders, as studied in [7], is computed and rendered.

When a relatively small inclusion is introduced into this domain, it can be interactively scaled up to reveal its heptagonal shape as a heat source (see Fig. 2). During this dynamic scaling process, the underlying function and corresponding level curves are recalculated in real time.

The shapes of small cut-outs can be examined in greater detail by scaling them up, regardless of whether they are elliptical, have nearly parallel edges, or take on another form defined by the underlying basis function (see Figs. 3 and 4).

The specific measurements corresponding to the charts presented in this paper are provided in Table 1.

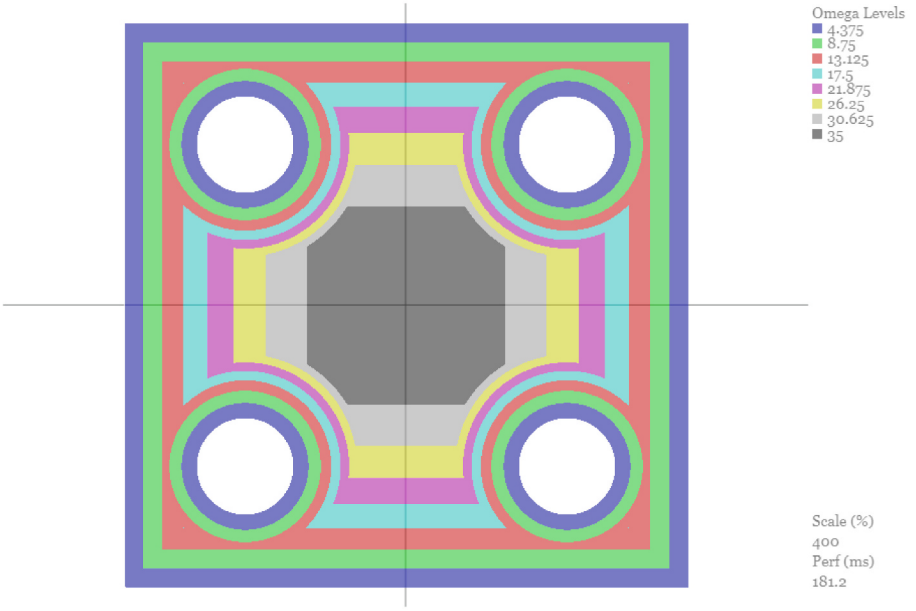

Fig. 1. Four heated cylinders in a cold square porous cavity, with the Cartesian grid scaled by 400%.

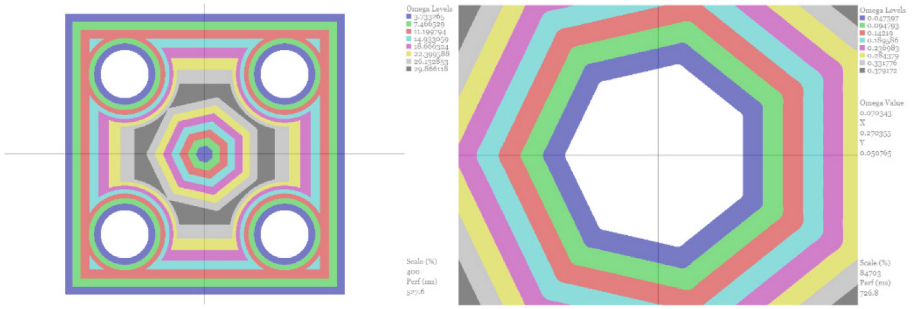

Fig. 2. Four heated cylinders with heptagonal inclusion in the center, with the Cartesian grid scaled by 400% (left) and 84,703% (right).

Moreover, the computational framework allows for real-time modification and visualization of the domain by dynamically adjusting key parameters. These include the number, positions, and sizes of the base geometric primitives. Each time the domain configuration is altered, the analytical function is automatically recomputed and re-rendered almost instantaneously, maintaining sub-second response times. This responsiveness is particularly valuable for parametric studies, interactive simulations, and design optimization tasks, where iterative adjustments to the geometry are common.

This rapid performance highlights the effectiveness of the JavaScript-based implementation in handling complex geometries and function evaluations without requiring

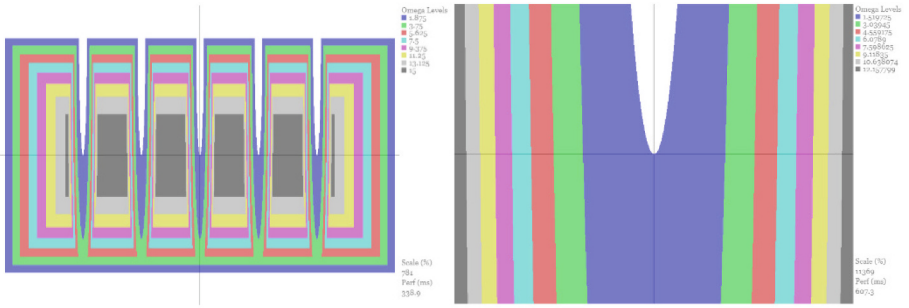

Fig. 3. Small elliptical cut-outs embedded within a rectangular domain, with the Cartesian grid scaled by 781% (left) and 11,369% (right).

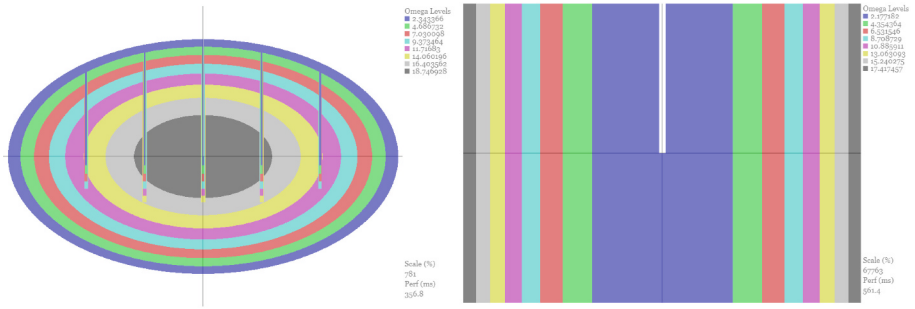

Fig. 4. Small rectangular cut-outs embedded in an elliptical domain, with the Cartesian grid scaled by 781% (left) and 67,763% (right).

Table 1. Efficiency of chart generation and rendering processes

Chart	Scale (%)	Basis functions (qty)	Performance (ms)
Figure 1	400	5	181.2
Figure 2 (left)	400	6	527.6
Figure 2 (right)	84,703	6	726.8
Figure 3 (left)	781	6	338.9
Figure 3 (right)	11,369	6	607.3
Figure 4 (left)	781	6	356.8
Figure 4 (right)	67,763	6	561.4

specialized computational resources. The use of R-functions enables this flexibility by providing a robust mathematical foundation for constructing and manipulating complex domain shapes through algebraic expressions. As a result, the visualization process becomes not only computationally efficient but also highly adaptable, supporting

exploratory analysis and rapid prototyping in applications such as heat transfer, fluid flow, and structural mechanics.

5 Conclusions

This study presents a lightweight, browser-based framework that integrates R-functions theory with modern JavaScript to model and visualize heat transfer domains. The approach enables key features for analyzing complex geometries in engineering applications such as exact boundary enforcement, smooth domain representation, and real-time rendering.

Unlike commercial tools (e.g., Altair Inspire, nTop, SimScale) that may be restricted by proprietary access or hardware demands, and open-source projects (e.g., ImplicitCAD, ImpliSolid) that require setup and lack browser-native interactivity, this framework offers a fully client-side solution. It allows researchers to evaluate analytical solutions at user-defined points within R-function-based domains, with interactive scaling and modification capabilities.

The platform is especially suited for iterative design, parametric studies, and educational use, avoiding the need for compilers or specialized simulation software. Future development directions include extending the framework to transient and 3D problems, incorporating additional physical phenomena, and integrating optimization tools.

To encourage community engagement, the core components are planned for open-source release, promoting broader adoption and collaborative development. Overall, this work shows that complex thermal modeling can be made accessible and dynamic through web technologies, highlighting the value of interdisciplinary, geometry-aware tools in modern engineering analysis.

References

1. Luo, J.-W., Chen, L., He, A., Tao, W.Q.: Topology optimization of convective heat transfer by the lattice Boltzmann method. Int. J. Numer. Meth. Fluids **95**(3), 421–452 (2023). https://doi.org/10.1002/fld.5153
2. Yan, K., Wang, Y., Yan, J.: Topology optimization of two fluid heat transfer problems for heat exchanger design. Comput. Model. Eng. Sci. **140**(2), 1949–1974 (2024). https://doi.org/10.32604/cmes.2024.048877
3. Barakat, A., Sun, B.B.: Enhanced convective heat transfer in new triply periodic minimal surface structures: numerical and experimental investigation. Int. J. Heat Mass Transf. **227**, 125538 (2024). https://doi.org/10.1016/j.ijheatmasstransfer.2024.125538
4. Sarath, K.P., Osman, M.F., Mukhesh, R., Manu, K.V., Deepu, M.: A review of the recent advances in the heat transfer physics in latent heat storage systems. Therm. Sci. Eng. Prog. **42**, 101886 (2023). https://doi.org/10.1016/j.tsep.2023.101886
5. Shakur, E., Marzok, A.: Isogeometric finite volume method for heat transfer simulations on curved spline-based geometries. Eng. Comput. (2025). https://doi.org/10.1007/s00366-025-02167-3
6. Yu, H., Li, T., Zeng, X., He, T., Mao, N.: A critical review on geometric improvements for heat transfer augmentation of microchannels. Energies **15**(24), 9474 (2022). https://doi.org/10.3390/en15249474

7. Nammi, G., Deka, D.K., Pati, S., Baranyi, L.: Natural convection heat transfer within a square porous enclosure with four heated cylinders. Case Stud. Therm. Eng. **30**, 101733 (2022). https://doi.org/10.1016/j.csite.2021.101733
8. Maksymenko-Sheiko, K.V., Sheiko, T.I., Lisin, D.O., Dudinov, T.B.: Mathematical and computer modeling of convective heat transfer in fuel cartridges of fuel elements with different shapes and packing of rods. J. Mech. Eng. **25**(1), 40–54 (2022). https://doi.org/10.15407/pmach2022.01.040
9. Kurpa, L., Shmatko, T.: Application of the R-functions method and shell theory of the higher-order to study free vibration of functionally graded shallow shells. In: Altenbach, H., et al. (eds.) CAMPE 2021, LNME, pp. 188–197. Springer, Cham (2023). https://doi.org/10.1007/978-3-031-18487-1_19
10. Kurpa, L., Pellicano, F., Shmatko, T., Zippo, A.: Free vibration analysis of porous functionally graded material plates with variable thickness on an elastic foundation using the r-functions method. Math. Comput. Appl. **29**(1), 10 (2024). https://doi.org/10.3390/mca29010010
11. Vescovini, R.: The R-functions combined with the Ritz method: an assessment on the integration schemes. Compos. Struct. **362**, 119066 (2025). https://doi.org/10.1016/j.compstruct.2025.119066
12. Vescovini, R., Foligno, P.P.: Geometrically nonlinear analysis of variable-stiffness plates using the R-functions combined with the Ritz method. Acta Mech. (2025). https://doi.org/10.1007/s00707-025-04412-8
13. Kucherenko, S., Shah, N., Klymenko, O.V.: Identification of feasible regions using R-functions. J. Process. Control. **154**, 103539 (2025). https://doi.org/10.1016/j.jprocont.2025.103539
14. Kucherenko, S., Shah, N., Klymenko, O.V.: Analytical identification of process design spaces using R-functions. Comput. Chem. Eng. **198**, 109112 (2025). https://doi.org/10.1016/j.compchemeng.2025.109112
15. Heat Transfer Finite Element Simulations in JavaScript using FEAScript by Nikos Chamakos. https://scribbler.live/2025/08/25/Heat-Transfer-Finite-Element-Simulations-in-JavaScript-using-FEAScript.html. Accessed 01 Sept 2025
16. ImpliSolid Homepage. https://sohale.github.io/implisolid/. Accessed 01 Sept 2025
17. ImplicitCAD Homepage. https://implicitcad.org/. Accessed 01 Sept 2025

Modelling of Effective Electroelastic and Dissipative Properties of Layered Piezocomposites

Oleh Derkach(✉)

Department of Oscillations and Vibrational Reliability, G.S. Pisarenko Institute for Problems of Strength of the National Academy of Sciences of Ukraine, Kyiv, Ukraine
derkach@ipp.kiev.ua

Abstract. In the present study an analytical method for the determination of effective elastic moduli, piezoelectric and dielectric constants of layered piezocomposites made of viscoelastic and electroviscoelastic materials is considered. The proposed method combines the Voigt and Reuss homogenization hypotheses for mechanical and electrical variables with the Fourier integral transform applied to hereditary-type constitutive equations and the Gauss elimination procedure. The concept of complex moduli is used to modelling of the effective dissipative properties. In order to take into account frequency-dependent properties of electroviscoelastic composites their effective properties modelling was provided in the Fourier frequency domain, which allows to derive properties of materials directly in the analysis without their additional transformations. Numerical results including effective electromechanical properties and elastic loss factor for periodic piezoceramic reinforced epoxy composites are presented. The model predicted results were compared with various experimentally obtained data for 2–2 and 1–3 piezocomposites. Qualitative agreement for the model results with known experimental data is shown. Proposed model can be employed in analysis of passive and active vibration damping of viscoelastic and electroviscoelastic heterogeneous structural elements with frequency-dependent elastic and dielectric energy losses.

Keywords: layered piezocomposite · electroviscoelastic material · effective properties; complex modulus · loss factor

1 Introduction

Piezoceramic composite transducers have numerous technical applications. Their composite structure is used to achieve high electromechanical properties. In particular, effective actuation and sensing capabilities in structural elements also can be achieved by using piezoelectric composites with transversely aligned piezoceramic reinforced elements in an epoxy matrix [1–3]. For example, well-known macro-fiber composites (MFC) [4] are one dimensional periodic piezoceramic fiber-reinforced layered actuator, in which combines the high electromechanical properties of piezoceramic materials with the flexibility

H. Altenbach et al. (Eds.): CAMPE 2025, LNME, pp. 333–343, 2026.
https://doi.org/10.1007/978-3-032-16381-3_32

and low specific weight of epoxy matrix. They have been serves as sensors and actuators in so-called smart structures in area of structural health monitoring, shape control, noise attenuation and active vibration control, etc. Two-dimensional periodic composites are usually composed of fibers made of polarized piezoelectric ceramic material and non-piezoelectric polymer matrix. This type of piezocomposites has been used as transducers for the underwater acoustic and bio-medical applications [1–3, 5].

The determination of the full set electromechanical properties of piezoelectric composites by given volume fractions, materials properties of the phases and their geometry are an important problem in the designing process of new sensors and actuators. For this purpose, analytical and numerical approaches have been applied. Exact analytical solutions of the problem are based on micromechanical models of composite materials are possible only for few particular types of the phases [6, 7]. Numerical approach consists on approximate determination of strain and stress state of the representative volume element at the taken boundary conditions. Although the abilities of contemporary computational equipments, this technique is still related with high computational efforts, especially in the case of time dependent properties of materials. In view of this effective properties of composites have been employed. To analyze the effective electromechanical constants, the average physical variables of the representative volume element to a uniform in-plane or out-of-plane mechanical and electrical loads are considered [6–9]. Based on the Voigt and Reuss hypotheses, the upper and lower bounds of the effective elastic, dielectric, and coupled properties can be obtained, respectively [7]. The combination of these hypotheses, as demonstrated in particular in [9, 10], makes it possible for a regular composite structure with plane parallel layers to determine effective properties that coincide with the exact values obtained from three-dimensional modeling of the representative volume element of the composite material.

Though, as is has been mentioned above the piezoceramic reinforced epoxy composites and piezoelectric polymers, which can be described by electroviscoelastic model of material have numerous technical applications experimental studies of their dissipative properties by using complex elastic, dielectric and piezoelectric constants are limited. On the actuality, lack of investigations and necessity of solving of this problem have been pointed out in [3]. There are very few analytical and numerical studies on the effective dissipative and electroviscoelastic properties of piezoelectric composite materials [9–12]. At the same time, complex constants of homogeneous piezoelectric and non-piezoelectric materials, which forms composite, can be relatively easy determined and used to modelling of effective properties of electroviscoelastic composites. The possibility of this approach has been demonstrated in [3, 11]. Besides, this approach seems attractive in view of which effective complex frequency-dependent moduli can be directly applied for analysis of non-stationary vibrations in the Fourier frequency domain.

The aim of this work is to develop a model of layered piezocomposites, based on the system of Voigt and Reuss hypotheses, for evaluating the complex-valued effective elastic, piezoelectric, and dielectric constants. Expressions for the effective moduli were obtained by using conditions of homogeneity for mechanical and electrical field variables, i.e. assuming that at certain loading conditions corresponding components of stress and strain vectors, and also components of electric displacement and electric field

vectors throughout the layered composite have to be constant. Energy losses in materials of composite layers were taken into account by using complex elastic moduli, complex piezoelectric and dielectric constants which are presented directly in the Fourier frequency domain. The approach to effective complex moduli obtaining is based on the usage of correspondence principle between quasistatic electro-viscoelasticity and static electroelasticity [3]. Hence, modelling of effective complex elastic moduli, piezoelectric and dielectric constants is carried out in terms of physical variables transformed in the frequency domain. To demonstrate the applicability of obtained expressions, numerical analysis of effective moduli, electromechanical coupling parameters, and effective elastic loss factors for one- and two-dimensional periodic piezoceramic reinforced epoxy composites are presented and compared with measurements which have been published in the literature.

2 Method of Analysis

Let consider a N-phased composite material consisting of perfectly bonded layers in the general case anisotropic electroviscoelastic materials. Element (Fig. 1) of layered composite is represented in an orthogonal coordinate system x_1, x_2, and x_3 so that the layers are parallel to the x_1x_3 plane.

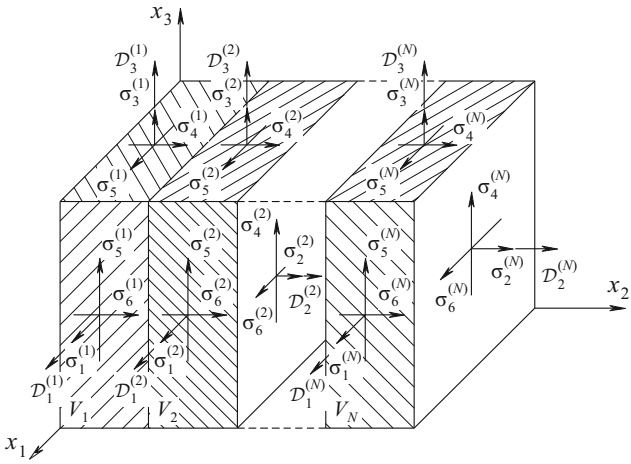

Fig. 1. Element of one dimensional periodic layered composite material.

The physical relations for k-th component of layered composite made of electroviscoelastic can be presented by using hereditary-type integral equation [3, 10]. However, they direct using for effective properties analysis is connected with the necessity of determination of relaxation functions parameters. This circumstance complicates an implementation of obtained effective properties of viscoelastic and electroviscoelastic materials for the vibration analysis of composite structural elements. Therefore, the usage of methods of direct analysis in the transformed Laplace or Fourier domains are

advisable with established correspondence principle [3]. Wherein, in [13] have been shown, that at the usage of Fourier frequency domain allows to take into account correctly experimentally obtained the complex moduli of materials without their additional transformations at an analysis of transient vibration. Thus, taking the Fourier transform ($\mathcal{F}$) to linear constitutive equations [3] of k-phase (layer) made of electroviscoelastic material we obtain constitutive equations in the transformed complex quantities in the Fourier frequency domain:

$$\begin{aligned}\hat{\sigma}^{(k)}(i\omega) &= \mathcal{F}\left(\boldsymbol{R}_C^{\mathcal{E}(k)} * \dot{\varepsilon}^{(k)} - \boldsymbol{R}_e^{(k)\boldsymbol{T}} * \dot{\mathcal{E}}^{(k)}\right) \equiv \\ &\equiv \hat{\boldsymbol{C}}^{\mathcal{E}(k)}(\omega)\hat{\boldsymbol{\varepsilon}}^{(k)}(i\omega) - \hat{\boldsymbol{e}}^{(k)\boldsymbol{T}}(\omega)\hat{\mathcal{E}}^{(k)}(i\omega);\end{aligned} \tag{1a}$$

$$\begin{aligned}\hat{\mathcal{D}}^{(k)}(i\omega) &= \mathcal{F}\left(\boldsymbol{R}_e^{(k)} * \dot{\varepsilon}^{(k)} + \boldsymbol{R}_\kappa^{\varepsilon(k)} * \dot{\mathcal{E}}^{(k)}\right) \equiv \\ &\equiv \hat{e}^{(k)}(\omega)\hat{\varepsilon}^{(k)}(i\omega) + \hat{\kappa}^{\varepsilon(k)}(\omega)\hat{\mathcal{E}}^{(k)}(i\omega),\end{aligned} \tag{1b}$$

where $\hat{\boldsymbol{\sigma}}^{(k)} = \left\{\hat{\sigma}_1^{(k)}\ \hat{\sigma}_2^{(k)}\ \cdots\ \hat{\sigma}_6^{(k)}\right\}^{\boldsymbol{T}}$ and $\hat{\boldsymbol{\varepsilon}}^{(k)} = \left\{\hat{\varepsilon}_1^{(k)}\ \hat{\varepsilon}_2^{(k)}\ \cdots\ \hat{\varepsilon}_6^{(k)}\right\}^{\boldsymbol{T}}$ are the representations of stress and strain vectors for k-phase ($k = 1, 2, \ldots, N$) in the space of Fourier transforms and $\hat{\mathcal{D}}^{(k)} = \left\{\hat{\mathcal{D}}_1^{(k)}\ \hat{\mathcal{D}}_2^{(k)}\ \hat{\mathcal{D}}_3^{(k)}\right\}^{\boldsymbol{T}}$, $\hat{\mathcal{E}}^{(k)} = \left\{\hat{\mathcal{E}}_1^{(k)}\ \hat{\mathcal{E}}_2^{(k)}\ \hat{\mathcal{E}}_3^{(k)}\right\}^{\boldsymbol{T}}$ are the same representations for electric displacement and electric field vectors (T is the transpose sign); $\boldsymbol{a} * \boldsymbol{b} \equiv \int_{-\infty}^{t} \boldsymbol{a}(t-\tau)\boldsymbol{b}(\tau)d\tau$ is the convolution of two vector-functions; $\dot{\boldsymbol{a}} \equiv d\boldsymbol{a}/d\tau$; t is the time; ω is circular frequency.

Obtained constitutive Eqs. (1) are similar to those which in linear theory of electroelasticity are, which exception that physical field variables, elastic moduli, dielectric and piezoelectric coefficients have been replaced by their complex values[1]: $\hat{C}^{\mathcal{E}(k)} = C^{\mathcal{E}(k)\prime} + iC^{\mathcal{E}(k)\prime\prime}$ and $\hat{\kappa}^{\epsilon(k)} = \kappa^{\epsilon(k)\prime} + i\kappa^{\epsilon(k)\prime\prime}$ are symmetric 6×6 and 3×3 non-Hermitian matrices of complex frequency-dependent elastic moduli and dielectric constants respectively; $\hat{\boldsymbol{e}}^{(k)} = \boldsymbol{e}^{(k)\prime} + i\boldsymbol{e}^{(k)\prime\prime}$ is 3×6 matrix of complex piezoelectric constants; $i = \sqrt{-1}$. Their real and imagine parts are positive definite and denoted by a prime and a double prime. They are sine and cosines Fourier transform of correspondent relaxation function matrices: $\boldsymbol{R}_C^{\mathcal{E}(k)}$, $\boldsymbol{R}_e^{(k)}$, and $\boldsymbol{R}_\kappa^{\varepsilon(k)}$.

The problem of obtaining the effective properties of composite electroviscoelastic material consists in determining the corresponding complex elements of the matrices $\hat{\boldsymbol{C}}^{\mathcal{E}}$, $\hat{\boldsymbol{\kappa}}^{\varepsilon}$, and $\hat{\boldsymbol{e}}$ from the known complex-valued matrices $\hat{\boldsymbol{C}}^{\mathcal{E}(k)}$, $\hat{\boldsymbol{\kappa}}^{\varepsilon(k)}$, and $\hat{\boldsymbol{e}}^{(k)}$ for each phase of composite material. Solution of this problem follows from the hypotheses, that at the certain homogeneous mechanical and electrical loadings the corresponding of physical variables in the composite material are constant through the layered structure [6, 7, 9].

Hence, for the layered representative volume element (Fig. 1) with one-dimensional periodic structure (2–2 connection type) we assume that continuity of physical fields across the interfaces is satisfied. For this purpose, the certain components of the strain $\hat{\boldsymbol{\varepsilon}}_s$ ($s = 2, 4, 6$) and stress $\hat{\boldsymbol{\sigma}}_r$ ($r = 1, 3, 5$) vectors at the corresponding uniform loadings

[1] For simplicity of notation, here and below we denote frequency domain values without circular frequency.

along (Voigt composite) and across (Reuss composite) the layers are take homogeneous. Other components of strain and stress vectors are obtained from the condition of static equilibrium of representative volume element [6, 9]. Due to the laminate configuration of composite, is assumed that the electric fields $\hat{\mathcal{E}}_p$ $(p = 1, 3)$ distributed uniformly in the layers. Thus, the electric displacement $\hat{\mathcal{D}}_n$ $(n = 3)$ is continuous across phase boundaries in the laminate [6–8]. It should be noted that the present homogenization assumptions are applicable to sufficiently thin layers compared with their in-plane dimensions. When the ratio of layer thickness to in-plane size increases, the mismatch of out-of-plane strains between adjacent layers may cause additional interlaminar stresses and alter the effective properties. To emphasize the main coupling effects within the bulk layers while avoiding additional uncertainties, the present model neglects the presence of an interphase layer with distinct mechanical and dissipative properties, which could partially accommodate the out-of-plane strain mismatch and influence the effective response.

The advantage of the proposed method, which combines the Voigt and Reuss hypotheses with a subsequent Gauss elimination procedure applied to complex-valued matrix equations, lies in the fact that the evaluation of the effective constants does not require the stationarity of the potential energy functional of the considered system. This makes it possible to avoid the problem of ensuring the correctness of the obtained solutions, which arises from the fact that the energy functional of a non-conservative system is sesquilinear, and the reliability of the numerical solution usually requires more sophisticated approaches, such as the introduction of internal variables or the construction of an appropriate functional space [14, 15]. However, it should be noted that the application of the approaches considered in the present work requires a proper Gauss elimination procedure for non-Hermitian matrices, which can be controlled during the computations.

From the prescribed above conditions of continuity for the stresses and strains, electric induction and electric field vectors there we have the following equations:

$$\hat{\boldsymbol{\sigma}}_r = \sum_{k=1}^{N} v_k \hat{\boldsymbol{\sigma}}_r^{(k)}, \hat{\boldsymbol{\varepsilon}}_s = \sum_{k=1}^{N} v_k \hat{\boldsymbol{\varepsilon}}_s^{(k)}, \hat{\boldsymbol{\varepsilon}}_r = \hat{\boldsymbol{\varepsilon}}_r^{(k)}, \hat{\boldsymbol{\sigma}}_s = \hat{\boldsymbol{\sigma}}_s^{(k)} \quad (r = 1, 3, 5;\ s = 2, 4, 6); \tag{2a}$$

$$\hat{\mathcal{D}}_p = \sum_{k=1}^{N} v_k \hat{\mathcal{D}}_p^{(k)}, \hat{\mathcal{E}}_n = \sum_{k=1}^{N} v_k \hat{\mathcal{E}}_n^{(k)}, \hat{\mathcal{E}}_p = \hat{\mathcal{E}}_p^{(k)}, \hat{\mathcal{D}}_n = \hat{\mathcal{D}}_n^{(k)} \quad (p = 1, 3;\ n = 2), \tag{2b}$$

where $v_k = V_k \Big/ \sum_{k=1}^{N} V_k$ are the coefficients of reinforcement determining the volume fraction of the k-th phase.

In order to get compact form of the Eq. (2), the vectors of physical variables were represented in the form of block matrices:

$$\hat{\boldsymbol{S}}_i = \sum_{k=1}^{N} v_k \hat{\boldsymbol{S}}_i^{(k)},\ \hat{\boldsymbol{S}}_j = \hat{\boldsymbol{S}}_j^{(k)}\ (i \leftrightarrow r, p;\ j \leftrightarrow s, n); \tag{3}$$

$$\hat{\boldsymbol{P}}_j = \sum_{k=1}^{N} v_k \hat{\boldsymbol{P}}_j^{(k)},\ \hat{\boldsymbol{P}}_i = \hat{\boldsymbol{P}}_i^{(k)}\ (i \leftrightarrow r, p;\ j \leftrightarrow s, n) \tag{4}$$

where

$$\hat{\boldsymbol{S}}_i = \left[\hat{\boldsymbol{\sigma}}_r\ \hat{\mathcal{E}}_n\right]^{\boldsymbol{T}},\ \hat{\boldsymbol{S}}_j = \left[\hat{\boldsymbol{\sigma}}_s\ \hat{\mathcal{E}}_p\right]^{\boldsymbol{T}};\ \hat{\boldsymbol{P}}_i = \left[\hat{\boldsymbol{\varepsilon}}_r\ \hat{\mathcal{D}}_n\right]^{\boldsymbol{T}},\ \hat{\boldsymbol{P}}_j = \left[\hat{\boldsymbol{\varepsilon}}_s\ \hat{\mathcal{D}}_p\right]^{\boldsymbol{T}}.$$

The physical relations (1) we also represent in block form, corresponding to the division of the vectors (3) and (4):

$$\begin{aligned}\hat{\boldsymbol{S}}_i^{(k)} &= \hat{\boldsymbol{L}}_{ii}^{(k)}\hat{\boldsymbol{P}}_i^{(k)} + \hat{\boldsymbol{L}}_{ij}^{(k)}\hat{\boldsymbol{P}}_j^{(k)};\\ \hat{\boldsymbol{S}}_j^{(k)} &= \hat{\boldsymbol{L}}_{ji}^{(k)}\hat{\boldsymbol{P}}_i^{(k)} + \hat{\boldsymbol{L}}_{jj}^{(k)}\hat{\boldsymbol{P}}_j^{(k)},\end{aligned} \tag{5}$$

where each block-matrix $\hat{\boldsymbol{L}}^{(k)}$ is portioned into four blocks, which in turn were obtained from matrices of complex coefficients of material:

$$\hat{\boldsymbol{L}}_{ii}^{(k)} = \begin{bmatrix} \hat{\boldsymbol{C}}_{rr}^{\mathcal{D}(k)} & -\hat{\boldsymbol{h}}_{rn}^{(k)} \\ -\hat{\boldsymbol{h}}_{nr}^{(k)} & \hat{\boldsymbol{\beta}}_{nn}^{\varepsilon(k)} \end{bmatrix}, \hat{\boldsymbol{L}}_{ij}^{(k)} = \begin{bmatrix} \hat{\boldsymbol{C}}_{rs}^{\mathcal{D}(k)} & -\hat{\boldsymbol{h}}_{rp}^{(k)} \\ -\hat{\boldsymbol{h}}_{ns}^{(k)} & \hat{\boldsymbol{\beta}}_{np}^{\varepsilon(k)} \end{bmatrix}, \hat{\boldsymbol{L}}_{jj}^{(k)} = \begin{bmatrix} \hat{\boldsymbol{C}}_{ss}^{\mathcal{D}(k)} & -\hat{\boldsymbol{h}}_{sn}^{(k)} \\ -\hat{\boldsymbol{h}}_{ns}^{(k)} & \hat{\beta}_{nn}^{\varepsilon(k)} \end{bmatrix}. \tag{6}$$

In Eq. (6) the following dependencies were used:

$$\hat{\boldsymbol{C}}^{\mathcal{D}} = \hat{\boldsymbol{C}}^{\mathcal{E}} + \hat{\boldsymbol{e}}^T\hat{\boldsymbol{h}}, \hat{\boldsymbol{h}} = \hat{\boldsymbol{\beta}}^{\varepsilon}\hat{\boldsymbol{e}},\ \hat{\boldsymbol{\beta}}^{\varepsilon} = \left(\hat{\boldsymbol{\kappa}}^{\varepsilon}\right)^{-1}. \tag{7}$$

Substituting derived results into Eqs. (3)–(4) we obtain representations in the space of Fourier transforms of some physical field's variables (stress, strain, electric displacement and electric field) averaged over the representative element of layered composite made of electroviscoelastic material. Their dependence can be represented in the form of the following system of equations with complex coefficients:

$$\begin{aligned}\hat{\boldsymbol{S}}_i &= \hat{\boldsymbol{L}}_{ii}\hat{\boldsymbol{P}}_i + \hat{\boldsymbol{L}}_{ij}\hat{\boldsymbol{P}}_j;\\ \hat{\boldsymbol{S}}_j &= \hat{\boldsymbol{L}}_{ji}\hat{\boldsymbol{P}}_i + \hat{\boldsymbol{L}}_{jj}\hat{\boldsymbol{P}}_j,\end{aligned} \tag{8}$$

where

$$\begin{aligned}\hat{\boldsymbol{L}}_{ii} &= \sum\nolimits_{k=1}^{N}\left(\hat{\boldsymbol{L}}_{ii}^{(k)} - \hat{\boldsymbol{L}}_{ij}^{(k)}\left(\hat{\boldsymbol{L}}_{jj}^{(k)}\right)^{-1}\hat{\boldsymbol{L}}_{ji}^{(k)}\right) + \hat{\boldsymbol{L}}_{ij}\hat{\boldsymbol{L}}_{jj}\hat{\boldsymbol{L}}_{ji},\\ \hat{\boldsymbol{L}}_{ij} &= \left(\sum\nolimits_{k=1}^{N}\hat{\boldsymbol{L}}_{ij}^{(k)}\left(\hat{\boldsymbol{L}}_{jj}^{(k)}\right)^{-1}\right)\hat{\boldsymbol{L}}_{jj},\ \hat{\boldsymbol{L}}_{ji} = \hat{\boldsymbol{L}}_{ij},\ \hat{\boldsymbol{L}}_{jj}^{(k)} = \left(\sum\nolimits_{k=1}^{N}\left(\hat{\boldsymbol{L}}_{jj}^{(k)}\right)^{-1}\right)^{-1}.\end{aligned} \tag{9}$$

Hence, in Eq. (8) the relation between the vectors of averaged mechanical and electrical variables by means matrices of effective complex elastic moduli, complex piezoelectric and dielectric coefficients is establishing.

3 Comparison Between Model Predicted and Experimental Results

To give a validation of the presented model of layered composite material, effective properties of a two-phase lossless electroelastic and dissipative electroviscoelastic composites are analyzed and compared with experimental data reported in the literature [1–3, 12, 13]. We will focus on capturing the effect of piezoceramic fibers (1–3 piezocomposite) and layers (2–2 piezocomposite) volume fraction in the non-piezoelectric epoxy and piezoelectric copolymer matrices on effective electromechanical and damping properties. Elastic moduli, piezoelectric coefficients and relative values of the dielectric permittivity coefficients of the piezoelectric materials used in calculations are shown in Table 1.

The basic material constants and electromechanical coupling parameters, such as short-circuit $\left(C_{33}^{\mathcal{E}}\right)$ and open-circuit $\left(C_{33}^{\mathcal{D}}\right)$ elastic moduli, thickness electromechanical coupling constant ($k_t = \sqrt{1 - C_{33}^{\mathcal{E}\prime} / C_{33}^{\mathcal{D}\prime}}$), and piezoelectric ($d_{33}$) constants are taken for comparative analysis.

Primarily we made comparative analysis of a set of the test values with computed results of the effective moduli of an 1–3 piezocomposite, whose fibers are aligned along the direction x_3, and both the piezoceramic fibers and matrix made of piezopolymer are poled along the same direction. Figure 2 illustrate the variation in the short-circuit and open-circuit elastic moduli, electromechanical coupling constant, and relative dielectric permittivity at constant strain, their model predicted values and experimental data [2] for TZL-5/VDF-TrFE piezocomposite (Table 1). The solid and dashed lines indicate the computed results, and the symbols denote the experimental data; a good agreement between the two sets of results is observed.

Table 1. Material data of the piezoelectric materials.

Parameter	TZL-5 [2]	VDF [2]	PZT 7A [1]	PZT-5A [3]	PZT P188 [12]
$C^{\varepsilon}{}_{11} = C^{\varepsilon}{}_{22}$ (GPa)	126	8.5	148.0	$121.0 + i\bullet 0.885$	$145.33 + i\bullet 1.82$
$C^{\varepsilon}{}_{12}$ (GPa)	79.5	3.6	76.2	$75.2 + i\bullet 0.061$	$102.57 + i\bullet 1.28$
$C^{\varepsilon}{}_{13} = C^{\varepsilon}{}_{23}$ (GPa)	84.1	3.6	74.2	$75.2 + i\bullet 0.061$	$98.65 + i\bullet 1.23$
$C^{\varepsilon}{}_{33}$ (GPa)	109	9.9	131.0	$111.0 + i\bullet 0.71$	$129.8 + i\bullet 1.63$
$C^{\varepsilon}{}_{44} = C^{\varepsilon}{}_{55}$ (GPa)	23	1.9	25.4	$21.1 + i\bullet 0.634$	$20.12 + i\bullet 0.25$
$C^{\varepsilon}{}_{66}$ (GPa)	23.5	2.45	35.9	$21.1 + i\bullet 0.634$	$20.53 + i\bullet 0.26$
$e_{15} = e_{24}$ (C/m2)	17	− 0.002	9.2	$12.3 - i\bullet 0.291$	12.37
$e_{31} = e_{32}$ (C/m^2)	− 6.5	0.008	− 2.1	$-5.4 + i\bullet 0.574$	− 8.03
e_{33} (C/m^2)	24.8	− 0.29	9.5	$15.8 + i\bullet 0.27$	15.5
$\kappa^{\varepsilon}{}_{11}/\kappa_0$[1] = $\kappa^{\varepsilon}{}_{22}/\kappa_0$	4200	9.0	235	$916 - i\bullet 18.3$	16.2
$\kappa\varepsilon_{33}/\kappa_0$	4200	9.0	235	$830 - i\bullet 16.3$	14.15

[1] $\kappa_0 = 8.85\bullet 10^{-12}$ F/m

The model also covers calculation of effective piezoelectric charge constant d_{33} of fiber-reinforced PZT 7A/Araldite D 1–3 (Fig. 3, a) and laminated PZT-5A/Cement 2–2 composite materials (Fig. 3, b). Electromechanical parameters of piezoelectric reinforced elements are prescribed in Table 1. Bulk and shear moduli of Araldite D matrix [2] are 5.6 GPa and 1.8 GPa, respectively; relative dielectric permittivity is 4. The cement matrix equating with following properties [16]: Young's modulus is 13.9 GPa, Poisson's ratio

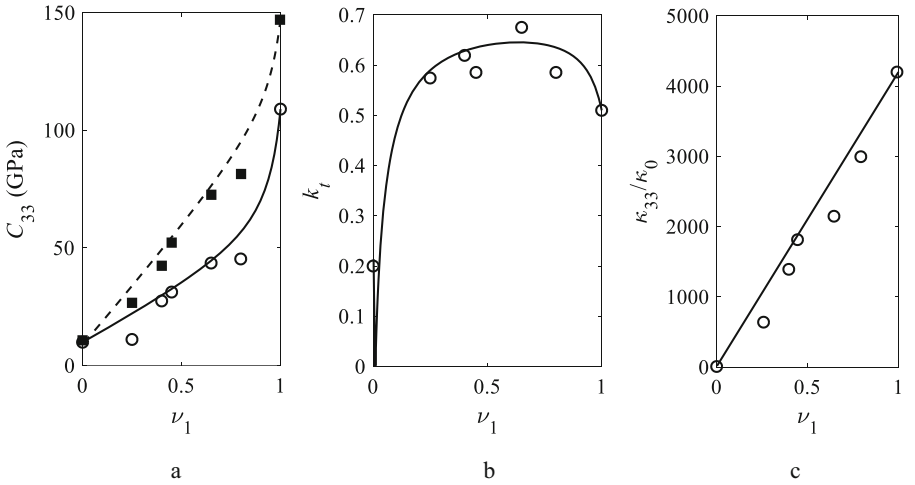

Fig. 2. Comparison between model predictions (lines) and measured values (symbols) [2] of TZL-5/ VDF-TrFE composite properties as a function of piezoceramic volume fraction: short-circuit elastic modulus $C^{\mathcal{E}}{}_{33}$ (solid line) and open-circuit elastic modulus $\left(C^{\mathcal{D}}_{33}\right)$ (dashed line) (a); thickness coupling constant k_t (b); relative dielectric permittivity ($\kappa_0 = 8.85{\cdot}10^{-12}$ F/m) (c).

is 0.2; relative dielectric permittivity is 19. Only the inclusion phase was polarized. As can be seen, the predicted effective properties are in good agreement with experimental data obtained for 1–3 and 2–2 composites.

Although experimental studies of energy dissipation in electroviscoelastic composite materials are limited, in order to demonstrate applicability of proposed model to these purposes we established dependencies of the effective loss factor and made their matching with known experimental [3] and numerical [12] results. In Fig. 5, the effective loss factor of the PZT/epoxy composites are shown for varying volume fraction of the PZT fibers. The loss factor was evaluated by the formula [3].

$$\eta = \mathrm{Im}\left(\hat{C}^{\mathcal{E}}_{11} - \left(\hat{C}^{\mathcal{E}}_{13}\right)^2 \Big/ \hat{C}^{\mathcal{E}}_{33}\right) \Big/ \mathrm{Re}\left(\hat{C}^{\mathcal{E}}_{11} - \left(\hat{C}^{\mathcal{E}}_{13}\right)^2 \Big/ \hat{C}^{\mathcal{E}}_{33}\right).$$

Experimentally obtained [3] values of loss factors (Fig. 4, a) were established for PZT-5A/Epoxy FM 73 layered electroviscoelastic composite. Parameters of reinforced piezoceramic material are prescribed in Table 1, properties of epoxy matrix are follow [3]: complex Young's modulus is $2.72{\cdot}(1 + i{\bullet}0.039)$ GPa; Poisson's ratio is 0.3; relative values of complex dielectric permittivity are $\kappa^{\mathcal{E}}{}_{11}/\kappa_0 = \kappa^{\mathcal{E}}{}_{22}/\kappa_0 = (4.43 + i{\bullet}0.059)$, $\kappa^{\mathcal{E}}{}_{33}/\kappa_0 = 4.43$.

In [12] 3-D finite element method (FEM) analysis of lossless piezoceramic PZT 188 (Table 1) fiber element periodically reinforced in the dissipative epoxy (EPON828) matrix was implemented for loss factor dependence on piezoceramic volume fraction (Fig. 4, b). The viscoelastic epoxy matrix with the following parameters was considered: complex Young's modulus is $2.69{\cdot}(1 + i{\cdot}0.039)$ GPa; Poisson's ratio is 0.36; dielectric permittivity is $44{\cdot}10^{-6}$ F/m.

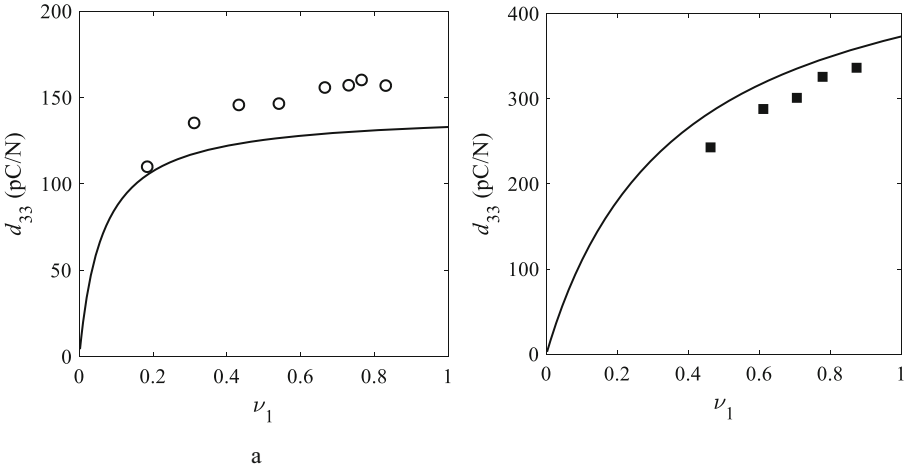

a

Fig. 3. Effective piezoelectric charge constant d_{33} for PZT 7A/Araldite D 1–3 piezocomposite (a) [1], and PZT-5A/Cement 2–2 piezocomposite (b) [16]: predicted (lines) and experimental data (symbols).

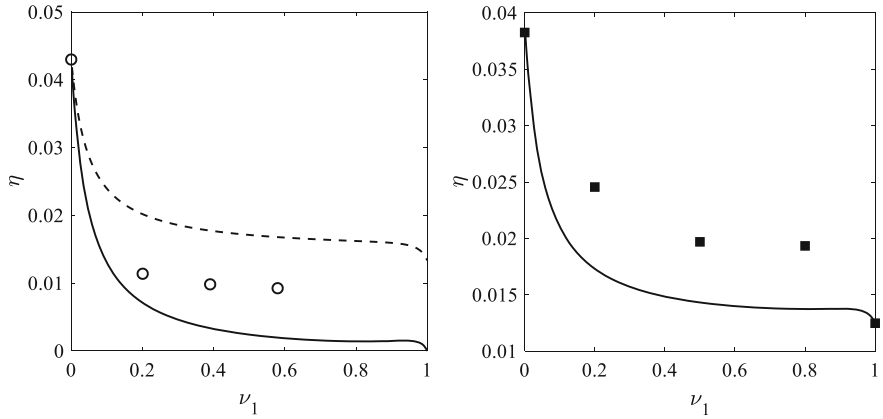

a b

Fig. 4. Loss factor η of piezoceramic reinforced epoxy laminate as a function of piezoceramic volume fraction: PZT-5A reinforced FM 73 epoxy (a), experimental data (circles) [3], predicted with (dashed line) and without (solid line) ceramic damping; PZT 188/EPON828 composite (b) obtained using FEM [12] (squares) and predicted (solid line).

4 Summary

A model of layered electroviscoelastic composites has been presented, based on the direct use of complex elastic, dielectric, and piezoelectric coefficients in the Fourier frequency-domain formulation and solved using Gauss elimination. Transformed in the frequency domain equations were derived that provide a framework for modelling of the effective

complex elastic moduli, complex-valued piezoelectric and dielectric constants which are required for energy dissipation analysis in nonhomogeneous materials, piezocomposite sensors and actuators with electroviscoelastic properties.

The model predicted results were compared with various experimentally obtained data which have been presented in the literature. Effective properties of piezoceramic reinforced epoxy composites are also analyzed. Their agreed with published results was shown. For simplicity, a mathematical model was developed for the one-dimensional periodic layered composites (2–2 type connectivity), but it is shown, that the conclusions are also valid for the two-dimensional composite structures (1–3 type composite).

Proposed model can be employed in analysis of passive and active vibration damping of viscoelastic and electroviscoelastic heterogeneous structural elements, to evaluate frequency-dependent elastic and dielectric energy losses, and losses caused by the electromechanical transformations in piezoelectric composite elements subjected to non-stationary electromechanical loads [13].

References

1. Chan, H.L.W., Unsworth, J.: Simple model for piezoelectric ceramic/polymer 1–3 composites used in ultrasonic transducer application. IEEE Trans. Ultrason. Ferroelectr. Freq. Cont. **36**, 434–441 (1989)
2. Taunaumang, H., Guy, I.L.: Electromechanical properties of 1–3 piezoelectric ceramic/piezoelectric polymer composites. J. Appl. Phys. **76**, 484–489 (1994)
3. Li, J., Dunn, M.L.: Viscoelastic behavior of heterogeneous piezoelectric solids. J. Appl. Phys. **89**, 2893–2903 (2001)
4. Bent, A.A.: Piezoelectric Fiber Composites For Structural Actuation. MIT (1994)
5. Ramos, R.R., Otero Hernandez, J.A., Castillero, J.B., Sabina, F.J.: Electromechanical properties of laminated piezoelectric composite. Mech. of Compos. Mat. **32**, 286–291 (1996)
6. Chen, T.: Exact moduli of layered piezoelectric media. Int. J. Solids Struct. **34**, 847–858 (1997)
7. Kim, B.-C., Baltazar, A., Kim, J.-Y.: Effective properties of multi-layered multi-functional composites. Adv. Compos. Mat. **18**, 153–166 (2009)
8. Sakthivel, M., Arockiarajan, A.: An analytical model for predicting thermo-electro-mechanical response of 1–3 piezoelectric composites. Comp. Mat. Sci. **41**, 759–767 (2010)
9. Derkach, O.L., Zinkovskii, A.P., Savchenko, K.V., Onyshchenko, Ye.O.: Evaluation of the effective characteristics of energy dissipation in layered composites. Mater. Sci. **57**. 782–791 (2022)
10. Derkach, O., Zinkovskii, A., Onyshchenko, Ye., Kobzar, V.: On the application of energy method for the numerical evaluation of the effective dissipative properties of composites. In: 2022 IEEE 3rd KhPI Week on Advanced Technology (KhPIWeek), 3–7 Oct. 2022, 343–347 (2022)
11. Jiang, B., Batra, R.C.: Effective electroelastic properties of a piezocomposite with viscoelastic and dielectric relaxing matrix. J. of Int. Mat. Syst. and Struct. **12**, 847–866 (2001)
12. Pastor, J., Richard, C., Nguyen Viet, H.: Predicting the losses and the efficiency of a 1–3 piezo-composite transducer through a partial homogenization method. Bol. Soc. Esp. Cerám. Vidrio. **41**, 171–176 (2002)
13. Derkach, O.L., Zinkovskyi, A.P., Savchenko, O.V.: Active damping of nonstationary vibrations of a three-layer electro-viscoelastic composite plate. Strength Mater. **52**, 876–888 (2020)

14. Simo, J.C., Hughes, T.J.R.: Computational Inelasticity, 1st edn. Springer, New York, NY (1998)
15. Amendola, G., Fabrizio, M., Golden, J.M.: Thermodynamics of Materials with Memory. 2nd edn. Springer Cham, Switzerland (2021)
16. Fu, C., Wang, Z., Jin, X., Zhu, X., Zhu, J.: Effective piezoelectric coefficients of cement-based 2–2 type piezoelectric composites based on a multiscale homogenization model. Comp. Struct. **194**, 170–177 (2018)

Strength Analysis of Nuclear Power Plant Protective Elements During Airplane Crash

Natalia Smetankina[1](✉), Anatolii Vasiliev[1], and Wei Han[2]

[1] Anatolii Pidhornyi Institute of Power Machines and Systems of the National Academy of Sciences of Ukraine, 2/10, Komunalnykiv Street, Kharkiv 61046, Ukraine
nsmet@ipmach.kharkov.ua

[2] Jinlin University, Road Huojv, 75, Changchun, China

Abstract. Ensuring reliable and accident-free performance is the foremost condition for nuclear power plant operation. This entails preventing the release of radioactive materials beyond established safety limits under all normal and emergency conditions, as well as under any internal or external influences. When designing nuclear power facilities, engineers carefully analyze the possible influences of natural phenomena and anthropogenic events. One of the mandatory modern safety considerations is the assessment of potential aircraft impacts on nuclear power plant structures. Due to the challenges and limitations associated with carrying out large-scale experiments, numerical modeling of protective components under normal and extreme conditions has become particularly relevant. This paper proposes a simulation-based approach for studying the load-bearing capacity of nuclear containment structures in case of a military aircraft impact. The study investigates the influence of the containment's design and structural configuration on its overall strength and resistance to impact loads. The results make it possible to identify the most effective and promising design options from the standpoint of safety and structural integrity.

Keywords: High-Risk Facility · Protective Cover · Airplane Strike

1 Introduction

Energy is one of the key pillars of stable economic development for the global community [1, 2]. A special role belongs to nuclear power plants (NPPs), which offer significant advantages over hydroelectric and thermal power facilities. This, in turn, highlights the importance of maintaining operational safety and reliability of NPPs [3]. To achieve this, it is essential to establish a comprehensive safety system [4, 5] capable of withstanding both external and internal impacts.

Recommendations are continuously being developed to assess NPPs vulnerability to accidental external events that were not foreseen in the original design under the auspices of the International Atomic Energy Agency (IAEA). Such events may include both natural and human-induced impacts, such as explosions at industrial sites, pipeline ruptures, hazardous material leaks from storage tanks, and the crash of an aircraft or its

H. Altenbach et al. (Eds.): CAMPE 2025, LNME, pp. 344–351, 2026.
https://doi.org/10.1007/978-3-032-16381-3_33

debris [6, 7]. Although the probability of an aircraft crash impacting a nuclear facility is extremely low, such an event would impose significant dynamic loads on the plant's structures and equipment.

In earlier designs of NPPs, the mass of a potentially impacting aircraft was assumed to be approximately 5 tons. Modern NPPs, however, are designed to account for the possible impact of an aircraft with a mass of up to 20 tons. Due to the complexity of numerical simulations, the collision between an aircraft and NPP protective structures is often modeled using a simplified one-dimensional representation of a flying body [8, 9], and is typically treated as a quasi-static process. Although full-scale experimental tests are extremely resource-intensive, they continue to be conducted to validate and substantiate the adequacy of computational models. Currently, analyses commonly consider the potential impact of military, commercial, and civil aircraft on nuclear facilities.

Most modern containment structures are made of reinforced or pre-stressed reinforced concrete, typically in the form of large cylindrical shells. Several design configurations for containment domes are used: (1) a flat dome, (2) a hemispherical dome, and (3) a flat cover. The shells generally include a steel liner on the inner surface, and in some cases, an additional outer liner.

This study aims to analyze the structural integrity of a nuclear power plant containment cover of the third type – namely, the flat cover – under the aircraft impact conditions. The problem solution is derived from a multilayer structures theory and incorporates data from in-situ tests [10].

2 Literature Review

In analyzing aircraft impacts on NPP protective barriers, one must consider the dynamic loads arising from the collision resulting from the destruction of the fuselage and engines, as well as the potential explosion of aviation fuel. In such cases, irreversible deformations within the structures are permissible, and the width of concrete cracks is not limited, provided that these deformations do not compromise the overall safety conditions of the NPP. Consequently, the problem of assessing the structural strength of containment systems is highly complex. Research devoted to evaluating the effects of aircraft impacts on NPP containment structures is therefore of particular current relevance.

In [5], the aircraft impact on reinforced concrete barrier was investigated. Finite element fracture modeling was combined with the Smoothed Particle Hydrodynamics. The degree of structural damage during impact was quantified as the proportion of the destroyed volume using an integrated deterministic–probabilistic approach.

In [10], the finite element analysis was carried out to examine the reactor containment's response to impacts from various aircraft types. Normal impacts along the containment surface and near the dome–cylindrical junction were considered. A three-dimensional deformable reinforced concrete structure was modeled, and the aircraft load was defined using the corresponding time-dependent response curve. The analysis showed that the protective structure would collapse if struck by a large commercial airplane.

In another study [11], numerical simulations of reinforced concrete containment structure using the finite element method were concluded. Simulations considered impact

points at cylindrical section center, between spherical dome and cylinder junction, and closer to foundation. The dynamic load from the aircraft was modeled using a time-dependent response function, with elastic–plastic deformation of the steel reinforcement included. It was found that the central part of the protective dome and the cylindrical wall experience the most significant deformations.

Further research [12, 13] focused on creating finite element models to simulate the impact of large aircraft on reinforced concrete containment structures. The studies examined the influence of aircraft velocity, impact angle, and collision height on the dynamic response of the containment system.

Overall, the strength analysis of NPP structures is most frequently conducted using discretization-based methods such as the finite element approach. However, development of analytical methods to evaluate NPP structures strength taking into account their heterogeneous composition remains an urgent and important task. Such approaches would contribute to reducing both the design time and the overall cost of constructing nuclear power plant containment structures.

3 Research Methodology

In this study, the third type of NPP containment cover – a flat circular plate – is considered. This configuration is commonly used in several European Community countries [14] because it provides convenient access to internal equipment and facilitates maintenance operations.

As the impact load pulse, the "IAEA Pulse" [14, 15] was selected, as it is considered the most reliable and experimentally validated model for simulating aircraft impacts. Figure 1 illustrates the IAEA-recommended time dependence of the impact load $P_{\text{ipm}}(t)$ (Fig. 1a) and the corresponding area of load application $S_{\text{ipm}}(t)$ (Fig. 1b), which accounts for deformation of the impacting body during a vertical collision of an aircraft with a mass of 20 tons on a flat surface.

This loading profile corresponds to experimental data obtained from full-scale impact tests involving a Phantom RF-4E fighter jet. The results of these experiments demonstrated that approximately 94% of the aircraft's kinetic energy was dissipated in its own destruction, while only the remaining 6% contributed to damage in the impacted structure.

An analysis is performed for a multilayer NPP containment structure, which comprises several interacting layers. The plate occupies a domain Ω enclosed by an arbitrary contour B:

$$x_B = x_B(\theta), \;\; y_B = y_B(\theta).$$

The first layer outer surface is taken as the reference coordinate surface.

The plate is subjected to nonstationary loads $\mathbf{F} = \{f_\alpha(t)\}$, $\alpha = \overline{1,\ 3\text{I}+3}$, where t is time. In particular, the impact load is given $f_3 = P_{\text{ipm}}(t)$ as shown in Fig. 1a. This load is applied over a circular area $S_{\text{ipm}}(t)$ (Fig. 1b).

The kinematic hypotheses of shear deformation, thickness compression and inertia of rotation of normal elements within each layer are used to describe the deformation of

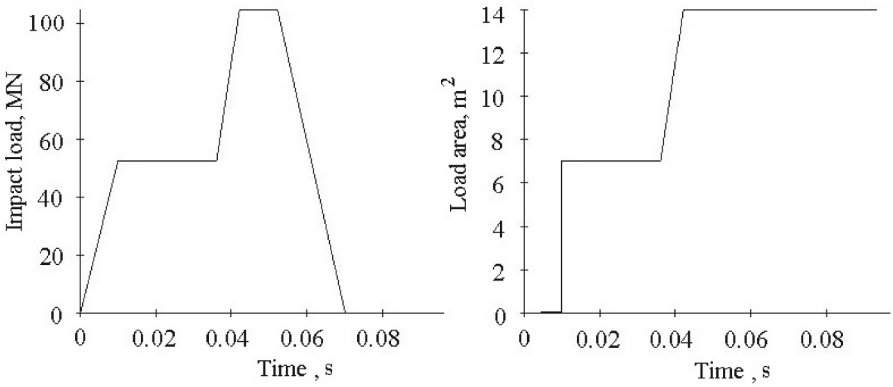

Fig. 1. Dynamic characteristics of the IAEA shock pulse.

the plate. The displacement of a point in the ι-th layer is expressed by

$$\xi_\kappa^\iota = \xi_\kappa + \sum_{\alpha=1}^{\iota-1} h_\alpha \xi_{3+\mathrm{I}(\kappa-1)+\alpha} + (z-\zeta_{\iota-1})\xi_{3+\mathrm{I}(\kappa-1)+\iota},\ \kappa = 1,\ 2,\ 3,\quad \iota = \overline{1,\mathrm{I}}. \tag{1}$$

Here $\xi_\kappa (\kappa = 1, 2, 3)$ are reference surface point displacements in coordinate axes directions; $\xi_{3+\mathrm{I}(\kappa+1)+\alpha}$ $(\kappa = 1, 2)$ are the rotations of the normal element relative to the axes in the ι-th layer; $\xi_{3+2\mathrm{I}+\iota}$ represents through-thickness compression of the normal element; $\zeta_\iota = \sum\limits_{\alpha=1}^{\iota} h_\alpha,\quad \zeta_{\iota-1} \le z \le \zeta_\iota,\ \iota = \overline{1,\ \mathrm{I}}$.

For each layer, the strain components are expressed according to Cauchy's relations, while the corresponding stresses are determined via Hooke's law. The governing equations of movement under nonstationary loading and the boundary conditions on B are obtained from the Hamilton variational principle

$$\left[\mathrm{K}^\rho\right]\boldsymbol{\Xi}_{,tt} - [\mathrm{H}]\,\boldsymbol{\Xi} = \mathbf{F},\quad \boldsymbol{\Xi}_{,t} = \boldsymbol{\Xi} = 0, \tag{2}$$

$$\left[\mathbf{C}^B\right]\boldsymbol{\Xi} = \mathbf{F}^B. \tag{3}$$

Here, $[\mathrm{K}^\rho]$ and $[\mathrm{H}]$ are symmetric square matrices, $\boldsymbol{\Xi} = \{\xi_\iota\}$ $\left(\iota = \overline{1,\ 3\mathrm{I}+3}\right)$ is the displacement vector, and the forms of $\left[\mathbf{C}^\Gamma\right]$ and $\left[\mathbf{F}^\Gamma\right]$ depend on the boundary conditions.

The vibration problem (2), (3) for the plate with arbitrary geometry and boundary conditions is solved using the expansion method [16, 17]. The original plate is mapped to an auxiliary rectangular plate with hinged boundaries, which allows the solution to be expressed in terms of trigonometric series. The auxiliary plate retains the same layer structure and loading as the original plate, while the geometry of the original domain is accounted for analytically through compensating loads $p_\alpha^{\mathrm{comp}}(\theta,\ t)$ $(\alpha = \overline{1,\ 3\mathrm{I}+3})$:

$$f_\alpha^{\mathrm{comp}}(t) = \int_{\theta_0}^{\theta_1} L_{\alpha\kappa} p_\kappa^{\mathrm{comp}}(\theta, t)\,\delta(x-x_B, y-y_B)\,\mathrm{d}\theta,\quad \alpha, \kappa = \overline{1,\ 3\mathrm{I}+3},$$

where $\delta(x - x_B, y - y_B)$ is two-dimensional Dirac function. These compensating loads ensure that the stress-strain state in the domain Ω of the auxiliary plate is identical to that of the original plate.

By expanding the compensating loads and boundary terms into trigonometric series, the system of integral equations is reduced to a set of algebraic equations for the corresponding load coefficients. Simultaneously, the equations of motion are converted into a second-order system of ordinary differential equations, which are solved using the Taylor series expansion method [17].

4 Results

The strength of the NPP containment cover of the third type, modeled as a circular plate, was investigated. The plate diameter was of 45 m, with the height of the cylindrical part of the containment shell of 68 m. The cover is constructed of reinforced concrete and lined internally with carbon steel of from 6 to 10 mm thickness. Additional steel structures are present on the exterior. Consequently, the containment cover can be represented as a multilayer circular plate and described within the framework of the kinematic hypotheses (1) outlined in Sect. 3. The connection conditions between the cylindrical part of the containment and the cover allow the plate to be considered rigidly fixed.

Two design variants of the plate were analyzed: a two-layer plate and a three-layer plate, subjected to the impact load $P_{\text{ipm}}(t)$ described in Fig. 1a. The plate contour is circular, with a radius r, while the dimensions of the auxiliary plate used for analytical modeling are A and B in plan:

$$x(\theta) = A/2 + r\cos\theta\ ,\ \ y(\theta) = B/2 + r\sin\theta\ .$$

The mechanical characteristics of the reinforced concrete were established using the averaging method and have the following values: modulus of elasticity $2.0 \cdot 10^4$ MPa; Poisson's ratio 0.25, and density 500 kg/m^3. The steel cladding is characterized by modulus of elasticity $2.1 \cdot 10^5$ MPa, Poisson's ratio of 0.3, with density of $7.85 \cdot 10^3$ kg/m^3.

Since experimental studies have shown [18, 19] that the strength of the protective shell depends on the properties of both the reinforcement and the metal cladding, the fourth strength theory was employed to evaluate the overall structural strength of the containment cover.

Figure 2 illustrates the time variation of the deflection $w(t)$ (Fig. 2a) and the stress $\sigma_i^2(t)$ (Fig. 2b) at the central point of the steel cladding for the two-layer plate at $h = 4$ m.

Table 1 shows the maximum deflections and stress intensity at the center point of the steel cladding of the two- and three-layer covers at different thicknesses of the reinforced concrete layer. The two-layer plate includes a steel cladding with a thickness of 10 mm, the three-layer plate contains outer and inner steel cladding with thicknesses of 0.5 cm and 1 cm, in each case accordingly.

The analysis of stresses in the two-layer plate showed that, for a reinforced concrete layer thickness of 3 m, the stress intensity does not exceed the steel yield strength 250 MPa. Increasing the thickness further leads to a substantial reduction in stress intensity throughout the cover.

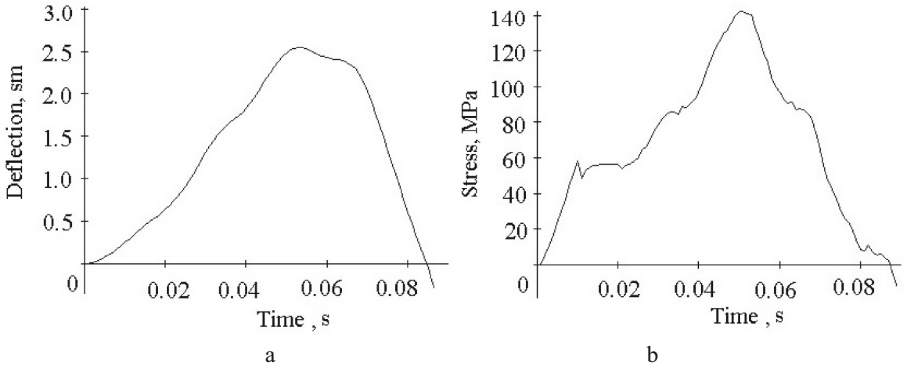

Fig. 2. Time variation of deflection and stress in a two-layer plate.

For the three-layer structure, the results indicate only a minor decrease in deflections and stresses in the inner steel cladding, suggesting that the additional outer layer has little effect on the overall structural strength. Therefore, the thickness of the reinforced concrete layer in both designs should be at least 3 m.

Table 1. Effect of design parameters on deflections and stress intensities in steel cladding

Two-layer plate						
Thickness h, m	1.0	2.0	3.0	4.0	5.0	6.0
Deflection w, m	$7.43 \cdot 10^{-1}$	$1.65 \cdot 10^{-1}$	$5.85 \cdot 10^{-2}$	$2.55 \cdot 10^{-2}$	$1.22 \cdot 10^{-2}$	$6.42 \cdot 10^{-3}$
Stress σ_i^2, MPa	1099.3	449.33	219.23	142.61	87.361	54.441
Three-layer plate						
Thickness h, m	1.0	2.0	3.0	4.0	5.0	6.0
Deflection w, m	$6.64 \cdot 10^{-1}$	$1.55 \cdot 10^{-1}$	$5.59 \cdot 10^{-2}$	$2.46 \cdot 10^{-2}$	$1.18 \cdot 10^{-2}$	$6.26 \cdot 10^{-3}$
Stress σ_i^3, MPa	1107.7	450.00	213.72	141.79	87.469	54.125

The results presented in Table 1 can be used in optimal design of NPP protective structures taking into account additional factors [20, 21].

5 Conclusions

An approach for investigating the strength of third-type NPP containment structures under aircraft impact has been proposed. The containment shell was modeled as a multilayer plate, and its dynamic behavior was described using the refined theory of multilayer plates. The problem of plate vibrations was solved using the expansion method.

The impact load was simulated using the "IAEA Pulse." The stress–strain response of two- and three-layer protective covers was analyzed at different time points during the

impact. Strength assessments of the various cover designs indicated that the multilayer configuration provides the most effective protection against unsteady dynamic loads.

The outcomes of this study may serve as a basis for optimizing the design of protective envelope structures capable of absorbing the impact of high-speed military aircraft with relatively small mass, thereby enhancing the safety and resilience of NPP containment systems.

References

1. Rusanov, A., Rusanov, R., Klonowicz, P., Lampart, P., Żywica, G., Borsukiewicz. A.: Development and experimental validation of real fluid models for CFD calculation of ORC and steam turbine flows. Mater. **14**(22), 6879 (2021). https://doi.org/10.3390/ma14226879
2. Sierikova, O., Strelnikova, E., Degtyariov, K.: Numerical simulation of strength and aerodynamic characteristics of small wind turbine blades. In: Nechyporuk, M., Pavlikov, V., Kritskiy, D. (eds.) Integrated Computer Technologies in Mechanical Engineering - 2022. ICTM 2022. Lecture Notes in Networks and Systems, vol. 657, pp. 357–370. Springer, Cham (2023). https://doi.org/10.1007/978-3-031-36201-9_31
3. Rawsan, A., Maiti, P.R.: Behavior of nuclear power plant containment under aircraft crash. Iran. J. Sci. Technol., Trans. Civil Eng. **45**, 207–218 (2021). https://doi.org/10.1007/s40996-020-00468-9
4. Bo, X.: Experimental study on the impact of thermal stress on aircraft structural performance. In: Halgamuge, S.K., Zhang, H., Zhao, D., Bian, Y. (eds.) The 8th International Conference on Advances in Construction Machinery and Vehicle Engineering. ICACMVE 2023. Lecture Notes in Mechanical Engineering. Springer, Singapore (2024).https://doi.org/10.1007/978-981-97-1876-4_101
5. Almomani, B., Kim, T.-Y., Chang, Y.-S.: Global damage evaluation of a dry storage structure subjected to postulated aircraft crashes. Prog. Nucl. Energy **156**, 104554 (2023). https://doi.org/10.1016/j.pnucene.2022.104554
6. Li, Z.R., et al.: Damage and vibrations of nuclear power plant buildings subjected to aircraft crash part II: numerical simulations. Nucl. Eng. Technol. **53**(9), 3085–3099 (2021). https://doi.org/10.1016/j.net.2021.03.008
7. Bogdanov, V.L., Guz, A.N., Nazarenko, V.M.: Fracture of materials loaded along cracks: approach and results. Adv. Mech. Adv. Struct. Mater. **191**, 51–89 (2023). https://doi.org/10.1007/978-3-031-37313-8-4
8. Riera, J.D., Zorn, N.F., Schueller, G.I.: An approach to evaluate the design load time history for normal engine impact taking into account the crash-velocity distribution. Nucl. Eng. Des. **71**(3), 311–316 (1982)
9. Siefert, A., Henkel, F.O.: Nonlinear analysis of commercial aircraft impact on a reactor building - comparison between integral and decoupled crash simulation. Nucl. Eng. Des. **269**, 130–135 (2014). https://doi.org/10.1016/j.nucengdes.2013.08.018
10. Qu, Y.G., Wu, H., Xu, Z.Y., Liu, X., Dong, Z.F., Fang, Q.: Safety assessment of generation III nuclear power plant buildings subjected to commercial aircraft crash part II: Structural damage and vibrations. Nucl. Eng. Technol. **52**(2), 397–416 (2020). https://doi.org/10.1016/j.net.2019.07.015
11. Saberi, R., Alinejad, M., Mahdavi, M.O., Sepanloo, K.: Numerical analysis of nuclear power plant structure subjected to aircraft crash. Int. J. Adv. Struct. Eng. **9**(4), 341–352 (2017). https://doi.org/10.1007/s40091-017-0170-0
12. Zhou, L., Li, X., Yan, Q., Li, X.: Study on the dynamic response of reinforced concrete nuclear containment under the impact of large aircraft. Nucl. Eng. Des. **417**, 112880 (2024). https://doi.org/10.1016/j.nucengdes.2023.112880

13. Wang, F., et al.: Numerical analysis of reinforced concrete nuclear power plant model tests under a large aircraft impact and the influence assessment of transverse reinforcement. Structures **70**, 107604 (2024). https://doi.org/10.1016/j.istruc.2024.107604
14. External Human-Induced Events in Site Evaluation for Nuclear Power Plants. IAEA Safety Standards Series. Safety Guide No. NS-G-3.1 / International Atomic Energy Agency. Vienna (2002)
15. Drittler, K., Gruner, P.: The force resulting from impact of fast-flying military aircraft upon a rigid wall. Nucl. Eng. Des. **37**(2), 245–248 (1976). https://doi.org/10.1016/0029-5493(76)90019-4
16. Kurennov, S., Smetankina, N.: Stress-strain state of a double lap joint of circular form. axisymmetric model. In: Nechyporuk, M., Pavlikov, V., Kritskiy, D. (eds.) Integrated Computer Technologies in Mechanical Engineering-2021. ICTM 2021. Lecture Notes in Networks and Systems, vol. 367, pp. 36–46. Springer, Cham (2022). https://doi.org/10.1007/978-3-030-94259-5_4
17. Ugrimov, S., Smetankina, N., Kravchenko, O., Yareshchenko, V., Kruszka, L.: A study of the dynamic response of materials and multilayer structures to shock loads. In: Advances in Mechanical and Power Engineering. CAMPE 2021. Lecture Notes in Mechanical Engineering, pp. 304–313. Springer, Cham (2023). https://doi.org/10.1007/978-3-031-18487-1_31
18. Kondratiev, A., et al.: Effect of ply orientation on the mechanical performance of carbon fibre honeycomb cores. Polymers **15**(11), 2503 (2023). https://doi.org/10.3390/polym15112503
19. International Atomic Energy Agency. Design of Nuclear Installations against External Events Excluding Earthquakes, Specific Safety Guide SSG 68, Vienna (2021)
20. Kuznetsov B.I., Kutsenko A.S., Nikitina T.B., Bovdui I.V., Kolomiets V.V., Kobylianskyi B.B.: Method for design of two-level system of active shielding of power frequency magnetic field based on a quasi-static model. Electr. Eng. Electromech. **2**, 31–39 (2024). https://doi.org/10.20998/2074-272X.2024.2.05
21. Melnyk, O., Onishchenko, O., Onyshchenko, S., Yaremenko, N., Maliuha, E., Honcharuk, I., Shamov, O.: Innovative technologies for the maritime industry: hydrogen fuel as a promising direction. In: Boichenko, S., Zaporozhets, A., Yakovlieva, A., Shkilniuk, I. (eds.) Modern Technologies in Energy and Transport. Studies in Systems, Decision and Control, vol. 510, pp. 23–34. Springer, Cham (2024). https://doi.org/10.1007/978-3-031-44351-0_3

Investigation of Crack Kinetics Under Multi-mode Cyclic Loading

Pavlo Hontarovskyi[1], Nataliia Garmash[1(✉)], Iryna Melezhyk[1], Tetiana Protasova[1], and Kateryna Ugrimova[2]

[1] Anatolii Pidhornyi Institute of Power Machines and Systems of the National Academy of Sciences of Ukraine, 2/10 Komunalnykiv Street, Kharkiv 61046, Ukraine
garm.nataly@gmail.com

[2] Simon Kuznets Kharkiv National University of Economics, Nauky Avenue 9A, Kharkiv 61166, Ukraine

Abstract. An advanced method for calculating crack growth in plate-like and axisymmetric structural elements under repeated loading conditions modeled using elastic–plastic material behavior, based on the principle of accumulation of distributed damage in the material is proposed. Near the crack tip, the processes of alternating elastic-plastic deformation and crack resistance of the material are modeled based on experimental results obtained from fatigue testing on smooth samples. Finite element analysis is conducted to determine the thermal and mechanical responses of the structure under different loading conditions. To assess accumulated metal damage from low-cycle fatigue, an improved method is used that takes into account the loading history. The ranges of equivalent elastic-plastic deformations are determined according to the Neuber's rule. Damage is assessed using low-cycle fatigue curves based on the hypothesis of linear damage accumulation. At the same time, crack propagation during both the tensile and compressive stages and possible contact between the crack edges are taken into account. As the damage accumulates to a critical magnitude at the crack tip, the material is considered destroyed, and the crack grows stepwise. The developed method has significant advantages, since it does not impose restrictions on the size of the plastic zone and small crack depth. The results of calculations are compared with data obtained using the Newman's formula.

Keywords: Crack Kinetics · Cyclic Loading · Elastic-Plastic Deformation

1 Introductions

One of the most important tasks in the design and manufacture of aviation, transport and power engineering structures is to increase their strength and reliability under cyclic loading. Ensuring the reliable operation of these structures demands' a calculated assessment of durability and the thermal stability of their components, built on the application of new calculation models and methods that consider a number of important factors, continuing heterogeneity of material properties, damageability, the presence of cracks, and the influence of non-stationary temperature fields. Among the most hazardous defects affecting

H. Altenbach et al. (Eds.): CAMPE 2025, LNME, pp. 352–363, 2026.
https://doi.org/10.1007/978-3-032-16381-3_34

operational safety are the initiation and propagation of cracks. Modern achievements in the mechanics of material deformation and the solution of boundary value problems make it possible to obtain improved methods for predicting the behavior of structures with cracks under complex loads.

The calculated survivability of power equipment, aviation and transport technology components is critical when determining their service life and the intervals between maintenance inspections [1]. Kinetic fatigue fracture diagrams and their governing equations are widely used to assess crack growth kinetics under cyclic loading. Determining the crack resistance parameters included in these equations (e.g., Paris' equation) requires laborious testing of special samples with cracks [2–7]. This complicates and restricts the analysis of the durability of a structure in conditions of insufficient experimental data on the behavior of samples with cracks. It should be noted that in classical fracture mechanics, the size of the plasticity zone at the crack tip is assumed to be small compared to its depth, which is not always true. Moreover, it is assumed that the crack does not propagate in a half-cycle of compressive loads, and calculations are performed for a zero cycle [8, 9]. At the same time, a number of studies on crack propagation under alternating loading cycles have shown that the compressive half-cycle also influences crack growth.

Therefore, it is important to develop a method for calculating the kinetics of cracks in structural elements under multi-mode asymmetric repeated loading in an elastic-plastic formulation based on the principle of accumulation of scattered damage in the material and data from fatigue failure diagrams of conventional cylindrical samples.

2 Method for Calculating Crack Kinetics

Taking into account the survivability of equipment elements with cracks is important when assessing their reliable operation. Usually, to assess crack kinetics under cyclic loading, the principles of brittle fracture mechanics are widely used, using stress intensity factors K_{I} and Paris equations

$$\frac{dl}{dN} = C\Delta K_{\mathrm{I}}^{n}, \tag{1}$$

where:

l is crack length;

C, n are constants of material;

N is number of loading cycles;

$\Delta K_{\mathrm{I}} = K_{\mathrm{Imax}} - K_{\mathrm{Imin}}$ is stress intensity factor range;

$K_{\mathrm{I}max}$ is maximum stress intensity factor (SIF) in the cycle;

$K_{\mathrm{I}min}$ is minimum SIF in the cycle.

The kinetic diagram of fatigue failure are determined by a large number of experimental tests of special samples with cracks at operating temperatures and loads, which requires the use of complex equipment and a significant amount of time.

Most often, the crack resistance characteristics of materials required for calculating the service life of elements are not available in reference data. It should be noted that in this case, the plasticity zone at the crack tip is assumed to be small compared to the

crack length, which, as shown by numerous researches, the results of which are given below, does not always correspond to reality.

The crack growth rate, in addition to the amplitude ΔK_{I}, depends on the load cycle asymmetry coefficient R:

$$R = \frac{K_{\mathrm{Imin}}}{K_{\mathrm{Imax}}},$$

which is taken into account in the refined formulas of the Paris' type [6].

The SIF is calculated based on the solutions of elasticity theory problems, and its sign corresponds to the sign of the stresses that open the crack. In brittle fracture mechanics, it is assumed that compressive stresses do not affect the kinetics of a fatigue crack [6]. It is believed that under compressive forces, the crack edges close and the crack closes along its entire length, so calculations should only be performed for a zero cycle ($R = 0$). The same approach is proposed in the ASME recommendations [8]. According to elasticity theory, under tensile stresses, the crack edges diverge, and under compressive stresses, they converge. In the case of compressive stresses, the stress intensity factor $K_{\mathrm{I}} = 0$ and the crack does not develop. However, it has been experimentally shown that the compressive stage of loading affects the crack growth rate under cyclic loading, albeit to a much lesser extent than tensile loading. When the crack edges interpenetrate under compressive stresses, the SIF becomes negative. Taking into account the full range ΔK_{I} in Paris' equations, the calculations give an underestimated design life of the material. The error will be significantly smaller for a zero cycle, although the calculated resource will be slightly overestimated.

Due to plastic deformation, the edges of the crack remain open when tensile stresses are completely removed, while compressive stresses appear in the crack tip area, which in some investigations has been termed the phenomenon of crack 'closure' [6, 9–11]. In works [10], equations are proposed that take into account the cyclic load asymmetry coefficient R and are based on the phenomenon of crack 'closure'. 'Closure' of a crack in this case is not a suitable term because only compressive stresses occur at the crack tip, and the crack edges do not contact each other. Experimental data [10] show that negative stresses at the crack tip also occur under tensile loads.

Another approach to calculating crack kinetics is based on assessing the accumulation of scattered damage in the material during elastic-plastic cyclic deformation and creep, and on using data from tests on smooth samples [12]. This approach uses the characteristics of the elastic-plastic behaviour of the material and the accumulation of damage in the area of the crack tip along the crack propagation path, which are determined numerically using the finite element method (FEM) with mesh refinement at the crack tip [1, 13, 14].

In the proposed method, the thermal and stress-strain state of the structure is determined using FEM for different load modes. To assess the accumulated damage to the metal from low-cycle fatigue, the method [1, 14] recommended for assessing the service life of rotors and turbine housings is used. Low-cycle fatigue is assessed by the maximum value of local elastic stresses, reduced to the design temperature, which is taken as the maximum temperature in this area under steady-state operation. The ranges of equivalent elastic-plastic deformations are determined according to the Neuber's rule [15].

According to this principle, using experimental fatigue curves for an isothermal symmetrical load cycle, the number of cycles before a crack appears is found. The damage assessment under multi-mode cyclic loading is determined using the linear damage summation hypothesis. When the damage parameter value close to unity is reached in one of the elements, it is excluded from further consideration. It is assumed that this element was destroyed and the crack propagates stepwise along its entire length. At the same time, the damage achieved in other structural elements is recorded. Then, the stress-strain state of the structure is recalculated with the new crack length. The structure is subjected to further multi-mode cyclic loading. At the same time, the accumulation of damage in all elements along the crack propagation path is assessed, which is summed up with the damage achieved in them during the last destruction of the element. When critical damage is reached in one of the following elements, it is excluded from further consideration, and the above calculation procedure is repeated until the avalanche-like destruction of the structure.

The calculation procedure is given below. For all load modes, the FEM is used to calculate the stress state in an elastic setting in the crack propagation area at several possible crack lengths.

Finite element discretization is performed with refinement at the crack tip. The minimum element size is taken to be 0.05 mm, which is consistent with previous investigations on the convergence of results. The crack is modelled by a notch with a width of 0.1 mm. Haywood's experiments [16] show that a radius of curvature at the crack tip of less than 0.1 mm does not affect fatigue strength. Based on this, to determine the stress-strain state near the crack tip with sufficient accuracy, the dimensions of the minimum finite elements should be 0.1–0.2 mm. Figure 1 shows a fragment of the finite element discretization in the crack tip area.

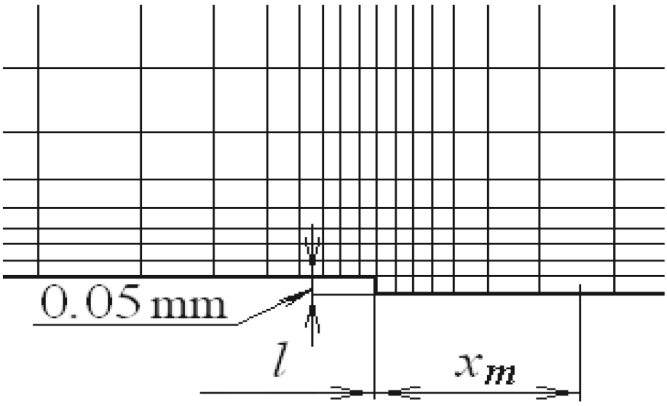

Fig. 1. Finite element discretization in the vicinity of the crack tip: l – crack length; x_m – distance from the crack tip to the centres of the finite elements.

The software package developed by the authors for solving plane and axisymmetric problems using the FEM [14] allows solving elastic-plastic problems taking into account

alternating loads. The boundary value problem is solved using the method of steps in time of loading.

The selected crack propagation direction is divided evenly into small segments d_l – steps of jump-like crack growth. A generalized load cycle is introduced, which averages the damage from all load modes. Each j-th mode is characterized by the interval of combined elastic and plastic deformation, which are determined at the centres x_i of the segments d_l by quadratic interpolation through their values obtained at the centres of the finite elements in the direction of crack propagation. The number of cycles to failure N_{pj} from the j-th loading condition is obtained from fatigue diagrams corresponding to the relevant temperature.

The damage increments from the j-th load mode in the generalized cycle are found by the formula

$$\Delta\Pi_j(x_j) = \frac{1}{N_{pj}(x_i)} d_{Nj},$$

where $d_{N\,j} = N_j \big/ N$ is the relative share of cycles of the j-th mode in the generalized number N of cycles.

The damage increment per generalized cycle from all load modes

$$\Delta\Pi(x_i) = \sum_{j=1}^{K_N} \Delta\Pi_j(x_i).$$

The number of cycles to failure in the element d_l closest to the crack tip with a length l_t is determined by the formula

$$N_i = \frac{1 - \Pi(x_1)}{\Delta\Pi(x_1)},$$

where $\Pi(x_1)$ the damage accumulation adjacent to the fracture zone during crack growth to the current depth l_t. The total cycle count during which the crack reached a depth of l_t is determined as follows:

$$N(l_t) = \sum N_i.$$

Damage at other points x_i on the crack growth path after the failure of the next element d_l is determined:

$$\Pi(x_{i+1}) = \Pi(x_{i+1}) + \Delta\Pi(x_{i+1}) N_t.$$

Next, the calculation is repeated for a crack with a depth of $t_l = t_l + d_l$ until its next growth.

The proposed methodology was tested on a series of calculated estimates of crack development in simple-shaped elements under various cyclic loads.

3 Calculating Crack Kinetics Taking into Account the Contact Between Their Edges and the Elastic-Plastic Deformation of the Material in the Crack Tip Zone

The growth of a surface crack with an initial length of $l = 2$ cm in a strip (Fig. 2.) subjected to loads whose patterns are shown in Fig. 3. (conventionally denoted as Type I and Type II), are investigated. The formation of cycles is determined by the rainflow method [17]. Here $\sigma_{1z\max}$, $\sigma_{1z\min}$ are the maximum and minimum stresses in the first load cycle; $\sigma_{2z\max}$, $\sigma_{2z\min}$ are the analogical stresses in the second load cycle.

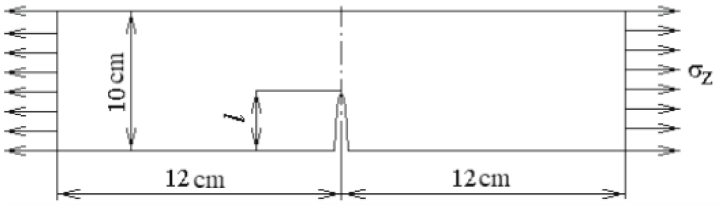

Fig. 2. Scheme of a plate with a crack

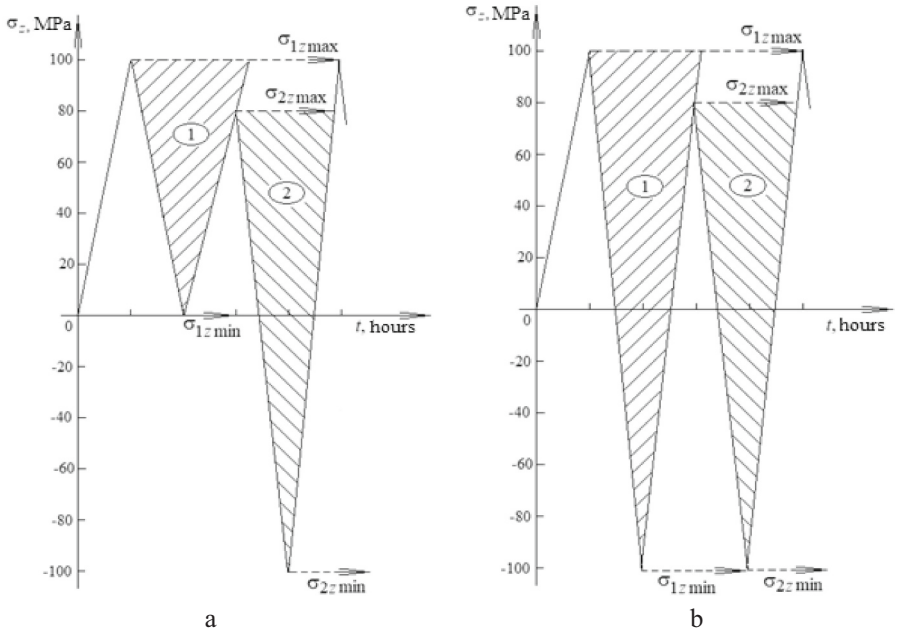

Fig. 3. Loading schemes for the plate: a – Type I loading; b – Type II loading

Tables 1 and 2 present the values of strain intensity amplitudes for Type I and Type II loading, respectively. In Tables 1 and 2, the numerators give the values for the first loading cycle, and the denominators – for the second loading cycle (Fig. 3.).

The plate material is 25Kh1M1F steel. Low-cycle fatigue diagrams at various temperatures are given in Fig. 4.

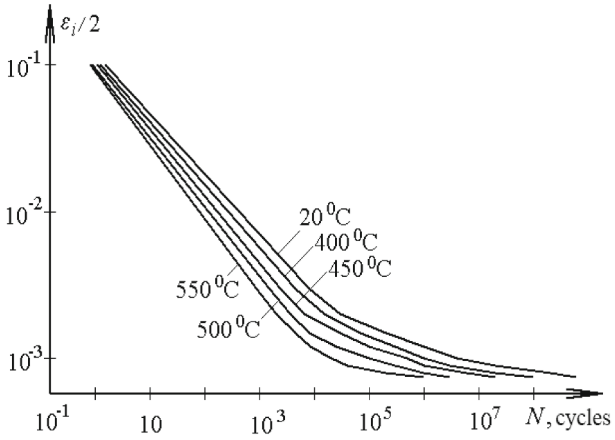

Fig. 4. Low-cycle fatigue curves for 25Kh1M1F material

The obtained crack growth results are compared with those calculated using Newman's method. The constants in the Eq. (1) were taken as follows: $C = 42.69 \times 10^{-10}$, $n = 3.8457$. The stress intensity factor ΔK_{I} are equal to 34.24; 50.81; 74.73; 112.04 MPa·$(\mathrm{m})^{1/2}$ for cracks with lengths of 2; 3; 4; and 5 cm, respectively.

Figure 5 presents the results of crack growth in the strip under Type I loading (Fig. 5, a) and Type II loading (Fig. 5, b). Solid lines indicate results obtained using the present methodology, while dashed lines show results obtained by Newman's method.

The results obtained using the proposed method and Newman's method are satisfactorily consistent. The discrepancy between the results can be explained by the inconsistency of material properties when determining kinetic and fatigue diagrams, as well as by the difference in the material failure models used in the calculation methods.

Table 1. Values of strain intensity amplitudes ε_{ia} for Type I loading of the plate

x_m, mm	Amplitudes of strain intensities ε_{ia}, %				
	$l = 20$ mm	$l = 30$ mm	$l = 40$ mm	$l = 45$ mm	$l = 50$ mm
0.0250	1.3185 1.3381	2.2391 2.3388	3.6169 4.1192	4.5826 5.6135	5.4757 8.4311
0.0750	0.5167 0.5200	0.9398 0.9768	1.6122 1.8492	2.1041 2.6082	3.1732 4.0691
0.1800	0.1405 0.1462	0.2392 0.2446	0.4074 0.4680	0.5452 0.6857	1.2383 1.1457
0.2550	0.1028 0.1104	0.1614 0.1619	0.2510 0.2844	0.3178 0.3938	0.7079 0.6296
0.5456	0.0662 0.0768	0.0974 0.1031	0.1446 0.1432	0.1754 0.2094	0.2709 0.2912
1.1281	0.0428 0.0538	0.0677 0.0788	0.0983 0.1088	0.1193 0.1327	0.1735 0.2018
2.2699	0.0296 0.0416	0.0450 0.0574	0.0695 0.0837	0.0842 0.1015	0.1146 0.1393
6.3353	0.0208 0.0364	0.0264 0.0398	0.0370 0.0524	0.0467 0.0661	0.0541 0.0837
11.6887	0.0189 0.0357	0.0209 0.0365	0.0244 0.0390	0.0280 0.0443	0.0372 0.0575
14.8932	0.0187 0.0357	0.0197 0.0359	0.0212 0.0361	0.0224 0.0381	0.0417 0.0474

Table 2. Values of strain intensity amplitudes ε_{ia} for Type II loading of the plate

x_m, mm	Amplitudes of strain intensities ε_{ia}, %				
	$l = 20$ mm	$l = 30$ mm	$l = 40$ mm	$l = 45$ mm	$l = 50$ mm
0.0250	1.3381 1.7387	2.3388 2.9580	4.1192 5.0219	5.6135 6.9438	8.4311 10.2975
0.0750	0.5200 0.6985	0.9768 1.2711	1.8492 2.3107	2.6082 3.2929	4.0691 5.0373
0.1800	0.1462 0.1874	0.2446 0.3164	0.4680 0.5969	0.6857 0.8946	1.1457 1.4652
0.2550	0.1104 0.1336	0.1619 0.2073	0.2844 0.3464	0.3938 0.4989	0.6296 0.8073
0.5456	0.0768 0.0930	0.1031 0.1272	0.1432 0.1919	0.2094 0.2465	0.2912 0.3525
1.1281	0.0538 0.0711	0.0788 0.0935	0.1088 0.1349	0.1327 0.1750	0.2018 0.2374
2.2699	0.0416 0.0513	0.0574 0.0689	0.0837 0.0938	0.1015 0.1226	0.1393 0.1683
6.3353	0.0364 0.0389	0.0398 0.0471	0.0524 0.0637	0.0661 0.0761	0.0837 0.0936
11.6887	0.0357 0.0392	0.0365 0.0387	0.0390 0.0492	0.0443 0.0553	0.0575 0.0677
14.8932	0.0357 0.0394	0.0359 0.0387	0.0361 0.0438	0.0381 0.0474	0.0474 0.0579

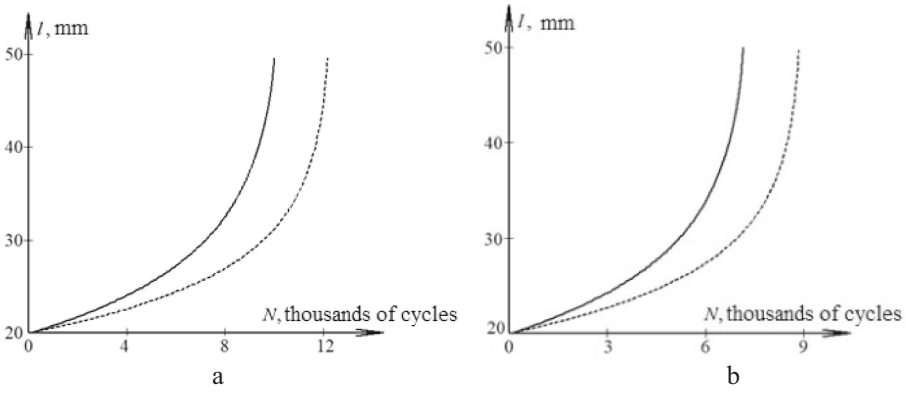

Fig. 5. Crack growth: a – Type I loading; b – Type II loading

4 Conclusion

The proposed method for assessing crack kinetics under cyclic loading using scattered damage parameters takes into account the amplitude of plastic deformations near the crack tip during contact interaction of its edges. To calculate crack kinetics in flat and axisymmetric structures, low-cycle fatigue curves for conventional crack-free specimens are used. Plastic deformation zones are determined using the FEM. The crack growth rates for different cycle asymmetry coefficients correspond to the data obtained by the Paris' equation and the Newman technique, which use experimental constants for cracked specimens.

The presented method allows taking into account the stage of crack initiation from a stress concentrator, which can be used in assessing the service life of structures. Its application will reduce the cost of designing new equipment, determine the survivability of structures, ensure operational reliability, reduce the number of experimental studies [18], and contribute to increasing the competitiveness of domestic equipment [14]. The results obtained can be useful in the design of structures for of power equipment and aircraft construction [1].

In the future, it may be possible to develop the proposed methodology for studying the nonlinear behaviour of materials under cyclic loading conditions. Conducting experimental studies is of particular scientific interest, as it will provide additional validation of the reliability of the results obtained.

This method will be used to conduct computational investigations of the residual durability of an aircraft engine fan disc when varying the parameters of the initial crack under conditions of multi-mode cyclic loading within the framework on IEMS-2025/3 project of the Specialised Scientific and Technical Programme of Defence Research of the National Academy of Sciences of Ukraine.

References

1. Hontarovsky, P.P., Smetankina, N.V., Ugrimov, S.V., Harmash, N.H., Melezhyk, I.I.: Simulation of the crack resistance of ion-exchange strengthened silicate glass subject to bending strain. Int. Appl. Mech. **58**(6), 715–724 (2022)
2. Degtyariov, K., Gnitko, V., Steinwolf, A., Vierushkin, I.: Boundary and finite element methods in crack propagation analysis. In: Altenbach, H., Gao, XW., Syngellakis, S., Cheng, A.HD., Lampart, P., Tkachuk, A. (eds.) Advances in Mechanical and Power Engineering II. CAMPE 2023. LLNME. Springer, Cham. pp. 299–300 (2025). https://doi.org/10.1007/978-3-031-82979-6_29
3. Sierikova, O., Kriutchenko, D., Vandyshev, K., Vierushkin, I.: Structure elements with crack-type defects durability estimation. In: Altenbach, H., Gao, XW., Syngellakis, S., Cheng, A.HD., Lampart, P., Tkachuk, A. (eds.) Advances in Mechanical and Power Engineering II. CAMPE 2023. LNME. Springer, Cham, pp. 301–311 (2025). https://doi.org/10.1007/978-3-031-82979-6_30
4. Fageehi, Y. \A.: Prediction of fatigue crack growth rate and stress intensity factors using the finite element method. Adv. Mater. Sci. Eng., Article ID 2705240 (2022). https://doi.org/10.1155/2022/2705240
5. Wen, L.-F., Tian, R., Wang, L.-X., Feng, C.: Improved XFEM for multiple crack analysis: accurate and efficient implementations for stress intensity factors. Comput. Methods Appli. Mech. Eng. **411**. Article 116045 (2023). https://doi.org/10.1016/j.cma.2023.116045
6. Ritchie, R.O., Liu, D.: Introduction to Fracture Mechanics. Elsevier (2021). https://doi.org/10.1016/C2020-0-03038-0
7. Herasymchuk, O.M., Kononuchenko, O.V.: A model for estimating the fatigue crack growth stage duration in metal specimens under variable cyclic stress ranges. Strength Mater. **57**, 1–13 (2025). https://doi.org/10.1007/s11223-025-00740-1
8. ASME Boiler and Pressure Vessel Code: Section XI, Appendix A. The American Society of Mechanical Engineers. New York, Addenda (1990)
9. Qin, D., Geng, X., Jie, Z., Yaoyu, H.: Experimental and numerical study on crack propagation of cracked plates under low cycle fatigue loads. J. Mar. Sci. Eng. **11**, 1436 (2023). https://doi.org/10.3390/jmse11071436
10. Alshoaibi, A.M., Fageehi, Y.A.: Numerical analysis on fatigue crack growth at negative and positive stress ratios. Materials. **16**, article 3669 (2023). https://doi.org/10.3390/ma16103669
11. Sun, R., Keller, S., Zhu, Y., Guo, W., Kashaev, N., Klusemann, B.: Experimental-numerical study of laser-shock-peening-induced retardation of fatigue crack propagation in Ti-17 titanium alloy. Int. J. Fatigue **145**, 106081 (2021). https://doi.org/10.1016/j.ijfatigue.2020.106081
12. Tsybanyov, G.V.: Computational monitoring of an initial fatigue crack incubation and growth in a smooth specimen. Strength Mater. **56**, 961–969 (2024). https://doi.org/10.1007/s11223-024-00707-8
13. Bobyr, M.I., Koval', V.V., Fam, D.K.: Continuum damage mechanics in problems of prediction of structural members load-bearing capacity. Int Appl Mech. **61**, 114–125 (2025). https://doi.org/10.1007/s10778-025-01338-5
14. Gontarovskyi, P.P., Smetankina, N.V., Garmash, N.G., Melezhyk, I.I., Protasova, T.V.: Three-dimensional stress-strain state analysis of the bimetallic launch vehicle propellant tank shell. Strength Mater. **55**(5), 916–926 (2023). https://doi.org/10.1007/s11223-023-00582-9
15. Burghardt, R., Masendorf, L., Esderts, A.: Determination of local stresses and strains within the notch strain approach: efficient implementation of notch root approximations. Appl. Sci. **11**(21), 10339 (2021). https://doi.org/10.3390/app112110339

16. Heywood, R.B.: Designing Against Fatigue of Metals Publisher. Reinhold Publishing Corporation, New York (1962)
17. ASTM E1049–85. Standard Practices for Cycle Counting in Fatigue Analysis. ASTM International, West Conshohocken, PA, USA (Reapproved 2017)
18. Ugrimov, S., Smetankina, N., Kravchenko, O., Yareshchenko, V., Kruszka, L.: A study of the dynamic response of materials and multilayer structures to shock loads. In: Altenbach, H., et al.(eds) Advances in Mechanical and Power Engineering. CAMPE 2021, LNME. Springer, Cham, pp. 304–313 (2022) https://doi.org/10.1007/978-3-031-18487-1_31

Investigation of the Dynamic Properties of Materials Under High-Rate Strain Conditions

Sergiy Ugrimov[1](✉), Volodimir Yareshchenko[1], Olexander Yareshchenko[1], and Ihor Derevianko[2]

[1] Anatolii Pidhornyi Institute of Power Machines and Systems of the National Academy of Sciences of Ukraine, 2/10 Komunalnykiv Street, Kharkiv 61046, Ukraine
sugrimov@ipmach.kharkov.ua

[2] Yuzhnoye State Design Office, 3, Krivorizka Street, Dnipro 49008, Ukraine

Abstract. The method and results of the study of the mechanical properties of some materials during high-speed deformation are presented. The methodology used is based on the indirect determination of material tensile curves under conditions of constant deformation rate of test specimens. Deformations are measured on a dynamometer rod and then converted into stresses in the specimens. The research is conducted on dog-bone-shaped specimens whose geometric dimensions are significantly smaller than those of samples used for static testing. A pneumatic gun is used to ensure the required strain rates, and the strains are measured using broadband strain gauges. Experimental determination of the strength limits of a number of materials used in aircraft construction has been carried out under tension at different strain rates. The dynamic mechanical properties of aluminum alloy and carbon fiber reinforced plastic have been investigated. The results for high strain rate are compared with data obtained using the classical quasi-static approach. The problems arising in the investigation of the dynamic behavior of isotropic and anisotropic materials are discussed, as well as some features of carbon fiber composite failure under impact loading. It has been shown that the strength limit of the materials under study increases with increasing deformation rate. This proves that the study of the dynamic properties of materials should become an essential component of strength assessment for structures operating under rapidly changing loads.

Keywords: Strength · Stress-Strain Curve · Tensile Strength · Experiment

1 Introduction

One of the main tasks in designing structures for modern aircraft and space-rocket construction is to increase their strength and reliability while reducing weight, which allows for an increase in the payload of aerospace vehicles [1]. This can be achieved through the rational design of structures and the use of new materials. In some cases (explosive forces, various emergency situations etc.), structural elements of aerospace vehicles are subjected to intense impact loads [2]. They all have a common feature: a rapid increase in pressure on the contact surface from zero to a maximum value. Quite

H. Altenbach et al. (Eds.): CAMPE 2025, LNME, pp. 364–373, 2026.
https://doi.org/10.1007/978-3-032-16381-3_35

often, such loads are characterized by high intensity of influence and lead to high-speed deformation of structures. At the same time, depending on the type of load, the strain rate of the structure in a short time varies in a wide range from 0 to 10^6 s^{-1} (sometimes this range is even wider). The physics of the processes occurring in structural elements under the action of such loads is quite complex and has not been sufficiently studied. This is especially relevant for promising and new materials (e.g. composite, polymer, and additive materials).

To analyze the strength of structures under dynamic loads, it is necessary to create an extensive database of the mechanical properties of materials at high strain rates. It is not always acceptable to rely on existing values of material properties obtained for static deformation, as this can lead to an incorrect assessment of their strength. Such data are available for classical materials. At the same time, for new materials, which often have anisotropic properties, the results are insufficient and sometimes contradictory. Therefore, the theoretical and experimental studies of the behavior of materials during high strain rate are one of the most pressing tasks in continuum mechanics.

The aim of this work is to determine the dynamic properties of materials for aircraft construction during high strain rates.

2 Literature Review

To date, numerous results of experimental studies of the properties of materials (usually metals and metal alloys) under dynamic loads have been accumulated [3–6]. These studies have shown that the mechanical characteristics of materials significantly depend on the deformation rate [3, 5]. As a result, a number of dependencies $\sigma = \sigma(\varepsilon, d\varepsilon/dt)$ between stresses and strains were identified, that take into account the deformation rate. Among the most well-known such models are the Cowper-Symonds [7] and Johnson-Cook [8] relationships. A more detailed description of these models and the definition of parameters for some materials are given in the works [9–11].

Currently, scientists are paying considerable attention to the theoretical and experimental study of the properties of new materials, the improvement of experimental methods for studying the transient processes of their deformation, as well as mathematical models and computational methods for analyzing the processes occurring in them [11–14].

Experimental studies of high-rate strain of materials, especially anisotropic ones, are quite complex. They require appropriate equipment capable of providing the necessary loading conditions and reliable recording of strains (stresses). In addition, effective methods are needed for the reliable processing of dynamic dependencies.

Currently, there are no standardized approaches to these studies. The most widespread use in practice is the Hopkinson bar and its modifications [15–20]. The basic principles of conducting experiments using the Hopkinson bar and processing the results obtained are described in paper [21].

Another way to study stresses in a test specimen under tension at a constant strain rate is to use a long measuring rod-waveguide on a vertical acceleration device and direct or indirect strain gauging [22]. A similar approach is used in this work.

3 Research Methodology

The research methodology is based on the indirect determination of stress-strain curve for tensile materials under conditions of constant strain rate. Material tensile curves are determined for different constant strain rates of the test specimen. This makes it easy to compare the tensile curves obtained for different deformation rates. As a result of a number of experiments at different strain rates, the deformation surface of the material $\sigma = \sigma(\varepsilon, d\varepsilon/dt)$ is determined (Fig. 1). On this surface, the deformation process at variable rates will be represented by some curve Γ.

The experimental research method consists of impact stretching of the test specimen, one end of which is fixed in a rigid anvil, and the other in a dynamometer rod. A simplified test setup for high rate tensile of the linear specimens is shown in Fig. 2 (1 – projectile; 2 – anvil; 3 – specimen; 4 – strain gauges; 5 – dynamometer rod).

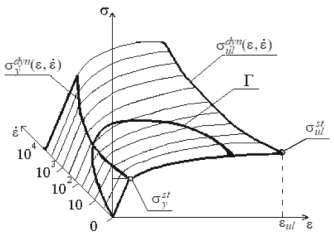

Fig. 1. Stress-strain surface

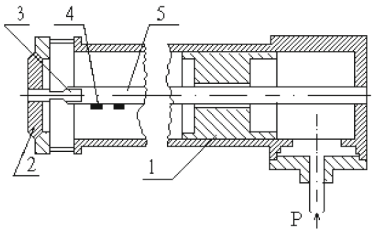

Fig. 2. Test setup for linear specimens

The longitudinal force in the specimens is determined based on the deformation data recorded on the dynamometer rod. The anvil is subjected to impact by a projectile with kinetic energy sufficient to ensure a constant strain rate of deformation of the specimen until it destruction. For this purpose, the kinetic energy of the projectile must significantly exceed the work required for the dynamic deformation of the specimen until its destruction, i.e.

$$Q_{projectile} > 10 \cdot Q_{destruction} = \int \sigma_i(\varepsilon, \dot{\varepsilon}) d\varepsilon,$$

where σ_i is the stress intensity; $\dot{\varepsilon} = d\varepsilon \big/ dt$.

In this case, the specimen elongation changes linearly vs time $\Delta l = (d\varepsilon/dt) \cdot t$, and the strain rate is equal to $d\varepsilon/dt = V_0 / l$, where l is length of narrow section of specimen.

For a qualitative determination of the magnitude of longitudinal forces in the specimen during tension, based on the measurements of bar strain, it is necessary that the bar be long enough so that the deformation waves reflected from its attachment point do not interfere with the tension process under study. Therefore, the length L of the rod must be such that at the studied speed V_0 it satisfies the condition

$$L > C_{1d} \cdot \varepsilon_{un} \cdot l/2 \cdot V_0 \tag{1}$$

where C_{1d} is the velocity of wave deformation in the rod;ε_{un} is the limiting uniform strain of the specimen.

The geometric dimensions of the test specimens are selected in such so as to ensure that condition (1) is satisfied and to ensure a practically uniform state of deformation. For a rapid transition of wave processes to a practically uniform state, the working part (narrow section) of the specimen must be relatively small. Moreover, the higher the strain rate under study, the shorter the working zone of the specimen should be.

The sought dependencies $\sigma = \sigma(\varepsilon, d\varepsilon/dt)$ for the specimens are determined based on the results of measurements of the strain of the dynamometer rod by a simple mathematical transformations, which is based on the equality of the longitudinal forces in the specimens N_z^{spec} and the rod N_z^{rod}.

$$N_z^{spec}(z_1, t) = N_z^{rod}(z_2, t - t_1)$$

where z_1, z_2 are axial coordinates of sections; t_1 is the time lag of the start of the rod deformation process relative to the specimen deformation process.

Longitudinal forces in the specimen and the rod are determined by the formulas

$$N_z^{spec} = \sigma_z^{spec}(z_1, t) \cdot S^{spec}(z_1, t), \tag{2}$$

$$N_z^{rod} = \sigma_z^{rod}(z_2, t - t_1) \cdot S^{rod}(z_2, t - t_1) = E \cdot \varepsilon_z^{\exp}(z_2, t - t_1) \cdot S^{rod}(z_2, t - t_1), \tag{3}$$

where $\sigma_z^{spec}(z_1, t)$, $S^{spec}(z_1, t)$ are the axial component of the stress tensor and the area of cross section in the specimen correspondingly; $\sigma_z^{rod}(z_2, t - t_1)$, $S^{rod}(z_2, t - t_1)$ are similar parameters of the rod; E is the Young's modulus of the dynamometer rod; $\varepsilon_z^{\exp}$ is the longitudinal component of strains of the rod.

In general cases, formula (2) is more complex. For the test specimen with general anisotropy, it is impossible to ensure a uniform distribution of stresses across the cross section. It is known that in anisotropic rods under the action of tensile force, rotation and bulging of the cross section can be observed. In some cases, uniformity can be ensured by manufacturing test specimens in the direction of the principal axes of anisotropy.

In result, taking into account dependencies (2) and (3), to determine the unknown stresses in the specimen, we obtain.

$$\sigma(z_1, t) = \chi \cdot E \cdot \varepsilon_z^{\exp}, \quad \chi = S^{rod} \Big/ S^{spec}.$$

Thus, to obtain a stress-strain curve at a constant strain rate, it is sufficient to measure the longitudinal strains of the rod and determine the cross-sectional areas of the specimen during deformation.

At a constant deformation rate of the end of the specimen, the longitudinal deformation of the specimen changes over time according to the formula $\varepsilon_z{}^{spec} = (d\varepsilon/dt) \cdot t$. Using the law of conservation of mass, the cross-sectional area of a round isotropic test specimen can be determined by the formula $S^{spec} = \pi R^2{}_0 \, [1 - 2(V_0/l)t]$, where R_0 is the initial radius of the specimen.

4 Experimental Stands and Test Specimens

Experimental setups for static and dynamic tests are presented in Fig. 3 and Fig. 4, respectively. A universal testing machine MRM-10C (Fig. 3) was used for static tests. During the static tests, the external loading and strains of the specimen along and across

the load axis were fixed. For high strain rate tests, a pneumatic acceleration device [22] was used (Fig. 4). The longitudinal strains of the dynamometer rod were recorded by the measuring strain gauge complex. The detailed description of this complex is given in [22].

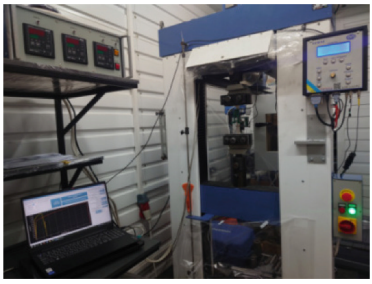

Fig. 3. Tensile testing machine

Fig. 4. Pneumatic gun

The mechanical parameters of specimen made of aluminum alloy and carbon fiber reinforced plastic were studied. Rectangular cross-section specimens were used.

For static tests of aluminum alloy, the length of the working part was 120 mm, the width was 20 mm, and the thickness was 1.4 mm. Dynamic tests were performed on two types of specimens with a working area length of 10 mm, a thickness of 1.4 mm, and a width of 8 mm and 5 mm.

The carbon fiber reinforced plastic is an orthotropic material. This complicates the selection of the length and width of the test specimen for dynamic studies. The specimens for both static and dynamic studies were cut in the same direction from a 2.1 mm thick carbon fiber reinforced plastic plate. The carbon fiber reinforced plastic was made from a simple weave carbon fabric of the T33K200P brand with a density of 200 g/m^2 and a fiber tensile strength of 4480 MPa and compounds CHS-EPODUR 525–0269 and CHS-EPODUR C55. Layers of fabric with a thickness of 0.25 mm were laid out in the 0 and 90° directions alternately, thus ensuring equal strength of the material in the longitudinal and transverse directions. After that, a polymerization mode under pressure was carried out. The density of the resulting carbon fiber sheet is 1.5 g/cm^3. Specimens with a width of 15 mm were used for static tests. For dynamic tests, specimens with different working area sizes, 8–10 mm long and 2.1–5 mm wide, were used. Figure 5 shows some types of carbon fiber composite test specimens (Fig. 5, a) and their fixation during testing (Fig. 5, b). During the experiments, it was found that specimens with greater thickness were destroyed not in the working area, but at the fastening point. Therefore, most of the results presented below were obtained on experimental samples with a thin working area (2.1 mm).

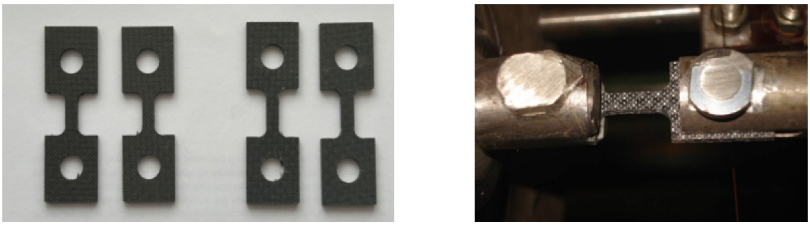

a b

Fig. 5. Dog-bone-shaped composite specimens and their fixation in setup

5 Results and Discussion

Figure 6 shows experimentally obtained tensile curves in static testing for aluminum alloy (Fig. 6, a) and carbon fiber reinforced plastic (Fig. 6, b). Deformations are given in percentages, and force is given in Newtons. It can be seen that aluminum alloy is a very ductile material, while carbon fiber reinforced plastic is a brittle material.

As a result of static tests, it was established that the elastic modulus of aluminum alloy is 69.47 GPa, the yield strength is 324.3 MPa, and the tensile strength is 461.94 MPa. For carbon fiber reinforced plastic, the elastic modulus is 63.12 GPa, and the tensile strength is 717 MPa. Thus, the elastic moduli of carbon fiber and aluminum alloy are almost identical, but the strength of carbon fiber reinforced plastic exceeds that of aluminum alloy by more than 50%, while its weight is 1.8 times less.

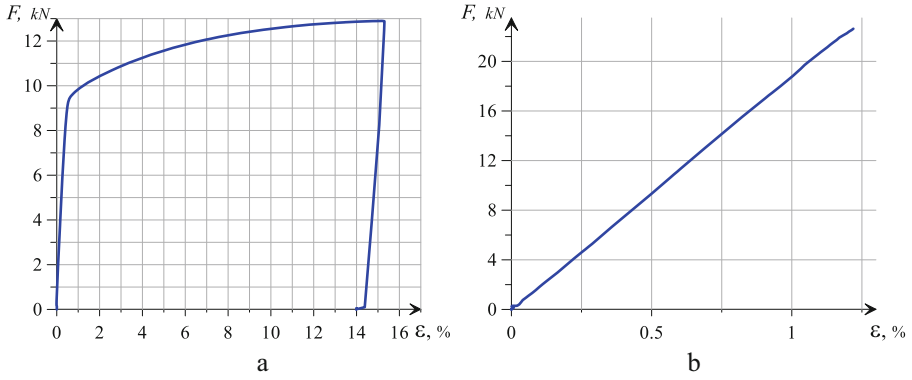

Fig. 6. Dependence of strains on force

Figure 7 shows the characteristic deformations of the dynamometer rod as a function of time for the specimen from aluminum alloy (Fig. 7, a) and the specimen from carbon fiber reinforced plastic (Fig. 7, b). The results are given for two deformation rates. For the aluminum alloy specimens, the strains rates are $0.303 \cdot 10^3$ s^{-1} (solid line) and $1.96 \cdot 10^3$ s^{-1} (dotted line). Results for specimens from carbon fiber reinforced plastic are presented for strain rate $0.403 \cdot 10^3$ s^{-1} (solid line) and $2.135 \cdot 10^3$ s^{-1} (dotted line).

It can be seen that an increase in the deformation rate is accompanied by a decrease in the time required from the start of specimen deformation to its destruction.

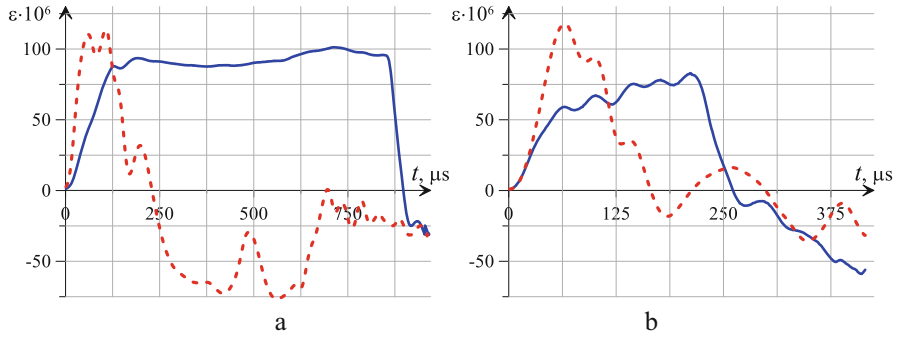

Fig. 7. Strains of the dynamometer rod depending on time

Figure 8 show an enlarged image of the place of destruction of the test specimens. It can be seen that noticeable residual deformations are observed for the aluminum alloy (Fig. 8, a). The destruction of carbon-plastic specimens is a process of tearing apart individual layers, which in some experiments was accompanied by significant delamination and pulling out of individual fibers (Fig. 8, b).

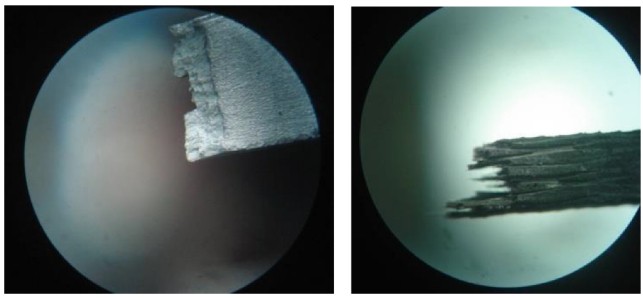

Fig. 8. Failure surface for aluminum alloy (a) and composite (b) specimens

Table 1 shows the obtained stress limits for aluminum alloy without and with consideration of the change in sectional area during deformation. It can be seen that as the speed increases, the ultimate values also rise. For an impact at a speed of 19.6 m/s, the strength of the aluminum alloy is at least 1.48 times higher than the similar values obtained for the static case. In the considered speed range, an increase in the strength of the aluminum alloy is observed.

Table 1. Strength of aluminum alloy under dynamic loading (without/taking into account the change in the cross-section of the specimen)

Deformation rate, s^{-1}	Yield strength, MPa	Ultimate strength, MPa	Strength enhancement factor
$0.303 \cdot 10^3$	528,7/539,3	610/681,8	1,32/1,47
$1{,}960 \cdot 10^3$	596,7/623,0	685,6/763,3	1,48/1,65

The stress limit values for composite are given in Table 2. As the deformation rate of carbon plastic increases, a significant increase in its strength is observed. When the deformation rate is $2.135 \cdot 10^3$ s^{-1}, the strength limit exceeds the corresponding static characteristics by at least 57%.

Table 2. Strength of carbon fiber reinforced plastic under dynamic loading without/taking into account the change in the cross-section of the specimen)

Deformation rate, s^{-1}	Ultimate strength, MPa	Strength enhancement factor
$0.403 \cdot 10^3$	788.82 / 828.69	1.10 / 1.16
$2.135 \cdot 10^3$	1128.52 / 1212.44	1.57 / 1.69

6 Conclusions

The study of material behavior under intense short-term loads is a relevant and complex problem in modern mechanics. Theoretical and experimental studies of the dynamic behavior of new materials under high strain rate are of particular importance.

A theoretical and experimental study of the strength of materials used in aerospace structures has been conducted. The limit values of the strength of aluminum alloy and carbon fiber reinforced plastic at different constant deformation rates have been obtained. The former is a highly ductile material, while the latter is characterized by brittle fracture. It has been shown that as the strain rate increases, the strength of these materials increases significantly relative to the characteristics obtained for static tests. At a strain rate of approximately $2 \cdot 10^3$ s^{-1}, the increase in strength for aluminum alloy is more than 48%, and for carbon fiber reinforced plastic – 57%. For the carbon-plastic sample, this increase is more noticeable compared to the aluminum alloy. However, the destruction of carbon-plastic is more complex and depends on the orientation of the fibers. The destruction of carbon-plastic is accompanied by partial delamination of the layers, cracking of its matrix, and sometimes pulling out of fibers. Research into the dynamic properties of carbon fiber reinforced plastic is accompanied by a greater spread of experimental values than for aluminum alloy specimens, which is explained by the heterogeneous structure of the specimens under consideration. This is further complicated by the use of small (in size) specimens for dynamic testing.

A significant increase in the strength of the studied materials with an increase in strain rate proves that when studying the strength of structures made of these materials,

it is necessary to take into account the dependence of mechanical properties on the strain rate.

The results obtained can be useful in the design of aviation constructions for the accurate determination of the strength of structures under the influence of high-speed loads.

Acknowledgment. The authors greatly acknowledge the National Academy of Sciences of Ukraine for supporting the research projects "IPMACH 2024/1" (State Registration No. 0124U002502) and "Development of methodological support for assessing the strength and service life of modern elements of power equipment, aviation and space rocket equipment with possible imperfection under intensive temperature and force load" (State Registration No. 0125U000513).

References

1. Gontarovskyi, P.P., Smetankina, N.V., Garmash, N.G., Melezhyk, I.I., Protasova, T.V.: Three-dimensional stress-strain state analysis of the bimetallic launch vehicle propellant tank shell. Strength Mater. **55**(5), 916–926 (2023)
2. Smetankina, N., Ustuhov, D., Zhyriakov, D., Ugrimov, S., Garmash, N.: Simulating of bird strike on stabilizer leading edge of transport category aircraft. In: Lytvynov, O., Pavlikov, V., Krytskyi, D. (eds.) ICTM 2024. LNME, vol 1474. Springer, Cham (2025). https://doi.org/10.1007/978-3-031-94852-7_48
3. Armstrong, R.W., Walley, S.M.: High strain rate properties of metals and alloys. Int. Mater. Rev. **53**(3), 105–128 (2008)
4. Lea, L.J., Walley, S.M.: High strain rate metal plasticity. In: Altenbach, H., Öchsner, A. (eds.) Encyclopedia of Continuum Mechanics, pp. 1072–1090. Springer, Berlin, Heidelberg (2020). https://doi.org/10.1007/978-3-662-55771-6_219
5. Zubov, V.I., Stepanov, G.V., Shirokov, A.V.: Effect of the strain rate on the yield strength of steels of different strength. Strength Mater. **35**, 514–520 (2003)
6. Meyers, M.A.: Dynamics behavior of materials. Wiley, New York (1994)
7. Cowper, G., Symonds, P.: Strain hardening and strain-rate effects in the impact loading of cantilever beams. Tech. Rep. Brown University, Division of Applied Mathematics (1957)
8. Johnson, G.R., Cook, W.H.: A constitutive model and data for metals subjected to large strains, high strain rates, and high temperatures. In: Proceedings 7th International Symposium on Ballistics, pp. 541–547 Hague, The Netherlands (1983)
9. Škrlec, A., Panić, B., Nagode, M., Klemenc, J.: Estimating the Cowper-Symonds parameters for high-strength steel using dic combined with integral measures of deviation. Metals **14**, 992 (2024)
10. Hernandez, C., Maranon, A., Ashcroft, I.A., Casas-Rodriguez, J.P.: A computational determination of the Cowper-Symonds parameters from a single Taylor test. Appl. Math. Model. **37**(7), 4698–4708 (2013)
11. Bergström, J. S.: Mechanics of Solid Polymers. Theory and Computational Modeling. Norwich, William Andrew (2015)
12. Siviour, C.R., Jordan, J.L.: High strain rate mechanics of polymers: a review. J. Dyn. Behav. Mater. **2**(1), 15–32 (2016)
13. Gualberto, R., Manjaiah, M., Bongao, H., et al.: High-strain-rate response of alloys fabricated by conventional and additive manufacturing techniques. Prog Addit Manuf **10**, 5787–5811 (2025)

14. Sasso, M. et al.: High-strain-rate behavior of 3D-printed CuCrZr. In: Mates, S., Eliasson, V., Allison, P. (eds.) Dynamic Behavior of Materials, Volume 1. SEM 2022. Conference . Proceedings of the Society for Experimental Mechanics Series, pp. 85–91, Springer, Cham (2023). https://doi.org/10.1007/978-3-031-17453-7_13
15. Wang, L., Yang, L., Dong, X., Jiang, X.: Dynamics of Materials Experiments. Academic Press, Models and Applications (2019)
16. Shin, H., Kim, J.-B.: Evolution of specimen strain rate in split Hopkinson bar test. Proc. Institut. Mech. Eng. Part C: J. Mech. Eng. Sci. **233**(13), pp. 4667–4687 (2019)
17. Acosta-Flores, M., et al.: Experimental method for obtaining the elastic properties of components of a laminated composite. Results in Phys. **12**, 1500–1505 (2019)
18. Miao, Y.-G., et al.: Determination of dynamic elastic modulus of polymeric materials using vertical split Hopkinson pressure bar. Int. J. Mech. Sci. **108–109**, 188–196 (2016)
19. Casem, D., Meredith, C., Magagnosc, D.: A tensile kolsky bar for submillimeter gage lengths. In: Mates, S., Eliasson, V., Allison, P. (eds.) Dynamic Behavior of Materials, Volume 1. SEM 2022. Conference Proceedings of the Society for Experimental Mechanics Series. Springer, Cham (2023)
20. Li, W., Chen, H.: Tensile performance of normal and high-strength structural steels at high strain rates. Thin-Walled Struct. **184**, 110457 (2023)
21. Chen, W., Song, B.: Split Hopkinson (Kolsky) Bar Design, Testing and Applications. Springer New York (2011)
22. Ugrimov, S., Smetankina, N., Kravchenko, O., Yareshchenko, V., Kruszka, L.: A study of the dynamic response of materials and multilayer structures to shock loads. In: Altenbach, H., et al. (eds.) A CAMPE 2021. LNME. Springer, Cham (2023). https://doi.org/10.1007/978-3-031-18487-1_31

Author Index

H. Altenbach et al. (Eds.): CAMPE 2025, LNME, pp. 375–376, 2026.
https://doi.org/10.1007/978-3-032-16381-3